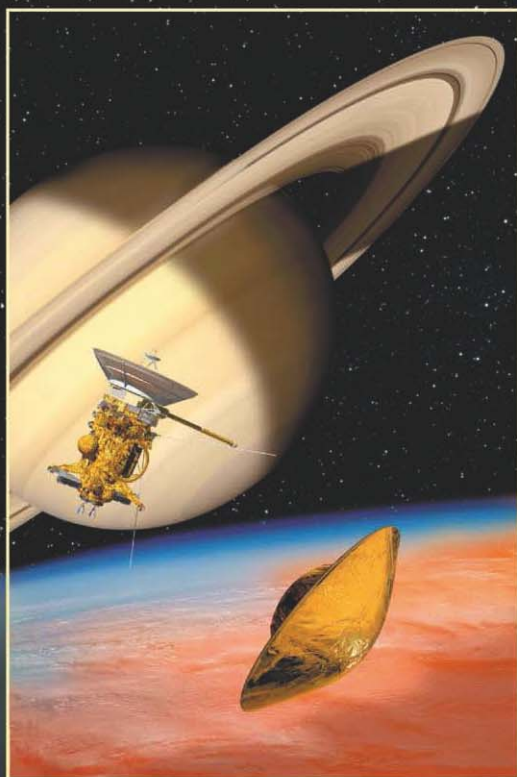


# The Cassini-Huygens Mission

**Orbiter Remote Sensing Investigations**

**Editor: C.T. Russell**



Springer

## THE CASSINI-HUYGENS MISSION

**THE CASSINI-HUYGENS MISSION**

*Orbiter Remote Sensing Investigations*

*Volume 3*

*Edited by*

CHRISTOPHER T. RUSSELL  
*University of California, California, U.S.A.*

Reprinted from *Space Science Reviews*, Volume 115, Nos. 1–4, 2004



**KLUWER ACADEMIC PUBLISHERS**

DORDRECHT / BOSTON / LONDON

A.C.I.P. Catalogue record for this book is available from the Library of Congress

ISBN: 1-4020-3147-5

---

Published by Kluwer Academic Publishers  
P.O. Box 17, 3300 AA Dordrecht, The Netherlands

Sold and distributed in North, Central and South America  
by Kluwer Academic Publishers,  
101 Philip Drive, Norwell, MA 02061, U.S.A.

In all other countries, sold and distributed  
by Kluwer Academic Publishers,  
P.O. Box 322, 3300 AH Dordrecht, The Netherlands

*Printed on acid-free paper*

*Cover illustration:* Courtesy of ESA

All Rights Reserved

© 2004 Kluwer Academic Publishers

No part of the material protected by this copyright notice may be reproduced or  
utilised in any form or by any means, electronic or mechanical,  
including photocopying, recording or by any information storage and  
retrieval system, without written permission from the copyright owner

Printed in the Netherlands



## TABLE OF CONTENTS

Foreword	vii
A.J. KLIORE, J.D. ANDERSON, J.W. ARMSTRONG, S.W. ASMAR, C.L. HAMILTON, N.J. RAPPAPORT, H.D. WAHLQUIST, R. AMBROSINI, F.M. FLASAR, R.G. FRENCH, L. IESS, E.A. MAROUF AND A.F. NAGY / Cassini Radio Science	1–70
C. ELACHI, M.D. ALLISON, L. BORGARELLI, P. ENCRENAZ, E. IM, M.A. JANSSEN, W.T.K. JOHNSON, R.L. KIRK, R.D. LORENZ, J.I. LUNINE, D.O. MUHLEMAN, S.J. OSTRO, G. PICARDI, F. POSA, C.G. RAPLEY, L.E. ROTH, R. SEU, L.A. SODERBLOM, S. VETRELLA, S.D. WALL, C.A. WOOD and H.A. ZEBKER / Radar: The Cassini Titan Radar Mapper	71–110
R.H. BROWN, K.H. BAINES, G. BELLUCCI, J.-P. BIBRING, B.J. BURATTI, F. CAPACCIONI, P. CERRONI, R.N. CLARK, A. CORADINI, D.P. CRUIKSHANK, P. DROSSART, V. FORMISANO, R. JAUMANN, Y. LANGEVIN, D.L. MATSON, T.B. MCCORD, V. MENNELLA, E. MILLER, R.M. NELSON, P.D. NICHOLSON, B. SICARDY and C. SOTIN / The Cassini Visual and Infrared Mapping Spectrometer (VIMS) Investigation	111–168
F.M. FLASAR, V.G. KUNDE, M.M. ABBAS, R.K. ACHTERBERG, P. ADE, A. BARUCCI, B. BÉZARD, G.L. BJORAKER, J.C. BRASUNAS, S. CALCUTT, R. CARLSON, C.J. CÉSARSKY, B.J. CONRATH, A. CORADINI, R. COURTIN, A. COUSTENIS, S. EDBERG, S. EDGINGTON, C. FERRARI, T. FOUCHET, D. GAUTIER, P.J. GIERASCH, K. GROSSMAN, P. IRWIN, D.E. JENNINGS, E. LELLOUCH, A.A. MAMOUTKINE, A. MARTEN, J.P. MEYER, C.A. NIXON, G.S. ORTON, T.C. OWEN, J.C. PEARL, R. PRANGÉ, F. RAULIN, P.L. READ, P.N. ROMANI, R.E. SAMUELSON, M.E. SEGURA, M.R. SHOWALTER, A.A. SIMON-MILLER, M.D. SMITH, J.R. SPENCER, L.J. SPILKER and F.W. TAYLOR / Exploring the Saturn System in the Thermal Infrared: The Composite Infrared Spectrometer	169–297
L.W. ESPOSITO, C.A. BARTH, J.E. COLWELL, G.M. LAWRENCE, W.E. McCLINTOCK, A.I.F. STEWART, H.U. KELLER, A. KORTH, H. LAUCHE, M.C. FESTOU, A.L. LANE, C.J. HANSEN, J.N. MAKI, R.A. WEST, H. JAHN, R. REULKE, K.	

WARLICH, D.E. SHEMANSKY and Y.L. YUNG / The Cassini Ultraviolet Imaging Spectrograph Investigation	299–361
C.C. PORCO, R.A. WEST, S. SQUYRES, A. McEWEN, P. THOMAS, C.D. MURRAY, A. DELGENIO, A.P. INGERSOLL, T.V. JOHNSON, G. NEUKUM, J. VEVERKA, L. DONES, A. BRAHIC, J.A. BURNS, V. HAEMMERLE, B. KNOWLES, D. DAWSON, T. ROATSCH, K. BEURLE and W. OWEN / Cassini Imaging Science: Instrument Characteristics and Anticipated Scientific Investigations at Saturn	363–497

## Foreword

At this writing the Cassini spacecraft has fired its engine and successfully inserted itself and its precious cargo of scientific instruments into orbit, the first step of its exploration of the Saturnian system. The suspense is not over, however. While exciting images of the rings have been captured, an exotic composition of Phoebe sensed by the mapping spectrometer and unexpected panoply of magnetic waves and plasma dynamics encountered on the incoming trajectory and initial orbit, the Huygens probe is still on board and the first close flyby of Titan has not taken place. Not until Christmas Day will the probe be released. Navigators are still checking their calculations, worrying about known unknowns like the mass of Saturn's moons that could cause ever so small a deviation from the planned trajectory of the probe. The orbiter investigators are also anxious but they get their taste of Titan earlier, on October 26. How well will they detect the surface? How thick is the atmosphere? Does Titan have a magnetic field? Is there lightning in the atmosphere of Titan? While terrestrial and Hubble Space Telescope pictures have improved greatly over the years, they cannot match the resolution obtainable from orbit about the planet, and much of the data is simply unobtainable without direct in situ sensing.

Volume 1 of this three volume set described the Cassini/Huygens mission, its scientific objectives and the Huygens probe that will soon enter the Titan atmosphere. Volume 2 described the in situ investigations on the orbiter. In this, the third and final volume of the compendium, we describe the remote sensing investigations: radio science, radar, visible and infrared spectroscopy, thermal infrared studies, ultraviolet spectroscopy and visible imagery.

This volume completes our description of this most ambitious mission. For the editor, this has been a very ambitious task, extending over an eight-year period. We trust that the reader will find these pages beneficial, gaining insight into the how and why of the Cassini investigations and allowing the broader scientific community to share in the advance in our understanding that the mission brings. As with Volumes 1 and 2, this volume is due to the efforts of many individuals especially the referees and authors who have helped produce a very readable and complete descriptions of the investigations. We especially wish to thank Anne McGlynn who assisted in the initial stage of the assembly of this collection and Marjorie Sowmendran who completed the effort upon Anne's retirement. Lastly, none of this would have been possible without the years of labor by the women and men of the Cassini/Huygens project who built the spacecraft, tested it, programmed the software, and navigated and operated the spacecraft so flawlessly.

C. T. Russell  
University of California  
Los Angeles, CA  
September 2004



## CASSINI RADIO SCIENCE

A. J. KLIORÉ<sup>1,\*</sup>, J. D. ANDERSON<sup>1</sup>, J. W. ARMSTRONG<sup>1</sup>, S. W. ASMAR<sup>1</sup>,  
C. L. HAMILTON<sup>1</sup>, N. J. RAPPAPORT<sup>1</sup>, H. D. WAHLQUIST<sup>1</sup>, R. AMBROSINI<sup>2</sup>,  
F. M. FLASAR<sup>3</sup>, R. G. FRENCH<sup>4</sup>, L. IESS<sup>5</sup>, E. A. MAROUF<sup>6</sup> and A. F. NAGY<sup>7</sup>

<sup>1</sup>*Jet Propulsion Laboratory, California Institute of Technology, 4800 Oak Grove Drive,  
Pasadena, CA 91109, USA*

<sup>2</sup>*Istituto di Radioastronomia CNR, Via Gobetti 101, I-40129, Bologna, Italy*

<sup>3</sup>*NASA-Goddard Space Flight Center, Greenbelt, MD 20771, USA*

<sup>4</sup>*Wellesley College, Wellesley, MA 02481, USA*

<sup>5</sup>*Università di Roma 'La Sapienza', Via Eudossiana 18, I-00184 Roma, Italy*

<sup>6</sup>*San Jose State University, One Washington Square, San Jose, CA 95192, USA*

<sup>7</sup>*University of Michigan, 2455 Hayward Avenue, Ann Arbor, MI 48109, USA*

(\*author for correspondence, e-mail: akliore@jpl.nasa.gov)

(Received 29 December 1999; Accepted in final form 4 April 2002)

**Abstract.** Cassini radio science investigations will be conducted both during the cruise (gravitational wave and conjunction experiments) and the Saturnian tour of the mission (atmospheric and ionospheric occultations, ring occultations, determinations of masses and gravity fields). New technologies in the construction of the instrument, which consists of a portion on-board the spacecraft and another portion on the ground, including the use of the Ka-band signal in addition to that of the S- and X-bands, open opportunities for important discoveries in each of the above scientific areas, due to increased accuracy, resolution, sensitivity, and dynamic range.

**Keywords:** atmospheres, Cassini, gravitational fields, gravitational waves, general relativity, ionospheres, occultations, planetary rings, radio science, Saturn, Titan

### 1. Introduction

This paper, produced by the Cassini Radio Science Team during the early cruise of the Cassini spacecraft en route for the Saturnian system, records major reference information concerning the investigations to be conducted, and the instrument that will be operated to conduct these investigations. Section 2 describes the radio science investigations. Section 3 is devoted to the radio science instrument. Section 4 contains a brief conclusion.

### 2. Radio Science Investigations

For each of the radio science investigations:

- Gravitational wave experiments,
- Conjunction experiments (a new test of general relativity, study of the solar corona),



*Space Science Reviews* **115**: 1–70, 2004.

© 2004 Kluwer Academic Publishers. Printed in the Netherlands.

- Gravitational field measurements and celestial mechanics experiments (pertaining to Saturn, Titan, and the Icy Satellites),
- Ring occultation experiments,
- Atmospheric and ionospheric occultation experiments (pertaining to Saturn, Titan, and the icy satellites),

we describe the scientific objectives with respect to the present state of knowledge, the techniques, and the major requirements.

## 2.1. GRAVITATIONAL WAVE EXPERIMENTS

### 2.1.1. *Scientific Objectives*

This section of the paper outlines the method and experimental setup of the Cassini Gravitational Wave Experiment (GWE).

The extensive and stringent tests of gravitation theories carried out in the solar system, together with observations of binary pulsars, have dispelled most doubts about Einstein’s theory of general relativity and the existence of the gravitational waves it predicts. The direct detection of gravitational waves constitutes an outstanding challenge for experimental physics, however, and – when successful – will open up a new window for observational astronomy (Thorne, 1987). Since gravitational waves are virtually unaffected by intervening matter, their observation will probe the dynamics of cataclysmic events in the deep interiors of, for example, supernovae and active galactic nuclei, regions which are inaccessible to electromagnetic observations.

There are three main frequency bands of astronomical interest:

- The “high” frequency band, around 1 kHz, where the sources include supernovae and stellar coalescences;
- The “low” frequency band, around 1 mHz, where the sources include compact binary systems such as a binary pulsar, the formation of super-massive black holes, and the coalescence of supermassive binary black holes;
- The “very low” frequency band,  $<1 \mu\text{Hz}$ , where one might expect a stochastic background of waves from the superposition of stellar binaries, distant past collapse events, and possibly the red-shifted remnant of a primordial cosmic background created by density fluctuations in the Big Bang. (See Armstrong *et al.*, 2003 for results from Cassini’s GWE).

The variety of possible sources in the low-frequency band accessible to spacecraft Doppler tracking necessitates using a variety of signal detection techniques. This is especially true because it is a search conducted largely “in the dark”; while astronomical observations and theory almost guarantee the existence of gravitational waves, it is still beyond our capability to predict the shape, or even the likely strength, of waves from these sources. So the best one can do is to do a systematic search for a variety of plausible waveforms (wide-band pulses, periodic and quasi-periodic waveforms, stochastic backgrounds).

For detection purposes, an ideal source would be the binary pulsar 1913 + 16. Binary pulsars are objects for which clear evidence of gravitational radiation already exists and everything one needs to know about the system is available to predict precisely the observed signal (Wahlquist, 1987). The wave frequency of the strongest harmonic of the periodic signal from 1913 + 16 falls exactly where the Doppler method is most sensitive. Unfortunately, the predicted amplitude of the signal from 1913 + 16 is too weak to detect at Cassini's sensitivity by many orders of magnitude.

In addition to being of great intrinsic astrophysical interest, supermassive binary black hole systems may be the most promising sources for detection with Cassini. Clean binary systems, not too close to coalescence, are sufficiently simple that detailed comparison of theory and observation is possible. Of course, since the parameters of the system are not known in advance, it is necessary to employ a large ensemble of signal templates to search for waves from one of these systems. Near coalescence, the amplitude and frequency of the wave increase with time; special methods to extract these "chirp" signals from both random and systematic noises have been developed (Tinto and Armstrong, 1991; Anderson *et al.*, 1993; Bertotti *et al.*, 1994; Bertotti, 1997; Iess and Armstrong, 1997; Bertotti *et al.*, 1999). Very close to coalescence, physical processes become more complicated and templates may at best be a rough approximation to the emitted waveforms.

The existence of binary sources has become increasingly plausible with the recent observations of supermassive objects in galactic nuclei, together with evidence for the frequent merging of galaxies in the early universe when their spatial density was much higher than at present. Cassini should be able to detect signals of this type, if they are present in the Doppler frequency band with the expected strength, well beyond the Virgo cluster ( $\approx 17$  Mpc), thus including thousands of candidate galaxies.

The gravitational wave search on the Cassini mission has been the most sensitive Doppler experiment ever performed. The experiment has been repeated three times during the cruise period from Jupiter to Saturn; i.e., when the spacecraft was the antisolar direction from earth (November 2001–January 2002; December 2002–January 2003; December 2003–January 2004). At each opposition, Cassini has been Doppler-tracked as continuously as possible for 40 days. Around-the-clock tracking required using all three deep space network (DSN) complexes (Goldstone, Madrid, Canberra), and may be supported additionally by non-DSN radio antennas in Italy. The highest sensitivity was achieved with DSS-25, a beam waveguide antenna located at the Goldstone complex, which has been carefully designed for the utmost in frequency stability and which has Ka-band uplink, precision frequency standards, and advanced tropospheric correction equipment.

Cassini at opposition became one of the largest gravitational wave antenna's ever used ( $\approx 8$  AU in length), attaining by far the highest sensitivity to date for gravitational waves at the lower end of the low-frequency band.

### 2.1.2. Techniques

Detection methods for gravitational radiation depend on the time scale of the radiation. At high frequencies the main techniques are resonant bars and laser interferometers. These techniques achieve excellent sensitivity in the Fourier frequency band where they operate. For frequencies lower than about 10 Hz, however, it becomes prohibitively difficult to isolate these detectors from seismic noise, other acoustic noise in the environment, and from fluctuating gravity gradients. For observations of sources radiating in the low frequency band (approximately 0.0001 Hz, or lower, to 0.01 Hz), the detector must be spaceborne. Although at the moment the low-frequency band is explored by means of Doppler tracking, the next generation of space-based detectors will soon become a reality with the launch of the USA mission, jointly funded by NASA and ESA (Bender *et al.*, 1998). For very-low frequencies (below about  $10^{-6}$  Hz) pulsar timing can be used to search for stochastic gravitational waves.

In the spacecraft technique, the earth and a distant spacecraft act as separated test masses. The Doppler tracking system measures the relative dimensionless velocity of the earth with respect to the spacecraft

$$2\frac{\Delta v}{c} = \frac{\Delta v}{v_0} = y \quad (1)$$

as a function of time;  $\Delta v$  is the perturbation of the Doppler frequency from  $\Delta v_0$ , the nominal radio frequency. A gravitational wave of amplitude  $h$  incident on the system causes small perturbations in the tracking record. These perturbations are of order  $h$  in  $y$  and are replicated three times in the Doppler data (Estabrook and Wahlquist, 1975). That is, the gravitational wave signal in the observed Doppler time series is the convolution of the waveform

$$s(t) = (1 - \mu^2)^{-1} \mathbf{n} \cdot [h_+(t)\mathbf{e}_+ + h_\times(t)\mathbf{e}_\times] \cdot \mathbf{n} \quad (2)$$

with the three-pulse response function

$$r(t) = \frac{\mu - 1}{2} \delta(t) - \mu \delta\left(t - (1 + \mu)\frac{L}{c}\right) + \frac{1 + \mu}{2} \delta\left(t - 2\frac{L}{c}\right) \quad (3)$$

Here  $\mu$  is the cosine of the angle between the earth–spacecraft vector and the gravity wavevector,  $L$  is the earth–spacecraft distance,  $\mathbf{n}$  is the unit vector from the earth to the spacecraft,  $h_+(t)$  and  $h_\times(t)$  are the gravity waveforms for each polarization and  $\mathbf{e}_+$  and  $\mathbf{e}_\times$  are transverse, traceless polarization tensors (Estabrook and Wahlquist, 1975; Wahlquist *et al.*, 1977; Wahlquist, 1987). The sum of the three pulses is zero; hence burst waves having a duration longer than about  $L/c$  overlap in the tracking record and the net response cancels to first order. The tracking system thus has a passband where it has maximum sensitivity: below about  $c/L$ , by pulse cancellation, the response is proportional to  $f$ ; thermal

noise in the radio system and the short-term stability of the frequency standard to which the Doppler system is referenced limits the high-frequency response to  $f \approx 0.1$  Hz.

### 2.1.3. Major Requirements

The anticipated signal amplitudes depend on the source generating the wave and the earth–source distance, but are in any case expected to be small. Since the resulting perturbations in the Doppler record are also expected to be small, careful attention to noise and systematics is required.

Non-signal fluctuations in the Doppler time series are caused by charged particle scintillation, tropospheric scintillation, antenna mechanical noise, clock noise, spacecraft unmodeled motion, ground electronic noise, thermal noise in the radio link, spacecraft electronics noise, and systematic errors. The extent to which these noises affect the ultimate sensitivity, depends on the gravity waveform because the noises enter the observable with different transfer functions (e.g., Wahlquist *et al.*, 1977; Estabrook, 1978; Armstrong, 1989; Bertotti *et al.*, 1999). However, it is clearly important to minimize the absolute level of the noises. (A more complete discussion of the error budget for precision Doppler tracking, with particular attention to the Cassini gravitational wave experiment, is given in Armstrong (1998), Tinto and Armstrong (1998) and Asmar *et al.* (2004)).

Obviously any unmodeled motion of the spacecraft itself enters directly in the Doppler record. Thus the Cassini gravitational wave experiment requires that activity on the spacecraft causing unmodeled motions be minimized during gravitational wave observations.

Propagation noise (“scintillation”) arises from irregularities in the refractive index along the radio path. These fluctuations randomly advance and retard the phase of the wave and thus cause frequency fluctuations. Charged particle scintillation, which is dominated by solar wind scintillation, can be minimized by observing at large sun-earth-spacecraft angles and by observing at high-radio frequency. The Cassini gravitational wave experiment thus requires that observations be made in the antisolar direction. The Cassini gravitational wave experiment has been the first scientific user of Ka-band ( $\approx 32$  GHz) up and downlinks. This has dramatically reduced the contribution of charged particle scintillation relative to previous experiment. Scintillation in the neutral atmosphere is an important noise source. Cassini gravitational wave experiments requires water-vapor radiometers colocated with DSS-25 (the DSN Ka-band uplink station) to estimate and remove the tropospheric scintillation to acceptable levels.

Clock noise is fluctuation in the frequency standard that drives the Doppler system. This noise is fundamental and must be minimized for a successful experiment. Cassini-era frequency standards have been engineered for excellent stability in the Fourier band of interest to the gravitational wave experiment and are expected to enter the observable at a noise level less than or comparable to the other principal noise sources.



Antenna mechanical noise is physical motion of the antenna and feed system as the ground antenna moves to track the spacecraft, deforms under gravity, distorts due to wind, etc. This noise source has been negligible in previous gravitational wave experiments, but has been detected at the excellent sensitivity of the Cassini Ka-band system.

## 2.2. CONJUNCTION EXPERIMENTS

Radio science experiments near solar conjunctions have been exploited for tests of general relativity and probing of the solar corona. The unique radio system of Cassini allows singling out plasma effects on carrier phase and is therefore especially suited for Doppler measurements near the sun. The 2002 Cassini solar conjunction experiment has yielded the most accurate test of general relativity so far.

### 2.2.1. A New Test of General Relativity

*2.2.1.1. Scientific Objectives.* The gravitational deflection of light rays, a crucial test of the theory of general relativity, has been performed so far with two methods:

- by measuring the differential deflection of the apparent position of stars or radio sources near the Sun;
- by measuring the change in the light transit time from a spacecraft near solar conjunction.

Within the parametrized post-Newtonian (PPN) (Will, 1993) approximation in its minimal form, in which the metric depends on two dimensionless parameters  $\gamma$  and  $\beta$ , these effects are controlled by  $\gamma$ . Before the Cassini experiment this parameter was constrained to be within  $10^{-3}$  of unity, the general relativistic value. Several experiments have been done in the past, all more or less with similar results, and it was apparent that new ideas and instrumentation were needed to obtain a major increase in accuracy. It is remarkable that the test performed more than 20 years ago by measuring the two-way travel time of radio signals from the earth to the Viking landers (Reasenberg *et al.*, 1979; Borderies *et al.*, 1980) has been marginally improved only very recently (Eubanks *et al.*, 1997), using more accurate VLBI (very-long-baseline interferometry) techniques for precision deflection measurements.

In the past, these experiments have played an essential role in the rejection of several alternative theories of gravity and in strengthening our confidence in the theory of general relativity. The main candidate for an alternative theory within this constraint is a scalar field coupled to the metric, which is the most obvious way to produce an inflationary cosmology; as the Universe starts its decelerated expansion phase, this field becomes progressively weaker, but its remnant, still present today, determines a small correction to the parameters  $\gamma$  and  $\beta$ . In the absence of a

reliable theory of inflation, it is difficult to assess the order of magnitude of these corrections; however, values from  $10^{-7}$  to  $10^{-5}$  have been considered (Damour and Nordtvedt, 1993). It is therefore most important to devise new methods to improve the measurement of  $\gamma$ .

The new technological developments required by the Cassini mission, in particular, the use of Ka-band radio links have allowed us to test general relativity to a substantially greater accuracy. The outstanding radio system of the spacecraft and ground station allows a nearly complete calibration of the plasma noise and an unprecedented stability of the interplanetary link. A crude estimation of the expected accuracies (Iess *et al.*, 1999) indicated that  $\gamma$  could be measured to levels of about  $10^{-5}$ , almost two orders of magnitude better than the previous experimental accuracy. The analysis of the data acquired between June 6 and July 5, 2002 fully confirmed the expectations: the experimental value for  $\gamma$  was found to be  $1 + (2.1 \pm 2.3) 10^{(-5)}$  (Bertotti *et al.*, 2003).

**2.2.1.2. Techniques.** The measurement of  $\gamma$  with Cassini is based upon a third, new observable: the frequency shift induced on a radio wave when the spacecraft is near solar conjunction (Bertotti and Giampieri, 1992; Iess *et al.*, 1999). Solar gravity has an effect on the frequencies of photons, since the relative frequency shift  $y = \Delta\nu/\nu$  due to the solar metric is just a time derivative of the delay of radio signals measured in space experiments:

$$y = \frac{d}{dt} \Delta\tau, \quad (4)$$

where

$$\Delta\tau = (1 + \gamma)M_{\odot} \ln \frac{r_1 + r_2 + r_{12}}{r_1 + r_2 - r_{12}}, \quad (5)$$

expressed in terms of the geometrical units in which  $G = c = 1$  and  $M_{\odot} = 5 \mu\text{s}$ , has the well-known dependence on the sun–earth, sun–spacecraft and earth–spacecraft distances  $r_1$ ,  $r_2$  and  $r_{12}$ . For a two-way link, as in the case of Cassini,  $y$  is actually the sum of two contributions, respectively from the uplink and the downlink. Near conjunctions, Equation (5) can be approximated using the impact parameter  $b$  of the beam:

$$\Delta\tau \approx 2(1 + \gamma)M_{\odot} \ln \frac{4r_1 r_2}{b^2}. \quad (6)$$

The corresponding value of  $y$  is therefore

$$y \approx 4(1 + \gamma) \frac{M_{\odot}}{b} \dot{b}. \quad (7)$$

In the case of Cassini, with a nearly grazing conjunction,  $y \approx 10^{-9}$ , five orders of magnitude larger than the expected stability of the radio link at time scales of  $10^4$  s ( $\sigma_y = 3 \times 10^{-15}$ ). This rough comparison indicated that the Cassini experiment could lead to a test of general relativity with unprecedented accuracy.

Another instructive way of looking at this experiment is to consider the effect on the frequencies as a consequence of the solar gravitational deflection. For a beam with impact parameter  $b$ , the deflection angle

$$\delta = 2(1 + \gamma) \frac{M_{\odot}}{b} \quad (8)$$

changes in time, therefore producing a variation in the direction of arrival  $\mathbf{n}$  of photons. Since the observable quantity is essentially the radial velocity  $\mathbf{v} \cdot \mathbf{n}$  of the spacecraft with respect to the earth, a deflection by an angle  $\delta$  changes  $\mathbf{n}$  and therefore produces an additional velocity along the line of sight of order  $v\delta$ . Again, for a grazing incidence, this amounts to approximately  $10^{-9}$ .

The relativistic Doppler signal evolves over time scales of order  $b/(\text{orbital velocity}) \approx 10^5$  s. Thus, a Doppler experiment requires short observation periods to minimize the effects of non-gravitational accelerations. On the other hand, large Doppler signals are obtained only at small impact parameters, when the radio beam, well inside the solar corona, undergoes strong frequency fluctuations. Until the recent implementation of multi-frequency radio links at X- and Ka-bands, which allows a full plasma calibration, Doppler experiments could not compete with the more familiar tests based on range measurements.

The main hindrance to precise measurements near conjunctions is indeed the solar corona, whose large and changing electron density induces severe propagation effects. In the past, spacecraft tracking near solar conjunction using S- and X-band radio links has provided important information about the coronal plasma. Since the coronal contribution to the fractional frequency change  $y$  is inversely proportional to the square of the carrier frequency  $\nu$ , the noise due to the corona is particularly large at the lower frequencies, such as S-band. With Cassini, besides the standard communication link in X-band (7.1–8.4 GHz), an additional link in Ka-band (32–34 GHz) was available, with two neighbouring downlink carriers driven by the Ka-band uplink and the X-band uplink, respectively. This configuration, with multi-frequency transmission from the ground and the spacecraft, will allow for the first time a complete plasma calibration both in the uplink and the downlink (Bertotti *et al.*, 1993). Moreover, the use of higher frequency carriers makes the link nearly immune to frequency jitter and cycle slips. The experimental results showed an excellent phase stability (about  $2 \times 10^{-14}$  or smaller), a value generally obtained close to solar opposition (Tortora *et al.*, 2003; Tortora *et al.*, 2004).

**2.2.1.3. Major Requirements.** The experiment was planned during two useful conjunctions in the cruise phase, in June 2002 and June 2003, at times when there was very little activity on the spacecraft. Unfortunately, due to a malfunction of the key onboard instrument (the Ka/Ka frequency translator, see sect. 3.2), only the data collected in 2002 have been used. The very small inclination of the Cassini orbit makes the geometry of the experiment particularly favorable, with a minimum impact parameters of  $1.6 R_{\odot}$ . The main tracking station was DSS-25, the only DSN

station capable of supporting a full multi-frequency link (with uplink both at X- and Ka-band).

Measuring  $\gamma$  to levels of  $10^{-5}$  requires a very stable radio link, with an accurate calibration for the effects of the media (solar corona and troposphere). The instrumental specifications set by the gravitational wave experiments are adequate, but now the complete multifrequency link becomes essential.

While the two experiments share a good degree of commonality (after all, they are based upon the same observable), the different time scales of the signal introduce new and subtle problems in the analysis of conjunction data. As the relativistic effect evolves overtime scales of, say,  $10^5$  s (i.e., longer than the period of gravitational waves considered so far) the orbital contribution to the Doppler shift needs to be determined with great accuracy. Polar motion, earth solid tides and errors in the station locations give important effects to be accounted for. Other contributions come from non-gravitational accelerations, which are a potentially large source of errors in an experiment based on a free flying spacecraft. Fortunately, the large distance from the sun and the nearly constant solar aspect angle make these errors quite small or easily accounted for in the data analysis.

### 2.2.2. *Study of the Solar Corona*

Tracking interplanetary spacecraft near solar conjunction has provided a wealth of information on the structure of the solar corona and the origin of the solar wind. This powerful tool, in combination with SOHO's ultraviolet coronagraph spectrometer, has been used recently to locate the sources of the slow wind, which stems from the stalks, narrow structures of the sun's streamer belt (Woo and Habbal, 1997). The same measurements seem to indicate also that the conventional understanding of the nature of the fast wind needs to be modified. It is likely that in the next years new measurements and observations will be required to confirm the new, emerging views on the solar wind.

The outstanding radio system of Cassini provides a unique opportunity for solar physics as well, without any additional allocation of resources from the spacecraft and the DSN. The effects of the solar plasma on Doppler signals are known with great precision separately for the uplink and the down-link paths, thanks to the multifrequency radio link (Bertotti and Giampieri, 1998). Moreover, the use of higher frequency carriers will strongly reduce the difficulties and the instrumental problems encountered when tracking near the sun.

## 2.3. GRAVITATIONAL FIELD MEASUREMENTS AND CELESTIAL MECHANICS EXPERIMENTS

### 2.3.1. *Scientific Objectives*

**2.3.1.1. Introduction.** Over the past 35 years, radio Doppler data generated with interplanetary spacecraft have yielded masses and densities for all the planets, except Pluto, as well as masses for all the larger satellites, and higher-order

gravitational moments are available for the planets and for Jupiter’s Galilean satellites (Anderson *et al.*, 1996a,b, 1997a,b). With the addition of Doppler data from the Cassini mission we expect to improve the description of Saturn’s gravitational field, as well as to map Titan’s second-order field in detail.

If a planet or satellite were perfectly spherical, its total mass would be sufficient to describe its external gravitational field. However all natural bodies deviate from spheres at some level, so what is needed is a general potential function that satisfies Laplace’s equation for an arbitrary distribution of mass. With the origin at the center of mass and coordinates  $r$  for radius,  $\phi$  for latitude, and  $\lambda$  for longitude, the standard form for the gravitational potential is written as follows in terms of spherical harmonics and the Legendre functions  $P_{nm}$

$$V(r, \phi, \lambda) = \frac{GM}{r} \left[ 1 + \sum_{n=2}^{\infty} \sum_{m=0}^n \left( \frac{R}{r} \right)^n (C_{nm} \cos m\lambda + S_{nm} \sin m\lambda) P_{nm}(\sin \phi) \right], \quad (9)$$

where  $M$  is the planet or satellite’s mass, the external field is referred to a reference radius  $R$  (usually the planet’s mean equatorial radius, but sometimes the semi-major axis of a reference ellipsoid);  $G$  is the gravitational constant. The gravity coefficients  $C_{nm}$  and  $S_{nm}$  are determined from the Doppler data by iterative linear weighted least squares. A particular coefficient with indices  $nm$  is referred to as a gravity harmonic of order  $m$  and degree  $n$ . Coefficients with  $m = 0$  are called zonal harmonics, coefficients with  $n = m$  are called sectorial harmonics, and the rest are called tesseral harmonics. Zonal harmonics divide the surface of the sphere into  $m + 1$  zones of latitude, sectorial harmonics into sectors of longitude or “orange slices,” and tesseral harmonics into a checker-board pattern.

The outer planets and their larger satellites are effectively in hydrostatic equilibrium. As a result, measured gravity harmonics provide important boundary conditions on their interior structure. If the giant Jovian planets and their satellites were in hydrostatic equilibrium and did not rotate, and if they were not subjected to external forces, their gravitational fields would provide no information on internal structure. However, because the giant planets rotate rapidly, their shapes and gravity fields yield information on the distribution of density with depth. The Galilean satellites and Titan are influenced by comparable tidal forces from their parent planet, and so both rotation and tides must be accounted for. For the giant planets, the two parameters for shape and rotation are the flattening  $f$  and the rotation parameter  $q$  defined by,

$$f = \frac{a - b}{a}, \quad (10)$$

$$q = \frac{\omega^2 a^3}{GM}, \quad (11)$$

where  $a$  is the planet's equatorial radius,  $b$  its polar radius,  $\omega$  its rotational angular velocity, and  $G$  is the gravitational constant. Even without gravity measurements, the ratio  $f/q$  would yield some limited information on interior structure because it has a minimum value of  $1/2$  for a body with an extreme mass concentration at its center, and a maximum value of  $5/4$  for a homogeneous body. For a spinning planet in hydrostatic equilibrium, we assume that only the even zonal gravity harmonics  $J_n = -C_{n0}$  ( $n = 2, 4, 6, \dots$ ) are non-zero. The importance of the gravity coefficients  $J_n$  is that they are related to the internal density distribution by the following volume integral over the planet's interior

$$J_n = -\frac{1}{MR^n} \int_v \rho(r, \phi, \lambda) r^n P_n(\sin \phi) dv \quad (n = 2, 4, 6 \dots). \quad (12)$$

The  $J_n$  coefficients represent boundary conditions that must be satisfied for any viable interior model. The deep interior stimulates the second zonal harmonic  $J_2$ , while the outer layer is sounded by higher harmonics to a depth of about 3100 km for Jupiter and 3600 km for Saturn. For example, in a simple polytrope of index one, a reasonably good first-order approximation for Jupiter and Saturn's outer layers, the pressure  $p$  and density  $\rho$  are related by,

$$p = K\rho^2, \quad (13)$$

and the constant  $K$  is determined from the measured gravity coefficients  $J_2$  and  $J_4$  by the expression,

$$K = -\frac{2\pi G b^2}{35J_4} \left( J_2 + \frac{q}{3} \right)^2. \quad (14)$$

For nonpolytropic models, a general density distribution with depth can be derived from measured gravity coefficients  $J_2$  and  $J_4$ . The coefficient  $J_6$  may also be useful, although differential rotation and deep atmospheric winds may complicate its interpretation. With a given density distribution, the pressure can be computed under the assumption of hydrostatic equilibrium, and the temperature follows from the equation of state for the assumed material in the outer layer.

2.3.1.2. *Objectives for Saturn.* The scientific objectives at Saturn are to:

- determine the mass of Saturn and its zonal gravitational harmonics, at least through degree six;
- constrain models of Saturn’s interior.

The product of the gravitational constant by Saturn’s mass,  $GM_S$ , has been determined to considerable accuracy from Pioneer and Voyager flybys (Campbell and Anderson, 1989). After dividing by  $G = 6.67259 \times 10^{-20} \text{ km}^3 \text{ s}^{-2} \text{ kg}^{-1}$  (Cohen and Taylor, 1987), we obtain a total mass  $M_S = (5.68464 \pm 0.0003) \times 10^{26} \text{ kg}$ . A fundamental constraint on interior models is that this total mass must be contained within an equipotential surface defined by Saturn’s mean equatorial radius,  $R_S = 60,268 \text{ km}$  (Lindal *et al.*, 1985). The shape of the equipotential surface is defined by the zonal harmonics, which also serve as additional boundary conditions on interior models. The current unnormalized values, in units of  $10^{-6}$ , from Pioneer and Voyager Doppler data are (Campbell and Anderson, 1989)

$$J_2 = 16332 \pm 10, \quad (15)$$

$$J_4 = -919 \pm 40, \quad (16)$$

$$J_6 = 104 \pm 50. \quad (17)$$

Current interior models based on these values are nonunique (Guillot *et al.*, 1994), although some fail to satisfy the more rigid observational constraint given by Campbell and Anderson (1989),

$$|0.23\delta J_2 + 2.20\delta J_4 - 3.13\delta J_6| \leq 1, \quad (18)$$

where the  $\delta$  corrections are with respect to the values of Equations (15)–(17). Because interior models are fundamentally constrained by the gravitational moments, improvements in accuracy by means of Cassini radio Doppler data may yield a better understanding of Saturn’s interior. The Cassini mission can provide improved determinations for all three zonal harmonics. Our best estimate of the expected one-sigma accuracy, again in units of  $10^{-6}$ , is  $\pm 0.1$  for  $J_2$ ,  $\pm 0.4$  for  $J_4$ , and  $\pm 1.5$  for  $J_6$ . In addition, the Cassini mission should improve other important parameters, most notably the rotational period of Saturn’s magnetic field (10.6549 h) (Davies *et al.*, 1983), its intrinsic power output ( $8.63 \times 10^{16} \text{ J s}^{-1}$ ) and internal energy flux ( $2.01 \text{ J m}^{-2} \text{ s}^{-1}$ ) (Hanel *et al.*, 1983), the temperature of the atmosphere at the one bar level (134 K) (Lindal *et al.*, 1985), and the mean equatorial radius. These various boundary conditions must be satisfied by solving the nonlinear differential equations for the interior structure (see for example Guillot *et al.*, 1994). Post-Cassini models may lead to a better understanding of the energy transport in Saturn’s interior and consequently to a better understanding of its cooling history and evolution.



2.3.1.3. *Objectives for Titan.* The Radio Science gravitational scientific objectives at Titan are to:

- determine the mass of Titan and its low degree and order gravitational harmonics ( $J_2, C_{22}$ );
- measure the tidal variation of Titan’s gravitational quadrupole moments;
- constrain models of Titan’s interior.

*a) Determine Titan’s mass and low degree and order gravity field:* The most accurate determination of Titan’s mass  $M_T$  has been obtained by a combination of radio Doppler data from Pioneer 11, Voyager 1 and Voyager 2 (Campbell and Anderson, 1989). Voyager 1 encountered Titan at a closest approach distance of 6500 km. Pioneer 11 and Voyager 2 encountered Titan at much farther distances of 363,000 and 666,000 km, respectively. The best current value of GMT is  $8978.2 \pm 1 \text{ km}^3 \text{ s}^{-2}$ .

None of the Titan encounters has yielded any information on gravitational harmonics beyond the zero-degree mass term. The values of  $J_2$  and  $C_{22}$  can be derived theoretically by assuming that Titan’s low degree and order gravitational field reects the satellite adjustment to the perturbing potentials excited by Titan’s rotation and by Saturn’s tides. The static part of the perturbing potential produces a permanent deformation of the body with coefficients (Rappaport *et al.*, 1997)

$$J_2 = \frac{5k_f M_S}{6 M_T} \left( \frac{R_T}{a_T} \right)^3 = \left( \frac{k_f}{1.5} \right) 0.49 \times 10^{-4}, \quad (19)$$

$$C_{22} = \frac{k_f M_S}{4 M_T} \left( \frac{R_T}{a_T} \right)^3 = \left( \frac{k_f}{1.5} \right) 0.15 \times 10^{-4}, \quad (20)$$

in Titan’s principal axes of inertia frame. In Equations (19) and (20),  $R_T$  is Titan’s equatorial radius,  $a_T$  is Titan’s orbital semi-major axis, and  $k_f$  is the fluid Love number. For a homogeneous uid,  $k_f = 3/2$ , but it could be as much as two times smaller if there were substantial central condensation in the interior of Titan. Note that for all possible internal mass distributions in hydrostatic equilibrium,  $J_2$  is exactly 10/3 of  $C_{22}$ .

An order of magnitude calculation (Rappaport *et al.*, 1997) indicates that measurements of the Doppler frequency shift in the two-way radio signal between the Cassini spacecraft and a ground station will allow an excellent determination of  $J_2$  and  $C_{22}$  with absolute accuracy of order

$$\sigma_2 = \frac{cbv}{GM_T} \left( \frac{b}{R_T} \right)^2 \sigma_y \simeq 4 \times 10^{-8}, \quad (21)$$

where we assume the distance at closest approach  $b$  is twice Titan’s radius  $R_T$ ,  $c$  is the speed of light, the spacecraft’s speed  $v \simeq 5 \text{ km s}^{-1}$ , and the Allan deviation of the Cassini radio signal over a typical Doppler integration time is  $\sigma_y \simeq 10^{-14}$ .



Equation (21) is consistent with results for Ganymede obtained with the Galileo spacecraft (Anderson *et al.*, 1996b).

An analytical covariance analysis (Rappaport *et al.*, 1997) suggests that  $J_2$  and  $C_{22}$  can be measured with the Cassini mission to an absolute accuracy between  $10^{-8}$  and  $10^{-9}$ , which is consistent with the rough estimate of Equation (21). That covariance analysis allows us to estimate the accuracy afforded by various flyby geometries. Favorable conditions include a small impact parameter, a small flyby velocity, a velocity at closest approach not too far from the line of sight, and an asymmetric flyby with respect to Titan's principal axes of inertia.

*b) Determine tidal variation of Titan's quadrupole moments:* In addition to a permanent deformation, Titan must undergo a periodic deformation in response to the changing tidal force caused by the significant eccentricity of Titan's orbit. The periodic tidal perturbation has a frequency equal to Titan's orbital angular frequency, and Titan's response is fundamentally different from its static response. While Titan responds more or less as a fluid body to the static potential, it responds as an elastic body to the periodic potential.

The tidal variation of Titan's quadrupole moment is described in terms of (Rappaport *et al.*, 1997)

$$\Delta J_2 = \frac{3k_2}{2} \frac{M_S}{M_T} \left( \frac{R_T}{a_T} \right)^3 e \cos f = \left( \frac{k_2}{0.015} \right) \times 2.58 \times 10^{-8} \cos f, \quad (22)$$

$$\Delta C_{22} = \frac{3k_2}{4} \frac{M_S}{M_T} \left( \frac{R_T}{a_T} \right)^3 e \cos f = \left( \frac{k_2}{0.015} \right) \times 1.29 \times 10^{-8} \cos f, \quad (23)$$

where  $e = 0.029$  is Titan's orbital eccentricity,  $f$  is its true anomaly, and  $k_2$  is the Love number of degree 2 (Love, 1906). For an incompressible body with uniform density  $\rho$  (for Titan,  $\rho = 1.88 \text{ g cm}^{-3}$ ) and elastic shear modulus (or rigidity)  $\mu$ ,

$$k_2 = \frac{3/2}{1 + 19\mu R_T / 2GM_T \rho}. \quad (24)$$

While deviations from incompressibility and homogeneous density require only small corrections to Equation (24) (Kaula 1964), a varying rigidity has important consequences (Cassen *et al.*, 1982).

The rigidity of Titan is highly uncertain. For a range of rigidity's values from  $\mu = 4 \times 10^{10} \text{ dyne cm}^{-2}$  (appropriate for an icy body) to  $\mu = 7 \times 10^{11} \text{ dyne cm}^{-2}$  (appropriate for a rocky body) we obtain a range of values of  $k_2$  from 0.22 to 0.015. It follows that the amplitudes of variations of  $J_2$  and  $C_{22}$  (estimated in Equations (22) and (23) to be  $2.6 \times 10^{-8}$  and  $1.3 \times 10^{-8}$ , respectively) could be as much as 15 times larger. From covariance analysis results we conclude that a determination of  $k_2$  to within 0.05 absolute accuracy is possible.

*c) Constrain models of Titan's interior:* The assumption of hydrostatic equilibrium will be tested by determining  $J_2$  and  $C_{22}$  (Hubbard and Anderson, 1978).

Indeed, important departures from hydrostatic equilibrium would invalidate the relationship between  $J_2$  and  $C_{22}$ .

If the assumption of hydrostatic equilibrium is verified, then the value of  $k_f$  will provide the value of the greatest moment of inertia  $C$  from the Radau equation (see Hubbard, 1984)

$$\frac{C}{M_T R_T^2} = \frac{2}{3} \left[ 1 - \frac{2}{5} \left( \frac{5}{k_f + 1} - 1 \right)^{1/2} \right]. \quad (25)$$

The value of  $C/(M_T R_T^2)$  depends on the degree of differentiation of the body. It will be compared to values predicted by various models of internal structure (e.g., Sohl *et al.*, 1995).

Finally, the value of  $k_2$  will be used to distinguish between volatile-rich and volatile-poor models of Titan (Stevenson, 1992). The above-mentioned range of  $k_2$  values (from 0.22 to 0.015) represent the extreme range from volatile rich to volatile poor models. Volatile-rich models are so-called because they have a deep, internal, water–ammonia ocean (Lunine and Stevenson, 1987; Cynn *et al.*, 1989; Grasset and Sotin, 1996). These models are supported by our ideas of the formation of satellites, but imply large amounts of methane which could be present in part as surface hydrocarbon oceans. These seem inconsistent with a primordial origin of Titan’s orbital eccentricity (Sohl *et al.*, 1995). Indeed, oceanic tidal friction would have circularized Titan’s orbit by now.

On the other hand, the volatile-poor models, in which Titan’s mantle is completely solid, are consistent with a primordial orbital eccentricity, but have cosmogonic problems described by Stevenson (1992).

These problems lead us to briefly re-examine underlying assumptions concerning Titan’s orbital eccentricity and Titan’s formation; such ideas can be tested by the gravity measurements.

Early work by Sagan and Dermott (1982) implicitly assumed that Titan’s orbital eccentricity is primordial. These authors identified two scenarios consistent with the persistence of eccentricity in the presence of tidal dissipation: either Titan is covered by a nearly global methane ocean deeper than 400 m, or there is no methane ocean on the surface. The first picture was favored because such an ocean would resupply the atmosphere in methane and hence balance atmospheric methane destruction by photolysis, which will remove the present atmospheric inventory in 107–108 years (Yung *et al.*, 1984).

However, the speculated global ocean was dispelled by radar (Grossman and Muhleman, 1992; Muhleman *et al.*, 1990, 1992) and infrared (Griffith, 1993; Lemmon *et al.*, 1993; Coustenis *et al.*, 1994; Han and Owen, 1994; Smith *et al.*, 1994) observations of Titan, although these allow for seas or lakes.

Sears (1995), using a more sophisticated tidal dissipation model than Sagan and Dermott (1982), concluded that even ignoring land masses, the present orbital eccentricity of Titan requires that the depth of any global ocean be at least 500 m.

Dermott and Sagan (1995) found that confining the fluid on Titan to a number of disconnected seas or crater lakes greatly extends the damping timescale of Titan's orbital eccentricity. One problem with this idea is that restricted seas and crater lakes may not contain sufficient amount of methane to resupply the atmosphere over the age of the solar system (Lunine, 1996). Stevenson (1992) suggested that the hydrocarbon ocean is stored in porous spaces and caverns within the upper crust of Titan. This model may reconcile the need for a reservoir of hydrocarbons with the tidal argument against a global ocean, though it demands a rather porous crust.

Lorenz *et al.* (1997) proposed the idea that Titan's atmosphere may be unstable and exists only episodically in its present extensive state. This model may be able to solve the eccentricity problem if Titan's surface remains frozen for long periods of time corresponding to epochs in which the atmosphere is collapsed.

Finally, the possibility remains that Titan's orbital eccentricity was produced recently (less than several hundred million years ago) by a large impact, though few bodies large enough to do so are expected to exist on highly eccentric orbits.

If Titan formed around Saturn, an ammonia–water layer may have formed inside Titan and persisted (Grasset and Sotin, 1996).

However, Prentice (1980, 1984) suggested that Titan could be a captured moon of Saturn. Lewis and Prinn (1980) showed that only small amounts of methane and ammonia were present in the solar nebula, so that Titan could have formed as a volatile-poor body. If produced from solar nebula material in the vicinity of Saturn's orbit, then Zahnle *et al.* (1992) and Griffith and Zahnle (1995) showed that volatiles could have been delivered to Titan by comets. Impact-driven chemistry (Jones and Lewis, 1987) would have led to production of organic compounds in a manner which may or may not be compatible with Titan's atmosphere and surface composition, but some comets themselves contain significant complements of organic compounds which may survive impact on Titan.

*2.3.1.4. Objectives for the Icy Satellites.* The radio science gravitational scientific objectives at the icy satellite are to:

- determine the gravity fields of Enceladus and Rhea ( $J_2$ ,  $C_{22}$ );
- determine the masses of Mimas, Tethys, Dione, Hyperion and Phoebe.

*a) Enceladus' gravity field:* Enceladus is a special focus of interdisciplinary science in the Cassini mission. Indeed, two major objectives of the Cassini Satellite Surface Working Group are to acquire optical remote sensing observations of Enceladus and to measure its gravity field.

This interest is explained by the intriguing characteristics of Enceladus, among which figures the remarkably high and uniform albedo and the presence of old and recent terrains. The mean geometric albedo is close to unity, and the total range of albedo over the surface is 20%. This is even more intriguing considering that Enceladus topography contains both old cratered terrains dating from the period of heavy bombardment and smooth terrains recently resurfaced, indicating endogenic

activity. Buratti (1988) investigated the photometric properties of Enceladus and concluded that the satellite is completely covered by a young, bright surface layer. Buratti argues that the E-ring, whose thickness peaks at the orbit of Enceladus, is the most likely source for this layer, and that the E-ring itself is probably the result of active surface processes on Enceladus. Alternatively, the bright surface of Enceladus may result from dissipation associated with tidal interactions, perhaps with Dione.

Enceladus's mean radius is  $\simeq 250$  km. How can such a small satellite have undergone substantial evolution? This may be due to the fact that ammonia ice, which plays an important role in lowering the melting point, may have been incorporated into Enceladus. Evidently, the surface properties alone are insufficient to provide information on the interior composition. To understand the nature and history of Enceladus and the other Saturn's satellites, modeling of the interiors and of the thermal evolutions is in order.

As far as Enceladus is concerned, even the most basic parameter, i.e., the mass density, is very poorly known. Indeed, the mass of Enceladus is known with about 50% accuracy. Assuming  $GM_E = 4.9 \text{ km}^3 \text{ s}^{-2}$  (Campbell and Anderson, 1989), hydrostatic equilibrium, and a value of the fluid Love number equal to half its value for a homogeneous body, we obtain  $J_2 = 0.0056$  and  $C_{22} = 0.0017$ .

A determination of the mass of Enceladus and of its harmonic coefficients of degree 2 from data acquired during a targeted flyby will allow us to determine the greatest moment of inertia from Equation (25), and hence to constrain models of internal structure.

*b) Rhea's gravity field:* With a radius of 765 km, Rhea is the largest satellite of Saturn after Titan. This is the reason why Rhea was selected for gravity field determination. Recently, Anderson *et al.* (1996a, 1996b) came to the surprising but inescapable conclusion that both Io and Ganymede contain large metallic cores. It will be very interesting to find out whether the smaller Rhea is differentiated and to compare its internal structure to that of Titan and Enceladus. In this regard, note that distinct terrain ages and endogenic resurfacing were suggested by Plescia and Boyce's (1982) discovery that two polar regions have retained large craters while they are absent in another region near the equator.

*c) Icy satellites' masses:* The objective is to determine the masses of the icy satellites (especially Mimas, Tethys, Dione, Hyperion and Phoebe) in order to determine their mean density to high accuracy, and hence constrain their bulk composition. This is essential for an improved understanding of their dynamical behavior and evolution. Tyler *et al.* (1981) determined the masses of Titan and Rhea from Voyager 1 radio science measurements at Saturn, and Voyager 2 permitted Tyler *et al.* (1982) to determine the masses of Tethys and Iapetus. Using the mass of Tethys in combination with the theory of the Tethys-Mimas resonance, they derived the mass of Mimas. Campbell and Anderson (1989) used the combined data set of Pioneer and Voyager data to redetermine the masses of Tethys, Rhea, Titan and

TABLE I  
Masses of the large icy satellites of Saturn.

Satellite	Mass ( $\times 10^{23}$ g)	Reference	Mean Radius ( $\times 10^5$ cm)	Reference	Density (g cm $^{-3}$ )
Mimas	$0.46 \pm 0.05$	Tyler <i>et al.</i> , 1982 (derived)	$196 \pm 3$	Smith <i>et al.</i> , 1982	$1.46 \pm 0.23$
	$0.375 \pm 0.009$	Kozai, 1976	$198.6 \pm 0.6$	Davies <i>et al.</i> , 1996	$1.14 \pm 0.04$
Enceladus	$0.74 \pm 0.36$	Kozai, 1976	$250 \pm 10$	Smith <i>et al.</i> , 1982	$1.13 \pm 0.69$
	$0.74 \pm 0.36$	Kozai, 1976	$249.4 \pm 0.3$	Davies <i>et al.</i> , 1996	$1.14 \pm 0.56$
Tethys	$7.55 \pm 0.90$	Tyler <i>et al.</i> , 1982	$530 \pm 10$	Smith <i>et al.</i> , 1982	$1.21 \pm 0.21$
	$6.22 \pm 0.13$	Kozai, 1976	$529.8 \pm 1.5$	Davies <i>et al.</i> , 1996	$1.00 \pm 0.03$
Dione	$10.52 \pm 0.33$	Kozai, 1976	$560 \pm 5$	Smith <i>et al.</i> , 1982	$1.43 \pm 0.08$
	$10.52 \pm 0.33$	Kozai, 1976	$560 \pm 5$	Davies <i>et al.</i> , 1996	$1.43 \pm 0.08$
Rhea	$24.9 \pm 1.5$	Tyler <i>et al.</i> , 1981	$760 \pm 5$	Smith <i>et al.</i> , 1982	$1.33 \pm 0.11$
	$23.1 \pm 0.6$	Campbell and Anderson, 1989	$764 \pm 4$	Davies <i>et al.</i> , 1996	$1.24 \pm 0.05$
Iapetus	$18.8 \pm 1.2$	Tyler <i>et al.</i> , 1982	$730 \pm 10$	Smith <i>et al.</i> , 1982	$1.15 \pm 0.12$
	$15.9 \pm 1.5$	Campbell and Anderson, 1989	$718 \pm 8$	Davies <i>et al.</i> , 1996	$1.02 \pm 0.13$

Iapetus, but recommended the earlier ground-based determination (Kozai, 1957) for Tethys. No mission has yet yielded the masses of Mimas, Enceladus, Dione, Hyperion and Phoebe.

Mass, size and density for the intermediate-size satellites are listed in Table I. For each satellite, the density on the first line is computed from the mass determined or recommended by Tyler *et al.* (1982) and the mean radius determined by Smith *et al.* (1982) from Voyager images. The density on the second line is computed from the mass determined or recommended by Campbell and Anderson (1989) and the mean radius from Davies *et al.* (1996).

Phoebe, on an inclined, retrograde orbit, may be a captured object. Determining the density of Phoebe is important to find out whether or not Phoebe is asteroidal in nature.

### 2.3.2. Techniques

2.3.2.1. *Saturn.* Cassini will orbit Saturn at a fairly wide range of periapsis radii between 1.3 and 7.3  $R_S$ , at inclinations between  $0^\circ$  and  $85^\circ$ , and with a wide range of orbital periods from 3 months to 8 days. By fitting a second degree and order gravitational field, in addition to  $J_4$  and  $J_6$ , to the radio Doppler data, the mapping of Saturn's gravitational field will be complete.

Flybys of Saturn on previous NASA missions occurred at periapsis radii of 1.34  $R_S$  for Pioneer 11, 3.05  $R_S$  for Voyager 1, and 2.67  $R_S$  for Voyager 2. However, the Pioneer 11 Doppler noise is a factor of 260 times that expected from the Cassini X-band data, while the Voyager noise is a factor of 12 larger than the expected Cassini noise. Given the improved Doppler accuracy for Cassini, and the expected smaller non-gravitational accelerations, plus the advantage of multiple orbits of Saturn, it is realistic to expect a factor of 100 improvement over Pioneer 11 and Voyager in our knowledge of Saturn's gravitational moments.

The radio Doppler data may be complemented by the reduction and analysis of imaging data for the study of the orbital mechanics of smaller inner satellites and eccentric ringlets. It was demonstrated during the Voyager mission that such orbital data can place independent constraints on Saturn's gravitational field (Nicholson and Porco, 1988), which when combined with the radio Doppler data, provide significantly better determinations of the higher-order gravitational moments.

2.3.2.2. *Satellites.* The gravity fields of Titan, Enceladus and Rhea will be determined by the same type of global technique as used for Saturn.

The tidal variation of the low degree and order gravity field will be measured from independent determinations of  $J_2$  and  $C_{22}$  obtained from flybys occurring near Titan's periapsis and apoapsis.

### 2.3.3. Major Requirements

2.3.3.1. *Saturn Requirements.* The major requirement for the determination of the gravitational moments is to obtain coherent X-band Doppler data over an interval of 5 h, centered on the closest approach in each Saturn orbit. Outside of closest approach, the data do not need to be continuous, but we require as nearly continuous data as possible for an interval of  $\pm 4$  h. Although our covariance analysis, based on an assumed Allan deviation of  $2 \times 10^{-14}$  at a 1000 s integration time, is valid for X-band tracking only, the determination of Saturn's gravitational field will most likely be improved further with a dual-band radio capability at X- and Ka-bands. The most significant enhancement will be the relative insensitivity of the data noise to solar elongation angle, thereby enabling a high quality moment determination on every orbital revolution.

The best orbits of opportunity are those with periapsis radii of less than 4.5  $R_S$ . About 40 such opportunities are anticipated. The first and closest orbit at 1.3  $R_S$  will receive the highest priority. A wide range of inclination angles is practically

assured because of the mission requirement to raise the inclination to a near polar orbit during orbits 34–59.

In principle, we require that there be no spacecraft maneuvers or momentum dumps of the reaction wheels during the two days of data acquisition for Saturn radio science. In practice, this may not be achieved. But when it is, we anticipate that the RSS total unmodeled acceleration by spacecraft subsystems, particularly the attitude and articulation control subsystem and the propulsion module subsystem, when inactive, will be less than  $5 \times 10^{-14} \text{ km s}^{-2}$ , about 100 times smaller than comparable acceleration noise on the Voyager spacecraft.

#### 2.3.3.2. Titan Requirements.

*a) Tour requirements and flybys selection:* The tour must contain at least four Titan flybys in the following conditions:

- The spacecraft must not be occulted by Titan during  $\pm 2$  h around closest approach. This is to allow us to track the spacecraft.
- The distance at closest approach  $b$  must be such that  $1.5 \leq b/R_T \leq 2$ . As a matter of fact, a flyby such that  $b < 1.5R_T$  would require firing the thrusters, which would introduce noise in the data. On the other hand, given that the accuracy of the determination is proportional to  $(b/R_T)^3$  (see Equation (21)), there is a rapid loss of sensitivity as the flyby's altitude is raised.
- Two flybys must occur near Titan's periapsis, and include one flyby at low inclination with respect to Titan and another one at high inclination. Two other flybys must occur near Titan's apoapsis, with the same inclination requirement. The inclination requirement will allow a good separation of  $J_2$  from  $C_{22}$ . The Titan's periapsis and apoapsis requirement will allow us to determine the tidal variations of Titan's quadrupole moments.
- The flybys should occur far from solar conjunction to minimize the effects of plasma noise. For example, plasma noise increases by two orders of magnitude between sun–earth–spacecraft angles of  $120^\circ$  and  $7^\circ$ .
- Goldstone viewing by the deep space station DSS-25 is desirable because the use of Ka-band afforded by this station reduces the plasma noise by one order of magnitude.

*b) Tracking requirements:* Tracking data must be acquired continuously for  $\pm 2$  h around the time of closest approach.

#### 2.3.3.3. Icy Satellite Requirements.

- The determination of Enceladus and Rhea's gravity fields requires that one targeted flyby of each satellite be dedicated to gravity field measurements.
- Mass determination can be performed with non-targeted flybys which have a distance at closest approach smaller than 50,000 km and preferably smaller than 25,000 km. Tracking data of Phoebe will be acquired during the Phoebe flyby, 19 days before Saturn orbit insertion.



## 2.4. RING OCCULTATION EXPERIMENTS

### 2.4.1. Objectives

Voyager observation of Saturn's rings in 1980 provided the only radio occultation observation available to date of the remarkable Saturnian ring system (Tyler *et al.*, 1980). All features of the main ring system were probed using coherent 3.6 and 13-cm wavelengths sinusoidal signals. Cassini ring observations will significantly expand on the Voyager observations, primarily taking advantage of new three simultaneous wavelengths capability (0.94, 3.6, and 13 cm, or Ka-, X-, and S-bands, respectively) as well as multiple occultation opportunities at large, intermediate, and small ring opening angle  $B$ .

*2.4.1.1. Ring Structure and Physical Properties.* Analysis of the Voyager radio occultation observations has contributed a wealth of information regarding radial ring structure (Tyler *et al.*, 1983; Marouf *et al.*, 1986; see also maps in Rosen, 1989), the particle size distribution of several broad ring features (Marouf *et al.*, 1983; Zebker *et al.*, 1985), physical ring thickness (Marouf *et al.*, 1982; Zebker and Tyler, 1984; Zebker *et al.*, 1985), and ring dynamics (Marouf and Tyler, 1986; Marouf *et al.*, 1987; Gresh *et al.*, 1986; Rosen and Lissauer, 1988; Rosen *et al.*, 1991a,b).

A small ring opening angle  $B = 5.9^\circ$  (angle between a unit vector in the Earth direction and the ring plane) at the time of the Voyager observations increased the effective path length of the radio signal through the rings by a factor of about 10 relative to its normal value. The increased length enhanced sensitivity to regions of small to moderate optical depth (Rings C, Cassini Division, and Ring A), but accentuated signal attenuation over most of Ring B as well as other optically thick ring features (Tyler *et al.*, 1983).

Accurate, high spatial resolution, multiple wavelengths characterization of ring structure and of its variability with ring longitude, ring opening angle, and time are major objectives of the Cassini radio science ring observations. The characterization is at the heart of understanding of ongoing physical and dynamical processes and is of prime importance for eventual understanding of ring origin and evolution.

Radio occultation opportunities implemented early in the Cassini tour when the rings are nearly fully open ( $B \approx 20\text{--}24^\circ$ ) will overcome a major Voyager limitation, allowing for the first time probing at radio wavelengths of the optically thick Ring B, which dominates the overall mass of the ring system. The optimized near-diametric geometry of these occultations will yield an order of magnitude resolution improvement in mapping the radial structure of ring features compared with Voyager. Other occultations later in the mission at intermediate and small ring opening angle  $B$  will provide complementary information regarding vertical ring structure, optical depth profiles of tenuous ring features, and the variability of ring structure with longitude and time.



The Cassini observations will also determine the particle size distribution of major ring features, including Ring B, over the millimeters to tens of meters size range. Knowledge of the size distribution constrains the surface mass density of a ring feature if the ring material is assumed to be solid water ice. Alternatively, the size information may be used to constrain the material density of ring particles if independent estimates of the surface mass density are available from analysis of local dynamical features.

The multi-wavelength observations will also yield high spatial resolution information regarding the abundance of millimeter to decimeter size particles within local ring features, a unique capability of the radio occultation observations. Of particular interest is mapping the possible variability in the abundance of this particle population within dynamically active ring features (density and bending waves, wakes of embedded satellites, resonant edges, etc.). Interesting sorting of particle sizes across narrow ring features has been noted in the Voyager observations (Tyler *et al.*, 1983; Marouf *et al.*, 1986) and has motivated the proposal of innovative ring models to explain the observations (Eshleman, 1983; Eshleman *et al.*, 1983; Michel, 1982).

Specific objectives include:

- High-resolution profiling of radial ring structure and characterization of its variability with wavelength, longitude, ring opening angle, and time. Profiling of the relative abundance of millimeter to decimeter radius particles and characterizing of their variability across resolved ring features.
- Determination of the full particle size distribution over the approximate size range 1 mm to 20 m of broad ring features that can be resolved in the spectra of the near-forward scattered signal. Determination of the vertical ring structure, of the physical ring thickness, and of the particle packing fraction within such features.
- Determination of ring surface mass density, ring viscosity, and bulk density of particle material. Characterization of the variability of these parameters among global ring features (A, B, C, . . .) and within local broad features.
- Characterization of the dust abundance within the main rings, especially in dynamically active regions, through collective analysis of radio, stellar, and solar ring occultation observations.

#### 2.4.1.2. *Ring Kinematics and Dynamics.*

*a) Geometry of the ring system:* The Voyager 1 and 2 encounters provided a detailed view of Saturn's complex ring system, with its density and bending waves and its non-circular features, and gave some indications about the composition and particle size distributions of the rings, but additional observations are required to refine the determination of ring orbits, the planetary gravitational field, and the orientation of the ring plane. This is in part because a long time baseline between observations is required for accurate measurement of the precession rates of nearly circular ring features, and also because a suite of different viewing geometries is

needed to constrain the direction of the planet's spin axis. An important goal of the radio science ring occultation observations is to determine the absolute radius scale of the ring system and the instantaneous direction of Saturn's pole to high accuracy.

Surprisingly, the radius scale of Saturn's rings has a much larger uncertainty – about 1 km – than the Uranian rings, whose orbital radii are accurate to a few hundred meters or less. This is because the Uranian rings have been observed using dozens of stellar occultations over a twenty-year period, providing a dense set of measurements of ring occultation event times. In contrast, stellar occultations by Saturn are much more difficult to observe because of the brightness of the rings in reflected sunlight. Ground-based observations of the 1989 occultation of a very bright star, 28 Sgr (French *et al.*, 1993; Hubbard *et al.*, 1993), and subsequent occultations observed from the Hubble Space Telescope (HST) (Elliot *et al.*, 1992; Bosh and Olkin, 1996), have provided the only post-Voyager occultations with sufficient Signal-to-Noise Ratio (SNR) to be used for refinement of the ring orbits.

An accurate radius scale for Saturn's rings is essential for detailed dynamical investigations of the rings, as well as accurate inter-comparisons of individual occultation profiles. Since the radial dependence of eccentric ringlet free precession rates is governed by the gravitational harmonics  $J_2, J_4, J_6, \dots$ , (Longaretti and Borderies, 1991; Borderies-Rappaport and Longaretti, 1994) a long time series of precise measurements of non-circular features can be used to determine the low-order gravitational harmonics of Saturn. As pointed out above, these give important information about the internal mass distribution of the planet.

The determination of the radius scale is strongly coupled to the assumed pole direction of the mean ring plane, and thus we must solve for both from the occultation observations. From their analysis of the 28 Sgr and Voyager observations, French *et al.* (1993) concluded that the pole direction had shifted measurably between the 1980/1981 Voyager epochs and the stellar occultation in 1989, and they interpreted this as evidence for precession of Saturn's pole. Although the solar torque exerted on Saturn itself is quite small, the Sun also exerts a torque on the satellites, principally Titan, which effectively increases the  $J_2$  of the system by a factor of  $\simeq 4$  and reduces the precession period by a comparable factor. They found that the rate of motion of Saturn's pole on the sky was  $0.86 \pm 0.31$  times the predicted rate of  $0.339''$  per year. The principal uncertainty in the theoretical value is Saturn's moment of inertia. By incorporating the full set of Cassini occultation observations of the rings, both from radio science measurements and from stellar occultations observed by other Cassini instruments, we have the prospect of greatly improving the accuracy of the precession rate of the pole, with the ultimate goal of determining the principal moment of inertia of Saturn to within a few percent.

For earth-based stellar occultations, the a priori uncertainty in the stellar position relative to the planet is relatively large, and least-squares fits for the occultation geometry must include the offset between the star and planet as a pair of free

parameters. For spacecraft occultations, the analogous uncertainty is in the spacecraft location with respect to the planet's center. Errors in the assumed spacecraft trajectory map directly into errors in the derived ring plane radius scale. For this reason, we place a very high value on accurate reconstruction of Cassini's trajectory.

*b) Ring morphology:* A major goal of ring dynamics studies is to explain the presence of nonaxisymmetric features such as eccentric ringlets and density waves, and nonequatorial features such as inclined ringlets and bending waves. Since the Keplerian shear, the differential precession of periapses and nodes, and viscous diffusion tend to erase these features on short time scales, the existing ones must be dynamically maintained.

Satellites are responsible for shaping a number of morphological features. They give rise to density waves (Goldreich and Tremaine, 1978a,b, 1979a; Shu, 1984; Borderies *et al.*, 1986; Longaretti and Borderies, 1986) and bending waves (Shu *et al.*, 1983), open gaps (Goldreich and Tremaine, 1978a; Borderies *et al.*, 1982, 1988), shepherd rings (Goldreich and Tremaine, 1979c; Hanninen and Salo, 1994, 1995; Goldreich *et al.*, 1995), excite eccentricities and inclinations in narrow rings (Goldreich and Tremaine, 1981; Borderies *et al.*, 1983b, 1984a), create ring arcs (Goldreich *et al.*, 1986), and sometimes perturb rings by penetrating them (Borderies *et al.*, 1983c).

The above effects of satellites on rings require that particles behave in a collective manner, which is insured by the ring self-gravity and viscous stresses. Self-gravity is invoked to explain the rigid precession of eccentric and inclined ringlets (Goldreich and Tremaine, 1979b; Borderies *et al.*, 1983a, b). Viscous stresses can lead to instabilities (Lin and Bodenheimer, 1981; Lukkari, 1981; Ward, 1981; Borderies *et al.*, 1985) or over-stabilities (Longaretti and Rappaport, 1995).

The objectives are:

- To test theoretical models for density waves, bending waves, shepherding, excitation of eccentricities and inclinations, ring arcs, precession of elliptical and inclined ringlets, viscous instabilities, etc.
- To identify profiles of gravitational wakes of embedded satellites (Showalter *et al.*, 1986; Marouf *et al.*, 1986; Marouf and Tyler, 1986). Characterize the evolution of profile morphology with longitude and its dependence on background optical depth. Determine the masses and orbits of identified satellites.
- To explain the presence in the C ring and the Cassini Division of several ringlets which are not associated with any known satellite. Study their interaction with the surrounding rings (Rappaport, 1998).
- To explain the presence in the B ring of non-axisymmetric features which are not associated with any known satellite (Lane *et al.*, 1982; Borderies *et al.*, 1984b).

*c) Ring evolution:* Angular momentum and energy are transferred between the rings and the satellites with which they interact (Goldreich and Tremaine, 1980). The small satellites outside the main rings of Saturn are repelled outwards over a time scale of a few tens of millions of years. This short-time scale suggests that

the interaction between rings and satellites includes accretion and disruption of satellites and that Saturn's rings as we observe them now may be recent. Alternatively, ring/satellite systems may be maintained by effects that we do not understand yet.

A key parameter in modeling this evolution is the ring's viscosity. This parameter has been measured indirectly from the damping of density and bending waves (Cuzzi *et al.*, 1981; Lane *et al.*, 1982; Lissauer *et al.*, 1982; Shu *et al.*, 1983). Cassini will allow us a more direct determination (Borderies, 1992).

The objectives are:

- To characterize and model viscous stresses.
- To characterize the transport of angular momentum and energy within the rings and their transfer between rings and satellites.

#### 2.4.2. Techniques

Observables during a ring occultation experiment can be derived from the effects of ring material on a sinusoidal signal linking the spacecraft and an earth receiving stations of the DSN (Marouf *et al.*, 1982). Temporal coherence of the radio link is ensured through the use of an ultrastable oscillator (USO) onboard the spacecraft and an atomic frequency standard at the ground receiving station. During an occultation, Cassini generates and transmits through the rings three coherent sinusoidal signals (wavelength of 0.94, 3.6, and 13 cm, or Ka-, X-, and S-bands, respectively) using the USO as a common reference for all three signals. The coherency of the signals allows measurement on the ground of the complex amplitude (magnitude and phase) of the perturbed signals.

Modeled as a discrete random medium, the collective effects of ring particles on an incident sinusoidal signal are well characterized (Marouf *et al.*, 1982; Tyler *et al.*, 1983; Marouf *et al.*, 1983; Simpson *et al.*, 1984; Zebker *et al.*, 1985; Marouf *et al.*, 1986; Tyler, 1987; Gresh *et al.*, 1989). Two main signal components may be identified and separated in the spectrum of the observed perturbed signal. The first is the direct or coherent signal, a sinusoidal component whose amplitude and phase can be measured relative to the corresponding values of the incident sinusoid. The direct signal characterizes the average effect of ring particles on the incident signal. The time history of its amplitude and phase provides information regarding detailed radial ring structure. The differential amplitude and phase of two signals of wavelength  $\lambda_1$  and  $\lambda_2$  provide information about the relative abundance of particles of radius  $a$  determined by  $\lambda_1$ ,  $\lambda_2$ , and the refractive index of particle material (Marouf *et al.*, 1982, 1983).

Initial measurements of the coherent signal amplitude and phase are diffraction-limited (Marouf and Tyler, 1982). Measurement of the direct signal phase allows reconstruction of the observations to remove diffraction effects, yielding high-resolution profiles of the complex ring transmittance, hence of optical depth and phase-shift profiles (Marouf *et al.*, 1986). Achievable resolution is a small fraction of

the corresponding Fresnel scale of diffraction and is determined by several factors, including geometry of the occultation orbit, stability of the reference phase, SNR of the observations, and processing complexity (Marouf *et al.*, 1986). A better Cassini USO and an optimized set of Cassini occultation orbits promise significant improvements in achievable resolution over the Voyager observations.

The second component of the perturbed signal is the scattered or incoherent signal, a spectral-broadened component that represents the fraction of average power scattered by ring particles and intercepted by the ground receiving station (Marouf *et al.*, 1982). The spectral broadening is caused by the Doppler shift introduced by the relative motion of the spacecraft and ring particles. Its time history (spectrogram) provides information regarding the relative abundance of meter size particles within broad ring features that can be resolved in the measured spectrograms.

The measured near-forward scattered signal of a resolved ring feature provides significant information about the distribution of particle sizes that populate the feature, its physical thickness, and the degree of particle crowding, among other physical parameters. Procedures have been developed to invert the measurements to recover physical model parameters for the classical many-particle-thick ring model (Marouf *et al.*, 1982, 1983) and for the thin-layers ring model (Zebker *et al.*, 1983, 1985). The more general problem of crowded and clustered ring models of arbitrary thickness is a subject of continued investigation (Marouf, 1994, 1996, 1997).

Contribution to the scattered signal measured during occultation is dominated by the diffraction lobes of large ring particles. Particles of radius  $a$  larger than the spacecraft antenna radius (2 m) have diffraction lobes of width narrower than the spacecraft antenna beamwidth, and information regarding their size distribution is captured in scattered signal measurements. The limit on the upper particle size captured is set by the sampling interval of the measured collective diffraction-pattern, hence by the SNR of the measurement, and is typically few to several tens of meters. Thus, scattered signal measurement during occultation yields the particle size distribution over the range  $2 \text{ m} < a < \text{several tens of meters}$ . Other techniques are used to extend the distribution to the range  $a < 2 \text{ m}$ .

Over the millimeter to decimeter size range, measurement of the differential extinction and phase shift of the X-, S-, and Ka-bands coherent may be used to constrain the size distribution. In the case of Voyager, measured differential optical depth and phase shift of the coherent X- and S-band signals ( $3.6$  and  $13 \text{ cm-}\lambda$ ) provided clear evidence for the presence of ring particles of sizes in the centimeter to decimeter radius range, both in local and global ring features (Tyler *et al.*, 1983; Marouf and Tyler, 1985; Marouf *et al.*, 1986). The additional availability of the Ka-band ( $0.94 \text{ cm-}\lambda$ ) signal on Cassini will allow similar inference of the abundance of the population of millimeters to centimeters size ring particles.

Particles of size in the decimeter to meter size range do not differentially affect the coherent signals significantly and have diffraction lobes that are essentially isotropic over the spacecraft antenna beam width. Determination of their size distribution is based on a yet different technique, referred to here as the bistatic-scattering

technique. It relies on observation of the scattered signal with the direction of the boresight of the spacecraft antenna shifted away from the earth direction so as to sample the broader diffraction lobes of particles in this range. Because the width of a diffraction lobe of a particle of diameter  $D = 2a$  observed at wavelength  $\lambda$  is roughly  $\lambda/D$ , the maximum angular shift of the spacecraft antenna boresight is determined by the minimum particle size whose diffraction lobe is to be sampled and is wavelength dependent.

Sampling the diffraction lobes of particles of radius  $a \geq 20$  cm, for example, requires bistatic-scattering observations over a maximum angular range equal to approximately five times the antenna beamwidth at the wavelength of interest. Thus, for both X- and Ka-bands, maneuvers to shift the antenna boresight away from the earth direction are limited to no more than a few degrees change in the antenna boresight direction. The exact limit is set by available SNR. Optimal maneuver strategies to observe bistatic-scattering given available SNR are still under development.

The capability of determination of the particle size distribution of resolved ring features over the millimeters to tens of meters range (millimeter to decimeter using differential extinction, decimeters to meters using bistatic scattering, and meters to tens of meters using forward-scattering) is a unique capability of the radio science ring observations. For ring features for which bistatic scattering may be noise limited or not available, a selfconsistent model fitting approach that bridges the lower and upper ends of the distribution provides a viable alternative (Marouf *et al.*, 1983; Zebker *et al.*, 1985).

#### 2.4.3. Major Requirements

The quality of ring occultation observations is determined by the phase and amplitude stability of the radio link, available SNR, and the geometry of occultation orbits, among other factors. These impose stringent requirements on the performance of the radio subsystems on board the spacecraft and at the ground receiving stations, as well as on the design of the Cassini tour.

Consider first the requirements on the phase stability of the radio link, a critical parameter for successful reconstruction of the diffraction-limited direct signal measurements. In the absence of phase noise, the limit on achievable radial resolution  $\Delta R$  is set by the Fresnel scale of diffraction  $F$  and the width  $W$  of the radial interval over which diffraction limited measurements are processed, where  $\Delta R = 2F^2/W$  (Marouf *et al.*, 1986). In reality, finite phase instability over  $W$  limits actual achievable resolution to a larger value  $\Delta R_\phi > \Delta R$ , where  $\Delta R_\phi$  is determined by the nature of the random reference phase fluctuations, usually dominated by the behavior of the USO onboard the spacecraft (Marouf *et al.*, 1986).

In the Voyager case, phase stability of the USO (Allan deviation  $\sigma_y \simeq 5 \times 10^{-12}$  at 1 s time interval) limited  $\Delta R_\phi$  to the range  $\Delta R_\phi \geq 250$  m (Marouf *et al.*, 1986). The Cassini USO is over ten times better than Voyager ( $\sigma_y \simeq 2 \times 10^{-13}$  at 1 s). Calculations based on the assumptions of a random walk phase noise model (white



frequency noise) and likely Cassini occultation orbits indicate that  $\Delta R_\phi \geq 10$  m, more than an order of magnitude improvement over Voyager. A requirement that the Allan deviations of the atomic frequency standard used at the earth receiving stations be at least three times better than that of the USO ensures that the latter is the limiting factor. Actual Cassini resolution will depend, of course, on in-flight performance of the USO and ability to model and remove long term phase drift, and other factors including the degree of variability of  $F$  over  $W$  and available SNR (Marouf *et al.*, 1986).

Like Voyager, Cassini conducts all occultations in a downlink mode (that is, transmission from the spacecraft and reception on the earth), hence the available free-space signal-to-noise ratio  $\text{SNR}_0$  is limited by the relatively small transmitted power. Indeed, both spacecraft have comparable  $\text{SNR}_0$  (for Cassini,  $\text{SNR}_0 \simeq 52, 40, 41$  dB/Hz for the X-, S-, and Ka-band signals, respectively). Unlike Voyager, Cassini enjoys the advantage of arriving at Saturn when the ring system is almost fully open as seen from the earth (ring opening angle  $B \simeq -24^\circ$ ), and remains in orbit as  $B$  gradually increases to a Voyager-like value of about  $-6^\circ$  over the four-year mission lifetime. Given a ring feature of normal optical depth  $\tau$ , the actual measurement SNR is reduced from its free-space value  $\text{SNR}_0$  by the factor  $\exp[-\tau/\sin(B)]$  (due to attenuation by ring particles). For a  $\tau = 1$  ring feature, for example, the measurement SNR is a factor of 1200 higher at  $B = 24^\circ$  than at a Voyager-like  $B = 6^\circ$ ; the SNR is 1.5 million times higher for  $\tau = 2$ !

Given the extreme sensitivity of the measured SNR on the ring opening angle, a major requirement on the Cassini tour design was to implement a set of radio occultation orbits as early as possible after Saturn orbit insertion (SOI). The early occultations take full advantage of a unique opportunity provided by nature to probe all ring features, including the B Ring, with the limited available  $\text{SNR}_0$ . An additional requirement of an occultation distance  $D \simeq 4 - 6R_S$  ensures moderate Fresnel scale  $F$ , hence moderate complexity in reconstruction of the diffraction limited observations. A remarkable set of early near-diametric occultation orbits was designed and implemented by the Mission Design Team and is an integral part of the selected orbital tour. The orbits span the range  $24^\circ < B < 20^\circ$ . Exceptional X-band radial resolution of 100 m or better is expected everywhere, including regions of Ring B of normal optical depth  $\tau \leq 2.5$ , an order of magnitude improvement over Voyager. Requirements for two additional occultation opportunities at intermediate ( $B \simeq 15^\circ$ ) and small ( $B < 10^\circ$ ) ring opening angle complement the first set and allow more complete characterization of the variability of the observables with  $B$ , longitude, and time.

Additional requirements on occultation orbit geometry are necessary to improve the spatial resolution of scattered signal measurements. As indicated before, the intrinsic resolution is determined by the size of the spacecraft antenna “footprint” on the ring plane. The footprint can be very large (with a characteristic scale of thousands to hundreds of thousands of km, depending on wavelength, the spacecraft distance  $D$  behind the ring, and the ring opening angle  $B$ ). The resolution may be

improved if contours of constant Doppler shift over the footprint align closely with boundaries of ring features so that the contribution of a given feature may be identified in the measured spectrograms (Marouf *et al.*, 1982). The Voyager flyby trajectory was optimized in part to enhance this alignment (Marouf *et al.*, 1982), allowing spatial resolution in the range 1000–6000 km to be achieved (Marouf *et al.*, 1983; Zebker *et al.*, 1985). Similarly, Cassini early occultation orbits have been optimized to provide good Doppler contour alignment with ring boundaries. Spatial resolution as good as 500–1000 km is expected for some occultations.

## 2.5. ATMOSPHERIC AND IONOSPHERIC OCCULTATION EXPERIMENTS

The refraction of monochromatic radiation emitted from the spacecraft toward earth as it passes through a spherical or oblate atmosphere produces Doppler shifts in the received frequency that allow the retrieval of refractivity as a function of altitude. This in turn leads to vertical profiles of electron density in the ionosphere and of density, pressure, and temperature in the neutral atmosphere. Much of the value of occultation profiles lies in their high vertical resolution, typically better than 1 km. This is to be contrasted with that achievable from passive remote sounders, for which the vertical resolution is more comparable to a scale height.

### 2.5.1. Scientific Objectives

#### 2.5.1.1. Atmospheres.

*a) Saturn:* The Pioneer 11 spacecraft provided the first radio occultation of Saturn's ionosphere and atmosphere (Kliore *et al.*, 1980a; Kliore and Patel, 1980), with ingress and egress soundings both at equatorial latitudes. Later, Voyager 1 and 2 gave two additional occultations, which sounded latitudes near the equator, at 36°N, 31°S, and 73°S (Lindal *et al.*, 1985; Tyler *et al.*, 1981, 1982).

All the retrieved temperature profiles (Figure 1) in the neutral atmosphere have a well-defined troposphere (where temperature decreases with altitude), a tropopause, or temperature minimum, located at the  $\approx 60$ –80 mbar level, and a stratosphere (where temperature increases with latitude). The Voyager occultations, which had higher signal-to-noise ratio than those from Pioneer 11, gave atmospheric profiles that extended from a few tenths of 1 mbar to 1.3 bar. The lower pressure limit was dictated by the USO stability on the spacecraft, signal-to-noise ratio, and the resulting ability to separate the effects of the neutral atmosphere from the ionosphere on the refractivity. The limit at 1.3 bar resulted from absorption by  $\text{NH}_3$ , which extinguished the signal transmitted from the spacecraft to earth.

Both the Pioneer and Voyager temperature profiles at low latitudes exhibit a marked undulatory structure in the upper troposphere and stratosphere that is suggestive of vertically propagating waves. Vertical wavelengths are  $\sim 2$  scale heights, although smaller-scale behavior is also present. The undulations are more subdued at mid and high latitudes. This structure has not been interpreted or analyzed in



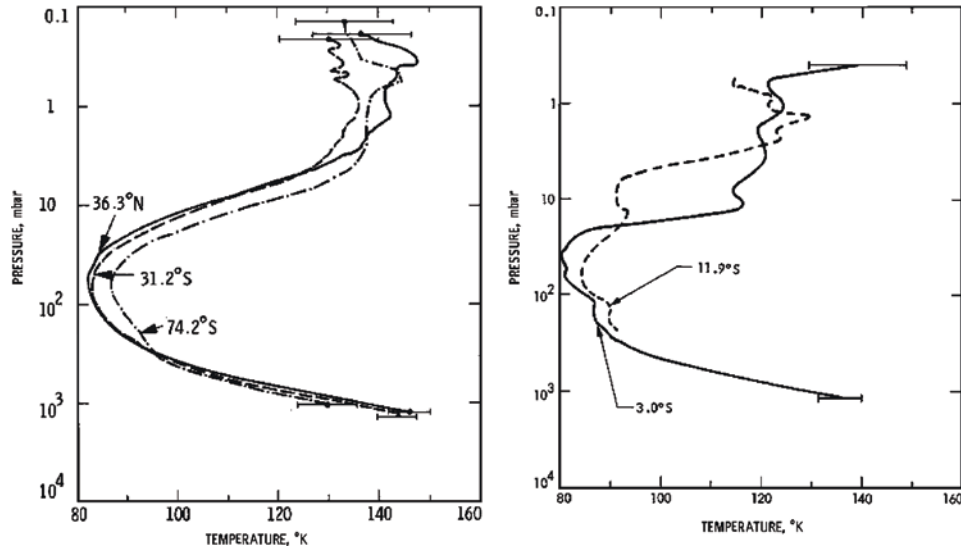


Figure 1. Temperature profiles in Saturn's atmosphere retrieved from Voyager and Pioneer 11. The dashed curve in the right panel is from the Pioneer egress (Kliore *et al.*, 1980b). After Lindal *et al.* (1985).

any depth. In their analysis of the zonal (i.e., east-west) variations of temperatures retrieved from the Voyager infrared spectroscopy experiment (IRIS), Achterberg and Flasar (1996) found evidence of a coherent wave structure in the tropopause region that extended from  $40^{\circ}\text{N}$  to low latitudes. They deduced that it was most probably a Rossby wave, forced by a critical-layer instability at the more northern latitude. The wave amplitude they derived,  $\pm 1\text{ K}$ , seems consistent with the reduced amplitude seen in the mid-latitude radio-occultation profiles. Coverage of the equatorial region, particularly at southern latitudes, by IRIS, which was primarily a nadir-viewing instrument, was minimal, because of interference from Saturn's rings and, for Voyager 2, a malfunction of the remote-sensing scan platform. Temperatures retrieved from radio occultations show structure in Jupiter's atmosphere that is similar to Saturn's (Lindal *et al.*, 1981). Allison (1990) has suggested that the structure in the equatorial profiles of Jupiter is produced by Rossby waves.

Waves are meteorologically significant, because they can be sensitive indicators of the conditions of the background mean atmosphere through which they propagate. In their study, Achterberg and Flasar (1996) were able to relate the observed meridional structure of the thermal wave they identified to the thermal structure of Saturn's atmosphere and spatial variation of its zonal winds. Waves can also be dynamically important, as they typically transport angular momentum over large distances. This could be an important factor in maintaining the large-scale zonal

wind system on Saturn, which is not well understood. Cassini is expected to provide occultations yielding temperature profiles at nearly 50 locations on Saturn, with a reasonably good distribution in latitude. This is far denser coverage than has been realized to date. With the zonal structure provided by the mapping capabilities of the composite infrared spectrometer (CIRS), wave structure in Saturn's troposphere and stratosphere should be well characterized.

Knowledge of temperature and pressure as functions of altitude and latitude leads to the zonal wind  $u$  through the gradient wind equation,

$$u \sin \Lambda \left( 2\Omega + \frac{u}{r \cos \Lambda_{pc}} \right) = -\frac{1}{\rho r} \left( \frac{\partial P}{\partial \Lambda} \right)_{\phi}, \quad (26)$$

and the thermal wind equation,

$$\frac{\partial}{\partial \ln P} \left( u \sin \Lambda \left( 2\Omega + \frac{u}{r \cos \Lambda_{pc}} \right) \right) = \frac{R}{mr} \left( \frac{\partial T}{\partial \Lambda} \right)_p. \quad (27)$$

Here  $r$  is radius to the planet's center of mass, and  $\Omega$  is the internal uniform planetary rotation rate of Saturn, presumably equal to that implied by the kilometric radiation modulation ( $= 1.66 \times 10^{-4} \text{ s}^{-1}$ );  $P$  is pressure,  $\rho$  is atmospheric mass density,  $T$  is temperature,  $R$  is the universal gas constant, and  $m$  is the mean molecular weight of the atmosphere;  $\Lambda$  is the planetographic latitude, determined by the intersection of the local normal to the equipotential surface, and  $\Lambda_{pc}$  is planetocentric latitude, determined by the intersection of the line to the planet center of mass with the equatorial plane;  $\phi$  denotes the geopotential,

$$\phi = \int_0^z g \, dz', \quad (28)$$

where  $g$  is the local effective gravitational acceleration, representing both gravitational attraction and the centrifugal repulsion associated with the uniform planetary rotation. The geopotential function  $\phi$ , therefore incorporates both gravity and uniform rotation; the altitude coordinate  $z$  is normal to the geopotential surface. Note that in Equation (26) the gradient in pressure is at constant altitude relative to the geopotential associated with uniform rotation. In Equation (27) the gradient in temperature is along isobars. Because of Saturn's rapid planetary rotation, the geostrophic term, the one containing  $2\Omega$  on the left-hand sides of Equations (26) and (27), generally dominates.

The Pioneer 11 and Voyager soundings were too sparse for inferring winds, but the much denser coverage afforded by the Cassini radio occultations make this much more feasible. Although the occultations will not densely sample longitude, they will sample latitude very well. Temperatures retrieved from the Voyager IRIS spectra indicate that, at least in the upper troposphere and lower stratosphere, the zonal variations of temperature are smaller than the variation with latitude. Thus the latitude variations in the pressure and temperature fields are fairly good indicators of the zonal winds on Saturn. Comparison with the temperatures retrieved from the

CIRS instrument, which can obtain global maps, will facilitate this derivation. A very important advantage for radio science lies in the capability to retrieve pressure as a function of altitude, and hence obtain the zonal winds directly through the application of Equation (26) (c.f., Newman *et al.*, 1984). When using temperatures to infer winds from Equation (27), as, for example CIRS must do, the winds need to be specified along a (usually lower) boundary. Winds will also be derived with high spatial resolution from cloud tracking using both the visible (ISS) and perhaps the near infrared (VIMS) images. In this analysis there always remains some ambiguity in the altitudes probed at a particular observing wavelength. Comparison of the winds derived from cloud tracking with those obtained from Equation (26) using radio science data should greatly facilitate the altitude assignment in the cloud-tracking studies.

The sensitivity of the radio signal passing through Saturn's atmosphere to absorption by gaseous ammonia permits the retrieval of vertical profiles of  $\text{NH}_3$  below the 1-bar level. Lindal *et al.* (1985) have presented such profiles from the Voyager Saturn occultations, as well as from those for Jupiter (Lindal *et al.*, 1981). The large number of Cassini occultations will permit a mapping of the three-dimensional distribution. Both passive ground-based microwave observations and observations at infrared and visible wavelengths have indicated that gaseous and condensed  $\text{NH}_3$  vary latitudinally over Saturn and Jupiter. These variations are probably indicative of the vertical motion field near the 1-bar level. Particularly intriguing in the observed radiances at radio and far-infrared wavelengths is a "warm" broad band on Saturn that is centered about  $30^\circ\text{N}$  (Conrath and Pirraglia, 1983; Grossman *et al.*, 1990). The corresponding latitude range in the southern hemisphere is much colder. This has been interpreted as caused by a diminution in cloud opacity and ammonia gas in the northern latitude range. Curiously, the Voyager radio occultation data at  $36^\circ\text{N}$  and  $31^\circ\text{S}$  give no hint of such asymmetry in the derived  $\text{NH}_3$  abundance (Lindal *et al.*, 1985). Whether an "atypical" region at the northern latitude was sounded by the radio occultations is open to question. The more complete coverage of Cassini should help address questions like this.

The helium abundance of the giant planets is an important indicator of their formation and evolution. One of the more sensitive methods to determine the helium abundances of the atmospheres of the outer planets from remote sensing has entailed the combination of radio-occultation soundings with far infrared spectra. The radio occultations provide profiles of the refractivity versus altitude, from which  $T(z)$  is derived. For uniform composition, the quantity  $T(z)/m$  is invariant. To first order, varying the assumed composition shifts the profile  $T(z)$  towards higher or lower values without changing its shape. If the source of infrared opacity of the atmosphere is known, a synthetic infrared spectrum can be computed and compared to an observed spectrum.

Comparison of Voyager radio occultation retrievals with IRIS spectra led to values of helium that were slightly depleted relative to solar abundance on Jupiter (Gautier *et al.*, 1981) and quite depleted on Saturn (Conrath *et al.*, 1984). This

appeared to be consistent with the notion that differentiation of the heavier helium from hydrogen was occurring in the planets' interiors.

Recently, however, direct determinations of the helium abundance from the Galileo probe (Niemann *et al.*, 1996; von Zahn and Hunten, 1996) have yielded values that are higher than that determined from Voyager and more nearly solar. Recent planetary evolution models (Hubbard *et al.*, 1999) have also called into question the low value of helium derived for Saturn, and they suggest that the current value of Saturn's intrinsic luminosity, which derives from cooling of its interior, is more consistent with a larger helium abundance for Saturn's atmosphere than was derived from Voyager data. Conrath and Gautier (2000) have also re-examined the helium retrieval from Voyager IRIS observations of Saturn. In this analysis, they used the redundant information in the IRIS spectrum between 200 and 600  $\text{cm}^{-1}$  to simultaneously retrieve profiles of temperature, the parafraction of hydrogen, and the helium abundance. In this spectral region the principal opacity is from absorption by the pressure-induced dipole of molecular hydrogen, caused by collisions with other hydrogen molecules and with helium. The absorption is sensitive to all three of the aforementioned atmospheric variables. Although this "internal" method of determining the helium abundance is not as sensitive as combining radio-occultation profiles with infrared spectra, Conrath and Gautier (2000) nonetheless were able to conclude the helium abundance must be higher than the value derived earlier.

Evidently there is some as yet unidentified source of systematic error in the earlier determination. Having CIRS spectra at the numerous locations of Cassini radio occultations, where the haze structure varies, may help elucidate the source of the problem and produce a more reliable determination of the helium abundance. There are no planned *in situ* measurements of helium on Saturn in the foreseeable future, so a reliable determination via remote sensing remains a high priority.

*b) Titan:* Prior to the arrival of the Voyager 1 spacecraft at Saturn, the surface pressure and temperature of Titan's atmosphere were not well determined. Indeed, predictions of the surface pressure differed by a factor of 100 (Danielson *et al.*, 1973; Caldwell, 1977; Hunten, 1978). In traversing the Saturn system, Voyager 1 flew behind Titan and provided a diametric occultation near the equator as viewed by Earth. Because of the gross uncertainty in the atmosphere base pressure, one could not perform a normal limbtracking maneuver (see Section 2.5.2.2), in which the spacecraft attitude is continually adjusted to ensure that the refracted radio waves reach Earth. This would have required a reasonably accurate model of the mean vertical structure of Titan's atmosphere for predicting the attitude control. Instead, the Voyager team hedged its bets, using constant offsets of the spacecraft antenna boresight from the line of sight to Earth,  $0.1^\circ$  during the ingress, and  $2.4^\circ$  during the egress (Lindal *et al.*, 1983; Hinson *et al.*, 1983). It turns out that the bending angle in the neutral atmosphere increases more or less monotonically with depth, reaching  $2^\circ$  for the ray that grazes the surface. The Voyager spacecraft antenna transmitted at both S- and X-bands. The S-band data, for which the half-power full width of

the antenna was  $2.5^\circ$ , covered the full range of atmospheric pressures during both ingress and egress, whereas the X-band data, with an antenna width of  $0.6^\circ$ , only proved useful in limited altitude ranges, above 28 km during ingress and within a few km of the surface during egress.

The Voyager 1 soundings provided vertical profiles of temperature and pressure at altitudes below 200 km. As discussed in Section 2.5.2, the refractivity profile is the fundamental quantity retrieved from the soundings, and obtaining temperature and pressure profiles requires that the atmospheric bulk composition be specified. The combination of data from the thermal infrared spectrometer (IRIS) with the radio occultation data led to the conclusion that the mean molecular weight of Titan's atmosphere is  $\sim 28$  AMU, highly suggestive of  $N_2$  as the dominant constituent (Tyler *et al.*, 1981; Hanel *et al.*, 1981; Vervack *et al.*, 1999). This was supported by the identification of several nitriles in the IRIS spectra, as well as the detection of atomic and molecular nitrogen in the thermosphere by the ultraviolet spectrometer on Voyager (Broadfoot *et al.*, 1981). Lindal *et al.* (1983) retrieved vertical profiles of temperature and pressure from the Voyager soundings, assuming an atmosphere of pure  $N_2$ . The ingress and egress soundings were nearly identical in the troposphere, and they obtained a surface temperature and pressure of 94 K and 1.5 bar, respectively. Below 4 km the lapse rate in temperature was nearly dry adiabatic, suggesting efficient mixing by small-scale convection.

The effect of composition on the retrieved temperature profiles is an important consideration for Titan. When the composition is spatially uniform, the retrieved temperature, as a function of altitude, scales linearly with the molecular mass (see Equation (54)). However, when there is a spatially varying condensible, such as  $CH_4$ , contributing to the refractivity, the behavior of temperature with altitude can be markedly different. Flasar (1983) retrieved temperatures for atmospheres with different  $N_2$ – $CH_4$  mixtures. He demonstrated that a vertical profile of saturated  $CH_4$  implied increasing lapse rates of temperature near the surface. By imposing the stability constraint that the lapse rate not exceed the dry adiabat, he deduced that the lowest 4 km of Titan's atmosphere had to be unsaturated and the maximum  $CH_4$  mole fraction just above the surface was  $\sim 0.09$  or less. Later, Lellouch *et al.* (1989) did a systematic study of  $N_2$ – $CH_4$ – $^{36,38}Ar$  atmospheres. Retrieving temperature profiles from the radio occultation refractivity profiles, they found a range of possible surface temperatures, from 92.5 to 101 K, and tropopause temperatures in the range 70.5–74.5 K. All the profiles were qualitatively similar in shape to that for the  $N_2$  atmosphere. Although Ar was initially thought to be a bulk constituent of Titan's atmosphere (see e.g., Samuelson *et al.*, 1981), no evidence of it has turned up, and indeed, recent work (Strobel *et al.*, 1993; Courtin *et al.*, 1995; Samuelson *et al.*, 1997) suggests that the Ar mole fraction may be quite low,  $< 0.01$ . For atmospheres composed of  $N_2$  and  $CH_4$ , Lellouch *et al.* (1989) found the range of allowable temperatures to be smaller: maximum temperatures are 71.8 K at the tropopause and 95.2 K just above the surface; the minimum possible temperatures are unchanged from before. Although the implied range of uncertainty amounts

to only  $\sim 3$  K, the IRIS spectra indicate that this is comparable to the meridional contrast seen at the surface and in the troposphere (Flasar *et al.*, 1981). Because of the likely spatial variation of tropospheric  $\text{CH}_4$ , it is important to reduce the current uncertainty in the radio occultation results, which are mostly attributable to uncertainty in the composition.

Despite this limitation, the Voyager radio-occultation profiles have formed the basis of much of the analysis of Titan's atmospheric structure, for example, in constructing global radiative-equilibrium and radiative-convective models (Samuelson, 1983; McKay *et al.*, 1989). The occultation profiles have also been directly used in the interpretation of IRIS spectra. Radiances in the thermal infrared depend both on atmospheric temperature and the infrared opacity. In the absence of independent information, the separation of these two effects requires redundancy in the infrared spectrum. This was generally not the case for the IRIS spectra, because much of the thermal infrared spectrum accessible to IRIS was dominated by aerosol opacity, whose heterogeneous distribution is not known (see Flasar (1998b) for a discussion). Hence, it was not possible to retrieve atmospheric temperatures from the spectra over most altitudes. Temperatures could only be retrieved in the upper stratosphere, using the  $\nu_4$ -band of  $\text{CH}_4$  as a "thermometer", under the assumption of a uniform abundance of  $\text{CH}_4$  in the stratosphere (Flasar, 1998a). Some information on physical temperatures was also available at the tropopause and at the surface (Flasar *et al.*, 1981). The latter was possible because of a "window" that occurs in the thermal infrared spectrum near  $530\text{ cm}^{-1}$ . Although surface emission is an important component of the radiances here, the stratospheric emission is not negligible.

Several studies of the spatial distribution of stratospheric compounds, based on emission lines in the mid-infrared portion of the IRIS spectra, have relied on the radio occultation refractivity profiles. For instance, Coustenis and Bézard (1995), in retrieving the meridional distribution of several hydrocarbons and nitriles, started with a mean temperature profile based on the equatorial radio-occultation profiles. They assumed that temperatures in the troposphere did not vary meridionally, but rescaled temperatures in the stratosphere to vary linearly with altitude from the radio-occultation profiles at the 40-mbar level, just above the tropopause, to the temperatures retrieved from the IRIS spectra in the upper stratosphere. Similarly, Courtin *et al.* (1995) and Samuelson *et al.* (1997) compared synthetic spectra, computed from temperature profiles derived from the radio occultation refractivities, with IRIS spectra in the far-infrared ( $200\text{--}600\text{ cm}^{-1}$ ) to constrain the distribution of tropospheric  $\text{CH}_4$ . They both reached the amazing result that, in a global sense,  $\text{CH}_4$  in the middle and upper troposphere must be supersaturated to provide the opacity needed to yield a good match between the synthetic and observed spectra. Samuelson *et al.* (1997) went on to derive the meridional distribution of tropospheric  $\text{CH}_4$ , including that near the surface. To do this, they had to account somehow for temperature variations in the troposphere. In effect, they used the IRIS spectra to constrain the temperatures at the tropopause and at the surface, and assumed that



occultation profiles retained their general shape with latitude. Although this is not unreasonable, it still remains an educated guess.

The Voyager 1 radio occultation data provided one of the few indications of waves in Titan's atmosphere. Hinson *et al.* (1983) analyzed the intensity scintillations found in the occultation profiles. They found a region of weak scintillation extending from 25 to 90 km altitude that they attributed to a vertically propagating internal gravity wave with little or no attenuation. At 44 km, near the tropopause, the implied vertical and horizontal wavelengths were 1 km and 4 km, respectively, and the wave amplitude was  $\sim 1$  K. They also detected strong scintillations over the altitude range 5–10 km. Later simulations by Friedson (1994) suggested that these might be attributed to an internal gravity wave that saturates and breaks near 15 km (see Flasar (1998b) for a more detailed review). Hinson and Magalhães (1991) have discussed how an atmospheric wave modulates a radio wave as it traverses an occulting atmosphere and is refracted. The amplitude response of the signal is dominated by diffraction effects, and it is most sensitive to atmospheric structure on scales that are smaller than the diameter of the first Fresnel zone,  $2\sqrt{\lambda D}$ , where  $\lambda$  is the wavelength of the radio wave, and  $D$  the distance of the spacecraft to the occulting limb. The contribution from larger-scale fluctuations is filtered out. For the Voyager occultation,  $2\sqrt{\lambda D} \approx 1\text{--}3$  km at the S- and X-band wavelengths, and it is not surprising that Hinson *et al.* (1983) detected waves with a vertical scale that was comparable to this. The phase response of the received signal, on the other hand, is dominated by atmospheric structure with vertical scales that are large compared to the Fresnel scale, for which diffraction effects are small. The temperature profiles of Titan's atmosphere retrieved from the Voyager occultations do suggest some larger-scale wave-like structure (Lindal *et al.*, 1983), but the characterization of this is incomplete. While systematic analyses of the phase scintillations have been performed on radio occultation soundings of some of the outer planets (Hinson and Magalhães, 1991, 1993), such a study has yet to be undertaken for the Titan data.

The Cassini radio science experiment is more capable than Voyager's, and it has several attractive features relevant to the issues discussed. One of the most important is that the orbiter will provide a distribution of Titan occultations with latitude, so that temperature profiles can be retrieved from measurements instead of from inspired guesswork. The Cassini thermal infrared spectrometer, CIRS, is also much improved from its predecessor, IRIS. It extends to longer wavelengths through the submillimeter portion of the spectrum, which will permit the pressure-induced  $S(0)$  line of  $N_2$  to be used as another "thermometer," probing the upper troposphere and middle and lower stratosphere (Flasar *et al.*, 2004). However, except for the surface, CIRS cannot retrieve temperatures below 30 km altitude. The radio occultation soundings provide the only means of doing so from the orbiter. By virtue of its limb sounding capability, CIRS can use the  $530\text{ cm}^{-1}$  radiances observed on the limb, for which deep space is the background, to subtract the stratospheric contribution to the radiances observed in nadir viewing, so that the surface emission and temperature can be better determined. The combination of this with radio occultation refractivity



profiles will permit a more accurate determination of the distribution of  $\text{CH}_4$  in the lower troposphere.

The latitude coverage will also provide important information on the zonal wind field, through application of Equations (26) and (27) to the retrieved pressures and temperatures, as discussed earlier for Saturn. With only two equatorial occultations, this was not possible with the Voyager data. The ability to assign a reference altitude scale to the zonal wind velocities may be even more important for Titan than for Saturn, as the identification and tracking of discrete features by the ISS and VIMS experiments to determine horizontal wind velocities will probably be more difficult for the former body.

Figure 2 depicts the characteristic vertical resolution of the occultations over the altitude range in which temperature and pressure profiles will be retrieved. Because the USO on Cassini is a factor of 20 more accurate than the one used by Voyager, atmospheric refraction should be detectable at higher altitudes, and temperature and pressure profiles up to 300 km altitude should be achievable. In the stratosphere, the vertical resolution is  $2\sqrt{\lambda D}$ . The vertical resolution is higher in the troposphere, because differential refraction and defocusing become important, and the Fresnel zone flattens vertically (Haugstad, 1978; Karayel and Hinson, 1997). Figure 2 indicates that vertical resolution lies between  $\sim 1$  km and 100 m, depending on the altitude and wavelength used, with Ka-band soundings providing the higher resolution. As discussed earlier, in Section 2.4, higher resolution is possible through inverse Fresnel reconstruction techniques. Although planetary atmospheres present

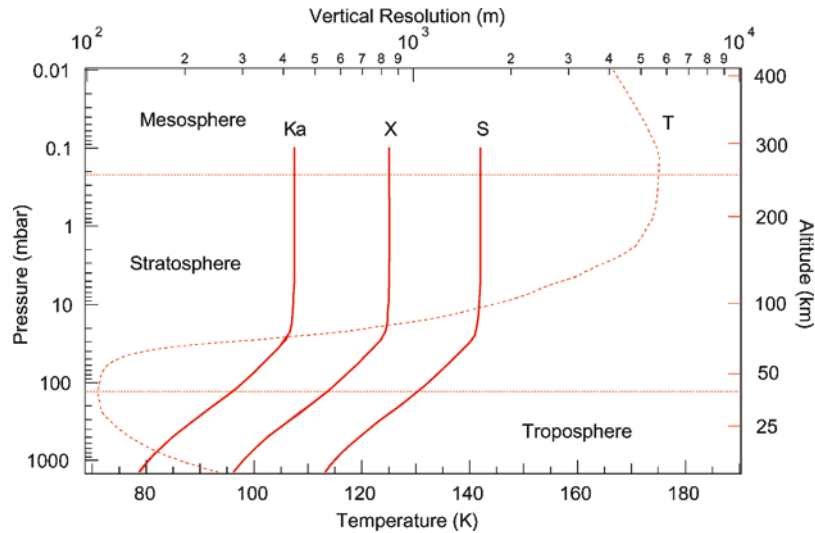


Figure 2. Vertical resolution (solid curves) of temperature profiles on Titan retrieved from radio occultations at S-, X-, and Ka-bands, for a nominal spacecraft-to-occluding limb distance of 5000 km. Dashed curve: temperature retrieved from Voyager radio occultation soundings below 200 km, after Lellouch *et al.* (1989); above 200 km, temperatures are from Yelle's (1991) model.

a more complex situation than rings, which behave as sharp edges in a vacuum, recent work on sub-Fresnel-scale inversion for atmospheres has been encouraging (Karayel and Hinson, 1997).

The high vertical resolution afforded by radio science is important for elucidating several atmospheric phenomena. In addition to resolving a large spectrum of vertically propagating waves, already discussed, the occultation soundings should be able to detect any thin cloud or aerosol layers in the stratosphere or troposphere, provided they have sufficient opacity to modify the temperature profile. The structure of the convectively mixed planetary boundary layer is of interest in understanding the exchange of heat and volatiles between the atmosphere and surface. The Voyager occultations indicate that the mixed layer extends to  $\sim 4$  km altitude at the equator, but its altitude probably varies with latitude. On Earth, the structure of the planetary boundary layer is complex, reflecting both dry and moist convective processes. Often the upper boundary is marked by a sharp stable inversion as, for example, at the top of the trade cumulus layer at subtropical latitudes (see e.g., Augstein, 1978). The latitude variation of the top of the planetary boundary layer can be indicative of meridional circulations in the troposphere, with subsiding regions characterized by lower heights of the boundary layer. Aside from the Huygens atmosphere structure investigation on the probe, which will take data at only one location, radio occultations will provide the highest resolution of tropospheric vertical structure.

The addition of a new wavelength [Ka band, 0.94 cm] should prove very important for atmospheric studies. In addition to providing the highest vertical resolution, it may prove to be an important probe of atmospheric absorption. Voyager occultations gave no indication of atmospheric absorption at S- and X-bands (Lindal *et al.*, 1983), but the absorption properties of Titan's atmosphere in the Ka-band are not known.

#### 2.5.1.2. Ionospheres.

*a) Introduction:* Any object in our solar system that has a neutral gas envelope surrounding it, due either to gravitational attraction (e.g., planets) or some other processes such as sublimation (e.g., comets), has an ionosphere. Radio occultation observations during the flybys of the Pioneer 11 (Saturn) and Voyager 1 and 2 spacecraft have clearly established the existence of a robust ionosphere around Saturn.

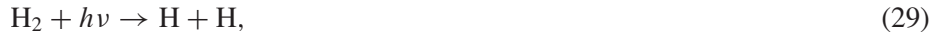
The retrieved electron density profiles exhibit primary maxima at altitudes 2000–3000 km above the 1-bar level. Those from Pioneer, in particular, exhibit a complex structure that suggest multiple layers of ionization. Multiple-layer structure in the Voyager ionospheric profiles is much more subdued, but this may be in part due to the fact that they were inverted only for higher altitudes. Originally, these profiles were retrieved only for 1500 km or higher (one profile from Voyager 2 did extend down to 700 km) (Eshleman *et al.*, 1979a,b). Recently, Hinson *et al.* (1998a) have extended the electron density retrievals from the Voyager 2 occultations by Jupiter down to 300 km, and at the lower altitudes layered structure is quite in evidence.

The Pioneer measurements were carried out using a single frequency S-band signal, the Voyager measurements employed dual frequencies at S and X-bands. The signal-to-noise ratios achieved in the Voyager observations were significantly better than the Pioneer ones. Furthermore the dual frequency technique is particularly advantageous in the signal analysis/inversion process in the presence of sharp ionospheric layers, which may lead to multipath propagation.

The three-frequency Cassini radio science subsystem will provide opportunities to obtain a significant number of new and high quality electron density profiles with a good coverage of latitudes and local time. These density profiles, combined with information on the time variation of the peak electron density values, to be deduced from the observations of Saturn electrostatic discharges (SED's) by the plasma radio wave experiment, will help to advance our understanding of the physical and chemical processes controlling the behavior Saturn's ionosphere. Furthermore, ionospheric information, combined with upper atmospheric data from the UV occultation experiment will also help to elucidate the aeronomy of Saturn's upper atmosphere.

The radio occultation data from the flyby of Titan by the Voyager 1 spacecraft provided an estimate of the peak electron density at a solar zenith angle near the terminator. Cassini will provide, during its baseline mission, further occultation opportunities, with improved signal-to-noise ratios. The information from these occultations, combined with *in situ* measurements of the ionospheric plasma, will lead to major advances in describing Titan's aeronomy.

*b) Saturn:* As indicated above our presently available direct information regarding the ionosphere of Saturn is based on a handful of electron density profiles obtained by radio occultation measurements and peak electron density values deduced from SED's. This information, combined with neutral atmospheric data obtained mainly from UV occultation measurements, has been used develop our present understanding of Saturn's ionosphere. The major neutral constituent in Saturn's upper atmosphere is molecular hydrogen, therefore the major primary ion, which is formed by either photoionization or particle impact, is  $H_2^+$ . In the equatorial and low-latitude regions electron-ion pair production is believed to be mainly due to solar EUV radiation, while at higher latitudes impact ionization by precipitating particles becomes very important. Although over 90% of all initial ions produced are  $H_2^+$ , their actual concentration is very small, because they undergo rapid charge transfer reactions. The rest of the discussion in this section will be based, for the sake of brevity, on photoionization (photodissociation) only, because particle ionization leads to similar products and processes. Solar radiation with wavelength short of 2768, 804, and 686 Å, respectively, leads to



The resulting neutral atomic hydrogen can also be ionized



At high altitudes where hydrogen atoms are the dominant neutral gas species,  $\text{H}^+$  can only recombine directly via radiative recombination, which is a very slow process, given the recombination rate of order  $\sim 10^{-12} \text{ cm}^{-3} \text{ s}^{-1}$ . It was suggested some time ago that  $\text{H}^+$  could charge-exchange with  $\text{H}_2$  excited to a vibrational state  $v > 4$ . The vibrational distribution of  $\text{H}_2$  is not known, but recent calculations (Cravens, 1987) appear to indicate that, while there are some vibrationally excited molecules present at Saturn, the corresponding charge exchange rate is not significant.  $\text{H}_2$  is very rapidly transformed to  $\text{H}_3^+$ , especially at the lower altitudes where  $\text{H}_2$  is dominant;  $\text{H}_3^+$  then in turn undergoes dissociative recombination



Significant uncertainties have been associated with the dissociative recombination rate of  $\text{H}_3^+$ . However, recent measurements have shown that the rate is rapid, even if the ion is in its lowest vibrational state (Sundstrom *et al.*, 1994). Models based upon the above discussed processes predict an ionosphere which is predominantly  $\text{H}^+$ , because of its long lifetime ( $\sim 10^6 \text{ s}$ ). In these models  $\text{H}^+$  is removed by downward diffusion to the vicinity of the homopause ( $\sim 1,100 \text{ km}$ ), where it undergoes charge exchange with heavier gases, mostly hydrocarbons such as methane, which in turn are lost rapidly via dissociative recombination. The main difficulties with these models are:

1. the calculated ionospheric density at the apparent main peak is about an order of magnitude larger than the observed one;
2. the altitude of the calculated ionospheric main peak is much lower than the observed one; and,
3. the predicted long lifetime of  $\text{H}^+$  is inconsistent with the observed large diurnal variations in the electron density peak.

A number of suggestions have been put forward during the last decade in order to overcome these difficulties. The most recent and successful models are based on the suggestion/assumption that water from the rings is being transported into Saturn's upper atmosphere, which then modifies the chemistry of the ionosphere. The presence of  $\text{H}_2\text{O}$  results in the following catalytic process



A block diagram of the chemistry scheme involving water is shown in Figure 3. The models which take into account this water chemistry and the recent values of

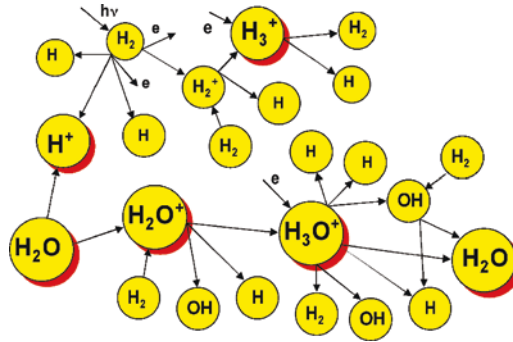


Figure 3. Block diagram of the chemistry scheme, including water (from Schunk and Nagy, 2000).

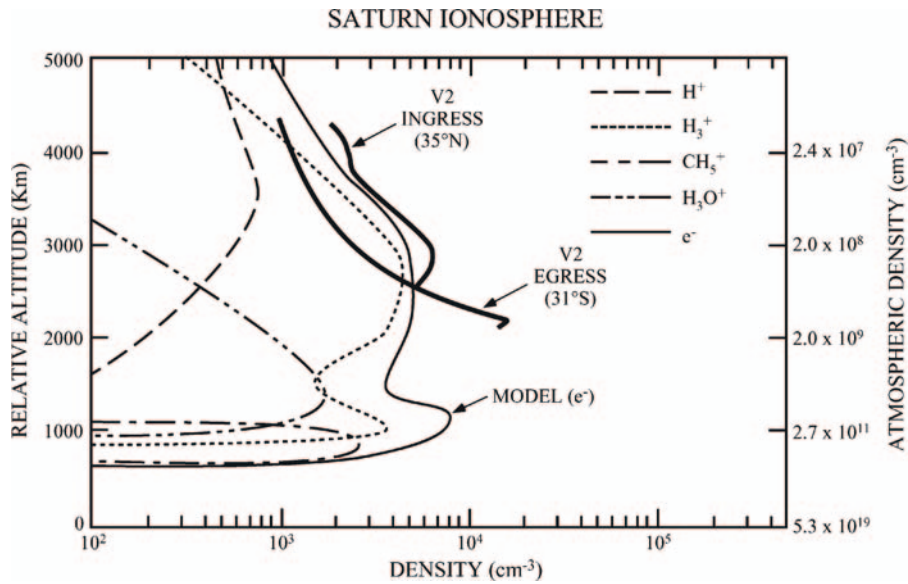


Figure 4. Calculated and measured (solid lines) ion densities for the ionosphere of Saturn. The calculations take into account the influx of water and a soft electron precipitation source (from Waite and Cravens, 1987).

the recombination rate for  $\text{H}_3^+$ , lead to ionospheres consisting mainly of  $\text{H}^+$ ,  $\text{H}_3^+$  and  $\text{H}_3\text{O}^+$ . It was shown that a downward flux of water from the rings into the atmosphere of the order of  $1\text{--}10 \times 10^7 \text{ cm}^{-2} \text{ s}^{-1}$  leads to electron density values consistent with the observations (see Figure 4); however, no current model has been able to reproduce the implied large diurnal variations (Majeed and McConnell, 1996).

*c) Titan:* Titan is surrounded by a substantial atmosphere and therefore one expects a correspondingly significant ionosphere. The only opportunity for a radio

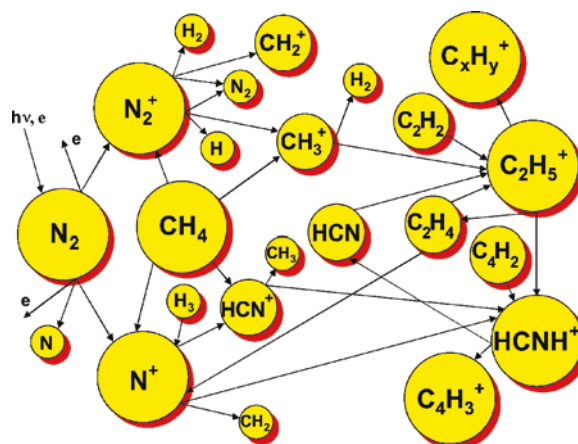
occultation measurement of such an ionosphere occurred when Voyager 1 was occulted by Titan. A careful analysis of those data by Bird *et al.* (1997) found that the peak electron density is about  $2.4 \times 10^3 \text{ cm}^{-3}$ .

Indirect evidence of the existence of an ionosphere was also obtained by the low-energy plasma analyzer measurements in the plasma wake. The various ionization sources which may be responsible for the formation of Titan's ionosphere are solar Extreme Ultra-Violet (EUV) radiation, photoelectrons produced by this radiation, and magnetospheric electrons. Cosmic rays can cause some low altitude ionization (e.g., Capone *et al.*, 1976) and proton and other ion precipitation may also make some contributions. To complicate matters even further, it is possible that under certain circumstances, e.g., high solar wind pressure, Titan will be beyond the magnetopause and in the magnetosheath of Saturn. Under these circumstances, the nature and intensity of the particle impact ionization source will be quite different. Calculations to date have concentrated on EUV and magnetospheric electron impact ionization, the two sources believed to be the dominant ones.

The next question which needs to be addressed is how do magnetospheric electrons reach the upper atmosphere. Gan *et al.* (1992) considered draped magnetic field lines and assumed that electrons enter these field lines far down the wake region at the "end" of these field tubes, for ram conditions, but can enter in a radial fashion on the wakeside. Keller *et al.* (1992) found that, contrary to earlier suggestions, photoionization is the main source for the dayside ionosphere, followed by photoelectron impact, and finally magnetospheric electron sources. Of course, magnetospheric electrons must dominate in the nightside ionosphere. The comprehensive photochemical calculations of Keller *et al.* (1992), found that the electron density peak is about  $5 \times 10^3 \text{ cm}^{-3}$  at an altitude around 1,100 km, for  $\chi = 60^\circ$ , and that the peak density is  $3 \times 10^3 \text{ cm}^{-3}$ , at an altitude of about 1,195 km, for  $\chi = 90^\circ$ , close to the Voyager results. Similar results were obtained by Ip (1990), using his model published a few years earlier. Both Ip (1990) and Keller *et al.* (1992) predicted that  $\text{HCNH}^+$  is the major ion near the density peak. The block diagram shown in Figure 5 indicates the production and loss pathways leading to  $\text{HCNH}^+$ . Fox and Yelle (1997) and Keller *et al.* (1998) have published results from their new Titan ionospheric models. The Fox and Yelle (1997) results indicate that the pseudo-ion  $\text{C}_x\text{H}_y^+$  (this is the sum of all ions with three or more carbon atoms) is the major one. Their result is shown in Figure 6. The Keller *et al.* (1998) model gives very similar electron densities and peak altitude. However, they still predict that  $\text{HCNH}^+$  is the major ion in a narrow region near the peak; the sum of the heavy hydrocarbon ions is also very significant in their model.

A variety of different studies examined the issue of the transition from chemical to diffusive control in the ionosphere. Simple time constant considerations, as well as more detailed model solutions, have indicated that the transition from chemical to diffusive control takes place in the altitude region around 1,500 km. The magnetospheric plasma velocity ( $\sim 120 \text{ km s}^{-1}$ ) is subsonic ( $\sim 210 \text{ km s}^{-1}$ ) and





superalfvenic ( $\sim 64 \text{ km s}^{-1}$ ), therefore, no bow shock is formed and the magnetic field is gradually slowed as it enters Titan's exosphere by mass loading. The magnetic field strength increases, piles up and eventually drapes around Titan. This piled up magnetic field, similar to the so-called magnetic barrier at Venus, is expected to be the dominant source of pressure against the ionosphere. Using reasonable magnetospheric parameters Keller *et al.* (1994) found that the total incident magnetospheric pressure is about  $1.6 \times 10^{-9} \text{ dynes cm}^{-2}$ . Using a peak electron density of  $5 \times 10^3 \text{ cm}^{-3}$ , this means that if the corresponding plasma temperature is greater than 700 K, the ionosphere is capable of holding off the external plasma. This pressure corresponds to about 20 nT, much of which is convected into the upper ram ionosphere, resulting in near-horizontal magnetic fields. Figure 7 is a pictorial



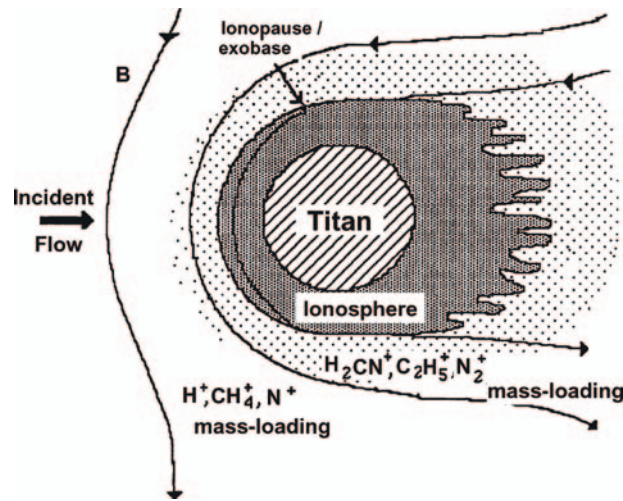


Figure 7. Pictorial representation of the interaction of Titan's ionosphere with magnetospheric plasma on the ram side (from Keller *et al.*, 1994).

representation of the situation for the ramside ionosphere. As indicated earlier, there are a large number of cases that can be considered, such as full solar and magnetospheric ionization sources, near-terminator conditions, and only magnetospheric sources.

*d) Icy satellites:* The environments of the icy satellites of Jupiter, Europa, Ganymede, and Callisto, have been observed through radio occultations of the Galileo spacecraft. Europa, and probably Callisto, were found to have a very tenuous ionosphere (Kliore *et al.*, 1997) most likely produced by the sputtering effects of Jupiter's magnetospheric particles upon their icy surfaces (Johnson *et al.*, 1998). There are no deliberate occultations of Cassini by any of Saturn's icy satellites designed into the current satellite tour.

## 2.5.2. Techniques

**2.5.2.1. The Radio Occultation Technique.** Radio occultation, in which a spacecraft emitting one or more coherent monochromatic radio signals, appears to move behind a planet or satellite as seen from the earth, affords an opportunity for the spacecraft-to-earth radio links to traverse the ionosphere and atmosphere of the occulting body. The interpretation of the observed effects of refraction by the planetary atmosphere and ionosphere allows one to determine the vertical electron density structure in the ionosphere and the temperature–pressure profiles and absorption characteristics of the neutral atmosphere (c.f., Fjeldbo, 1964; Kliore *et al.*, 1964).

This technique has been applied successfully to measure the characteristics of the ionospheres and atmospheres of Mars (Fjeldbo *et al.*, 1968; Kliore *et al.*, 1965;

Kliore *et al.*, 1969; Kliore *et al.*, 1972a; Kolosov *et al.*, 1975; Lindal *et al.*, 1979), Venus (Fjeldbo *et al.*, 1971; Howard *et al.*, 1974b; Kliore *et al.*, 1967; Kolosov *et al.*, 1976; Kliore *et al.*, 1979; Kliore and Patel, 1980a, 1982; Savich *et al.*, 1986; Jenkins *et al.*, 1993; Kliore and Mullen, 1989; Kliore and Luhmann, 1991; Yakovlev *et al.*, 1991), Mercury (Fjeldbo *et al.*, 1976a; Howard *et al.*, 1974a), Jupiter (Kliore *et al.*, 1974; Fjeldbo *et al.*, 1975; Fjeldbo *et al.*, 1976b; Kliore *et al.*, 1976, 1977; Eshleman *et al.*, 1979a,b; Hinson *et al.*, 1997; Lindal *et al.*, 1980, 1981; Flasar *et al.*, 1998), Saturn (Kliore *et al.*, 1980b; Lindal *et al.*, 1985; Tyler *et al.*, 1981), Uranus (Lindal *et al.*, 1987; Tyler *et al.*, 1986), Neptune and Triton (Tyler *et al.*, 1989; Lindal, 1992), Titan (Lindal *et al.*, 1983), Saturn's rings (Marouf and Tyler, 1985), and Jupiter's satellites Io, Europa, Ganymede, and Callisto (Kliore *et al.*, 1975; Hinson *et al.*, 1998a, in press; Kliore *et al.*, 1997; Kliore *et al.*, 1998a, b). The radio occultation technique depends on being able to invert the observed changes in the frequency and amplitude of the radio signals during the time of the occultation to produce vertical profiles of the index of refraction and absorption coefficient. For the case of spherical symmetry, in which the atmospheric structure depends only on the radial distance from the center of the planet, the inversion techniques have been firmly established (c.f., Fjeldbo and Eshleman, 1968; Kliore, 1972b). This technique also provides a good approximation in the case of oblate planets, in which case the center of refraction is determined by the local radius of curvature at the occultation location (c.f., Kliore *et al.*, 1976, 1977). The method by means of which the refraction angle, or bending angle,  $\epsilon$ , and the ray asymptote distance,  $p$ , are determined for each time  $t_0$  can be deduced with reference to Figure 8.

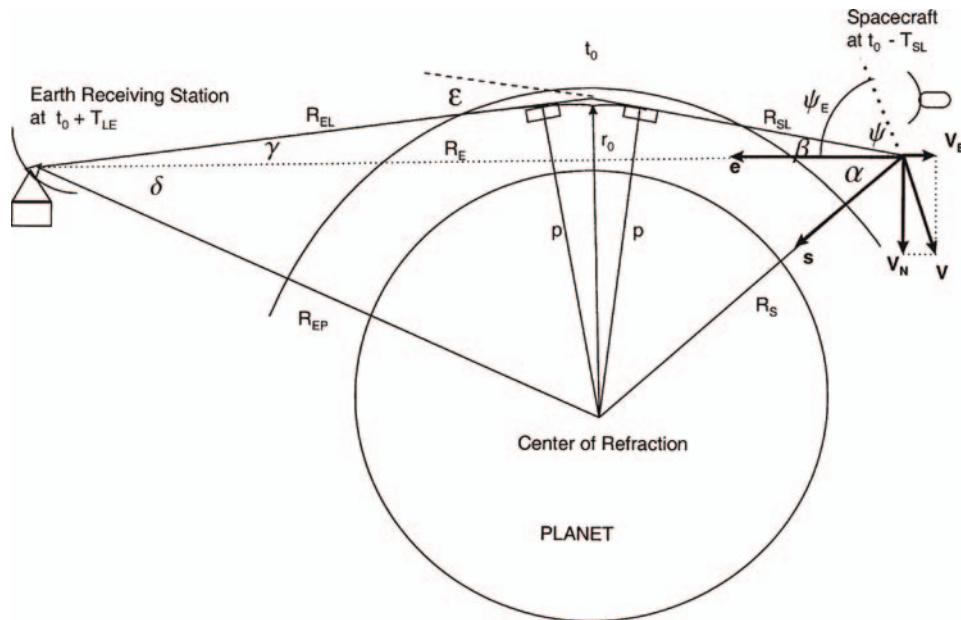


Figure 8. Geometry of a radio occultation observation.

Figure 8 displays the geometry in a plane defined by the position of the center of refraction at time  $t_0$  (the time at which the photon in question came closest to the center of refraction), the position of the spacecraft at time  $t_0 - T_{SL}$  (the time when the photon was emitted from the spacecraft antenna), and the position of the receiving antenna on earth at time  $t_0 + T_{LE}$  (the time when the photon reached the receiving station, i.e., the time of the observation). These times and positions are iteratively computed from the ephemerides of the spacecraft, the planet center, and the earth center relative to the Sun, as well as the exact location of the receiving station. This defines the plane of refraction at  $t_0$ . Referring to Figure 8, the Doppler frequency observed with no refraction is

$$\nu_E = \frac{v_0}{c} v_E, \quad (38)$$

where  $v_E$  is  $\mathbf{v} \cdot \hat{\mathbf{e}}$ , the component of the planetocentric inertial spacecraft velocity  $\mathbf{v}$  in the plane of refraction, in the direction of the virtual earth (receiving station at time of observation). If  $\delta\nu$  is defined as the frequency residual, relative to the “free space” Doppler frequency, that is caused by a refractive bending angle  $\varepsilon$ , then it may be shown that (c.f., Phinney and Anderson, 1968)

$$\cos(\psi_E - \beta) = \frac{\nu_E + \delta\nu}{\nu_S}, \quad (39)$$

where

$$\nu_S = \frac{v_0}{c} v, \quad (40)$$

and,

$$\psi_E = \arccos\left(\frac{v_E}{v}\right). \quad (41)$$

Equation (39) can then be used to determine the angle  $\beta$ , which under the usual condition of  $R_{EL} \gg R_{SL}$  is equal to the bending angle,  $\varepsilon$ . The corresponding ray asymptote distance (ray parameter),  $p$ , can then be computed as

$$p = R_S \sin(\alpha + \beta), \quad (42)$$

where

$$\cos \alpha = \hat{\mathbf{e}} \cdot \hat{\mathbf{s}}, \quad (43)$$

and  $\hat{\mathbf{s}}$  is the unit vector from the spacecraft position to the center of refraction. The actual bending angle is then

$$\varepsilon = \beta + \arcsin\left(\frac{R_{SL}}{R_{EL}} \sin \beta\right) \quad (44)$$

Thus, for each time of observation  $t_{0i}$  one can determine the corresponding bending angle and ray parameter,  $(\varepsilon_i, p_i)$ . In order to invert these data to obtain a vertical profile of the index of refraction, it is necessary to make use of the Abel

integral transform (c.f., Fjeldbo and Eshleman, 1968; Fjeldbo *et al.*, 1971; Kliore, 1972b). In a spherically stratified medium, the refractive bending angle can be expressed as

$$\varepsilon(p) = -2p \int_p^\infty \frac{dn}{d\chi} \frac{d\chi}{n\sqrt{\chi^2 - p^2}}. \quad (45)$$

where  $n$  is the index of refraction. The inverse transform is then

$$\ln n(p) = \frac{1}{\pi} \int_p^\infty \frac{\varepsilon(\xi) d\xi}{\sqrt{\xi^2 - p^2}}, \quad (46)$$

and the radius of closest approach of the ray,  $r_0$ , corresponding to  $n(r_0)$  is

$$r_0 = \frac{p}{n(p)}. \quad (47)$$

The index of refraction in an atmosphere is very nearly 1.0, therefore it is more convenient to work with the refractivity, which is defined as

$$N = (n - 1) \times 10^6. \quad (48)$$

In order to calculate profiles of pressure and temperature from the refractivity, it is necessary to define the chemical composition of the atmosphere. For the outer planets, the neutral atmosphere can be assumed to consist of hydrogen and helium. Under those conditions, the mass density,  $\rho$ , in  $\text{g cm}^{-3}$  is related to the refractivity by

$$\rho = \frac{\bar{m}N}{Rq}, \quad (49)$$

where  $\bar{m}$  is the mean molecular weight

$$\bar{m} = f_{\text{H}_2}m_{\text{H}_2} + (1 - f_{\text{H}_2})m_{\text{He}}; \quad (50)$$

and  $q$  is the specific refractivity

$$q = 0.26943(135.77f_{\text{H}_2} + 34.51(1 - f_{\text{H}_2})). \quad (51)$$

In the above equations,  $f_{\text{H}_2}$  is the number fraction of hydrogen in the atmosphere, the numerical refractivities of hydrogen and helium in Equation (51) are from Newell and Baird (1965), and  $R$  is the universal gas constant. Assuming that the atmosphere is in hydrostatic equilibrium

$$dP = g(z)\rho(z)dz, \quad (52)$$

and hence

$$P(r) = P_0 + \int_r^{r_0} P(z)g(z)dz, \quad (53)$$

and the temperature is computed from the perfect gas law, as follows:

$$T(r) = T_0 \frac{N(r_0)}{N(r)} + \frac{\bar{m}}{R N(r)} \int_r^{r_0} N(z) g(z) dz. \quad (54)$$

Thus, once one has a profile of the index of refraction in an atmosphere, and its chemical composition, any other geophysical property of the atmosphere can be readily computed. In case of the ionosphere, since the index of refraction is dependent only on the number of free electrons, it is independent of the ion composition of the ionosphere, and so the refractivity is directly related to the electron density, as follows:

$$n_e(r) = 2.479 \times 10^{-14} N(r) v_0^2, \quad (55)$$

where  $v_0$  is the transmitted frequency in Hz,  $N(r)$  is the refractivity in n-units, and  $n_e(r)$  is the electron density in  $\text{cm}^{-3}$ .

The effects of absorption and scattering in a planetary atmosphere can be described by the absorptivity (or, absorption coefficient),  $(\sigma)(r)$ , having units of  $\text{dB km}^{-1}$ , as follows:

$$\tau(r) = 2 \int_r^\infty \sigma ds. \quad (56)$$

In Equation (56),  $\tau$  represents the total absorptive attenuation, or extinction along the path of the ray, in dB as follows:

$$10 \log \left( \frac{I}{I_0} \right) = -\tau \quad (57)$$

where  $I$  is the intensity of the signal. For a refracted ray tangentially propagating through a spherically stratified atmosphere with index of refraction  $n(r)$ , Equation (56) becomes

$$\tau(p) = 2 \int_p^\infty \frac{\sigma(\chi) \left( \frac{dr(\chi)}{dp} \right) \chi d\chi}{\sqrt{\chi^2 - p^2}}, \quad (58)$$

and this can be inverted by using the Abel integral transform pair, c.f., (Jenkins *et al.*, 1993) to yield the absorptivity

$$\sigma(p) = -\frac{1}{\pi P} \left( \frac{dp(r)}{dr} \right) \frac{d}{dp} \int_p^\infty \frac{\tau(\xi) \xi d\xi}{\sqrt{\xi^2 - p^2}}. \quad (59)$$

It is customary to express the attenuation of a radio frequency signal in decibels relative to an unattenuated signal power level,  $W_0$

$$A(z) = 10 \log \frac{W_0}{W(z)} \quad (60)$$

The attenuation due to absorption is obtained by subtracting refractive defocusing attenuation and correcting for antenna mispointing

$$\tau(z) = A(z) - A_{\text{def}}(z) + A_{\text{corr}}(z), \quad (61)$$

where

$$A_{\text{def}}(z) = 10 \log \left( 1 - D(z) \frac{d\varepsilon(z)}{dz} \right), \quad (62)$$

and

$$D(z) = R_S(z) \cos(\alpha + \beta) + p(z) \tan \frac{\varepsilon(z)}{2}. \quad (63)$$

The value of the optical depth,  $\tau(z)$  is then

$$\tau(z) = A_a(z) \frac{\ln 10}{10} \simeq 0.23026 A_a. \quad (64)$$

When a profile of the absorptivity,  $\sigma(z)$  is obtained through the procedure outlined above, it can be used to infer the abundances of specific absorbers in the atmosphere, such as  $\text{NH}_3$  and  $\text{PH}_3$  in the atmosphere of Saturn, and the three frequencies available on Cassini will make it possible to determine their relative abundances. Radio occultation data from oblate or otherwise not spherically symmetrical bodies can also be inverted by applying raytracing techniques (Lindal, 1992; Melbourne *et al.*, 1994)

*2.5.2.2. Limb Tracking Maneuvers.* During an occultation experiment, monochromatic waves at X, S, and/or Ka bands are downlinked to earth by the spacecraft high-gain antenna, using the onboard ultrastable oscillator to maintain coherence. When a planetary body with an atmosphere begins to occult the spacecraft, the radio wave transmitted from the spacecraft to earth traverses the atmosphere and is refracted. In a neutral atmosphere, the molecular constituents raise the index of refraction above one, and the wave is refracted toward higher atmospheric densities, more or less inward along the potential gradient. In an ionosphere, the electrons dominate refraction, and decrease the index of refraction to less than one. In this case the wave is refracted away from high electron densities. In general, the ionospheric electron density does not increase monotonically with depth, and there can be isolated peaks in electron density. The refraction of radio waves away from these peaks can cause complicated diffraction patterns, leading to so-called multipath effects with different frequencies being detected simultaneously at earth (see e.g., Fjeldbo *et al.*, 1971; Hinson *et al.*, 1997).

The effects of the atmosphere on the index of refraction are small. In the neutral portion of the atmosphere, these are largest at the highest barometric pressures traversed by the radio waves. At the surface of Titan ( $\approx 1.5$  bar) or at the 1–2 bar level on Saturn, where  $\text{NH}_3$  will likely extinguish the received signal, the index of refraction deviates from 1 by only  $10^{-3}$ . In ionospheres, the differences are even smaller, typically  $10^{-6}$  at S-band for an electron densities of  $1 \times 10^5 \text{ cm}^{-3}$ , less at X and Ka wavelengths. (The change to the index of refraction induced by electrons is proportional to the square of the wavelength in the radio spectrum; in a neutral atmosphere, the change is independent of wavelength.) However, these

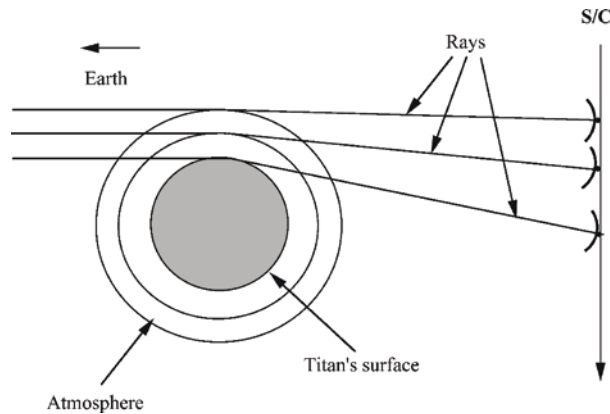


Figure 9. Idealized geometry for that portion of the entry phase of an occultation when the radio waves traverse the neutral portion of an atmosphere.

small differences, particularly in the neutral atmosphere, can induce large enough changes in the direction of the propagation of the radio wave and in its frequency in the earth-fixed frame of reference, relative to what would occur in the absence of the atmosphere, that an active strategy is required to avoid loss of the received signal.

Figure 9 illustrates an idealized geometry for that portion of the entry phase of an occultation when the radio waves traverse the neutral portion of an atmosphere. Here, the spacecraft moves on a trajectory perpendicular to the earth-spacecraft line of sight, but this does not materially affect the following discussion. During entry the radio waves, depicted as rays in the figure, progressively traverse deeper layers of the atmosphere, and the bending angle,  $\varepsilon$ , increases. At the surface of Titan, the bending angle amounts to  $2^\circ \approx 34$  mrad, and this is also comparable to that at the 2-bar level in Saturn's atmosphere. This angle is close to the full-width at half power of the S-band diffraction limited spacecraft high-gain antenna pattern, but much larger than those at X-band (9 mrad) and Ka-band (2 mrad, designed to be slightly defocussed from the diffraction limit).

Hence the spacecraft high-gain antenna must continuously track the virtual image of earth on the occulting limb in order to avoid loss of the signal. This is necessary not only to maintain lock in the Doppler tracking, but also to measure the signal intensity accurately. The observed attenuation is the sum of that from refractive defocusing and that from absorption by the atmosphere. The former results from the rays being refracted through larger angles as they successively lie deeper in the atmosphere (Figure 9). This can be computed once the Doppler shifts in frequencies from refraction in the atmosphere are determined. The absorption is the difference between the observed attenuation and that computed from defocusing. It is important to distinguish between variations in signal intensity from atmospheric effects and those associated with errors in maintaining the virtual image of earth in the boresight of the antenna beam. Inevitably errors in both spacecraft



pointing control (currently 2 mrad) and reconstruction (much smaller) arise during an occultation, and these need to be minimized.

The effects of refraction must also be taken into account when selecting the frequencies from the local oscillator to mix with the received signal at the DSN tracking station and the bandwidth to be used for the digitized recordings. The mixing must be done in order to convert the GHz frequencies of the received signal to the kHz, or audio-range, so that digitization of the signal is possible. From Figure 9, the Doppler shift in frequency from refraction is given approximately as:

$$\delta\nu = \nu_0 \frac{v}{c} \varepsilon \quad (65)$$

for small  $\varepsilon$  to first order in  $v/c$ , where  $v$  denotes the planetocentric spacecraft velocity component normal to the earth direction in the plane of refraction. For typical Titan occultations, this velocity is at most  $5.6 \text{ km s}^{-1}$ . With  $\varepsilon \approx 34 \text{ mrad}$ ,  $\Delta\nu/\nu \sim 6 \times 10^{-7}$ , or  $\Delta\nu \sim 1.5 \text{ kHz}$  at S-band.

Generating the local oscillator frequency record for the receiving station thus requires a model atmosphere for the occulting body to simulate the effects of refraction on the frequency shift, so as to maintain the mixed signal near the center of the audio-range recording bandwidth. The bandwidth itself is selected to account for navigation errors and actual variations in atmospheric properties from the model. Typically, this is chosen as conservatively as possible to minimize the possibility of signal loss without making the digitized recordings intractable. For example, Galileo radio occultations by Jupiter and its satellites were recorded with a 2.5-kHz bandwidth at S-band (see e.g., Hinson *et al.*, 1997; Kliore *et al.*, 1997). Voyager occultations of the outer planets and Titan were recorded at larger bandwidths, as these atmospheres were less well characterized at the time: 5–25 kHz was typical at S-band, with the exception of 50 kHz for Saturn, because of the wider bandwidth required for the adjacent occultation of its rings (Lindal *et al.*, 1981, 1983, 1985a, b, 1987, Lindal, 1992).

### 2.5.3. Major Requirements

As in the case of ring occultations, the quality of atmospheric and ionospheric occultation data depends on the phase and amplitude stability of the three radio links, the signal-to-noise ratio available on these links, and the orbital geometry which defines the occultation locations on the target body and their characteristics. Since atmospheric and ionospheric occultations will be conducted only in the one-way mode, the discussion of the USO stability and the SNR in Section 2.4.3 applies equally here. The requirements on the orbital geometry are given below.

The requirements for Saturn occultations are as follows:

1. A sufficient number of Saturn occultations well spaced in latitude in both the Northern and the Southern hemispheres. This is needed to provide data on zonal wind speeds at different altitudes and latitudes, as well as to sample the ionosphere structure and the ammonia abundance at different latitudes.

The requirements for Titan occultations are:

1. A sufficient number of Titan occultations well spaced in latitude in both hemispheres to provide data for the derivation of the global zonal circulation of Titan's atmosphere.
2. An adequate sampling of the ionosphere at different locations relative to the magnetospheric ram direction.
3. Occultations that are not fast enough to require the use of thrusters to carry out the limb-tracking maneuvers (Section 2.5.2.2).

### 3. Radio Science Instrument

#### 3.1. OVERVIEW

Among the Cassini instruments, the radio science instrument is unique in that is not confined to the spacecraft, and that part which is on the spacecraft is distributed among several subsystems. It can be regarded as a solar-system-sized instrument observing at microwave frequencies, with one end of the radio path on the spacecraft and the other end at DSN stations on the ground.

##### 3.1.1. *Functional Description*

Figure 10 shows a functional block diagram abstracting those elements of the Cassini orbiter and the DSN that make up the radio science instrument. The instrument operates in two fundamental ways, distinguished by whether the microwave optical path has one or two legs.

For two-way measurements, the uplink can be a single carrier signal at either X-band ( $\sim 7.2$  GHz) or Ka-band ( $\sim 34$  GHz), or both carriers can be transmitted at the same time. These signals are generated by the DSN receiver/exciter system, using as a reference the local frequency and timing system. The DSN frequency standard is a combination of a Hydrogen Maser and a Sapphire Cavity Oscillator. The uplink signals are amplified, radiated through feed horns, and collimated by a large parabolic ground antenna, which is continuously aimed at the Cassini spacecraft. The actual transmission frequencies can be adjusted to allow the spacecraft receivers to lock to the uplink signals and to compensate, finite steps, for the main part of the Doppler effect between the earth and the Cassini Orbiter. In this mode spacecraft radio equipment forms a repeater, collecting the carrier signal with the spacecraft's high gain antenna (HGA), transforming it to one or more downlink frequencies (2.3 GHz, 8.4 GHz, or 32 GHz) that are coherent with the uplink, amplifying and re-collimating it, and sending it back to earth. The returning signal is detected using DSN ground receiving equipment, amplified and downconverted, and recorded for later analysis. In a variant of the two-way mode, the downlink is received at a different ground station; this three-way technique has been found very

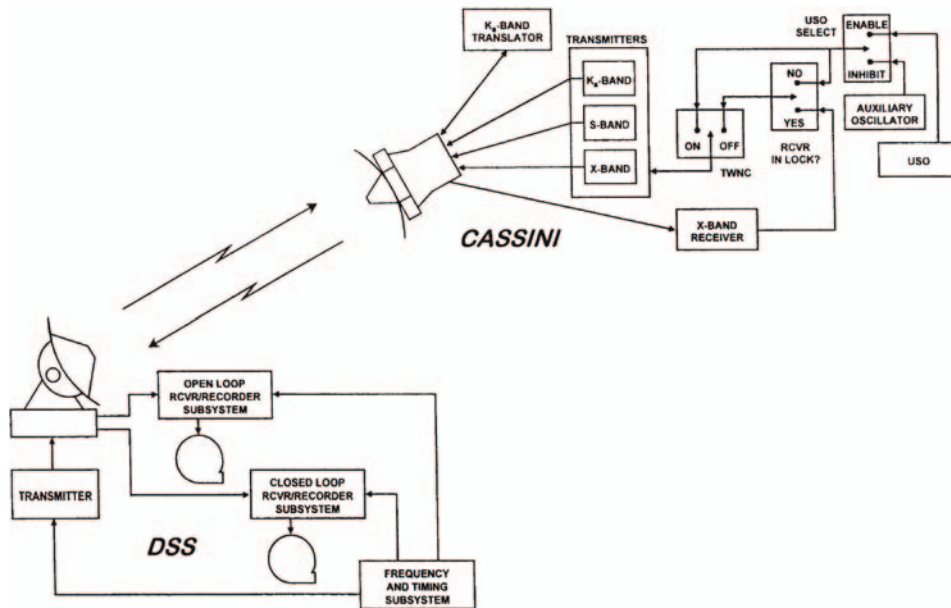


Figure 10. The distributed radio science instrument.

useful to isolate anomalous noise sources and to improve the science return from most of the radio science experiments.

For one-way measurements, the signal source is on board the Cassini orbiter. The output from on-board ultrastable oscillator (USO) is transformed to down-links at S-band (2.3 GHz), X-band (8.4 GHz), or Ka-band (32 GHz) by elements in the radio frequency subsystem (RFS) and radio frequency instrument subsystem (RFIS). These signals are amplified and radiated through the HGA toward earth. After passing through the medium of interest, the perturbed signal is collected by a DSN antenna, amplified and downconverted, and recorded for later analysis.

### 3.1.2. Measurements

The scientific observables are phase, frequency, and amplitude perturbations on the S-, X-, and Ka-band signals that are transmitted between the spacecraft and the ground. These perturbations are induced by:

- passage through atmospheres, ionospheres, plasmas, and populations of particles (rings);
- gravitational accelerations of the spacecraft caused by nearby masses;
- relativistic effects.

Because the perturbations induced by the phenomena under investigation are very small, it is essential that sources of obscuring noise be minimized. The

contribution of the Doppler effect due to the spacecraft and ground antenna motions must be removed, which is a key step in the processing of the data. In the spacecraft and ground equipment, this means that all components have to preserve as much dimensional and electrical stability as can be accomplished within mass, power, and environmental constraints. The key characteristics of the radio frequency (RF) signals have to be maintained over short and long integration times. Short-term stability is generally measured as phase noise. Stability over longer integration times is described by the so-called Allan deviation parameter  $\sigma_y$ , a statistical measure of contiguous differences of frequency measurements. In general, the requirements are that phase noise be  $\geq 60$  dB below the carrier in the frequency bands where radio science measurements are made, and that the Allan deviation range from  $2 \times 10^{-13}$  at 1-second integration time to  $1 \times 10^{-15}$  at 1000-second integration time.

Investigations dealing with the composition, chemistry, and dynamics of planetary atmospheres and ionospheres use the instrument in its one-way mode at all three downlink frequencies. Ring studies and measurement of general relativistic time delay during solar conjunction are also conducted using the non-coherent mode. Data samples for these experiments are integrated over short times ( $\leq 1$ –100 s), where the USO-driven signal provides the best stability. In the one-way mode, measurements can be started immediately after the spacecraft emerges from behind a planet or satellite. Using the one-way mode avoids potential lock up problems associated with a deep egress atmospheric occultation. The one-way path also avoids complications that would be introduced into data analysis by two passages, separated in time and space, through the target under study.

Two-way Doppler experiments in cruise and during the tour use the same link system, X-band and Ka-band (when available) uplink and downlink. An additional observable is provided by the possibility of locking to the X-band uplink an additional Ka-band carrier downlink as shown in the Riley report (Riley *et al.*, 1990). This will allow essentially complete calibration of the plasma contribution to the noise, which is the crucial factor in two way experiments, especially during conjunction experiments, when the signal propagates through the heavily ionized and turbulent medium of the solar corona. This is a necessary condition for the coherent reconstruction of the signal over the long duration of the experiment.

### 3.2. SPACECRAFT ELEMENTS

On the Cassini Orbiter, the radio science instrument is encompassed in the radio science subsystem (RSS). RSS is really a virtual subsystem in that it is composed of elements from three spacecraft subsystems, two of which have other functions to perform as well. The subsystems that participate in RSS are the RFIS, the RFS, and the Antenna Subsystem. Figure 11 illustrates the elements of the subsystems that make up RSS, and the RF paths through the instrument that are involved in

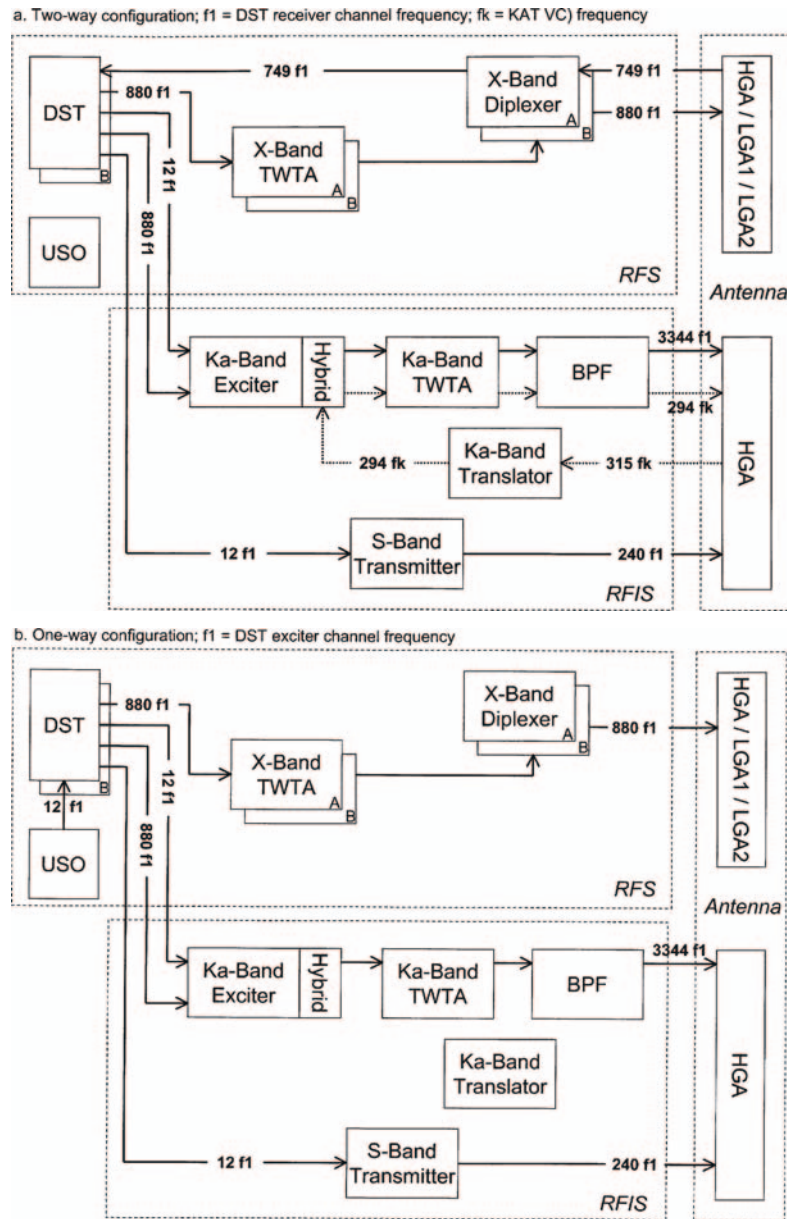


Figure 11. Radio frequency paths through the Cassini Orbiter radio science subsystem for two-way configuration (a) and one-way configuration (b).

its various operational modes. Figure 11a shows the signal paths available when the instrument is in two-way configuration, while Figure 11b shows those for the one-way configuration. In each case the active signal paths and subassemblies are depicted in bold.

### 3.2.1. *Radio Frequency Subsystem*

The primary function of the RFS, a redundant critical engineering subsystem, is to support spacecraft telecommunications. RFS receives commands and transmits telemetry at X-band; its carrier is also the source of the X-band downlink signals used by radio science. For radio science purposes, the key components are the USO, the deep space transponders (DSTs) and the X-band traveling wave tube amplifiers (X-TWTAs).

The RFS has three modes of operation:

- two-way coherent mode, where the receiver in the DST is locked to the uplink and the downlink is referenced to, or coherent with, that uplink;
- two-way noncoherent mode, where the receiver is locked to the uplink and the exciter in the DST is referenced to either the USO or the transponder's auxiliary oscillator; and
- one-way mode, where there is no uplink and the exciter is referenced to either the USO or the transponder's auxiliary oscillator.

When RSS is operating in two-way mode, RFS is in its two-way coherent mode. The active DST receives a 7.2 GHz uplink signal from the HGA or one of the two low gain antennas (LGAs), amplifies it, and translates it by the ratio 880/749 into an 8.4 GHz downlink. The precise frequency of the uplink of course depends on the Doppler shift experienced in its transit from the ground. The DSTs are capable of locking onto a signal as low as -155.8 dBm. The DST also generates input signals, coherent with the uplink, for the S-band transmitter (SBT) and the Ka-band exciter (KEX) in the RFIS. For the SBT, a single input at 115 MHz is supplied. The KEX receives input at 8.4 GHz and a reference signal at 115 MHz.

For one-way radio science experiments, RFS will be in either one-way or two-way noncoherent mode. The USO (the DST's auxiliary oscillator is not stable enough to use for radio science) provides a 115 MHz input to the DST exciter, which multiplies it to 8.4 GHz for the X-band downlink and for the 8.4 GHz input to the KEX. The SBT input and the 115 MHz reference signal for the KEX are sent directly from the USO.

Cassini's USO is a crystal oscillator based on a carefully selected 4.8 MHz quartz resonator, which is housed along with its oscillator circuit and oven control circuit in a titanium Dewar whose internal temperature is maintained constant to within 0.001°C by a proportionally controlled oven. The USO's 114.9 MHz output provides a reference signal for the DST, SBT, and KEX that has exceptional short-term phase and frequency stability.

The X-band downlink from the DST is amplified by the X-TWTA to 15.8 W, and radiated to earth through the HGA or whichever of the two LGAs is active. X-band is the only frequency available to radio science when the spacecraft is not using the HGA.



### 3.2.2. *Radio Frequency Instrument Subsystem*

The elements in the RFIS are devoted exclusively to radio science. They include the SBT, the KEX, the Ka-band Translator (KAT) and the Ka-band TWTA (K-TWTA). Primary application of the SBT and the KEX is in one-way experiments, though the KEX will also be used in two-way (X-up, Ka-down) mode. The SBT transmits a 13.5W, 2.3 GHz carrier derived from the 115 MHz reference provided by the DST, through a diplexer contained in the probe receiver front end (RFE), to the HGA. The KEX multiplies its 115 MHz reference by 11/3, mixes the result with its 8.4 GHz input, and multiplies by 4 to produce 32 GHz. That output is routed through a hybrid coupler contained in the KEX subassembly to the K-TWTA.

Used only in two-way mode, the KAT turns a 34 GHz uplink signal from the HGA into a coherent 32-GHz downlink using a 14/15 translation ratio. The translator is capable of generating a downlink with 1000-second Allan deviation of  $3 \times 10^{-15}$  from input signals as low as  $-132$  dBm. KAT output goes through the hybrid coupler in the KEX subassembly and then to the K-TWTA. Amplification of Ka-band output from both the KEX and the KAT, singly or simultaneously, is accomplished in the K-TWTA. The amplifier produces a total output power of 7.2 W when operating with one carrier and 5.7 W in dual-carrier mode. Like the SBT, it feeds the HGA only.

### 3.2.3. *High Gain Antenna*

While all the Cassini Orbiter antennas are usable at X-band, only the HGA transmits all the radio science frequencies. In addition to supporting telecommunications and radio science, the HGA also serves as the transmit and receive antenna for the Cassini Radar and for the probe relay link. It is the most complex antenna ever flown on a planetary spacecraft, functioning at S-band, X-band, Ka-band, and Ku-band. Its functions are illustrated in Figure 12. The portions used for radio science experiments or in-flight tests are highlighted.

Carrier signals transmitted between the spacecraft and the ground are all circularly polarized. X-band signals are received and transmitted with right-hand circular polarization through the RFS A-string diplexer and with left-hand circular polarization through the B-string diplexer. The Ka-band uplink is left-hand circularly polarized, the downlink right-hand circularly polarized. The S-band downlink is right-hand circularly polarized. The S-band transmit signal path is shared between the probe relay link and radio science.

## 3.3. GROUND ELEMENTS

### 3.3.1. *Deep Space Network*

The DSN comprises three complexes around the globe, called the deep space communication complexes (DSCC), located in the desert of Southern California, near Madrid, Spain, and near Canberra, Australia. Each complex is equipped with several tracking stations of different aperture size and different capabilities. Each



### ANTENNA SUBSYSTEM FUNCTIONAL BLOCK DIAGRAM

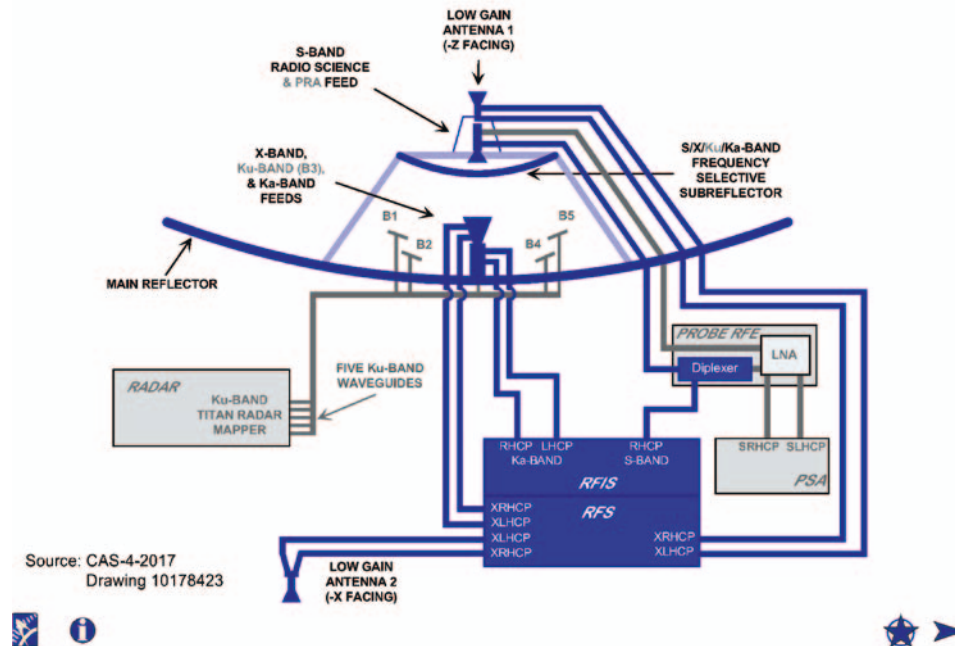


Figure 12. The Cassini antenna subsystem, with radio science functions emphasized.

complex has one 70-m diameter station, one 34-m high-efficiency (HEF) station, and at least one 34-m beam-wave-guide (BWG) station. Though their primary functions are to send commands to and to receive telemetry from space probes, these complexes have been designed to be an integral part of the radio science instrument (Asmar and Renzetti, 1993). As such, their performance and proper calibration directly determine the accuracy of Radio science experiments. The following subsystems of the DSN stations are relevant to acquisition of radio science data (see Figure 13): the monitor and control subsystem, the antenna mechanical subsystem, microwave subsystem, receiver–exciter subsystem, transmitter subsystem, tracking subsystem, spectrum processing subsystem, and frequency and timing subsystem.

The monitor and control subsystem receives and archives information sent to the complex from the control center at JPL. It also handles and displays responses to directives for configuration or information. Operator control consoles at the complex central processing center allow centralized control of all station subsystems within that complex. The center receives and distributes schedules of activities, sequence of events, prediction files for pointing the antennas and tuning the receivers, and other information.

The antenna surface performs two functions. As part of the receiving function, it acts as a large aperture to collect incoming energy transmitted from a spacecraft and

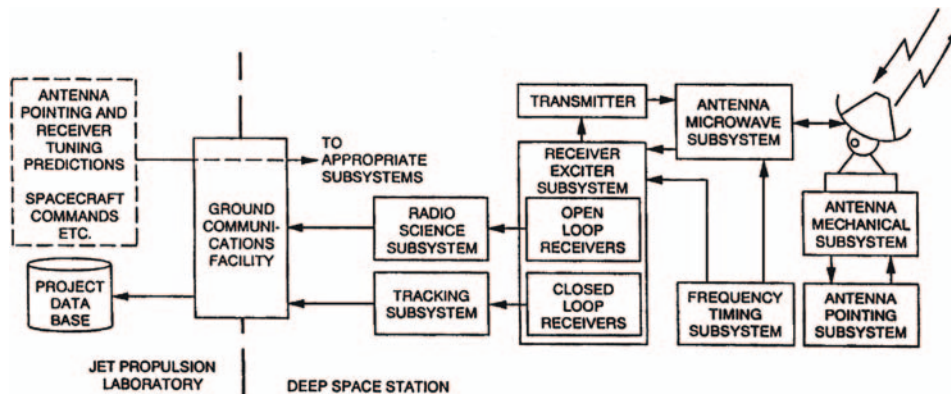


Figure 13. DSN subsystems relevant to the acquisition of radio science data.

focus it onto the feed horns. The subreflector is adjustable in the axial and angular positions in order to correct for gravitational deformation due to the motion of the antenna between zenith and the horizon. The primary surface is a paraboloid, modified for optimized illumination and signal stability. As part of the transmitting function, the antenna surface is used to form a narrow microwave beam that is directed to the spacecraft.

The electronics handles the received signal in two main steps. First the microwave subsystem accepts the S-, X-, and/or Ka-bands (depending on the station) and directs them via polarizer plates and microwave mirrors to low-noise amplifiers. Then the amplified signals are downconverted by local oscillators and routed to the receivers. These two processes set the electronics contribution to the overall amplitude sensitivity (usually measured as system noise temperature) and frequency/phase stability (generally quantified in terms of Allan deviation and phase noise respectively).

Two types of receivers (part of the receiver–exciter system) can be used: closed-loop and open-loop. (The distinction is that the closed-loop receiver estimates parameters such as phase and amplitude in real time with standardized values of receiver bandwidths and time constants; the open-loop receivers record the pre-detection electric field for subsequent non-real time processing.) The closed-loop receiver (Block V Receiver) is the primary DSN receiver for telemetry and tracking data. It phase-locks to the signal carrier and demodulates science data, engineering data, and ranging signals transmitted by the spacecraft. The tracking subsystem measures Doppler shifts and ranging information based on the closed-loop receiver output.

The open-loop receiver (called the radio science receiver) downconverts and digitizes a selected bandwidth of the spectrum centered around the carrier signal. It utilizes a fixed first local oscillator and a tunable second local oscillator that is driven by a tuning “predict set” (predicted downlink frequency versus time) that

takes into account the relative motion between the spacecraft and ground station. The predict set can also take into account the atmospheric effects of the planet under study. With no real-time signal detection requirements, the open-loop system provides flexibility in post-processing of the data. It is also designed with stringent requirements on amplitude, frequency and phase noise stability. Additional advantages of the open-loop reception include the simultaneous handling of signals in two polarization states as well as capturing multiple signals resulting from multipath propagation between the spacecraft transmission and the earth reception.

The transmitter subsystem utilizes a frequency reference to synthesize the uplink frequency channel assigned to a specific spacecraft. It also has the capability to tune the uplink to account for the Doppler shift on the uplink. The DSN can transmit at S-, X- or Ka-bands depending on the transmitting station and the receiving spacecraft. A record of the transmitted frequencies is saved for post-processing of the two-way Doppler observable, as necessary.

The frequency and timing subsystem provides a reference that drives the local oscillator devices throughout the complex. Global positioning system (GPS) satellites are utilized for inter-complex timing calibration. Currently centered on hydrogen masers, the frequency and timing system will be upgraded to include additional devices to meet the Cassini requirements including a linear trapped ions standard with a cryogenic local oscillator and a feedback-stabilized frequency distribution. Performance of the frequency and timing subsystem to fractional frequency stabilities of order  $10^{-15}$  for integration times of 1000 s, as well as phase noise lower than  $-75$  dBc at 100 Hz from a Ka-band carrier, is fundamental to many radio science observations.

### 3.3.2. 70-m Stations

The 70-m diameter stations of the DSN (DSS-14, DSS-63, and DSS-43) are currently equipped for transmission at the S-band frequencies and reception at S- and X-band frequencies. Future upgrades to transmit at X-band are possible. The microwave subsystem allows reception at both polarizations such that the right circular polarization (RCP) and left circular polarization (LCP) components of each band can be received via the radio science System. Accurate pointing of the 70-m stations is achieved by either active conical scanning or via blind pointing, driven by predictions of the spacecraft's position on the sky. It is anticipated that the 70-m stations will be used for occultation and other experiments requiring S-band reception from the Cassini spacecraft. The new BWG stations in Spain and Australia also may be used for occultation measurements.

### 3.3.3. Beam Wave-Guide Stations

The 34-m diameter BWG stations have been recently added to the DSN. Several BWG stations will exist at the California DSCC and one station each will be at the Spanish and Australian complexes. It is anticipated that only one BWG station will be instrumented for transmission and reception at Ka-band frequencies. This

station in California (DSS-25) was developed to meet stringent Radio Science requirements on all of its components, including special structural and pointing requirements unique to a high-precision two-way Ka-band capability. In time for Saturn's tour, it is expected that Ka-band downlink will be available at 34-m BWG stations DSS-54 and DSS-34 in Spain and Australia, respectively.

#### 3.3.4. *High-Efficiency Stations*

The 34-meter diameter high-efficiency DSN stations (DSS-15, DSS-65, and DSS-45) are equipped for transmission at X-band and are optimized for reception at X-band. The microwave and receiver subsystems allow for the reception of two channels simultaneously. The station pointing capabilities and strategies are similar to those of the 70-m stations.

#### 3.3.5. *Media Calibration System*

The earth's atmosphere contributes phase and amplitude noise to a spacecraft radio signal received at a ground station. A system to calibrate the effects of the atmosphere on the phase of the microwave signal is under development especially for Cassini radio science experiments utilizing Ka-band, where excellent end-to-end frequency and phase stability is required. The purpose of this media calibration system is to provide a line-of-sight calibration of the water vapor delay (responsible for most of the atmosphere induced phase fluctuations at microwave frequencies) during DSS-25 radio science experiment passes. It will also provide estimates of the total zenith delay and delay fluctuation. This will be accomplished via several components of the system. An advanced water vapor radiometer will sense the number of water vapor molecules along the line-of-sight, a microwave temperature profiler will sense the vertical temperature distribution, a surface meteorology package will measure the temperature, pressure, and humidity, and a GPS receiver will provide the total zenith delay estimates.

#### 3.3.6. *Other Stations*

The utility of stations other than those of NASA's DSN has been proven for several radio science experiments on past missions. For example, arraying of different antennas has improved the signal strength coming from an extremely distant spacecraft (as during the Voyager Neptune encounter, where Australian and Japanese stations also recorded the received signals in collaboration with the ight project and science team.)

More recently, the contribution of an Italian station and a Japanese station has proven valuable to the radio science experiments on the Ulysses mission. These stations are normally equipped with a dual S- and X-bands receiver and a hydrogen maser frequency standard in order to perform very long baseline interferometry studies. Adding a dedicated instrument to these radio telescopes made it possible to measure the phase and amplitude of the S- and X-band carrier signals transmitted from Ulysses. This instrument, called a digital tone extractor, has been used at

both the Medicina 32-m parabola in Italy and at the Kashima observatory in Japan. Medicina successfully participated in the three measuring campaigns of the 1991, 1992 and 1993 opposition and conjunction experiments made with Ulysses. The operation started with the transfer of trajectory information from JPL to the station where pointing coordinates and the downlink Doppler shifts were computed. The acquired data were comparable in quality to the DSN data for those experiments.

The information collected at these two stations enabled the sampling of a propagation path across a substantially different region of the troposphere and ionosphere than those of the DSN stations. Furthermore, the data were useful in understanding the DSN-acquired data at times of unusual behavior of the signal or equipment.

The availability of non-DSN stations, capable of operation up to Ka-band and available for limited times during specific mission events, has become crucial since existing plans allow for only one DSN station (DSS-25, discussed earlier) expressly dedicated to the Cassini radio science experiments at Ka-band. The possible future availability of an Italian station, located more than  $120^\circ$  away in longitude from Goldstone, would almost double the tracking time at Ka-band for Cassini. This could significantly improve the integration time for gravitational wave experiments, as well as benefit other radio science research. Availability of such non-DSN stations might open new opportunities during the cruise and tour phase of the Cassini mission, in addition to reducing the tracking load on the DSN under critical conditions.

#### **4. Conclusion**

At the time this paper is being written, a partial check-out of the radio science instrument indicates very good performance, and scientific data were obtained during the flybys of Venus and Earth. The investigators are working at planning future observations and looking forward to successful cruise and tour experiments.

#### **Acknowledgments**

The Radio Science instrumentation on the Cassini Orbiter represents a truly global effort, with contributions from organizations all over the world. The DST was developed for JPL by Motorola. Both X-band and Ka band TWTAs were provided by Hughes Electronics; the Ka band TWTA utilized a design developed from research done at NASA Lewis Research Center. The USO was designed and built by the Johns Hopkins University Applied Physics Laboratory. The KEX was designed and built at JPL. The SBT and KAT were provided by the Italian firm Alenia Spazio for our partner, the Italian Space Agency (ASI), and Alenia Spazio integrated and tested the RFIS. The Radio-Science Team wishes to particularly thank B. Bertotti, now retired from the Radio Science Team, for his important efforts leading to Cassini's superb radio system, his work on the cruise experiments, and his work in preparation for the Tour.

We also thank the Cassini engineers in JPL's Radio Science Systems Group: Aseel Anabtawi, Elias Barbinis, Don Fleischman, Gene Goltz, Randy Herrera, Trina Ray, and the personnel of the DSN for their efforts and support of the experiments described in this paper. The Radio Science Team thanks G. Comoretto, F. B. Estabrook, J. Lunine, M. Tinto, and R. Woo for discussions and collaborations.

## References

- Achterberg, R. K. and Flasar, F. M.: 1996, *Icarus* **119**, 359–369.
- Allison, M. D.: 1990, *Icarus* **83**, 282–307.
- Anderson, J. D., Armstrong, J. W., and Lau, E. L.: 1993, *ApJ* **408**, 287–292.
- Anderson, J. D., Sjogren, W. L., and Schubert, G.: 1996a, *Science* **272**, 709–712.
- Anderson, J. D., Lau, E. L., Sjogren, W. L., Schubert, G., and Moore, W. B.: 1996b, *Nature* **384**, 541–543.
- Anderson, J. D., Lau, E. L., Sjogren, W. L., Schubert, G., and Moore, W. B.: 1997a, *Nature* **387**, 264–266.
- Anderson, J. D., Lau, E. L., Sjogren, W. L., Schubert, G., and Moore, W. B.: 1997b, *Science* **276**, 1236–1239.
- Armstrong, J. W.: 1989, Schutz, B. (ed.), *Gravitational Wave Data Analysis*, Kluwer, Dordrecht, 153–172.
- Armstrong, J. W.: 1998, *Radio Science* **33**, 1727–1738.
- Armstrong, J. W., Iess, L., Tortora, P., and Bertotti, B.: 2003, *Astrophysics J.* **599**, 806–813.
- Asmar, S. W., and Renzetti, N. A.: 1993, *JPL Publication 80-93 Rev. 1*, Jet Propulsion Laboratory, Pasadena, California.
- Aswar, S. W., Armstrong, J. W., Iess, L., and Tortora, P.: 2004, *Radio Science* (submitted).
- Augstein, E.: 1978, Shaw, D. B. (ed.) *Meteorology Over the Tropical Oceans*, Royal Meteorological Society, pp. 73–103.
- Bender, P., Brillet, A., Ciufoloni, I., Cruise, A. M., *et al.*: 1998, *Pre-Phase A Report (Second Edition)*, Max-Planck-Institut fur Quantenoptik, Garching, MPQ 233.
- Bertotti B., and Giampieri, G.: 1992, *Class. Quantum Grav.* **9**, 777–793.
- Bertotti B., Comoretto, G., and Iess, L.: 1993, *Astron. Astrophys.* **269**, 608–616.
- Bertotti, B., Ambrosini, R., Armstrong, J. W., Asmar, S., Comoretto, G., Giampieri, G. *et al.*: 1995, *Astron. Astrophys.* **296**, 13–25.
- Bertotti, B.: 1997, Francaviglia, M., *et al.* (eds.), *Proceedings of 14th International Conference on General Relativity and Gravitation*, World Scientific, Singapore, New Jersey, London, Hong Kong, pp. 79–101.
- Bertotti, B., Iess, L., and Tortora, P.: 2003, A test of general Relativity using Radio Links with the Cassini spacecraft, *Nature*, **425**, 374–376.
- Bertotti B., and Giampieri, G.: 1998, *Solar Physics* **178**, 85–107.
- Bertotti B., Vecchio, A., and Iess, L.: 1999, *Phys. Rev. D* **5908**(8), 2001.
- Bird, M. K., Dutta-Roy, R., Asmar, S. W., and Rebold, T. A.: 1997, *Icarus* **130**, 426–436.
- Borderies, N., Balmino, G., Castel, L., and Moynot, B.: 1980, *Moon Planet.* **22**, 191–200.
- Borderies, N., Goldreich, P., and Tremaine, S.: 1982, *Science* **299**, 209–211.
- Borderies, N., Goldreich, P., and Tremaine, S.: 1983a, *Astron. J.* **88**, 226–228.
- Borderies, N., Goldreich, P., and Tremaine, S.: 1983b, *Astron. J.* **88**, 1560–1568.
- Borderies, N., Goldreich, P., and Tremaine, S.: 1983c, *Icarus* **53**, 84–89.
- Borderies, N., Goldreich, P., and Tremaine, S.: 1983d, *Icarus* **55**, 124–132.
- Borderies, N., Goldreich, P., and Tremaine, S.: 1984a, *Astrophys. J.* **284**, 429–434.



- Borderies, N., Goldreich, P., and Tremaine, S.: 1984b, Greenberg, R. and Brahic, A., (eds.), *Planetary Rings*, University of Arizona Press, Tucson, pp. 713–734.
- Borderies, N., Goldreich, P., and Tremaine, S.: 1985, *Icarus* **63**, 406–420.
- Borderies, N., Goldreich, P., and Tremaine, S.: 1986, *Icarus* **68**, 522–533.
- Borderies, N., and Longaretti, P.-Y.: 1987, *Icarus* **72**, 593–603.
- Borderies, N., Goldreich, P., and Tremaine, S.: 1988, *Icarus* **80**, 344–360.
- Borderies, N.: 1992, Ferraz-Mello, S., (eds.), *Proceedings of IAU Symposium No. 152, 'Chaos, Resonance and Collective Dynamical Phenomena in the Solar System'* (Angra Dos Reis, Brazil, July 15–19, 1991), Kluwer Academic Publishers: Dordrecht, pp. 53–64.
- Borderies-Rappaport, N., and Longaretti, P.-Y.: 1994, *Icarus* **107**, 129–141.
- Bosh, A. S. and Olkin, C. B.: 1996, *Bull. Am. Astron. Soc.* **28**, 1124–1124.
- Broadfoot, A. L., *et al.*: 1981, *Science* **212**, 206–211.
- Brouwer, D. and Clemence, G. M.: 1961, *Methods of Celestial Mechanics*, Academic Press, New York.
- Buratti, B. J.: 1988, *Icarus* **75**, 113–126.
- Caldwell, J.: 1977, Burns, J., (ed.), *Planetary Satellites*, University of Arizona Press, Tucson, pp. 438–450.
- Campbell, J. K., and Anderson, J. D.: 1989, *Astron. J.* **97**, 1485–1495.
- Capone, L. A., Whitten, R. C., Dubach, J., Prasad, S. S., and Huntress, W. T.: 1976, *Icarus* **28**, 367.
- Cassen, P. M., Peale, S. J., and Reynolds, R. T.: 1982, Morrison, D., (ed.), *Satellites of Jupiter*, University of Arizona Press, Tucson, pp. 193–128.
- Cohen, E. R., and Taylor, B. N.: 1987, *Rev. Mod. Phys.* **59**, 1121–1148.
- Conrath, B. J., Gautier, D., Hanel, R. A., and Hornstein, J. S.: 1984, *Astrophys. J.* **282**, 807–815.
- Conrath, B. J., and Gautier, D.: 2000, *Icarus* **144**, 124–134.
- Conrath, B. J., and Pirraglia, J. A.: 1983, *Icarus* **53**, 286–292.
- Courtin, R., Gautier, D., and McKay, C. P.: 1995, *Icarus* **114**, 114–162.
- Coustonis, A., Lellouch, E., Maillard, J.-P., and McKay, C. P.: 1994, *Bull. Am. Astron. Soc.* **26**, 1181.
- Coustonis, A., and B. Bézard: 1995, *Icarus* **115**, 126–140.
- Cravens, T. E.: 1987, *J. Geophys. Res.* **92**, 11083.
- Cuzzi, J. N., Lissauer, J. J., and Shu, F. H.: 1981, *Nature* **292**, 703–707.
- Cuzzi, J. N., Lissauer, J. J., Esposito, L. W., Holberg, J. B., Marouf, E. A., Tyler, G. L. *et al.*: 1984, Greenberg, R. and Brahic, A., (eds.), *Planetary Rings*, University of Arizona Press, Tucson, pp. 73–199.
- Cynn, H. C., Boone, S., Koumvakalis, A., Nicol, M., and Stevenson, D. J.: 1989, *Proceedings of the 19th Lunar and Planetary Science Conference*, pp. 443–441.
- Damour T. and Nordtvedt, K.: 1993, *Phys. Rev. Lett.* **70**, 2217–2219.
- Danielson, R. E., Caldwell, J., and Larach, D. R.: 1973, *Icarus* **20**, 437–443.
- Davies, M. E., Abalakin, V. K., Lieske, J. H., Seidelmann, P. K., Sinclair, A. T., Sinzi, A. M. *et al.*: 1983, *Cel. Mech.* **29**, 309–321.
- Davies, M. E., Abalakin, V. K., Bursa, M., Lieske, J. H., Morando, B., Morrison, D. *et al.*: 1996, *Cel. Mech.* **63**, 127–148.
- Dermott, S. F., and Thomas, P. C.: 1994, *Icarus* **109**, 241–257.
- Elliot, J. L., Frogel, J., Elias, J., Glass, I., French, R. G., Mink, D. J. *et al.*: 1981, *Astron. J.* **86**, 127–134.
- Elliot, J. L., French, R. G., Frogel, J., Elias, J., Mink, D. J., and Liller, W.: 1981, *Astron. J.* **86**, 444–455.
- Elliot, J. L., Elias, J. H., French, R. G., Frogel, J., Liller, W., Matthews, K. *et al.*: 1983, *Icarus* **56**, 202–208.
- Elliot, J. L., French, R. G., Meech, K. J., and Elias, J. H.: 1984, *Astron. J.* **89**, 1587–1603.
- Elliot, J. L., Glass, I. S., French, R. G., and Kangas, J. A.: 1987, *Icarus* **71**, 91–102.



- Elliot, J. L., Bosh, A. S., Cooke, M. L., Bless, R. C., Nelson, M., Percival, J. W. *et al.*: 1992, *EOS Trans. Am. Geophys. U.* **73**(14), 176.
- Eshleman, V. R., Tyler, G. L., Wood, G. E., Lindal, G. F., Anderson, J. D., Levy, G. S., *et al.*: 1979a, *Science* **204**, 976–978.
- Eshleman, V. R., Tyler, G. L., Wood, G. E., Lindal, G. F., Anderson, J. D., Levy, G. S., *et al.*: 1979b, *Science* **206**, 959–962.
- Eshleman, V. R.: 1983, *Science* **221**, 361–364.
- Eshleman, V. R., Breakwell, J. V., Tyler, G. L., and Marouf, E. A.: 1983, *Icarus* **54**, 212–226.
- Esposito, L. W., Borderies, N., Goldreich, P., Cuzzi, J. N., Holberg, J. B., Lane, A. L., Pomphrey, R. B., Terrile, R. J., Lissauer, J. J., Marouf, E. A., and Tyler, G. L.: 1983, *Science* **222**, 57–60.
- Esposito, L. W., Cuzzi, J. N., Holberg, J. B., Marouf, E. A., Tyler, G. L., and Porco, C. C.: 1984, Gehrels, T. and Matthews, M. S., (eds.), *Saturn*, University of Arizona Press, Tucson, pp. 463–545.
- Esposito, L. W., Brahic, A., Burns, J. A., and Marouf, E. A.: 1991, *Uranus*, pp. 439–447.
- Estabrook, F. B., and Wahlquist, H. D.: 1975, *Gen. Rel. Grav.* **6**, 439–447.
- Estabrook, F. B.: 1978, Neugebauer, M. and Davies, R. W. (eds.), *A Close-Up of the Sun*, JPL Publication 78–70, Pasadena, pp. 441–449.
- Eubanks, T. M., Matsakis, D. N., Martin, J. O., Archinal, B. A., Fey, A. L., Josties, F. J., *et al.*: 1997, *Joint APS/AAPT Meeting*, Washington April, D.C. 18–21, Paper K11.05.
- Fjeldbo, G.: 1964, *Report No. SU-64-025*, Stanford Electronics Laboratories, Stanford, CA.
- Fjeldbo, G., Eshleman, V. R., Garriott, O. K., and Smith, F. L., III: 1965, *J. Geophys. Res.* **70**, 3701–3710.
- Fjeldbo, G., and Eshleman, V. R.: 1968, *Planet. Space Sci.* **16**, 1035–1059.
- Fjeldbo, G., Kliore, A. J., and Eshleman, V. R.: 1971, *Astron. J.* **76**, 123.
- Fjeldbo, G., Kliore, A. J., Seidel, B. L., Sweetnam, D. N., and Cain, D. L.: 1975, *Astron. and Astrophys.* **39**, 91–96.
- Fjeldbo, G., Kliore, A. J., Sweetnam, D. N., Esposito, P. B., Seidel, B. L., and Howard, H. T.: 1976a, *Icarus* **29**, 439–444.
- Fjeldbo, G., Kliore, A. J., Seidel, B. L., Sweetnam, D. N., and Woiceshyn, P. M.: 1976b, Gehrels, T. (ed.), *Jupiter*, The University of Arizona Press, Tucson, Arizona, pp. 238–246.
- Flasar, F. M., Samuelson, R. E., and Conrath, B. J.: 1981, *Nature* **292**, 693–698.
- Flasar, F. M.: 1983, *Science* **221**, 55–57.
- Flasar, F. M.: 1998a, *Planet Space Sci.* **46**, 1109–1124.
- Flasar, F. M.: 1998b, *Planet Space Sci.* **46**, 1125–1147.
- Flasar, F. M., Hinson, D. P., Kliore, A. J., Schinder, P. J., Twicken, J. D., Herrera, R. G., *et al.*: 1998, ‘Galileo radio occultation measurements of Jupiter’s highly variable Ionosphere’, in International Symposium The Jovian System after Galileo – The Saturnian System before Cassini-Huygens, Nantes, France.
- Flasar, F. M. *et al.*: 2004, Exploring the Saturn system in the thermal infrared: The composite infrared spectrometer. *Space Sci. Rev.* **115**, 169–297.
- Fox, J. L., and Yelle, R. V.: 1997, *Geophys. Res. Lett.* **24**, 2179.
- French, R. G., Elliot, J. L., and Allen, D. A.: 1982, *Nature* **298**, 827–828.
- French, R. G., Kangas, J. A., and Elliot, J. L.: 1986a, *Science* **231**, 480–483.
- French, R. G., Elliot, J. L., and Levine, S. E.: 1986b, *Icarus* **67**, 134–163.
- French, R. G., Jones, T. J., and Hyland, A. R.: 1987, *Icarus* **69**, 499–505.
- French, R. G., Elliot, J. L., French, L. M., Kangas, J. A., Meech, K. J., Ressler, M. E., *et al.*: 1988, *Icarus* **73**, 349–378.
- French, R. G., Clark, M. A., Tollestrup, E., Robinson, E., Harvey, P., Heilman, L., *et al.*: 1989, *Bull. Am. Astron. Soc.* **21**, 928.
- French, R. G., Chanover, N. J., Clark, M. A., Tollestrup, E., and Baron, R. L.: 1990, *Bull. Am. Astron. Soc.* **22**, 1069–1070.

- French, R. G., Nicholson, P. D., Porco, C. C., and Marouf, E. A.: 1991, *Uranus*, 327–409.
- French, R. G., Nicholson, P. D., Cooke, M. L., Elliot, J. L., Matthews, K., Perković, O., *et al.*: 1993, *Icarus* **103**, 163–214.
- Friedson, A. J.: 1994, *Icarus* **109**, 40–57.
- Gan, L., Keller, C. N., and Cravens, T. E.: 1992, *J. Geophys. Res.* **97**, 12.
- Gautier, D., *et al.* 1981.
- Goldreich, P., and Tremaine, S.: 1978a, *Icarus* **34**, 240–253.
- Goldreich, P., and Tremaine, S.: 1978b, *Astrophys. J.* **222**, 850–858.
- Goldreich, P., and Tremaine, S.: 1979a, *Astrophys. J.* **233**, 857–871.
- Goldreich, P., and Tremaine, S.: 1979b, *Astron. J.* **84**, 1638–1641.
- Goldreich, P., and Tremaine, S.: 1979c, *Nature* **277**, 97–99.
- Goldreich, P., and Tremaine, S.: 1980, *Astrophys. J.* **241**, 425–441.
- Goldreich, P., and Tremaine, S.: 1981, *Astrophys. J.* **243**, 1062–1075.
- Goldreich, P., Tremaine, S., and Borderies, N.: 1986, *Astron. J.* **92**, 490–494.
- Goldreich, P., Rappaport, N., and Sicardy, B.: 1995, *Icarus* **118**, 414–417.
- Grasset, O., and Sotin, C.: 1996, *Icarus* **123**, 101–112.
- Gresh, D. L., Rosen, P. A., Tyler, G. L., and Lissauer, J. J.: 1986, *Icarus* **68**, 481–502.
- Gresh, D. L., Marouf, E. A., Tyler, G. L., Rosen, P. A., and Simpson, R. A.: 1989, *Icarus* **78**, 131–168.
- Griffith, C. A.: 1993, *Nature* **364**, 511–514.
- Griffith, C. A., and Zahnle, K.: 1995, *Geophys. J. Res.* **100**, 16, 907–16,922.
- Grossman, A. W., Muhleman, D. O., and Berge, G. L.: 1990, *Science* **245**, 1211–1215.
- Grossman, A. W., and Muhleman, D. O.: 1992, *Bull. Am. Astron. Soc.* **24**, 954.
- Guillot, T., Chabrier, G., Morel, P., and Gautier, D.: 1994, *Icarus* **112**, 354–367.
- Habbal, S. R., Woo, R., Fineschi, S., O’Neal, R., Kohl, J., Noci, G., *et al.*: 1997, *Astrophys. J.* **489**, L103–L106.
- Han, B., and Owen, T.: 1994, *Bull. Am. Astron. Soc.* **26**, 1181.
- Hanel, R. A., Conrath, B., Flasar, F. M., Kunde, V., Maguire, W., Pearl, J., Pirraglia, J., Samuelson, R., Herath, L., Allison, M., Cruikshank, D., Gautier, D., Gierasch, P., Horn, L., Koppany, R., and Ponnampertuma, C.: 1981, *Science* **212**, 192–200.
- Hanel, R. A., Conrath, B. J., Kunde, V. G., Pearl, J. C., and Pirraglia, J. A.: 1983, *Icarus* **53**, 262–285.
- Hanninen, J., and Salo, H.: 1994, *Icarus* **108**, 325–346.
- Hanninen, J., and Salo, H.: 1995, *Icarus* **117**, 435–438.
- Haugstad, B. S.: 1978, *Radio Sci.* **13**, 435–440.
- Hinson, D. P., Flasar, F. M., Kliore, A. J., Schinder, P. J., Twicken, J. D., and Herrera, R. G.: 1977, *Geophys. Res. Lett.* **24**, 2107–2110.
- Hinson, D. P., and Tyler, G. L., *et al.*: 1983, *Icarus* **54**, 337–352.
- Hinson, D. P., and Magalhães, J. A.: 1991, *Icarus* **94**, 64–91.
- Hinson, D. P., and Magalhães, J. A.: 1993, *Icarus* **105**, 142–161.
- Hinson, D. P., Flasar, F. M., Kliore, A. J., Schinder, P. J., Twicken, J. D., and Herrera, R. G.: 1997, *Geophys. Res. Lett.* **24**, 2107–2110.
- Hinson, D. P., Twicken, J. D., and Karayel, E. T.: 1998a, *J. Geophys. Res.* **103**, 9505–9520.
- Hinson, D. P., Kliore, A. J., Flasar, F. M., Twicken, J. D., Schinder, P. J., and Herrera, R. G.: 1998, *J. Geophys. Res. Space Phys.* **103**, 29343–29357.
- Holberg, J. B., Nicholson, P. D., French, R. G., and Elliot, J. L.: 1987, *Astron. J.* **94**, 178–188.
- Howard, H. T., Tyler, G. L., Fjeldbo, G., Kliore, A. J., Levy, G. S., Brunn, D. L., *et al.*: 1974a, *Science* **183**, 1297–1301.
- Howard, H. T., Tyler, G. L., Fjeldbo, G., Kliore, A. J., Levy, G. S., Brunn, D. L., *et al.*: 1974b, *Science* **185**, 179–180.
- Hubbard, W. B., and Anderson, J. D.: 1978, *Icarus* **33**, 336–341.
- Hubbard, W. B.: 1984, *Planetary Interiors*, Van Nostrand Reinhold Company, New York

- Hubbard, W. B., Porco, C. C., Hunten, D. M., Rieke, G. H., Rieke, M. J., McCarthy, D. W., *et al.*: 1993, *Icarus* **103**, 215–234.
- Hubbard, W.B., Guillot, T., Marley, M. S., Burrows, A., Lunine, J. I., and Saumon, D. S: 1999, Plan. Space Sci., submitted.
- Hunten, D. M.: 1978, Hunten, D. M and Morrison, D. (eds.), *The Saturn System*, NASA Conf. Publ. 2068, pp. 127–140.
- Iess, L., and Armstrong, J. W.: 1997, Ciufolini, I. and Fidecaro, F. (eds.), *Proceedings of the Conference on Gravitational Waves: Sources and Detectors*, Cascina, Italy, 19–23 March 1996, World Scientific, 323–343
- Iess, L., Giampieri, G., Anderson, J. D., and Bertotti, B.: 1999, *Clas. Quantum Grav.* **16**, 14870–1502.
- Ip, W. H.: 1990, *Astropys. J.* **362**, 354.
- Jacobson, R. A.: 1996, *Bull. Am. Astron. Soc.* **28**, 1185.
- Jenkins, J. M., Steffes, P. G., Twicken, J. D., Hinson, D. P., and Tyler, G. L.: 1994, *Icarus* **110**, 79–94.
- Johnson, R. E., Killeen, R. M., Waite, J. H., Jr., and Lewis, W. S.: 1998, *Geophys. Res. Lett.* **25**, 3,257–3,260.
- Jones, T. D., and Lewis, J. S.: 1987, *Icarus* **72**, 381–393.
- Karayel, E. T., and Hinson, D. P.: 1997, *Radio Sci.* **32**, 411–423.
- Kaula, W. M.: 1964, *Rev. Geophys.* **2**, 661–685.
- Keller, C. N., Cravens, T. E., and Gan, L.: 1992, *J. Geophys. Res.* **97**, 12117–12135.
- Keller, C. N., Cravens, T. E., and Gan, L.: 1994, *J. Geophys. Res.* **99**, 6511–6525.
- Keller, C. N., Anicich, V. G., and Cravens, T. E.: 1998, *Planet. Space Sci.* **46**, 1157–1174.
- Kliore, A. J., Cain, D. L., and Hamilton, T. W.: 1964, *Determination of Some Physical Properties of the Atmosphere of Mars from Changes in the Doppler Signal of a Spacecraft on an Earth – Occultation Trajectory*, No. T. R.. 32-674, Jet Propulsion Laboratory, Pasadena, CA.
- Kliore, A. J., Cain, D. L., Levy, G. S., Eshleman, V. R., Fjeldbo, G., and Drake, F. D.: 1965, *Science* **149**, 1243–1248.
- Kliore, A. J., Levy, G. S., Cain, D. L., Fjeldbo, G., and Rasool, S. I.: 1967, *Science* **158**, 1683–1688.
- Kliore, A. J., Fjeldbo, G., Seidel, B. L., and Rasool, S. I.: 1969, *Science* **166**, 1393–1397.
- Kliore, A. J., Cain, D. L., Fjeldbo, G., Seidel, B. L., and Rasool, S. I.: 1972a, *Icarus* **12**, 484–516.
- Kliore, A. J.: 1972b, Colin, L. (ed.), *The Mathematics of Profile Inversion*, NASA TM X-62,150, NASA Ames Research Center, Moffett Field, CA, pp. 3-2–3-17.
- Kliore, A. J., Cain, D. L., Fjeldbo, G., Seidel, B. L., and Rasool, S. I.: 1974, *Science* **183**, 323–324.
- Kliore, A. J., Fjeldbo, G., Seidel, B. L., Sweetnam, D. N., Sesplaukis, T. T., Woiceshyn, P. M., *et al.*: 1975, *Icarus* **24**, 407–410.
- Kliore, A. J., Woiceshyn, P. M., and Hubbard, W. B.: 1976, *Geophys. Res. Lett.* **3**, 113–116.
- Kliore, A. J., Woiceshyn, P. M., and Hubbard, W. B.: 1977, Pergamon Press, Oxford and New York, pp. 703–710.
- Kliore, A. J., Patel, I. R., Nagy, A. F., Cravens, T. E., and Gombosi, T. I.: 1979, *Science* **205**, 99–102.
- Kliore, A. J., Patel, I. R., Lindal, G. F., Sweetnam, D. N., Hotz, H. B., Waite, J. H., Jr., *et al.*: 1980a, *J. Geophys. Res.* **85**, 5857–5870.
- Kliore, A. J., and Patel, I. R.: 1980, *J. Geophys. Res.* **85**, 7957–7962.
- Kliore, A. J., Lindal, G. F., Sweetnam, D. N., Hotz, H. B., and McDonough, T. R.: 1980b, *Science* **207**, 446–449.
- Kliore, A. J., and Patel, I. R.: 1982, *Icarus* **52**, 320–334.
- Kliore, A. J., and Mullen, L. F.: 1989, *J. Geophys. Res.* **94**, 13339–13351.
- Kliore, A. J., and Luhmann, J. G : 1991, *J. Geophys. Res.* **96**, 21281–21289.
- Kliore, A. J., Hinson, D. P., Flasar, F. M., Nagy, A. F., and Cravens, T. E.: 1997, *Science* **277**, 355.
- Kliore, A. J.: 1998a, Andersen, J. (ed.), *Andersen Highlights in Astronomy*, International Astronomical Union, pp.1065–1069.
- Kliore, A. J., Herrera, R. G., Hinson, D. P., Twicken, J. D., Flasar, F. M., and Schinder, P. J.: 1998b, 30th DPS Meeting, Madison, WI.

- Kolosov, M. A., Yakovlev, O. I., Yakovleva, G. D., Efimov, A. I., Trusov, B. P., Timofeyava, T. S., *et al.*: 1975, *Cosmic Res.* **13**, 46.
- Kolosov, M. A., Yakovlev, O. I., Matyugov, S. S., Timofeyava, T. S., Yakovleva, G. D., and Kalashnikov, I. E.: 1976, *Cosmic Res.* **16**, 221.
- Kozai, Y.: 1957, *Ann. Tokyo Obs. Ser.* **25**, 73.
- Lane, A. L., Hord, C. W., West, R. A., Esposito, L. W., Coffeen, D. L., Sato, M., Simmons, K. E., Pomphrey, R. B., and Morris, R. B.: 1982, *Science* **215**, 537–543.
- Lellouch, E., Coustenis, A., Gautier, D., Raulin, F., Dubouloz, N., and Frère, C.: 1989, *Icarus* **79**, 328–349.
- Lemmon, M. T., Karkoschka, E., and Tomasko, M.: 1993, *Icarus* **103**, 329–332.
- Lewis, J. S., and Prinn, R. G.: 1980, *Astrophys. J.* **238**, 357–364.
- Lin, D. N. C., and Bodenheimer, P.: 1981, *Astrophys. J. Lett.* **248**, L83–L86.
- Lindal, G. F., Hotz, H. B., Sweetnam, D. N., Shippony, Z., Brenkle, J. P., Hartsell, G. V., *et al.*: 1979, *J. Geophys. Res.* **84**, 8443–8456.
- Lindal, G. F., Wood, G. E., Levy, G. S., Anderson, J. D., Sweetnam, D. N., Hotz, H. B., *et al.*: 1981, *J. Geophys. Res.* **86**, 8721–8727.
- Lindal, G. F., Wood, G. E., Hotz, H. B., Sweetnam, D. N., Eshleman, V. R., and Tyler, G. L.: 1983, *Icarus* **53**, 348–363.
- Lindal, G. F., Sweetnam, D. N., and Eshleman, V. R.: 1985, *Astron. J.* **90**, 1136–1146.
- Lindal, G. F., Sweetnam, D. N., and Eshleman, V. R.: 1985a, *J. Geophys. Res.* **92**, 14987–15001.
- Lindal, G. F., Sweetnam, D. N., and Eshleman, V. R.: 1985b, *Astron. J.* **90**, 1136–1146.
- Lindal, G. F., Lyons, J. R., Sweetnam, D. N., Eshleman, V. R., D P. Hinson, and Tyler, G. L.: 1987, *J. Geophys. Res.* **92**, 14987–15001.
- Lindal, G. F.: 1992, *Astron. J.* **103**, 967–982.
- Lissauer, J. J., Shu, F. H., and Cuzzi, J. N.: 1982., Brahic, A., (ed.), *Proceedings of IAU Colloquium 75, 'Planetary Rings' (Toulouse, France, August 1992)*, Cepadues Editions, Toulouse, pp. 385–392.
- Longaretti, P.-Y., and Borderies, N.: 1986, *Icarus* **67**, 211–223.
- Longaretti, P.-Y., and Borderies, N.: 1991, *Icarus* **94**, 165–170.
- Longaretti, P.-Y., and Rappaport, N.: 1995, *Icarus* **116**, 376–396.
- Lorenz, R. D., McKay, C. P., and Lunine, J. L.: 1997, *Science* **275**, 642–644.
- Love, A. E. H.: 1906, *A Treatise on the Mathematical Theory of Elasticity*, Cambridge University Press, Cambridge
- Lukkari, J.: 1981, *Nature* **292**, 433–435.
- Lunine, J. I., and Stevenson, D. J.: 1987, *Icarus* **70**, 61–77.
- Lunine, J. I.: 1996, Ambrosini, R. (ed.), *Proceedings of The Cassini-Huygens Mission: The Exploration of the Saturn System, (Bologna, Italy, November 19–22, 1996)*, Arti Grafiche S. Marcello srl: Roma, 14.
- Majeed, T., and McConnell, J. C.: 1996, *J. Geophys. Res.* **101**, 7589.
- Marouf, E. A., Tyler, G. L. and Eshleman, V. R.: 1982, *Icarus* **49**, 161–193.
- Marouf, E. A., and Tyler, G. L.: 1982, *Science* **217**, 243–245.
- Marouf, E. A., Tyler, G. L., Zebker, H. A., Simpson, R. A., and Eshleman, V. R.: 1983, *Icarus* **54**, 189–211.
- Marouf, E. A., and Tyler, G. L.: 1985, *Adv. Space Res.* **5**, 117–120.
- Marouf, E. A., Tyler, G. L., and Rosen, P. A.: 1986, *Icarus* **68**, 120–166.
- Marouf, E. A., and Tyler, G. L.: 1986, *Nature* **323**, 31–35.
- Marouf, E. A., Gresh, D. L., and Tyler, G. L.: 1987, *Bull. Am. Astron. Soc.* **19**, 883.
- Marouf, E. A.: 1994, *Bull. Am. Astron. Soc.* **26**, 1150.
- Marouf, E. A.: 1996, *Bull. Am. Astron. Soc.* **28**, 1126.
- Marouf, E. A.: 1997, *Bull. Am. Astron. Soc.* **29**, 1000.
- McElroy, M. B.: 1973, *Space Sci. Rev.* **14**, 460.

- McKay, C. P., Pollack, J. B., and Courtin, R.: 1989, *Icarus* **80**, 23–53.
- Melbourne, W. G., Davis, E. S., Duncan, C. B., Hajj, G. A., Hardy, K. R., Kursinski, E. R., *et al.*: 1994, *The Application of Spaceborne GPS to Atmospheric Limb Sounding and Global Change Monitoring*, JPL Pub. 94-18, Jet Propulsion Laboratory, California Institute of Technology, Pasadena, CA.
- Michel, F. C.: 1982, *Astrophys. Lett.* **22**, 101–102.
- Muhleman, D. O., Grossman, A. W., Butler, B. J., and Slade, M. A. 1990, *Science* **248**, 975–980.
- Muhleman, D. O., Grossman, A. W., Slade, M. A., and Butler, B. J.: 1992, *Bull. Am. Astron. Soc.* **24**, 954.
- Muller, P. M., and Sjogren, W. L.: 1968, *Science* **161**, 680–684.
- Nagy, A. F., and Cravens, T. E.: 1998, *Planet. Space Sci* **46**, 1149–1156.
- Newell, A. C., and Baird, R. C.: 1965, *J. Appl. Phys.* **36**, 3751–3759.
- Newman, M., Schubert, G., Kliore, A. J., and Patel, I. R.: 1984, *J. Atmos. Sci.* **41**, 1901–1913.
- Nicholson, P., and Porco, C.: 1988, *J. Geophys. Res.* **93**, 209.
- Niemann, H. B., Atreya, S. K., *et al.*: 1996, *Science* **272**, 848–849.
- Phinney, R. A., and Anderson, D. L.: 1968, *J. Geophys. Res.* **73**, 1819.
- Plescia, J. B., and Boyce, J. M.: 1982, *Nature* **295**, 285–290.
- Porco, C., Nicholson, P. D., Borderies, N., Danielson, G. E., Goldreich, P., Holberg, J. B., *et al.*: 1984, *Icarus* **60**, 1–16.
- Porco, C. C., and Nicholson, P. D.: 1987, *Icarus* **72**, 437–467.
- Prentice, A. J. R.: 1980, *JPL Publication*, 80–80.
- Prentice, A. J. R.: 1984, *Earth Moon Planets* **30**, 209–228.
- Rappaport, N.: 1994, *JPL Interoffice Memorandum* 314.6-1549.
- Rappaport, N.: 1995, *JPL Interoffice Memorandum* 312.D-95-105.
- Rappaport, N., Bertotti, B., Giampieri, G., and Anderson, J. D.: 1997, *Icarus* **126**, 313–323.
- Rappaport, N.: 1998, *Icarus* **132**, 36–42.
- Reasenberg, R. D., Shapiro, I. I., MacNeil, P. E., Goldstein, R. B., Breidenthal, J. C., Brenkle, J. P., Cain, D. L., *et al.*: 1979, *Astrophys. J.* **234**, L219–L221.
- Riley, A. L., Antsos, S., Armstrong, J., Kinman, P., Wahlquist, H., Bertotti, B., *et al.*: 1990, *Cassini Ka-band Doppler and Enhanced Telecommunications System Study*, Report jointly sponsored by NASA and ASI.
- Rosen, P. A.: 1989, *Waves in Saturn's Rings Probed by Radio Occultation*, Ph.D. Dissertation, Stanford University, Stanford, CA.
- Rosen, P. A., and Lissauer, J. J.: 1988, *Science* **241**, 690–694.
- Rosen, P. A., Tyler, G. L., and Marouf, E. A.: 1991a, *Icarus* **93**, 3–24.
- Rosen, P. A., Tyler, G. L., and Marouf, E. A.: 1991b, *Icarus* **93**, 25–44.
- Sagan, C., and Dermott, S. F.: 1982, *Nature* **300**, 731–733.
- Samuelson, R. E., Hanel, R. A., Kunde, V. G., and Maguire, W. C.: 1981, *Nature* **292**, 688–693.
- Samuelson, R. E.: 1983, *Icarus* **53**, 364–387.
- Samuelson, R. E., Nath, N. R., and Borysow, A.: 1997, *Planet. Space Sci.* **45**, 959–980.
- Savich, N. A., *et al.*: 1986, *Radiotekhnika i Elektronika* **31**, 2113.
- Schubert, G., Limonadi, D., Anderson, J. D., Campbell, J. K., and Giampieri, G.: 1994, *Icarus* **111**, 433–440.
- Schubert, G., Limonadi, D., Anderson, J. D., Campbell, J. K., and Giampieri, G.: 1994, *Icarus* **111**, 433–440.
- Schunk, R. W. and Nagy, A. F.: 2000, *Ionospheres: Physical, Plasma and Chemical Processes*, Cambridge University Press, Cambridge.
- Showalter, M. R., Cuzzi, J. N., Marouf, E. A., and Esposito, L. W.: 1986, *Icarus* **66**, 297–323.
- Shu, F. H., Cuzzi, J. N., and Lissauer, J. J.: 1983, *Icarus* **53**, 185–206.
- Shu, F. H.: 1984, in: Greenberg, R. and Brahic, A., (eds.), *Planetary Rings*, University of Arizona Press, Tucson, pp. 513–561.

- Simpson, R. A., Tyler, G. L., Marouf, E. A., Zebker, H. A., and Eshleman, V. R.: 1984, *IEEE Trans. Geosci. Remote Sens.* **22**, 656–665.
- Smith, B. A., Soderblom, L., Batson, R., Bridges, P., Inge, J., Masursky, H., *et al.*: 1982, *Science* **215**, 504–537.
- Smith, P. H., Lemmon, M. T., Caldwell, J. J., Allison, M. D., and Sromovsky, L. A.: 1994, *Bull. Am. Astron. Soc.* **26**, 1181.
- Sohl, F., Sears, W. D., and Lorenz, R. D.: 1995, *Icarus* **115**, 278–294.
- Stevenson, D. J.: 1992, *Proceedings of Symposium on 'Titan' (Toulouse, France, 9–12 September 1991)*, ESA Publication: #338, pp. 29–33.
- Strobel, D. F., Hall, D. T., Zhu, X., and Summers, M. E.: 1993, *Icarus* **103**, 333–336.
- Sundstrom, G., *et al.*: 1994, *Science* **263**, 785–787.
- Synnott, S. P., Peters, C. F., Smith, B. A., and Morabito, L. A.: 1981, *Science* **212**, 191–192.
- Thorne, K. S.: 1987, Hawking, S., and Israel, W. (eds.), *300 Years of Gravitation*, Cambridge University Press, Cambridge, pp.330–458.
- Tinto, M. and Armstrong, J. W.: 1991, *Ap. J.* **372**, 545–553.
- Tinto, M. and Armstrong, J. W.: 1998, *Phys. Rev. D*, **58** 042002.
- Tortora, P., Iess, L., and Ekelund, J. E.: 2003, The Cassini multifrequency link performance during 2002 Solar Conjunction Proceedings, IEEE Aerospace Conference, Big Sky, Montana, March 8–15, 2003.
- Tortora, P., Iess, L., Bordi, J. J., Ekelund, J. E., and Roth, D.C.: Precise Cassini Navigation during Solar Conjunctions through multifrequency plasma calibrations, *J. Guidance, Control and Dyn.* **27**, 251–257.
- Tyler, G. L., Eshleman, V. R., Anderson, J. D., Levy, G. S., Lindal, G. F., Wood, G. E., *et al.*: 1981, *Science* **212**, 201–206.
- Tyler, G. L., Eshleman, V. R., Anderson, J. D., Levy, G. S., Lindal, G. F., Wood, G. E., *et al.*: 1982, *Science* **215**, 553–558.
- Tyler, G. L., Marouf, E. A., Simpson, R. A., Zebker, H. A., and Eshleman, V. R.: 1983, *Icarus* **54**, 160–188.
- Tyler, G. L., Sweetnam, D. N., Anderson, J. D., Campbell, J. K., Eshleman, V. R., Hinson, D. P., *et al.*: 1986, *Science* **233**, 79–84.
- Tyler, G. L.: 1987, *Proc. IEEE* **75**, 1404–1431.
- Tyler, G. L., Sweetnam, D. N., Anderson, J. D., E. Borutzki, Campbell, J. K., Kursinski, E. R., *et al.*: 1989, *Science* **246**, 1466–1473.
- Vervack, Jr, R. J., and Sandel, B. R.: 1998, *B.A.A.S.*, **30**.
- Vervack, Jr, R. J., Sandel, B. R., and Strobel, D. F.: 2004, *Icarus* **170**, 91–112.
- Wahlquist, H. D., Anderson, J. D., Estabrook, F. B., and Thorne, K. S.: 1977, *Atti dei Convegni Lincei* **34**, 335–350.
- Wahlquist, H. D.: 1987, *Gen. Rel. Grav.* **19**, 1101–1113.
- Waite J. A., Jr., and Cravens, T. E.: 1987, *Adv. Space Res.* **7**, 119.
- Ward, W. R.: 1981, *Geophys. Res. Lett.* **8**, 641–643.
- Will, C. M.: 1993, *Theory and Experiment in Gravitational Physics*, Cambridge University Press, Cambridge.
- Woo, R., and Habbal, S. R.: 1997, *Geophys. Res. Lett.* **24**, 1159–1162.
- Yakovlev, O. I., Matyugov, S. S., and Gubenko, V. N.: 1991, *Icarus* **94**, 493–510.
- Yelle, R. V: 1991, *Astrophys. J.* **383**, 380–400.
- Yung, Y. L., Allen, M., and Pinto, J. P.: 1984, *Ap. J. Supp.* **55**, 465–506.
- von Zahn, U., and Hunten, D. M.: 1996, *Science* **272**, 849–851.
- Zahnle, K., Pollack, J. B., D. Grinspon, and Dones, L.: 1992, *Icarus* **95**, 1–23.
- Zebker, H. A., Tyler, G. L., and Marouf, E. A.: 1983, *Icarus* **56**, 209–228.
- Zebker, H. A., and Tyler, G. L.: 1984, *Science* **223**, 396–398.
- Zebker, H. A., Marouf, E. A., and Tyler, G. L.: 1985, *Icarus* **64**, 531–548.



## RADAR: THE CASSINI TITAN RADAR MAPPER

C. ELACHI<sup>1,†</sup>, M. D. ALLISON<sup>2</sup>, L. BORGARELLI<sup>3</sup>, P. ENCRENAZ<sup>4</sup>, E. IM<sup>1</sup>,  
M. A. JANSSEN<sup>1</sup>, W. T. K. JOHNSON<sup>1</sup>, R. L. KIRK<sup>5</sup>, R. D. LORENZ<sup>6</sup>, J. I. LUNINE<sup>6</sup>,  
D. O. MUHLEMAN<sup>7</sup>, S. J. OSTRO<sup>1</sup>, G. PICARDI<sup>8</sup>, F. POSA<sup>9</sup>, C. G. RAPLEY<sup>10</sup>,  
L. E. ROTH<sup>1</sup>, R. SEU<sup>8</sup>, L. A. SODERBLOM<sup>5</sup>, S. VETRELLA<sup>11</sup>, S. D. WALL<sup>1,\*</sup>,  
C. A. WOOD<sup>12</sup> and H. A. ZEBKER<sup>13</sup>

<sup>1</sup>*Jet Propulsion Laboratory, California Institute of Technology, Pasadena, CA 91109, U.S.A.*

<sup>2</sup>*Goddard Institute for Space Studies, National Aeronautics and Space Administration, New York,  
NY 10025, U.S.A.*

<sup>3</sup>*Alenia Aerospazio, 00131 Rome, Italy*

<sup>4</sup>*Observatoire de Paris, 92195 Meudon, France*

<sup>5</sup>*U. S. Geological Survey, Flagstaff, AZ 86001, U.S.A.*

<sup>6</sup>*Lunar and Planetary Laboratory, University of Arizona, Tucson, AZ 85721, U.S.A.*

<sup>7</sup>*Division of Geological and Planetary Sciences, California Institute of Technology,  
Pasadena, CA 91125, U.S.A.*

<sup>8</sup>*Università La Sapienza, 00184 Rome, Italy*

<sup>9</sup>*Dip. Interateneo di Fisica, Politecnico di Bari, 70126 Bari, Italy*

<sup>10</sup>*British Antarctic Survey, CB3 0ET Cambridge, U.K.*

<sup>11</sup>*Facoltà di Ingegneria, 80125 Naples, Italy*

<sup>12</sup>*University of North Dakota, Grand Forks, ND 58202, U.S.A.*

<sup>13</sup>*Stanford University, Stanford, CA 94305, U.S.A.*

*\*(Author for correspondence: E-mail address: stephen.d.wall@jpl.nasa.gov)*

*†RADAR Team Leader*

(Received 23 January 1998; Accepted in final form 3 June 1999)

**Abstract.** The Cassini RADAR instrument is a multimode 13.8 GHz multiple-beam sensor that can operate as a synthetic-aperture radar (SAR) imager, altimeter, scatterometer, and radiometer. The principal objective of the RADAR is to map the surface of Titan. This will be done in the imaging, scatterometer, and radiometer modes. The RADAR altimeter data will provide information on relative elevations in selected areas. Surfaces of the Saturn's icy satellites will be explored utilizing the RADAR radiometer and scatterometer modes. Saturn's atmosphere and rings will be probed in the radiometer mode only. The instrument is a joint development by JPL/NASA and ASI. The RADAR design features significant autonomy and data compression capabilities. It is expected that the instrument will detect surfaces with backscatter coefficient as low as  $-40$  dB.

### 1. Introduction

The Cassini spacecraft, launched on October 15, 1997, carries a multimode Ku-band (13.8 GHz,  $\lambda 2.17$ -cm) radar instrument (RADAR) designed to probe Titan's surface and other targets in the Saturn system. It is distinguished by a number of novel features which accommodate the large geometric variations in flyby trajectories and the wide range of uncertainty in surface properties, and which efficiently utilize





the limited spacecraft resources such as the data rates, the data volumes, and power. This article describes the science objectives, operational modes, and general design of the RADAR; the description given here updates the report published previously (Elachi *et al.*, 1991).

The RADAR will investigate the surface of Titan using all four of its operational modes—imaging, altimetry, scatterometry, and radiometry. The radiometry and scatterometry will also be used to investigate other targets. The utility of radar imaging of solar-system objects, inaccessible to remote sensing at visible wavelengths has been demonstrated most dramatically by the success of the Magellan radar experiment at Venus (Johnson, 1991; Pettengill *et al.*, 1991; Saunders *et al.*, 1992). It has been known since the early 1960s (e.g. Pettengill *et al.*, 1962) that the cloud-shrouded surface of Venus is solid. The correspondence in the radar cross-sections between Venus and the Moon, Mars, and Mercury (see, e.g. Ostro, 1993) indicated a gross similarity—both compositional and morphological—of Venus' surface to the surfaces of the inner planets. The Arecibo and Goldstone radars had produced impressive images of the part of Venus that faces the Earth when the two planets are closest and hence when Venus radar echoes are strongest (see, e.g. Campbell *et al.*, 1983). Thus, even prior to the launch of the Magellan mission (and the Pioneer Venus and Venera 15/16 missions before) the expected return signal was fairly well understood and the results of the imaging operations anticipated. That situation does not prevail in the case of Titan, though some globally averaged radar reflectivity information exists.

Historically, the telescopic appearance of Titan has been compared to that of Mars and ascribed to the same physical causes. In the words of the discoverer of the atmosphere on Titan (Kuiper, 1944), “the color of Titan is orange, in marked contrast to Saturn and its other satellites or with Jupiter and its satellites. It seems likely that the color is due to the action of the atmosphere on the surface itself, analogous to the oxidation supposed to be responsible for the orange color of Mars.” The Voyager images confirmed that the ball of Titan was indeed orange but the color has been attributed to the suspended products of the photo- and radiation-induced dissociation of atmospheric methane. As far-fetched as the idea of Titan made of iron oxides may seem, it was justified by the density estimates current in Kuiper's time, which made Titan even denser than the Moon (see Table 2 in Kuiper, 1944). The post-Voyager value of Titan's density,  $1.88 \text{ g cm}^{-3}$  (Tyler *et al.*, 1981; Lindal *et al.*, 1983), allows for a silicate abundance comparable to or less than that of ices and organics together. The suspended aerosol particles represent one end state of the photolysis of methane, which also results in the escape of hydrogen from the planet. Post-Voyager estimates put the loss time of all the atmospheric methane at about 1% of the age of the solar system. To account for the supply of methane in the atmosphere, a family of models proposed to date require (or admit) the existence on the Titan's surface of a massive, perhaps global, methane reservoir, along with ethane, propane, and other hydrocarbons (Lunine *et al.*, 1983; Dubouloz *et al.*, 1989; Lunine and Rizk, 1989; Lunine, 1993). But the 1.7 dielectric constant of most light

hydrocarbons at 90 K (e.g. Straty and Goodwin, 1973; Sen *et al.*, 1992), implies that the reflectivity of an ethane–methane mixture is equal to 0.02. Titan, if it were indeed covered by a smooth, deep ethane–methane ocean, would generate a weak, specular, longitude-independent radar echo. The results of the  $\lambda$ 3.5-cm Goldstone/VLA Titan radar experiments indicate otherwise: Titan has been found to return a relatively strong, diffuse, and longitude-dependent echo (Muhleman *et al.*, 1990, 1992, 1993, 1995). On the average, Titan behaves in a manner similar to a Lambertian scatterer, with echoes returned by nearly the entire Earth-facing hemisphere. The radar cross-section peaks around longitude 90°W (Figure 16 in Muhleman *et al.*, 1995), suggesting that a sizeable segment of the Titan’s leading hemisphere is free of liquid hydrocarbons. Measurements of the  $\lambda$ 3.5-cm radio emission from Titan have yielded emissivity of  $0.88 \pm 0.03$ ; this corresponds to materials with the dielectric constant of  $2.9 \pm 0.6$  (Grossman and Muhleman, 1992). Taken alone, the  $\lambda$ 3.5-cm reflectivity and the angular scattering behavior of Titan are closer to those of Callisto than other radar-studied targets (Figure 17 in Muhleman *et al.*, 1995). When the circular polarization ratio (i.e., the ratio of the same-sense to the opposite-sense circularly polarized cross-sections),  $\mu_c$ , is also taken into account, the main-belt asteroid 4 Vesta, believed to have basaltic crust, emerges as the closest radar analog to Titan (Mitchell *et al.*, 1996; Figure 1). Kuiper erred in assessing the reasons for the optical appearance of Titan, but he seems to have anticipated Titan’s radar properties—perhaps for wrong reasons also. Contamination by silicates may be responsible for the Vesta-like radar characteristics of Titan, as might coating by solid photolytic debris. (For a review of the dielectric properties of higher hydrocarbons, see Thomson and Squyres, 1990.) As a consequence of the Goldstone/VLA measurements a global ocean on Titan should be seen as improbable, but discrete ethane–methane lakes or inland seas are by no means ruled out. Telescopic observations in the 0.9, 1.1, 1.3, 1.6, and 2.0  $\mu$ m methane windows confirm the apparent heterogeneity of Titan’s surface (Griffith *et al.*, 1991; Griffith, 1993; Lemmon *et al.*, 1993, 1995). Regional albedoes might be consistent with the presence of the water/ammonia ice and of an unspecified dark material—possibly the debris left behind by the methane photochemistry. The 0.9 and 1.1  $\mu$ m Hubble Space Telescope maps of Titan (Smith and Lemmon, 1993; Smith *et al.*, 1996) show a feature with an albedo of about 8% above the background, centered at the longitude of 110°W, and covering  $10^7$  km<sup>2</sup> (i.e. 10% of the total area of Titan). The feature is located on the surface itself and coincides with the source region of the strong Goldstone/VLA radar echoes (Figure 8 in Smith *et al.*, 1996). The demise of the notion of a global ocean makes the case for orbital imaging of Titan even more compelling. Given the contrast between the higher-permittivity “bedrock” and the lower-permittivity liquid hydrocarbons, detection of ethane–methane lakes in the RADAR data should be a straightforward matter.

The bright IR/radar feature has been referred to as a “continent,” but its actual physical nature is unknown. Neither an impact-related excavation of cleaner ice nor a volcanic resurfacing of the (presumably) tholin-coated bedrock are deemed to be

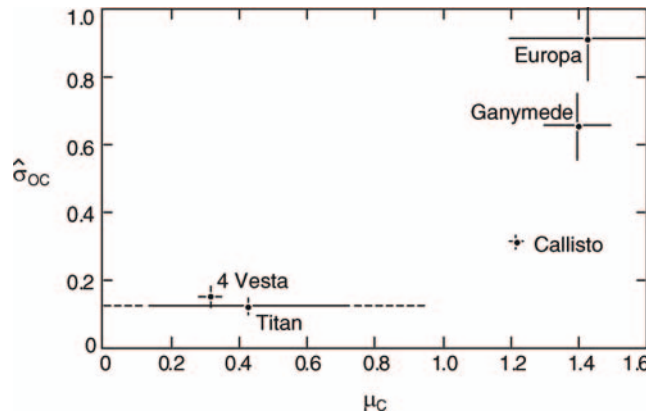


Figure 1. The  $\lambda 3.5$ -cm opposite-sense radar albedo,  $\sigma_{oc}$ , vs. the circular polarization ratio,  $\mu_c$ , for the Moon, Titan, 4 Vesta, Callisto, Europa, and Ganymede. Data sources: The Moon, Table 3 in Harmon and Ostro (1985) and Table 1 in Pettengill (1978); Vesta, Table 7 and Figure 11 in Mitchell *et al.* (1996); Callisto, Europa and Ganymede, Table 8 in Ostro *et al.* (1992). The value for the mean cross-section of Titan is from Muhleman *et al.* (1995), p. 369. The error bar on  $\mu_c$  for Titan was computed from data in Table 1 in Muhleman *et al.* (1995). Ganymede and Europa are included for comparison, as the objects with the most extreme radar properties.

the likely generation mechanism of the feature (Smith *et al.*, 1996). Since methane precipitation is possible on Titan (Toon *et al.*, 1988), and the associated limitations on the erosion rates are at least qualitatively understood (Lorenz, 1995a; Lorenz and Lunine, 1996), the bright feature has tentatively been identified as a topographic high exposed to the cleansing effect of methane rainfall (Smith *et al.*, 1996). Since that cleansing would wash away tholin deposits, the enhanced strength of the radar echo, returned presumably by clean (or cleaner) ice, could then be easily explained. The seasonal hemispheric brightness variability, the other telescopically observed phenomenon on Titan, is probably related to processes taking place well above the surface (Caldwell *et al.*, 1992; Lorenz *et al.*, 1997), and thus is of no immediate interest to RADAR.

## 2. Science Objectives

The overall science objectives of the Cassini mission include five Titan-specific objectives. Two of these—the determination of the physical state, topography, and composition of the Titan's surface; and the measurement of global temperatures and general circulation on Titan—constitute the overriding goal of the RADAR experiment. Whenever feasible, the RADAR will also conduct observations of the icy satellites, Saturn's rings, and Saturn itself. The Titan observations, however, constitute the highest scientific priority for the RADAR, and they drive its design.

## 2.1. TITAN

The general objective of the RADAR experiment is to carry out the first-order geological reconnaissance of Titan's surface and to derive a quantitative characterization of the surface. The approach is to use microwave radiation to penetrate opaque atmosphere, map the surface, and, combining RADAR data with the data from the Cassini optical remote sensing instruments, obtain a comprehensive understanding of Titan's physical condition. An important early objective is to acquire coverage of the Huygen's landing site. The purpose here is to give regional context to the data generated by the probe payload and particularly to the topography measurements from the probe's own (optical) imager and radar altimeter.

A global view of Titan and its geological and climatological history will result from mapping in all four RADAR modes. Special attention will be paid to the moon's cratering record. The crater size distribution, particularly as a function of elevation, will provide a constraint on the duration and extent of any episodes of atmospheric collapse (Engel *et al.*, 1995). Crater morphology is an indicator of subsurface structure and, by implication, of Titan's thermal history. The likelihood of surface liquids suggests that there may be hydroblemes (seabed impact craters) and tsunami deposits. Although only a fraction—about 25%—of Titan's surface will be mapped in the SAR mode, the long, thin coverage swaths are an efficient means of establishing the crater distribution—a large impact crater is more likely to be cut by a long, thin swath than by a square patch of the same area (Lorenz, 1995b).

The polar regions of Titan are also important targets for RADAR SAR imaging. The polar climate may have experienced more variability than the global average. The reason for this is that Titan's obliquity is fractionally larger than the Earth's, and although its present atmosphere damps out seasonal changes, a thinner past atmosphere may have allowed the polar temperatures to swing widely. A recent re-analysis of Voyager IR data suggests that the poles may experience more precipitation than the equatorial regions, raising the likelihood of surface liquids and erosional features. The seasonal effects on the polar hazes (Samuelson *et al.*, 1997) may also make these regions more difficult to observe at optical wavelengths.

The RADAR altimetry data will provide information on relative elevations along portions of the suborbital tracks. The SAR and altimetry data will be examined to seek evidence for the effects of crustal processes such as viscous relaxation and cryovolcanism. Volumes of the cryovolcanic constructs identified in the altimetry data, may indirectly constrain Titan's hydrocarbon budget, while morphometry of erosional features may provide information about the rates at which volatiles are recycled.

The high-resolution (350–720 m) SAR images will permit identification of features and terrain types that will be observed in varying locations on Titan and in different viewing geometries. RADAR scatterometer data will reveal the backscatter efficiency versus incidence angle for a large fraction of Titan's surface, although

the spatial resolution may be coarse (as in the radiometer mode). Nonetheless, scatterometer data will constrain surface slope distribution and the density of the uppermost decimeter of the surface. Scatterometer data will also be most similar to the data taken with the upgraded Arecibo radar during the coming decade and therefore will allow Titan's global radar properties to be defined in detail.

In its radiometric mode, RADAR will produce thermal emission (brightness temperature) maps of essentially the entire surface of Titan. To this end, the spacecraft will be commanded to execute spiral scanning maneuvers. The spiral scanning will be expanded in targeted areas by rolling the spacecraft about the  $z$ -axis. The emissivity and the integrated reflectivity are complementary (but anti-correlated) quantities. Because the radar backscatter that is measured by the instrument is also related (although weakly) to the integrated reflectivity, the radiometer data may be expected to provide additional information on the nature of Titan's surface. The radiometric brightness temperature and its dependence on polarization and angle of incidence will be used to discriminate among surfaces of smooth and broken ice fields, liquid hydrocarbon lakes, and ice coated with organic precipitates from the atmosphere. Specifically, we will augment the interpretation of the active-modes RADAR data by constraining large-scale (10–30 km) surface composition from dielectric properties measured along radar tracks. Emissivity (as well as radar reflectivity) of a given substance is a strong function of the density; thus an emissivity map can be interpreted as a surface density map. We hope to discriminate between ice and snow or rock and soil in this way. A procedure which is being developed to interpret the RADAR radiometry data will also be used to model observations of comet Wirtanen with the Microwave Instrument for the Rosetta Orbiter (MIRO). Finally, taking advantage of the repeated opportunities to collect radiometer data over the entire disk of Titan, we will investigate global circulations and thermal transport by determining physical temperature contrasts between equator and poles, and between night and day.

The RADAR is a single-polarization instrument, but information about the polarization state of echoes is often needed to make unambiguous statements about physical properties. Arecibo's  $\lambda 12.6$ -cm data will provide a very accurate curve of Titan's disk-integrated radar cross-section in two polarizations for subradar tracks near the equator (as well as nearly global maps with resolutions of order of several hundreds of kilometers). The availability of Cassini RADAR disk-integrated cross-sections will permit direct, model-independent calibration of Cassini and Arecibo data against each other, and also will define a solid boundary condition on models of the backscattering function's variation over the surface. Titan fills the RADAR center beam, at about a million kilometers, so disk-integrated measurements should be made no closer than that. At that distance, even a 1 s integration with the scatterometer will produce an echo much stronger than what Arecibo can obtain on any given date.

In order to make the results of the RADAR experiment easily accessible, we will devise means of placing the data in a consistent spatial framework in which

the individual datasets (SAR, thermal emission, and altimetry/scatterometry) will be combined with one another and with the optical remote sensing data. As part of this objective, we will construct a global geodetic control network for Titan. This is needed to compare the various types of observations, and it will allow determination of the spin pole direction and rotation period of Titan (cf. Hubbard *et al.*, 1993; Lemmon *et al.*, 1993, 1995). Cartographic products will be generated from individual observations, mosaics of like data, and composites of different, coregistered datasets. Digital maps in sinusoidal and oblique sinusoidal projections, and hardcopy products in conformal projections, will be produced at a range of scales, with appropriate divisions of the surface of Titan. Also, topographic mapping of Titan will be attempted by digital stereogrammetry (where overlapping SAR images are obtained with favorable geometry), and by radarclinometry (shape from shading in single images). Ganymede, which is similar in size to Titan and has been observed at resolutions comparable to those of the RADAR (Inge and Batson, 1992), provides the initial model for the Titan cartographic program.

## 2.2. ICY SATELLITES

In general, the IR measurements of icy satellites are most sensitive to the conditions in the upper few centimeters of the surface. Measurements around all phase angles contain information to depths of up to several tens of centimeters, which can be retrieved in only a model-dependent way, e.g. on the assumption of constant density and thermal parameters over that depth. Measurements at microwave frequencies are sensitive to temperatures down to the depth of about 1 m if the ice is dense and several meters if the ice is under-dense. The thermal properties of the surface regolith, e.g. the ability to retain heat, may further be constrained by temperature measurements as a function of local time. Therefore an objective of the Cassini RADAR is to conduct radiometric observation of icy satellites during untargeted flybys at distances of less than about 100,000 km. Operations at closer ranges, when the satellite disk can be covered by a sufficient number of footprints, will give an opportunity to identify “hot spots” if there is cryovolcanic activity as is conceivable at least for Enceladus.

The Earth-based radar backscatter measurements in the outer solar system have been limited to the Galilean satellites and Titan (for a review, see Ostro, 1993). The RADAR scatterometry mode allows backscatter measurements on Saturn’s icy satellites also. This can be seen from a simple comparison of the Cassini RADAR with the Goldstone radar—the least sensitive of the three Earth-based planetary radar systems (Goldstone, Goldstone/VLA, Arecibo). The RADAR’s emitted power is about  $10^{-4}$  of the power emitted by Goldstone, and the gain of the Cassini Orbiter High Gain Antenna (HGA) is about  $10^{-5}$  of the gain of the Goldstone 70 m dish. The deficit of nine orders of magnitude can be compensated for by the fact that even during distant flybys (100,000 km) of icy satellites the RADAR is about  $10^4$  times closer to these targets than are the Earth-based radars. Taking into account the  $r^{-4}$



dependence of the received power, the RADAR might thus be about  $10^7$  times more sensitive than the Goldstone system. As an example, the RADAR scatterometer can obtain a signal-to noise ratio equal to 2 (comparable to that obtained by the Goldstone/VLA observations of Titan; see Muhleman *et al.*, 1990) by integrating only 1400 pulses from 500 km objects (Dione, Tethys) at a range of 300,000 km. Much higher signal-to-noise and spatially resolved measurements can be achieved at shorter ranges. Since radar cross-sections are equivalent to microwave albedoes, these measurements will complement the measurements of the visible and IR albedoes obtained by the Cassini optical remote sensing instruments. Furthermore, the RADAR scatterometer observations of icy satellites may be conducted at ranges too large to be useful to optical remote sensing. (Tour 18-5 offers 138 flybys of icy satellites at ranges from 100,000 to 300,000 km.) This would contribute to the optimal utilization of all available tour segments.

### 2.3. SATURN'S RINGS

Microwave flux due to the thermal emission by the rings particles and to scattering by the same particles of the emission from the deep atmosphere of Saturn will be sensed in the RADAR radiometer mode. Microwave emission from the ring particles uniquely probes through the mass of the particles because the  $\lambda$ 2-cm wavelength penetration depth is of the order of 1 m. Thus, the RADAR radiometer presents the best way to measure the ice-to-dust ratio of the particles, as a function of radial distance from Saturn. Several radial scans of the ring system will be required during high-inclination Saturn passes.

### 2.4. SATURN

The deep subcloud region of Saturn is inaccessible to observation by means other than the measurement of thermal emission that originates in that region. The RADAR objective is to map variations in ammonia humidity in the subcloud region, which can be achieved through RADAR radiometer mapping. Ammonia is a tracer of atmospheric motions and provides unique insight into the dynamics of Saturn's atmosphere. Also, the radiometer provides a deeper, and hence complementary, weighting function to other Cassini instruments that operate at shorter wavelengths, and makes an essential contribution to the sounding of Saturn's atmosphere.

Microwave imaging of Saturn at centimeter wavelengths from the Very Large Array (VLA) (Grossman *et al.*, 1989) reveals significant latitudinal structure, plausibly interpreted as a decrease in the ammonia vapor abundance at the cloud deck from equator to pole (Grossman, 1990). VLA images of Saturn are compromised, however, by the geometrical foreshortening of the polar region as well as the aperture synthesis and necessary 3 h integration of zonally smeared observations, and



are limited to a 2% variation in their dynamic range. Polar observations at a near-normal viewing angle by the Cassini RADAR radiometer can resolve the horizontal ammonia structure in the region of the Saturn polar hexagon (Allison *et al.*, 1990) and with complementary mapping from low-inclination orbits potentially afford characterization of vertical variations apparent at differing emission angles. The further prospects for these observations would include their possible interpretation as tracer-maps of Saturn's "potential vorticity" distribution (cf. Allison *et al.*, 1995).

High-inclination flybys will be required for polar imaging, low-inclination flybys for acquiring a full longitudinal image of the planet. To conduct radiometric observations, the preferred range of distances to Saturn is anticipated to be between about  $5R_S$  and  $15R_S$ , where  $R_S$  is the equatorial radius of Saturn, roughly 60,000 km. It is also the objective of RADAR to obtain synoptic thermal-emission images of Saturn's disk. These images will be used to calibrate the radiometer for the Titan radiometric mapping.

### 3. Experiment Description

Since the RADAR will operate almost exclusively during close flybys of its targets, altitudes will change rapidly throughout the data collection periods. Under such conditions, operations in a multiplicity of modes are a necessity. The instrument was designed to incorporate four modes: imaging (either high- or low-resolution), altimetry, scatterometry, and radiometry. The basics of operations in these modes are outlined below; the system design considerations are summarized in Sections 4 and 5.

An optimum Titan flyby scenario, in which all RADAR modes are exercised and a maximum volume of data is collected, calls for about 10 h of uninterrupted operations. At 5 h away from the closest approach, the spacecraft is about 100,000 km from Titan (Figure 2). At that distance the RADAR is used in the radiometer-only mode. As the spacecraft approaches Titan, the remaining modes are activated; first scatterometry, followed by altimetry, and, finally, imaging. Upon receding

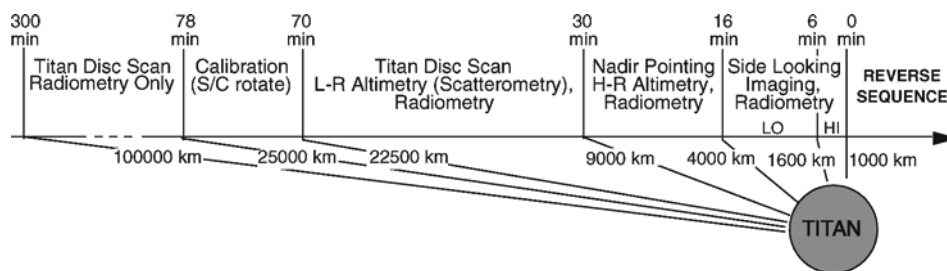


Figure 2. Sequence of the RADAR operational modes during a nominal Titan flyby. To the RADAR, the term "nominal" designates a flyby with the closest-approach altitude of 1,000 km.

TABLE I  
Cassini RADAR Data Characteristics

	Altitude (km)	Incidence angle (°)	Resolution		NE $\sigma_0$ (at boresight) (dB)	Number of looks	Surface coverage (%)
			Azimuth (km)	Range (km)			
SAR							
High resolution	1,000–1,600	21–30	0.35–0.41	0.48–0.64	N/A	2–3	≤1.1
Low resolution	1,600–4,000	15–28	0.41–0.72	0.48–2.70	N/A	2–7	≤1.1
Altimeter	4,000–9,000	0	24–27	24–27	60	16–36	N/A
Scatterometer	9,000–22,500	0–30	55–140	55–140	N/A	N/A	20
Radiometer	1,000–100,000	0–80	6–600	6–600	N/A	N/A	40

N/A: Not applicable.

from Titan, the order of modes is reversed. A detailed description of the RADAR observational strategy is presented in Section 3.5 below.

### 3.1. IMAGING

The RADAR imaging mode provides low-to-high resolution synthetic aperture (SAR) images. The meaning of the terms “low” and “high” in the present context is clarified in Table I. Reference to appropriate analogs may be of further help. Thus, when considering the absolute pixel size, the low-resolution RADAR images will be comparable to the Venera-15/16 and Arecibo radar images of Venus, and the high-resolution RADAR images will be similar in resolution to the Mariner-9 optical images of Mars.

As the SAR data are being acquired, the spacecraft is pointed to the left or right of the nadir track. The way in which this off-nadir angle is varied is referred to as the look-angle profile, where look angle is the angle between boresight and nadir. Look angle is used to calculate the incidence angle—the angle between the antenna boresight and local surface normal. For typical natural surfaces, larger incidence angles tend to better reveal surface topography. From a mission standpoint, the profile of incidence (or look) angle used during SAR datataking is unconstrained except for limitations on spacecraft turning rates. One likely algorithm is to keep the largest incidence angle possible, consistent with a given received signal-to-noise ratio. This rule was followed during the primary mapping phase of the Magellan mission. An alternative philosophy is to maintain constant incidence angle with respect to the surface; this facilitates comparisons of images from different areas. For more detailed information on the principles of SAR imaging and interpretation, see, e.g. Elachi (1987, 1988) and Johnson (1991).

The total width of the RADAR swath is created by combining the five individually illuminated sub-swaths (see Section 5.4) and ranges from 120 to 450 km at the spacecraft altitude,  $h$ , of 1,000 to 4,000 km. Each 1,000 km flyby of the RADAR will yield a SAR strip about 5,000 km long. Each such strip will image about 1.1% of Titan’s surface. Over a tour in which, say, 25 close flybys would be available to the RADAR, at least 25% of Titan’s surface could be imaged. This statement, although true in principle, needs to be qualified. As the example of the tours 18-5 and 19-1, introduced in Figure 3, illustrates, the SAR coverage is sensitive to the characteristics of a given tour—the segment of Titan repeatedly imaged in one tour may be invisible to the RADAR in another tour. Furthermore, the unavoidable overlap dictated by orbital dynamics reduces the aggregate SAR coverage in each tour.

### 3.2. ALTIMETRY

The altimetry mode will typically employ only the central, narrow antenna beam, to make time-of-flight measurements of the relative surface elevations along suborbital

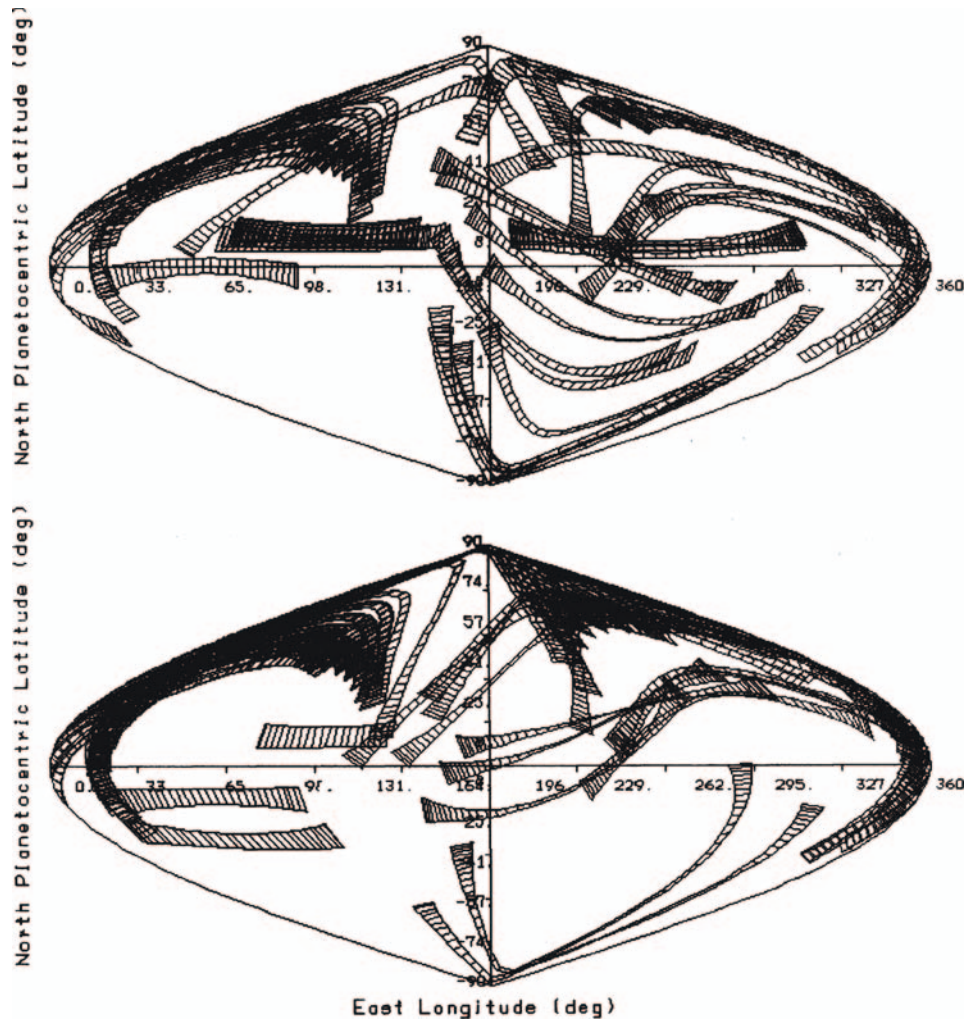


Figure 3. Mapping of Titan in the RADAR high- and low-resolution imaging modes. Included are only flybys with the close-approach altitudes  $< 4,000$  km; incidence angle  $20^\circ$ . (Top): Tour 18-5, (Bottom): Tour 19-1.

(nadir) tracks. Tight spacecraft pointing toward Titan's center of mass is required during the time altimetric observations are in progress. The primary information from the altimetry echoes is the range from spacecraft to surface which, taken together with the knowledge of the spacecraft and Titan ephemerides, will be converted into Titan's radii along the subradar track. Relative topographic accuracy will approach 150 m (see Section 4.1.2); absolute accuracy of radii will depend on the postflight ephemeris reconstruction accuracy, which has not yet been evaluated. Since complete return echoes are relayed to Earth, it is also possible to apply

appropriate scattering models to infer surface microtopography and reflecting properties, as has been done with the Magellan altimetry data (Ford and Pettengill, 1992; Tyler *et al.*, 1992). The full length of a suborbital track for the spacecraft moving from the altitude of 10,000 km, through closest approach at 1,000 km, back to 10,000 km, is about 6,500 km. That is the maximum length of a topographic profile that can be obtained, assuming imaging is sacrificed to altimetry. For comparison, the currently available Goldstone altimetry profiles of Mars span no more than about 6,000 km (Downs *et al.*, 1975). During a nominal Titan flyby (Figure 2), the two topographic profiles collected at the tail ends of imaging runs will each span about 750 km.

### 3.3. SCATTEROMETRY

The RADAR scatterometer mode measures the surface backscatter coefficient,  $\sigma_0$  (radar cross-section normalized to the illuminated surface area), as a function of the incidence angle. From the instrument standpoint, this mode does not differ from the altimetry mode except for the reduced resolution; it has in fact often been referred to as “low-resolution altimetry.” Since echoes at multiple incidence angles are desired, the spacecraft is commanded to scan preselected portions of Titan’s disk between the nadir and limb, as during the RADAR radiometer observations. This mode allows radar echoes to be obtained from anywhere on Titan at a variety of incidence angles, albeit at resolutions much coarser than in the other active modes. An alternate mode manner of scatterometer operations, in which the RADAR central beam illuminates the icy satellites from a considerable distance, has been briefly outlined in Section 2.2.

### 3.4. RADIOMETRY

To acquire the RADAR radiometry data, three types of scans will be executed. Each will trace a spiral track on the surface of the target body. In two of these scans, only the central RADAR beam will be utilized; the third scan may involve one, three, or five beams. The first of the two central-beam scans is defined by a constant cone angle  $\varphi$ . The constant cone-angle scan yields data with a footprint of continuously varying sizes (Figure 4 (top)). In the second central-beam scan, the spacecraft is maneuvered so that the High Gain Antenna (HGA) describes an outward spiral and the boresight sweeps through a cone of increasing angular radius. Using parameters for the maneuvers appropriate to the approach velocity results in a nearly constant-resolution scan, balancing the decreasing range to Titan with increasing cone angle (Figure 4 (bottom)). Almost global coverage of Titan, at a resolution of about 500 km, is possible in a few judiciously selected flybys. Global coverage with a higher resolution will require scanning of Titan during each RADAR flyby.

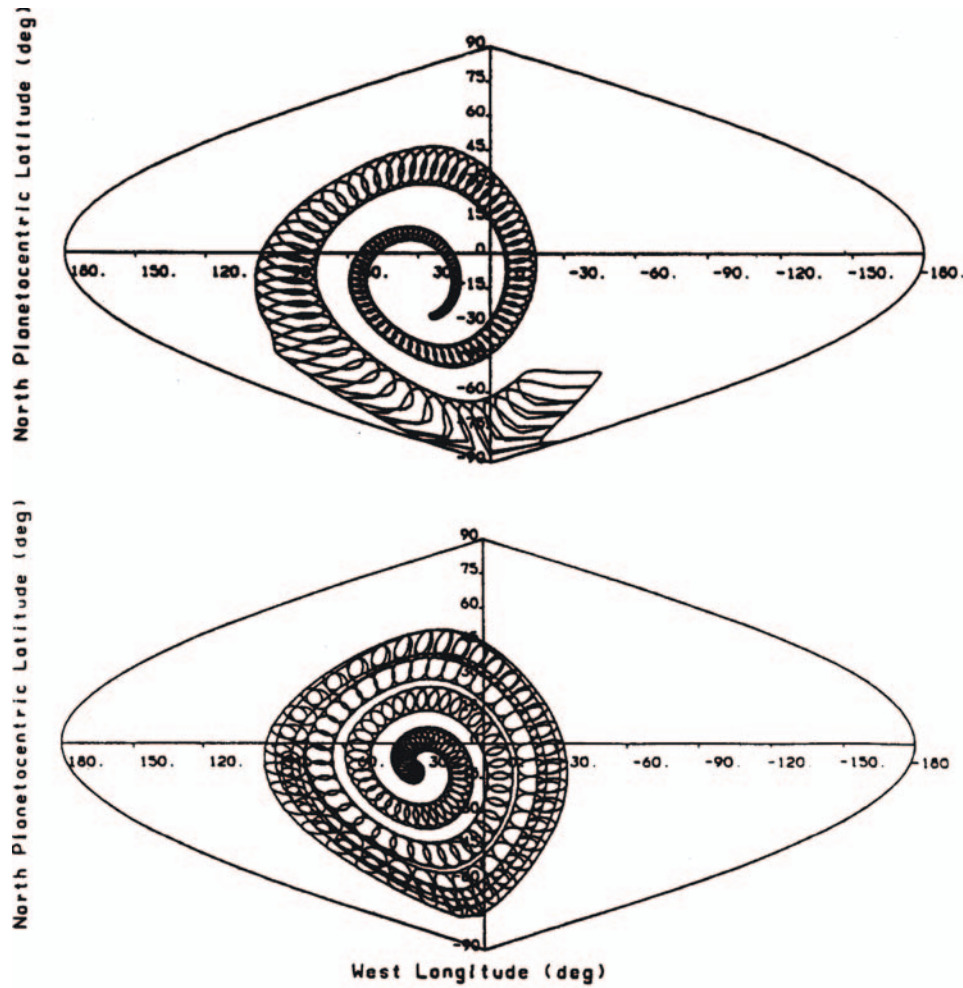


Figure 4. Scanning of Titan with the RADAR central beam. (Top): Constant cone angle; distance 100,000 km–10,000 km, clock rate  $0.05^\circ \text{ s}^{-1}$ . (Bottom): Variable cone angle; distance 80,000–25,000 km, clock rate  $0.20^\circ \text{ s}^{-1}$ .

When only the central beam aligned with the ( $-z$ )-axis is used during a scan, the spiral can be followed using small cyclic rotations about the  $x$ - and  $y$ -axis. The HGA nods in a circular motion, tracing out the spiral, but there is no cumulative rotation about the antenna boresight. In the third type of RADAR scan, when several beams are brought into play, the plane of the beam must be held perpendicular to the motion of the track. Consequently, as the spiral is followed, an additional rotation about the  $z$ -axis is also necessary. The rate and acceleration limits governing spacecraft under Reaction Control System (RCS) control (Table 8.8 in the Cassini Mission Plan, PD 699-100) place bounds on how rapidly the clock angle of the spiral in



either of the three scans can change. If  $\omega$  is the clock rate, then  $\omega\varphi$  must be less than  $0.4^\circ \text{ s}^{-1}$  and  $\omega^2\varphi$  must be less than  $0.01^\circ \text{ s}^{-2}$ , at all times. Either of the three RADAR scans can be commanded by representing the surface track relative to the center of the target body as a sequence of vector polynomial segments in the Attitude and Articulation Control Subsystem (AACS) inertial vector table. An additional constraint that is imposed by the maximum frequency content of vector representations in AACS limits  $\omega$  to less than  $3.6^\circ \text{ s}^{-1}$ . Radiometry data will also be acquired during each of the active modes through the same beam used in the active mode (i.e. when transmitting) for that radar burst. The data will be acquired between the bursts.

### 3.5. DATA ACQUISITION SCENARIOS

The RADAR will conduct its observations in the mission's RADAR/INMS operational mode. Because of similar requirements on Titan flyby geometry, the RADAR and the Ion and Neutral Mass Spectrometer (INMS) have been combined into a single mission operational mode; for the definitions of the mission operational modes, see Tables 8.1 and 8.4 in PD 699-100. Use of the RADAR modes depends primarily on (1) pass assignment; (2) flyby altitude; (3) science objectives; and (4) agreed-upon priorities among the instruments within the RADAR/INMS mode. Sharing Titan passes with other investigations may allow optimizing Titan observations for all parties, although these opportunities depend on, for example, the spacecraft being able to turn and change operational modes rapidly enough that the cost in overhead is small compared with the incremental science gain. The final observation strategy will be determined before arrival at Saturn; combined scenarios may indeed turn out to be attractive in their ability to maximize the amount of science data collected.

Ideally, the RADAR's full capabilities would be realized in a RADAR-dedicated Titan pass with a flyby altitude of 1,000 km or lower (Figure 2). In the interval between  $-6$  and  $-5$  h relative to the closest approach to Titan, and after the RADAR receiver had sufficiently warmed up, external radiometric calibration is performed by pointing the HGA at one or more predetermined calibration targets (cold sky, the Sun, the disk of Saturn, or a galactic radio source) and gathering thermal energy emitted by those targets. About 6 h before the closest approach, radar sequences are loaded. The subsequent operations are autonomous although coordinated with spacecraft maneuvers. At about  $-5$  h ( $h = 100,000$  km), the instrument commences observations in the radiometer mode as the spacecraft creates a scan pattern. Reception of thermal emission continues even when the RADAR is in active modes, but scanning using the spacecraft becomes less useful as the angular movement relative to Titan increases. At about  $-78$  min ( $h = 25,000$  km), the instrument begins active scatterometric observations. Depending on available maneuver time and desired targeting, either single- or multiple-beam observations



may be pursued. At about  $-30$  min ( $h = 9,000$  km), the spacecraft maneuvers to point the HGA in the direction of the Titan's center of mass. After this maneuver has been accomplished, altimetry begins. At about  $-16$  min ( $h = 4,000$  km), altimetry ends, the HGA is pointed  $10-20^\circ$  to one side of the ground track, and the low-resolution SAR imaging begins as the spacecraft executes the planned look-angle profile. At about  $-6$  min, the spacecraft drops below an altitude of  $1,600$  km and the acquisition of high-resolution SAR images begins. This mode of operation will continue through the closest approach of Titan at altitude of  $1,000$  km. As the spacecraft recedes, the same sequence of the RADAR modes is executed in reverse.

While a few of the actual flybys of Titan may follow the standard sequence described above, there are at least three reasons for other, non-standard sequences. First, orbital dynamics is the driving factor for designing close Titan approaches into the tour and setting the dynamically optimal flyby altitudes. Thus, a number of flybys may occur at altitudes higher than  $4,000$  km, making SAR data acquisition unfeasible. Second, once the general physiography of Titan is known it may be more scientifically profitable to collect data in the other RADAR modes, over a particular target area. This may disrupt the standard sequence. Third, the needs of other instruments or an urgent spacecraft activity may interfere. For instance, in the vicinity of Titan, the principal non-science activity will be spacecraft tracking, which requires the HGA be pointed at Earth. As a result, the RADAR sequence may have to be truncated. In many cases, therefore, parts of the standard sequence may be mixed with other activities.

#### 4. Radar Operations

The anticipated uncertainties in the spacecraft ephemeris and attitude predictions have led to a "burst timing" design for signal transmission and reception. In this timing approach, as shown in the lower portion of Figure 5, the radar transmits a series of pulses for a given time period and is then switched to receive the return echo burst. After reception, the radar switches to the radiometer mode to collect the surface-radiation measurements. With such an approach, the uncertainty in timing due to ephemeris and pointing errors will be accommodated by adjusting the burst period and data window rather than the pulse-to-pulse timing as in the case of the conventional pulse interleave approach. The chosen approach is expected to be more effective in utilizing the allocated data rate/volume, as well as in lowering the probability of data loss. The upper portion of Figure 5 illustrates the sequence of bursts as each antenna beam is used. For each beam the bursts overlap to give the multiple looks necessary in SAR in order that the speckle noise be reduced. A flyby with a closest approach altitude is used as an example in the following discussion but during actual operations the predicted profile will be used to set all the RADAR parameters for each pass.

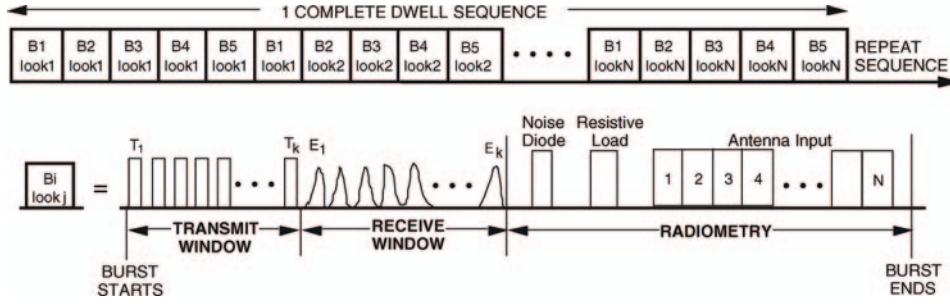


Figure 5. Non-interleaved multi-beam pulse burst timing for radar and radiometer operations.

#### 4.1. RADAR MODES DESIGN

The motivation for the RADAR modes design is the desire to accommodate the potentially different types of surfaces on Titan (or other targets). Given the uncertainties in the ephemeris and in Titan's radar properties, the RADAR system performance must be robust. Since the radar range will be constantly varying within a single flyby as well as from flyby to flyby, the radar parameters such as pulse width, bandwidth, receiver gain, pulse repetition frequency, and other timing must be updated at regular intervals in order to maintain sufficient signal-to-noise ratio on the radar echoes. The major system parameters for each of the four instrument modes are listed in Table II.

##### 4.1.1. Imaging mode

During radar imaging, the spacecraft will roll to either the left- or right-side of the suborbital track according to the pre-determined sequence, and five antenna beams will be utilized, one at a time, to obtain the maximum possible cross-track swath coverage (Figure 6). The azimuth image resolution will be accomplished by unfocussed SAR processing of the echo bursts. With the designed burst timing and processing schemes, the azimuth resolution,  $d_{az}$ , can be expressed as

$$d_{az} = \frac{\lambda R}{2L_{SAR}} = \frac{\lambda R}{2} \frac{1}{T_B} \frac{1}{v_{sc} \sin \theta} = \frac{\lambda R}{2} \frac{c}{2R} \frac{1}{v_{sc} \sin \theta} = \frac{\lambda c}{4v_{sc} \sin \theta}$$

where  $\lambda$  is the radar wavelength,  $R$  the range,  $L_{SAR}$  the unfocussed SAR aperture,  $T_B$  the echo burst period,  $c$  the pulse propagation speed,  $v_{sc}$  the spacecraft velocity,  $\theta$  is the radar azimuth pitch angle, and  $v_{sc} \sin \theta$  is the spacecraft velocity component perpendicular to the radar line of sight (Im *et al.*, 1993). The azimuth resolution is estimated to be between 350 and 720 m throughout the imaging period of each flyby.

TABLE II  
System Parameters for the Cassini RADAR Modes

Frequency (GHz)	Peak power (W)	No. of beams	Look angle (°)		PRF (kHz)	Pulse width (ms)	Bandwidth (MHz)
			Cross-track	Along-track			
Imaging	46.2	All 5	5–20	0	1.8–6.0	200–400	0.43, 0.85
Altimeter	46.2	Beam 3	0	0	4.7–5.6	150	4.25
Scatterometer	46.2	Beam 3	±6 to ±12	±6 to ±12	1.0–3.0	500	0.11
Radiometer	N/A	All 5	±6 to ±12	±6 to ±12	N/A	N/A	135

N/A: Not available.

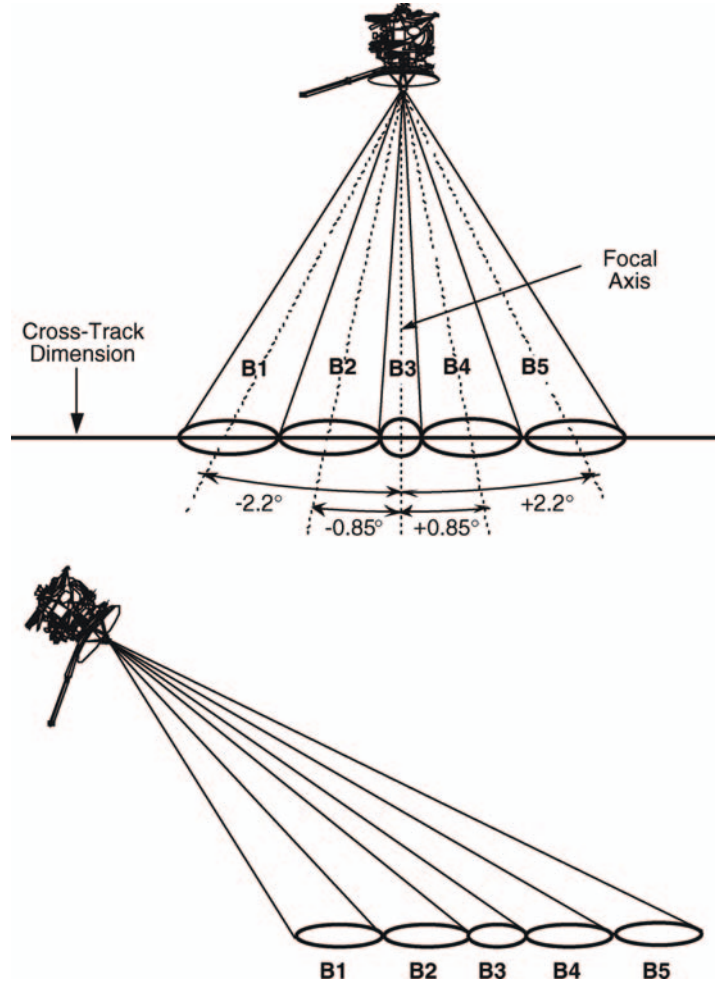


Figure 6. Antenna beam configuration for the Cassini RADAR. (Top): Nadir pointing for altimetry. (Bottom): Side-pointing for imaging.

The range resolution,  $d_r$ , is accomplished through range compression of the chirp signals:

$$d_r = \frac{c}{2B \sin \phi}$$

where  $B$  is the chirp bandwidth and  $\phi$  is the incidence angle. In order to enhance the signal-to-noise ratio, a 850 kHz bandwidth will be used when the spacecraft altitude is 1600 km or less, and a 425 kHz bandwidth will be used at spacecraft altitudes between 1,600 and 4,000 km. The corresponding  $d_r$  is estimated to be between 420 m and 640 m at  $h < 1,600$  km, and between 420 and 2,700 m at  $1,600 \text{ km} < h < 4,000$  km.

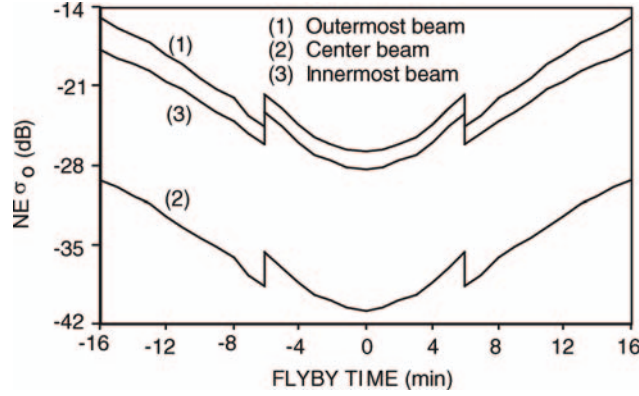


Figure 7. The  $\sigma_0$  noise equivalent ( $NE\sigma_0$ ) of the RADAR images during a nominal Titan flyby, with  $h = 4,000$  km at  $t = \pm 16$  min.

Due to the imperfect knowledge of the surface backscatter characteristics of Titan, we choose to use the so-called noise-equivalent backscattering coefficient,  $NE\sigma_0$ , as a measure of the signal detection sensitivity. This quantity is defined as the normalized surface cross-section which gives rise to a unity single-look thermal signal-to-noise ratio. That is,

$$NE\sigma_0 = \frac{2(4\pi)^3 k T B R^3 l_{\text{atm}}^2 \sin \phi}{P_T G^2 \lambda^2 r_a c t}$$

where  $k$  is the Boltzmann's constant,  $T$  the system noise temperature,  $l_{\text{atm}}^2$  the round-trip atmospheric loss,  $P_T$  the radiated peak power,  $G$  the antenna gain,  $r_a$  the 3 dB along-track beamwidth, and  $t$  the pulse duration. Figure 7 shows  $NE\sigma_0$  as a function of the flyby time for a typical Titan flyby with spacecraft altitude at the closest approach,  $h_0$ , equals 1,000 km. Due to the continuous change in both the range and Doppler contours as well as the irregular isogain contour of the offset antenna beams, the image ambiguity varies substantially throughout a Titan flyby. The total signal-to-ambiguity ratio is estimated to be  $\geq 15$  dB for all images obtained by the Cassini RADAR (Hensley and Im, 1993).

#### 4.1.2. Altimeter mode

This mode will be used to generate relative elevations profile along the Cassini spacecraft sub-orbital track. Operating at spacecraft altitudes between 4,000 km and 9,000 km, this mode will utilize the nadir-pointing central antenna beam (Beam 3) for transmission and reception of chirp pulse signals at a system bandwidth of 4.25 MHz. The altimetric measurements along the sub-nadir ground track are expected to have horizontal resolution (pulse-limited radar footprints) ranging between 24 and 27 km and vertical resolution of about 50 m. The relative height change,  $\Delta h$ , over a surface region illuminated by two successive radar footprints

can be expressed as

$$\Delta h = (h_2 - h_1) - \frac{c(t_2 - t_1)}{2}$$

where  $h_2$  and  $h_1$  are the radar altitudes, deduced from spacecraft trajectory, at two points of interest and  $t_2$  and  $t_1$  are the corresponding round-trip flight times of the radar pulses. Since the trajectory perturbation is likely to be small,  $(h_2 - h_1)$ , and therefore  $\Delta h$ , can be deduced quite accurately during ground processing. We expect that an overall accuracy of 150 m can be achieved.

#### 4.1.3. *Scatterometer mode*

The lack of reliable information on the backscattering characteristics of Titan's surface has been of major concern in the course of the RADAR design work. In order to compensate for the possibility that parts of Titan's surface are unexpectedly radar-dark, and to ensure credible measurements of the surface backscatter variations, we have incorporated a dedicated scatterometer mode into the overall design. The functional concept of the scatterometer mode is similar to that of the altimeter except for one major difference—the scatterometer bandwidth is but 106 kHz, to give sufficient signal-to-noise ratio at long ranges. The RADAR will operate in the scatterometer mode at altitudes between 9,000 km and 25,000 km. The spacecraft will be required to execute specified scanning maneuvers (spiral or circular). Both the backscatter and noise-only measurements will be collected, so that the surface backscatter coefficient,  $\sigma_0$ , can be estimated. Depending on the range distance and angle of incidence, this mode will detect  $\sigma_0$  as low as  $-35$  dB. The long-distance scatterometer observations of icy satellites, whose objective is to measure the disk-integrated radar albedoes, may also require execution of limited conical scans.

#### 4.1.4. *Radiometer mode*

While operating in the radiometry mode, at a bandwidth of 135 MHz, the RADAR will measure the 13.8 GHz emissivity of Titan and targets of opportunity. The radiometer mode can be used alone or in conjunction with other RADAR modes. The data are collected as shown in Figure 7. During each burst, after the active portion of the radar cycle is completed, the radiometer first switches to the noise diode as input, and then to the resistive load in the Front End Electronics (FEE). Each of these calibration sources are sampled once per burst, and the integration times are set to yield between 2,000 and 3,500 counts in a 12-bit (4095) counter. After the two calibration measurements are made, multiple measurements (up to 255) are made through the antenna port. These multiple 12-bit values are summed to give one 20-bit value per burst. Thus, during each burst three radiometer data-points are recorded. Before and after each radiometer only data-taking the HGA will be turned to “cold-space” for an absolute calibration of the antenna-input relative to the internal calibration sources. According to our estimates, the RADAR radiometer is capable of measuring brightness temperature with an error of less than 3 K.

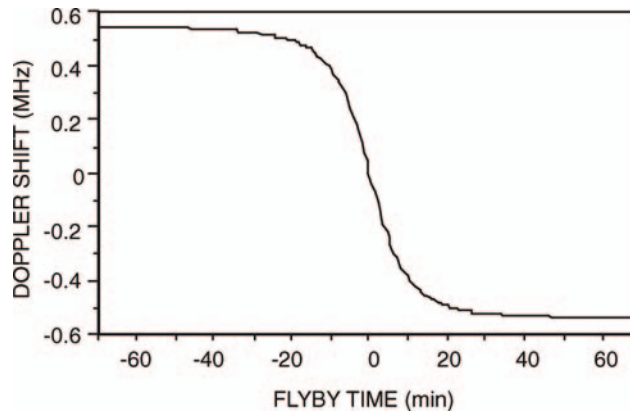


Figure 8. The Doppler shift during a nominal Titan flyby, with  $h = 22,500$  km at  $t = \pm 70$  min.

#### 4.2. DOPPLER TRACKING

Due to the spacecraft motion, the received radar signal will be Doppler-shifted. The extent of the shift depends on the antenna pointing, frequency, and orbit geometry. Assuming that the antenna is pointed toward the center of Titan at any time during a flyby, the maximum Doppler shift,  $\Delta f$ , will be less than  $\pm 600$  kHz, for a flyby altitude of 1,000 km at closest approach. The Doppler shift profile versus flyby time is plotted in Figure 8. In our current design, the chirp signals will be generated digitally with center frequency shifted by an amount equal to  $-\Delta f$  in order to compensate for the shift. Other factors such as the trajectory perturbations, finite-time updates, and off-nadir antenna pointing will also contribute to the shift. The receiver filters compensate for these shift residues.

#### 4.3. ONBOARD DATA REDUCTION

Signals to be acquired by the active radar modes will initially be quantized to 8 bits. In order to satisfy the allocated output data rate constraint, the radar data will be re-quantized onboard to a lesser number of bits, using the block-adaptive quantization (BAQ) scheme similar to the one used by the Magellan radar. In this scheme, the 8-bit digital samples per interpulse period are divided into a finite number of blocks. After signal averaging over a number of pulse periods, the averaged power in each block is estimated and a threshold is determined. The 8-bit data are then scaled with respect to the threshold and the scaling factor is quantized to  $k$  bits ( $k < 8$ ). Both the scaling factor and the threshold values, after quantization, will be downlinked for signal reconstruction purpose. This, together with the lesser number of bits used for the scaling factors, reduces the output data rate substantially. Our current estimates of the output data rates are: 195 and 250 kbps in the imaging mode, low



and high resolution, respectively, (8-to-2 reduction), 30 kbps in the altimeter and scatterometer modes (8-to-4 reduction). We use a larger number of bits for altimetry and scatterometry due to the fact that in these modes less data are averaged and the initial data rates are lower.

#### 4.4. CONTROL INSTRUCTIONS

The timing, gain, antenna port selection, and other setup parameters of the RADAR are controlled through a set of instructions which are calculated on the ground and uplinked to the spacecraft prior to a flyby. After the RADAR is turned on and the FSW loaded and started, the Instruction Execution Block (IEB) is loaded and triggered. The block contains all the instructions the FSW will execute during a flyby. There are three types of instructions: Power—to control the power states of the RADAR; Telemetry & Command—to set up special modes, including diagnostic instructions; and Slow and Fast instructions. The last two are combined into one setup instruction for the RADAR configuration. The reason for the fast and slow types was to reduce the number of instructions necessary to uplink by recognizing that some parameters vary faster than others.

Tables III and IV present a list of the slow and fast instructions and their meaning. A much more detailed description of each parameter is in the Cassini RADAR Digital Subsystem High Level Design Document (DSS-HLD). During a typical flyby it is expected that each Fast Field will change as often as every 15 s while each Slow Field will change as often as every 3 min. The execution time for each instruction is controlled by the flight software, using the relative time from the initial trigger (TFI) of the RADAR. The combined instruction is sent to the Control and Timing Unit (CTU) for its actual control of the RADAR. The TRIGGER command is the last command the RADAR, received from the spacecraft Command and Data System (CDS) prior to RADAR operations and from that point on, until the RADAR is turned off, the RADAR operates autonomously.

#### 4.5. INSTRUMENT DATA MODES

The RADAR sends data to the spacecraft CDS for storage on the Solid State Recorder (SSR) through two channels. The first, low-rate (10–20 bps), channel is called “Housekeeping” and is used whenever the RADAR is on. The Housekeeping channel carries engineering data only. It becomes active approximately 80 s after the DSS is turned on and continues until the DSS is turned off. During normal operations a complete sample of RADAR engineering data is received every 2–4 min. The second channel is the High Rate Science channel with data rates as high as 365 kbps. All RADAR science data, including the engineering data in the science headers, are sent through this channel. The spacecraft CDS picks up packets from the RADAR at the maximum rate of 365 kbps but only stores

TABLE III  
Slow Field Instruction Structure

Parameter Name	Bits	Range
Time from trigger	16	0–18.2 h in 1.0 s steps
Instruction type	2	11 <sub>2</sub> (fixed)
Data take number	8	0–255
Slow field instruction number	8	0–255
Radar mode	4	0: LALTL, 1: LALTH, 2: SARL, . . .
Calibration source	4	0: Norm, 1: Ant, 2: Noise diode, . . .
Adc sample rate	2	0: 0.25, 1: 1.0, 2: 2.0, 3: 10.0 MHz
Receiver bandwidth	2	0: 0.12, 1: 0.47, 2: 0.94, 3: 4.68 MHz
Transmit/receive window offset	4	–8 to +7 PRIs
Data compression mode	3	0: 8/2, 1: 8/1, 2: 8/1MSB, . . .
Beam mask	5	00100 <sub>2</sub> : beam 3, 11111 <sub>2</sub> : all beams
Receiver attenuation (beams 1 and 2)	12	0–74 dB in 1 dB steps
Receiver attenuation (beam 3)	12	0–74 dB in 1 dB steps
Receiver attenuation (beams 4 and 5)	12	0–74 dB in 1 dB steps
Radiometer integration period length	4	10–75 ms in 5 ms steps
Number of radiometer integration periods	8	1–255 periods
Chirp step duration	8	0.67–9.47 $\mu$ s in 0.67 $\mu$ s steps
Chirp step quantity	12	2–750 steps
Chirp frequency step size	16	0–117.2 kHz in 1.788 Hz steps

TABLE IV  
Fast Field Instruction Structure

Parameter Name	Bits	Range
Time from trigger	16	0–18.2 h in 1.0 s steps
Instruction type	2	10 <sub>2</sub> (fixed)
Fast field instruction number	8	0–255
Bursts in instruction	8	1–255 bursts
Pulses in transmit burst	8	0–255 pulses
Burst period	12	10–4095 ms
Receiver window delay	10	0–1023 PRIs
Pulse repetition interval	10	0–1023 clock periods
Chirp start frequency	16	0–30 MHz (458 Hz steps)

those packets that have real data included. The other packets are identified as “0-filled” by the RADAR and are discarded. The valid data are produced by the RADAR at variable rates; typically 1 kbps for radiometer only, 30 kbps for scatterometer and altimeter, and up to 260 kbps for imaging. It is up to the RADAR to insure that the total volume of data allocated to the RADAR is not exceeded during the RADAR data collection time. The total volume of data the RADAR would produce in the course of a nominal Titan flyby (i.e. a 1,000 km flyby) is about 1 GB.

During the cruise period, when only a simple preventive maintenance test is performed every three months, the only data-type available is housekeeping. Normal operations of the RADAR will be executed during infrequent special checkout periods.

#### 4.6. MAINTENANCE SEQUENCE

The maintenance sequence the RADAR will execute every three months during the cruise phase of the mission is shown in Figure 9. The figure illustrates how the CDS and the RADAR interact during this sequence, and is also illustrative of how the RADAR will be operated during science data taking. The thick center line represents

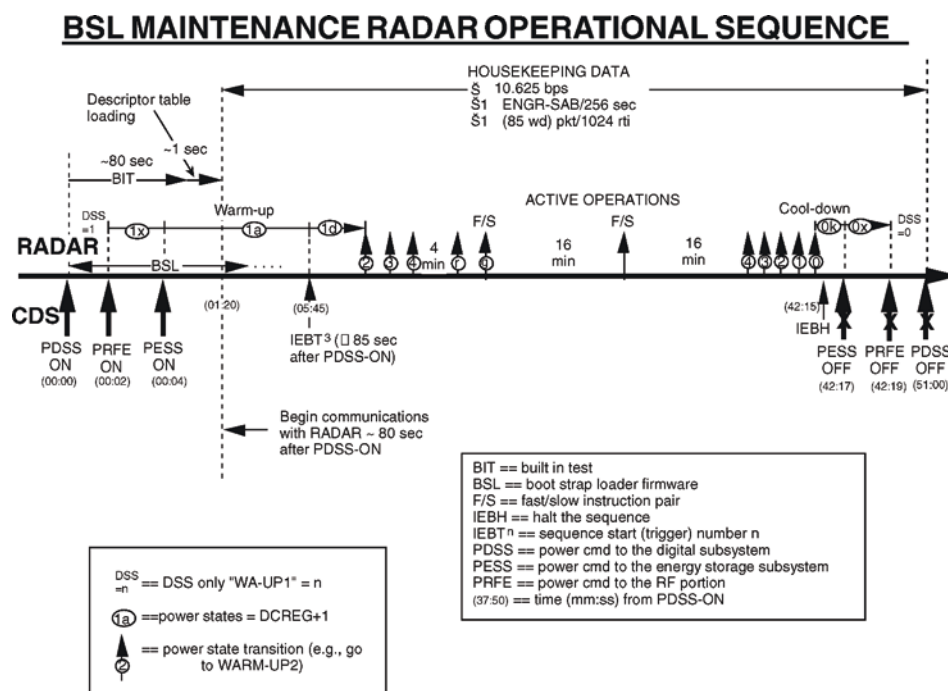


Figure 9. The RADAR Bootstrap Loader Maintenance Sequence.

a timeline interface between the RADAR and the CDS; the CDS actions are below the line, the RADAR actions above. The times after the DSS turn-on are shown with each command from the CDS. The three RADAR power switches are quickly turned on to start the RADAR. The RADAR DSS goes through an initialization procedure during which a sequence of built-in tests is run. After these tests are completed the RADAR loads a descriptor table into the CDS/RADAR interface, and communication with the RADAR can begin. It is at this point that the housekeeping data start to be sent to the CDS. As the maintenance sequence runs from PROM (the Bootstrap Loader), no flight software or an IEB table are necessary to be loaded prior to operations.

The RADAR comes up in a power state called Warmup-1. This power state has several substates, depending on which commands have been sent by the CDS. As soon as the RADAR receives a trigger, the PROM sequence of instructions begins to run. These are illustrated by the short up-arrows above the time line. The numbers embedded in these arrows indicate a transition instruction to that power state. These power states are for the RFES portion of the RADAR. The transition to the Warmup-4 includes a 4 min wait to allow for time to warm up the Traveling Wave Tube Amplifier (TWTA). The last power instruction puts the DSS in the state to sequence the RFES. The first fast/slow (F/S) instruction then commands the transmitter to commence transmitting.

In the maintenance sequence there are only two fast/slow field pairs which operate for 16 min each. The RADAR transmits and receives, but no science data are collected. After the end of the second 16 min period the power instructions reverse the order to put the RADAR in Warmup-0 mode, and make it ready for the power to be disconnected by the CDS commands to the power subsystem of the spacecraft. The housekeeping data transmission ends when the DSS is turned off but, in reality, the last housekeeping packet received represents the state of the RADAR several minutes before shutoff.

## 5. RADAR Design Considerations

The Cassini/Huygens mission is a joint undertaking of the National Aeronautics and Space Administration (NASA), European Space Agency (ESA), and the Italian Space Agency (ASI). The RADAR instrument was developed in partnership between NASA and ASI. ASI selected Alenia Aerospazio in Rome as the contractor for both the spacecraft High Gain Antenna (HGA) and the RADAR Radio Frequency Electronics Subsystem (RFES). Alenia in turn selected subcontractors such as FIAR in Milan and EMS in Atlanta, Georgia, for the component units of the RFES. The overall responsibility for the RADAR system design and spacecraft interfaces rested with the Jet Propulsion Laboratory (JPL). The complexity of the instrument called for a number of special design considerations. We treat here the following: power, mass, space and location, antenna, pointing and ephemeris

accuracies, target-flyby geometries, instrument control method, data rates and volumes, and the limited number of Titan flybys.

### 5.1. POWER

The Cassini spacecraft power system uses radioactive thermal generators (RTGs) for all its electrical power and no batteries for power buffering. The RADAR has high (195 W) peak power requirements which could not be accommodated by the spacecraft power system. Early design of the instrument included an internal battery which would provide most of the transmitter energy requirements during a 10 h Titan flyby. Both battery size and long life considerations led to a battery substitute, called the Energy Storage Subsystem (ESS), which is a bank of capacitors. The design of the ESS called for energy to be stored for a “transmit burst,” 90–3,000 ms. The transmit portion of the burst lasts no more than about 10% of the total burst time, thus, the 90% non-transmit time is used to recharge the capacitor bank of the ESS. The peak transmitter power requirement was thus reduced from 195 to 30 W by use of the ESS. The RADAR power requirement is 86 W.

### 5.2. MASS

As in all planetary missions, mass has been a severe constraint on the RADAR design. Conservative design for an 11-year mission and radiation environments near 100 krad dictated the use of low-density components. This resulted in the total mass of 43.3 kg for the RADAR instrument.

### 5.3. SPACE AND LOCATION

The spacecraft was designed to have 12 electronic bays. The RADAR occupies Bay 11 and a specially constructed appendage to the main body of the spacecraft, the “penthouse” (Figure 10). The use of the penthouse required a thermal interface through a baseplate to the spacecraft; it further required additional thermal blankets, louvers, and radioactive heating units (RHUs) to control the thermal environment of the RFES. The DSS and ESS, located in Bay 11, share the thermal design of the spacecraft bays.

### 5.4. ANTENNA

Tight constraints on mass and volume required that the RADAR share the 4 m telecommunications antenna (HGA), as did the radar on the Magellan mission. The system design also dictated that a single feed or beam could not meet the per-flyby requirements of imaging and other modes simultaneously. A five-feed, five-beam design was decided upon, in which the center, highest-gain beam would be used in

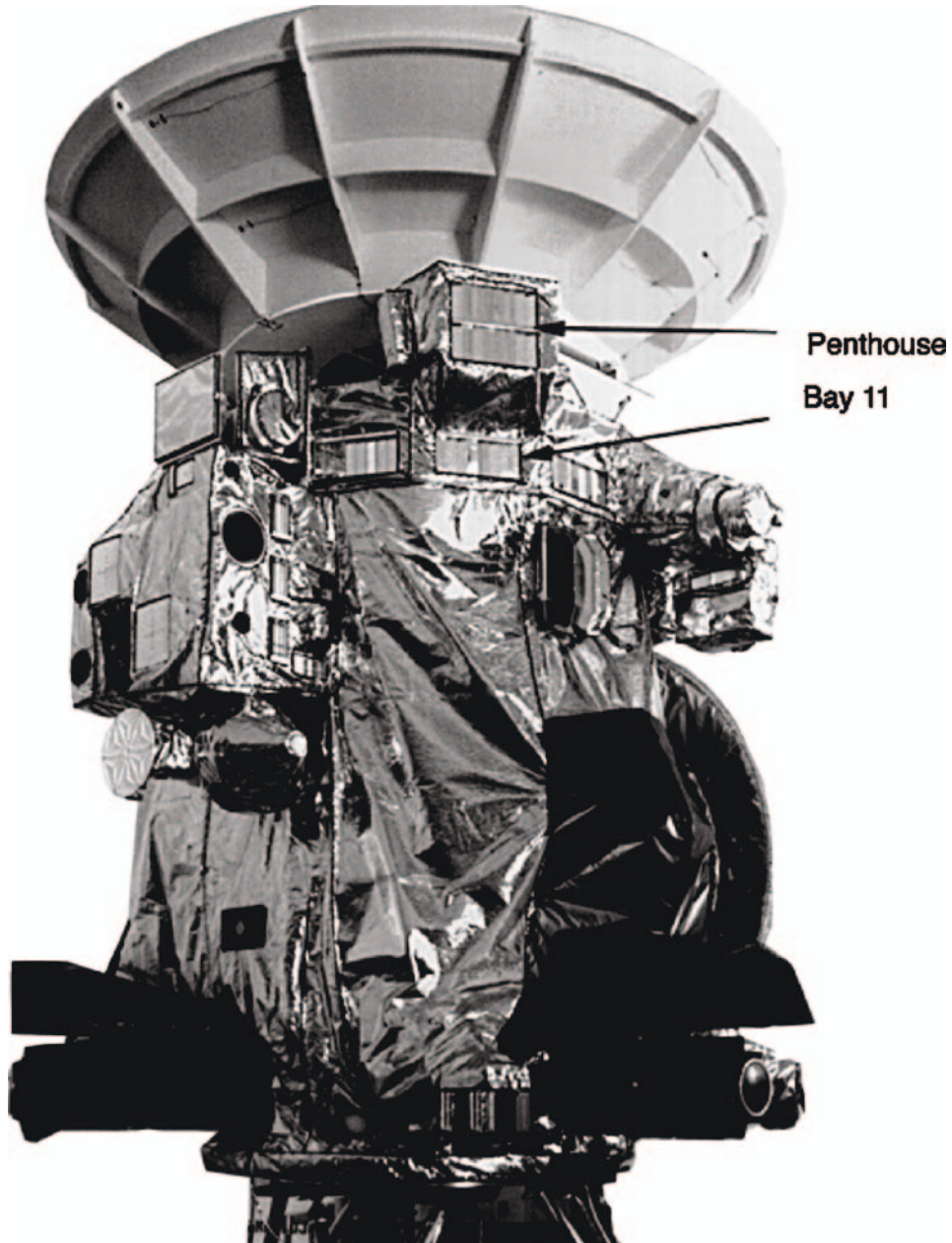


*Figure 10.* The locations on the spacecraft of the RADAR RFES (Penthouse) and DSS/ESS (Bay 11).



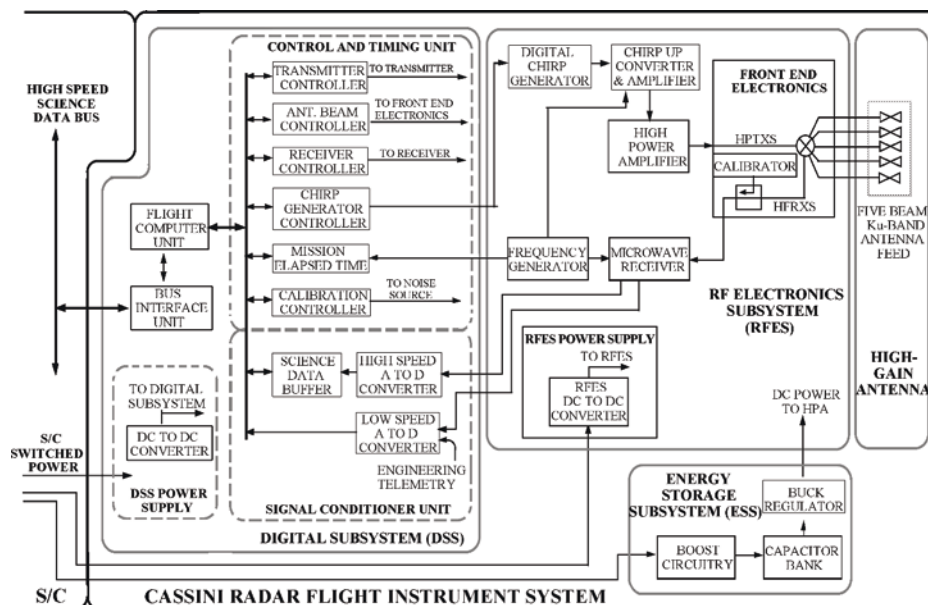


Figure 11. Cassini RADAR block diagram.

all modes. The additional four beams would be used in the imaging mode, creating a wide swath. Beam switching would be done inside the RADAR. The five-beam design required five waveguides into the HGA, each with a separate feed. Other methods of beam scanning were considered, such as the phased-array feeds, but were rejected. The five feeds were accommodated into the four-frequency HGA (Figure 11). The switching of the beams is accomplished in the RFES by the Front End Electronics, which is a compact set of twisted waveguides and circulators. No moving parts were used.

### 5.5. POINTING AND EPHEMERIS

In order to automatically record the echo data the RADAR needs to have available accurately predicted ranges to the targets of interest. This is achieved by knowing at any instant the spacecraft position relative to the target and the HGA pointing. Since the Cassini spacecraft is in orbit around Saturn, and Titan is the target of interest, the accuracy of the ephemeris is expected to be insufficient by Earth-observing or Magellan radar standards. The same is true for pointing, which is done relative to a star field or a fuzzy limb rather than the center of Titan, and is thus degraded for radar use. These inaccuracies demanded a design in which the radar echoes are not interleaved with transmissions, as would be required for high-resolution imaging. Thus, the radar transmits for a set number of pulses and pulse rate until



the prediction indicates the first echo will have returned, and then the receiver is activated and all echoes received.

#### 5.6. FLYBY GEOMETRY

As described in Section 4.6, the timing of the radar must be set properly to receive the echo. It is also necessary that the frequency of the echo be within the range of the receiver. If the target is moving with respect to the transmitter or the receiver, the echo is Doppler-frequency shifted proportional to the velocity and radar frequency. Normally this shift is only a small fraction of the bandwidth and can be neglected. For the Cassini RADAR, the bandwidth is as low as 0.1 MHz and the Doppler shift as high as  $\pm 0.6$  MHz. It is a requirement on the design to take into account this effect.

#### 5.7. CONTROL METHOD

The control of the radar can be performed by several means including remotely, based upon predictions, and automatically, based upon actual data. The radar echoes and radiometric settings, it was felt, would be too difficult for an automatic system to set up and hold to all the system constraints, especially that of the total data volume. A computer was available on the project list, called the Engineering Flight Computer (EFC), which had most of the capability required for radar operations. It was decided that the radar parameters would be table-driven from a time-ordered set of parameters, which would control all the radar parameters such as gain, antenna port, pulsewidth, and bandwidth. Each entry in the table is calculated by ground software, called the Radar Mapping Sequencing Software (RMSS), which takes inputs such as science desires spacecraft pointing, ephemeris, and data rate. The RMSS outputs the Instruction Execution Block (IEB) table. Each RADAR observation (a Titan flyby, an icy-satellite flyby, etc.) has a unique table which is transmitted to the spacecraft as part of the regular uplink process prior to a flyby.

Another aspect of RADAR control is the program, which runs in EFC. This program is called the Cassini RADAR Operational Control Flight Software (CROCFSW), or Flight Software (FSW) for short. The FSW, to be described later in this paper, is a major contributor to the functionality and testability of the RADAR hardware.

#### 5.8. DATA RATES AND VOLUMES

In addition to mass and power, the data rates and volumes are the most limiting resources planetary missions impose. During each RADAR flyby of Titan about 1 Gbit will be recorded on the spacecraft's Solid State Recorder (SSR) for later playback. These data include all spacecraft packet formats, radar formats, engineering

telemetry, and science data. The science portion will be approximately 90% of the total. In order to pack as much information as possible into these bits the echo data are compressed using a method pioneered on the Magellan mission called the Block Adaptive Quantizer (BAQ) (Kwok and Johnson, 1989). On Magellan, the method used was 8-bits-in/2-bits-out (8/2), in a fixed hardware design. In the case of the Cassini RADAR the hardware method was dropped and a software method added to the system. Since the BAQ was implemented in software, it has much more flexibility than the Magellan hardware method; in fact, other modes are available such as 8/4, 8/1, and 8/0. The 8/4 mode will be used for altimetry and scatterometry, the 8/1 mode could be used for imaging in order to sacrifice amplitude resolution in return for finer spatial resolution, and the 8/0 mode (which produces no data) is used for test purposes.

#### 5.9. LIMITED NUMBER OF FLYBYS

The RADAR lacks opportunity to acquire processable echoes prior to its first data-collecting flyby of Titan, likely to take place in 2005. Radar-operational flybys of Venus and Earth would allow the first closed-loop test of the RADAR system. As helpful as these tests could be, they would still simulate operations at targets vastly different from Titan. The review in Section 1 showed how little we know about the surface characteristics of Titan. We know even less about the performance of the RADAR radiometer and about the thermal effect of a 10 h RADAR flyby of Titan on the performance of the spacecraft systems. During the Science Cruise (i.e. in the period of 2 years prior to the Saturn Orbit Insertion), we expect to run extensive “dress rehearsal” tests to simulate full Titan flybys. During a Titan flyby the HGA is pointed at Titan, and no data are received at Earth. Thus, there is no opportunity to correct problems during the data collection, and if there indeed are problems, the RADAR flyby will, most likely, be sacrificed and the correction will have to wait until the next downlink/uplink cycle is completed. To make this process efficient, the RADAR has been designed to be as autonomous as possible and monitor and report all aspects of its operation while collecting the science data.

Prior to each flyby the RADAR is powered up, at which time it performs a series of built-in tests (BITs). The results of the BITs are reported in the low-rate housekeeping data. Next, the FSW is loaded, followed by the IEB table and by the trigger to start. If any of these processes does not go to completion the RADAR cannot report that fact to the spacecraft and the science-data flyby will be lost. If a problem occurs after the trigger, the FSW should recognize that fact and recovery might be possible, depending upon the nature of the problem.

In addition to potential hardware (or software) faults the data themselves can be examined by the FSW to determine if the settings of the radar system parameters are correct. The three areas which were examined for automatic control (onboard

processing) were the timing of the receive window position, receiver gain, and radiometer integration period. It was felt that it would be difficult to set the timing correctly in an automatic system in all cases and that the pointing and ephemeris would be good enough for data capture so automatic timing control was rejected. Receive gain control was examined and determined to be a candidate for automatic control. Consequently, automatic gain (really attenuation) was implemented as well as automatic radiometer integration-time setting. Each of these software modules reads the input science data and determines a change in the setting, which will bring the level closer to the ideal.

## 6. Hardware Design

The Cassini RADAR consists of four subsystems: the Digital Subsystem (DSS), Radio Frequency Electronics Subsystem (RFES), Energy Storage Subsystem (ESS), and High Gain Antenna (HGA) (Figure 11). The DSS, built at JPL, contains the interfaces to the spacecraft data bus, the control electronics for all the radar, the analog-to-digital converters for both science data and engineering telemetry, and the flight software for all RADAR operations. These operations include data assembly and data processing such as gain adjustment and data compression. The RFES, built by Alenia Aerospazio, contains all the analog RF components of the RADAR as well as the digital chirp generator (DCG) and the Ultra-Stable Oscillator (USO)—the timing reference for the whole RADAR. The RFES responds to digital signals from the DSS, to set its operating parameters. The ESS, built at JPL, is a battery substitute for the transmitter of the RFES. The HGA, built by Alenia Aerospazio, has four frequency bands (S, X, Ku, and Ka) to provide services for radar science (Ku-band) and radio science and telecommunications operations (the remaining bands).

### 6.1. DIGITAL SUBSYSTEM

The Digital Subsystem performs all the digital functions of the RADAR, which include accepting commands from the spacecraft Command and Data System (CDS), executing the flight software, operating the entire system as specified in the uplinked instruction table, collecting and processing science data, and collecting engineering telemetry data. The DSS is located in a portion of Bay 11, one of the 12 bays, which make up the spacecraft instrument bus. The DSS is made up of five circuit chassis which contain the following: the Flight Computer Unit (FCU), the Science Analog-to-Digital Converter (SADC), the Telemetry Analog-to-Digital Converter (TADC), the Science Data Buffer (SDB), the Control and Timing Unit (CTU), the Power Converter Unit (PCU), and the RFES interfaces. The functions of each of these units are explained below.

#### 6.1.1. *Flight computer unit*

The Flight Computer Unit is made up of the project-supplied Engineering Flight Computer (EFC), the Bus Interface Unit (BIU), and Startup Read Only Memory (SUROM). The function of the FCU is to accept and interpret commands from the spacecraft CDS. The commands include the RADAR flight software and the table that contains the time-ordered set of instructions to operate the RADAR. The FCU controls both science and engineering telemetry data flow, compresses the science data using a software algorithm known as the Block Adaptive Quantizer (BAQ), and formats the data into RADAR units known as SAR-Altitude Bursts (SAB) and then into the smaller CDS transport packets.

#### 6.1.2. *Science analog-to-digital converter*

The Science Analog-to-Digital Converter (SADC) is known as the “Science ADC” to distinguish it from the ADCs for the telemetry subsystem and the radiometer. The Science ADC consists of three parts: an input buffer amplifier, the high-speed ADC, and the digital code conversion circuitry and output buffers. The input buffer amplifier receives the video signal from the receiver, amplifies it, and level-shifts it to a value that is compatible with input voltage range of the ADC. The digital circuitry receives and transmits all control and timing signals required by the Science ADC Subsystem.

#### 6.1.3. *Telemetry analog-to-digital converter*

The purpose of the Telemetry ADC Subsystem (TADC) is to provide the Engineering Flight Computer (EFC) with up-to-the-second data on the performance of the Cassini RADAR System. The TADC samples analog voltages from DSS, ESS, RFES, and external waveguides, converting them into digitized equivalents with an analog-to-digital converter, and then it transfers those digitized data into RAM memory. The TADC also accepts the radiometer DC signals from the RFES and processes them for inclusion in the SAB footer.

#### 6.1.4. *Science data buffer*

The Science Data Buffer (SDB) is a 16K-word, high-speed RAM buffer that acts as a rate buffer for science data from the high-speed A/D converter (SADC) enroute to the FCU. The SDB appears in the address space of the FCU as a 16K-word (one “word” equals two bytes) block. During the receive-window of a burst, the SDB is filled with raw, 8-bit, time-domain samples (packed two samples per word) from the SADC. When the receive-window closes, the FSW transfers the burst of data from the SDB into the local memory of the FCU.

#### 6.1.5. *Control and timing unit*

The Control and Timing Unit (CTU) sets all the timing functions of the RADAR. It accepts a formatted instruction from the software running in the FCU and stores it in a register until the previous instruction runs out. The CTU sets all the high-speed

logic in the RADAR such as when to transmit, when to receive, or when to move data to the RFES. The CTU runs off a 10 MHz clock that is derived from the 30 MHz Ultra-Stable Oscillator (USO) in the RFES.

#### 6.1.6. *Power converter unit*

The Power Converter Unit (PCU) takes the 30 VDC power from the spacecraft power bus and converts it to the various voltages used in the DSS:  $\pm 5$  VDC,  $\pm 9$  VDC,  $-12$  VDC, and  $\pm 15$  VDC. The power into the PCU comes from the spacecraft via a solid-state power switch, one of the three used to control the RADAR.

#### 6.1.7. *RFES interfaces*

The electrical interfaces to the Radio Frequency Electronics Subsystem (RFES) are all with the DSS, except for the power interfaces to the spacecraft and to the RADAR Energy Storage Subsystem (ESS) and the RF interface with the HGA. There are 22 control and timing signals from the DSS-CTU which, among other things, control the beam-select and receive-window. In the RFES the signals fan out to the various units such as the Front End Electronics for beam-select and Microwave Receiver for receive-window. A high-speed logic line also controls the waveform generation start in the Digital Chirp Generator. The DSS accepts analog inputs from the RFES such as the downconverted waveform going to the SADC, and the radiometer and engineering telemetry voltages going to the TADC.

### 6.2. RADIO FREQUENCY ELECTRONICS SUBSYSTEM

The Radio Frequency Electronics Subsystem (RFES) is that portion of the RADAR that converts the chirp waveform data from the DSS into high-powered pulsed waveforms which, in turn, are sent to the proper antenna port. The echoes are received through the same port and captured by the sensitive receiver. The physical location of the RFES is in a “penthouse” located above Bay 11 (which houses the DSS), below the backside of the HGA (see Figure 10). The penthouse is attached thermally to the spacecraft through a baseplate and has additional thermal control through the use of thermal blankets, a louvered outer cover, and five 3 W, radioactive heating units (RHU) attached to the outer surface of the RFES. The units which make up the RFES are the Frequency Generator (FG) (which contains the Ultra-Stable Oscillator), the Digital Chirp Generator (DCG), the Chirp Upconverter and Amplifier (CUCA), the High-Power Amplifier (HPA), the Front End Electronics (FEE), the Microwave Receiver (MR), and the Power Converter. The operation of these units will be explained below.

#### 6.2.1. *Frequency generator*

The Frequency Generator Unit (FGU) contains the 30-MHz USO that is placed in an oven controlled to  $85^\circ\text{C}$ . The signals from this unit are sent to three destinations.

First, they are sent to the CUCA, to provide upconversion frequencies for construction of the transmit waveform. Second, they are sent to the MR, to downconvert the received signal to baseband. Third, they are sent to the DSS for all digital timing signals control, including the digitization of the science data.

#### 6.2.2. *Digital chirp generator*

The Digital Chirp Generator (DCG) is the device that generates the frequency-modulated signal, the “chirp.” The chirp is the pulse expansion necessary in high-performance radar in order to achieve high average power with relatively low peak power. The inputs to the DCG come from the DSS; they are the parameters of a pulsed radar chirp—such as the start frequency, number of frequency steps, frequency step length, and frequency step size. The last three parameters control the pulse length and bandwidth, while the first controls the frequency offset due to the high Doppler frequencies on this mission.

#### 6.2.3. *Chirp upconverter and amplifier*

The chirp signal coming from the DCG is at baseband frequency and of low level. In order to drive the transmitter, the chirp waveform must be upconverted to 13.8 GHz and amplified. The Chirp Upconverter and Amplifier receive the low-level chirp from the DCG. It uses the 30 MHz signal and derivatives to arrive at 13.8 GHz, and then the signal is amplified to the proper level.

#### 6.2.4. *High power amplifier*

The amplified chirped signal from the CUCA is further amplified by the High Powered Amplifier (HPA) to approximately 65 W peak power. The HPA uses a traveling wave tube amplifier (TWT). This tube operates at high voltages (4,000 VDC) in order to get sufficient amplification. The high voltages are generated within this unit. The output of the HPA is fed through waveguides to reduce losses.

#### 6.2.5. *Front end electronics*

The purpose of the FEE is to route the transmitted signal through one of the five output waveguides and to switch a few milliseconds later to route the echo to the receiver. The FEE is a complex set of 13 circulators and waveguides, which allow selection of single beams a large number of times without deterioration of function. The FEE also contains the resistive load calibration for the radiometer and the routing circuit for the injection of the noise diode calibration. The noise diode itself is located in the MR.

#### 6.2.6. *Microwave receiver*

The most complex unit in the RFES is the Microwave Receiver. This unit contains the low-noise amplifiers (LNA), downconverter, amplifiers, bandpass and bandwidth filters, variable attenuators, and the radiometer detection circuit and noise diode calibration source. Because of its extreme sensitivity, a limiter was added

before the LNA to reduce the possibility of catastrophic failure caused by high signals entering the MR. The LNA were specially designed and mounted in gold foil to reduce gain changes that might result from the ground-plane motion. To protect the LNAs during normal operations, pin-diode switches block signals except when reception is desired. A combination of high-gain amplifiers and attenuators, controlled from the DSS, allow for precise control of the signal levels going to the DSS-SADC.

The radiometer detector circuit operates at the full 135 MHz bandwidth of the receiver. The circuit contains a special noise diode, an integrator, and a reset circuit. Particular consideration was given to all these components to yield a stable system. The noise diode has undergone special gold foil application for grounding to reduce gain jumps. The diode is mounted in a kovar frame, and its signal goes to the FEE where it joins the input to the MR.

#### 6.2.7. *Power converter*

The Power Converter Unit (PCU) supplies all the low-voltage application in the RFES except the ESS-supplied 35 VDC which powers the HPA. A separate spacecraft solid-state power switch turns on the RFES.

### 6.3. ENERGY STORAGE SUBSYSTEM

The Energy Storage Subsystem (ESS) is a battery substitute for the HPA of the RFES, used to reduce the peak-power required by the RADAR during transmission. The ESS does this by boosting the 30 VDC, supplied by the spacecraft, to approximately 80 VDC for storage in a capacitor bank, and then bucks the 80 VDC to 35 VDC for use by the HPA. The boost to 80 VDC is necessary to more effectively store the energy and give some “headroom” so that when the energy is drawn from the capacitor bank the voltage stays above the 35 VDC required. The input to the ESS is limited to 34 W, while the output is approximately 200 W. The RADAR transmits at a <75% duty cycle for 10–50 ms and then waits for approximately 10 times this interval, until the next transmission occurs. During this “quiet” time the voltage in the ESS builds back up. A separate spacecraft solid-state switch turns on the ESS.

### 6.4. HIGH GAIN ANTENNA

Due to volume and mass constraints, the Cassini RADAR uses the spacecraft’s high-gain, 4 m diameter telecommunications antenna. To extend the imaging coverage, a multiple radar feed structure at 13.8 GHz is mounted on the antenna reflector to generate five beams. The beams are adjacent to one another in the cross-track dimension, as is shown in Figure 12. The beam configuration is illustrated in Figure 6. In this figure, the central, circular beam (B3) is generated by illuminating the entire



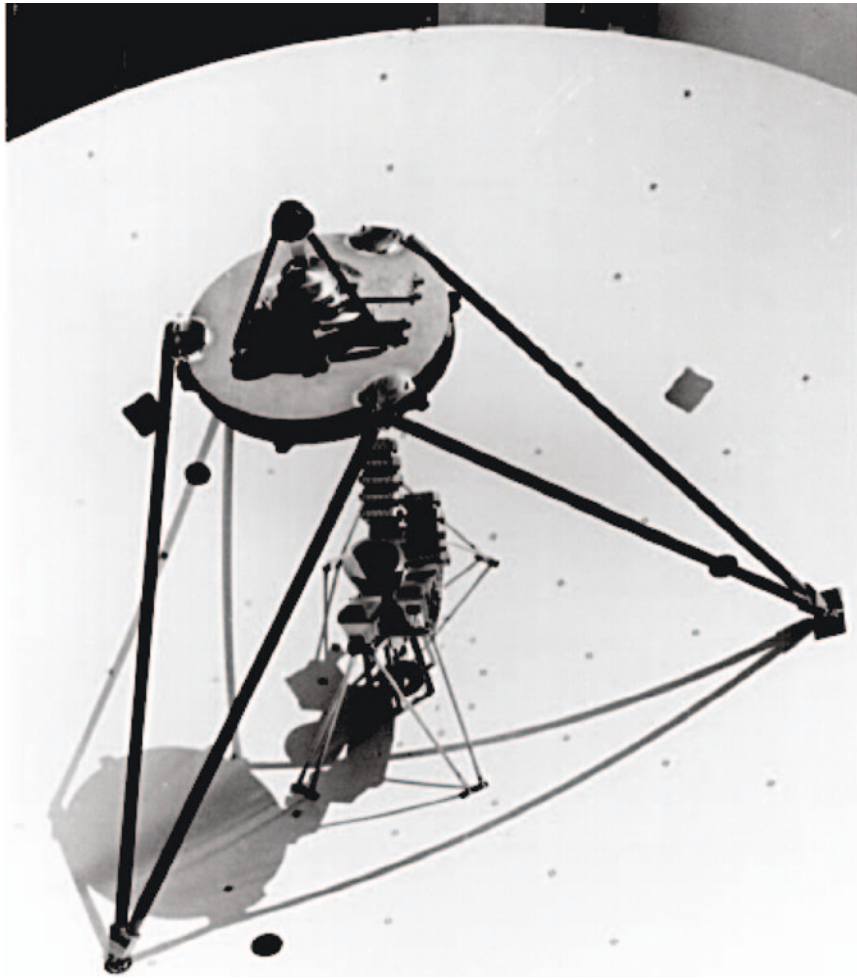


*Figure 12.* The four-wavelength feed assembly of the Cassini High Gain Antenna. The RADAR Ku-band feeds B1, B2, B4, and B5 are placed—the sides from the antenna's axis.

reflector with a feed that is located at reflector's focal point, and the side-looking beams are generated by partially illuminating the reflector with four feeds that are located away from the focal axis. The expected performance characteristics of the five antenna beams of the Cassini RADAR are given in Table V. During operation, only one beam will be utilized during a radar burst, from 90 to 3,000 ms.

## 7. Summary

The RADAR experiment will provide a comprehensive set of data that will allow a significant enhancement of our understanding of the present state and evolution of

TABLE V  
Cassini RADAR Antenna Performance Characteristics

	Peak gain (dB)	Azimuth beamwidth (°)	Cross-track beamwidth (°)	Angle from focal axis (°)	Peak sidelobe (dB)	Peak cross-pol (dB)
Beams 1 and 5	42.0	0.35	1.35	2.2	−12	−20
Beams 2 and 4	42.1	0.35	1.35	0.85	−13	−20
Beam 3	49.1	0.35	1.35	0	−16	−20

the surface of Titan, by acquiring global radiometric maps and high-to-moderate resolution imaging of about 25% of the moon's surface. The RADAR sensor was designed to have flexibility to respond to a wide range of the presently unknown surface characteristics. As we acquire the first set of data, during the first flybys of Titan, the RADAR sensor configuration and parameters will be reset to optimize the science yield of the data acquired during the subsequent flybys. By the end of the Cassini mission, the RADAR will have provided significant imaging coverage of the last major body in the solar system save the still unmapped Pluto/Charon.

### Acknowledgements

We acknowledge the contributions made by the Cassini RADAR Instrument Development Teams both at Alenia Aerospazio and at JPL, and we also acknowledge the support from the Cassini Program. The Alenia portion of the work was carried out under the sponsorship of the Italian Space Agency (ASI); the JPL portion was performed under contract with National Aeronautics and Space Administration (NASA).

### References

- Allison, M., Godfrey, D. A., and Beebe, R. F.: 1990, 'A wave dynamical interpretation of Saturn's polar hexagon', *Science* **247**, 1061–1063.
- Allison, M., Del Genio, A. D., and Zhou, W.: 1995, 'Richardson number constraints for the Jupiter and outer planet wind regime', *Geophys. Res. Lett.* **22**, 2957–2960.
- Caldwell, J., Cunningham, C. C., Anthony, D., White, P. H., Groth, E. J., Hassan, H., *et al.*: 1992, 'Titan: Evidence for seasonal change—a comparison of Hubble Space Telescope and Voyager images', *Icarus* **96**, 1–9.
- Campbell, D. B., Head, J. W., Harmon, J. K., and Hine, A. A.: 1983, 'Venus: Identification of banded terrain in the mountains of Ishtar Terra', *Science* **221**, 644–647.
- Downs, G. S., Reichley, P. E., and Green, R. R.: 1975, 'Radar measurements of Martian topography and surface properties: The 1971 and 1973 oppositions', *Icarus* **26**, 273–312.

- Dubouloz, N., Raulin, F., Lellouch, E., and Gautier, D.: 1989, 'Titan's hypothesized ocean properties: The influence of surface temperature and atmospheric composition uncertainties', *Icarus* **82**, 81–96.
- Elachi, C.: 1987, *Introduction to the Physics and Techniques of Remote Sensing*, New York: Wiley.
- Elachi, C.: 1988, *Spaceborne Radar Remote Sensing: Applications and Techniques*, New York: IEEE Press.
- Elachi, C., Im, E., Roth, L. E., and Werner, C. L.: 1991, 'Cassini Titan Radar Mapper', *Proc. IEEE* **79**, 867–880.
- Engel, S., Lunine, J. I., and Hartmann, W. K.: 1995, 'Cratering on Titan and implications for Titan's atmospheric history', *Planet. Space Sci.* **43**, 1059–1066.
- Ford, P. G., and Pettengill, G. H.: 1992, 'Venus topography and kilometer-scale slopes', *J. Geophys. Res.* **97**, 13,103–13,114.
- Griffith, C. A.: 1993, 'Evidence for surface heterogeneity on Titan', *Nature* **364**, 511–514.
- Griffith, C. A., Owen, T., and Wagener, R.: 1991, 'Titan's surface and troposphere, investigated with ground-based, near-infrared observation', *Icarus* **93**, 362–378.
- Grossman, A. W.: 1990, 'Microwave imaging of Saturn's deep atmosphere and rings', Doctoral Dissertation, California Institute of Technology.
- Grossman, A. W., and Muhleman, D. O.: 1992, 'Observation of Titan's radio light-curve at 3.5-cm', *Bull. Am. Astron. Soc.* **24**, 954.
- Grossman, A. W., Muhleman, D. O., and Berge, G. L.: 1989, 'High-resolution microwave imaging of Saturn', *Science* **245**, 1211–1215.
- Harmon, J. K., and Ostro, S.J.: 1985, 'Mars: Dual-polarization radar observations with extended coverage', *Icarus* **62**(1985), 110–128.
- Hensley, S., and Im, E.: 1993, 'SAR ambiguity study for the Cassini Radar', *Proceedings of IGARSS'93*.
- Hubbard, W. B., and 45 others: 1993, 'The occultation of 28 Sgr by Titan', *Astron. Astrophys.* **269**, 541–563.
- Im, E., Johnson, W. T. K., and Hensley, S.: 1993, 'Cassini Radar for remote sensing of Titan - design considerations', *Proceedings of IGARSS'93*.
- Inge, J. L., and Batson, R.M.: 1992, 'Indexes of maps of the planets and satellites', *NASA TM* **4395**, 96–98.
- Johnson, W. T. K.: 1991, 'Magellan imaging radar mission to Venus', *Proc. IEEE* **79**, 777.
- Kuiper, G. P.: 1944, 'Titan: A satellite with an atmosphere', *Astrophys. J.* **100**, 378–383.
- Kwok, R., and Johnson, W. T. K.: 1989, 'Block adaptive quantization of Magellan SAR data', *IEEE Trans. Geosci. Remote Sens.* **27**, 375–383.
- Lemmon, M. T., Karkoscka, E., and Tomasko, M.: 1993, 'Titan's rotation: Surface feature observed', *Icarus* **103**, 329–332.
- Lemmon, M. T., Karkoscka, E., and Tomasko, M.: 1995, 'Titan's rotational light-curve', *Icarus* **113**, 27–38.
- Lindal, G. F., Wood, G. E., Hotz, H. B., Sweetnam, D. N., Eshleman, V. R., and Tyler, G. L.: 1983, 'The atmosphere of Titan: An analysis of the Voyager 1 radio occultation measurements', *Icarus* **53**, 348–363.
- Lorenz, R. D.: 1995a, 'Raindrops on Titan', *Adv. Space Res.* **15**, (3)317–(3)320.
- Lorenz, R. D.: 1995b, 'Cassini mission: Radar sensing of craters on Titan', *Lunar Planet. Sci.* **XXVI**, 775–776.
- Lorenz, R. D., and Lunine, J. I.: 1996, 'Erosion on Titan: Past and present', *Icarus* **122**, 79–91.
- Lorenz, R. D., Smith, P. H., Lemmon, M. T., Karkoschka, E., Lockwood, G. W., and Caldwell, J.: 1997, 'Titan's north-south asymmetry from HST and Voyager imaging: Comparison with models and ground-based photometry', *Icarus* **127**, 173–189.

- Lunine, J. I.: 1993, 'Does Titan have an ocean? A review of current understanding of Titan's surface', *Revs. Geophys.* **31**, 133–149.
- Lunine, J. I., and Rizk, B.: 1989, 'Thermal evolution of Titan's atmosphere', *Icarus* **80**, 370–389.
- Lunine, J. I., Stevenson, D. J., and Yung, Y. L.: 1983, 'Ethane ocean on Titan', *Science* **222**, 1229–1230.
- Mitchell, D. L., Ostro, S. J., Hudson, R. S., Rosema, K. D., Campbell, D. B., Vélez, R., *et al.*: 1996, 'Radar observations of asteroids 1 Ceres, 2 Pallas, and 4 Vesta', *Icarus* **124**, 113–133.
- Muhleman, D. O., Grossman, A. W., Butler, B. J., and Slade, M. A.: 1990, 'Radar reflectivity of Titan', *Science* **248**, 975–980.
- Muhleman, D. O., Grossman, A. W., Slade, M. A., and Butler, B. J.: 1992, 'The surface of Titan and Titan's rotation: What is radar telling us?', *Bull. Am. Astron. Soc.* **24**, 954.
- Muhleman, D. O., Grossman, A. W., Slade, M. A., and Butler, B. J.: 1993, 'Titan's radar reflectivity and rotation', *Bull. Am. Astron. Soc.* **25**, 1009.
- Muhleman, D. O., Grossman, A. W., and Butler, B. J.: 1995, 'Radar investigation of Mars, Mercury, and Titan', *Annu. Rev. Earth Planet. Sci.* **23**, 337–374.
- Ostro, S. J.: 1993, 'Planetary Radar Astronomy', *Revs. Mod. Phys.* **65**, 1235–1279.
- Ostro, S. J., Campbell, D. B., Simpson, R. A., Hudson, R. S., Chandler, J. F., Rosema, K. D., *et al.*: 1992, 'Europa, Ganymede, and Callisto: New radar results from Arecibo and Goldstone', *J. Geophys. Res.* **97**, 18,227–18,244.
- Pettengill, G. H.: 1978, 'Physical properties of the planets and satellites from radar observations', *Ann. Rev. Astron. Astrophys.* **16**, 265–292.
- Pettengill, G. H., Briscoe, H. W., Evans, J. V., Gehrels, E., Hyde, G. M., Kraft, L. G., Price, R., and Smith, W. B.: 1962, 'A radar investigation of Venus', *Astron. J.* **67**, 181–190.
- Pettengill, G. H., Ford, P. G., Johnson, W. T. K., Raney, K. R., and Soderblom, L. A.: 1991, 'Magellan: Radar performance and data products', *Science* **252**, 260–265.
- Samuelson, R. E., and Mayo, L. A.: 1997, 'Steady-state model for methane condensation in Titan's troposphere', *Planet. Space Sci.* **45**, 949–958.
- Saunders, R. S., and 26 others: 1992, 'The Magellan Mission summary', *J. Geophys. Res.* **97**, 13,067–13,090.
- Sen, A. D., Anicich, V. G., and Arakelian, T.: 1992, 'Dielectric constant of liquid alkanes and hydrocarbon mixtures', *J. Phys. D: Appl. Phys.* **25**, 516–521.
- Smith, P. H., and Lemmon, M. T.: 1993, 'HST images of Titan', *Bull. Am. Astron. Soc.* **25**, 1105.
- Smith, P. H., Lemmon, M. T., Lorenz, R. D., Sromovsky, L. A., Caldwell, J. J., and Allison, M. D.: 1996, 'Titan's surface, revealed by HST images', *Icarus* **119**, 336–349.
- Straty, G. C., and Goodwin, R. D.: 1973, 'Dielectric constant and polarizability of saturated and compressed fluid methane', *Cryogenics* **13**, 712–715.
- Thomson, W. R., and Squyres, S. W.: 1990, 'Titan and other icy satellites: Dielectric properties of constituent materials and implications for radar sounding', *Icarus* **86**, 336–354.
- Toon, O. B., McKay, C. P., Courtin, R., and Ackerman, T. P.: 1988, 'Methane rain on Titan', *Icarus* **75**, 255–284.
- Tyler, G. L., Eshleman, V. R., Anderson, J. D., Levy, G. S., Lindal, G. F., Wood, G. E., *et al.*: 1981, 'Radio science investigations of the Saturn system with Voyager 1: Preliminary results', *Science* **212**, 201–206.
- Tyler, G. L., Simpson, R. A., Maurer, M. J., and Holman, E.: 1992, 'Scattering properties of the Venusian surface: Preliminary results from Magellan', *J. Geophys. Res.* **97**, 13,115–13,139.

# THE CASSINI VISUAL AND INFRARED MAPPING SPECTROMETER (VIMS) INVESTIGATION

R. H. BROWN\*, K. H. BAINES, G. BELLUCCI, J.-P. BIBRING, B. J. BURATTI, F. CAPACCIONI, P. CERRONI, R. N. CLARK, A. CORADINI, D. P. CRUIKSHANK, P. DROSSART, V. FORMISANO, R. JAUMANN, Y. LANGEVIN, D. L. MATSON, T. B. MCCORD, V. MENNELLA, E. MILLER, R. M. NELSON, P. D. NICHOLSON, B. SICARDY AND C. SOTIN

*Department of Planetary Sciences, 1629 University Boulevard, University of Arizona, Tucson, AZ 85721, U.S.A.*

*(\*Author for correspondence: E-mail address: rhb@lpl.arizona.edu)*

(Received 5 April 2002; Accepted in final form 2 January 2004)

**Abstract.** The *Cassini* visual and infrared mapping spectrometer (VIMS) investigation is a multidisciplinary study of the Saturnian system. Visual and near-infrared imaging spectroscopy and high-speed spectrophotometry are the observational techniques. The scope of the investigation includes the rings, the surfaces of the icy satellites and Titan, and the atmospheres of Saturn and Titan. In this paper, we will elucidate the major scientific and measurement goals of the investigation, the major characteristics of the *Cassini* VIMS instrument, the instrument calibration, and operation, and the results of the recent *Cassini* flybys of Venus and the Earth–Moon system.

**Keywords:** Cassini, Saturn, infrared mapping spectrometer

## 1. Introduction

The visual and infrared mapping spectrometer (VIMS) is a state-of-the-art, imaging spectrometer that spans the 0.3–5.1  $\mu\text{m}$  wavelength range. It obtains observations of targets in the Saturnian system. These data are used by the team members to carry out many, different, multidisciplinary investigations. These studies, for example, seek to increase our knowledge about atmospheric processes, the nature of the rings, and the mineralogical composition of surfaces.

The VIMS strategy is to measure scattered and emitted light from surfaces and atmospheres. While the spectral domain is emphasized, spatial resolution is also important particularly when it allows the correlation of the spectral characteristics with surface or atmospheric features. Since the spatial domain is important for understanding and interpreting the data, close collaboration is maintained with other, primarily imaging, investigations that are aboard *Cassini*. The addition of data of relatively high-spatial resolution, but of modest spectral resolution, to a data set of high spectral resolution and modest spatial resolution results in synergistic scientific advances well beyond those which could be accomplished using either data set separately. Conversely, very-high spectral-resolution instruments (e.g. CIRS) on



*Space Science Reviews* **115**: 111–168, 2004.

© 2004 Kluwer Academic Publishers. Printed in the Netherlands.

the *Cassini* spacecraft offer a different set of synergistic interactions for VIMS. Thus, the *Cassini* VIMS investigation will perform much of its work with an eye toward the synergy it has with other experiments.

### 1.1. TECHNICAL HERITAGE OF THE VIMS INSTRUMENT

The *Cassini* VIMS instrument has its roots in a long line of proposed imaging spectrometers, starting with a rudimentary instrument proposed for the *Lunar Polar Orbiter* in 1974. A more refined concept was proposed for the *Mariner Jupiter Uranus* (MJU) mission in 1975. This design was accepted for the *Jupiter Orbiter Probe* (JOP, later named *Galileo*) Mission in 1977. After selection, this design rapidly evolved into that of the NIMS instrument. Further consideration of these concepts for terrestrial applications led the Jet Propulsion Laboratory to propose to design and develop the airborne visible/infrared spectrometer (AVIRIS) in 1983. In 1987 this system measured its first spectral images (Green *et al.*, 1998). Also, in the early 1980's, an instrument development program for future planetary missions was setup at JPL and headed by Larry Soderblom as principal investigator.

This collaboration resulted in several similar instruments optimized for different planetary targets, most notably the OMEGA instrument, the Mars Observer VIMS, and the CRAF VIMS. Mars Observer VIMS and CRAF VIMS are *Cassini* VIMS' most immediate forbearers, but changes made in the VIMS instrument design in response to NASA's demands to reduce the cost of the strawman *Cassini* VIMS resulted in a substantial heritage from Galileo NIMS. Despite that heritage, which goes so far as to include parts from the Galileo NIMS engineering model, *Cassini* VIMS is a substantial step beyond NIMS in the evolution of visual and infrared imaging spectrometers.

This program developed imaging spectrometer designs for the *Comet Rendezvous Asteroid Flyby* (CRAF), the *Mars Observer* (MO), and the *Cassini* missions. While these spectrometers were selected as facility instruments on all three missions, the CRAF mission was cancelled and the MO instrument was removed from the payload in favor of the remaining payload elements that never reached Mars. Only the *Cassini* instrument survived and flew in space.

*Cassini* VIMS has inherited much from the NIMS instrument, including mechanical and optical parts from the original NIMS engineering model. VIMS nevertheless represents a substantial improvement over the state of the art as marked by the NIMS instrument. In particular, where the NIMS instrument incorporates a moving grating that scans a multiple-order spectrum across a linear array of discrete detectors, the VIMS instrument includes a fixed, multiply blazed grating and array detectors in both its visual and near-infrared channels. Another important improvement is the way the visual and infrared channels scan spatial targets. The VIMS-VIS (visual channel) uses a two-dimensional array detector and a scanned slit (literally scanning a two-dimensional scene across the spectrometer slit) to provide two-dimensional spatial coverage. The infrared channel has only a linear array



of detectors and therefore must use a two-dimensional scanning secondary mirror to obtain the same spatial coverage. The NIMS instrument by contrast scans a scene in only one direction while using the relative motion between the target and the spacecraft to scan the other spatial dimension.

The major differences between the *Cassini* VIMS and the Galileo NIMS lie in the incorporation of a separate visual channel using a frame-transfer, silicon CCD detector with separate foreoptics and analog/control electronics, the inclusion of a radically improved infrared detector with improved order sorting and thermal background rejection, an improved infrared focal plane cooler design, an improved main electronics design, a two-dimensional, voice-coil-actuator-driven, scanning secondary mirror in the infrared foreoptics, a fixed, triply blazed grating in the infrared, a redundant 16-megabit buffer, and a redundant, lossless, hardware data compressor using a unique compression algorithm developed by Yves Langevin. These improvements result in an instrument with substantially greater capability for planetary imaging spectroscopy—so much so that *Cassini* VIMS is the most capable and complex imaging spectrometer presently flying on a NASA planetary spacecraft.

## 1.2. INTERNATIONAL COOPERATION

The VIMS investigation is truly an international enterprise. The instrument resulted from the best thinking and skill of scientists and engineers in the United States, Italy, France, and Germany. The bonds of cooperation and friendship formed during the design, construction, and testing of this pioneering instrument have now resulted in the closely knit team that is using this instrument to obtain new knowledge about the Saturnian system.

### 1.2.1. *The VIMS Engineering Team*

The *Cassini* VIMS Development Project began with the *Cassini* instrument selections in November 1990 and ended 30 days after the *Cassini* launch on October 15, 1997. Overall management responsibility was awarded to the NASA Jet Propulsion Laboratory, but soon after that selection, agencies of Italy and France were invited to join the instrument engineering team. In the resulting division of responsibilities, VIMS-VIS (visual spectral region component) was designed and built by *Officine Galileo* in Florence Italy for the *Agenzia Spaziale Italiana* (ASI); the VIMS data compressors and data buffers were supplied by the *Institut d'Astrophysique Spatiale* (IAS) in Orsay, France for the *Centre National de la Recherche Scientifique* (CNRS); and VIMS-IR (infrared spectral region component) was designed and built by the *NASA Jet Propulsion Laboratory* (JPL) in Pasadena, California. JPL also conducted the integration, test, and calibration of the instrument with involvement by the science team and members of all the engineering teams.



Note that throughout this document we denote the visible spectral region component (channel) of VIMS as VIMS-VIS, and the infrared component (channel) as VIMS-IR.

The original VIMS project manager at JPL was Robert F. Lockhart. Mr. Lockhart was later asked to lead the effort to build the entire suite of four *Cassini* facility instruments, including VIMS, and Dr. Gail Klein, then the deputy project manager for VIMS, assumed the VIMS project manager role. David Juergens continued in the role of instrument manager and Edward Miller continued as the senior VIMS system engineer. In Italy, Enrico Flamini of the Agenzia Spaziale Italiana directed the VIMS-VIS Visual Channel (VIMS-VIS) project, with Romeo DeVidi as the VIMS-VIS project manager at Officine Galileo. Francis Reininger served as the Visual Channel system engineer. In France, Alain Soufflot and Yves Langevin led the development of the VIMS data compressor and buffer hardware at IAS.

In total, over 50 engineers in France, Italy, and the US collaborated to design and build the VIMS instrument. The instrument has to date operated flawlessly en route to Saturn, a testament to the cohesion and dedication of the engineering team.

#### 1.2.2. *The VIMS Investigation (Science) Team*

The VIMS Science Team came into existence on November 5, 1990 when the US National Aeronautics and Space Administration announced the selections of the various instrument and investigation teams for the *Cassini* Orbiter. The original VIMS science team consisted of: Robert H. Brown (Team Leader), Kevin H. Baines, Jean-Pierre Bibring, Andrea Carusi, Roger N. Clark, Michael Combes, Angioletta Coradini, Dale P. Cruikshank, Pierre Drossart, Vittorio Formisano, Ralf Jaumann, Yves Langevin, Dennis L. Matson, Robert M. Nelson, Bruno Sicardy, and Christophe Sotin.<sup>1</sup>

There have been some changes since the original selection. Added to team membership were: Alberto Adriani, Giancarlo Bellucci, Bonnie J. Buratti, Ezio

<sup>1</sup>Institutional affiliations are as follows (in alphabetical order by last name): Alberto Adriani (CNR Istituto di Astrofisica Spaziale, Italy), Kevin H. Baines (NASA Jet Propulsion Laboratory), Jean-Pierre Bibring (Universite de Paris Sud-Orsay, France), Giancarlo Bellucci (CNR Istituto Fisica Spazio Interplanetario, Italy), Bonnie J. Buratti (NASA Jet Propulsion Laboratory), Robert H. Brown (University of Arizona, Team Leader), Ezio Bussoletti (Istituto Universitario Navale, Italy), Fabrizio Capaccioni (CNR Istituto di Astrofisica Spaziale, Italy), Andrea Carusi (CNR Istituto di Astrofisica Spaziale, Italy), Priscilla Cerroni (CNR Istituto di Astrofisica Spaziale, Italy), Roger N. Clark (U.S. Geological Survey, Denver), Michael Combes (Observatoire de Paris-Meudon, France), Angioletta Coradini (CNR Istituto di Astrofisica Spaziale, Italy), Dale P. Cruikshank (NASA Ames Research Center), Pierre Drossart (Observatoire de Paris-Meudon, France), Vittorio Formisano (CNR Istituto Fisica Spazio Interplanetario, Italy), Ralf Jaumann (Institute for Planetary Exploration, DLR, Berlin, Germany), Yves Langevin (Universite de Paris Sud-Orsay, France), Thomas B. McCord (University of Hawaii, Honolulu), Dennis L. Matson, (NASA Jet Propulsion Laboratory), Vito Mennella (Osservatorio Astronomico di Capodimonte, Italy), Phillip D. Nicholson (Cornell University), Robert M. Nelson (NASA Jet Propulsion Laboratory), Bruno Sicardy (Observatoire de Paris-Meudon, France) Christophe Sotin (Universite de Nantes, Nantes France).

Bussoletti, Fabrizio Capaccioni, Priscilla Cerroni, Thomas B. McCord, Vito Men-  
nella, and Phillip D. Nicholson.<sup>1</sup> Resignations were received from Andrea Carusi,  
Alberto Adriani, and Ezio Bussoletti.

The VIMS science team members' scientific interests range over three major  
areas: planetary surfaces, atmospheres and rings. The combined scientific goals of  
the VIMS scientific team are discussed later in this paper.

## 2. Scientific Goals of the Vims Investigation

At the time of this writing, the *Cassini* spacecraft has flown by Venus twice, the  
Earth once, and Jupiter once. Later in this paper we describe some of the obser-  
vations made for the purposes of instrument test-and-calibration during the Venus  
encounters and the Earth flyby. Scientific results derived from the flybys of Venus  
and Jupiter are published elsewhere (Baines *et al.*, 2000; Brown *et al.*, 2003; Mc-  
Cord *et al.*, 2004). Now we discuss the scientific goals addressed during the cruise  
phase and orbital tour of Saturn.

### 2.1. VENUS

The specific scientific objectives for Venus arose from VIMS unique ability to  
peer into Venus' turbulent middle atmosphere as well as the cloud-covered upper  
atmosphere. Unfortunately, the fact that VIMS-IR was not operational at Venus,  
combined with the restricted attitude of the spacecraft dictated by the need to protect  
the *Huygens* probe from excessive insolation, made it impossible to obtain a data  
set at Venus which would allow us to address the list of scientific goals originally  
envisioned for Venus. Nevertheless, useful data were obtained with VIMS-VIS. In  
particular, VIMS-VIS saw the surface of Venus for the first time at multiple sub-  
micrometer wavelengths, proving that sub-micrometer spectroscopy of the Venus  
surface is possible. In Section 6 we detail the results obtained during the second  
Venus flyby (see also Baines *et al.*, 2000).

### 2.2. JUPITER

The VIMS scientific objectives for Jupiter were built upon the results obtained by  
the Galileo investigations (up until the late fall of 2000). VIMS extended this cov-  
erage in time and illumination/emission geometries, as well as provided contiguous  
spectral coverage into the visual and ultraviolet. Overall, the unique circumstances  
of the several-month-long *Cassini* fly-by enabled full global maps of Jupiter over  
both, a large and continuous range of wavelengths spanning nearly the entire so-  
lar spectrum, and over a large range of phase angles. Specific VIMS scientific  
objectives at Jupiter were:

1. Determine the vertical aerosol distributions and microphysical(optical aerosol  
properties of Jupiter's atmosphere as a function of latitude and longitude.

2. Determine the temporal and spatial variations in constituent gases, including condensables (ammonia, water), and disequilibrium gases (phosphine and ortho/para hydrogen).
3. Investigate the temporal and spatial distribution of lightning, and measure the emission spectrum of lightning from the UV to the near infrared.
4. Determine the vertical and horizontal solar flux deposition in Jupiter's atmosphere to constrain the role of solar energy in Jupiter's meteorology.
5. Investigate auroral and polar haze phenomena, particularly the polar aerosol burden and the abundance of  $\text{H}_3^+\text{Z}$ .
6. Study the temporal evolution of the surfaces of the satellites of Jupiter, particularly that of Io, using VIMS data compared to those of the Galileo NIMS instrument.
7. Investigate time variations in the Io torus.
8. Measure the spectrum of Himalia.
9. Measure the spectrum of Jupiter's Ring.

### 2.3. THE ORBITAL TOUR OF THE SATURNIAN SYSTEM

The overall objectives of VIMS for Saturn and Titan are to investigate ongoing chemical and dynamical processes in a diverse range of planetary and satellite atmospheres, and determine constraints on planetary formation processes and evolutionary histories. The multi-dimensional characteristics of VIMS data acquisition—namely, the ability to acquire two-dimensional spectral maps in 352 wavelengths from the ultraviolet to the thermal infrared allows the instrument to obtain three-dimensional views of atmospheric thermal, aerosol, and chemical structures. Furthermore, these will be over a wide variety of illuminations, and over many emission angles. Meaningful parameters and relationships can be rendered into two-dimensional maps. These then become the tools that enable diverse investigations of chemical, dynamical, and geophysical phenomena. Important targets include the surface and atmosphere of Titan, the cloud-rich atmosphere of the planet itself, its rings, and the plethora of icy moons. Observations of both the day and night sides of these objects shall lead to increased insights into various phenomena involving both reflection and emission of radiation. Occultations of the Sun and stars by these objects should provide new insights into the nature of tenuous stratospheric hazes on Saturn and Titan, the structure of faint rings, and atmospheric composition. Thus, the Saturnian system provides VIMS with many opportunities.

#### 2.3.1. *Titan*

VIMS data will constrain gas and aerosol distributions in Titan's atmosphere as well as their variability with time, and the operative chemical and dynamical processes (Baines *et al.*, 1992). In addition, it is now known that VIMS will be able to see the surface of Titan through atmospheric windows in the infrared (e.g. Tomasko *et al.*, 1989; Griffith and Owen, 1992; Stammes, 1992; Baines *et al.*, 1992; Meier

*et al.*, 2000). Therefore, VIMS studies of Titan will include both the surface and atmosphere and will help in the study of the surface-atmosphere interactions. VIMS objectives for Titan include:

1. Determination of Titan's surface properties using VIMS data obtained at the wavelengths of near-infrared atmospheric windows in Titan's atmosphere (e.g. 0.95, 1.1, 1.3, 1.6, 2.0, 2.7  $\mu\text{m}$ ).
2. Measurement of the vertical distribution of condensable and chemically active gas species, including methane, ethane, and acetylene, along with their spatial and temporal variability. In particular, studies of distributions at microbar and millibar levels using stellar occultation measurements.
3. Determination of stratospheric temperature profiles from multispectral occultation measurements.
4. Determination of equipotential surfaces near the 1 mbar level, and inference of geostrophic winds.
5. Determination of vertical aerosol distributions and associated microphysical and optical properties, over latitude/longitude and time. Studies of stratospheric aerosol distributions from stellar occultation measurements.
6. Determination of the bolometric Bond albedo for comparison to CIRS-determined temperature measurements.
7. Determination of the three-dimensional distribution of solar flux deposition rates to constrain the role of solar energy in powering dynamics at various levels, and to constrain the surface solar energy flux over latitude, longitude, and time.
8. Determination of wind fields as revealed by movements of spatially varying clouds and hazes.
9. Determine the composition of Titan's surface, and map that composition as a function of longitude and latitude.
10. Studies of the geology of Titan's surface and any correlation between geomorphology and composition.
11. Searches for signs of active volcanism and tectonism on Titan's surface.

#### 2.3.2. *Saturn*

VIMS will take advantage of the unique geometry of the *Cassini* orbital tour (encompassing both near-polar and equatorial Saturnian orbits) and the 4-year time window to obtain detailed four-dimensional views (i.e. over latitude, longitude, altitude, and time) of Saturn's atmospheric phenomena. Specific VIMS scientific objectives for Saturn include:

1. Determination of vertical aerosol distributions, and associated microphysical and optical properties, over latitude, longitude and time. In addition, provide enhanced accuracy in the determination of stratospheric aerosol properties using stellar occultation measurements.

2. Detection and characterization of spectrally identifiable ammonia cloud features. In particular, determine their spatial distribution and vertical and micro-physical properties. Such localized clouds have been identified on Jupiter by Galileo NIMS (c.f., Baines *et al.*, 2002). Using similar techniques, their presence on Saturn should be readily observed by *Cassini* VIMS. Also, the detection and determination of water clouds (recently identified in infrared observations by Simon-Miller *et al.*, 2000) will be attempted.
3. Determination of the vertical distributions of variable gas species, including condensables (ammonia and perhaps water) and disequilibrium species (phosphine and ortho/para hydrogen), over latitude, longitude and time. Follow the lead of Galileo NIMS (e.g. Roos-Serote *et al.*, 1999, 2000) in such analyses. In addition, study hydrocarbon and other gas distributions at microbar and millibar levels using stellar occultation measurements.
4. Determination of stratospheric temperature profiles from multispectral occultation measurements.
5. Determination of equipotential surfaces near the 1 mbar level, and inference of geostrophic winds.
6. Determination, over time, of wind fields near the ammonia cloud tops and, perhaps, lower-lying clouds as probed by near-infrared wavelengths. Constrain vertical wind components from cloud top altitude variations.
7. Improve the determination of the bolometric bond albedo of Saturn, and use in constraining the magnitude of Saturn's internal heat source.
8. Investigation of the three-dimensional distribution of lightning, and measurement of the emission spectrum of lightning from the UV to the near infrared.
9. Place constraints on chemical/dynamical mechanisms from spatial/temporal variability in atmospheric phenomena. Specifically, investigate links between disequilibrium and condensable gas variations, as well as variations in cloud opacities and vertical distributions.
10. Determination of the three-dimensional solar flux deposition rate to constrain the role of solar energy in powering dynamics at various levels.
11. Investigation of links between polar aerosol burden and composition, and magnetospheric phenomena utilizing charged particle flux estimates from *Cassini* plasma investigations.

### 2.3.3. *Icy Satellites*

Objectives for the icy satellites are:

1. Determine or constrain the mineralogical compositions of the satellite surfaces at maximum spatial resolution.
2. Determine the composition of the Iapetus dark side material and constrain the origin and evolution of Iapetus and its surface.
3. Relate the compositions of Saturn's icy satellites to that of icy satellites of other planets (i.e. Jupiter, Uranus, Neptune, Pluto)

4. Constrain the insolation absorbed by the satellites of Saturn and thereby constrain the photometric and thermal properties of their regoliths.
5. For the smaller Saturnian satellites, obtain spectral data for comparison with the larger satellites, the ring system, and other small bodies of the outer Solar System.
6. Determine the composition of any dark material on Saturn's satellites, especially Iapetus, Hyperion and Phoebe, and relate the composition of this primitive/organic material to that on other solar system bodies, and to groundbased measurements of objects thought to have primitive material on their surfaces as well as to relevant laboratory data.

#### 2.3.4. *Rings*

Ring objectives are:

1. Determine or constrain the mineralogical composition and grain-size distribution of small (micrometer-sized) as well as large (millimeter- and larger-sized) particles in the rings of Saturn using absorption features found in reflected solar radiation. For rings that are optically thin, constrain, map variations in, and determine the size distribution of small (micrometer-sized) particles via multi-wavelength optical-depth measurements obtained from stellar and solar occultations.
2. Map the radial, azimuthal, and vertical distribution of ring material using stellar occultations, at radial resolutions of 0.1–1 km.
3. Probe dynamical phenomena responsible for ring structure and evolution, including density and bending waves, wakes due to embedded satellites, and resonantly forced ring edges and narrow ringlets, using multiple stellar occultation profiles.
4. Characterize the size distribution of ring particles by imaging the diffraction aureole during stellar occultations.
5. Establish the surface properties (grain size, degree of crystallinity, packing, etc.) of the bodies composing the rings using spectral reflectance measurements.
6. Set bounds on the insolation absorbed by the rings, and thereby constrain their photometric and thermal properties.
7. Determine the composition of any dark material in Saturn's rings and relate its composition to that of other primitive/organic material elsewhere in the solar system and in the laboratory.

### 3. Measurement Goals

#### 3.1. SURFACES

##### 3.1.1. *Spectral Imaging*

The measurements required to meet the scientific objectives for surfaces can be divided into four broad classes:

*Type S1:* High-spectral- and low-spatial-resolution data acquired at great distances from the target. These data will provide orbital phase spectral information and will permit longitudinal mapping of the object at scales greater than  $5^\circ$  spherical lunes. Such observations, performed shortly after arrival at Saturn will provide a preliminary database for defining the spectral regions to be studied during subsequent targeted encounters.

*Type S2:* Observations with high spectral and modest spatial resolution on approach to a targeted satellite encounter until the object fills one VIMS field of view, or until mosaicing is required to obtain full areal coverage. The spatial resolution in this case ranges from  $\sim 10$  to  $\sim 20$  km. This will provide the best global coverage at highest spectral resolution.

*Type S3:* Observations with the highest spatial and spectral resolution allowing coverage of the entire illuminated hemisphere of the object in a limited time. In essence, this amounts to constructing the highest spatial resolution map at full spectral resolution in the shortest possible time consistent with the constraints of a given flyby. These types of observations will usually be made during targeted icy satellite flybys far enough ahead of closest approach that full coverage of the object can be made. The spectral ranges and resolutions and targeting will be the product of tradeoffs determined during observations of *Types S1* and *S2* above.

*Type S4:* High spatial and spectral resolution observations with limited coverage. This type of observation will occur near closest approach during a “close” flyby of an object. This observation type concentrates on obtaining high spatial resolution (at the expense of areal coverage). In practice, we envision riding along with the imaging science subsystem (ISS) and producing a complete VIMS image for each narrow-angle camera frame taken by the ISS. In terms of specific observations of objects in the Jupiter and Saturnian systems, the following discussion of essential observations is presented as a minimal requirement to fulfill the goals of this investigation. As the requirements of the total mission develop and are addressed, this list of observations will be augmented, particularly through obvious resource economies such as joint observations with other instruments.

### 3.1.2. *The Galilean Satellites*

Although the spatial resolution attained by VIMS during the *Cassini* Jupiter flyby was limited to at best 1 pixel at closest approach, VIMS was able to provide information in the visual and near IR spectral range that was not obtained by either Voyager or the Galileo NIMS spectrometer. During the Jupiter flyby, a full set of *Type S1* observations of the Galilean satellites were obtained. The reader is referred to Brown *et al.* (2003) for a discussion of the results.

### 3.1.3. *The Saturnian Satellites*

The Phoebe flyby, prior to the start of the *Cassini* orbital tour, will permit observations of *Types S1* through *S3*. Observations will commence in *Type S1* and end up in *Type S3* depending upon the closest approach distance.



The *Cassini* orbital tour will provide a variety of opportunities for *Type S1* observations of the icy Saturnian satellites at solar phase angles from near zero to the maximum solar cone angle constraint ( $\sim 160\text{--}170^\circ$ ). The minimum requirement is that these observations be made on both hemispheres of all objects at  $5^\circ$  increments in solar phase angle and orbital phase angle. The close satellite encounters will permit *Types S2, S3 and S4* observations of each object. This will yield the near complete spectral mapping of each satellite. Significant support imagery from the ISS will be required for the success of this investigation, much of which will occur as a matter of course as a result of these data being taken simultaneously with the imaging data (VIMS-imaging ride-along mode).

Many *Type S1* observations will be made of Saturn's satellites in order to construct full solar and orbital phase curves. This can be done at times of low spacecraft activity, reducing competition for spacecraft resources.

The typical, targeted satellite flyby will be so fast that, in the time required for a complete VIMS frame to be taken, large changes in phase angle will occur. In addition, the size of the target will change by a large factor. The high spatial resolution data obtained will be a singular event for best definition for subsequent compositional mapping done in concert with ISS NA images. During the period of such an encounter, continuous images will be taken beginning with sub-pixel spatial resolution through the time of closest approach.

#### 3.1.4. *Titan*

During each flyby of Titan, VIMS observations can commence several hours before closest approach. Titan's surface can be mapped at the wavelengths of near infrared windows in Titan's atmosphere. *Type S4* observations will be performed in order to obtain increasing spatial resolution as *Cassini* gets closer to Titan. Mosaics composed of four images taken approximately 4 h before closest approach will allow complete coverage of Titan's hemisphere. Different integration times will be used to measure the opacity of Titan's atmosphere at the wavelengths of near-infrared windows in Titan's atmospheric spectrum. A resolution of about 10 km per pixel can be achieved at 0.5 h before closest approach. A high-resolution mosaic of Titan's surface can be obtained using *image cubes* obtained on successive flybys. This information will complement the observations of Titan's surface by other *Cassini* instruments and will allow the creation of a geological map of Titan's surface based on all *Cassini* observations.

Observations obtained during the first Titan flyby will help characterize the landing site of the *Huygens* probe. Also, at wavelengths longward of  $3\text{ }\mu\text{m}$ , it will be possible to map temperature variations expected to result from any ice diapirs exposed at Titan's surface. It may also be possible to sense the release of volatiles from the interior of the satellite. Lenticulae on Europa are features attributed to ice diapirs and have diameters around 10 km. Such a resolution can be obtained by VIMS about half an hour before closest approach. Therefore, such observations during selected flybys will be carried out so as to characterize such

areas. In addition to observations dedicated for VIMS, we will acquire observations while other imaging instruments have control of the spacecraft pointing.

### 3.2. ATMOSPHERES OF SATURN AND TITAN AND ATMOSPHERE MODES

For atmospheres there are two major types of measurement objectives with respect to Saturn and Titan: spectral imaging and stellar occultation. A third type, that of measuring solar occultations, may also be periodically undertaken. Spectral imaging will be used to map and study trace gas and aerosol distributions, microphysical properties of aerosols, aurorae, lightning production and associated spectral/chemical characteristics, and, for Titan, surface mineralogy and topography. Stellar occultations by the atmospheres of Saturn and Titan and observed by VIMS will be used to study the vertical distribution of trace constituents (e.g. CH<sub>4</sub>, C<sub>2</sub>H<sub>2</sub>, CO, and CO<sub>2</sub>) and aerosols, particularly in Titan's stratosphere. Some thermal profile information may also be forthcoming from spectral regions where refraction is the primary extinction mechanism.

#### 3.2.1. *Spectral Imaging—Spatial Distributions*

Measurements for atmospheres largely follow those for satellite surfaces, in that various combinations of spectral and spatial resolutions will be utilized, depending on the target-spacecraft distance. The actual combinations however are different, owing to the greater spectral activity in gases as compared to solids, the highest spectral resolution modes will be used most frequently.

*Type A1:* High-spectral-, high-spatial-resolution data sets acquired within 25 object radii. The full spectral/spatial resolution and spectral coverage of VIMS-VIS is utilized, as is the full (i.e. standard) spatial/spectral resolutions of VIMS-IR. The data may be limited to specific targeted regions (such as particular regions of belts and zones, storm systems, etc.). Multiple observations of these regions as a function of illumination and viewing geometry (i.e. center-to-limb observations as the feature rotates with respect to the spacecraft, and observations acquired at various phase angles) will enable the full three-dimensional character of the atmospheric region to be determined. For Saturn, such detailed sets of observations are referred to as *Feature Tracks* and *Feature Campaigns*. Specifically, a *Feature Track* is a set of center-to-limb observations acquired at one phase angle; A *Feature Campaign* comprises a set of *Feature Tracks*, obtained over the full range of available phase angles during one orbit. It is expected that at least one *Feature Campaign* will be acquired per orbit, comprised of at least five sets of *Feature Tracks*, with each *Feature Track* comprised of between three and seven individual *Type A1* observations, depending on the phase angle. In addition, a number of other *Feature Tracks* will be conducted per orbit, scrutinizing various other features for temporal variability and contextual relationship with primary *Feature Campaign* objects.

Some *Feature Tracks* are obtained at the same time that data for *Cylindrical Maps* are recorded. At these times large swaths of longitudes are mapped over a

relatively narrow range of latitudes. Other *Feature Tracks* are obtained in specific remote-sensing *Feature Track* observations in cooperation with other remote sensing instruments. These are typically accomplished at ranges less than seven Saturn radii ( $R_S$ ), in order to provide the necessary spatial resolution needed by the full complement of remote-sensing instrumentation onboard *Cassini*. Still others are accomplished during VIMS-specific *feature tracks*.

In practice, it is also expected that many of the *Feature Track* observations will be acquired in cooperative “ride-along” mode with other remote sensing instruments. VIMS’s ability to image a  $32 \times 32$  mrad field of view allows coverage of a wide range of latitudes and longitudes, particularly when outside of  $15 R_S$ , thus enabling many features to be captured within its field-of-view, even when spacecraft pointing is being directed at other places on Saturn by other instruments.

*Feature Campaigns* as done for Saturn will not be feasible for Titan, whose atmosphere is expected to rotate much more slowly than the 10-hr Saturnian period. The time when the spacecraft is within 25 Titan radii ( $R_T$ ) is relatively short (i.e. typically 2.5–5.5 h), but *Feature Tracks* will still be possible due to the rapidly varying spacecraft-target geometry as *Cassini* flies over Titan. Approximately a dozen such *Feature Tracks* are expected per Titan encounter.

*Type A2:* High-spectral- and moderate-spatial-resolution data acquired outside of 25 object radii, utilizing the highest spectral/spatial resolutions of VIMS. At this range, global mosaics will be acquired wherein the target is covered pole-to-pole. For Saturn, these mosaics may be built up from full-disk imaging or from a set of pole-to-pole images acquired over a limited range of solar-illumination/viewing geometry, taking advantage of the relatively rapid rotation rate of Saturn to enable the acquisition of global mosaics under nearly uniform lighting conditions. For Titan, full-disk imaging will be the norm. At least one mosaic of Saturn will be acquired per orbit, lasting ten hours with a duty cycle of some 20%.

*Type A3:* VIMS-IR only observations for nighttime thermal measurements. These will be used particularly on Saturn to acquire high spatial-resolution maps when periapsis occurs on the night side, primarily to map out tropospheric distributions of trace constituents (e.g.  $\text{PH}_3$ ,  $\text{NH}_3$ ). In particular, *Cylindrical Maps* will be obtained wherein nadir views of Saturn’s deep atmosphere will be acquired, peering through relative clearings in the clouds to deep-level “hot spots”. Ten hours of continuous observations may be needed, depending on periapsis distance.

*Type A4:* VIMS-IR long-integration observations for weak emissions. Methane fluorescence will be observed on the dayside, and  $\text{H}_3^+ Z$  emissions will be observed on the night side using this technique. Observations of high-altitude emissions are conducted within strong bands of atmospheric methane absorption. Integrations up to 10 s may be used.

*Type A5:* VIMS high-speed photometry mode for detection and characterization of lightning emissions. Under nighttime conditions, while relatively close to the planet (less than  $10 R_S$ ), VIMS stares at one location at a time, searching for lightning. When lightning strikes, the full spectrum is obtained, and acquiring data at

high rates (about 20 ms integrations), the chronological order of multiple lightning strikes in a single locale can, in principle, be ascertained. From analysis of the lightning emission spectrum in and out of methane absorption bands, it is hoped that the altitude of emission can be determined as well as the total energy for each lightning strike.

### 3.2.2. *Atmospheric Stellar Occultations*

Stellar occultations will be attempted periodically during Titan encounters, for a period of 5–10 min each. Integration times are typically 80 and 13 ms, respectively, for VIMS-VIS and VIMS-IR. These high sampling rates thus enable VIMS-VIS vertical resolutions of between 30 and 50 m for tangential spacecraft velocity components, relative to Titan, of 3–5 km/s. Observations last 3–6 min on average. Further details on particular occultation modes are discussed later.

## 3.3. RINGS

There are two major types of measurement objectives for the VIMS investigation with respect to Saturn's ring system: Spectral imaging and stellar occultation. Spectral imaging will be used to map and study the composition and mineralogy of Saturn's rings. Usually this will use *image*, *line*, or *point* instrument modes (see Section 5.2.1 for definitions). Stellar occultations by the rings and observed by VIMS will be used to study the dynamical structure of the rings. The *occultation* modes are used for these (see Section 5.2.2 where these modes are defined).

### 3.3.1. *Spectral Imaging of Rings*

The purpose of ring spectral imaging with VIMS is to determine the spatial distribution of various chemical species in Saturn's rings by mapping absorption bands in the visual and in the near infrared spectral regions. Radial mineralogical differentiation of the ring may be a key issue, related to ongoing transport phenomena in the rings, and related as well to the initial conditions through which the rings were formed (like a satellite breakup or the remnants of the protoplanetary nebula).

Another specific goal of VIMS is to characterize small-particle properties through the observation of the rings at various phase angles. Micrometer-sized particles are an important tracer of the ring dynamics because they are abundantly released during collisions, and also because they are sensitive to non-gravitational forces like radiation pressure or the Lorentz force. The visual and infrared channels of VIMS have access to the very wavelengths from which Mie scattering phase functions may be derived for these particles. Such functions yield some important physical properties of the particles (real and imaginary refractive index, size distribution).

Spectral identifications will require mapping the Saturnian ring system at the highest spectral and spatial resolution consistent with mission constraints. The best opportunity for spectral imaging of the rings occurs at Saturn Orbit Insertion when the spacecraft is closer to the rings than it will be for the rest of the Saturn Orbital

Tour. The present scenario calls for VIMS to be operated in line mode, using the shortest possible integration time consistent with useful signal precision (signal-to-noise ratio, or S/N). We note that VIMS-IR 2-D scan mirror is particularly convenient for that purpose since it allows us to choose the region of the ring which will be mapped, within the VIMS-IR 32 mrad field of view. During the rest of the orbital tour, ring regions to be mapped will be selected according to the orbit geometry, so as avoid redundancy and cover as much as possible of the ring system in the initial phases. In later phases, when interesting compositional and dynamical regions are discovered, they will be re-observed using a strategy specific to the phenomena being studied.

Some regions of dynamical interest will be mapped at the highest possible spatial resolution. In particular, spectral signatures near sharp edges, wave features, or narrow ringlets can provide evidence for the release of fresh material through enhanced collision rate. The radial width of the waves features is typically 100 km, i.e. barely resolvable by the VIMS instrument. Nevertheless, mineralogical differentiation near these regions can be detected, in particular during the close approach of the entrance orbit. On the other hand, the typical width of sharp edges is a few meters only. However, the streamline distortions near an edge are significant over radial distances of several tens of km. Thus, VIMS may detect and map mineralogical differentiation near edges also. Transient phenomena like clumps or braids in the narrow F ring will also be mapped by VIMS.

Depending on the precise orbital tour, VIMS observations of the rings will cover a complete range of phase angles, allowing the size range of small particles to be strongly constrained. The range of phase angles to be covered is  $0-165^\circ$ , the latter limit dictated by the need to keep direct sunlight off the VIMS focal plane.

Long exposures will also be made (consistent with the  $\sim 1.2$  s limit on the integration time in VIMS-IR) to map the structure and composition of faint rings like E ring, whose optical depth lies in the range  $10^{-4}$ – $10^{-5}$ . In addition, the comparison of the spectrum of Saturn's E ring to that of Enceladus will help to determine if Enceladus is indeed the source of the E-ring material as is presently thought.

### 3.3.2. *Stellar Occultations by Rings*

The purpose of ring-stellar-occultation observations with VIMS is to obtain high-S/N optical depth profiles of the rings, at a variety of longitudes, ring incidence angles, wavelengths and times during the *Cassini* orbital tour. The radial resolution is limited by the VIMS sampling time (13–100 ms, corresponding to 100 m–1 km typically), by Fresnel diffraction (typically 40 m, at  $3\text{-}\mu\text{m}$  wavelength and a distance of  $5 R_S$ ), and by the diameter subtended by the stellar disk at the rings (10–100 m). The S/N achieved will depend on the sampling time, the stellar brightness, and the background flux of sunlight reflected by the rings into the VIMS aperture. Simultaneous observations at two or more wavelengths will permit this background signal to be subtracted from the stellar signal, once the

appropriate calibration data are obtained. Typical occultation durations will be 30 min–5 h, with 2 h a good average for a complete ring occultation near pericenter. A similar experiment may be done using the Sun as a source using the VIMS-IR solar port, but in this case the primary purpose is to quantify the ring extinction as a function of wavelength between 1 and 5  $\mu\text{m}$ , at 300–1000 km spatial resolution.

During stellar occultations, VIMS will also obtain information on the ring particle size distribution by observing the 'aureole' of forward-scattered light surrounding the direct stellar line-of-sight. Utilizing the full VIMS wavelength range of 0.3–5  $\mu\text{m}$ , and obtaining  $32 \times 32$  mrad 'images', particle sizes between 2  $\mu\text{m}$  and 3 mm can be probed.

Because the angular size of the effective VIMS pixel ( $0.5 \times 0.5$  mrad) is comparable to the pointing command and control errors expected for the *Cassini* spacecraft, an active method is necessary in order to keep the instrument bore-sighted on the star during a ring occultation. This will be achieved by using the VIMS-IR 2-D scanning capability to periodically perform small ( $4 \times 4$ ) raster scans, identify the location corresponding to the maximum stellar signal, and then reset the mirror position accordingly. Because portions of the rings are likely to be effectively opaque (notably the middle B Ring) this 'auto-guiding' function can be turned off for short periods according to a specified schedule.

In order to correct the ring occultation data for the presence of reflected ring light, a spatial map of the ring reflectivity spectrum is required. For this purpose, 1-D drift scans across the rings will be conducted at a range of phase angles and lighting conditions (lit side/unlit side, as well as various incidence angles), using the identical data mode used to take ring occultation data. For these scans, standard spacecraft attitude control will be sufficient. In fact, these scans may be identical to regular 1-D spectral maps of the rings acquired for other scientific purposes.

Full IR spectral observations of the occultation stars prior to the actual occultation observations will be necessary for calibration purposes, and for final selection of suitable occultation candidates. Some stellar observations must therefore be done during the interplanetary cruise phase, prior to SOI.

VIMS packets containing occultation data also contain absolute timing signals derived from the ultra-stable oscillator (USO) in the radio science subsystem. The exact relation between the photon-arrival time of the first data point in the packet and the recorded clock signal will be known to  $\pm 1$  VIMS sample, or 13 ms. The absolute precision of the timing signals will be maintained to the same level, or better, and the VIMS sampling rate will be controlled and known to an accuracy such that the maximum cumulative timing error over one packet is appreciably less than 13 ms. The overall goal is that the photon arrival time for any specified occultation datum can be reconstructed to  $\pm 13$  ms, after the data is received on the ground.

Ring occultations can only be carried out on inclined orbits, and are thus concentrated within certain limited periods of the baseline orbital tour. Only the ingress of the star behind the rings is observed, so as to permit acquisition of the star via



the star tracker prior to the occultation. Similar opportunities exist on most inclined ( $i > 10^\circ$ ) orbits, and a great many more on the near-polar orbits in the last year of the baseline tour. A total of 50–100 stellar occultations by the rings may be observable during the nominal mission.

#### 4. Instrument Description

This section presents a broad overview of the technical aspects of the VIMS instrument. For a detailed technical description, the reader is referred to the literature (Miller *et al.*, 1996; Reininger *et al.*, 1994) and *Cassini* project documents that describe the technical aspects of the VIMS instrument in detail. For a complete discussion of the operational aspects of the *Cassini* VIMS the reader is directed to the *VIMS Users Manual* (JPL document D-14200).

##### 4.1. VIMS-VIS THE VISUAL CHANNEL

VIMS-VIS is a multispectral imager covering the spectral range from 0.30–1.05  $\mu\text{m}$ . VIMS-VIS is equipped with a frame transfer CCD matrix detector on which spatial and spectral information is simultaneously stored. The CCD is passively cooled in the range ( $-20$  to  $+40^\circ\text{C}$ ). Radiation collected from VIMS-VIS telescope is focused onto the spectrometer slit. The slit image is spectrally dispersed by a diffraction grating and then imaged on the CCD: thus, on each CCD column a monochromatic image of the slit is recorded. On-chip summing of pixels allows implementation of a large number of operating modes for different observing conditions.

The maximum capabilities of VIMS-VIS are a spectral resolution of 1.46 nm and a spatial resolution of 167  $\mu\text{rad}$  while in the high-resolution mode of operation. On-chip summing of five spectral  $\times$  three spatial pixels enables the normal mode of operation whereby VIMS-VIS achieves a spectral resolution of 7.3 nm and a spatial resolution of 500  $\mu\text{rad}$ . The total field of view of the instrument is  $2.4^\circ \times 2.4^\circ$ , although matching with VIMS-IR imposes the use of a  $1.8^\circ \times 1.8^\circ$  FOV. The main characteristics of the instrument are listed in Table I.

As seen in the functional block diagram (Figure 1), VIMS-VIS is composed of two modules, the optical head and the electronic assemblies, housed in separate boxes. The VIMS-VIS optical head, shown in Figure 2, consists of two units: a scanning telescope and a grating spectrometer, joined at the telescope focal plane where the spectrometer entrance slit is located. The telescope mirrors are mounted on an optical bench that also holds the spectrometer. In fact, the optical bench is the reference plane for the whole instrument.

The telescope primary mirror is mounted on a scan unit that accomplishes two specific tasks: (a) pointing and (b) scanning. The scanning capability enables the 500  $\mu\text{rad}$  IFOV of the nominal mode of operation by a two-step motion of the



TABLE I  
VIMS-VIS System Characteristics (After Reininger *et al.*, 1994).

Spectral coverage	350–1050 nm
Spectral sampling (VIMS-VIS capability)	1.46 nm
Spectral sampling ( <i>Cassini</i> requirements)	7.3 nm (5 pixel summing)
IFOV	$0.17 \times 0.17$ mrad
Effective IFOV	$0.5 \times 0.5$ mrad (3 $\times$ 3 pixel summing)
FOV ( <i>Cassini</i> requirements)	$1.83^\circ \times 1.83^\circ$
FOV (VIMS-VIS capability)	$2.4^\circ \times 2.4^\circ$

primary mirror during each integration time; images are produced by scanning across the object target in the down track direction (push-broom technique). The pointing capability is used to image selected target regions in a range about  $1.8^\circ$  around the optical axis, and to observe the Sun, through the solar port, during in-flight radiometric calibration.

An in-flight calibration unit is located at the entrance of the telescope. The unit consists of: (a) two LEDs for a two-point calibration of the spectral dispersion and (b) a solar port for direct solar imaging and hence for radiometric calibration. Because the remote sensing pallet is body-mounted to the spacecraft, to image the Sun the spacecraft is reoriented to form a  $20^\circ$  angle with the boresight direction of the instrument and the instrument scan mirror needs to be moved to an angle of  $4.8^\circ$  from boresight. Under these conditions light from the Sun passes through a cutout

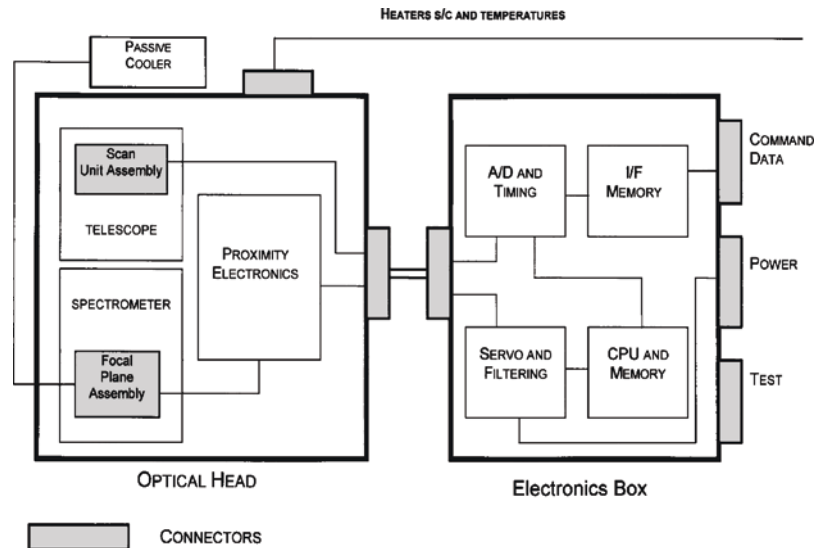


Figure 1. VIMS-VIS functional block diagram.

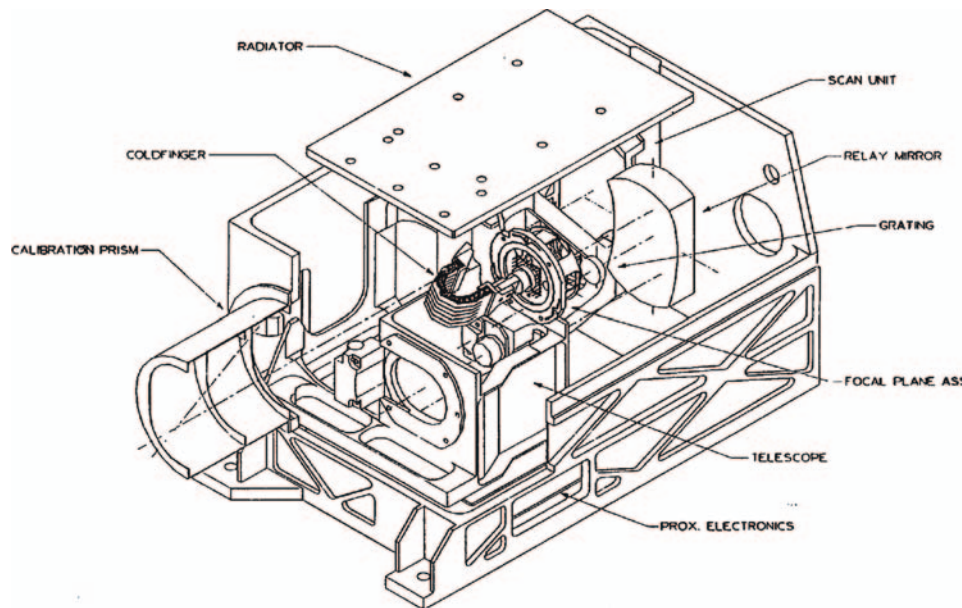


Figure 2. VIMS-VIS cutaway diagram.

in the instrument baffle and then through a prism that attenuates the solar radiation and redirects it towards the telescope primary mirror. Due to budget constraints, the high-resolution mode was been implemented and tested, but not calibrated. Calibration will be accomplished during the cruise phase to Saturn.

#### 4.2. VIMS-IR THE INFRARED CHANNEL

In Figure 3 is a wire-frame drawing of VIMS-IR showing the major optical components along with the light paths. At the top of Figure 3 can be seen the visual channel with its light path and foreoptics, and near the bottom of Figure 3 is the infrared channel with its light path and foreoptics. Also shown at the right is the cover for the VIMS-IR optics that was successfully deployed as of August 15, 1999, some 50 h before the time of closest approach during the *Cassini* Earth Swingby. VIMS-VIS and VIMS-IR are mounted to a palette that holds them in optical alignment and helps to thermally isolate the instrument from the *Cassini* spacecraft. Thermal isolation is particularly important for the infrared channel because thermal background radiation from the IR spectrometer, combined with shot noise from leakage current in the InSb photodiodes of the 256 element linear array detector of VIMS-IR are the chief sources of noise in measurements obtained with the IR channel. The nominal operating temperature for the VIMS-IR focal plane is 55–60 K and for the IR foreoptics and spectrometer optics 120 K.

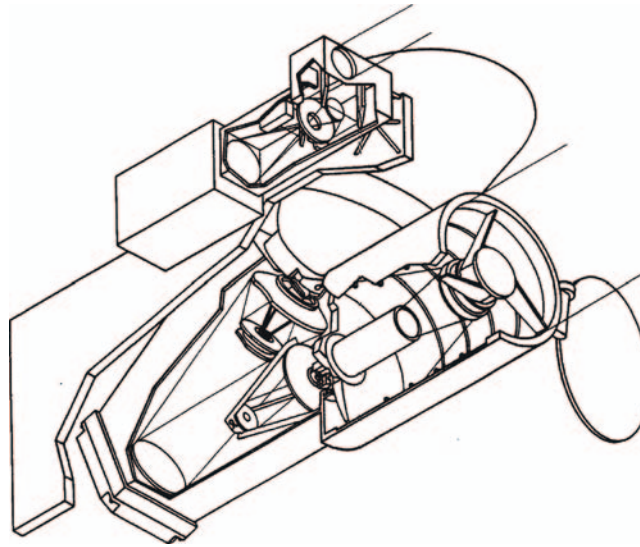


Figure 3. VIMS IR wire-frame drawing.

The VIMS instrument is mounted on the *Cassini* spacecraft by means of a palette (called the remote sensing palette or RSP) on which are also mounted the *Cassini* imaging science subsystem (ISS), the composite infrared spectrometer (CIRS), and the ultraviolet imaging spectrometer (UVIS). Mounting of all the *Cassini* remote sensing instruments on a common palette allows relatively precise boresight alignment of the four instruments, enhancing synergy between the four instruments.

Figures 4 and 5 are computer-aided design (CAD) models of the *Cassini* spacecraft with all of the major spacecraft components and their spatial relationship to the remote sensing palette indicated. Figure 4 specifically shows the mounting position and orientation of the VIMS instrument on *Cassini*. Figure 6 is a picture of the infrared channel very near the time that the VIMS instrument began its thermal vacuum and ground calibration tests prior to integration on the *Cassini* spacecraft. Also in Figure 6 are some of the nefarious characters that helped give birth to VIMS.

#### 4.3. FUNCTIONAL DIAGRAMS

Figure 7 is a functional block diagram of the entire VIMS instrument, with VIMS-VIS and VIMS-IR integrated on an optical pallet assembly (OPA).

#### 4.4. PERFORMANCE AND OPTICAL SPECIFICATIONS

##### 4.4.1. VIMS-VIS

The optical specifications of both components of the VIMS instrument are given in Table II. The VIMS-VIS telescope is a  $f/3.2$  system which uses a Shafer design to



Figure 4. CAD model of *Cassini* orbiter with VIMS shown.

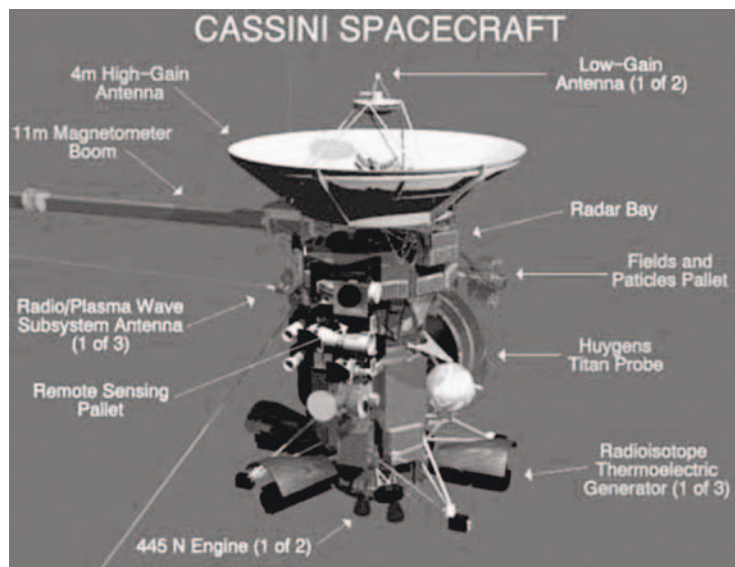


Figure 5. CAD model of *Cassini* with various subsystems indicated.

couple an inverted Burch telescope to an Offner relay system. The Burch telescope consists of a concave scanning primary mirror, a planar folding mirror, and a spherical convex secondary mirror. The Burch telescope produces a curved, anastigmatic virtual image which is fed to the Offner relay whose purpose is to produce a flat, real image on the telescope focal plane without losing the anastigmatic quality



Figure 6. VIMS-IR and some of the engineers.

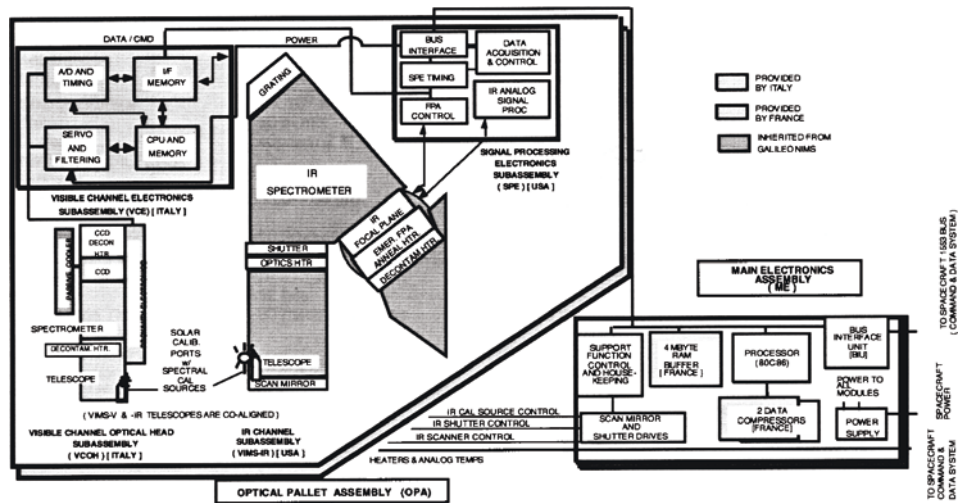


Figure 7. Integrated VIMS functional block diagram.

of the Burch telescope (See F. Reininger *et al.*, 1994). The telescope is effectively diffraction limited at  $0^\circ$  scan angle over the full field, the encircled energy at  $1.2^\circ$  off-axis (maximum VIMS-VIS capability) is 97.8% for a  $24 \mu\text{m}$  square (size of the CCD pixel); moreover, the geometrical spot sizes were under  $12 \mu\text{m}$  at  $0^\circ$  scan angle over the full field.

TABLE II  
VIMS-VIS and VIMS-IR optical system characteristics.

	VIMS-VIS	VIMS-IR	Total system
Spectral coverage	0.35–1.0 $\mu\text{m}$ (0.3–1.0 $\mu\text{m}$ by special command)	0.85–5.1 $\mu\text{m}$	0.35–5.1 $\mu\text{m}$ or 0.3–5.1 $\mu\text{m}$
Spectral sampling	7.3 nm/spectral (96 bands) ( $1 \times 5$ sum)	16.6 nm/spectral (256 bands)	
Spatial characteristics			
Instantaneous field of view (IFOV)	$0.17 \times 0.17$ mrad	$0.25 \times 0.5$ mrad	
Effective IFOV	$0.5 \times 0.5$ mrad ( $3 \times 3$ sum)	$0.5$ (0.5 mrad ( $1 \times 2$ sum)	$0.5 \times 0.5$ mrad
Total field of view	$64 \times 64$ pixels ( $32 \times 32$ mrad)	$64 \times 64$ pixels ( $32 \times 32$ mrad)	$32 \times 32$ mrad
Swath width	576 IFOVs ( $3 \times 3 \times 64$ )	128 IFOV ( $2 \times 64$ )	32 mrad
Image size modes (fast scan)	1–64 pixels	1–64 pixels	1–64 pixels
Image size modes (slow scan)	1–64 pixels	1–64 pixels	1–64 pixels



The focal plane of the telescope is the entrance object plane of the spectrometer. The spectrometer is an Offner relay matched to the telescope relay ( $f/3.2$ ) that utilizes a holographically recorded convex spherical diffraction grating as the secondary mirror of the Offner relay. The grooves of the grating have a rectangular profile. In addition, two different groove depths are used in adjacent sections of the grating to enhance the grating efficiency spectrum in the UV and IR regions. This compensates for the spectral response function of the CCD detector (quantum efficiency) and for the solar radiance (the peaks occur at about 675 and 475 nm, respectively). In 67.5% of the grating surface, there is a groove depth of 300 nm while the remaining 32.5% is covered with grooves of depth 440 nm. The spectrometer spot diagrams show that for a  $0^\circ$  scan angle all the energy falls inside a CCD pixel over the full angular and spectral fields.

The CCD detector is a  $512 \times 512$  Loral frame-transfer, front-side-illuminated device. The pixel size is  $24 \mu\text{m} \times 24 \mu\text{m}$ . Half of the detector is used for the frame transfer, and the effective sensitive area corresponds to a  $256 \text{ spatial} \times 480$  spectral pixels. To minimize second- and third-order light from the grating, two long-pass filters were deposited on a window used to seal the detector. The junction between the two filters (located at 601 nm) induces a dead zone on the detector of less than  $40 \mu\text{m}$  (a nominal spectral pixel is  $120 \mu\text{m}$  wide). To improve CCD detector responsivity in the UV region of the spectrum a Lumigen coating has been deposited on the CCD sensitive surface in the region 300–490 nm.

The performance of the instrument can be evaluated by its S/N for a given configuration of the instrument and for a given target scenario. VIMS-VIS has been designed to guarantee a  $S/N > 100$  under all observing conditions for the nominal mode of operation.

#### 4.4.2. VIMS-IR

The VIMS infrared channel optical design follows that of the Galileo NIMS instrument, but incorporates several improvements that result in much better performance than that of its predecessor. The IR foreoptics is a 23-cm diameter Ritchey Cretien telescope operating at  $f/3.5$ . It is equipped with a secondary mirror that can be scanned in two orthogonal directions, resulting in the scanning of  $64 \times 64$  mrad scene across a  $0.2 \times 0.4$  mm entrance slit. The entrance slit is coupled to a classical grating spectrometer using a  $f/3.5$  Dahl-Kirkham collimator. The spectrometer incorporates a triply-blazed grating whose blaze angles have been adjusted so as to compensate for the steep drop in intensity of the solar spectrum toward long wavelengths, thus resulting in a more uniform signal-to-noise ratio across the  $0.85\text{--}5.0 \mu\text{m}$  wavelength region when viewing spectrally neutral objects in sunlight. The dispersed light from the grating is imaged onto a  $1 \times 256$  array of InSb detectors using a  $f/1.8$ , all reflective, flat-field camera. The IR detector employs four filters, used both for order sorting and for blocking excess thermal radiation from the spectrometer optics. The secondary mirror of the VIMS foreoptics is articulated using a two-dimensional, voice-coil actuator capable of  $0.25$

mrad steps in the fast-scan direction and 0.5 mrad steps in the slow-scan direction. Because the optical performance and design of NIMS have been described in detail elsewhere (Aptaker, 1982; Macenka, 1982), we direct the interested reader to those discussions. Below we will focus in more detail on the optical improvements to the NIMS design.

The major areas in which the VIMS design improves on the NIMS design are: a two-axis, voice coil actuator for articulation of the telescope secondary mirror; a fixed, three-blaze grating; an improved shutter to replace the NIMS focal-plane chopper; on-board solar and spectral calibration; and an improved IR detector.

The two-axis scan mechanism employs four voice coil actuators for articulation and two linear variable displacement transformers for position sensing. The secondary mirror is mounted on a monolithic gimble ring supported by four flexures. The flexure life is predicted to be greater than 20 million cycles. The range of motion is 128 steps in the fast-scan direction and 64 steps in the slow-scan direction, both covering approximately 64 mrad in angular displacement. The step transition time is a maximum of 5 ms.

The grating is blazed in three separate zones designed to more evenly distribute the performance of the spectrometer over the large 0.85–5.1  $\mu\text{m}$  spectral region covered by the VIMS instrument. The groove spacing is 27.661/mm, and the first, second and third blazes cover 20, 40 and 40%, respectively of the area of the grating. The three zones are blazed at wavelengths of 1.3, 3.25 and 4.25  $\mu\text{m}$ , respectively.

The shutter mechanism of VIMS is a blade located just in front of the spectrometer slit. The shutter can be commanded to block the light from the foreoptics, thus allowing a specific measurement of the thermal background radiation and detector dark current that collects during a given integration period. In normal operation this is accomplished at the end of every fast scan, and the result is both subtracted from the open-shutter measurements, and downlinked with the data. A LED-photo-sensor pair is employed to detect blade position. Lifetime tests indicate a minimum life of  $7 \times 10^6$  cycles at the normal operating temperatures of 120–140 K.

The IR focal plane assembly is a linear array of 256 InSb photo detectors read by two FET multiplexers. Each detector is  $200 \times 103 \mu\text{m}$  in size and positioned on 123  $\mu\text{m}$  centers. Each multiplexer handles 128 detectors, and the two multiplexers are interdigitated; thus, each reads every other detector along the array. This arrangement was chosen to prevent the loss of half of the spectral range of the instrument if one of the multiplexers fails. The detector is housed in a Kovar package, specially constructed to mimic the dimensions of the NIMS detector, and to allow the employment of most of the original design of the NIMS passive cooler. To keep the detector dark current within the range necessary for observations at Saturn, the detector must be cooled to 60 K or less, and becomes non-operational for science observations at 77 K. Mounted in the Kovar package and over the detector array are four order-sorting filters that also reduce the amount of stray thermal radiation from the spectrometer optics incident on the detectors. The filters are arranged in four

contiguous segments, the lengths of which were carefully chosen so as to provide efficient order sorting and to place the slight gaps between the filters in places that would not have an adverse impact on science observations in the Saturn system. For more details on the filters (or on any of the above topics) the reader is referred to Miller *et al.* (1996).

The final two enhancements to the NIMS design are the addition of a port through which the Sun can be observed and a laser diode that is used for onboard wavelength calibration. Detailed descriptions of the solar port and the on-board spectral-calibration capability of VIMS appear later in this document.

#### 4.5. DATA HANDLING, COMPRESSION, AND BUFFERING

Reversible data compression for the VIMS instrument is performed by a dedicated module based on a digital signal processor working at 6 MHz that interfaces with the VIMS command and data processing unit through an input first-in-first-out buffer and an output first-in-first-out buffer. The data compression algorithm consists of a preprocessing routine and a Rice entropy encoder (Rice *et al.*, 1991). The data unit for compression is a series of 64 spectra (a slice) obtained during one scan (i.e., in nominal  $64 \times 64$  image mode or  $64 \times 1$  line mode) or a series of scans. This provides 64 pixels each with 352 spectels. Each slice is divided into 11 sub-slices of 32 spectels (three for the visual channel and eight for the IR channel), and each sub-slice is compressed independently. This restricts the impact of possible bit errors either in random access memory (single event upsets) or during transmission.

The preprocessing routine for the  $64 \text{ pixel} \times 32 \text{ spectel}$  sub-slice is based on the large entropy content of variations in lighting and albedo when compared to spectral signatures (more than 5 to 1). Four evenly distributed channels are summed and divided by four so as to obtain a representative “brightness line” for this spectral range. This line and the brightest spectrum are differenced, then Rice encoded into a header. The matrix product of the brightest spectrum by the brightness line provides a model rectangle where every pixel has the same brightness as the actual data and the same spectrum as the brightest pixel. The model rectangle is then subtracted from the actual data. The entropy of the resulting “spectral rectangle” is directly related to the variations in relative spectral characteristics. It is then differenced along the spatial direction and the  $63 \times 32$  differences are Rice encoded. Reconstitution on the ground first recovers the brightness line and brightest spectrum from the header, then the rectangle of  $63 \times 32$  differences, and finally the original data taking advantage of the fact that model and data are identical for the brightest spectrum. The compression ratio for fully reversible compression ranges between 2 and 3 depending on the actual entropy of the data.

Reversible compression is highly sensitive to over sampling of the noise. Each doubling of the data number (DN) level of the noise adds 1 bit per data element to the compressed string. After calibration, the shot noise can

be accurately predicted from the data itself. The algorithm provides the possibility of defining two DN limits, Lim2 and Lim4, above which the total noise is expected to exceed 2 (4) DN. Each datum in the spectral rectangle is divided by 2 if the model value exceeds Lim1 (Lim2) (4). The quantization noise after reconstitution is then  $2 \times 0.28$  DN ( $4 \times 0.28$  DN) instead of 0.28 DN hence the compression algorithm is able to automatically divide the actual gain by 2 (4) for DN levels associated with large shot noise. Setting Lim1 and Lim2 to 4096 (larger than any 12 bit data) provides fully reversible compression.

A data buffer of 4 Mb is used for buffering data between the VIMS processor and the spacecraft. Its full memory is divided into two redundant pages of 2 Mb, each consisting in 32 sectors organized as a matrix of four lines by eight columns. Each sector contains two  $32K \times 8$  RAM chips, connected in parallel to achieve a 16-bit architecture. Each sector can be specifically selected. The transfer is made via a direct memory access (DMA), with write and read maximum times of 240 and 140 ns, respectively. Each column includes an “anti-latchup” capability and over-current protection, which switches off the power autonomously in case of over-threshold current (100 mA in 11  $\mu$ s or 200 mA in 4.4  $\mu$ s).

Dassault Electronique of France developed the VIMS data buffer. It was qualified for radiation levels up to 20 krad, storage temperatures of  $(-55^{\circ}\text{C}, +125^{\circ}\text{C})$ , and operating (full functional) temperatures of  $(-40^{\circ}\text{C}, +80^{\circ}\text{C})$ . It consists of a single board, with one page on each side,  $162 \times 129 \times 17$  mm<sup>3</sup> in size, and 625 g in mass. With a  $5 \pm 0.25$  V supply voltage, its power consumption is 1.5 W in stand-by mode, and 2 W during operations.

## 5. Instrument Operation

### 5.1. GENERAL OPERATIONAL CONSIDERATIONS

#### 5.1.1. VIMS-VIS

VIMS-VIS operates in different operating states and in different modes. The CCD data acquisition mechanism combines pixels by summing them on chip, both in the spatial direction (along slit) and in spectral direction. The use of a scanning secondary mirror allows summation of pixels parallel to the slit. Thus square spatial pixels are generated in lower spatial resolution modes. There are five operating states of the instrument as a whole: science status, internal calibration, uploading, downloading, and off. The scientific data and the internal calibration data are in turn defined by different operating parameters that translate the scientific requirements for the data collection into the physical, electrical and optical characteristics of the instrument.

When VIMS-VIS is switched on it goes into the science state in the nominal mode. The commands to change the operating state are sent to the VIMS-VIS electronics together with the set of parameters relevant to define a new state. The scientific data set can be obtained in different “operative modes” according to the

different observation scenarios. For each mode the operating parameters define the characteristics of the data to be collected, such as spatial resolution, spectral resolution, and extent and location of the scene to be observed in the instrument FOVs. When the instrument is switched on, the combination of different parameters that define the different observation modes are loaded. The input parameters of the scientific data acquisition modes are:

- (a) Summing parameters,
- (b) Swath width,
- (c) Swath offset,
- (d) Spectral offset,
- (e) Swath length,
- (f) Exposure time,
- (g) Exposure time delay,
- (h) Mirror,
- (i) Gain,
- (j) Anti-blooming.

Different combinations of these parameters lead to several different operative modes.

#### 5.1.2. *VIMS-IR*

The two main considerations in the design of the IR component of VIMS are flexibility and compatibility with the other *Cassini* remote sensing instruments. A range of programmable parameters, including integration time, swath width and length, and mirror position enable the instrument to adapt to a variety of observing modes dictated by the scientific objectives of each phase of the *Cassini* mission, and by synergistic observations with other *Cassini* instruments. Software enhancements uploaded after launch provide more levels of flexibility, including spectral editing, additional image sizes, increased spectral resolution in the visual channel, and a doubling of the instrument's spatial resolution.

### 5.2. SPECIFIC OPERATIONAL MODES

*Image*, *line*, *point*, and *occultation* are instrumental modes of operation. An operational mode corresponds to specific instrumental parameter settings, as was illustrated in Section 5.1.1. The *image*, *line*, and *point* modes are the most frequently used. Observation types (Sections 3.1.1. and 3.2.1) are use oriented variations on single modes.

#### 5.2.1. *Image*, *line* and *point* mode descriptions

The majority of scientific observations by VIMS will be in the *image*, *line*, or *point* modes. Several modes were tested for a variety of integration times and instrument gain states. For image sizes smaller than  $64 \times 64$ , the scan mirror can be offset from the boresight in both the  $x$  and  $z$  directions. In the *image* mode, VIMS is a framing

instrument, producing a spectral cube of 352 images in the specified size. Three routinely used sizes for the images are a full  $64 \times 64$  IFOVs,  $12 \times 12$  IFOVs and a single ( $1 \times 1$ ) IFOV. The  $12 \times 12$  image size corresponds to the field of view of the image science subsystem's narrow angle camera (ISS NAC). This mode will be used to efficiently gather data simultaneously with ISS. The  $1 \times 1$  image size corresponds to *point* mode, which will be used primarily for stellar occultations or for the accumulation of spectra during a rapid flyby of a target for which motion compensation is not possible. Rectangular combinations of 12, 32, and 64 are also in the group of tested modes: these will be used during periods when the data rates or volume is constrained. It is possible to offset the position of the scan mirror so that "sub images" are gathered in a position offset from the center of the field of view. Compositional mapping and photometric studies of Saturn, the surfaces of the icy satellites, Titan, and the rings, and dynamical studies of Saturn and Titan will be performed primarily in the image modes.

The VIMS instrument was also designed to obtain data in single lines of either 12 or 64 IFOVs parallel to either the spacecraft's *x*- or *z*-direction. The line mode parallel to the *z*-direction will be used in synergistic studies such as atmospheric profiles of Saturn and Titan with CIRS and UVIS, both of which have slits parallel to this axis. *Line* mode can also be operated such that the spacecraft's motion scans a second spatial dimension. These modes of operation are useful, for example, in a rapid flyby where motion compensation is not possible.

### 5.2.2. Occultation Modes

VIMS is the only instrument on the *Cassini* payload capable of observing stellar occultations in the visual and near IR portion of the spectrum. Stellar occultations by the atmospheres of Titan and Saturn will be used to derive the vertical distribution and microphysical properties of aerosols, and the stratospheric temperature profiles of these two bodies. Stellar occultations of the rings of Saturn will provide a sensitive probe of their radial structure, optical depth, composition and physical properties.

Occultations will be executed in the point mode. Before each occultation a  $12 \times 12$  image of the star will be obtained. On-board software will seek the pixel with the maximum brightness. The instrument's mirror will be offset so that data is gathered in this pixel. If necessary, additional images can be gathered during long occultations to check that the star is still centered in the selected pixel. If the star has drifted, the mirror can be repositioned so that data are gathered from the pixel with the maximum brightness.

Three different modes of ring occultation observation are currently envisaged, with different data rates and spectral coverages:

*Occultation mode 1:* In this mode, which is applicable to stellar occultations by Saturn, Titan, and the rings, complete IR spectra are recorded, compressed, and either stored in the VIMS internal buffer or in the spacecraft on-board solid state recorder (SSR). The scan mirror oscillates so as to synthesize an effective 0.5-mrad square pixel for each spectrum. The sampling rate is adjusted, up to a maximum of



$\sim 10$  Hz (one complete spectrum every 0.1 s). The maximum data rate (2:1 compressed) is  $0.5 \times (256 \text{ channels} \times 12 \text{ bit} \times 10 \text{ Hz}) = 15.4 \text{ kb/s}$ . Typical data volumes are 5 Mb for a 300-s atmospheric occultation, and 110 Mb for a 2-h ring occultation. A modification of this mode, employed for the aureole observations, is to interrupt the regular occultation data stream with a full  $64 \times 64$  pixel spatial/spectral map of the starlight scattered by the rings into the instrument FOV. Such a map would require 8.6 Mb of data, compressed, and take  $\sim 450$  s at 100 ms sampling. Since each pixel subtends at least 150 km on the rings at  $5 R_S$ , the full image covers a patch about 9600 km square, about twice the distance the star travels across the rings in 450 s, and comparable to the largest homogeneous regions in the A, B and C rings.

*Occultation Mode O2:* In this mode, to be used primarily for ring occultations (but possibly also for icy satellite occultations), edited spectral averages are returned at the maximum VIMS sample rate of 77 Hz. Using spectral editing mode, a small number of spectral editing masks will be chosen, but a typical mask would require the co-addition of 15–30 contiguous spectral channels centered at four different wavelengths. A typical example might be 30 co-added channels centered at 2.00, 2.25, 2.90, and  $3.50 \mu\text{m}$ . As in *mode O1*, the internal mirror oscillates every 6.5 ms to synthesize a 0.5 mrad square pixel. The four co-added signals are stored or transmitted, uncompressed, every 13 ms, for a data rate of four channels  $\times 12 \text{ bit} \times 77 \text{ Hz} = 3.7 \text{ kb/s}$ , plus timing and housekeeping data. Total data volume is 27 Mb for a 2-h occultation.

*Occultation Mode O3:* Solar occultations. During a solar occultation experiment VIMS stares at the Sun through its solar calibration port, monitoring the extinction of sunlight by Saturn's rings, Saturn's atmosphere or Titan's atmosphere. Because the Sun has a large angular diameter even at Saturn's distance, (0.9 mrad at 10 AU), the maximum spatial resolution under these conditions is 300 km, and the necessary sampling time about 15 s or longer. Typical observations of the rings, for example, would result in full IR spectra every 15 s, for one spatial pixel, yielding a data rate (compressed) of 102 bps and a data volume of 740 kb for a 2-h occultation.

### 5.2.3. Solar Port

The solar port of VIMS was added late in the instrument design stage to recover some of the capability lost by the deletion of the *Cassini* spacecraft's calibration target. As a bonus, the solar port is capable of performing observations of solar occultations for atmospheric and ring studies.

The solar port strongly attenuates the solar spectrum that, once it passes through the solar port itself, follows the same path through the instrument as photons incident on the boresight. Its chief purpose is to acquire a solar spectrum that can be used to remove the effects of solar illumination from the VIMS data to obtain accurate scales of relative and absolute reflectance. The port's boresight is offset from VIMS main optical axis by  $20^\circ$ , to coincide with the optical axis of the UVIS instrument.

This configuration facilitates compatible operations between the two instruments for solar occultations of the atmospheres of Titan, Saturn, and of the rings.

The large attenuation factor is achieved by the small aperture of the solar port in comparison to the main beam, and by a series of one  $70^\circ$  and  $90^\circ$  reflections from right angle prisms made of ZnSe. Most of the incident flux is reflected back out of the entrance aperture by internal reflection in the prisms. The beam exiting the cal port is first focused by the primary and secondary telescope mirrors onto the VIMS-IR entrance slit, and then it enters the spectrometer. The incident solar radiation will illuminate only a small portion of the diffraction grating, because the cal port aperture samples only a portion of the main instrument's aperture. The optical design ensures that this region overlaps the short and medium-wavelength blaze regions on the grating, in the ratio of 1:3. The long-wavelength blaze is not illuminated. The predicted attenuation factor is  $1.35 \times 10^{-4}$  at  $0.85 \mu\text{m}$ ,  $1.09 \times 10^{-4}$  at  $3.0 \mu\text{m}$ , and  $1.04 \times 10^{-4}$  at  $5.0 \mu\text{m}$ . The actual attenuation factor in flight, measured by observing the Earth's moon in both the occultation port and the main aperture, is about  $2.5 \times 10^{-6}$ .

#### 5.2.4. *IR and VIS Timing and Coordination*

Although the infrared and visual channels have separate optics and detectors, the two data streams are combined in the instrument's electronics so that a single spectrum of the same physical area on the target is produced. The visual channel utilizes an area array so it is able to gather an entire line of data during a single integration. The same line synch pulse that initiates the IR scan synchronizes the acquisition of the visual line. After the first visual integration period is complete, the entire frame of data is transferred and stored within the CCD for initial processing. The line of visual data is then sequentially read out and digitized by the visual channel electronics. Three lines of visual data are accumulated during the time of the forward scan of the IR channel. These individual visual pixel elements are then summed three by five (both spatially and spectrally) to yield a line of square pixel elements of  $\sim 0.5$  mrad and with spectral channel widths of  $\sim 7$  nm. This line of visual data is transferred to the instrument's main electronics over the global bus in exactly the same fashion as the IR data. The integrated visual and infrared spectra are then stored in the control processor's RAM.

## 6. Instrument Calibration and Cruise Data Analysis

### 6.1. SYNOPSIS OF THE GROUND CALIBRATION

Spectral calibration of VIMS occurred in three separate steps. As above, we denote the visible spectral region component (channel) of VIMS as VIMS-VIS, and the infrared component (channel) as VIMS-IR. VIMS-VIS was calibrated separately in Italy prior to integration with VIMS-IR at JPL. VIMS-IR was calibrated in the thermal vacuum tests at JPL January 28–February 5, 1996. The integrated

instrument was further tested at the JPL thermal vacuum facility July 16–17, 1996. This final test only included filter transmission and mineral target tests.

The spectral calibration resulted in a specification of the wavelength position and bandpass of each VIMS spectral channel across the instrument field of view and as a function of temperature. The VIMS-IR spectral response is identical across the full field of view to within about a nanometer (nm) over the temperature range tested. The VIMS-IR sampling interval is about 16 nm in the IR, thus a 1-nm shift is a small fraction ( $<7\%$ ) of the sampling interval. VIMS-VIS has a sampling interval of  $\sim 7$  nm and tests show stability to better than about 0.3 nm.

The detailed plan for the VIMS ground calibration evolved over a period of approximately four years, being completed in mid-1995, roughly six months before the actual measurements were to commence. The time frame for the ground calibration was driven by the planned delivery date of the fully integrated VIMS instrument in the September–October period, 1996. As mentioned above, because VIMS-VIS was not completed at the time of the main calibration, only VIMS-IR was calibrated. As a result of the slip in the schedule for the delivery of VIMS-VIS, a substantial recalibration of the integrated instrument has been undertaken while Cassini is en route to Saturn. The details of the efforts to calibrate the VIMS instrument in flight appear later in this document.

The main ground calibration of the IR channel was carried out in six separate areas: radiometric/flat field response, geometric, polarimetric, spectral, and solar port response. In the early phases of the genesis of the VIMS ground calibration plan, measurement of VIMS stray light rejection performance was also envisioned, but practical difficulties in performing those measurements under vacuum and at the operational temperatures required necessitated elimination of the groundbased measurements in favor of measurements in flight. Those measurements are discussed later in this document.

The actual measurements were carried out in the JPL thermal vacuum testing facility in the largest thermal vacuum tank available. The in-flight thermal environment for VIMS was simulated by cooling the interior surfaces of the thermal vacuum tank with liquid  $N_2$ , and providing a cold target that filled the fields of view of the passive coolers of both VIMS-VIS and VIMS-IR with a high-emissivity surface cooled to 4 K. In retrospect, the thermal environment of the JPL thermal vacuum tank and the cold target was quite accurate because the temperatures of the instruments optics and focal planes in flight are within a few K of those measured while the instrument was in the test environment.

## 6.2. RADIOMETRIC CALIBRATION

### 6.2.1. *VIMS-IR*

The radiometric response of VIMS-IR was carried out before launch in the thermal vacuum facility at the Jet Propulsion Laboratory. A team of scientists, supported by the instrument engineering team at JPL, designed and carried out these

measurements. The team members responsible are Thomas B. McCord (lead), Robert Brown, Angioletta Coradini, Vittorio Formisano, and Ralf Jaumann. Also contributing were Giancarlo Bellucci, Bonnie Buratti, Frank Trauthan, Charles Hibbitts and Gary Hansen. Two sessions were conducted, one in January and the other in July of 1996. In-flight calibration efforts were conducted during the Venus, Earth and Jupiter flybys, and for two star observations. A workshop was held in Hawaii in February 2001 to review the information obtained. Additional people contributing post launch were Kevin Baines, Roger Clark, and Robert Nelson.

The equipment facility during the ground calibration included a JPL thermal vacuum chamber cooled by liquid nitrogen and containing the instrument, which viewed the outside through a window with known optical transmission. A reflecting collimator fed light from several sources to the instrument. The calibrated sources were a glow bar and a tungsten lamp; their energy delivered to the instrument was controlled by adjustable iris diaphragms at the exit of the lamps. The light sources and delivery system were covered to eliminate outside light and, during the first session, the tent was purged with dry nitrogen to reduce the effects of the atmosphere gas absorptions (mainly CO<sub>2</sub> and H<sub>2</sub>O). Measurements were made at several instrument and focal plane temperatures, but most measurements were made with the focal plane temperature in the range 60.7–61.69 K. Data were acquired at several light levels and integration times, including zero.

The characteristics of the instrument that were explored were dark current (detector thermal carrier generation and electronic off-sets), background signal (mostly thermal radiation from the chamber window and from outside), linearity of response, ratio of responses at the two gain states, performance of the detector for two different bias levels, and overall radiometric response over the spectral range. The instrument was determined to be linear within the measurement error to detector saturation. The dark current, background, gain ratios and behavior at different bias are reasonable, stable and as expected. The overall spectral responsivity was most difficult to calibrate due to several factors, including an unexpected and unknown (at the time) change in a light source during the calibration effort. This effort has been enhanced during in-flight calibration efforts and the responsivity calibration is converging.

In-flight calibrations were conducted at Venus only for the visual channel because the cooler cover was not yet removed from the IR channel radiator. The entire instrument calibration was tested at the Earth–Moon (for the Moon only) and the Jupiter fly-bys and for two star observations. The data are still being analyzed at this writing for the in-flight calibrations, but the general result so far is to further refine the calibrations and to gain better understanding of the instrument performance, which remains as expected.

One interesting characteristic experienced is the difficulty of achieving precise and stable calibration for sources smaller than the spectrometer slit width (sub-pixel sources). This is because the effective spectral resolution of the spectrometer and the exact location of the source image on the detectors depend on the size of the

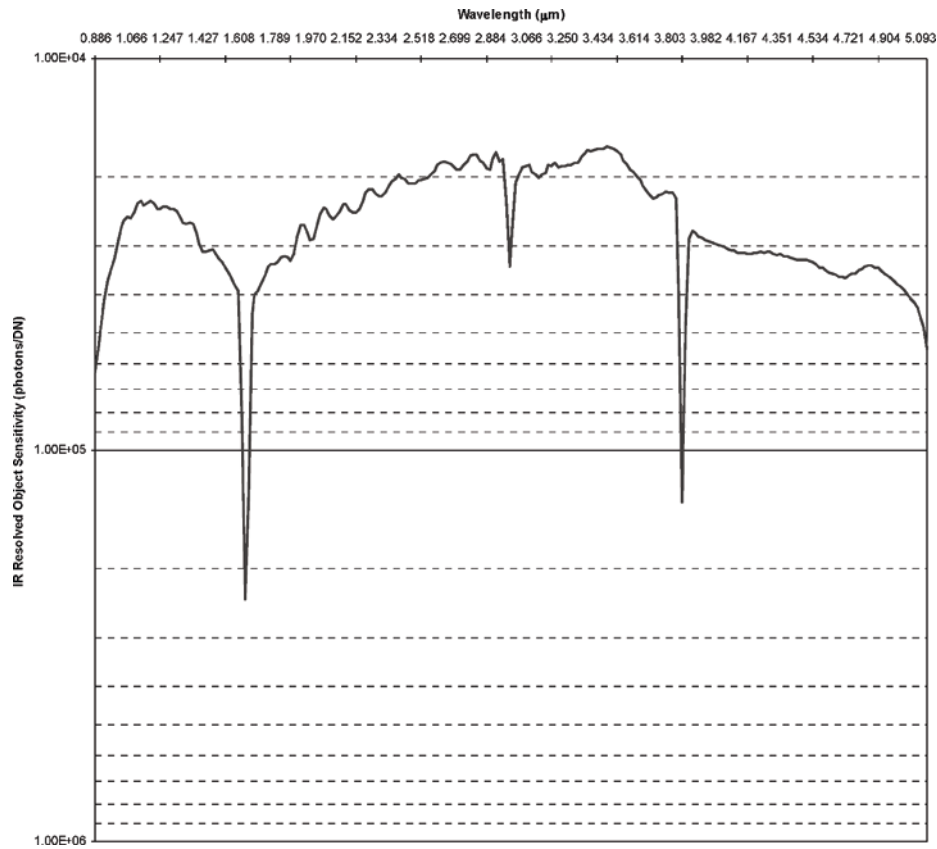


Figure 8. Spectro-radiometric response of the VIMS-IR channel as a function of wavelength in photons per data number. This plot represents the status of the calibration as of the writing of this article. Improvements and changes are expected with time and further analysis.

source and its exact location in the focal plane. Thus, it will be difficult to precisely predict radiometric performance for sub-pixel sources. Nevertheless, for sources that fill the slit, the instrument behavior is normal and as expected.

The spectro-radiometric response function as currently known is given in Figure 8. Improvements and changes are expected with time and more analysis. Thus, the reader is referred to the VIMS planetary data system (PDS) archive for appropriate calibrations to be used with flight data.

#### 6.2.2. VIMS-VIS

VIMS-VIS was constructed and calibrated in Italy, at Officine Galileo. It was calibrated in two phases: (1) at Officine Galileo prior to the integration with VIMS-IR, and (2) at JPL after the integration on the remote sensing palette. The activity carried out at JPL was mainly devoted to geometric measurements, that is, co-alignment of the two channels and measurement of the relative radiometric response.

Furthermore, the instrument spatial response (measurement of the image quality through the instrument modulation transfer function and point spread function) was evaluated as part of the full functional tests performed at Officine Galileo prior to the calibration activity.

VIMS-VIS was placed inside a vacuum chamber equipped with a thermally stabilized radiator connected to the CCD and capable of keeping the CCD at a temperature in the range  $-20$  to  $40^{\circ}\text{C}$  under a residual pressure  $<10^{-4}$  mbar. The chamber has a window made of TVC, with transparency better than 0.9 throughout the entire spectral range. VIMS-VIS was mounted on two computer-controlled rotating tables for fine positioning at a range of azimuthal and elevation angles. Two lamps were used to cover the full spectral range: a xenon lamp for the range  $0.3\text{--}0.4\text{ }\mu\text{m}$ , and a tungsten lamp between  $0.4$  and  $1.035\text{ }\mu\text{m}$ . The lamp with its housing, which includes a condenser and a diffusing screen to improve light uniformity, was positioned at the input slit of a Jobin-Yvon HR640 monochromator capable of better than  $0.05\text{-nm}$  resolution (band width at half height) over the VIMS-VIS spectral range. The monochromator output was then used to illuminate a slit, pinhole or test targets (corresponding to a specific type of test) placed at the focus of an off-axis collimator. The collimated beam was fed to the instrument inside the vacuum chamber. Unfortunately, the collimated beam had an unknown spectral irradiance; thus, we had to devise a method to measure it. This was achieved using a beam splitter of known optical properties, placed in the optical path at  $45^{\circ}$  in front of the chamber window. The reflected portion of the beam was collected by a calibrated photodiode to monitor the irradiance output of the light source. An additional calibrated photodiode was placed every  $50\text{ nm}$  (or  $50$  monochromator steps) directly in front of the collimator to have direct calibration at the collimator aperture.

Only one-sixth of the full VIMS-VIS FOV could be instantaneously illuminated with the available collimator, thus a time consuming procedure was implemented to repeat a full spectral sweep ( $0.3\text{--}1.05\text{ }\mu\text{m}$  in  $1\text{ nm}$  steps) to cover the field of view of the instrument.

The radiometric calibration of VIMS-VIS was as follows. The unit response (UR) of the instrument is defined as the output in data numbers (DN) when the instrument entrance pupil is fed with a light beam of  $1\text{ W cm}^{-2}$ , and this beam is collected entirely into a single spectel and into a unit solid angle, for an integration time of  $1\text{ s}$ . This quantity was directly measured along with its dependence on wavelength. The spectral calibration was performed in order to evaluate the spectrally weighted center of each channel as well as the spectral width. The spectral width of each spectel is  $7.33\text{ nm}$ . For a detailed discussion on the calibration see Capaccioni *et al.* (1998).

We note that the radiometric transfer function obtained at Officine Galileo during on ground calibration of VIMS-VIS when applied to the Moon and Venus illuminated side is insufficient to remove instrumental effects. Moreover two problems are apparent: a shift in wavelengths of about two nominal pixels and an inadequate



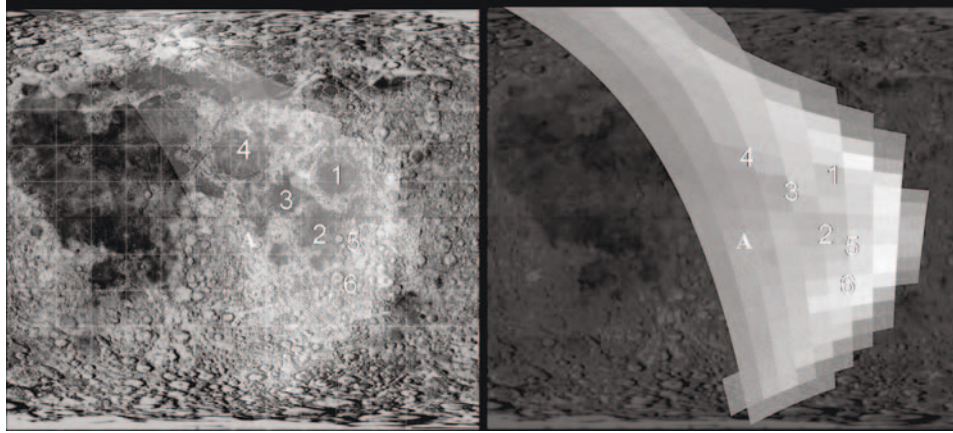


Figure 9. The VIMS-VIS field of view on the Moon during the flyby of August 18, 1999. Key: 1 Mare Crisium, 2 Mare Fecunditatis, 3 Mare Tranquillitatis, 4 Mare Serenitatis, 5 Langrenus, 6 Petavius, A Apollo 16 landing site.

removal of instrumental effects, particularly at short wavelengths. So we measured a new unit response function using the Venus and Moon data in the following way.

We use a telescopic reflectance spectrum (McCord and Adams, 1973) of the Apollo 16 landing site, which is a bright area in the highlands of the Moon's surface where the albedo is particularly high.

At this point on the Moon the signal is given by:

$$F_{\text{Moon}}(x^*, \lambda) = R_{\text{Moon}}(x^*, \lambda) \times S_{\text{Moon}}(\lambda) \cdot \text{UR}(x^*, \lambda), \quad (1)$$

where  $R_{\text{Moon}}$  is the lunar spectral reflectance computed at a point  $x^*$  in the lunar highlands (see Figure 9),  $S_{\text{Moon}}$  is the solar radiance at the mean Moon–Sun distance (1 A.U.) and UR is the unknown transfer function at the point  $x^*$ . Accordingly, the Unit Response transfer function is:

$$\text{UR}(x^*, \lambda) = \frac{F_{\text{Moon}}(x^*, \lambda)}{R_{\text{Moon}}(\lambda) \times S_{\text{Moon}}(\lambda)} \quad (2)$$

This is the transfer function for the point on the Moon  $x^*$  located in the slit center.

In order to obtain a target-independent UR function we have to consider a flat field. Assuming the uniformity of Venus' dayside atmosphere we define a flat field using the ratio between the signal  $F_{\text{Venus}}(x, \lambda)$  at some point  $x$  in the frame and  $F_{\text{Venus}}(x^* = 32, \lambda)$  in the center of the slit.

$$[F_{\text{Venus}}(x, \lambda)]_{\text{Norm}} = \frac{F_{\text{Venus}}(x, \lambda)}{F_{\text{Venus}}(x^*, \lambda)} \quad (3)$$

The signal on Venus is given by an expression analogous to (1) for the Moon:

$$F_{\text{Venus}}(x, \lambda) = \text{UR}(x, \lambda) \times R_{\text{Venus}}(\lambda) \times S_{\text{Venus}}(\lambda) \quad (4)$$

$$F_{\text{Venus}}(x^*, \lambda) = \text{UR}(x^*, \lambda) \times R_{\text{Venus}}(\lambda) \times S_{\text{Venus}}(\lambda) \quad (5)$$

where  $S_{\text{Venus}}$  is the solar radiance at the mean Venus-Sun distance (0.73 A.U.). Putting (4) and (5) into Equation (3) we obtain the normalized signal on Venus:

$$[F_{\text{Venus}}(x, \lambda)]_{\text{Norm}} = \left[ \frac{\text{UR}(x, \lambda)}{\text{UR}(x^*, \lambda)} \right] \quad (6)$$

Using this result it is possible to define the UR as the product of the transfer function computed for the Moon at point  $x^*$  (45, 33) and the transfer function normalized to the center  $x^*$  of the VIMS-VIS slit on Venus:

$$\text{UR}(x, \lambda) = \text{UR}(x^*, \lambda)_{\text{Moon}} \times [F_{\text{Venus}}(x, \lambda)]_{\text{Norm}} \quad (7)$$

Finally, we obtain the general UR:

$$\text{UR}(x, \lambda) = \text{UR}(x^*, \lambda)_{\text{Moon}} \times \left[ \frac{\text{UR}(x, \lambda)}{\text{UR}(x^*, \lambda)} \right]_{\text{Venus}} \quad (8)$$

Figure 10 shows the final UR transfer function for all the wavelengths: note that the UR is a function of the pixel position. The UR function permits conversion of DN to physical units.

### 6.2.3. Conclusions

Additional radiometric calibration improvements are expected as the Jupiter encounter data are analyzed and compared with the ground calibration results (see McCord *et al.*, 2004). During Cassini's Saturn tour, there will be many measurements for a variety of objects that will help identify and allow removal of any remaining artifacts in the spectral radiometric calibration. Users of VIMS data should consult later papers by the investigation team, as well as the VIMS website, for the most current versions of the calibration of the instrument.

## 6.3. GEOMETRIC CALIBRATION

For VIMS, the primary data product is, for each resolved pixel of a given target, the determination of both the pixel position and the full spectrum from 0.35 to 5.1  $\mu\text{m}$ . To build such spectral images, for each picture element of any given  $64 \times 64$  frame, the viewing direction of each of its 352 contiguous spectral elements (spectels) must be known. Thus, the prime goal of the geometric calibration of VIMS was to determine the relative viewing directions of all 96 VIMS-VIS and 256 VIMS-IR spectels within the full VIMS field of view (FOV), in a frame to be referenced to the Cassini spacecraft.

VIMS-VIS and VIMS-IR form images in two distinct ways. VIMS-VIS operates like a push-broom, acquiring an entire cross-track line simultaneously spread over

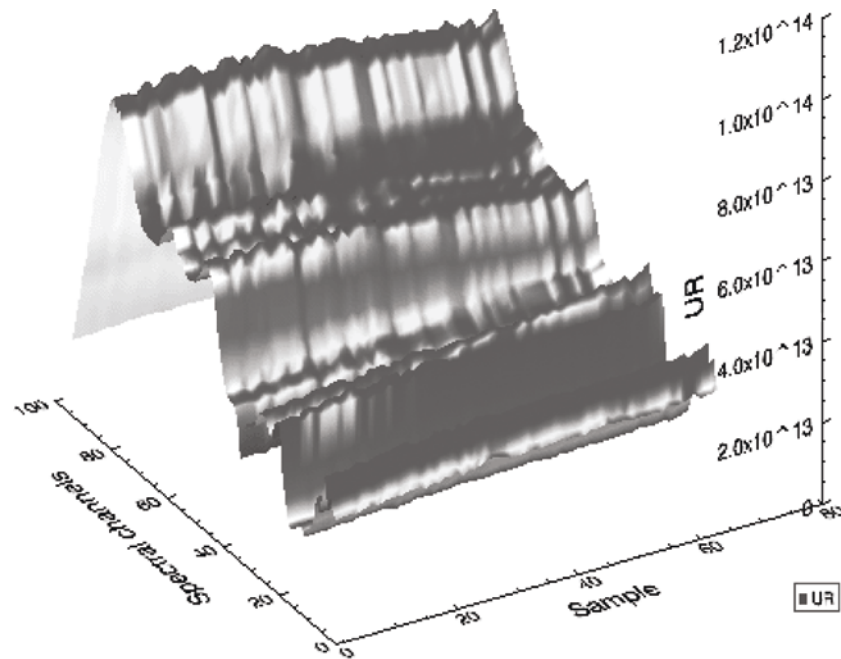


Figure 10. The computed UR transfer function.

its spectral dimension (from 0.35 to 1.0  $\mu\text{m}$ ) along the second dimension of its CCD detector. The second spatial dimension is acquired either using the spacecraft drift or the scanning of the VIMS-VIS telescope secondary mirror. VIMS-IR uses only a linear array detector, thus it acquires one pixel only spread over its spectral dimension (from 0.85 to 5.1  $\mu\text{m}$ ). The cross-track spatial dimension is acquired by scanning the telescope secondary mirror (whiskbroom mode), while the along track dimension is acquired (as for VIMS-VIS) using either spacecraft drift or scanning the IR telescope's secondary mirror in the second dimension. With two distinct scanning mechanisms, telescopes, and spectrometers, the boresight alignment and the Instantaneous Fields Of View (IFOV) within the full FOV are not identical by design, and, in principle, are wavelength dependent. The geometric calibration is thus intimately coupled to the determination of these spectral registration effects.

Due to the late delivery of VIMS-VIS, the ground geometric calibration was performed in steps: the in-depth geometric calibration of VIMS-IR was performed first, prior to the integration with VIMS-VIS, followed by the geometric calibration of VIMS-VIS after its integration. After integration, a large misalignment was observed, requiring a global mechanical realignment of both the IR and V channels (out of the calibration chamber), followed by a few final control measurements (back to the calibration chamber) prior to integration with the Cassini spacecraft. Some in-flight calibrations were performed to assess the actual geometrical characteristics of

both channels, when the instrument had reached its proper in-flight thermal regime, late during the cruise towards Jupiter.

During the ground calibration, VIMS was mounted on a fixed platform, thermally controlled and under vacuum. A collimator and optical bench assembly was constructed outside of the thermal-vacuum chamber, and viewed through a large window. For the geometric calibration, we chose to image with VIMS, two types of targets, both mounted on an  $X$ - $Y$  stage to allow coverage of the entire VIMS FOV. In the target projector plane, one VIMS pixel (0.5 mrad) corresponded to  $\sim 1$  mm. To cover the entire VIMS FOV, the target was 64 mm in size, and the stage was moved by steps of 0.1 mm (1/10 VIMS pixel). The first type of target consisted of linear blades to measure potential spectral registration effects by analyzing for each spectel the pixel response while the blade was moved across the pixel. The other target placed in the projector focal plane consisted of an opaque metal plate with a grid of sub-pixel sized pinholes (0.1 mm in diameter) evenly spaced, and back-illuminated by a tungsten lamp. The complete calibration data products are in the form of tables, one for each spectral channel, giving the viewing direction of each VIMS pixel. Below we summarize some of the main results.

The IFOVs of both channels were accurately measured. Averaged over all wavelengths within a given channel,  $\text{IFOV}_{\text{IR}} = 0.495 \pm 0.003$  mrad, and  $\text{IFOV}_{\text{VIS}} = 0.506 \pm 0.003$  mrad. Although the differences appear small ( $\sim 2\%$ ), they result in a misalignment of VIMS-VIS relative to VIMS-IR of more than one pixel over the 64-pixel FOV. This imposes the need for a thorough geometric re-sampling of all image cubes larger than 32 pixels. Prior to launch, the last geometric measurement showed a boresight alignment between VIMS-VIS and VIMS-IR of better than 0.3 pixels at all wavelengths. Images coincide independent of wavelength to within  $< 0.5$  pixel in frames up to  $12 \times 12$  pixels.

The first measurements in flight were performed using both channels to observe the Moon during the Cassini Earth-Moon fly-by (August 18, 1999). Those showed a boresight misalignment of VIMS-IR with respect to VIMS-VIS  $\Delta(X, \Delta Y) = (-1 \text{ pixels}, +2 \text{ pixels})$ . Because the VIMS-IR was warmer than its proper operating temperature at the time of the Earth-Moon flyby, it was concluded that at least part of misalignment resulted from thermal gradients in the IR channel that would lessen as the Cassini spacecraft moved farther from the Sun and the IR channel cooled. A more recent calibration using the Pleiades cluster and the star Fomalhaut (late March, 2001) showed boresight offsets of  $(\Delta X, \Delta Y) = (-1, 0)$  pixels. The Pleiades observation (Figure 11) demonstrates the misalignment variation within the FOV, showing the various stars in the visual (blue pixels, averaged over the first 30 VIS spectels) and the near IR (red pixels, averaged over the first 40 spectels).

The ground calibration yielded the VIMS-IR FOV for most IR spectels, leading to spectral geometric registration maps. For images up to  $32 \times 32$  pixels, all spectral images coincide to better than 1/3 pixel. Larger discrepancies appear in the bottom right and top left corners of the frame, where spectral misalignments up to half a pixel are present. This is illustrated in Figure 12, scaled in mrad, for

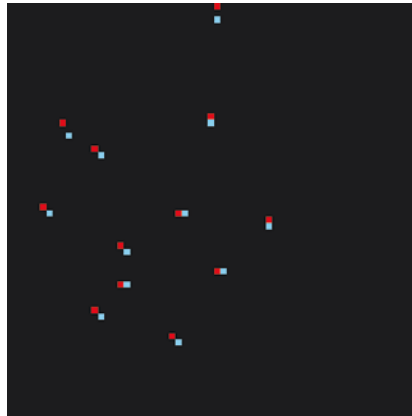


Figure 11. VIMS image of the Pleiades, showing the stars in the VIMS-VIS (blue pixels) and the VIMS-IR (red).

three IR wavelengths (spectels 103, 150 and 206, at  $0.98\ \mu\text{m}$ ,  $1.75\ \mu\text{m}$  and  $2.68\ \mu\text{m}$ , in red, blue and green respectively), enlarging the four corners and the center of the FOV geometric spectral responses. Finally, the spectral registration effects measured for the IR spectels were demonstrated to be very low, as illustrated in the figure: the very high sensitivity of the measurements allows detection of effects at a scale smaller than  $1/10$  pixel. With this resolution, the larger effects we see between contiguous spectels actually amount to  $1/10$  pixel, and in fact result from atmospheric contributions during the calibration (variation of  $\text{H}_2\text{O}$  and  $\text{CO}_2$  features). The only large-scale effect present (black curve) has a very low frequency (at the scale of the entire spectral range), and likely results optical aberrations within the IR spectrometer. It is both smooth and small enough to minimize the risk of misinterpreting potential large optical contrasts in the observed scene in terms of false spectral signatures.

#### 6.4. SPECTRAL CALIBRATION

##### 6.4.1. Summary of Tests

The goals of the spectral calibration of VIMS were to measure the spectral response of each VIMS spectral channel to determine the central wavelength and spectral profile of each detector, and its spectral stability as a function of temperature and spatial position within the field of view of the instrument. To achieve this, the tests included: (1) scanning a nearly monochromatic line (using a calibrated grating monochromator) over the VIMS wavelength range to map the spectral profile of each VIMS detector, (2) transmission spectra of materials with sharp absorption bands, and (3) measuring reflectance spectra of minerals and other targets with VIMS.

The monochromator scans were useful for a single position in the full VIMS field of view because the relatively large field of view of the VIMS could not be covered

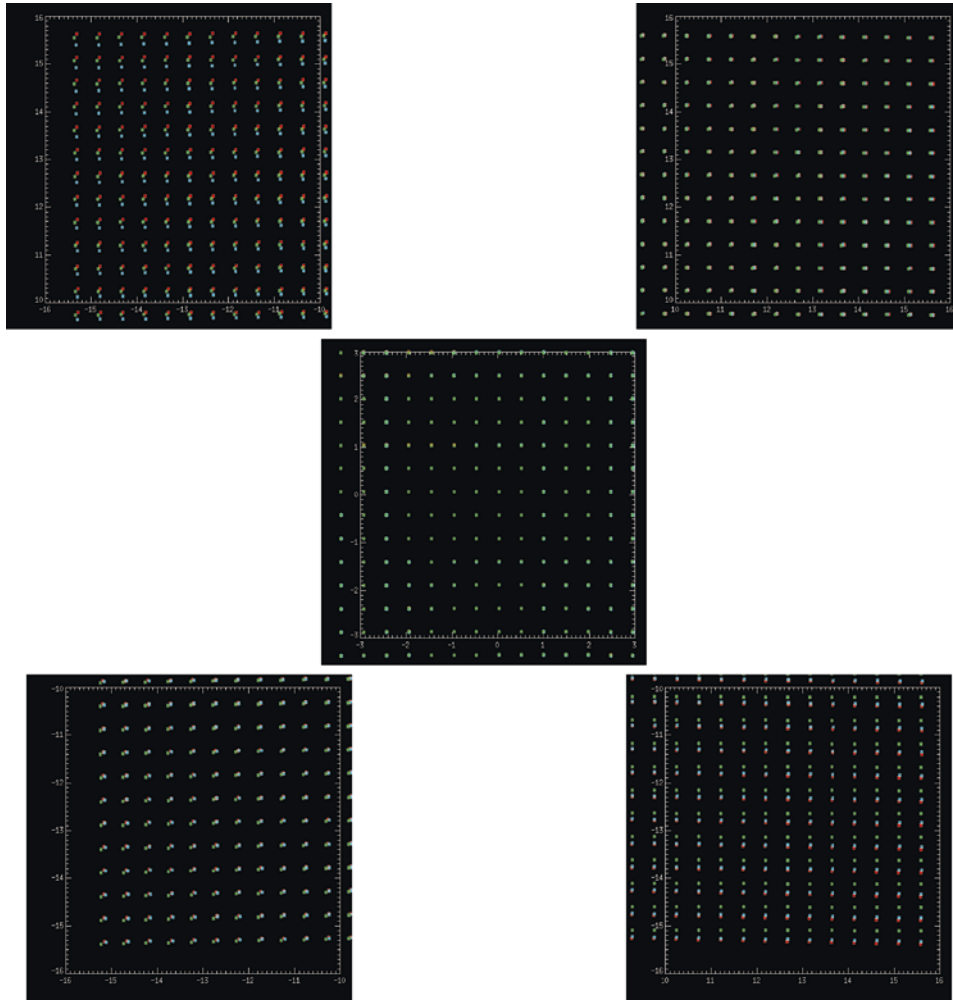


*Figure 12.* Spectral registration maps for five positions in the VIMS field of view. The position of each panel in the instrument focal plane can be seen from the coordinates in each square frame. The vertical and horizontal directions (relative to the upper left) correspond to the  $+Z$  and  $+X$  axes of the spacecraft coordinate system.

with the narrow exit slit of the monochromator, and small shifts in wavelength were observed in the monochromator as a function of position along the slit. This results because a change in direction along the slit results in a slight change in the field position in VIMS that corresponds to an angular movement. Such changes require a change in the light path through the monochromator with a corresponding change in the effective output wavelength of the monochromator. Thus the monochromator tests were done on-axis only. The monochromator was typically scanned at 1 nm increments to map out the profile of each VIMS spectral bandpass.



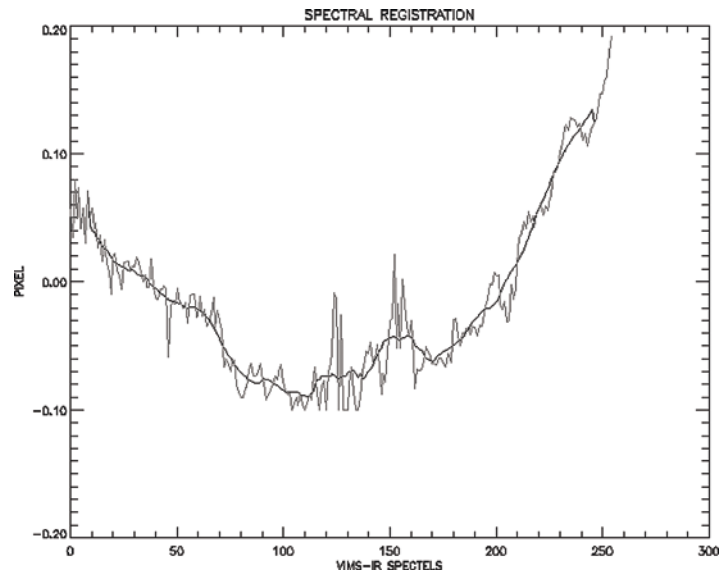


Figure 13. Plot of the deviation (calculated versus actual) for the pointing direction (in the direction of the boresight) as a function of wavelength (shown as spectel, or channel number). As examples, in the direction of the boresight, the IFOV of spectel number 1 deviates by +0.006 pixel, while spectel number 115 deviates by  $-0.08$  pixel.

Calibrated transmission filters consisting of a mylar sheet displaying sharp absorption bands in the  $1\text{--}3.5\ \mu\text{m}$  region, with broader features at longer wavelengths, and Corning glass filters containing rare-earth elements which give sharp absorption features in the visual and near-infrared wavelength regions, and broader absorptions at longer wavelengths were used to cover the full VIMS field of view. Because of their uniformity and stability, the filters were used to determine the stability of the VIMS wavelength response as a function of spatial position, temperature, and time (because two tests were done over a period of about six months).

To measure the response of VIMS to real targets with spectral features, a set of minerals and other materials were assembled into a spectral target and measured in reflectance. Because the calibration geometry was optimized for other tests, the setup for reflectance measurements was not ideal, so these tests were qualitative. The light source used to illuminate the samples was set up at relatively large angles to the normal to the surface of the highly scattering surface of the spectral target, but the exact viewing geometry was difficult to control. Furthermore, only samples mounted vertically could be measured, so it was not possible to measure the reflectance of unconstrained, loose particulate samples. Measurements were made of rocks and solid samples that typically had large grains, thus the absorption bands were deep and saturated, but the spectra of these rocks are quite identifiable with VIMS.

The spectral calibration tests showed that VIMS is a remarkable instrument, producing spectra comparable in quality to specialized laboratory spectrometers.

The large spectral range of the VIMS includes the region of increasing thermal emission at room temperature ( $\lambda \geq 3\mu\text{m}$ ) making the light reflected from the sample difficult to separate from the background thermal emission. The spectral range of VIMS is greater than the spectral output any single convenient laboratory light source, so tests were often done multiple times with different light sources.

#### 6.4.2. *Spectral Profiles*

The VIMS-IR spectral profiles are very close to Gaussian in shape, with small, Gaussian shaped side lobes (Figures 14a and 14b). The small side lobes are possibly caused by reflections in the order sorting filters. The side lobes are stronger on the short wavelength side at the short-wavelength end of the IR array, and are stronger on the long wavelength side on the long-wavelength end of the array. The side lobes are typically 2% or less of the strength of the central profile and can probably be ignored except for the most rigorous work. A set of spectral profiles for each spectral channel will be maintained on the Cassini VIMS team home page. Spectral profiles are somewhat distorted near the VIMS order-sorting filter gaps. These gaps occur at VIMS-IR channels 45–46, 128–129, and 183–183 (1.59, 2.96, and  $3.86\mu\text{m}$ ). At or near the filter gaps, the central portion of the spectral profile can be absorbed, leaving the main signal coming from the side lobes (Figure 15). Except for the side lobes, no out-of band signals were detected in the monochromator scans.

#### 6.4.3. *Cruise Spectral Calibration*

During cruise, high signal-to-noise spectra were obtained on the Moon, stars, Jupiter, and the Galilean satellites. Immediately apparent in these cruise data is that the wavelengths of VIMS-IR shifted after launch. A best fit that shows overlap consistency between VIMS-VIS and VIMS-IR using deep absorption bands in the spectra of Jupiter shows a 1.3 channel ( $\sim 21\text{ nm}$ ) shift in the IR wavelengths (Figure 16). The positions of absorption features in sub-pixel images of stars and the Galilean Satellites showed variability by up to 1/3 channel depending upon where the object was located in the slit. This adds difficulty in determining the wavelength calibration post launch to better than about 5 nm. Despite this difficulty, comparison with the Galileo NIMS data on the Galilean satellites confirms the 1.3 channel shift at the positions of the  $4.25\text{-}\mu\text{m}$   $\text{CO}_2$  feature and water-ice absorptions seen in spectra of Ganymede and Callisto. Analysis of absorption features throughout the VIMS-IR spectral range shows that the shift is consistent across the entire wavelength range of VIMS-IR. Calibrations using stars and other objects will be performed frequently throughout cruise and the orbital tour.

### 6.5. POLARIMETRIC CALIBRATION

The VIMS instrument contains no specific polarimetric capability, such as filters or grids, but the design of the grating spectrometer makes it inevitable that the instrument's response will be linearly polarized to some extent. The purpose of the

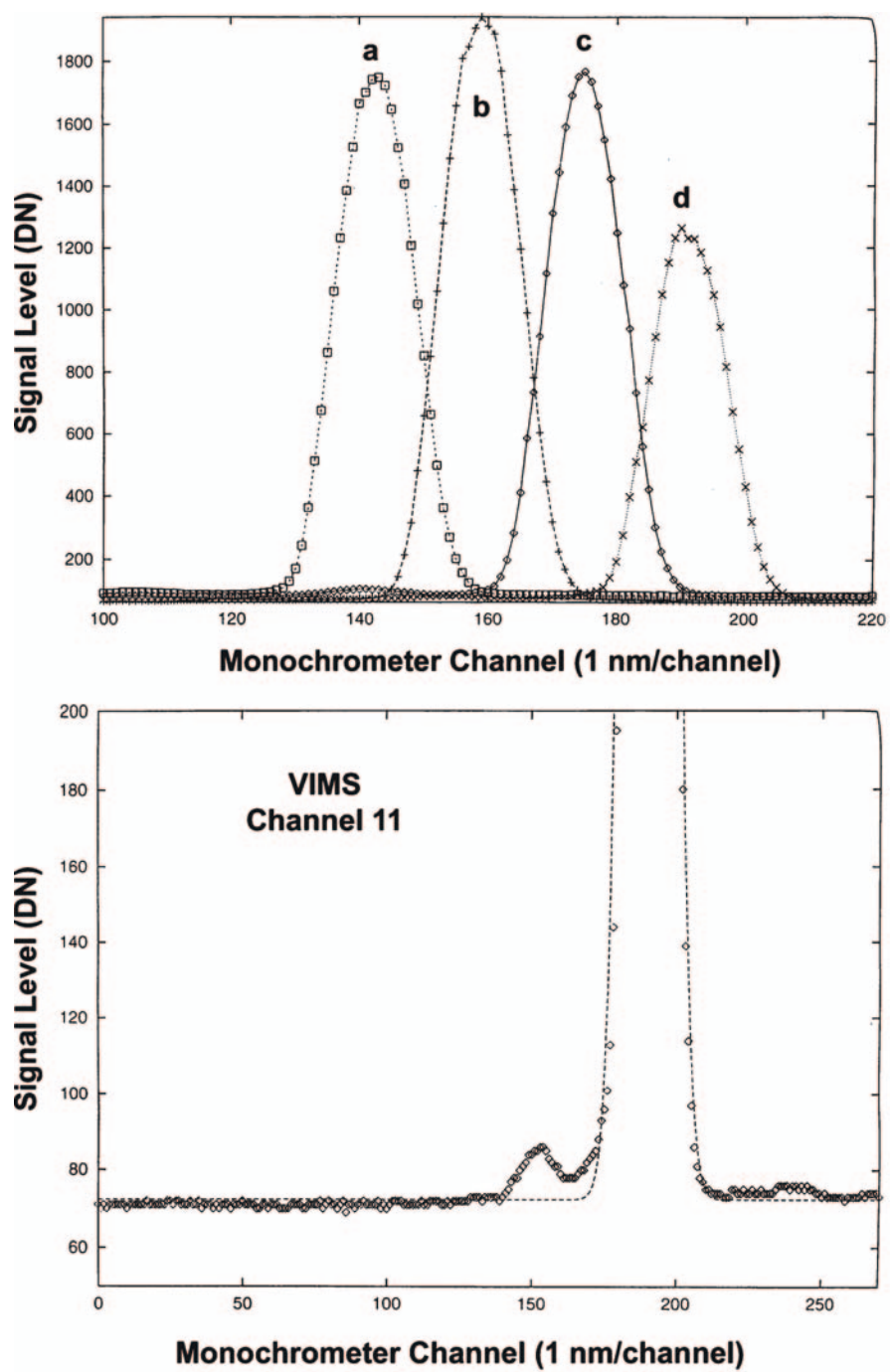


Figure 14. (a) VIMS-IR spectral profile at several wavelengths. (b) Enlargement of one profile to show the small side lobes.

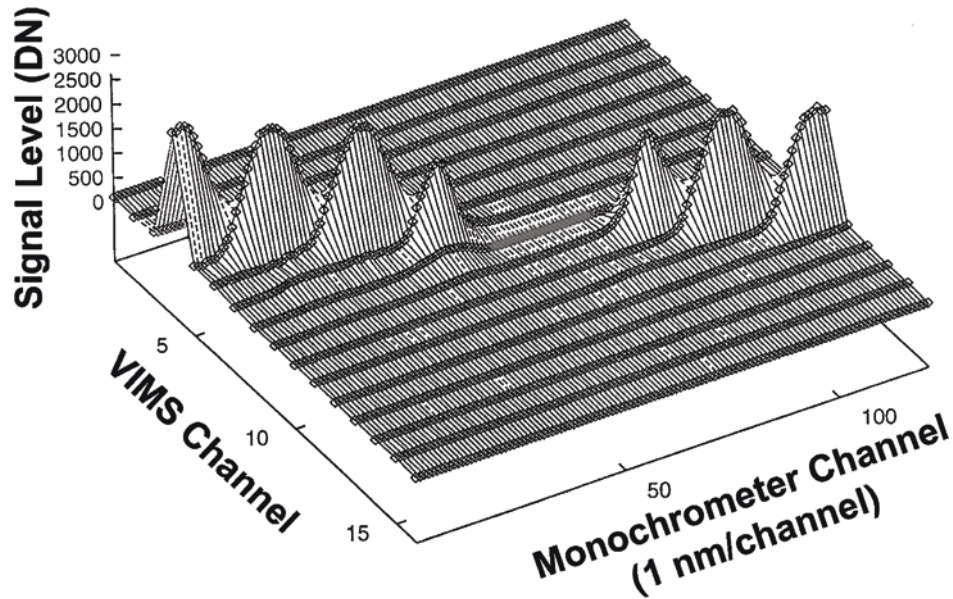


Figure 15. Monochromatic spectral image profiles for VIMS-IR near the filter gaps, as noted in the text.

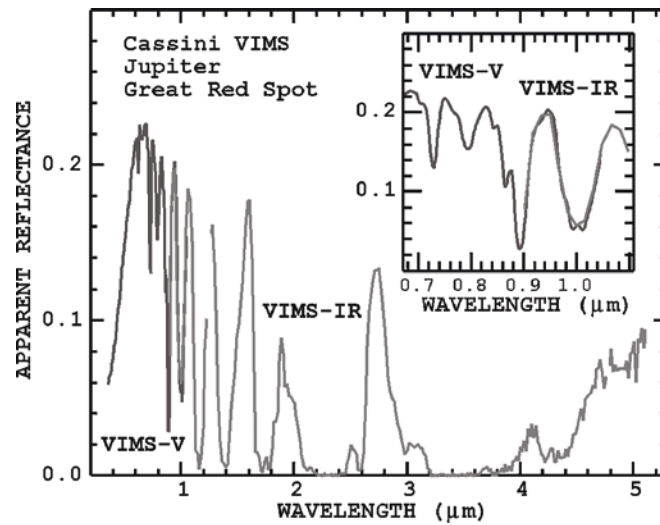


Figure 16. Spectra of Jupiter with VIMS-VIS and VIMS-IR. The inset shows an enlargement of the region of spectral overlap.

polarimetric calibrations was to characterize this sensitivity, so that its effect on the accuracy of spectra obtained for both polarized and non-polarized targets in the Saturnian system can be assessed. In general, spacecraft pointing constraints will determine the roll attitude of the optical remote sensing instruments during

targeted observations, leaving little opportunity for observations at multiple roll orientations.

Measurements for the polarization characterization of VIMS-IR were carried out in the 10-foot thermal-vacuum tank in Building 144 at JPL, during January 17–20, 1996. A target projector was set up with a 26-mm diameter IR linear polarizing filter at the focal plane of a collimator. The target was illuminated by the 1-inch output aperture of an integrating sphere, producing a polarized image of the exit aperture of the sphere at the VIMS focal plane. The polarizer consisted of a ZnSe substrate with a deposited aluminum pattern of parallel stripes, and its polarization efficiency is documented from 2.5  $\mu\text{m}$  to beyond 10  $\mu\text{m}$ . The average single-polarizer throughput is 38%, while the maximum cross-polarized throughput over the 2.5- to 5.0- $\mu\text{m}$  range is 1.5%. No data on the filter transmission were available below 2.5  $\mu\text{m}$ . A calibrated tungsten source with a Teflon-coated sphere provided adequate SNR out to about 2.5  $\mu\text{m}$ , while a glowbar source with a gold integrating sphere provided adequate SNR at all wavelengths beyond 1.5  $\mu\text{m}$ .

Measurements were made at five spatial positions of the source in the target plane, on boresight, and near the four corners of the VIMS field. For each source position, measurements were made at seven settings of the polarizer, at 30° intervals between (+90° and –90°, followed by a sequence of background measurements with the shutter on the light source closed. Only VIMS-IR was available for these measurements.

Three cubes per measurement were co-added and background-subtraction spectra were extracted both for a central spot in the image of the source and for a larger region which included the full output aperture of the sphere. This was accomplished at each orientation of the polarizer and for each source position.

Figure 17 shows 3-D surface plots of the normalized spectra for both light sources, measured on the boresight. At each wavelength, the measured intensity at a particular polarizer angle was divided by the average over all seven positions. From this figure, and similar ones constructed for other source positions, it is apparent that the maximum signal invariably occurs at an orientation of either 0° (polarizer parallel to the rulings on the grating) or 90°, but that the sense and magnitude of the polarized response vary smoothly with wavelength. We thus calculated the fractional polarization of VIMS-IR from the expression:

$$P(\lambda, \%) = \frac{2I(\lambda, 0^\circ) - I(\lambda, -90^\circ) - I(\lambda, +90^\circ)}{2I(\lambda, 0^\circ) + I(\lambda, -90^\circ) + I(\lambda, +90^\circ)} \times 100$$

Figure 18 shows the polarization determined from central-spot and full-aperture data from both sources, at two locations in the VIMS FOV. The results were found to be the same to within 1% or better for all source positions and aperture sizes, and essentially identical for both tungsten and glowbar sources in their region of overlap (1.2–2.5  $\mu\text{m}$ ).



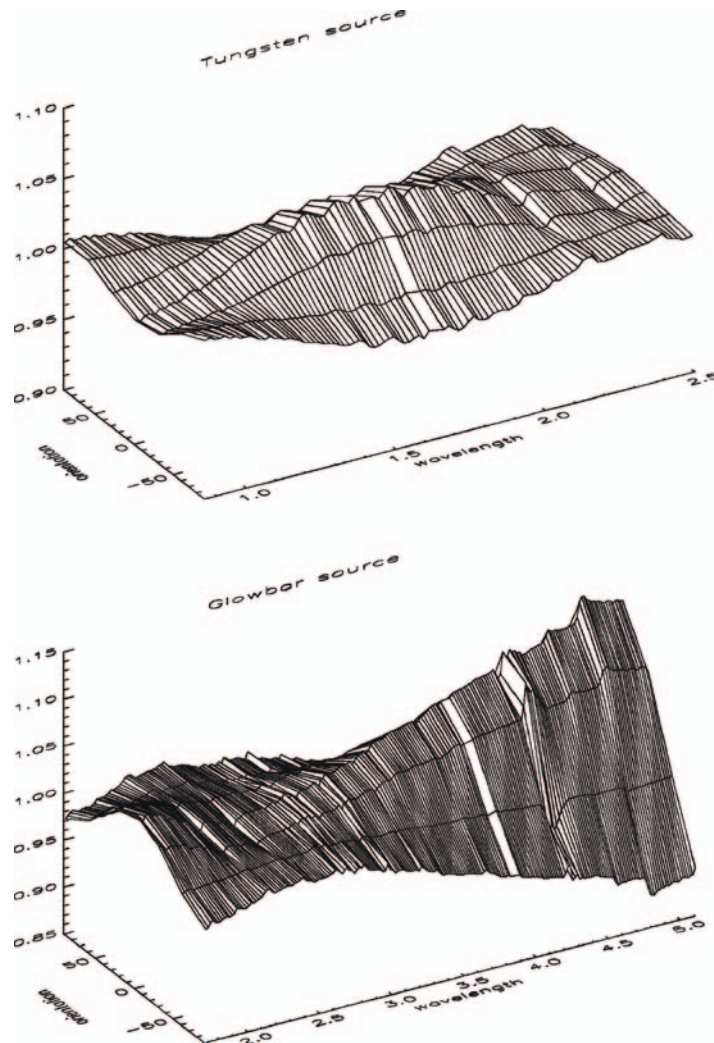


Figure 17. 3D surface plots of VIMS polarization measurements.

In summary, the calibration data showed the following:

1. The maximum polarization sensitivity is either parallel to (positive) or perpendicular to (negative) the rulings on the diffraction grating.
2. The polarization is positive for wavelengths of 1.1–2.1  $\mu\text{m}$ , and beyond 2.4  $\mu\text{m}$ , but negative below 1.1  $\mu\text{m}$ . Between 2.1 and 2.4  $\mu\text{m}$  the polarization is negligible (less than 1%). A peak in polarization occurs at 1.6  $\mu\text{m}$  (+3%). Beyond 2.5  $\mu\text{m}$ , the polarization increases linearly with wavelength, reaching a maximum of about 11% at 5.0  $\mu\text{m}$ .



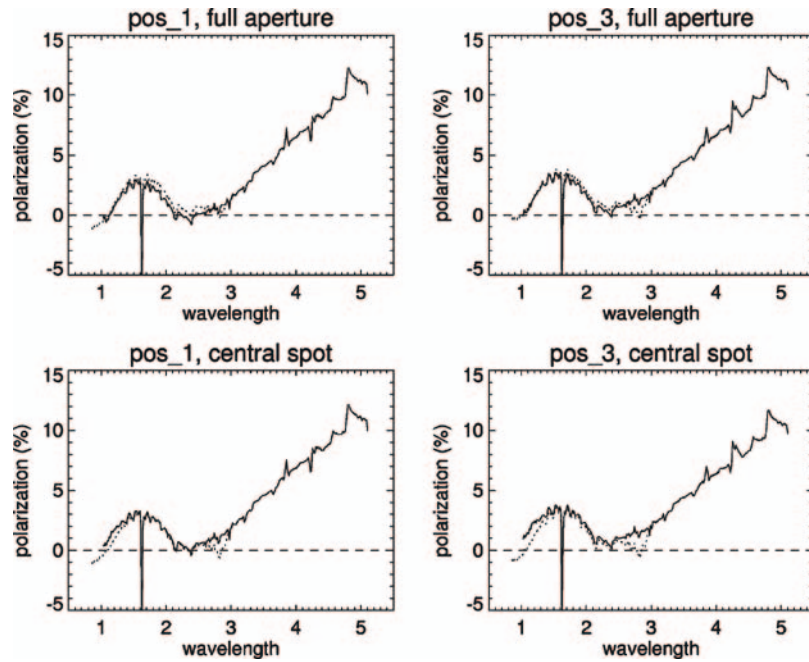


Figure 18. Results of polarization measurements.

3. Except for some artifacts at the segment boundaries of the blocking filter at 1.6 and 3.9  $\mu\text{m}$ , the level of polarization is continuous, suggesting that the polarization is not related to the filter.
4. The lack of a significant dependence of polarization on the particular light source used indicates that the origin of the polarization is not in the sources, although it could conceivably be in the window of the thermal-vacuum chamber.
5. The lack of variation of polarization with target position suggests that the polarization does not arise from the VIMS scan mirror.

These results suggest that the origin of the measured polarization is within the spectrometer, and most likely resides in the diffraction grating. Measurements of the ZnSe chamber window indicate no significant polarization, at least at wavelengths below 1.7  $\mu\text{m}$ .

To assess the implications for spectral observations, consider a source with a fractional linear polarization  $f$  in a direction  $\hat{e}$  with respect to the VIMS “zero angle”, as defined above. The parallel and perpendicular components of the incident intensity are then:

$$I_{\text{par}} = [0.5 + f \cos^2\theta]I_0 \text{ and } I_{\text{perp}} = [0.5 + f \sin^2\theta]I_0$$

The measured intensity of the source by VIMS is:

$$I(\theta) = (1 + P)I_{\text{par}} + (1 - P)I_{\text{perp}} = [1.0 + f + Pf \cos(2\theta)]I_0$$

The RMS fractional error in a single measurement of the intensity at an arbitrary orientation is:

$$\frac{\sigma(I)}{\langle I \rangle} = \frac{Pf}{\sqrt{2(1+f)}}$$

For the most severe case of  $P = 11\%$  (Figure 18), the RMS error is  $< 1\%$  for  $f < 0.15$ , which probably includes any natural source polarization likely to be encountered. At wavelengths below  $3.3 \mu\text{m}$ , the error will reach  $1\%$  only for  $f = 0.9$ , and is thus almost certainly negligible.

## 6.6. SOLAR PORT CALIBRATION

### 6.6.1. Ground Calibration

The solar calibration port (henceforth “cal port”) was installed within the VIMS-IR telescope to provide a strongly attenuated spectrum of the Sun during the Cassini mission, which facilitates reduction of VIMS spectra to an accurate scale of absolute reflectance. The cal port axis is offset by  $20^\circ$  from the telescope boresight in the  $-Z$  direction, aligned with the UVIS solar occultation port. Attenuation of the incident solar beam by a factor of  $\sim 2.5 - 10^7$  is achieved by (i) the small aperture of the cal port, compared to the main beam and (ii) a series of one  $70^\circ$  and five  $90^\circ$  reflections from right-angle prisms made of ZnSe. Most of the incident flux is directed back through the entrance aperture by internal reflection in the prisms. The beam exiting the cal port is focused by the telescope optics onto the VIMS-IR entrance slit, and then enters the spectrometer in the same way. But because the cal port aperture samples only a portion ( $\sim 0.3\%$ ) of the full instrument aperture, the collimated beam illuminates only a small part of the diffraction grating. The optical design ensures that this region overlaps the short- and medium-wavelength blaze regions on the grating, in the ratio 1:3. The cal port does not illuminate the long-wavelength blaze.

The predicted throughput of the stack of prisms varies smoothly from  $1.35 \times 10^{-4}$  at  $0.85 \mu\text{m}$  to  $1.09 \times 10^{-4}$  at  $3.0 \mu\text{m}$  and  $1.04 \times 10^{-4}$  at  $5.0 \mu\text{m}$ , for radiation linearly polarized in a plane perpendicular to the plane containing the incident and exit beams and to the rulings on the VIMS diffraction grating. The transmission of the orthogonal polarization is less than  $1.0 \times 10^{-7}$ . The output spectrum of a target seen through the cal port differs from that produced by the same source seen on the instrument boresight. This arises through a combination of polarization and partial illumination of the grating. Partial illumination of the grating results in a different set of contributions from the different blazes than occurs when the grating is fully illuminated. The purpose of the cal port calibrations is to establish the ratio of the spectrum of an unpolarized broadband source as seen through the cal port to that of the same source on the instrument boresight.

The simulated solar source used for the calibration runs was a high-power xenon lamp, illuminating a large, white, teflon-coated integrating sphere. The output of the sphere illuminated a 1-mrad diameter circular aperture in the focal plane of

the calibration projector (equal to the angular size of the sun at 9 AU), after a  $90^\circ$  reflection from an aluminum plate. One side of this plate was polished and oriented for specular reflection of the high-intensity beam onto the target for the cal port runs, while the other was sand-blasted to provide diffuse reflected illumination of the target for the boresight runs.

All measurements were made on July 12, 1996, in the 10-foot thermal-vacuum chamber at JPL. Inside the tank, a deployable periscope-like arrangement with two aluminum mirrors was used to redirect the input beam into the cal port's entrance aperture. The input signal to VIMS thus experienced identical atmospheric paths, with the same number of reflections, for both cal port and boresight runs. For each observation multiple  $8 \times 8$  image cubes were taken, centered manually on the image of the target. Only VIMS-IR was available for these runs; VIS-VIS was calibrated separately at Officine Galileo.

A total of 100 separate cal port image cubes were background subtracted and averaged in sets of ten, and all pixels co-added to produce spectra. Twenty boresight cubes were processed in identical fashion. Figure 19 shows the average boresight and solar port spectra, at the DN levels originally recorded. The resulting ratio spectrum is displayed in Figure 20, normalized to an average value of unity. Data for nine channels at the three filter segment boundaries have been interpolated in both plots.

The ratio spectrum shows that the cal port sensitivity is relatively low shortward of VIMS-IR channel 50 ( $1.7 \mu\text{m}$ ), increases rapidly between channels 50 and 70 to a peak at channel 80 ( $2.2 \mu\text{m}$ ), and then declines smoothly at longer wavelengths. Oscillations near  $2.7$  and  $4.3 \mu\text{m}$  are due to imperfect cancellation of  $\text{CO}_2$  absorption features in the raw spectra. The high-frequency structure beyond of  $4.0 \mu\text{m}$  is an artifact of the array readout.

The decline in sensitivity of the cal port relative to the main aperture at longer wavelengths is attributable to the lack of illumination of the long-wavelength grating blaze, and to the increasing polarization sensitivity of the VIMS-IR beyond  $3 \mu\text{m}$ . The steep drop shortward of  $2 \mu\text{m}$  is, on the other hand, unexplained. Neither the ZnSe prisms nor the several aluminum reflections seem to be capable of causing this effect. Additional experiments showed no indication of a misalignment in the projector illumination pattern. Previous calibration runs on June 26, 1996, which did not use the external Al plate, did not achieve sufficient SNR at the longer wavelengths. Nevertheless, these earlier results are not consistent with the final runs at short wavelengths, for reasons that are presently unknown. Thus, the cal port ratio spectrum in Figure 20 must be considered provisional, until in-flight experience is available.

Viewed through the VIMS-IR cal port, images of a circular target are noticeably elongated. FWHM dimensions are  $\sim 2.0$  pixels in X, but increase steadily from 2.8 pixels in the Z direction at  $1 \mu\text{m}$  to 4.1 pixels at  $5 \mu\text{m}$ . This may be compared with FWHM sizes for the boresight images of  $1.5 \times 2.2$  pixels for the same target. The elongation of the solar port images is due to diffraction at the elongated rectangular

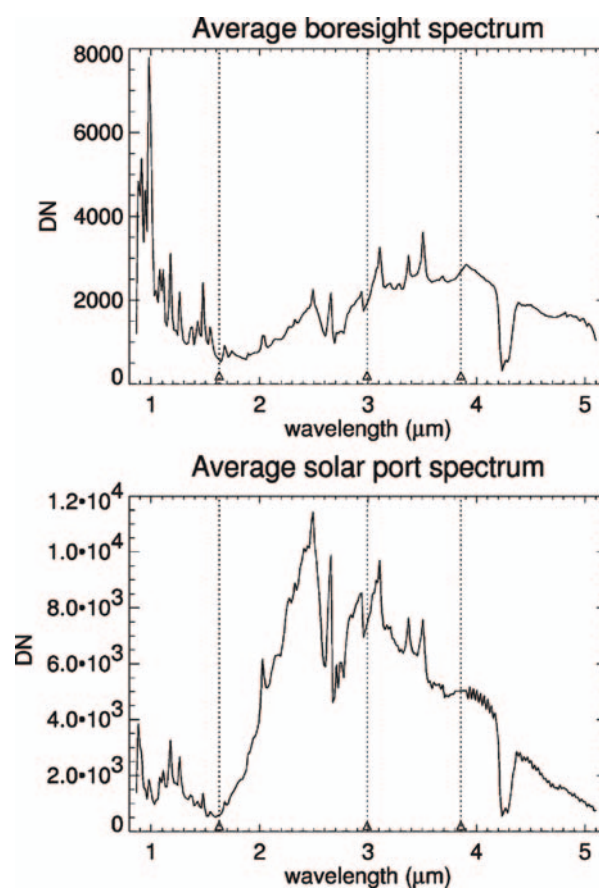


Figure 19. Average instrumental response through the boresight and solar port.

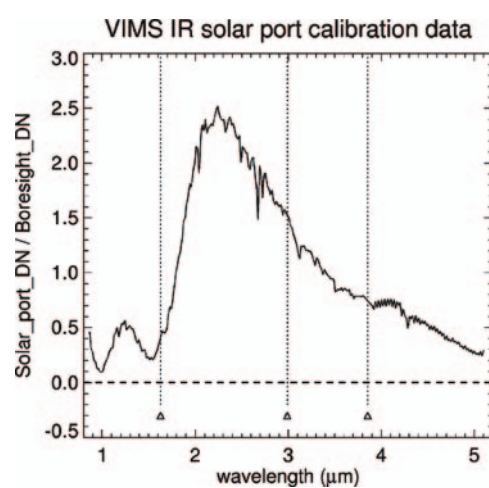


Figure 20. Ratio of response, solar calibration port (cal port) to boresight.

aperture of the cal port ( $30 \text{ mm} \times 5 \text{ mm}$ ). Image centroids are fairly stable, varying in  $X$  by at most 0.3 pixels and in  $Z$  by at most 0.2 pixels. Because of the variable size and slightly wavelength-dependent position of the solar image, it is recommended that solar cal port images be co-added over at least an  $8 \times 8$  pixel region in order to obtain a stable, well-defined spectrum. In-flight observations show that the solar calibration ports in VIMS-VIS and VIMS-IR are co-aligned to within 1 pixel, but offset by 10 mrad from the nominal pointing. This is well within the capability of the VIMS scan mirrors to correct, and will thus permit simultaneous solar occultation measurements with the UVIS instrument.

#### 6.6.2. *Results from Earth–Moon Flyby*

Due to the large attenuation factors incorporated in the design of the VIMS-VIS and VIMS-IR solar calibration ports, the only targets suitable for calibration observations after launch were Venus and the Moon. Prior to the Earth–Moon flyby and the deployment of the VIMS-IR covers, only the VIMS-VIS was operational. Although a short series of observations of Venus through the VIMS-VIS solar port was attempted during the V2 flyby on 24 June 1999, a software error prevented their successful execution. It appears, however, that light from Venus inadvertently entered the solar port during pre-encounter background calibration frames.

Approximately 95 min after Earth's close approach on 18 August 1999, the crescent Moon passed through the field of view of the VIMS solar port. Because full pointing control of the spacecraft was not possible at this time, actual data collection was limited to the period of  $\sim 5$  min. during which the Moon crossed the VIMS look direction. The observations were made in image mode, with the slits oriented perpendicular to the direction of the Moon's apparent motion across the focal plane (at 1.32 mrad/min), and with a VIS integration time of 20/sline and an IR integration time of 320 ms/pixel. A total of four full  $64 \times 64$  pixel image cubes were obtained over a period of 91 min, centered on the predicted observation time. Because the VIMS slow-scan direction is towards  $Z$ , and the Moon was drifting towards  $-Z$ , the Moon was expected to cross the spectrometer entrance slits in 2.8 min., with the lit crescent visible for perhaps one min.

The VIMS-VIS solar calibration port did indeed apparently detect the Moon in two successive 20 s. integrations acquired at approx. 5:13 UT, at an average signal level of  $22 \pm 4$  DN above the local sky background. At a distance of 460,000 km, the lunar diameter subtended 7.6 mrad, or 15 VIMS pixels, and the lit crescent completely filled the width of the 0.5 mrad entrance slit. Nevertheless, the design of the cal port prism diffuses the light uniformly along the slit, so no actual image was obtained. Figure 21 shows the resulting spectrum, averaged over all 64 spatial pixels along the slit and over both integrations. Plotted with the solar port spectrum is a spectrum of the bright lunar limb acquired by VIMS-VIS through its main aperture, suitably scaled. Although the illumination direction is the same for both spectra, it should be noted that the cal port observations were obtained at a phase angle of  $110^\circ$ , whereas the boresight spectrum was obtained at  $90^\circ$ .

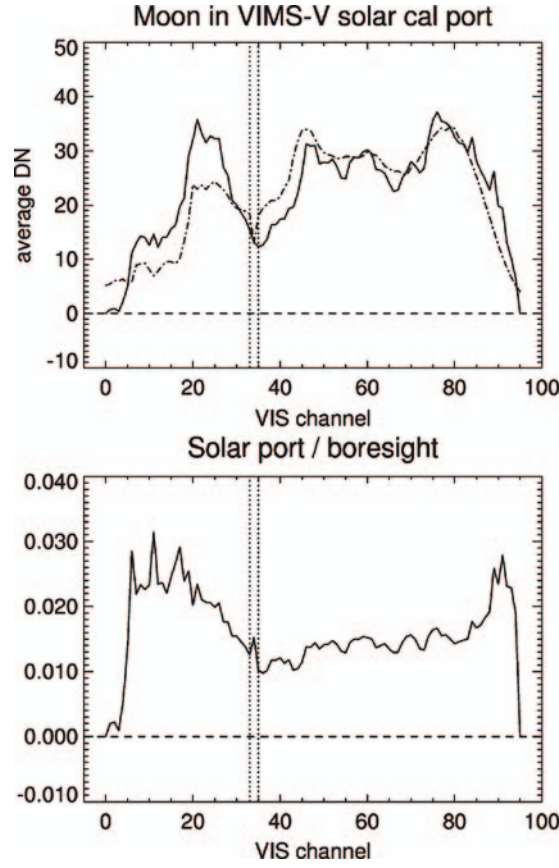


Figure 21. Solar port calibration at the Earth-Moon flyby.

The lower panel of Figure 21 shows that the ratio of lunar spectra obtained through the cal port and on boresight varies relatively smoothly with wavelength (within the SNR limitations of the data), and is highest in the UV. A rough estimate of the overall average attenuation by the VIMS-VIS cal port, taking into account the different integration times and instrument gain states, is,

$$R = \left( \frac{22\text{DN}}{1000\text{DN}} \right) \left( \frac{0.32s}{20s} \right) \times \left( \frac{1}{8} \right) = 4.5 \times 10^{-5}$$

at an effective wavelength of  $\sim 650$  nm. Unfortunately, all of the IR data were saturated because both the detector array and the entire spectrometer were too warm.

Although the data obtained at the Moon are of insufficient SNR to use for calibration purposes, they are valuable in (i) demonstrating the functionality of the VIMS-VIS cal port, (ii) confirming the validity of the ground calibration data in, and (iii) providing a basis for estimating solar exposure times at Saturn.



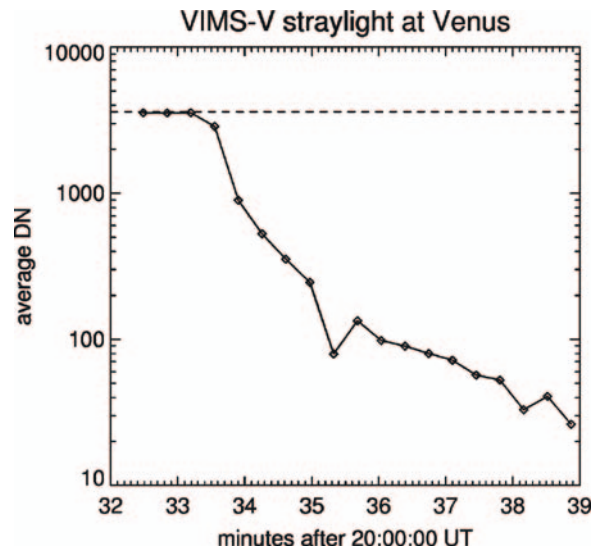


Figure 22. Scattered light measurements at Venus.

#### 6.7. SCATTERED LIGHT MEASUREMENTS FOR THE VISUAL CHANNEL

The Venus 2 flyby on June 24, 1999 provided an excellent opportunity for measurements of scattered light from a very bright off-axis source. Twenty seven integrations were executed by VIMS-VIS shortly after Venus close-approach, and immediately after the VIMS boresight moved off the bright limb of the planet onto dark sky. Operating in line mode with an integration time of 20 s, these observations spanned the period 20:32:29–20:42 UT and commenced with the VIMS boresight pointed  $4.9^\circ$  away from the nearest point on Venus' limb.

Data from the first three integrations, within  $10^\circ$  of the limb, are saturated in all 96 spectral channels and all 64 spatial pixels along the slit. Subsequent integrations show scattered light rapidly declining, as shown in Figure 22, until the sky background level was reached at around 20:39 UT. The signal had fallen by a factor of 10 by 20:35, when the VIMS boresight was pointed  $23.2^\circ$  off the limb.

Throughout the scattered light observations, the recorded spectrum remained essentially unchanged except for the absolute level, as shown in Figure 23. This spectrum, however, is virtually flat and does not show the characteristic spectral response of VIMS-VIS to broadband solar radiation, such as was observed at Venus and the Moon. The feature at channel 34 ( $\sim 600$  nm) is due to partial obscuration of the focal plane array at the segment boundary between the short- and long-wavelength blocking filters.

Further analysis strongly suggests that the measured signal is due to off-axis light from Venus which entered the entrance slit of the spectrometer enclosure directly (passing just above the fold mirror M2), without reflecting off the scanning

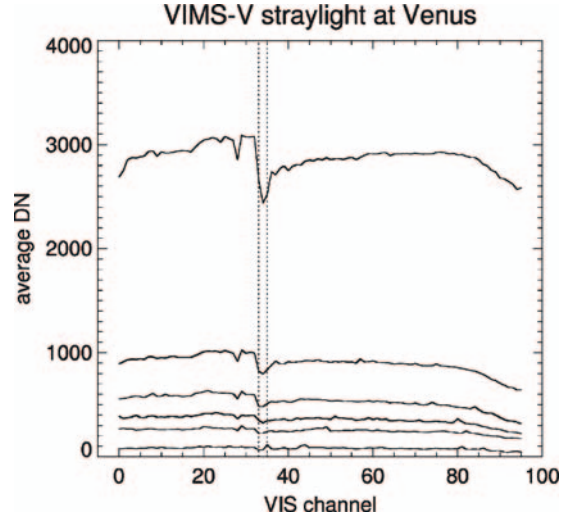


Figure 23. Non dispersed stray light.

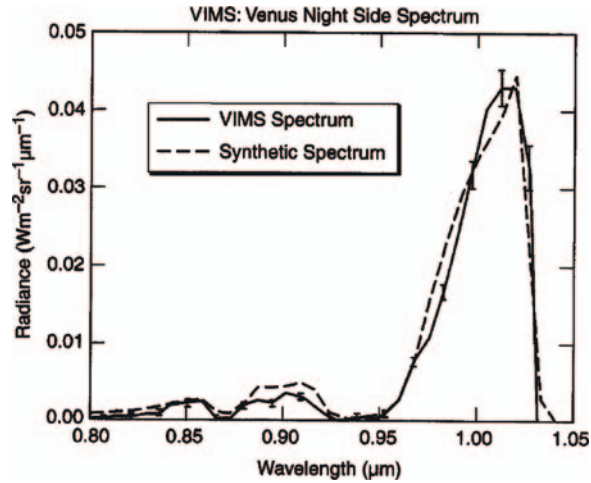


Figure 24. VIMS-VIS spectrum of the night side of Venus, compared to a synthetic spectrum (normalized at  $1.01 \mu\text{m}$ ). From Baines *et al.*, 2000.

mirror, and then was reflected by mirror M3 and the collimator directly to the FPA, bypassing the diffraction grating. At the time of the observations, Venus' disk subtended a radius of  $55\text{--}59^\circ$ , and the nearest point on the limb was located within a few degrees of the  $+Z$  direction from the VIMS boresight. 3-D ray-tracing indicates that undispersed scattered light may reach the FPA from an off-axis direction of  $\sim 17^\circ$  towards  $+Z$  and  $\pm 10^\circ$  in  $X$ , a location which would have fallen on the illuminated disk of Venus over a period which matches that of the observed signal in Figure 22.

A series of similar observations were made just as the VIMS boresight crossed the opposite limb of Venus to probe the planet's night side spectrum. These spectra, obtained when the illuminated disk of Venus was located between  $-Z$  and  $+X$ , relative to the boresight, and with the terminator  $10\text{--}15^\circ$  off axis, show no evidence of a significant component of scattered light similar to that in Figure 23.

Although very evident in long integrations, the level of scattered light is in fact fairly modest: at  $13^\circ$  from Venus' limb, and accounting for integration time and instrument gain, the measured signal was  $\sim 0.1\%$  of the average flux received directly from Venus. Similar situations are likely to be encountered during some Titan flybys, and perhaps for Saturn observations near periapse, and may warrant corrections for scattered light.

## 6.8. VENUS SURFACE AND ATMOSPHERE

The power of VIMS to make new discoveries was amply demonstrated by the very first planetary spectrum acquired by the instrument (Baines *et al.*, 2000). On June 24, 1999, during the Cassini flyby of Venus, the visual channel obtained a single long-duration (10 s) exposure of the planet's night side. This observation was centered near  $20^\circ\text{N}$ . latitude and  $60^\circ\text{E}$ . longitude, and for the first time quantitatively measured Venusian surface emissions at sub-micrometer wavelengths. As shown in Figure 24, the emission profiles of two spectral features predicted by Lecacheux *et al.* (1993) at  $0.85$  and  $0.90\text{ }\mu\text{m}$  were measured. As with other surface emissions previously observed near  $1.01$ ,  $1.10$ , and  $1.18\text{ }\mu\text{m}$  by ground-based observers and the near-infrared mapping spectrometer (NIMS) onboard the Galileo spacecraft (e.g. Carlson *et al.*, 1991, 1993a,b; Crisp *et al.*, 1991; Lecacheux *et al.*, 1993; Meadows and Crisp, 1996), these features are located in spectral windows devoid of atmospheric absorption through which radiation emitted from the hot ( $\sim 740\text{ K}$ ) surface passes through the  $\sim 90$  bars of  $\text{CO}_2$ -laden atmosphere into space. This spectrum is the first detection of the  $0.90\text{-}\mu\text{m}$  feature. The shorter wavelength feature at  $0.85\text{ }\mu\text{m}$  was provisionally detected in a single wavelength channel just above the detection limit by Galileo NIMS (Carlson *et al.*, 1991). In contrast, the VIMS spectral profile of this feature spans a wide range of wavelength at high signal-to-noise.

Adding to the previous work of NIMS and groundbased observers, VIMS thus demonstrated that the surface of Venus could be observed in five distinct windows between  $0.85$  and  $1.18\text{ }\mu\text{m}$ . As shown by Baines *et al.* (2000), compositional maps of the surface of Venus may be obtainable from future spacecraft that take advantage of this novel technique to observe the glowing surface of Venus under nighttime conditions. Future observations should take simultaneous measurements of the flux generated at several purely non-gas-absorbing atmospheric wavelengths (e.g.  $1.28$ ,  $1.74$ ,  $2.29\text{ }\mu\text{m}$ ) as well as within the five surface-detecting windows, so that the surface spectrum can be corrected for the highly-spatially-variable extinction due to overlying clouds. As previously demonstrated (e.g. Carlson *et al.*, 1993a,b), due to the spherical shape and non-absorbing nature of Venus's sulfuric

acid cloud particles, the wavelength-dependent extinction of Venus aerosols can be estimated over a large wavelength range from observations made at relatively long wavelengths (NIMS successfully used 1.73 and 2.4  $\mu\text{m}$  fluxes to determine cloud extinction at 1.18  $\mu\text{m}$ ). In the case of VIMS, observations longward of 1.05  $\mu\text{m}$  were unobtainable since the optics cover of VIMS-IR had not been opened as of the Venus encounter, as noted above. Thus, while the relative shape of various surface emission features could be observed by VIMS-VIS, absolute surface fluxes could not be determined. Nevertheless, the distinct advantage VIMS has over previous spectral instruments to the outer planets—in particular, its ability to simultaneously acquire all wavelengths of a spectrum, and its ability to take long exposures (e.g. 10 s here as opposed to enabled VIMS at Venus to make new discoveries with its very first observation, and portends well the making of new discoveries at the mission's major target, the Saturn system.

## 7. Conclusions

All indications to the writing of this document are that the VIMS instrument in flight has met or exceeded all of its preflight specifications. Measurements have been, and will continue to be, made of the instrument's performance throughout the roughly 6.5 years of Cassini's cruise to Saturn in preparation for the orbital tour. There is every reason to expect VIMS performance will meet or exceed expectations during the Saturn orbital tour, and that the science results produced from VIMS data will be both rich and exciting. It is indeed a privilege for all of the authors of this document to have participated in the VIMS adventure thus far, and we look forward to the exciting discoveries yet to be made at Saturn.

## Acknowledgements

The number of people who are responsible for the design, construction, test, launch and operation of the Cassini/Huygens Mission in general, and the VIMS instrument in particular, is truly enormous, and the brilliance of their contributions may sometimes get lost in the glare of the science discoveries that we all hope will result at Saturn. We cannot list them all here, but they know who they are, and the VIMS Science Team especially wants to acknowledge the enabling contributions of all of those bright and dedicated people who created VIMS, and those who are now helping us to operate it. Without them, none of what is possible with VIMS would be possible. Many thanks to all of you and we hope to see you at Saturn.

## References

Aptaker, I.: 1982, *SPIE Instrumentation in Astronomy IV Proceedings*, pp. 182–196.

- Baines, K. H., Brown, R. H., Matson, D. L., Nelson, R. M., Buratti, B. J., Bibring, J. P., *et al.*: 1992, *Symposium on Titan*, ESA SP-338, pp. 215–219.
- Baines, K. H., Bellucci, G., Bibring, J.-P., Brown, R. H., Buratti, B. J., Bussolletti, E., *et al.*: 2000, *Icarus* **148**, 307–311.
- Baines, K. H., Carlson, R. W., and Kamp, L. W.: 2002, *Icarus* **159**, 74–94.
- Brown, R. H., Baines, K. H., Bellucci, G., Bibring, J.-P., Buratti, B. J., Capaccioni, F., *et al.*: 2003, *Icarus* **164**, 461–470.
- Carlson, R. W., Baines, K. H., Kamp, L. W., Weissman, P. R., Smythe, W. D., Ocampo, A. C., *et al.*: 1991, *Science* **253**, 1541–1548.
- Carlson, R. W., Baines, K. H., Girard, M., Kamp, L. W., Drossart, P., Encrenaz, T., *et al.*: 1993a, *Proceedings of XXIV Lunar Planetary Science Conference*, 253.
- Carlson, R. W., Kamp, L. W., Baines, K. H., Pollack, J. B., Grinspoon, D. H., Encrenaz, T., *et al.*: 1993b, *Planet. Space Sci.* **41**, 477–485.
- Crisp, D., Allen, D. A., Grinspoon, D. H., and Pollack, J. B.: 1991, *Science* **253**, 1263–1266.
- Green, R. O., Eastwood, M. L., Sarture, C. M., Chrien, T. G., Aronsson, M., Chippendale, B. J., *et al.*: 1998, *Remote Sensing Environ.* **65**, 227–248.
- Griffith, C. A. and Owen, T.: 1992, *Symposium on Titan*, ESA SP-338, 199–204.
- Lecacheux, J., Drossart, P., Laques, P., Deladerriere, F., and Colas, F.: 1993, *Planet. Space Sci.* **41**, 543–549.
- McCord, T. B. and Adams, J. B.: 1973, *Moon* **7**, 453–474.
- McCord, T. B. and the VIMS Team: in press, *Icarus*.
- Meadows, V. S. and Crisp, D.: 1996, *J. Geophys. Res.* **101**, 4595–4622.
- Miller, E., Klein, G., Juergens, D., Mehaffey, K., Oseas, J., Garcia, R., *et al.*: 1996, *SPIE* **2803**, 206.
- Macenka, S.: 1982, *SPIE* **43**, 46.
- Meier, R., Smith, B. A., Owen, T. C., and Terrile, R. J.: 2000, *Icarus* **145**, 362–473.
- Pollack, J. B., Dalton, J. B., Grinspoon, D., Watson, R. B., Freedman, R., Crisp, D., Allen, D. A., *et al.*: 1993, *Icarus* **103**, 1–42.
- Reininger, F., Dami, M., Paolinetti, R., Pieri, S., and Falugiani, S.: 1994, *SPIE* **2198**, 239–250.
- Rice, R., Yeh, P., and Miller, W.: 1991, *Algorithms for a Very-High-Speed, Noiseless Encoding Module*. JPL Publication 91-1.
- Roos-Serote, M., Drossart, P., Encrenaz, T., Lellouch, E., Carlson, R. W., Baines, K. H., *et al.*: 1999, *J. Geophys. Res. Planets* **103**, 23023–23042.
- Roos-Serote, M., Vasavada, A. R., Kamp, L., Drossart, P., Irwin, P., Nixon, C., *et al.*: 2000, *Nature* **405**, 158–160.
- Simon-Miller, A. A., Conrath, B., Gierasch, P., and Beebe, R.: 2000, *Icarus* **45**, 454–461.
- Stammes, P.: 1992, *Symposium on Titan*, ESA SP-338, pp. 205–210.
- Tomasko, M., Pope, S., Kerola, D., Smith, P., and Giver, L.: 1989, *Bull. Amer. Astron. Soc.* **21**, 961–962.

## EXPLORING THE SATURN SYSTEM IN THE THERMAL INFRARED: THE COMPOSITE INFRARED SPECTROMETER

F. M. FLASAR<sup>1,\*</sup>, V. G. KUNDE<sup>2</sup>, M. M. ABBAS<sup>3</sup>, R. K. ACHTERBERG<sup>4</sup>, P. ADE<sup>5</sup>,  
A. BARUCCI<sup>6</sup>, B. BÉZARD<sup>6</sup>, G. L. BJORAKER<sup>1</sup>, J. C. BRASUNAS<sup>1</sup>, S. CALCUTT<sup>7</sup>,  
R. CARLSON<sup>4</sup>, C. J. CÉSARSKY<sup>8</sup>, B. J. CONRATH<sup>9</sup>, A. CORADINI<sup>10</sup>, R. COURTIN<sup>6</sup>,  
A. COUSTENIS<sup>6</sup>, S. EDBERG<sup>11</sup>, S. EDGINGTON<sup>11</sup>, C. FERRARI<sup>12</sup>, T. FOUCHET<sup>6</sup>,  
D. GAUTIER<sup>6</sup>, P. J. GIERASCH<sup>9</sup>, K. GROSSMAN<sup>13</sup>, P. IRWIN<sup>7</sup>, D. E. JENNINGS<sup>1</sup>,  
E. LELLOUCH<sup>6</sup>, A. A. MAMOUTKINE<sup>4</sup>, A. MARTEN<sup>6</sup>, J. P. MEYER<sup>12</sup>, C. A.  
NIXON<sup>2</sup>, G. S. ORTON<sup>11</sup>, T. C. OWEN<sup>14</sup>, J. C. PEARL<sup>1</sup>, R. PRANGÉ<sup>6</sup>, F. RAULIN<sup>15</sup>,  
P. L. READ<sup>7</sup>, P. N. ROMANI<sup>1</sup>, R. E. SAMUELSON<sup>2</sup>, M. E. SEGURA<sup>16</sup>, M. R.  
SHOWALTER<sup>17</sup>, A. A. SIMON-MILLER<sup>1</sup>, M. D. SMITH<sup>1</sup>, J. R. SPENCER<sup>18</sup>,  
L. J. SPILKER<sup>11</sup> and F. W. TAYLOR<sup>7</sup>

<sup>1</sup>Goddard Space Flight Center, Greenbelt, MD, 20771, U.S.A.

<sup>2</sup>University of Maryland, College Park, MD 20742, U.S.A.

<sup>3</sup>Marshall Space Flight Center, Huntsville, AL 35812, U.S.A.

<sup>4</sup>Science Systems and Applications Inc., Lanham, MD 20706, U.S.A.

<sup>5</sup>University of Cardiff, CF24 3YB, U.K.

<sup>6</sup>Observatoire de Paris-Meudon, F92195 Meudon Cedex, France

<sup>7</sup>Oxford University, OX1 3PU, U.K.

<sup>8</sup>European Southern Observatory, 85748 Garching bei Muenchen, Germany

<sup>9</sup>Cornell University, Ithaca, NY 14853, U.S.A.

<sup>10</sup>Istituto di Astrofisica Spaziale, Rome I-00133, Italy

<sup>11</sup>Jet Propulsion Laboratory, Pasadena, CA 91109, U.S.A.

<sup>12</sup>CEA/Service d'Astrophysique, 91191 Gif-sur-Yvette Cedex, France

<sup>13</sup>Gesamthochschule Wuppertal, 5600 Wuppertal 1, Germany

<sup>14</sup>University of Hawaii, Honolulu, HI 96822, U.S.A.

<sup>15</sup>Université de Paris 7 & 12, 94010 Creteil Cedex, France

<sup>16</sup>QSS Group, Inc, Lanham, MD 20706 U.S.A.

<sup>17</sup>Stanford University, Stanford, CA 94305 U.S.A.

<sup>18</sup>Southwest Research Institute, Boulder, CO 80302 U.S.A.

(\*Author for correspondence: E-mail: f.m.flasar@nasa.gov)

(Received 9 October 2003; Accepted in final form 2 January 2004)

**Abstract.** The Composite Infrared Spectrometer (CIRS) is a remote-sensing Fourier Transform Spectrometer (FTS) on the Cassini orbiter that measures thermal radiation over two decades in wavenumber, from 10 to 1400 cm<sup>-1</sup> (1 mm to 7 μm), with a spectral resolution that can be set from 0.5 to 15.5 cm<sup>-1</sup>. The far infrared portion of the spectrum (10–600 cm<sup>-1</sup>) is measured with a polarizing interferometer having thermopile detectors with a common 4-mrad field of view (FOV). The middle infrared portion is measured with a traditional Michelson interferometer having two focal planes (600–1100 cm<sup>-1</sup>, 1100–1400 cm<sup>-1</sup>). Each focal plane is composed of a 1 × 10 array of HgCdTe detectors, each detector having a 0.3-mrad FOV. CIRS observations will provide three-dimensional maps of temperature, gas composition, and aerosols/condensates of the atmospheres of Titan and Saturn with good vertical and horizontal resolution, from deep in their tropospheres to high in their mesospheres. CIRS's ability to observe atmospheres in the limb-viewing mode (in addition to nadir) offers the opportunity to



Space Science Reviews **115**: 169–297, 2004.

© 2004 Kluwer Academic Publishers. Printed in the Netherlands.



provide accurate and highly resolved vertical profiles of these atmospheric variables. The ability to observe with high-spectral resolution should facilitate the identification of new constituents. CIRS will also map the thermal and compositional properties of the surfaces of Saturn's icy satellites. It will similarly map Saturn's rings, characterizing their dynamical and spatial structure and constraining theories of their formation and evolution. The combination of broad spectral range, programmable spectral resolution, the small detector fields of view, and an orbiting spacecraft platform will allow CIRS to observe the Saturnian system in the thermal infrared at a level of detail not previously achieved.

**Keywords:** Infrared spectroscopy, Saturn, Titan, Saturn's rings, Saturn's moons, atmospheric temperatures, atmospheric composition, atmospheric dynamics, Cassini

## 1. Introduction

The Saturn system offers a rich variety of objects for exploration and study at infrared wavelengths. The atmospheres of Saturn and Titan, the surfaces of Titan and the icy satellites, and the rings, each pose unique challenges for a single instrument. In the wake of the highly successful Galileo mission to Jupiter, an important goal is to acquire a set of data at Saturn that will allow detailed comparisons between these two giants, providing insights that will sharpen our general ideas about the formation of planetary systems.

What are the key differences between the atmospheres of Jupiter and Saturn, and what accounts for them? Why does Titan, unlike all other planetary satellites, have such a thick atmosphere? How is the chemistry that occurs on it today related to prebiological chemical evolution on the early Earth? What governs the weather on this slowly rotating satellite, and how does it compare to that driving the circulations of Earth's and Venus' atmospheres? What relations exist among the various icy satellites and the rings and why is this satellite system so very different from Jupiter's? These are a few of the questions we hope to answer.

The Saturn system is well suited for exploration in the infrared. Saturn, its rings, and its satellites radiate most of their energy at mid- and far-infrared wavelengths, because their radiating temperatures are relatively cold: in the range 55–200 K. Most molecules have lines or bands of lines in this spectral region, arising from rotational or vibrational-rotational transitions. A spectrometer covering these wavelengths serves as a remote-sensing thermometer and assayer, allowing one to map temperatures and composition spatially and temporally. How well it can exploit this spectral region depends on its configuration and sensitivity, but key figures of merit include: high spectral resolution, to permit identification of trace constituents, including isotopic variants; broad spectral coverage, to encompass a large variation in the opacity of the target, whether it be an atmosphere, surface, or ring material; detectors having a small field of view (FOV) projected onto the sky; and close proximity to the target, as afforded by an orbiting spacecraft to provide a variety of geometric observing opportunities, including a broad range of phase-angle coverage.

The Composite Infrared Spectrometer (CIRS) is an infrared Fourier Transform Spectrometer (FTS) on the Cassini orbiter which measures thermal radiation over more than two decades in wavenumber ( $\nu$ ) from 10 to 1400  $\text{cm}^{-1}$  (1 mm to 7  $\mu\text{m}$ ). CIRS will measure thermal emission from the Saturn system with a spectral resolution that can be selected over the range from 0.5 to 15.5  $\text{cm}^{-1}$ . It will map the atmospheres of Saturn and its largest moon Titan temporally and spatially in three dimensions, including limb sounding, which will achieve a vertical resolution of one scale height or better. In addition, CIRS will map the thermal characteristics and composition of the other icy satellites and Saturn's rings.

The plan of this paper is as follows: Section 2 provides a brief overview of the instrument capabilities and its modes of operation. Section 3 discusses the science objectives of the CIRS investigation, in context of the current knowledge of Saturn, Titan, the other satellites, and the rings. We discuss how CIRS's unique capabilities can help address many of the important questions concerning these bodies. Section 4 describes in more detail the observations CIRS will make during the Saturn tour. The instrument itself is described in Section 5. Appendices describe the retrieval of atmospheric variables from infrared spectra, the spatial response across the far-infrared FOV of CIRS, and the equations used in calibrating the infrared spectra.

CIRS acquired data during the Jupiter swingby from October, 2000, to March, 2001, which resulted in approximately 600,000 calibrated spectra. Jupiter results are not discussed here, except in the context of Saturn system science. Instead, we refer the reader to the Jupiter results reported elsewhere by Flasar *et al.* (2004), Kunde *et al.* (2004), Wong *et al.* (2004), Abbas *et al.* (2004), Fouchet *et al.* (2004a,b) and Irwin *et al.* (2004).

## 2. Instrument Overview

The CIRS instrument consists of two interferometers, sharing a common telescope and scan mechanism. They operate in the far-infrared (10–600  $\text{cm}^{-1}$ ) and mid-infrared (600–1400  $\text{cm}^{-1}$ ) with a commandable apodized<sup>1</sup> spectral resolution as high as 0.5  $\text{cm}^{-1}$ . Table I summarizes the instrument properties. The far-IR interferometer is a polarization interferometer, with a focal plane consisting of two thermopile detectors with a 3.9-mrad FOV, labeled FP1. The mid-IR interferometer is a conventional Michelson interferometer with two focal plane arrays (FP3, FP4), each having 10 HgCdTe detectors, with 0.273-mrad FOV per pixel.

<sup>1</sup>Interferograms extend only over a finite distance, with maximum mirror displacement  $\delta_{\text{max}}$ . The reconstructed spectrum, obtained via Fourier transforms, will consist of the true spectrum convolved with  $\sin(2\pi\nu\delta_{\text{max}})/2\pi\nu\delta_{\text{max}}$ , which produces a “ringing” in the vicinity of strong narrow features. To avoid this, the interferogram is “tapered” by multiplying it by a quasi-triangular apodization function, so that displacement amplitudes are attenuated away from the  $\delta = 0$  central fringe. See, e.g., Hanel *et al.* (2003) for more discussion. A well-chosen apodization reduces the ringing considerably, but degrades the spectral resolution. In searching for weak features away from strong lines, it is often desirable to use unapodized spectra to maximize the contrast of the weak features. The search for HD rotational lines (see Section 3.1.1 and Figure 6) is one example of this.

TABLE I  
CIRS instrument characteristics.

Telescope diameter (cm)	50.8		
Interferometers	Far-IR	Mid-IR	
Type	Polarizing	Michelson	
Spectral range ( $\text{cm}^{-1}$ )	10—600	600—1400	
Spectral range ( $\mu\text{m}$ )	17—1000	7—17	
Spectral resolution ( $\text{cm}^{-1}$ )	0.5—15.5	0.5—15.5	
Integration time (s)	2—50	2—50	
Focal planes	FP1	FP3	FP4
Spectral range ( $\text{cm}^{-1}$ )	10—600	600—1100	1100—1400
Detectors	Thermopile	PC HgCdTe	PV HgCdTe
Pixels	2 <sup>a</sup>	$1 \times 10$	$1 \times 10$
Pixel FOV (mrad)	3.9	0.273	0.273
Peak D* ( $\text{cm Hz}^{1/2} \text{ W}^{-1}$ )	$4 \times 10^9$	$2 \times 10^{10}$	$5 \times 10^{11}$
Data telemetry rate (kbs)		2 and 4	
Instrument temperature (K)		170	
Focal planes 3 and 4 Temperature (K)		75—90	

<sup>a</sup>Single FOV, two polarizations.

Figure 1 depicts the CIRS FOVs as projected onto the sky. The instrument is described in more detail in Section 5.

CIRS derives much of its heritage from the Voyager Infrared Interferometer Spectrometer (IRIS: see Hanel *et al.*, 1980), but it has several important improvements:

- (I) *Extended far-infrared coverage:* The CIRS coverage between 10 and 180  $\text{cm}^{-1}$  was not accessible to IRIS. This will extend the vertical range of temperature sounding to include the upper troposphere of Titan and lower stratospheres of Saturn and Titan. It will also increase the chances of detecting previously undiscovered organic molecules. The enhanced spectral coverage will provide the ability to probe Saturn's ring particles in the poorly studied submillimeter region, where opacity decreases rapidly with increasing wavelength, and it will permit the thermal sounding of the first centimeter of the regoliths of the icy satellites.
- (II) *Higher spectral resolution:* The maximum CIRS resolution of 0.5  $\text{cm}^{-1}$  (apodized) is an order of magnitude higher than that of IRIS (4.3  $\text{cm}^{-1}$ ). This will increase the opportunity to detect new trace constituents including their isotopic variants, and will permit the improved retrieval of temperature and gas profiles by virtue of both the narrower contribution functions and of the higher altitudes probed.

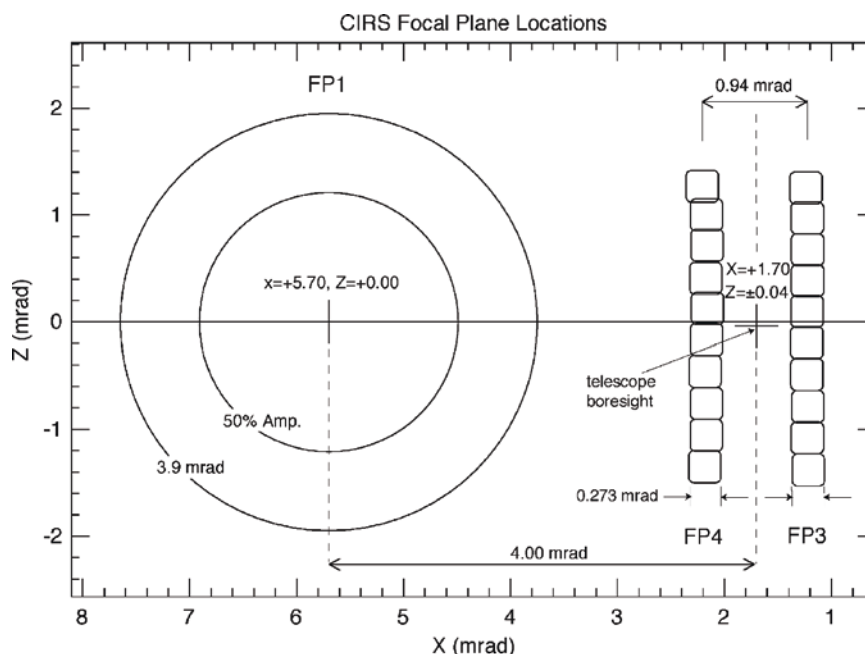


Figure 1. CIRS fields of view projected on the sky. FP1 is the far-IR focal plane. FP3 and FP4 are the mid-IR focal planes. The relative positions of the CIRS focal planes on the spacecraft have been determined by scans across a distant Jupiter and infrared stars (Section 5.2.2). The spacecraft  $-Y$  axis is at  $(X, Z) = (0, 0)$ . The boresight of the Cassini imaging science (ISS) Narrow Angle Camera (NAC) is approximately at  $X = 0.58$  mrad,  $Z = -0.17$  mrad. The mid-IR arrays are linear. The slight "wobble" is just the best fit to the scan data for each pixel. The full length of each array is 2.876 mrad.

- (III) *Improved sensitivity:* The CIRS sensitivity is much better than Voyager IRIS in the  $600\text{--}1400\text{ cm}^{-1}$  region, through the use of passively cooled HgCdTe detectors, instead of a thermopile. This allows the smaller  $0.27 \times 0.27$  mrad FOV's to be used, giving higher spatial resolution.
- (IV) *Limb-viewing capability:* The arrays and smaller detectors in the  $600\text{--}1400\text{ cm}^{-1}$  region permit limb sounding of both Saturn's and Titan's stratosphere and mesosphere with an altitude resolution better than one scale height, an improvement of 2–3 over the Voyager IRIS nadir soundings. In addition, the long absorber paths viewed against a cold space background greatly enhance sensitivity to minor constituents. Close passages of Titan will repeatedly allow limb sounding of that body at far infrared wavelengths with the larger 3.9-mrad FP1 FOV.
- (V) *Orbiting platform:* The Cassini spacecraft has an inherent advantage, in that it will orbit within the Saturn system for several years, while each of the Voyager spacecraft flew through only once. Hence CIRS will have the opportunity for global and seasonal mapping with spatial detail that was

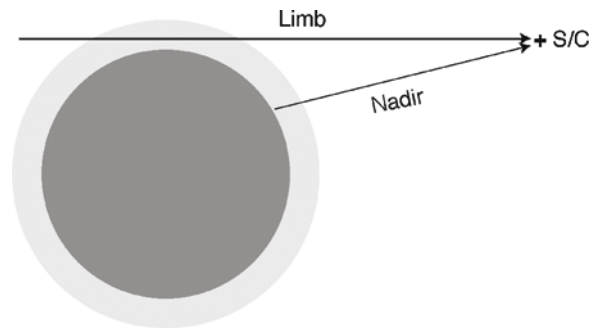


Figure 2. Schematic illustrating limb and nadir modes of observation.

simply not possible with IRIS. In addition, CIRS will be able to make refined investigations of newly discovered phenomena.

Figure 2 illustrates the nadir and limb-viewing modes CIRS will employ. The viewing mode and spectral resolution are dictated by the scientific objectives. The principal modes of observation of Saturn and Titan are:

- (1) *Nadir viewing, complete spectral range, full spectral resolution ( $0.5\text{ cm}^{-1}$ ).* Objectives: gas composition, isotopic ratios, general exploration.
- (2) *Nadir viewing, complete spectral range, reduced spectral resolution ( $3, 15.5\text{ cm}^{-1}$ ).* Objectives: maps of temperature, more abundant gas species, and aerosols.
- (3) *Limb viewing, complete spectral range, full spectral resolution ( $0.5\text{ cm}^{-1}$ ).* Objectives: Vertical profiles of trace constituents, identifications of new species, distinguishing vapor from condensed phases.
- (4) *Limb viewing, complete spectral range, reduced spectral resolution ( $3, 15.5\text{ cm}^{-1}$ ).* Objectives: Vertical profiles of temperature, aerosols, and more abundant gases to high altitudes (0.01 mbar).

For the satellites and rings, the primary observational modes are:

- (5) *Nadir viewing, complete spectral range, reduced spectral resolution ( $3.0\text{ cm}^{-1}$ ), stare.* Objectives: composition.
- (6) *Nadir viewing, FP1, low spectral resolution ( $15.5\text{ cm}^{-1}$ ), full disk, stare.* Objectives: disk temperatures for phase (“diurnal”) coverage; eclipse measurements to determine thermal inertia.
- (7) *Mapping of icy satellites at low spectral resolution ( $15.5\text{ cm}^{-1}$ ).* Objectives: composition; thermal probing of regolith to search for solid state greenhouse effects (FP1); thermal anomalies; high spatial resolution surface-temperature mapping and eclipse heating and cooling to determine the thermal inertia (FP3, FP4).

- (8) *Ring radial scans, complete spectral range, reduced spectral resolution ( $3\text{ cm}^{-1}$  and  $15.5\text{ cm}^{-1}$ ).* Objectives: Radial profiles of composition, temperature and opacity.
- (9) *Ring circumferential scans, complete spectral range, reduced spectral resolution ( $15.5\text{ cm}^{-1}$ ).* Objectives: Eclipse heating and cooling curves to obtain ring particle thermal inertia and rotation rate.
- (10) *Long integrations on rings, full and reduced spectral resolution ( $0.5\text{ cm}^{-1}$  and  $3.0\text{ cm}^{-1}$ ).* Objectives: composition of non-icy component of ring material, IR phase function, interior structure.

### 3. Scientific Background and Objectives

#### 3.1. SATURN

Saturn is like the Sun, in that it is composed primarily of hydrogen and helium. However, its mass – like Jupiter’s – is too small for its gravitational field to produce the high pressures and temperatures required for nuclear burning in its interior. Instead, it radiates thermal energy from its degenerate fluid interior, which was created during an earlier Kelvin contraction phase, and by gravitational separation of partially immiscible helium-rich and hydrogen-rich phases (see, e.g., Hubbard, 1980). Not long ago, the common perception was that the giant planets were formed directly from the gaseous material of the primitive solar nebula. The planets were massive enough to prevent the escape of any element, and hence the atmospheres should reflect solar composition. After hydrogen and helium, compounds of carbon, nitrogen, and oxygen should be the most abundant. Although, in a general sense, this model is correct, it does not hold up at the detailed level, reflecting a more complex scenario of planetary formation and evolution than originally envisioned (see, e.g., Gautier and Owen, 1989, for a review). The atmosphere of Saturn may be depleted in helium, because of the immiscibility and differentiation mentioned above that is occurring in its interior during the current epoch (see, e.g., Fortney and Hubbard, 2003). The relative abundances of carbon and nitrogen are above solar values by factors of two to four, suggesting that Saturn formed heterogeneously from the surrounding nebula (see, e.g., Pollack *et al.*, 1996). In the final phase of formation the hydrogen and planetesimals contained in the feeding zone of the planet (within the Hill radius) collapsed simultaneously, so that the resulting gaseous envelope was enriched in heavy elements (Magni and Coradini, 2003). Sulfur may also be enriched on Saturn by a factor of  $\sim 10\times$  solar (Briggs and Sackett, 1989), if the apparent depletion of  $\text{NH}_3$  in the upper troposphere is caused by the formation of dense  $\text{NH}_4\text{SH}$  clouds. These enrichments in heavy elements constrain the theories of the formation of Saturn, as well as the composition of grains embedded in the solar nebula.

Figure 3 depicts synthetic spectra of Saturn at low latitudes over the full CIRS spectral range at several resolutions; major spectral features are indicated. Observed



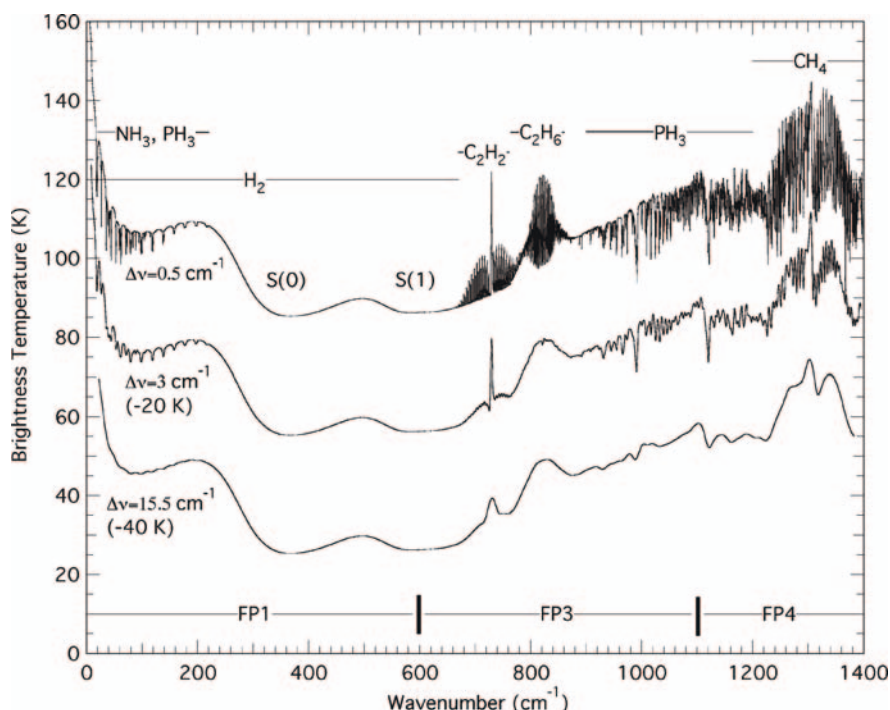


Figure 3. Synthetic spectrum of Saturn's equatorial atmosphere at three (apodized) resolutions. For ease of viewing the entire CIRS spectral range, brightness temperatures are depicted. The brightness temperatures of the lower-resolution spectra are offset vertically as indicated. The boundaries of the three focal planes (FP1, FP3, FP4) are shown at the bottom. At wavenumbers less than  $670\text{ cm}^{-1}$  the spectrum is dominated by tropospheric absorption. The broad spectral features are from pressure-induced absorption from the S(0) and S(1) lines of  $\text{H}_2$ , labeled in the figure, and from the translational continuum of  $\text{H}_2$  at lower wavenumbers. Superposed on this at wavenumbers less than  $220\text{ cm}^{-1}$  is absorption primarily from  $\text{NH}_3$  and  $\text{PH}_3$ .  $\text{PH}_3$  also appears in absorption between  $900$  and  $1200\text{ cm}^{-1}$ . Spectral features attributable to  $\text{C}_2\text{H}_2$ ,  $\text{C}_2\text{H}_6$ , and  $\text{CH}_4$  appear in emission, relative to the background continuum, because their line-formation regions are in the stratosphere. The spectral regions associated with pressure-induced  $\text{H}_2$  absorption and  $\text{CH}_4$  emission serve as the thermometers used to retrieve vertical profiles of atmospheric temperature.

spectra such as these will form the basis for addressing several of the scientific issues just raised.

Table II summarizes the scientific objectives of the CIRS investigation of Saturn. The first column lists major scientific objectives for Saturn, and the second column lists the physical variables that CIRS can retrieve to address those objectives. The last column lists the relevant measurement sequences, which are treated more fully in Section 4.2.

### 3.1.1. Formation, Evolution, and Internal Structure

CIRS spectra will contribute to this area in several ways. The first is through a better determination of the abundances of He, C, N, and S in Saturn's atmosphere.

TABLE II  
Saturn science and measurement objectives and observations.

Science objective	CIRS categories: Retrieved physical parameters	Observations
Formation, evolution, and internal structure		
Elemental abundances	He	Nadir occultation point, far-IR maps
	CH <sub>4</sub> , NH <sub>3</sub> , H <sub>2</sub> S	Comp integrations, far- and mid-IR nadir maps, regional nadir maps, limb integrations, limb maps
Isotopic abundances	HD, CH <sub>3</sub> D, <sup>15</sup> NH <sub>3</sub> , <sup>13</sup> CH <sub>4</sub>	" "
Internal heat	Temperatures	Far- and mid-IR nadir maps, regional nadir maps, feature tracks
Atmospheric gas composition		
Disequilibrium species	PH <sub>3</sub> , HCP, halides, stratospheric hydrocarbons, new molecules	Comp integrations, limb integrations, limb maps, feature tracks
	Ortho/para ratio	Far-IR nadir maps, regional nadir maps
Condensible gases	NH <sub>3</sub> , H <sub>2</sub> S	Comp integrations, far-IR and mid-IR nadir maps, feature tracks
External sources (e.g., rings)	Oxygen species: stratospheric H <sub>2</sub> O, CO <sub>2</sub> , CO	Comp integrations, far-IR nadir maps, regional nadir maps
Clouds/aerosols		
Composition	NH <sub>3</sub> , NH <sub>4</sub> SH, . . .	Far- and mid-IR nadir maps, regional nadir maps, limb maps
Microphysical properties	Aerosol/cloud properties	" "
Auroral hot spots		
Spatial and temporal distribution	Temperature and composition gradients	Feature tracks, limb maps, limb integrations, far- and mid-IR nadir maps, regional nadir maps, comp integrations
Spectral properties	New species	Feature tracks, limb integrations, comp integrations
Atmospheric structure		
Temperature, pressure, density	Temperature field	Far- and mid-IR nadir maps, regional nadir maps, limb maps
Circulation		
Zonal jets	Thermal winds	Far- and mid-IR nadir maps, regional nadir maps, limb maps
Meridional motion	Constituent tracers	Comp integrations, far- and mid-IR nadir maps, limb integrations
	Aerosols/diabatic heating and cooling	Far- and mid-IR nadir maps, limb maps
	Potential vorticity (temperature field)	Far- and mid-IR nadir maps, regional nadir maps, limb maps, feature tracks
Waves and vortices	Temperature and comp fields	Far- and mid-IR nadir maps, regional nadir maps, limb maps
Convection	Temperature variance	" "

*Helium.* Voyager spacecraft measurements have been used to determine the He abundance on all four giant planets, but recent Galileo probe measurements have raised some questions concerning these results. The primary technique employed with the Voyager measurements uses data from both IRIS and the radio occultation (RSS) experiments. If a particular atmospheric composition is assumed, then the atmospheric mean molecular mass and mean microwave refractivity coefficient can be specified, and a profile of temperature versus pressure can be obtained from the RSS measurements. A theoretical thermal emission spectrum, calculated from a radiative transfer code using this profile, is then compared with spectra measured by IRIS near the occultation point on the planet. The atmospheric composition is adjusted until the theoretical and measured spectra are brought into agreement. This technique yielded a He mass fraction of  $0.18 \pm 0.04$  for Jupiter and the remarkably low value of  $0.06 \pm 0.05$  for Saturn (Gautier *et al.*, 1981; Conrath *et al.*, 1984). Recently, the helium abundance detector (HAD) on the Galileo probe into Jupiter obtained results equivalent to a He mass fraction of  $0.238 \pm 0.007$  (von Zahn and Hunten, 1996), and the probe mass spectrometer measurements were identical to this value (Niemann *et al.*, 1996). Although the  $1\text{-}\sigma$  error bars associated with the Voyager and Galileo results are relatively near one another, close examination of the results suggests the possibility of systematic errors in the Voyager determination. When the Galileo value of the Jovian He abundance is used to calculate a temperature profile from the Voyager RSS results, the theoretical thermal emission spectrum calculated from that profile is about 2 K warmer in brightness temperature than the measured IRIS spectra throughout the entire spectral region  $300\text{--}800\text{ cm}^{-1}$  (Conrath and Gautier, 2000). The source of possible systematic errors has yet to be identified.

The possibility of systematic errors in the Voyager He abundance determination for Jupiter leads one to ask whether similar problems exist for the Voyager results for the other giant planets, including Saturn. For this reason, the re-determination of the Saturn He abundance has become a major scientific objective for *Cassini*. The same technique that was used in the *Voyager* analyses can be applied to combinations of *Cassini* CIRS spectra and radio occultation measurements (see Kliore *et al.*, 2003). However, in this case, many radio occultation profiles will be available, acquired under differing viewing geometries and at different locations on the planet. Such multiple determinations should be useful in identifying and eliminating possible systematic errors.

A second constraint on the He abundance is provided by the detailed shape of the measured thermal emission spectrum in the far infrared ( $\nu < 600\text{ cm}^{-1}$ ). The differential spectral dependence of the collision-induced  $\text{H}_2$  absorption in the S(0) and S(1) lines and the translational portion of the spectrum is a function of the relative contributions from  $\text{H}_2\text{--H}_2$  and  $\text{H}_2\text{--He}$  interactions. Ideally, this effect should permit simultaneous retrieval of both the temperature profile and the He abundance (Gautier and Grossman, 1972). This was done with the *Voyager* Jupiter thermal

emission spectra by Gautier *et al.* (1981). The shape of this portion of the spectrum is also sensitive to the molecular hydrogen *ortho/para* ratio (the ratio of molecular hydrogen in the odd rotational-quantum-number, or *ortho-hydrogen*, state to that in the even rotational-quantum-number, or *para-hydrogen*, state). Gautier *et al.* assumed this ratio to be the thermodynamic equilibrium value at the local temperature. However, it is now realized that the H<sub>2</sub> *ortho/para* ratio is not in equilibrium at many locations on Jupiter (Conrath and Gierasch, 1984; Carlson *et al.*, 1992). Within the portion of the hydrogen absorption spectrum on Jupiter that is free from cloud opacity and ammonia absorption, the effects of He and the hydrogen *ortho/para* ratio are similar, and it is not possible to constrain both parameters simultaneously. Saturn's troposphere, however, is colder than Jupiter's, and more ammonia precipitates out. The reduced cloud and gaseous ammonia absorption in the upper troposphere allows access to a larger portion of the H<sub>2</sub> translational continuum at lower wavenumbers. Measurements in this portion of the spectrum, combined with measurements in the S(0) and S(1) lines, do permit the simultaneous retrieval of temperature, the hydrogen *ortho/para* ratio, and the He abundance. Conrath and Gautier (2000) have reanalyzed Saturn IRIS spectra over its lowest wavenumber range, 200–600 cm<sup>-1</sup>, and derived a helium mass fraction of 0.18–0.25, considerably higher than the earlier IRIS-RSS result. This technique will be more sensitive using CIRS spectra, because of the additional spectral coverage of the translational continuum below 200 cm<sup>-1</sup>. Spectra from various locations on the planet can be analyzed, while imposing the additional constraint that, even though the temperature and *ortho/para* ratio vary with location, the He abundance should be the same everywhere. This approach will provide an independent determination. While the formal errors from these results will be larger than from those derived using both CIRS and RSS data, they should serve as a useful constraint in detecting any large systematic errors in the latter approach.

**Methane.** CH<sub>4</sub> is the primary repository of carbon on Saturn. Previous determinations of the atmospheric CH<sub>4</sub> abundance have relied on near-infrared reflection spectra obtained with ground-based telescopes. Most recent measurements (Karkoschka and Tomasko, 1992) indicate a methane mixing ratio of  $(3.0 \pm 0.6) \times 10^{-3}$ , yielding  $[C]/[H] = (1.3\text{--}2.0) \times 10^{-3}$ . This range represents a considerable enhancement relative to the solar value ( $4.7 \times 10^{-4}$ ), which, as noted earlier, would suggest a heterogeneous origin of Saturn. Scattering from clouds and aerosols complicates the interpretation of the near-infrared data, and this issue has been somewhat controversial (see Prinn *et al.*, 1984).

Retrievals of the CH<sub>4</sub> abundance from spectra obtained in the  $\nu_4$  band in the thermal infrared near 1300 cm<sup>-1</sup>, such as those obtained by Voyager IRIS ( $4.3^{+2.3}_{-1.8} \times 10^{-3}$ , Courtin *et al.*, 1984) and by the ISO/Short Wavelength Spectrometer ( $4.5^{+1.1}_{-2.1} \times 10^{-3}$ , Lellouch *et al.*, 2001) have been problematic, because of the difficulty in separating the effects of CH<sub>4</sub> abundance from those of temperature. This general problem is discussed in more detail in Appendix A. With only

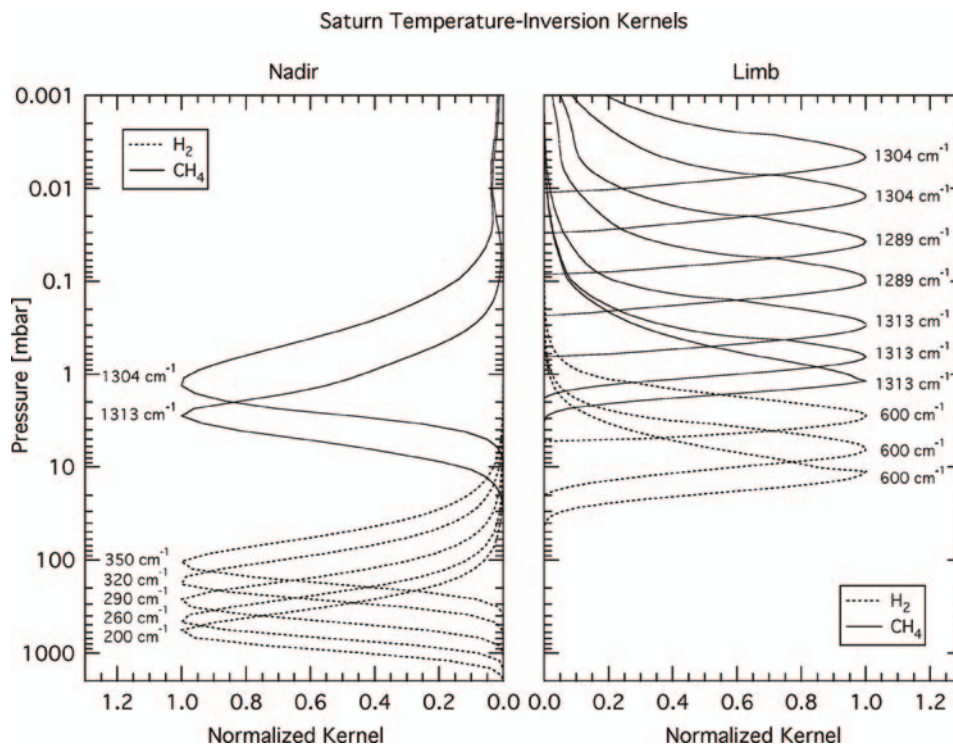


Figure 4. Inversion kernels for temperature sounding of Saturn. The kernels for limb viewing have been convolved with a finite FOV approximated as a Gaussian, whose full width at the  $1/e$  points, projected onto the horizon, equals one scale height.

nadir-viewing observations, as IRIS usually obtained, there is not sufficient redundancy in the spectra to determine  $[\text{CH}_4]$  uniquely. The capability of limb sounding changes all this. Figure 4 depicts the inversion kernels for temperature retrieval in Saturn's atmosphere from CIRS spectra for both nadir- and limb-viewing geometries. The requisite redundancy in the spectra is evidenced by the slight overlap in the stratosphere of the inversion kernels at  $600\text{ cm}^{-1}$  – attributable to absorption in the  $\text{S}(1)$  line of  $\text{H}_2$  – for the limb mode and those in the  $\nu_4$ -band of  $\text{CH}_4$  near  $1300\text{ cm}^{-1}$  for nadir viewing. Hence, the combination of CIRS spectra at the two viewing geometries should determine the stratospheric  $\text{CH}_4$  abundance. Additionally, the rotational lines of  $\text{CH}_4$ , in the far-infrared at  $60\text{--}120\text{ cm}^{-1}$ , illustrated in Figure 5, contain information on tropospheric methane. As methane does not condense in Saturn's atmosphere, the tropospheric and stratospheric abundances should be identical. The line-formation region of the centers of rotational lines, which are seen in absorption, is  $\sim 250\text{ mbar}$ , in the upper troposphere. The requisite redundancy here is afforded by the independent determination of temperature from the simultaneous nadir observations in the spectral region  $150\text{--}600\text{ cm}^{-1}$ , where pressure-induced absorption by  $\text{H}_2$  in the translational continuum and the

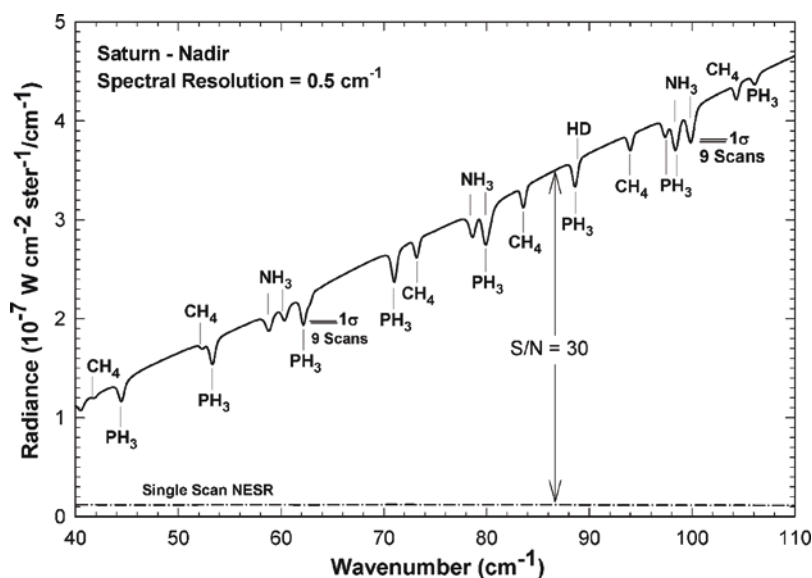


Figure 5. Synthetic far-infrared nadir spectrum of Saturn at high resolution ( $0.5 \text{ cm}^{-1}$ ) showing  $\text{NH}_3$ ,  $\text{PH}_3$ ,  $\text{CH}_4$ , and  $\text{HD}$  absorption lines, along with the NESR (Section 5.6.1) for a single spectrum and the  $1\text{-}\sigma$  errors for 9 averaged spectra.  $\text{NH}_3$  and  $\text{PH}_3$  variations across the disk of Saturn will be inferred from these spectral lines

$\text{S}(0)$  and  $\text{S}(1)$  lines dominates the opacity (see Appendix A). Hence, determination of stratospheric and tropospheric methane from two different spectral regions should provide an accurate determination of the atmospheric abundance of this compound.

**Ammonia.**  $\text{NH}_3$  is the principal reservoir of nitrogen on Saturn. Its abundance in Saturn's upper troposphere and higher is severely limited by condensation.  $\text{NH}_3$  is usually thought to be the main component of Saturn's visible clouds, although no definite evidence exists. It is photolyzed at pressures  $\leq 0.5$  bar and, coupled with  $\text{PH}_3$  and hydrocarbons, may be involved in complex chemical processes (Kaye and Strobel, 1984).  $\text{NH}_3$  varies laterally as well as vertically. Ground-based radio observations of Saturn at 6 cm, which probe the atmosphere between 1.3 and 5 bar, have shown enhanced emission within a broad latitude band extending from  $20^\circ \text{ N}$  to  $50^\circ \text{ N}$  (Grossman *et al.*, 1989). The band is thought to be depleted in gaseous  $\text{NH}_3$ , which permits emission from warmer and deeper regions of the troposphere to be observed. The 700-mbar temperatures retrieved from Voyager IRIS radiances near  $225 \text{ cm}^{-1}$  also indicated an apparent increase in the same region (Conrath and Pirraglia, 1983). However, the retrievals were based on the assumption that the collision-induced transitions of  $\text{H}_2$  provided all the infrared opacity, and they did not include the contributions of clouds. If the cloud opacity was not negligible, then it is likely that the enhanced temperatures at mid northern latitudes result from a minimum in the cloud opacity there, which would be consistent with the radio



observations. The spatial distribution of gaseous  $\text{NH}_3$  and clouds must result from atmospheric transport, coupled with condensation and photochemical processes. This cycle is still poorly understood.

CIRS spectra provide a sensitive means to determine the distribution of tropospheric  $\text{NH}_3$  on Saturn. Both the  $\nu_2$  vibrational band in the mid infrared near  $1000\text{ cm}^{-1}$  and the rotational lines visible in the far infrared from  $60$  to  $225\text{ cm}^{-1}$  can be used. Figure 5 depicts a synthetic nadir spectrum at high spectral resolution of the rotational  $\text{NH}_3$  lines at Saturn's equator. The high spectral resolution ( $0.5\text{ cm}^{-1}$ ) is needed to separate the multiplets of  $\text{PH}_3$  from those of  $\text{NH}_3$ , and give good discrimination of the weak  $\text{NH}_3$  lines against the underlying  $\text{H}_2$  continuum. The Noise Equivalent Spectral Radiance (NESR, see Section 5.6.1) is shown for a single high resolution scan (52 s). The  $\text{H}_2$  continuum to NESR ratio establishes the accuracy with which the temperature and cloud structure can be retrieved. Over most of the spectral range, the signal-to-noise ratio (SNR) is  $\sim 30$ . The  $1\text{-}\sigma$  error bar shown corresponds to the average of 9 scans, which decreases the NESR by a factor of three, and it indicates the accuracy with which the  $\text{NH}_3$  abundance can be retrieved. The SNR is quite adequate for retrieving the  $\text{NH}_3$  vertical profile from the observed Saturn radiances.  $\text{NH}_3$  abundances will be retrieved in a layer centered at 500 mbar with a vertical resolution comparable to the  $\text{NH}_3$  saturation vapor pressure scale height.

*Hydrogen sulfide.* The Galileo probe mass spectrometer detected  $\text{H}_2\text{S}$  at pressure levels between 8 and 20 bars in Jupiter's deep atmosphere (Niemann *et al.*, 1998). The only remote observation of  $\text{H}_2\text{S}$  on Jupiter was a tentative detection in the stratosphere immediately after the collision of comet Shoemaker-Levy 9 (Yelle and McGrath, 1996; Atreya *et al.*, 1995, claimed only an upper limit from the same ultraviolet data set.)  $\text{H}_2\text{S}$  has not been observed at all on Saturn. The difficulty arises from the depletion of  $\text{H}_2\text{S}$  from the chemical reaction with  $\text{NH}_3$  to form the  $\text{NH}_4\text{SH}$  cloud that is thought to exist at a pressure of several bars. Only at  $5\text{ }\mu\text{m}$  and beyond  $10\text{ cm}$  at radio wavelengths can one probe deeper than this cloud to levels where  $\text{H}_2\text{S}$  is expected to be abundant. However, there are no  $\text{H}_2\text{S}$  bands at  $5\text{ }\mu\text{m}$ , and beyond  $10\text{ cm}$ , there is a smeared out continuum that makes it nearly impossible to separate  $\text{NH}_3$ ,  $\text{PH}_3$ , and  $\text{H}_2\text{S}$ . There are strong rotational lines of  $\text{H}_2\text{S}$  between  $20$  and  $80\text{ cm}^{-1}$  within CIRS's FP1 bandpass – not shown in Figure 5 – that sound the  $\sim 1\text{-bar}$  level, which is well above the nominal  $\text{NH}_4\text{SH}$  cloud. Weisstein and Serabyn (1996) acquired whole-disk spectra of Saturn using the Caltech Submillimeter Observatory. They reported a stringent upper limit to  $\text{H}_2\text{S}$  on Saturn of 16 ppb using an absorption feature at  $687.3\text{ GHz}$  ( $22.93\text{ cm}^{-1}$ ). This is 3 orders of magnitude less than the solar abundance of sulfur, thus supporting the idea that sulfur is locked up in the  $\text{NH}_4\text{SH}$  cloud. Images of Saturn at  $5.2\text{ }\mu\text{m}$  reveal interesting spatial structure in the deepest cloud layers (Yanamandra-Fisher *et al.*, 2001), and it is possible for  $\text{H}_2\text{S}$  to be enhanced locally above the very low global average. Hence a search for  $\text{H}_2\text{S}$ , using the CIRS capability of high spectral and spatial resolution, is an important objective.

Isotopic abundances also bear on Saturn's formation and evolution:

*Deuterium.* It is widely recognized that an accurate determination of  $[D]/[H]$  can provide useful constraints on models for the origin and evolution of planetary atmospheres. As  $H_2$  dominates all other hydrogen-bearing constituents by a large margin on both Jupiter and Saturn, one expects the value of  $[D]/[H]$  in the  $H_2$  in these atmospheres to be identical to the value in the hydrogen that dominated the interstellar cloud from which the solar system formed. Neither of these giant planets is sufficiently massive to produce internal temperatures and pressures that would permit D-consuming nuclear reactions. The only disturbance of the original ratio would therefore come from other hydrogen compounds that were brought to the forming planet as solids (primarily in ices) in sufficient amounts.

Gautier and Owen (1989) adopted  $[D]/[H] = (1.7 + {}^{1.9}_{-1.0}) \times 10^{-5}$  on Saturn, based on various analyses of observations of  $CH_4$  and  $CH_3D$  bands (with a correction for the fractionation from hydrogen) by several different observers. More recently, ISO has also observed the rotational lines of HD in absorption in the far infrared (Griffin *et al.*, 1996; Lellouch *et al.*, 2001). Averaging the  $[D]/[H]$  retrieved from ISO observations of the R(2) and R(3) HD lines at  $265\text{ cm}^{-1}$  and  $351\text{ cm}^{-1}$ , respectively, with that retrieved from the observed emission in the  $CH_3D$  band near  $1150\text{ cm}^{-1}$ , Lellouch *et al.*, derived  $[D]/[H] = (1.70 + {}^{0.75}_{-0.45}) \times 10^{-5}$  on Saturn and  $(2.25 \pm 0.35) \times 10^{-5}$  on Jupiter. The latter ratio is in good agreement with that derived from direct measurements of HD and  $H_2$  in Jupiter's atmosphere with the mass spectrometer on the Galileo Probe (Mahaffy *et al.*, 1998):  $[D]/[H] = (2.6 \pm 0.7) \times 10^{-5}$ . The Jupiter ratios are significantly higher than the value of  $(1.5 \pm 0.1) \times 10^{-5}$  in local interstellar hydrogen today (Linsky, 1998), as expected from models for galactic evolution that predict the destruction of deuterium with time as a result of nuclear "burning" in stars.

The lower value of  $[D]/[H]$  on Saturn is surprising, although the relative errors are large. Interior models (Guillot, 1999) predict that  $(^{[D]}/_{[H]})_{\text{Saturn}} / (^{[D]}/_{[H]})_{\text{Jupiter}} \sim 1.25\text{--}1.35$ , because of mixing of solar nebular gas with D-rich ices at Saturn's orbit. It is important to increase the precision of the  $[D]/[H]$  measurement on Saturn in order to decide whether this has occurred. CIRS can accomplish this through improved measurements of HD and deuterated methane.

CIRS can observe the R(0), R(1), and R(2) rotational lines of HD in the far-infrared, illustrated in Figure 6. These have been tentatively identified in CIRS observations of Jupiter obtained during the recent Cassini swingby (Kunde *et al.*, 2004). Even with CIRS's high resolution, the higher spectral resolution ( $\sim 0.27\text{ cm}^{-1}$ ) afforded by unapodized spectra is needed to resolve these weak features. The R(0) feature appears as a notch in the wing of the stronger  $PH_3$  absorption. The R(1) absorption at  $178\text{ cm}^{-1}$  is small,  $\sim 2 \times 10^{-8}\text{ W cm}^{-2}\text{sr}^{-1}/\text{cm}^{-1}$ , and it is imbedded within a  $NH_3$  multiplet. However, a two-hour integration would yield a SNR of 10 for this feature. In addition to HD and  $NH_3$  gas, this part of the spectrum is sensitive to temperature, the para  $H_2$  fraction, He, and  $NH_3$  ice. All but HD and He vary with location. As with He (see above), the constancy of

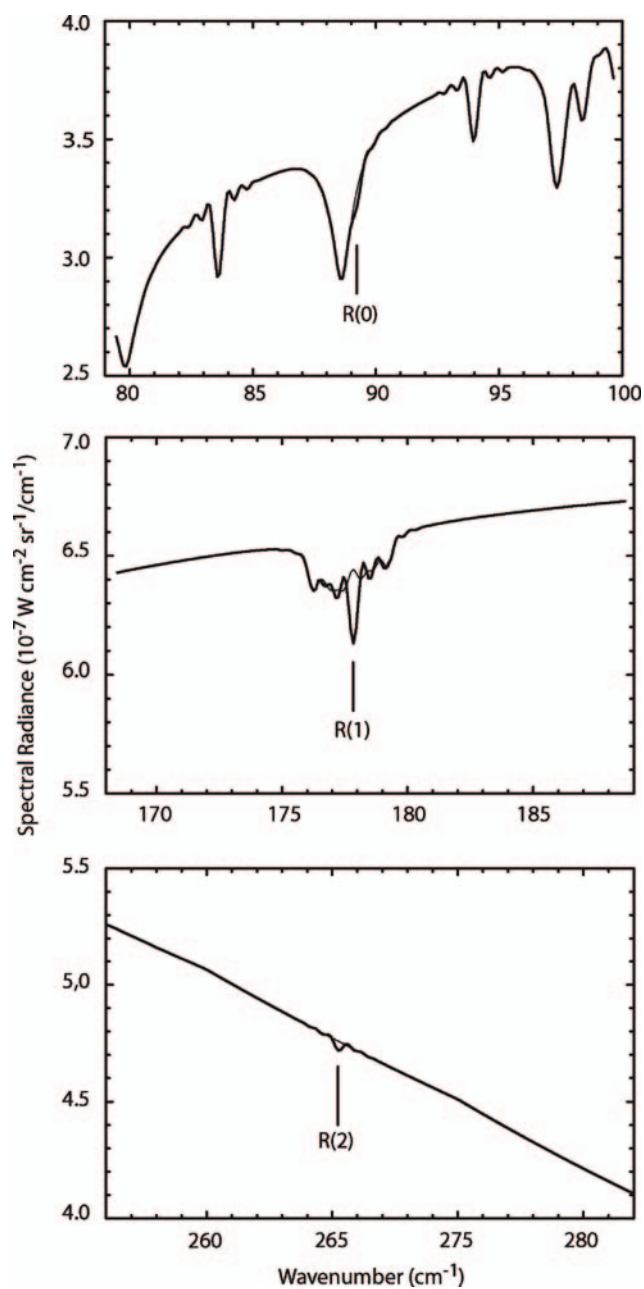


Figure 6. Unapodized  $0.27\text{ cm}^{-1}$  synthetic spectra in the far infrared, illustrating the R(0), R(1), and R(2) rotational lines of HD on Saturn. Spectra with and without the HD features are indicated. The R(0) line lies on the high-wavenumber side of a  $\text{PH}_3$  absorption, and the R(1) line is embedded within a  $\text{NH}_3$  absorption manifold.

HD can be leveraged to separate it from the other sources of opacity. Information on  $\text{NH}_3$  in both the gaseous and solid phases, temperature, and the para fraction can be obtained from other parts of the spectrum and also from different viewing geometries. CIRS should be able to surpass the accuracy of the ISO determination.

In addition,  $[\text{D}]/[\text{H}]$  in methane can be inferred from the determination of the  $[\text{CH}_3\text{D}]/[\text{CH}_4]$  ratio (e.g., Lellouch *et al.*, 2001); this comes from spectral regions near  $1150\text{ cm}^{-1}$  and  $1300\text{ cm}^{-1}$ , where the Q-branches of  $\text{CH}_3\text{D}$  and  $\text{CH}_4$  are located, respectively. The spectral resolution accessible to CIRS and the high sensitivity of its detectors in this region (Figure 37) will permit an improved determination of this ratio. In particular, CIRS should improve the ISO determination ( $2.0^{+1.4}_{-0.7} \times 10^{-5}$ ), which was hampered by the existence of temperature variations over Saturn's unresolved disk. Comparing this with  $[\text{D}]/[\text{H}]$  in  $\text{H}_2$  should allow one to evaluate the isotopic enrichment factor in methane in the upper troposphere of Saturn. This factor reflects the competition between chemical equilibration at deeper, hotter levels of Jupiter's and Saturn's atmospheres and rapid upward transport to colder levels where the equilibration is quenched (Lecluse *et al.*, 1996; Smith *et al.*, 1996a). A precise determination of this factor would better define the quenching level and the nature of the dynamics of the deep atmosphere, which presently are only poorly constrained. ISO observed both HD and  $\text{CH}_3\text{D}$  on Jupiter and Saturn, but the errors in the  $[\text{D}/\text{H}]$  ratios derived were large enough to preclude a meaningful determination of the enrichment factor (Lellouch *et al.*, 2001).

*Carbon isotopes.* The ratio  $[\text{^{13}C}]/[\text{^{12}C}]$  is of interest because it is indicative of conditions in the outer solar system (Gautier and Owen, 1983). Galileo probe measurements found  $[\text{^{13}C}]/[\text{^{12}C}] = 0.010820 \pm 0005$  on Jupiter (Niemann *et al.*, 1996, 1998; Atreya *et al.*, 1999, 2003), which is consistent with the solar value. Ground-based measurements in the near infrared (Combes *et al.*, 1997) indicate that the ratio for Saturn is also close to solar. CIRS can observe  $^{13}\text{CH}_4$  emission at several features between  $1290$  and  $1300\text{ cm}^{-1}$ . Courtin *et al.* (1983) used IRIS data in this spectral region to retrieve  $[\text{^{13}C}]/[\text{^{12}C}]$  on Jupiter, but their value was higher than the solar value. In part this bias stemmed from IRIS's limited spectral resolution of  $4.3\text{ cm}^{-1}$ , causing some blending of the  $^{13}\text{CH}_4$  and  $^{12}\text{CH}_4$  emission. With its higher spectral resolution, CIRS should be able to separate the emission from these isotopes better. CIRS spectra should also show emission from  $^{13}\text{C}^{12}\text{CH}_6$ , near  $820\text{ cm}^{-1}$ . As methane and ethane are parent and daughter molecules, respectively, any differences in  $[\text{^{13}C}]/[\text{^{12}C}]$  inferred from their emission may be indicative of fractionation processes.

*Internal heat.* Saturn radiates more energy in the thermal infrared than it absorbs from sunlight. From Voyager IRIS observations, Hanel *et al.* (1983) have made the most definitive determination of the ratio of emitted radiation to absorbed sunlight,  $= 1.78 \pm 0.09$ . The excess energy is thought to be from Saturn's interior, attributable to primordial heat loss associated with Saturn's cooling and slow contraction, and possibly the energy release associated with gravitational separation of hydrogen and

helium. The CIRS spectra can determine Saturn's thermal emission more accurately for two reasons. The first is that the far infrared spectrum measured by IRIS only extended down to  $200\text{ cm}^{-1}$ . At lower wavenumbers, Hanel *et al.*, used a synthetic spectrum, calculated from the temperatures retrieved from the radiances at higher wavenumbers. CIRS will measure the far-infrared spectra directly down to  $10\text{ cm}^{-1}$ . Secondly, the Voyager IRIS coverage for the heat balance study was obtained at a time when the entire disk of Saturn nearly filled the instrument FOV, and a fairly involved correction was required to remove the effects of its rings. The Cassini orbital tour offers an improvement, in that it allows viewing of the entire planet at high spatial resolution at different emission angles.

At the emission-to-space level (400 mbar), Saturn's (and Jupiter's) zonal-mean temperatures (averaged over longitude) are remarkably uniform with latitude. This has been attributed to the efficiency of convective transport of heat within the interior (see, e.g., Ingersoll and Porco, 1978). However, small meridional temperature variations on the scale of the zonal-wind structure are observed (see below). The local variations in the heat balance on these scales are diagnostic of local dynamics, as Pirraglia (1983) has shown for Jupiter, using Voyager IRIS spectra. Detailed thermal mapping by CIRS will elucidate the local variations in thermal emission on Saturn. Unlike IRIS, which had a single-channel visible radiometer, CIRS does not have any sensitivity at solar wavelengths. However, there are other orbiter instruments that measure ultraviolet (Esposito *et al.*, 2003), visible (Porco *et al.*, 2003), and near-infrared (Brown *et al.*, 2003) radiation with photometric precision, and these will provide an improved determination of Saturn's reflected solar radiation. Combining these with CIRS observations in the thermal infrared will more accurately determine Saturn's heat balance on global and smaller scales.

### 3.1.2. Atmospheric Gas Composition

*Disequilibrium compounds – troposphere.* The molecules phosphine ( $\text{PH}_3$ ), carbon monoxide (CO), germane ( $\text{GeH}_4$ ), and arsine ( $\text{AsH}_3$ ) have been identified in Saturn (Bregman *et al.*, 1975; Noll *et al.*, 1986; Noll and Larson, 1990; Bézard *et al.*, 1989). These compounds are not in thermochemical equilibrium at the pressures ( $\leq$  several bars) and temperatures ( $< 300\text{ K}$ ) at which they are observed, and their existence in this part of the atmosphere must result from rapid upward transport from the hotter interior. They therefore serve as valuable tracers of the strength of the deep convective transport and of the chemical state of the interior. In tandem with thermochemical-kinetic models, the observed abundances can constrain the composition of heavy elements in Saturn's interior, a key parameter for theories of its formation and evolution. However, the interpretation of the observed disequilibrium molecules is complicated by the interplay of photochemistry and dynamics at atmospheric levels accessible to short-wave solar radiation. Phosphine, which leads to the formation of more complex molecules and possibly chromophores, provides an illustrative example. The abundance of  $\text{PH}_3$  in the atmosphere at pressures  $< 1\text{ bar}$  is depleted compared to that measured in the 4–5 bar range (see, e.g., de

Graauw *et al.*, 1997). This depletion has been attributed to UV photolysis or more complex photochemical processes (Kaye and Strobel, 1984). The vertical profile of phosphine results from a balance between vertical mixing and photochemical destruction. Additionally there are probably horizontal variations from the competition between photochemistry and meridional and vertical transports. On Jupiter, phosphine was found to decrease slowly in the 600-mbar region from  $10^\circ$  S to  $35^\circ$  S, which suggests a decrease in the strength of vertical mixing there (Lara *et al.*, 1998). In addition, an enhancement of the deep mixing ratio, at pressures  $>1$  bar was found at high northern latitudes ( $\sim 50^\circ$  N) on Jupiter (Drossart *et al.*, 1990). Recently, Irwin *et al.* (2004) have analyzed CIRS Jupiter data at  $1000\text{--}1200\text{ cm}^{-1}$  obtained during the Cassini swingby. Although a rapid decrease of  $\text{PH}_3$  with altitude above the 1-bar level was consistent with the spectra, they concluded that the 1-bar abundance and fractional scale height retrieved from the nadir-viewing spectra were highly correlated. At low latitudes they observed an enhancement in the 1-bar abundance in the equatorial zone – presumably a region of upwelling – and a depletion over the north and south equatorial belts. Because of the distance ( $140 R_J$ ) of the Jupiter flyby, Irwin *et al.* were restricted to the middle infrared portion of the spectrum, for which the CIRS detector arrays could spatially resolve the planet for detailed mapping. During the Cassini tour, Saturn can also be mapped in the far infrared, permitting deeper levels of the atmosphere to be probed. Figure 5 illustrates that the far-infrared spectrum is as promising a region to retrieve the spatial distribution of  $\text{PH}_3$  as it is for  $\text{NH}_3$ . The magnitude of the  $\text{PH}_3$  rotational lines are comparable to those of  $\text{NH}_3$ , so the earlier SNR estimates for the latter molecule apply to  $\text{PH}_3$  as well.

Mapping the distribution of several non-equilibrium molecules on Saturn will help separate the effects of chemistry and dynamics in the deep atmosphere from those of photochemistry and dynamics in the upper troposphere and middle atmosphere. In addition to the aforementioned molecules,  $\text{H}_2\text{Se}$ ,  $\text{H}_2\text{S}$ , and halides (HF, HCl, HBr, HI) are promising candidates (Bézard *et al.*, 1986). None of these, however, have been seen by ISO. Thermochemical models predict that halogens in the observable atmosphere should be trapped in the condensed phase as ammonium salts. Showman (2001) modeled the rapid transport of halides from the deep atmosphere, and he concluded that nucleation and condensation are too rapid to lead to observable supersaturation of these species. Using the strongest lines below  $205\text{ cm}^{-1}$ , Fouchet *et al.* (2004a) have analyzed CIRS Jupiter spectra to place upper limits on the mole fractions of the hydrogen halides:  $[\text{HF}] < 2.7 \times 10^{-11}$ ,  $[\text{HCl}] < 2.3 \times 10^{-9}$ ,  $[\text{HBr}] < 1.4 \times 10^{-9}$ ,  $[\text{HI}] < 1.0 \times 10^{-8}$ . The upper limits on [HF] and [HCl] are well below the solar values, supporting the condensation hypothesis. A similar analysis using CIRS spectra of Saturn would be useful for comparative studies of these two planets.

*Disequilibrium compounds – Ortho-para  $\text{H}_2$  conversion.* The ortho-para ratio of molecular hydrogen is a parameter of keen interest in the study of the dynamics and



energetics of the upper tropospheres of the giant planets. At deeper levels where the temperature exceeds 300 K, the value of the ortho-para ratio should be near the 3:1 high temperature limit (called the “normal” value). Since ortho-para transitions are highly forbidden, a parcel of gas initially at a deeper level will tend to retain its initial para fraction when moved upward toward cooler levels, rather than immediately assuming the thermodynamic equilibrium value of the lower temperature (the para fraction at equilibrium increases with decreasing temperature). The extent of disequilibrium will depend on the ratio of the thermal equilibration time to the dynamical transport time, which is not well known in the outer planets. In the upper troposphere of Saturn, the equilibration time for pure molecular hydrogen is approximately  $3 \times 10^8$  s, but this time can be significantly shortened by catalytic processes, involving, for instance, ortho-para conversion at paramagnetic sites produced by solar photons on cloud particles (Massie and Hunten, 1982; Conrath and Gierasch, 1984). Slow para hydrogen conversion can be a significant factor in the thermodynamics of convective processes, acting essentially as a latent heat (Conrath and Gierasch, 1984; Gierasch and Conrath, 1987; Smith and Gierasch, 1995). Para hydrogen can also serve as a tracer of atmospheric motion; measurements of its spatial distribution can be used to study the upper tropospheric circulation diagnostically.

Previous efforts to determine the hydrogen para fraction in the observable layers of the atmospheres of the giant planets include analyses of measurements of reflected solar radiation in the near-infrared hydrogen lines (Baines and Bergstralh, 1986; Smith and Baines, 1990; Baines *et al.*, 1995) and analyses of emission measurements in the thermal infrared. Retrievals from *Voyager* IRIS thermal emission spectra mapped the para fraction in the upper troposphere at  $\sim 100$ –300 mbar. The para hydrogen was found to be in disequilibrium at low latitudes (Conrath and Gierasch, 1983, 1984; Carlson *et al.*, 1992). From these results, Gierasch *et al.* (1986) inferred the presence of a hemispheric zonal-mean Lagrangian circulation in the upper troposphere and lower stratosphere, with slow upwelling (vertical velocities  $\leq 10^{-1}$  mm s $^{-1}$ ) at low latitudes and subsidence in the polar regions. Recently, Conrath *et al.* (1998) have extended the analysis of *Voyager* IRIS data to include all four giant planets. Disequilibrium para hydrogen was found on Saturn, with the large scale spatial distribution showing possible seasonal asymmetries. However, the *Voyager* analysis was limited by both the signal to noise ratio of the measurements and incomplete spatial coverage, especially in the southern hemisphere, because of the fly-by geometry. The global average ortho-to-para ratio has also been derived in the stratospheres of the four giant planets, from emission in the H $_2$  S(0) and S(1) quadrupolar lines measured by ISO/SWS (Fouchet *et al.*, 2003). The measurements were full-disk, except for Jupiter, for which the SWS FOV subtended 30°N to 30°S. The stratospheric para fractions on Jupiter and Saturn were close to the average tropopause values, thus representing a departure from thermodynamical equilibrium.

*Disequilibrium compounds – stratospheric hydrocarbons.* The irradiation of CH<sub>4</sub> by solar ultraviolet photons leads to the irreversible production of more complex hydrocarbons. Figure 7 depicts the chemical pathways following the initial breakup of CH<sub>4</sub>. The first “tier” of stable products includes acetylene (C<sub>2</sub>H<sub>2</sub>), ethylene (C<sub>2</sub>H<sub>4</sub>), and ethane (C<sub>2</sub>H<sub>6</sub>). C<sub>2</sub>H<sub>2</sub> and C<sub>2</sub>H<sub>6</sub> were observed in Voyager IRIS

*Disequilibrium compounds – stratospheric hydrocarbons.* The irradiation of CH<sub>4</sub> by solar ultraviolet photons leads to the irreversible production of more complex hydrocarbons. Figure 7 depicts the chemical pathways following the initial breakup of CH<sub>4</sub>. The first “tier” of stable products includes acetylene (C<sub>2</sub>H<sub>2</sub>), ethylene (C<sub>2</sub>H<sub>4</sub>), and ethane (C<sub>2</sub>H<sub>6</sub>). C<sub>2</sub>H<sub>2</sub> and C<sub>2</sub>H<sub>6</sub> were observed in Voyager IRIS

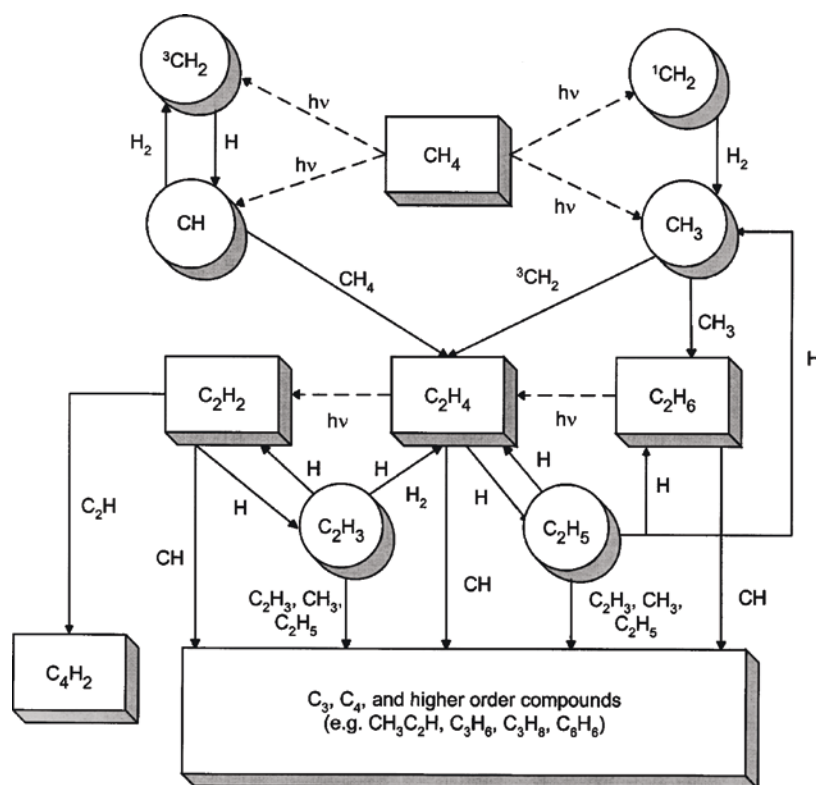


Figure 7. Photolytic reaction scheme for hydrocarbons in Saturn’s stratosphere. The rectangular boxes represent stable compounds, the circles denote free radicals, the solid lines indicate chemical reactions, and the dashed lines represent photolysis pathways.

spectra (see, e.g., Courtin *et al.*, 1984), but  $C_2H_4$  has only recently been detected (Bézard *et al.*, 2001a).  $C_2H_2$  is a key component, because it plays a role in the photosensitized destruction of  $CH_4$  to create  $C_6H_6$ , and it also leads to higher-order hydrocarbons, such as  $C_4H_2$  and  $C_6H_2$ , which are a potential source of the aerosol hazes in Saturn's stratosphere.  $C_2H_4$  is closely linked to  $C_2H_2$ , and current models (Moses *et al.*, 2000a) predict a column abundance of  $C_2H_4$  that is five times greater than that inferred from the observations. Uncertainties in some key reaction rates and in branching ratios associated with Ly- $\alpha$  photolysis may account for part of the discrepancy. Disk-average observations of Saturn by the ISO/SWS have also detected diacetylene ( $C_4H_2$ ), methylacetylene ( $CH_3C_2H$ ) (de Graauw *et al.*, 1997), and benzene (Bézard *et al.*, 2001b). Current photochemical modeling suggests that the creation and destruction of  $CH_3C_2H$  involves its allotrope, allene ( $CH_2CCH_2$ ), which has not been detected.

All these molecules are infrared active and contribute to the radiative balance of the stratosphere, thereby providing thermal feedback to the photochemistry. Because the Cassini observations will occur at a different season and level of solar activity than those by Voyager, they should provide constraints on the time constants of photochemical and dynamical transport processes. The best disk-resolved observations of Saturn in the thermal infrared are still those by Voyager IRIS. However, Saturn's stratosphere is sufficiently cold,  $<150$  K, that it was not possible to retrieve a meridional distribution of any hydrocarbon from the IRIS spectra. Figure 8 illustrates the mid-infrared spectrum of Saturn observed by CIRS at moderate spectral resolution in both the nadir- and limb-viewing geometries. The strong emission features seen from the hydrocarbons  $C_2H_2$ ,  $C_2H_6$ , and  $C_3H_8$  will be used to determine the spatial distributions for these gases. The nadir mode can quickly provide horizontal maps of column densities, but it will usually be necessary to make assumptions concerning the relative vertical profiles. Limb viewing affords much better vertical resolution. Figure 9 illustrates this and demonstrates that vertical profiles can be retrieved at pressure levels spanning 0.01 mbar to several tens of mbar. Figure 8 also shows the NESR for a single FP3 pixel for both viewing geometries (one scan, 10-s integration time). The limb-viewing panel (b) illustrates the  $1-\sigma$  noise error for an average of nine scans, and it shows that the SNR obtained is adequate to map these stronger species in 90 s. The use of individual pixels for the best vertical resolution is usually critical for limb observations, but nadir observations may be more amenable to pixel averaging, thereby degrading horizontal resolution to optimize the SNR. Figure 8a illustrates one possible strategy, namely averaging 5 pixels. The  $1-\sigma$  noise error is indicated for this spatial averaging and also for an average of 25 scans. The expected SNR is again very good.

The methyl radical ( $CH_3$ ) represents a key intermediate stage in the  $CH_4$  photochemistry. Formed by dissociation of  $CH_4$ , it ultimately recombines with itself in a three-body reaction to form  $C_2H_6$ . Its abundance is sensitive to the poorly known  $CH_3$  recombination rates and to the strength of vertical mixing near the  $CH_4$

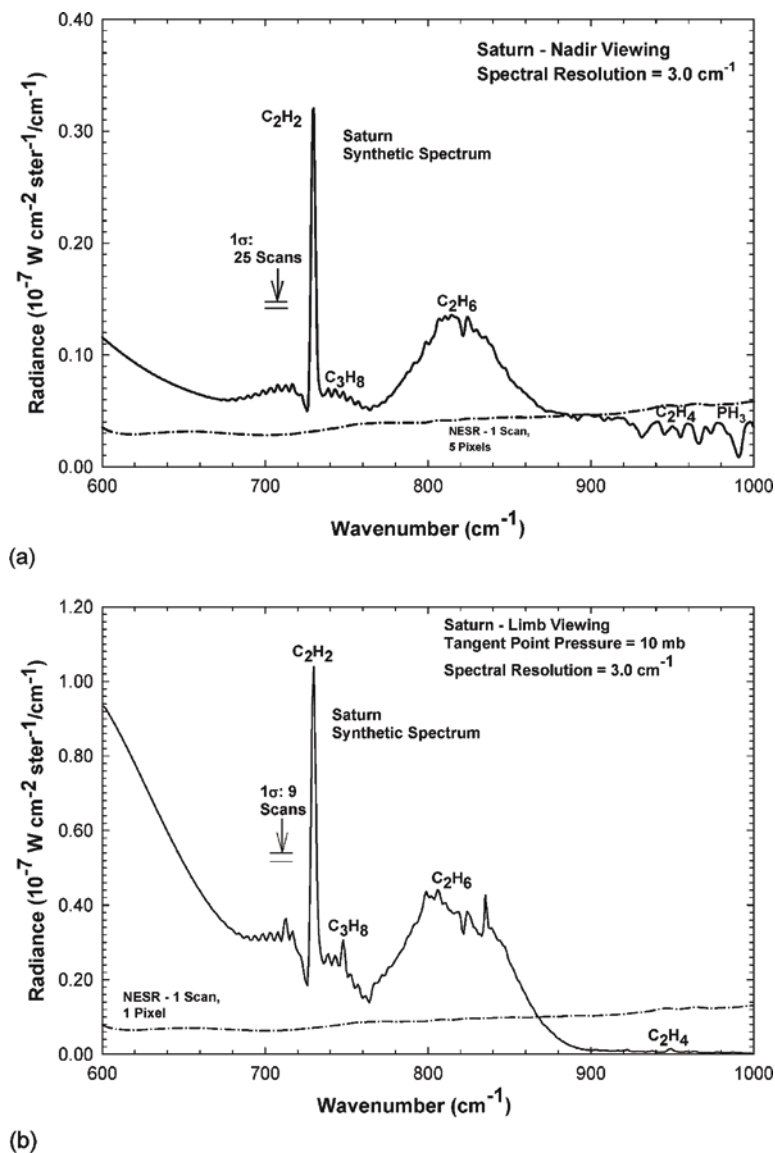


Figure 8. Synthetic mid-infrared spectrum in FP3 at an apodized resolution of  $3.0 \text{ cm}^{-1}$  for (a) nadir and (b) limb viewing of Saturn. Note the different vertical scales. The single-scan NESR for one pixel is indicated. The  $1\text{-}\sigma$  noise error is also shown for (a) an average of 5 pixels and 25 scans, and (b) a single pixel averaged over 9 scans.

homopause. ISO/SWS spectra of Saturn, with approximately disk-average resolution, led to the first detection of  $\text{CH}_3$  and a derived column abundance of  $1.5\text{--}7.5 \times 10^{13} \text{ molec. cm}^{-2}$  (Bézard *et al.*, 1998). The large uncertainty was primarily attributable to the 20% uncertainty in the flux calibration of the SWS spectra, not

only near the  $\text{CH}_3$  emission feature at  $16.5\ \mu\text{m}$ , but also in the fluxes in the  $\nu_4$  band of  $\text{CH}_4$  at  $7\ \mu\text{m}$ , which were used to constrain the temperature profile at the 0.15–5 mbar altitudes. Still, the ISO observations were enough to indicate that the  $\text{CH}_3$  recombination rates were either larger than those currently used in photochemical models, or else the vertical mixing near the homopause was much smaller than previously inferred from Voyager ultraviolet measurements (Bézard *et al.*, 1998). CIRS can improve on the ISO determination in three ways. First, because the optics and detectors are thermostatically controlled, the calibration accuracy is much higher (Section 5). Second, because of its closer proximity to Saturn,

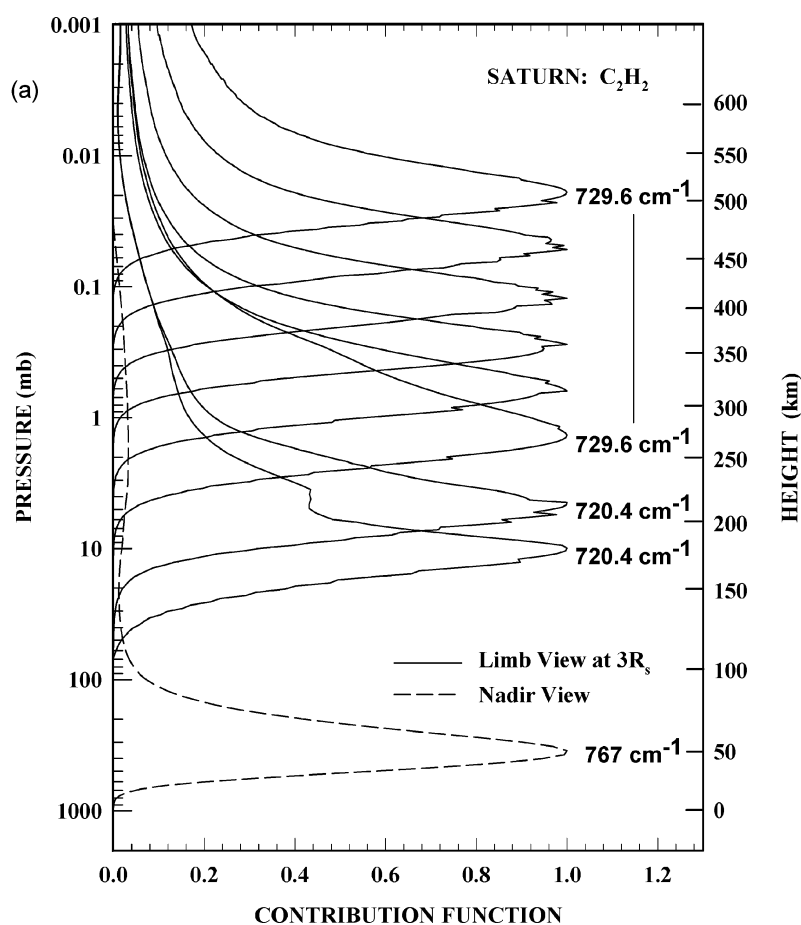


Figure 9. Hydrocarbon contribution functions for  $\text{C}_2\text{H}_2$  and  $\text{C}_2\text{H}_6$  for limb and nadir viewing of Saturn. The limb contribution functions have been convolved with a finite FOV whose full width projected onto the horizon equals one scale height. The opacity of tropospheric  $\text{H}_2$  accounts for the large peak in the normalized nadir contribution functions at several hundred millibars, but the smaller broad peaks above the 10-mbar level are attributable to the hydrocarbons.

(Continued on next page)

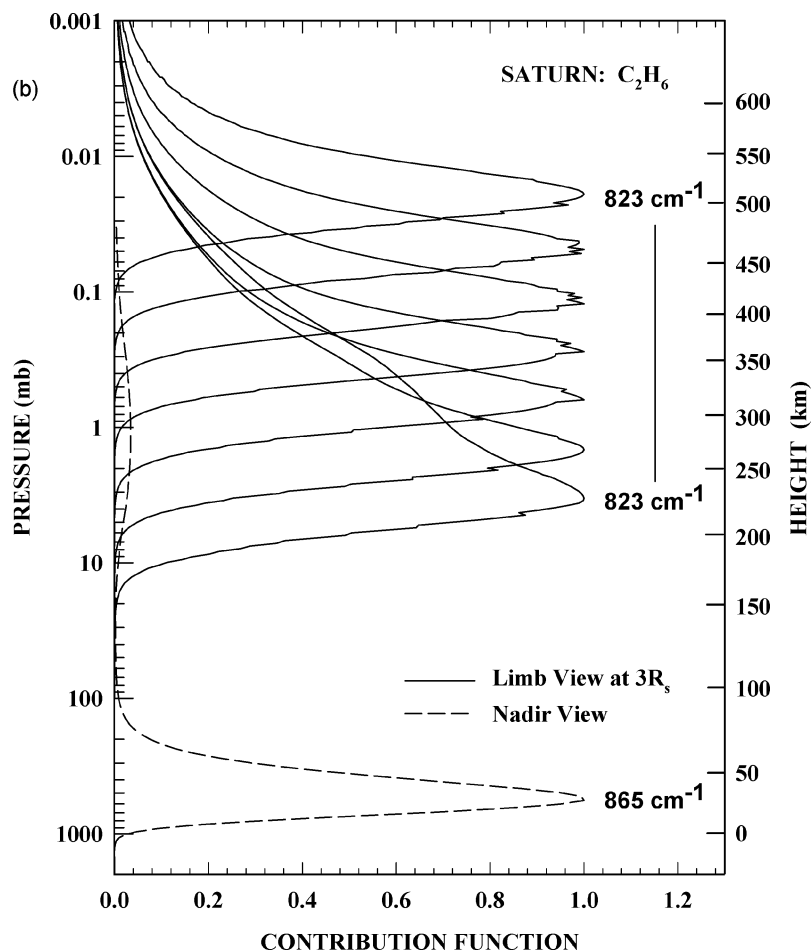


Figure 9. (Continued)

the horizontal spatial resolution is much higher, and heterogeneities in emission (e.g., isolating warmer regions) can be used to advantage for detection. This enabled CIRS to detect  $\text{CH}_3$  on Jupiter for the first time, within its auroral hot spots (Kunde *et al.*, 2004). Finally, near periapses, CIRS can actually observe Saturn in the limb mode, measuring radiances as high as the  $10\text{-}\mu\text{bar}$  level. This will be important in better constraining the temperature profile at high altitudes. Photochemical models suggest that the  $\text{CH}_3$  mole fraction is maximum near the  $\text{CH}_4$  homopause.

Coupling between  $\text{CH}_4$  and  $\text{PH}_3$  photochemistry could produce additional organics, mainly alkylphosphines and HCP, as suggested by laboratory experiments (Bossard *et al.*, 1986). These compounds have strong signatures in the mid-IR and could be detected by CIRS.



*External sources – oxygen compounds.* Although carbon monoxide in Saturn's atmosphere was discovered more than a decade ago (Noll *et al.*, 1986), its vertical distribution and origin are still unknown. Recently, the ISO/SWS detected H<sub>2</sub>O and CO<sub>2</sub> on Saturn (Feuchtgruber *et al.*, 1997). The H<sub>2</sub>O and CO<sub>2</sub> lines were seen in emission, indicating that the source of the emission was the stratosphere, where temperature increases with altitude. The inferred mixing ratio of H<sub>2</sub>O (Table III) is well above the saturation values near the tropopause, and this strongly suggests an external supply of oxygen in the form of H<sub>2</sub>O and perhaps O. The external source has not been unambiguously identified, as both interplanetary dust and material originating from the rings or satellites are plausible water-carriers. Determining the spatial distribution of H<sub>2</sub>O could discriminate among these possibilities. For example, while “interplanetary” water is expected to be horizontally uniform on the planetary disks, water from the rings should be locally enhanced at latitudes magnetically connected to the rings (Connerney and Waite, 1984). Indeed, FUV spectra recorded by HST at several latitudes suggest that H<sub>2</sub>O may not uniform over Saturn's disk, but be significantly enhanced at mid-southern latitudes (Fouchet *et al.*, 1996; Prangé *et al.*, 1999).

The CO<sub>2</sub> observed in Saturn's stratosphere could result from the infall of CO<sub>2</sub> ice contained in micrometeorite/ring/satellite material (Feuchtgruber *et al.*, 1997). Alternatively, secondary production from the reaction of CO and OH can serve as a source of CO<sub>2</sub>, where OH is produced from the photolysis of infalling H<sub>2</sub>O, and CO is at least partly deposited from external debris. Such a scheme has been proposed for Titan (see below). A recent detailed photochemical model (Moses *et al.*, 2000b) indicates that all these mechanisms could be at work. The derived mixing ratio of CO<sub>2</sub> is so small (Table III), that no condensation should occur at the tropopause and an interior source is theoretically possible. This would require rapid upward transport from the 1200 K level (Feuchtgruber *et al.*, 1997). In this case, the mixing ratio in the troposphere, as yet unmeasured, should be comparable to the stratospheric value. However, Lellouch *et al.* (2002) have estimated that an internal source accounts for only  $\sim 10^{-2} - 10^{-1}$  of the CO<sub>2</sub> observed on Jupiter.

Given the small fields of view and the viewing proximity afforded by the orbital tour, CIRS observations should determine the lateral variation of H<sub>2</sub>O and the vertical variation of CO<sub>2</sub>. The strongest H<sub>2</sub>O feature is the rotational line at 150.5 cm<sup>-1</sup>, in FP1 (see Figure 19, which illustrates this for Titan). Scaling disk-averaged ISO observations of H<sub>2</sub>O at 254 cm<sup>-1</sup>, it follows that 10 h of integration time should provide a SNR of 5. Several locations could be observed during the orbital tour. The vertical variation of CO<sub>2</sub> is best determined from limb observations at 667 cm<sup>-1</sup> with the FP3 arrays. Nadir observations would provide a column abundance. Again scaling the disk-average radiance observed by ISO, at this wavenumber, indicates that achieving a SNR = 5 requires 100 h of integration. This is fairly long, but it could be broken into shorter segments over a 4-year tour, and the spectra later averaged for analysis.

TABLE III  
Atmospheric composition of Saturn (mole fractions).

Gas	Chemical formula	Composition (mole fractions)
Helium	He	0.10–0.13 <sup>a</sup>
Methane	CH <sub>4</sub>	4.3(+2.3/–1.8) × 10 <sup>–3b</sup> (3.0 ± 0.6) × 10 <sup>–3c</sup> 4.5(+1.1/–2.1) × 10 <sup>–3d</sup>
Ammonia	NH <sub>3</sub>	~1 × 10 <sup>–4</sup> (3 bar) <sup>e</sup>
Hydrogen sulfide	H <sub>2</sub> S	Undetected
Phosphine	PH <sub>3</sub>	7(+3/–2) × 10 <sup>–6</sup> (p > 400 mbar) <sup>f</sup> ~ 4.2 × 10 <sup>–6</sup> (global, 3 bar); ~ 2.5 × 10 <sup>–6</sup> (global, 300 mbar) <sup>e</sup> ~ 7.4 × 10 <sup>–6</sup> (p > 630 mbar); ~ 4.3 × 10 <sup>–7</sup> (150 mbar) <sup>g</sup>
Arsine	AsH <sub>3</sub>	2.4(+1.4/–1.2) × 10 <sup>–9</sup> (3 bar) <sup>h</sup> (3 ± 1) × 10 <sup>–9</sup> (3 bar) <sup>f</sup>
Germane	GeH <sub>4</sub>	(4 ± 4) × 10 <sup>–10</sup> (3 bar) <sup>f</sup>
Methyl radical	CH <sub>3</sub>	4 (+2/–1.5) × 10 <sup>13</sup> molec cm <sup>–2</sup> (global, p ≤ 10 mbar) <sup>i</sup>
Ethane	C <sub>2</sub> H <sub>6</sub>	(3.0 ± 1.1) × 10 <sup>–6</sup> (N. hemisphere, p ≤ 20 mbar) <sup>b</sup> (9 ± 2.5) × 10 <sup>–6</sup> (global, 0.5 mbar) <sup>f</sup>
Acetylene	C <sub>2</sub> H <sub>2</sub>	(2.1 ± 1.4) × 10 <sup>–7</sup> (N. hemisphere, p ≤ 20 mbar) <sup>b</sup> 1.2(+0.9/–0.6) × 10 <sup>–6</sup> (global, 0.3 mbar) <sup>i</sup> (2.7 ± 0.8) × 10 <sup>–7</sup> (global, 1.4 mbar) <sup>i</sup>
Ethylene	C <sub>2</sub> H <sub>4</sub>	~ 3 × 10 <sup>15</sup> molec cm <sup>–2</sup> (non-auroral, p ≤ 10 mbar) <sup>j</sup>
Methylacetylene	CH <sub>3</sub> C <sub>2</sub> H	(1.1 ± 0.3) × 10 <sup>15</sup> molec cm <sup>–2</sup> (global, p ≤ 10 mbar) <sup>i</sup>
Propane	C <sub>3</sub> H <sub>8</sub>	detected <sup>k</sup>
Diacetylene	C <sub>4</sub> H <sub>2</sub>	(1.2 ± 0.3) × 10 <sup>14</sup> molec cm <sup>–2</sup> (global, p ≤ 10 mbar) <sup>i</sup>
Benzene	C <sub>6</sub> H <sub>6</sub>	4.7(+2.1/–1.1) × 10 <sup>13</sup> molec cm <sup>–2</sup> (global, p ≤ 10 mbar) <sup>l</sup>
Water	H <sub>2</sub> O	(1.4 ± 0.4) × 10 <sup>15</sup> molec cm <sup>–2</sup> (global, p ≤ 10 mbar) <sup>l</sup> ; ~ 2 × 10 <sup>–7</sup> (3–5 bar) <sup>e</sup> ; subsaturated at p < 3 bar <sup>e</sup>
Carbon monoxide	CO	(1 ± 0.3) × 10 <sup>–9</sup> (3 bar) <sup>f</sup>
Carbon dioxide	CO <sub>2</sub>	(6.3 ± 1) × 10 <sup>14</sup> molec cm <sup>–2</sup> (global, p ≤ 10 mbar) <sup>m</sup>

<sup>a</sup>Conrath and Gautier (2000).

<sup>b</sup>Courtin *et al.* (1984).

<sup>c</sup>Karkoschka and Tomasko (1992).

<sup>d</sup>Lellouch *et al.* (2001).

<sup>e</sup>de Graauw *et al.* (1997).

<sup>f</sup>Noll and Larson (1990).

<sup>g</sup>Orton *et al.* (2001).

<sup>h</sup>Bézard *et al.* (1989).

<sup>i</sup>Moses *et al.* (2000a).

<sup>j</sup>Bézard *et al.* (2001a).

<sup>k</sup>Greathouse *et al.* (2003).

<sup>l</sup>Bézard *et al.* (2001b).

<sup>m</sup>Moses *et al.* (2000b).

### 3.1.3. *Clouds and Aerosols*

Clouds on Saturn are expected to result from condensation of volatiles transported upward from deeper, warmer levels of the troposphere. Thus, a solid  $\text{NH}_3$  condensate cloud should form near or just above the 1-bar level (Tomasko *et al.*, 1984). Photochemical products, such as  $\text{C}_2\text{H}_2$ , form high in the atmosphere and can condense near the cold tropopause after being transported downward (Carlson *et al.*, 1988). Photochemistry and condensation may also produce solid  $\text{C}_4\text{H}_2$  or  $\text{P}_2\text{H}_4$  (West *et al.*, 1986). The characterization of the spatial distribution of cloud and haze material and their properties is an important task of the CIRS investigation for several reasons. First, clouds and aerosols affect the observed radiances within several spectral regions; accounting for their opacities accurately is often required for the retrieval of temperatures and gaseous abundances from CIRS and other remote sensing data. They also play an important role in the radiative heating and cooling of the atmosphere. An interesting goal will be to determine whether any intermediate-term (between seasonal and diurnal) changes in cloud properties take place in regions which are in or have recently undergone ring shadowing. Finally, the spatial distribution of clouds and aerosols is diagnostic of chemistry and dynamical transport.

CIRS spectra are most sensitive to particles greater than  $1\ \mu\text{m}$  in radius. The influence of tropospheric clouds will be detected in regions of weakest gaseous absorption. For the far infrared, a comparison of Voyager IRIS and radio occultation results (Conrath *et al.*, 1984, see Section 3.1.1), for example, suggested that the influence of tropospheric clouds was evident at frequencies less than about  $250\ \text{cm}^{-1}$ , ordinarily a spectral region sensitive to temperatures near 800 mbar. Since this is probably within the region of the atmosphere dominated by small-scale thermally driven convection, variations of brightness below  $250\ \text{cm}^{-1}$  are probably indicative of cloud variability, rather than major changes in the temperature lapse rate (Section 3.1.4). The size of particles can be determined in this spectral range by inspecting the spectral extent of the cloud influence. Consider, for example, two clouds with equal opacity at  $200\ \text{cm}^{-1}$ , one cloud composed of  $1\text{-}\mu\text{m}$  particles, and a second cloud with  $100\text{-}\mu\text{m}$  particles. While the first cloud may not influence the spectrum at wavenumbers less than  $130\ \text{cm}^{-1}$ , the  $100\text{-}\mu\text{m}$  cloud affects the spectrum out to  $80\ \text{cm}^{-1}$ . The distribution of these particles with altitude can be determined using observations at different emission angles. For instance, at a distance of 4 Saturn radii, spectra obtained with the emission angle as large as  $78^\circ$  at the center of the 4-mrad FP1 FOV will allow us to probe 1.6 pressure scale heights above emission detected from nadir observations. For such spectra, the airmass does not vary by more than 40% over the FOV, which is acceptable. Determination of the height dependence is particularly important to regions, such as the equator, where evidence for high cloud tops (Tomasko *et al.*, 1984) requires attention to distinguishing carefully between temperature and cloud variability above the 600-mbar level, where temperature sounding is generally considered “safe” from cloud influences.

Observations with  $15.5\text{-cm}^{-1}$  resolution are acceptable for wavenumbers at or greater than  $120\text{ cm}^{-1}$  and  $3\text{-cm}^{-1}$  resolution for wavenumbers less than  $120\text{ cm}^{-1}$  in order to avoid confusion by significant absorption features of  $\text{NH}_3$  or  $\text{PH}_3$ . Figure 5 shows that there is easily sufficient signal to accommodate these observations in rather short time intervals.

CIRS spectra can also be used to probe particulate opacity in the mid-infrared, for instance, near  $897\text{ cm}^{-1}$  (between  $\text{C}_2\text{H}_6$  emission and  $\text{PH}_3$  absorption, cf. Figure 3), near  $1100$  or  $1180\text{ cm}^{-1}$  (a region of  $\text{PH}_3$  and  $\text{CH}_4/\text{CH}_3\text{D}$  absorption), and near  $1392\text{ cm}^{-1}$  (where  $\text{CH}_4$  and  $\text{H}_2$  are the only gaseous absorbers). Information from these regions would provide an additional discriminator of particle size, allowing broader size distributions or multiple size distributions to be diagnosed. By virtue of the smaller FP3 and FP4 pixel sizes, it would facilitate cloud mapping at high spatial resolution, during nadir stratospheric temperature sounding maps, for example. It would permit cloud parameters to be determined with sufficient independence to separate the influences of clouds from temperature structure in the far infrared, allowing temperature sounding deeper than the 600-mbar level.

Limb spectra taken for stratospheric temperature sounding can be examined for evidence of emission from condensates and aerosols, which often have slowly varying absorption spectra. We would ordinarily expect stratospheric particles to be sub-micron in size and have little influence on the spectrum, but the exponential dependence of the Planck function for the warm stratosphere in FP3 and FP4 provides an increased sensitivity to slowly varying “continuum” absorption at low optical thickness. Difficulty in reconciling simultaneous Voyager IRIS and radio occultation results for latitude  $30^\circ\text{S}$  (Conrath *et al.*, 1984) could be explained by an emitting aerosol in the warm stratosphere (Section 3.1.1). Because the background is deep space, limb spectra would unambiguously probe the presence of such an aerosol.

#### 3.1.4. Atmospheric Structure and Circulation

*Temperatures and zonal winds.* Meteorological studies of Saturn have been limited, because winds and temperatures have for the most part only been measured at and above the visible cloud tops. Wind velocities have been retrieved from tracking discrete cloud features wherever they appeared. The most detailed results have been from Voyager (Smith *et al.*, 1981, 1982) and Hubble Space Telescope imaging observations (Barnet *et al.*, 1992; Sánchez-Lavega *et al.*, 2003). These indicate a pattern of zonal (i.e., east-west) currents roughly symmetric about the equator. In addition, there are several vortices and wave-like features.

Remote-sensing thermal-infrared and radio-occultation data have provided the means to retrieve temperatures in the upper troposphere and stratosphere of Saturn, mostly above the clouds. The flyby of Pioneer 11 in 1979 provided the first radio occultation that allowed retrieval of a temperature profile in the tropopause region and stratosphere, from  $\sim 200$  mbar to 2 mbar (Kliore *et al.*, 1980). The two Voyager flybys in 1980 and 1981 yielded two additional radio occultations (each with a

recorded ingress and egress), which obtained temperatures from 1 mbar to as deep as the 1.3-bar level, where the signal was extinguished by  $\text{NH}_3$  absorption (Lindal *et al.*, 1984). Infrared sounding has provided more extended spatial coverage, albeit with less vertical resolution, typically no better than 1 scale height. Ingersoll *et al.* (1984) summarize the earliest ground-based infrared studies, which had low spatial resolution. The Pioneer 11 infrared radiometer had two broad spectral bands at 20 and 45  $\mu\text{m}$ , which provided information on upper-tropospheric temperatures at low latitudes (Orton and Ingersoll, 1980; Ingersoll *et al.*, 1980). More extensive mapping of Saturn's atmospheric temperatures was provided by infrared spectra measured by IRIS on the Voyager spacecraft. IRIS usually observed in the nadir-viewing mode (Figure 2), and it had a spectral range from 200 to 2500  $\text{cm}^{-1}$  (50 to 4  $\mu\text{m}$ ) and a uniform spectral resolution of 4.3  $\text{cm}^{-1}$ . Figure 10 illustrates typical vertical profiles of temperature retrieved from IRIS spectra. The radiances between 200 and 700  $\text{cm}^{-1}$  lie within the S(0) and S(1) pressure-induced hydrogen rotation lines and part of the hydrogen translational continuum (Figure 3), and allow retrieval of temperatures in the troposphere and tropopause region between the 80 and 700 mbar levels. This is illustrated by the inversion kernels in the left panel of Figure 4. The radiances in the  $\nu_4$  band of  $\text{CH}_4$  (1200–1400  $\text{cm}^{-1}$ ) permit retrieval of temperatures in the upper stratosphere near the 1-mbar level. The spectra contain little information between 10 and 80 mbar, so the profiles within this region are more or less an interpolation between the bounding regions. The shape of the

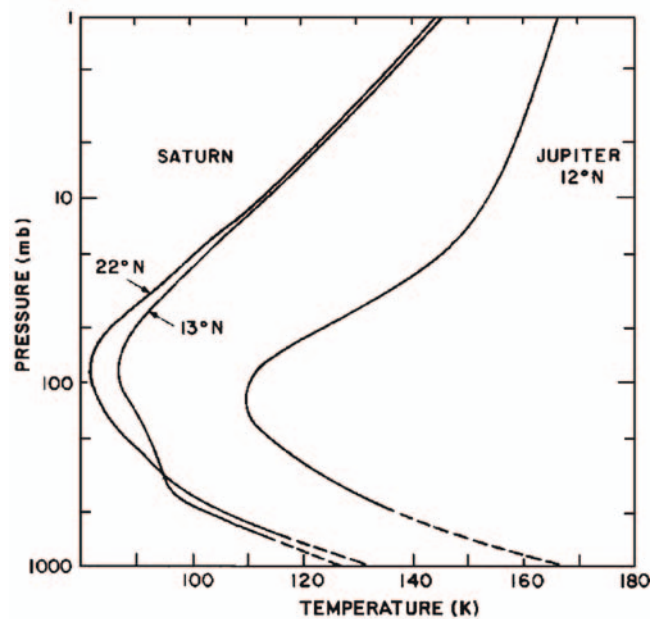


Figure 10. Vertical profiles of temperature for Saturn retrieved from Voyager IRIS observations, compared with Jupiter (Hanel *et al.*, 1980).

22°N profile in Figure 10 is typical of mid northern latitudes during the Voyager encounters. It exhibits a well-defined troposphere (where temperature decreases with altitude) below the 100-mbar level, overlain by a well-defined stratosphere (where temperature increases with altitude), which is similar to the thermal structure seen in Jupiter's atmosphere. The shape of the 13°N profile, on the other hand, typifies low latitudes and much of the southern hemisphere. It exhibits a distinct "knee" in the tropopause region. The cause of this shape difference has never been satisfactorily explained.

IRIS spectra also allowed mapping of temperatures with latitude, at least in the troposphere and tropopause region. Figure 11 illustrates temperatures at three pressure levels. At the deepest level shown, 730 mbar, temperature exhibits little structure with latitude, except for a 4 K warm anomaly at mid northern latitudes, discussed earlier. With increasing altitude, the meridional variation in temperature exhibited a progressively more pronounced north-south asymmetry and a smaller-scale structure that is correlated with the meridional variation of zonal winds that have been inferred from tracking discrete cloud features (Smith *et al.*, 1981). The hemispheric asymmetry is probably a consequence of the radiative-thermal inertia of the upper troposphere and lower stratosphere. At 730 mbar, the relaxation time is long compared to a season, and little seasonal variation is expected. The

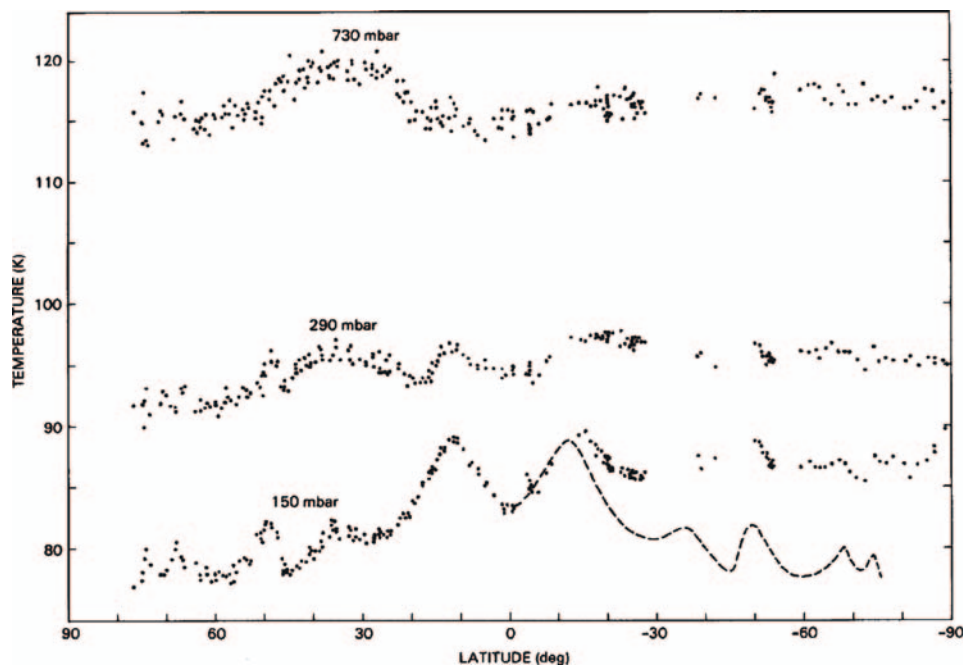


Figure 11. Saturn atmospheric temperatures at three pressure levels as function of latitude, derived from Voyager IRIS observations. The dashed curve in the southern hemisphere at the 150-mbar level is a reflection about the equator of the northern-hemisphere temperatures (Conrath and Pirraglia, 1983).



radiative relaxation time is  $2 \times 10^8$  s near 150 mbar, comparable to the seasonal time scale; the thermal response there is expected to lag that in radiative equilibrium with the current solar forcing (Conrath and Pirraglia, 1983; Bézard *et al.*, 1984). The Voyagers flew by Saturn shortly after Saturn's northern spring equinox, so the southern hemisphere should be warmer, which is what is observed. Two decades of ground-based observations of Saturn's stratosphere at  $7.7 \mu\text{m}$  ( $1300 \text{ cm}^{-1}$ ) have also displayed a seasonal lag of this magnitude (Orton *et al.*, 1989, 2003).

The wind and temperature fields in planetary atmospheres are dynamically coupled. In rotating systems, this gives rise to a diagnostic relation, the thermal wind equation, that relates horizontal temperature gradients to vertical shears in horizontal winds. For example, meridional gradients in temperature and zonal winds are related by (Holton, 1979):

$$\frac{\partial}{\partial \ln p} \left[ u \left( 2\Omega \sin \Lambda + u \frac{\tan \Lambda}{r} \right) \right] = \frac{R}{r} \left( \frac{\partial T / \mu}{\partial \Lambda} \right)_p \approx \frac{R}{r \mu} \left( \frac{\partial T}{\partial \Lambda} \right)_p, \quad (1)$$

where  $p$  is pressure,  $\Lambda$  is latitude,  $r$  is radius,  $R$  the universal gas constant,  $\mu$  is the molecular mass of Saturn's atmosphere,  $\Omega = 1.66 \times 10^{-4}$  s is the rotation rate of Saturn's interior, assumed identical to the Saturn Kilometric Radiation rotation rate (Desch and Kaiser, 1981),  $T$  is temperature, and  $u$  is the zonal wind velocity. The thermal wind equation permits the largely two-dimensional wind field derived from cloud-tracked studies to be extended to higher altitudes. From (1), the smaller-scale undulations in the 150-mbar temperatures in Figure 11 imply a slow decay of the zonal winds with altitude, with a vertical decay scale  $\sim 5$  pressure scale heights. Curiously, the decay in Saturn's stratosphere is toward a state of uniform angular velocity that is eastward with respect to the interior rotation (Conrath and Pirraglia, 1983). The retrieved tropopause temperatures for all the giant planets imply a decay of the zonal currents, at least in the tropopause region. Application of a simple axially symmetric linear model, parameterized with Newtonian cooling and Rayleigh friction, indicates that the zonal winds in this region can be interpreted as the response of frictional and radiative damping to a zonal wind system that is forced at deeper levels. The mechanism providing the vertical decay is not known. In the earth's middle atmosphere, momentum flux divergences associated with the decay of vertically propagating waves are known to be an important mechanism for damping zonal jets (see, e.g., Andrews *et al.*, 1987). Alternatively, Orsolini and Leovy (1989, 1993a,b) and Pirraglia (1989) have interpreted the vertical decay of the jets as a natural consequence when a deep zonal flow in the quasi-adiabatic atmosphere extends upward to the more stably stratified upper troposphere and stratosphere. Instabilities in the wind field generate eddy fluxes that stabilize the zonal winds by acting as a drag force, establishing a vertical decay in the flow profile.

Detailed mapping of the temperatures and winds of the stratospheres of the giant planets has been limited or nonexistent. Ground-based observations, using the  $\nu_4$ -band of  $\text{CH}_4$ , have not achieved good vertical resolution in the stratospheres, primarily because of telluric absorption. Voyager IRIS did not have this problem and had adequate spectral resolution to resolve vertical structure in the stratosphere better, but it lacked the sensitivity in the mid-infrared needed for global mapping. CIRS has both the requisite sensitivity and vertical resolution. The Cassini swingby of Jupiter in December 2000 has shown the complexity in the temperature and zonal-wind fields of that planet's stratosphere. The zonal winds derived from the retrieved temperatures do not exhibit the monotonic decay with altitude that characterizes the tropopause region. Indeed, the zonal wind field exhibits a strong equatorial jet centered in the upper stratosphere at 4 mbar (Flasar *et al.*, 2004), which may be driven by the stresses associated with vertically propagating waves (see below).

At Saturn, CIRS gains two additional advantages. First, the orbital geometry afforded by the Cassini tour will allow a more complete thermal spatial mapping of Saturn's atmosphere than previous spacecraft and ground-based observatories could provide. Second, at Saturn, CIRS can also acquire mid-infrared spectra on the limb, at least near periapsis, where the typical range is 3–6  $R_S$ , and the FP3 and FP4 pixel resolution is 1–2 scale heights. (CIRS spectra of Jupiter were largely limited to nadir-viewing observations, because of the 138  $R_J$  swingby distance.) The inversion kernels in the right panel of Figure 4 indicate that limb spectra not only fill in the gap between 10 and 80 mbar left by nadir spectra, but can also extend the range of altitudes up to the 0.01-mbar level. Appendix A discusses the retrieval of atmospheric temperatures from CIRS spectra in more detail.

*Meridional circulations.* Perhaps the best-known meridional circulation is the terrestrial Hadley circulation, in which high-altitude velocities are poleward, and near-surface velocities equatorward (see, e.g., Lorenz, 1967). This is an example of a thermally direct circulation: warm air near the equator rises, and colder air at mid-latitudes sinks. While one may think that radiative heating and cooling are the drivers of the Hadley circulation, even in this simple case friction is necessary to achieve a steady, balanced flow (see, e.g., Held and Hou, 1980). The tendency of air parcels to conserve axial angular momentum and spin up or down, depending on whether they move poleward or equatorward, is balanced by frictional coupling to the surface. More generally, terrestrial meteorological studies have indicated that zonal-mean meridional circulations are not always thermally direct, and the zonal momentum and heat deposition associated with eddies and propagating waves are important in driving these circulations. However, for zonal-mean flows in thermal wind balance (Equation (1)), the forced meridional circulations tend to cancel the heat and momentum transports by the eddies/waves themselves. In the limit in which the eddies/waves are conservative – not internally forced by some instability, not subject to dissipation or radiative damping – and steady, the cancellation is complete and the net effect of eddy/wave forcing on the zonal-mean flow is zero (Charney and Drazin, 1961; Eliassen and Palm, 1961; Andrews *et al.*, 1987). In

general, this limiting state is not fully realized. Nonetheless, it is the residual mean meridional circulation – the circulation with the eddy/wave fluxes of heat and momentum subtracted out – that is relevant for studies of the general circulation, because it, and not the zonal-mean Eulerian circulation, contains the relevant heat and momentum transports. Dunkerton (1978) has shown that the residual mean meridional circulation in the terrestrial stratosphere and mesosphere approximately corresponds to the Lagrangian circulation, which describes constituent transport.

The terrestrial studies are based on very general concepts, and they should be applicable to the atmospheres of the giant planets, perhaps not so much in the deep tropospheres where convection and dissipation are important, but certainly at higher altitudes, near the tropopause and in the stratospheres and mesospheres. CIRS spectra are well suited for probing the residual mean meridional circulations on Saturn in several ways:

1. *Gaseous and particulate tracers.* CIRS will acquire maps of several gaseous constituents with good vertical resolution. The discussion in Section 3.1.2 noted that the departure of the  $\text{H}_2$  para fraction from the local thermodynamic equilibrium value is a good indicator of vertical Lagrangian velocities. The retrieved para fractions from Voyager IRIS spectra of Jupiter implied a simple global-scale circulation in the tropopause region, with upwelling at low latitudes and subsidence at high latitudes in both hemispheres (Conrath and Gierasch, 1984). The IRIS spectra implied planetary-scale spatial structure in the para fraction on Saturn, and CIRS will provide more detailed mapping with higher sensitivity.

Gaseous  $\text{NH}_3$  is another good tracer of motions, because it condenses and is not uniformly distributed. Zonal mean abundances at the  $\sim 700$ -mbar level, retrieved from IRIS spectra of Jupiter in the far infrared at  $216\text{ cm}^{-1}$  (Gierasch *et al.*, 1986), showed a variation with latitude that was anti-correlated with temperatures, i.e., higher abundances occurred where the zonal-mean temperatures in the upper stratosphere were colder, an indicator of upwelling (see below). Using the more sensitive CIRS data in the mid-infrared near  $1000\text{ cm}^{-1}$ , from the Jupiter swingby, Achterberg *et al.* (2003) also concluded that enhanced zonally averaged  $\text{NH}_3$  abundances were correlated with colder temperatures. IRIS Saturn spectra did not have an adequate SNR to permit  $\text{NH}_3$  retrievals, but as noted earlier, this is not a problem for CIRS, which will obtain retrievals both in the mid- and far-infrared.  $\text{PH}_3$  is also a good tracer, as noted earlier.

Stratospheric hydrocarbons should provide a rich mix of motion indicators. Here the physics depends largely on the magnitude of the photochemical time constants relative to dynamical time scales. When the latter are smaller, lateral transports are efficient and constituent mole fractions should be laterally uniform. When the former are smaller, constituent abundances should be governed by photochemical processes and exhibit strong latitude variations. Consider  $\text{C}_2\text{H}_6$  and  $\text{C}_2\text{H}_2$ . The loss time constants for photochemical destruction are  $\sim 50$  years and 1 year, respectively, near 10 mbar. Estimates of the dynamical turnover times for

the upper troposphere on Jupiter and Saturn, based on the temperature and para-hydrogen fields (see below), are 70 years and 200 years, respectively (Conrath *et al.*, 1998). They may be smaller at higher altitudes in the stratosphere. Retrieved column abundances from CIRS nadir-viewing spectra of Jupiter indicate a meridional variation of stratospheric  $C_2H_6$  that is relatively flat, whereas the abundance of  $C_2H_2$  decreases from the equator toward both poles (Nixon *et al.*, 2004). The latter variation makes sense, given the relatively short photochemical time constant of  $C_2H_2$ . The flat distribution of  $C_2H_6$  suggests that stratospheric mixing is strong enough that the turnover time is less than the photochemical time scale. The trend for more sluggish motions and longer turnover times on Saturn (Conrath *et al.*, 1998) suggests that  $C_2H_6$  may exhibit stronger meridional variations there. CIRS will be able to determine this.

Condensates can be good indicators of vertical motions. Gierasch *et al.* (1986), analyzing Voyager IRIS data of Jupiter, found evidence of two cloud components. One of the components had optical depths that correlated well with the gaseous  $NH_3$  abundance. The optical depths were also largest where temperatures in the upper troposphere were colder, indicating upward motions (see below). The subsequent spreading of aerosols after the Comet Shoemaker-Levy 9 impacts in Jupiter's southern hemisphere has been used to infer the magnitude of meridional transport in Jupiter's lower stratosphere (Friedson *et al.*, 1999). Although the SL-9 impact provided an unusual injection of aerosols within a narrow latitude band, convective storms have been known to erupt and spread at low latitudes on Saturn Beebe *et al.*, 1992; Barnet *et al.*, 1992). The sensitivity of CIRS spectra to aerosols and condensates should complement their sensitivity to temperatures and help determine the circulations associated with these phenomena.

2. *Temperature and aerosol distribution.* In terms of the mean residual meridional circulation, the heat equation is (Dunkerton, 1978, Andrews *et al.*, 1987):

$$\frac{\partial T}{\partial t} + \left( \frac{dT_0}{dz} + \frac{RT_0}{C_p H} \right) w = \frac{J}{C_p} \approx \frac{T_e - T}{\tau_r} \quad (2)$$

where  $R$  and  $T$  have been defined for Equation (1),  $z$  is a vertical coordinate,  $C_p$  is the specific heat at constant pressure,  $H$  is a mean scale height,  $T_0(z)$  is the horizontally averaged temperature profile,  $w$  is the vertical velocity, and  $J$  is the net radiative heating and cooling rate. The right-most term is a simplified parameterization of the radiative term in terms of a radiative equilibrium temperature  $T_e$  and relaxation time,  $\tau_r$ . Equation (2) does not include the effects of heating associated with the lagged conversion between ortho- and para- $H_2$ . These can be included (Conrath *et al.*, 1998), but they are less important in the stratosphere than in the upper troposphere, where temperatures are colder and the energy release larger. Equation (2) indicates that detailed measurements of the temperature field can serve as a good diagnostic of vertical motions. The mean temperature profile,  $T_0$ , is well known, and estimates can be made of the radiative heating/cooling. These can be simple parameterizations in terms of  $\tau_r$ ,

which can be readily calculated if the infrared absorbers are known (Gierasch and Goody, 1969; Conrath *et al.*, 1998), or more detailed calculations can be made, using detailed radiative-transfer calculations and measurements of aerosol heating and cooling at infrared, visible, and ultraviolet wavelengths.

Often the heat Equation (2) takes a particularly simple form. For instance if one studies the latitude variation in temperature at the tropopause on the scale of the zonal winds, one can assume  $\partial/\partial t = 0$  to first order, since the winds are usually fairly steady. Then the balance in (2) is between the vertical advection term – representing adiabatic heating and cooling associated with vertical motions – and the radiative term on the left hand side. Near the tropopause,  $T_e$  is primarily due to infrared heating and cooling. Since temperatures in the upper troposphere are nearly uniform with latitude, as discussed earlier, the variation of  $T_e$  with latitude is small. Hence, vertical velocities tend to track temperature variations: colder temperatures indicate upwelling, warmer temperatures indicate subsidence (Conrath and Pirraglia, 1983). Saturn’s stratosphere has a hemispheric seasonal variation in temperature. If one wishes to analyze circulations on this temporal and spatial scale, then the  $\partial T/\partial t$  would be retained in (2).

### 3. Potential vorticity (Ertel potential vorticity),

$$q \approx -g(2\Omega \sin \Lambda + \hat{\mathbf{z}} \cdot \nabla \times \mathbf{u}) \frac{\partial \theta}{\partial p} \quad (3)$$

is conserved for single-component fluids when forcing and dissipation are relatively weak. The quantity  $\theta$  is the potential temperature:  $\theta = \text{constant} \times T p^{-\frac{\kappa}{c_p}}$ ,  $g$  is the magnitude of the gravitational acceleration, and  $\mathbf{u}$  is the (two-dimensional) horizontal velocity. In hydrogen atmospheres, the presence of ortho- and para- forms with lagged conversion means that there is a two-component fluid, varying spatially, and hence  $q$  is not strictly conserved (Gierasch *et al.*, 2003). This conservation-breaking is probably less important in Saturn’s upper stratosphere. The attractive feature of (3) is that  $q$  can be computed solely from the temperature field, provided  $\mathbf{u}$  is known at some reference level. In terrestrial studies, the potential vorticity has proven to be a very useful tracer of atmospheric motions and dynamical processes. An example is the interaction of air masses within the circumpolar vortices with those at low latitudes (Hoskins *et al.*, 1985; Andrews *et al.*, 1987). The polar vortices are marked by sharp gradients in  $q$  across their boundaries, and the distortion of the contours of constant  $q$  from quasi-circles about the pole can indicate stirring and ultimately irreversible mixing of low- and high-latitude air masses. Such vortices can be expected on the giant planets. Ground-based infrared observations have identified a cold region in Jupiter’s arctic region that is likely associated with a strong circumpolar vortex (Orton *et al.*, 2002). Similarly on Saturn, one may anticipate nearly discontinuous changes in  $q$  across analogous features, including the ribbon feature

and the polar hexagon mentioned below, and the detailed morphology of  $q$  may be indicative of fluid material transport across these features.

*Waves, eddies, and compact vortices.* Voyager images of Saturn at visible wavelengths provided several examples of large-scale wave motion at mid and high latitudes, including the so-called ‘ribbon wave’ at around  $40^\circ\text{N}$  (Smith *et al.*, 1982; Sromovsky *et al.*, 1983) and the ‘polar hexagon’ at around  $70^\circ\text{N}$  (Godfrey, 1988, 1990). These wave-like flows appear to be unique to Saturn, and may represent a form of zonally propagating Rossby wave in a “waveguide” produced by the zonal mean flow itself. From sequences of Voyager images, Sromovsky *et al.* (1983) showed that the “ribbon wave” feature appeared to satisfy a dispersion relation that was roughly compatible with that expected for Rossby waves. Observations of the “polar hexagon” from Voyager were limited to a single set of images, revealing a remarkably symmetric pattern centered on a westerly jet at  $\sim 70^\circ\text{N}$  with near-perfect six-fold symmetry about Saturn’s rotation axis. The hexagon appears to be associated with an adjacent compact, anticyclonic oval just south of it (Godfrey, 1988, 1990; Allison *et al.*, 1990), and both have persisted and appear in later Hubble Space Telescope and ground-based observations (Caldwell *et al.*, 1993; Sánchez-Lavega, 1993). Some support for this linkage comes from recent Hubble observations of Saturn’s south polar region, which show neither a hexagon nor an anticyclonic oval, although there is a moderately strong circumpolar jet (Sánchez-Lavega *et al.*, 2002). However, much remains unclear about the origin and vertical structure of the ribbon and hexagonal waves.

The evidence for Rossby waves in Saturn’s atmosphere was reinforced by the detection of wave structure in the temperature field by Achterberg and Flasar (1996). They identified a planetary wavenumber-2 (i.e., two wavelengths around a latitude circle) feature in upper-tropospheric temperatures retrieved from Voyager IRIS spectra. The feature extended from  $40^\circ\text{N}$  to equatorial latitudes with nearly constant zonal phase. Achterberg and Flasar determined that the feature was quasi-stationary with respect to Saturn’s interior rotation, and they concluded the wave properties were most consistent with Rossby-wave propagation. They suggested that the wave might be a meridionally trapped wave forced by a “critical-layer instability” at midlatitudes, where the (zero) zonal phase velocity of the wave matches the null in the latitude profile of the zonal wind.

A problem that has existed for previous studies is the absence of planetary data sets with adequate horizontal and vertical coverage. CIRS is well equipped to provide this in a 4-year mapping mission, with its vertical coverage from both limb- and nadir-sounding. This is important, as waves are more easily identified when both horizontal and vertical wavelengths can be determined, as well as the horizontal tilts of the constant phase surfaces with altitude. These, together with phase velocities determined from time-lapsed observations, provide a probe of the propagation characteristics of the waves. It is logical to search for waves in the temperature field, but wave structure in gaseous constituent and aerosol distributions should also provide important diagnostics.



Although wave activity on Saturn is not yet adequately characterized, the momentum transports associated with such waves are likely to be important in maintaining the zonal winds. One candidate is the strong prograde equatorial jet that has been observed in Voyager images. The jet is approximately four times the width and strength of the analogous feature on Jupiter, and its strongly prograde motion implies a considerable excess of axial angular momentum. Winds derived from HST images obtained a few weeks after the onset of the major 1990 equatorial disturbance on Saturn indicated changes in the zonal mean winds and an enhancement in the zonal variance of the winds within the jet from those in the Voyager epoch (Barnet *et al.*, 1992). Similar images from 1996–2002 indicate that Saturn's equatorial jet has decreased to  $\sim 200 \text{ m s}^{-1}$ , one half its earlier value (Sanchez-Lavega *et al.*, 2003). An interesting question is whether this variability (and the onset of the 1990 “storm”) could have resulted from changes in the interaction of the equatorial jet with upward-propagating equatorial planetary waves. This is an important source of cyclic variability in the Earth's stratosphere (the Quasi-Biennial Oscillation or QBO, e.g., Andrews *et al.*, 1987), where such oscillations have a characteristic signature in both the thermal structure of both the waves and zonal mean flow in the stratosphere. An analogous temporal oscillation in Jupiter's stratosphere has been reported (Orton *et al.*, 1991; Leovy *et al.*, 1991), with a period of around 4 years. As noted earlier, CIRS mapping during the Cassini swingby of Jupiter showed a high-speed equatorial jet centered in the upper stratosphere (Flasar *et al.*, 2004). Both the temporal oscillation and the spatial structure of the equatorial stratospheric zonal winds on Jupiter may be an atmospheric response to wave forcing. Temperatures retrieved from CIRS spectra will allow a systematic search for similar structure in Saturn's equatorial stratosphere.

Another important large-scale dynamical phenomenon observed in Saturn's atmosphere is the occurrence of long-lived, predominantly anticyclonic compact oval vortices. Such features were found at mid-latitudes on Saturn in Voyager images (Smith *et al.*, 1981, 1982), and appear to be the counterparts on Saturn of major long-lived vortices on Jupiter, such as the Great Red Spot and the White Ovals. On Jupiter, temperature measurements exhibited cold tropopauses over these features, indicating upwelling within the cores and subsidence in the surrounding environment (see, e.g., Flasar *et al.*, 1981b; Conrath *et al.*, 1981). Voyager, on the other hand, obtained little information on the thermal and vertical structure of Saturn's compact vortices. The possibility of obtaining near-simultaneous maps of temperatures and (from cloud-tracking) winds, allowing the computation of potential vorticity and maps of the concentrations of minor trace constituents in the vicinity of these features would provide information on the weak cross-isentropic Lagrangian circulation within these vortices. The latter could indicate the role and character of thermodynamic interactions with the buoyancy field within these vortices, and hence provide valuable insight into their origin and stability.

### 3.2. TITAN

Titan is Saturn's largest satellite. At 2575 km, its radius is nearly half Earth's. Since Comas Solá (1908) observed limb-darkening on Titan's disk, its atmosphere has attracted the interest of astronomers. CH<sub>4</sub> was the first constituent identified (Kuiper, 1944), from detection of its near-infrared bands. Further progress in characterizing Titan's atmosphere remained in abeyance for nearly 30 years, until ground-based narrow-band radiometric observations, and later high-precision spectrophotometric observations, began and identified several other hydrocarbons – ethane (C<sub>2</sub>H<sub>6</sub>), monodeuterated methane (CH<sub>3</sub>D), ethylene (C<sub>2</sub>H<sub>4</sub>), and acetylene (C<sub>2</sub>H<sub>2</sub>) – from their emission features in the thermal infrared (Gillett *et al.*, 1973; Low and Rieke, 1974; Gillett, 1975; Tokunaga, 1980). A leap in the characterization of Titan's atmosphere occurred when the Voyager spacecraft flew through the Saturn system in 1980 and 1981. Molecular nitrogen (N<sub>2</sub>) was determined to be the dominant atmospheric constituent, with CH<sub>4</sub> in second place at the few-percent level (Broadfoot *et al.*, 1981; Hanel *et al.*, 1981; Tyler *et al.*, 1981). IRIS also detected numerous organics in its range of sensitivity, below 300 km, expanding the list of hydrocarbons previously identified and adding several nitriles (Table IV). Titan thus has a mid-reducing atmosphere that resembles Earth's primordial atmosphere in several respects (Clarke and Ferris, 1997), albeit much colder. Being rich in organics – nitriles and hydrocarbons – it forms a natural laboratory to study prebiotic chemistry (Hunten *et al.*, 1984; Raulin and Owen, 2003).

Voyager provided the spatial resolution to characterize Titan's meteorology for the first time. It is a mix of that on Venus and Earth. Like Venus, Titan is a slow rotator, and it has a global cyclostrophic zonal wind system, with stratospheric winds corresponding to an angular velocity  $\sim 10$  times the surface rotation rate. However, its effective obliquity of 26° is much larger than Venus' and comparable to Earth's. Its stratospheric temperatures and winds should have large seasonal variations (Flasar *et al.*, 1981a; Flasar, 1998b). Titan also has a strong circumpolar vortex in the stratosphere, with condensed nitriles and enhanced hazes in the polar region. It may thus have an interaction of chemistry, condensation microphysics, and dynamical transport that is as complex as that in the terrestrial ozone hole in the Antarctic (Flasar, 1998a; Samuelson and Mayo, 1997). Finally, Titan likely has a "hydrological" cycle with cumulus convection, but involving CH<sub>4</sub>, not H<sub>2</sub>O (Awal and Lunine, 1994). There may be reservoirs of liquefied natural gas to drive the cycle, if not as global oceans, then as more localized lakes, perhaps subterranean (Lunine *et al.*, 1983; Dubouloz *et al.*, 1989). Voyager IRIS was a major player in elucidating the atmospheric composition and meteorology of Titan. CIRS is well equipped to extend this work substantively. Table V lists major scientific objectives for Titan, the physical variables that can be retrieved from CIRS spectra, and relevant measurement sequences, which are discussed in Section 4.3.

TABLE IV  
Atmospheric composition of Titan.

Gas	Chemical formula	Mole fraction		Comments-Reference
Major components				
Nitrogen	N <sub>2</sub>	0.85–0.98		Inferred indirectly <sup>a</sup>
Argon	Ar	<0.07		Inferred indirectly <sup>b</sup>
Methane	CH <sub>4</sub>	0.005–0.034		In the stratosphere <sup>b</sup>
		0.03–0.085		Near the surface <sup>b,1</sup>
Hydrogen	H <sub>2</sub>	0.0011–0.0013		<sup>b</sup>
Trace constituents		North Pole <sup>d</sup>		
		Equator <sup>e</sup>		
		0.5–20 mbar	~ 1.5 mbar	Disk-average <sup>e</sup>
Hydrocarbons				
Acetylene	C <sub>2</sub> H <sub>2</sub>	2.85 × 10 <sup>-6</sup>	4.7 × 10 <sup>-6</sup>	5.5 × 10 <sup>-6</sup>
Ethylene	C <sub>2</sub> H <sub>4</sub>	1.5 × 10 <sup>-7</sup>		1.2 × 10 <sup>-7</sup>
Ethane	C <sub>2</sub> H <sub>6</sub>	1.5 × 10 <sup>-5</sup>	1.5 × 10 <sup>-5</sup>	2.0 × 10 <sup>-5</sup>
Methylacetylene	C <sub>3</sub> H <sub>4</sub>	6.5 × 10 <sup>-9</sup>	6.2 × 10 <sup>-8</sup>	1.2 × 10 <sup>-8</sup>
Propane	C <sub>3</sub> H <sub>8</sub>	7.0 × 10 <sup>-7</sup>	5.0 × 10 <sup>-7</sup>	2.0 × 10 <sup>-7</sup>
Diacetylene	C <sub>4</sub> H <sub>2</sub>	1.5 × 10 <sup>-9</sup>	4.2 × 10 <sup>-8</sup>	2.0 × 10 <sup>-9</sup>
Benzene	C <sub>6</sub> H <sub>6</sub>			4.0 × 10 <sup>-10</sup>
Monodeuterated methane	CH <sub>3</sub> D	1.1 × 10 <sup>-5</sup>		6.7 × 10 <sup>-6</sup>
Nitriles				
Hydrogen cyanide	HCN	1.95 × 10 <sup>-7</sup>	2.3 × 10 <sup>-6</sup>	3.0 × 10 <sup>-7</sup>
Cyanoacetylene	HC <sub>3</sub> N	≤ 1 × 10 <sup>-9</sup>	2.5 × 10 <sup>-7</sup>	5.0 × 10 <sup>-10</sup>

Cyanogen	C <sub>2</sub> N <sub>2</sub>	$\leq 1 \times 10^{-9}$	$1.6 \times 10^{-8}$	$5.5 \times 10^{-9}$	$1 \times 10^{-8}$	At 1 mbar <sup>f</sup> k
Acetonitrile	CH <sub>3</sub> CN					
Dicyanoacetylene	C <sub>4</sub> N <sub>2</sub>		Solid phase			
Oxygen compounds						
Water vapor	H <sub>2</sub> O				$8 \times 10^{-9}$	At 0.01 mbar <sup>g</sup>
Carbon dioxide	CO <sub>2</sub>	$1.45 \times 10^{-8}$	$\leq 7 \times 10^{-9}$	$\leq 7 \times 10^{-9}$	$2.0 \times 10^{-8}$	In the troposphere <sup>h</sup>
Carbon monoxide	CO				$(2.2-4.2) \times 10^{-5}$	In the lower and in the upper stratosphere <sup>i</sup>
					$(2-3.9) \times 10^{-5}$ ; $(0.33-0.9) \times 10^{-5}$	In the upper stratosphere <sup>j</sup>
					$4-6 \times 10^{-5}$	In the upper stratosphere <sup>j</sup>

<sup>a</sup>Lindal *et al.* (1983), Broadfoot *et al.* (1981).

<sup>b</sup>Lellouch *et al.* (1989), Courtin *et al.* (1995), Samuelson *et al.* (1997b).

<sup>c</sup>Unless otherwise indicated in the 7th column, all the results are from Coustenis and Bézard (1995).

<sup>d</sup>Unless otherwise indicated in the 7th column, all the results are from Coustenis *et al.* (1991).

<sup>e</sup>Unless otherwise indicated in the 7th column, all the results are from Coustenis *et al.* (2003).

<sup>f</sup>Marten *et al.* (2002).

<sup>g</sup>Coustenis *et al.* (1998).

<sup>h</sup>Lellouch *et al.* (2003).

<sup>i</sup>Hidayat *et al.* (1998).

<sup>j</sup>Gurwell and Muhleman (1995).

<sup>k</sup>Khanna *et al.* (1987).

<sup>l</sup>Lemmon *et al.* (2002).

TABLE V  
Titan science and measurement objectives and observations.

Science objective	CIRS categories: Retrieved physical parameters	Observations
Formation and evolution		
Volatiles	CH <sub>4</sub>	Mid-IR nadir maps, far-IR nadir integrations and limb scans
Isotopes	CH <sub>3</sub> D, <sup>13</sup> CH <sub>4</sub> , <sup>13</sup> C <sup>12</sup> CH <sub>6</sub> , H <sup>13</sup> CN	Mid- and far-IR nadir and limb integrations
Atmospheric gas composition		
Photochemical cycle	Hydrocarbons (C <sub>2</sub> H <sub>2</sub> , C <sub>2</sub> H <sub>4</sub> , C <sub>2</sub> H <sub>6</sub> , C <sub>3</sub> H <sub>4</sub> , C <sub>3</sub> H <sub>8</sub> , C <sub>4</sub> H <sub>2</sub> , ...) and nitriles (HCN, HC <sub>3</sub> N, CH <sub>3</sub> CN, C <sub>2</sub> N <sub>2</sub> , ...), including new species (CH <sub>3</sub> , C <sub>6</sub> H <sub>6</sub> , CH <sub>2</sub> =C=CH <sub>2</sub> , ...)	Mid-IR nadir maps and integrations, far-IR nadir integrations, mid- and far-IR limb integrations
Oxygen compounds	CO, H <sub>2</sub> O, CO <sub>2</sub>	Far-IR limb integrations (CO and H <sub>2</sub> O), mid-IR limb and nadir maps (CO <sub>2</sub> )
New species/organics	H <sub>2</sub> CO, ...	Mid- and far-IR nadir and limb integrations
Aerosols and condensates		
Tropospheric clouds	CH <sub>4</sub> , ...	Far-IR nadir integrations and scans
Stratospheric condensates	C <sub>4</sub> N <sub>2</sub> , HC <sub>3</sub> N, ...	Mid- and far-IR limb integrations
Stratospheric aerosols	Far-IR haze properties	Mid-IR limb maps, far-IR limb scans
Atmospheric structure		
Temperature, pressure, density	Temperature field	Mid-IR nadir and limb maps, far-IR nadir and limb scans
Circulation		
Zonal winds	Thermal winds	Mid-IR nadir and limb maps, far-IR nadir and limb scans
Meridional motions	Constituent tracers	Mid-IR nadir and limb integrations, far-IR nadir and limb integrations
	Aerosols/diabatic heating and cooling	Mid-IR nadir and limb maps, far-IR nadir and limb scans
	Potential vorticity (temperature field)	Mid-IR nadir and limb maps, far-IR nadir and limb scans
Waves and eddies	Temperature and comp fields, variances	" "
Surface		
Structure	Temperature	Far-IR nadir and limb scans

### 3.2.1. Formation and Evolution

*Volatiles – Methane.* Aside from argon, which only has an upper limit placed on its abundance, CH<sub>4</sub> is the most common atmospheric constituent after N<sub>2</sub> (Table IV), and a key question is why it is present to the degree observed. Photolytic and catalytic dissociation would deplete the atmospheric inventory of CH<sub>4</sub> in only 10 million years (Strobel, 1982). The logical source to replenish the atmospheric CH<sub>4</sub> is Titan's surface or its interior, but how this occurs is not known. If a surface reservoir, the liquid is not likely to be pure CH<sub>4</sub> (Flasar, 1983), but instead liquefied natural gas (CH<sub>4</sub>, C<sub>2</sub>H<sub>6</sub>, C<sub>3</sub>H<sub>8</sub>, . . . , N<sub>2</sub>), with C<sub>2</sub>H<sub>6</sub> as one of the major components (Lunine *et al.*, 1983; Dubouloz *et al.*, 1989). C<sub>2</sub>H<sub>6</sub> and other hydrocarbons, produced by CH<sub>4</sub> dissociation in the upper atmosphere, end up at the surface by rainout after condensing in the lower stratosphere (Maguire *et al.*, 1981). Radar reflectivity studies (Muhleman *et al.*, 1990), however, are not consistent with a global ocean of liquefied natural gas. In addition, near-infrared spectroscopy and imaging indicate bright and dark albedo features that are fixed in location, suggesting a mostly solid surface (Lemmon *et al.*, 1993; Smith *et al.*, 1996b; Combes *et al.*, 1997; Meier *et al.*, 2000; Coustenis *et al.*, 2001; Roe *et al.*, 2002; Gendron *et al.*, 2004). Recent spectroscopic studies have indicated that water ice is extensively exposed (Griffith *et al.*, 2003). An ocean basin-continent configuration similar to Earth's also poses difficulties. It would efficiently circularize Titan's orbit by tidal dissipation, which is inconsistent with the observed 3% orbital eccentricity (Sagan and Dermott, 1982; Sears, 1995; Dermott and Sagan, 1995). Hence, surface reservoirs are likely to be localized lakes or even stored in the regolith (Lunine, 1993). Lorenz *et al.* (1997) have suggested that the atmospheric CH<sub>4</sub> abundance is episodic, with periods of depletion and enhanced outgassing. Atmospheric CH<sub>4</sub> should vary spatially, not only from a possible heterogeneous source distribution, but also because it can condense in the troposphere. CIRS observations can determine the distribution of both tropospheric and stratospheric CH<sub>4</sub>, thereby providing some clues to its source and also its transport in the atmosphere.

Information on the distribution of tropospheric CH<sub>4</sub> follows from an analysis of the collision-induced spectrum of CH<sub>4</sub> at 150–600 cm<sup>-1</sup>, using temperature profiles independently retrieved from radio occultation soundings. The combined method works because the far-infrared spectra and the temperatures retrieved from the radio occultations depend differently on the vertical distribution of CH<sub>4</sub>. The technique is fairly involved, and we refer the reader to Courtin *et al.* (1995), Samuelson *et al.* (1997b), and the review by Flasar (1998a) for details. Samuelson *et al.*, derived a CH<sub>4</sub> mole fraction near the equator  $\approx 0.06$ , which decreased with latitude in both hemispheres, by a factor of 3 near 60°. They used Voyager IRIS spectra and the temperatures retrieved from Voyager radio occultation soundings. The latter were equatorial, so they had to assume that the general shape of the temperature profile at other latitudes remained similar to the low-latitude temperature profiles. Both Courtin *et al.* (1995) and Samuelson *et al.* (1997b) found that plausible opacities



from tropospheric gases and condensates were not sufficient to account for the observed spectral radiances, unless  $\text{CH}_4$  was supersaturated by 50–100% in the middle and upper troposphere. Otherwise the brightness temperatures in the far-infrared portion of synthetic spectra would be too high compared to the observations, indicating that the emission level was too deep in the troposphere. However, the limited spatial coverage by IRIS and the existence of only one radio occultation sounding, with both ingress and egress were at equatorial latitudes, were a major impediment to these analyses. The mapping capability of CIRS, combined with several radio-occultation soundings by Cassini at different latitudes, will make this approach more viable.

Stratospheric  $\text{CH}_4$  can be retrieved using CIRS spectra alone obtained with both nadir- and limb-viewing geometries. Figure 12 depicts the inversion kernels for temperature retrieval in Titan's atmosphere. These derive from the far-infrared portion of the spectrum in which pressure-induced absorption by  $\text{N}_2$  dominates, and from the mid-infrared part of the spectrum near  $1300\text{ cm}^{-1}$  in the  $\nu_4$  band of  $\text{CH}_4$ . The situation is similar to that discussed earlier for Saturn (Section 3.1.1). The partial overlap of the far-infrared inversion kernels in the limb-viewing mode and with those in the mid-infrared in the nadir-viewing mode allows the simultaneous

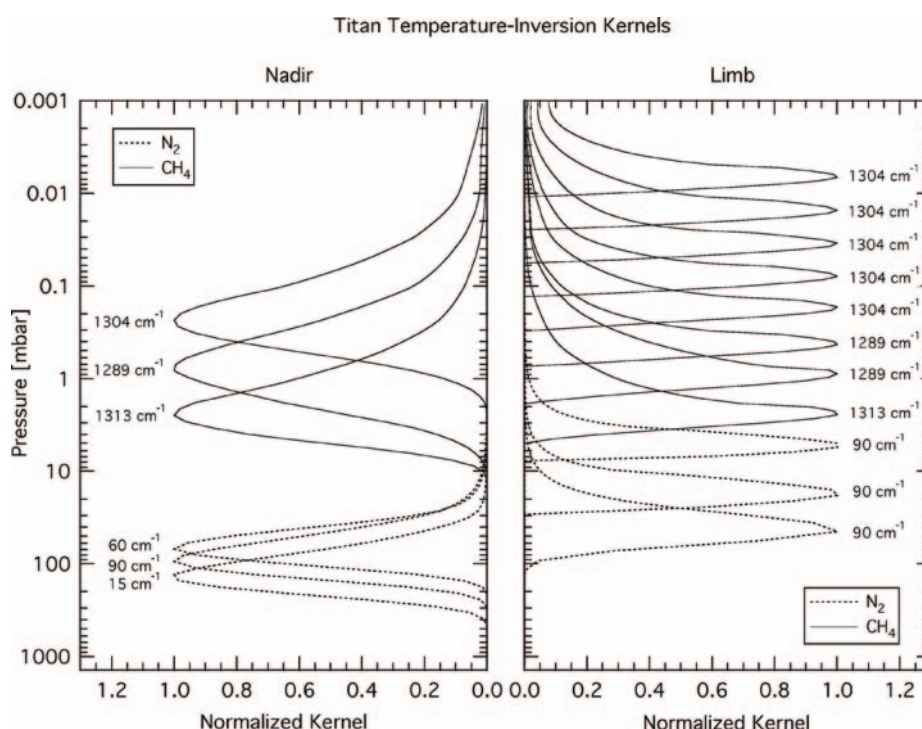


Figure 12. Inversion kernels for temperature sounding of Titan. The kernels for limb viewing have been convolved with a finite FOV approximated as a Gaussian, whose full width at the  $1/e$  points, projected onto the horizon, equals one scale height.

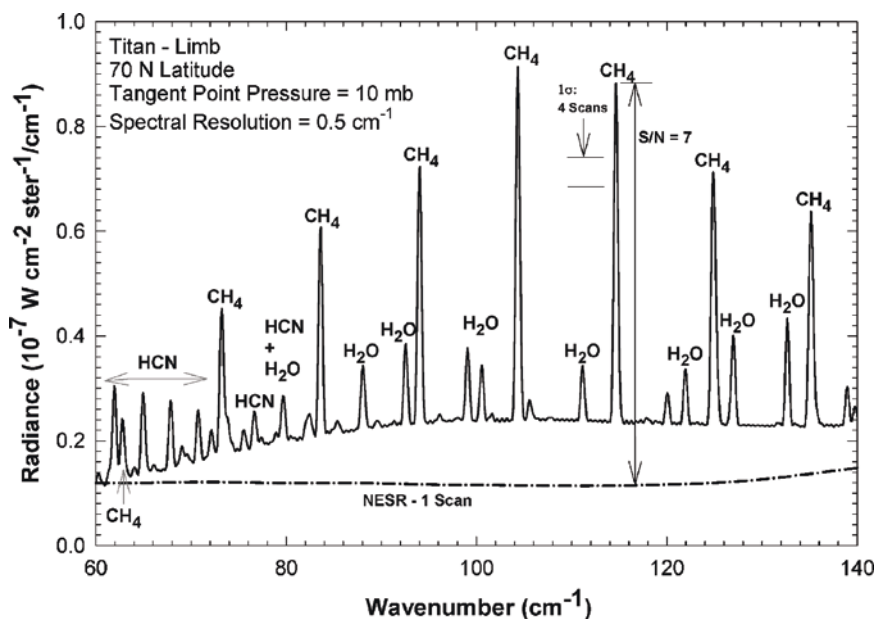


Figure 13. Synthetic far infrared limb spectrum between 60 and 140  $\text{cm}^{-1}$  of Titan at 70°N, under conditions observed by Voyager near N. spring equinox. The limb-tangent height is the 10-mbar level. The spectrum contains the rotational lines of  $\text{CH}_4$ ,  $\text{HCN}$ , and  $\text{H}_2\text{O}$ , seen in emission from the stratosphere, overlying the pressure-induced continuum of  $\text{N}_2$ . The NESR (Section 5.6.1) is shown for a single scan. The figure depicts the 1- $\sigma$  error bar corresponding to an average of 4 scans, indicating the accuracy with which the  $\text{CH}_4$  abundance can be retrieved.

retrieval of temperature and the mole fraction of gaseous  $\text{CH}_4$  near 4 mbar. The retrieval is discussed in greater detail in Appendix A. An alternate method entails the use of the rotational lines of  $\text{CH}_4$  in the far infrared at 60–140  $\text{cm}^{-1}$ . Figure 13 illustrates this region of the spectrum viewed on Titan's limb, with a tangent point at the 10-mbar level. The optically thin rotational lines ride on the  $\text{N}_2$  pressure-induced "continuum." Hence, temperature can be retrieved (as discussed in Section 3.2.4 and Appendix A) by using the radiances in the spectrum between the rotational lines, and temperature and  $\text{CH}_4$  abundance can be retrieved unambiguously. To observe the narrow rotational lines, spaced  $\sim 10 \text{ cm}^{-1}$  apart, a moderately high resolution is needed. Figure 13 corresponds to the full apodized CIRS resolution (0.5  $\text{cm}^{-1}$ ). In Figure 14, the  $\text{CH}_4$  emission probes the 10-mbar level; however, the lines will also be visible in nadir-viewing spectra, and those can probe  $\text{CH}_4$  in this region down to 20 mbar.

An unambiguous retrieval of stratospheric  $\text{CH}_4$  has never been done. Dynamical overturning times are short compared to the timescale for  $\text{CH}_4$  dissociation (see Flasar, 1998a), and this would suggest that it is well mixed in the stratosphere. However,  $\text{CH}_4$  condenses in the troposphere, and transport between the troposphere and stratosphere is poorly understood. The best fit of currently available data indicates

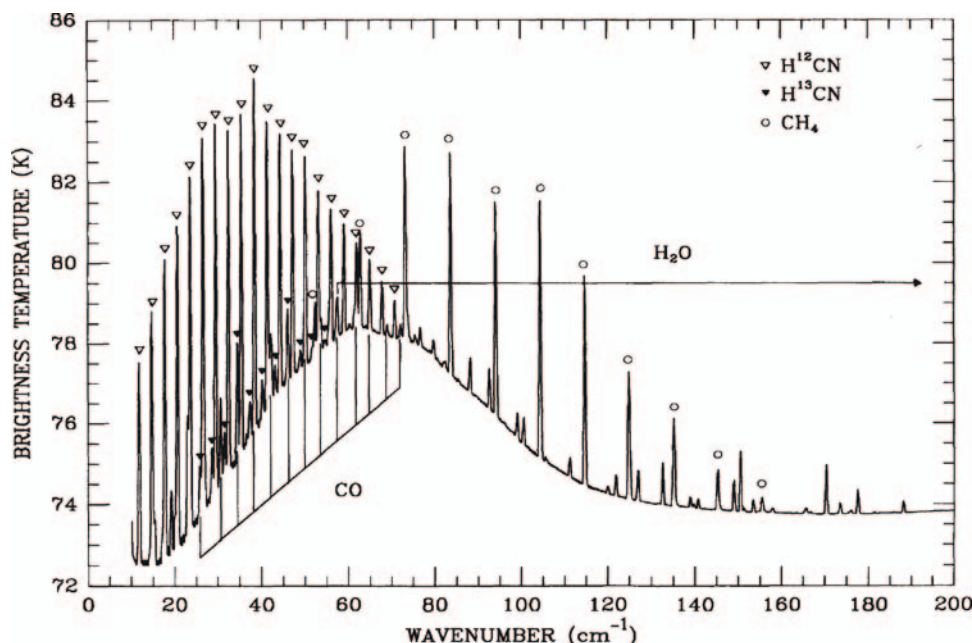


Figure 14. Synthetic nadir Titan spectrum at 10–200  $\text{cm}^{-1}$ , with viewing at an emission angle of  $48^\circ$ . Brightness temperatures are depicted for clarity in viewing rotational lines of  $\text{H}^{12}\text{CN}$ ,  $\text{CO}$ ,  $\text{CH}_4$ ,  $\text{H}^{13}\text{CN}$ , and  $\text{H}_2\text{O}$  (Coustenis *et al.*, 1993).

that the  $\text{CH}_4$  mole fraction varies between 0.5 and 3.4% above the cold trap (Table IV), although recent studies tend to constrain this value even more (1.0–1.7%). Determining the vertical and horizontal distribution of  $\text{CH}_4$  is critical for understanding several key atmospheric processes on Titan, and it is a major goal of CIRS measurements.

*Isotopes.* Other evidence in addition to  $\text{CH}_4$  replenishment requires that the bulk of Titan's atmosphere must have outgassed from its interior. Had the atmosphere been captured directly from the gas in the solar nebula, one would expect twice as many neon atoms as  $\text{N}_2$  molecules, which is not the case (Owen, 1982). Recent studies of carbon and nitrogen isotopes of HCN in Titan's atmosphere support this idea. From millimeter measurements, Hidayat *et al.* (1997) have shown that the ratio  $^{13}\text{C}/^{12}\text{C}$  in HCN lies between 0.008 and 0.014 and equals the terrestrial-solar value within the uncertainties of the measurements. However, Marten *et al.* (1997) and Meier *et al.* (1997) have found that the ratio  $^{15}\text{N}/^{14}\text{N}$  is greater than four times the terrestrial-solar value; more recently Marten *et al.* (2002) have found a ratio of 4.2. This fractionation implies a huge loss of nitrogen from Titan – 30 to 45 bars – much of which may have escaped from the satellite as a result of intense, early solar activity (Lunine *et al.*, 1999; Lammer *et al.*, 2000; Lammer and Bauer, 2003). If nitrogen has been escaping, carbon (and oxygen from  $\text{CO}$ ) should have gone with it. The absence of a comparable fractionation of the carbon isotopes implies a large

reservoir of methane, or some other hydrocarbons, from which atmospheric  $\text{CH}_4$  is continually replenished.

Rapid exchange of C between  $\text{CH}_4$  and CO prevents enrichment of  $^{13}\text{C}$  in CO as well (Wong *et al.*, 2002). Oxygen has been escaping, however, as demonstrated by the fact that  $^{18}\text{O}/^{16}\text{O} \sim$  twice the terrestrial value in CO (Owen *et al.*, 1999a; Wong *et al.*, 2002). The lower enrichment for  $^{18}\text{O}$  compared with  $^{15}\text{N}$  is presumably the result of an influx of oxygen from the outside (see below).

The far infrared is fertile ground for probing the carbon isotopes of HCN. Figure 14 illustrates a nadir-viewing spectrum between 10 and  $200\text{ cm}^{-1}$ . The far-infrared rotational lines are all optically thin, and they sit on the  $\text{N}_2$  pressure-induced continuum emission from the lower stratosphere and upper troposphere. The differences in the amplitudes of the lines of  $\text{H}^{12}\text{CN}$  and  $\text{H}^{13}\text{CN}$  are strictly attributable to their relative abundances. The line-formation region for both isotopes is 10–20 mbar. Hence CIRS should be able to retrieve  $[^{13}\text{C}]/[^{12}\text{C}]$  in the far infrared to a much higher accuracy than previously available. CIRS can also observe the ratio in the isotopic forms of  $\text{CH}_4$  and  $\text{C}_2\text{H}_6$  (Orton, 1992). As noted earlier for Saturn, the ability to observe  $^{13}\text{C}$  in both parent ( $\text{CH}_4$ ) and daughter ( $\text{C}_2\text{H}_6$ , HCN) molecules simultaneously may provide insight into any fractionation processes that have occurred.

The indirect evidence for a large internal reservoir to replenish atmospheric  $\text{CH}_4$  suggests that the present ratio of atmospheric  $[\text{D}]/[\text{H}]$  should represent the value corresponding to the inventory of this reservoir, rather than a value determined by fractionation in the atmosphere itself. The abundance of atmospheric  $\text{H}_2$  is too small to detect the rotational lines of HD in CIRS spectra, as can be done on Saturn. The same applies to  $\text{H}_2\text{O}$  and HDO (see below). However, the  $[\text{CH}_3\text{D}]/[\text{CH}_4]$  ratio can be determined from the Q-branches of  $\text{CH}_3\text{D}$  and  $\text{CH}_4$  near  $1150\text{ cm}^{-1}$  and  $1300\text{ cm}^{-1}$ , respectively. From Voyager IRIS data a value of  $1.5_{-0.5}^{+1.4} \times 10^{-4}$  was found for  $[\text{D}]/[\text{H}]$  in  $\text{CH}_4$  (Coustenis *et al.*, 1989b), recently revised from ISO/SWS disk-averaged spectra to something about 2 times less:  $8.7_{-1.9}^{+3.2} \times 10^{-5}$  (Coustenis *et al.*, 2003). Mousis *et al.* (2002) argued that this value is representative of the  $[\text{D}]/[\text{H}]$  ratio in methane trapped in crystalline ice in the solar nebula at 10 AU. If correct, this would constrain the value of  $[\text{D}]/[\text{H}]$  in methane in the presolar cloud. The high sensitivity of the CIRS detectors in this region (Figure 37) will permit an improved determination of this ratio in  $\text{CH}_4$ .

### 3.2.2. Atmospheric Composition

*Hydrocarbons and nitriles.* Titan's atmosphere has an active photochemical cycle. Photolytic and catalytic dissociation of  $\text{CH}_4$  in the upper atmosphere (mainly above 700 km altitude) lead to the formation of  $\text{C}_2\text{H}_6$ ,  $\text{C}_2\text{H}_2$ , and higher-order hydrocarbons, including the polyacetylenes and organic oligomers thought to make up the brownish haze observed at visible wavelengths. The concomitant dissociation of  $\text{N}_2$  by photolysis above 800 km and cosmic ray impact in the  $\sim 100$  km region leads to the production of nitriles, e.g., HCN,  $\text{HC}_3\text{N}$ ,  $\text{C}_2\text{N}_2$  (see, e.g., Lara *et al.*, 1996). Most of the hydrocarbons and nitriles condense (Maguire *et al.*, 1981) in

the lower stratosphere and tropopause region, where temperatures are coldest, as low as  $\sim 72$  K, and precipitate to the surface. As noted earlier, this and the relative ease with which hydrogen, freed in the dissociation cycle, can escape from the atmosphere, ensures that the total inventory of atmospheric  $\text{CH}_4$  is irreversibly lost in 10 million years in the absence of a source (Strobel, 1982).

The spatial distribution of the hydrocarbons and nitriles is a product of the coupling of photochemical processes and condensation with atmospheric transport. Voyager IRIS spectra indicated an enhancement of hydrocarbons (other than  $\text{CH}_4$ ) and nitriles at high northern latitudes (Hanel *et al.*, 1981; Kunde *et al.*, 1981; Maguire *et al.*, 1981; Samuelson *et al.*, 1983; Coustenis *et al.*, 1991; Coustenis and Bézard, 1995). Figure 15 illustrates the relative prominence of emission from these species at these latitudes. Note that they are most distinct in the limb-viewing

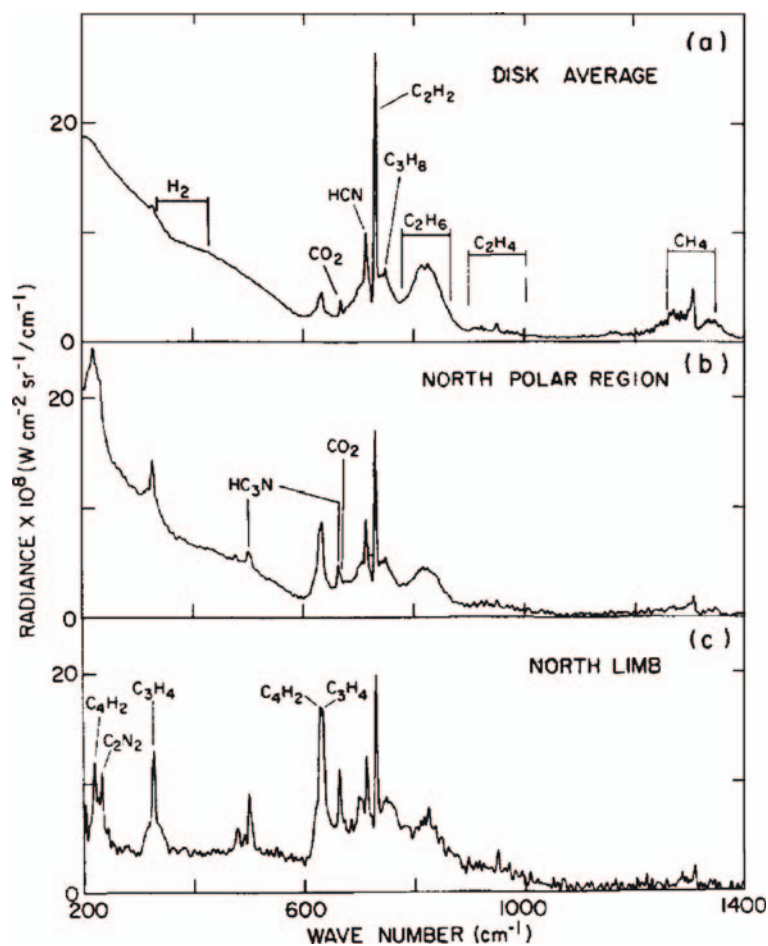


Figure 15. Voyager IRIS infrared spectrum of northern latitudes of Titan showing spectral emission features from hydrocarbons and nitriles.



spectrum, which is free of the underlying continuum from the troposphere. For several of these ( $\text{C}_2\text{H}_4$ ,  $\text{C}_3\text{H}_4$ ,  $\text{C}_4\text{H}_2$ ,  $\text{HCN}$ ,  $\text{HC}_3\text{N}$ , and  $\text{C}_2\text{N}_2$ ), the enhancement was a factor of 10 or greater (Coustenis *et al.*, 1991; Coustenis and Bézard, 1995). The temperatures retrieved at high northern latitudes are cold, suggesting strong circumpolar winds that may inhibit meridional transport between low and high latitudes (see below). Some information on the vertical profiles of the hydrocarbons and nitriles in the north polar region was available from the few IRIS limb spectra obtained, but these were fairly coarse, with 200-km altitude resolution. Several species, including all the aforementioned nitriles, showed a marked increase with altitude, at least in the region of sensitivity,  $\sim 1$  mbar to 0.1 mbar (Coustenis *et al.*, 1991). Although the ISO/SWS had higher sensitivity and spectral resolution than IRIS ( $0.3\text{--}0.8\text{ cm}^{-1}$ , comparable to that of CIRS), and detected new molecules, such as  $\text{H}_2\text{O}$  (Coustenis *et al.*, 1998) and – tentatively – benzene ( $\text{C}_6\text{H}_6$ ; Coustenis *et al.*, 2003), it was only capable of obtaining disk-average Titan spectra. As a consequence, it missed two of the nitriles that IRIS had detected ( $\text{C}_2\text{N}_2$ , and  $\text{C}_4\text{N}_2$ ). Adequate spatial resolution is key to studying these compounds.

The IRIS coverage of Titan was limited, and the vertical and horizontal distribution of the hydrocarbons and nitriles can be better retrieved from CIRS limb- and nadir-viewing spectra. Figure 16a shows a synthetic limb spectrum for a portion of the FP3 band pass at  $3\text{ cm}^{-1}$  resolution. This spectrum was computed for conditions representative of the high northern latitudes ( $70^\circ\text{N}$ ) during the Voyager encounter. The strong emission features seen from the hydrocarbons  $\text{C}_2\text{H}_2$ ,  $\text{C}_2\text{H}_6$ ,  $\text{C}_2\text{H}_4$ ,  $\text{C}_3\text{H}_4$ ,  $\text{C}_3\text{H}_8$ ,  $\text{C}_4\text{H}_2$  and nitriles  $\text{HCN}$  and  $\text{HC}_3\text{N}$  will be used to determine vertical profiles of these gases. For example, Figure 17 illustrates the limb contribution functions for  $\text{C}_2\text{H}_2$ ,  $\text{C}_2\text{H}_6$ , and  $\text{HCN}$ . These show good altitude coverage from 100–400 km. Adequate SNRs exist to map many of the strong species on the limb in 10 s time steps. Weaker features, such as  $\text{C}_2\text{H}_4$  and  $\text{C}_3\text{H}_8$ , will require time averages of about 250 s (25 spectra). Although the nadir mapping will have somewhat lower vertical resolution and more limited vertical coverage, it will generally be executed further from Titan and therefore will provide more complete horizontal coverage (Section 4.3). Figure 16b shows a synthetic nadir spectrum for FP3 at  $3\text{ cm}^{-1}$  spectral resolution, computed for conditions representative of Titan's equatorial region. The figure indicates that averaging over 16 scans (2.7 min) provides adequate SNR to determine the abundance of the weaker emission features, such as  $\text{C}_2\text{H}_4$  and  $\text{C}_3\text{H}_8$ .

*Oxygen compounds.* The observed distribution of  $\text{CO}$ ,  $\text{CO}_2$ , and  $\text{H}_2\text{O}$  bears on the question of whether oxygen in Titan's atmosphere has a primordial or external origin, or both.

Currently, there is some question on the spatial uniformity of  $\text{CO}$  in the troposphere and stratosphere (Table IV). A tropospheric value,  $q = 6 \times 10^{-5}$ , was inferred from spectra near  $1.6\text{ }\mu\text{m}$  (Lutz *et al.*, 1983). Recent  $5\text{-}\mu\text{m}$  spectra has indicated a tropospheric mole fraction  $q = 3.2 \pm 1.0 \times 10^{-5}$  (Lellouch *et al.*, 2003). In the stratosphere, observations of the 115-GHz  $\text{CO}$  1–0 rotational line by Marten *et al.* (1988) suggested a  $\text{CO}$  mole fraction,  $q = 2_{-1}^{+2} \times 10^{-6}$ . Later observations of



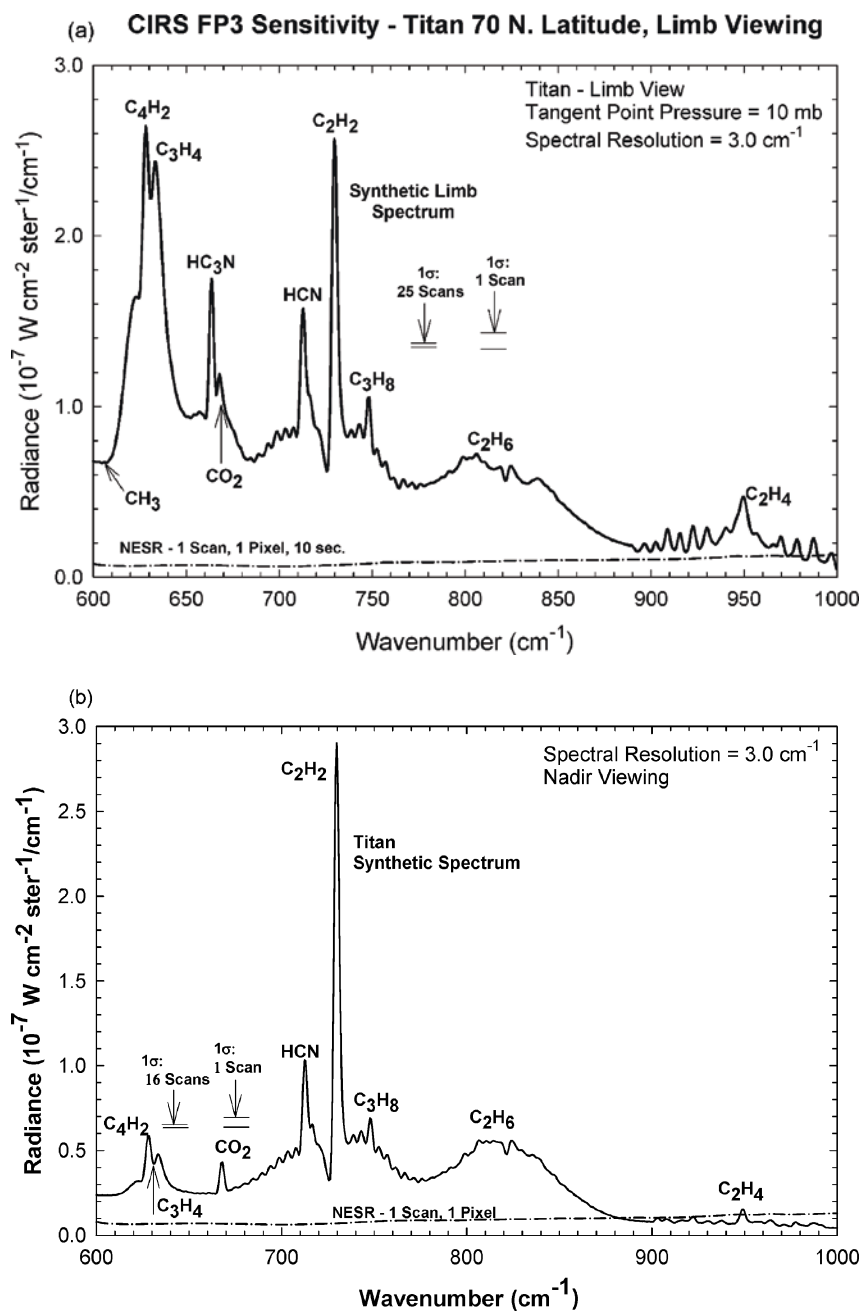


Figure 16. (a) Synthetic mid infrared spectrum (3.0 cm $^{-1}$ ) for FP3 for Titan limb viewing. The NESR is shown for a single FP3 pixel for a single-scan 10-s integration time. The 1- $\sigma$  error bars are indicated for both 1 and 25 scans. (b) Synthetic mid infrared spectrum (3.0 cm $^{-1}$ ) for FP3 for Titan nadir viewing. The NESR for a single pixel and a single scan is indicated. The 1- $\sigma$  error bars are shown for both 1 and 16 scans.

the 115 GHz line by Gurwell and Muhleman (1995) indicate a much higher stratospheric abundance,  $q = 5 \pm 1 \times 10^{-5}$ . Hidayat *et al.* (1998) used observations at 115 GHz and several other lines of  $^{12}\text{CO}$  and  $^{13}\text{CO}$  in the millimeter and submillimeter range, to retrieve a vertical profile of CO above the tropopause. They concluded that  $q = 2.9^{+0.9}_{-0.5} \times 10^{-5}$  at 60-km altitude, decreasing to  $q = 2.4 \pm 0.5 \times 10^{-5}$  at 175 km, and falling to  $q = 4.8^{+3.8}_{-1.5} \times 10^{-6}$  at 350 km. The 60-km number is in agreement with Lellouch *et al.* but are smaller than those found by Gurwell and Muhleman, Lellouch *et al.* (2003) emphasize that with the observed influx of  $\text{H}_2\text{O}$  of  $3 \times 10^6 \text{ cm}^{-2} \text{ s}^{-1}$ , and a mixing ratio of 30 ppm, CO on Titan is not in

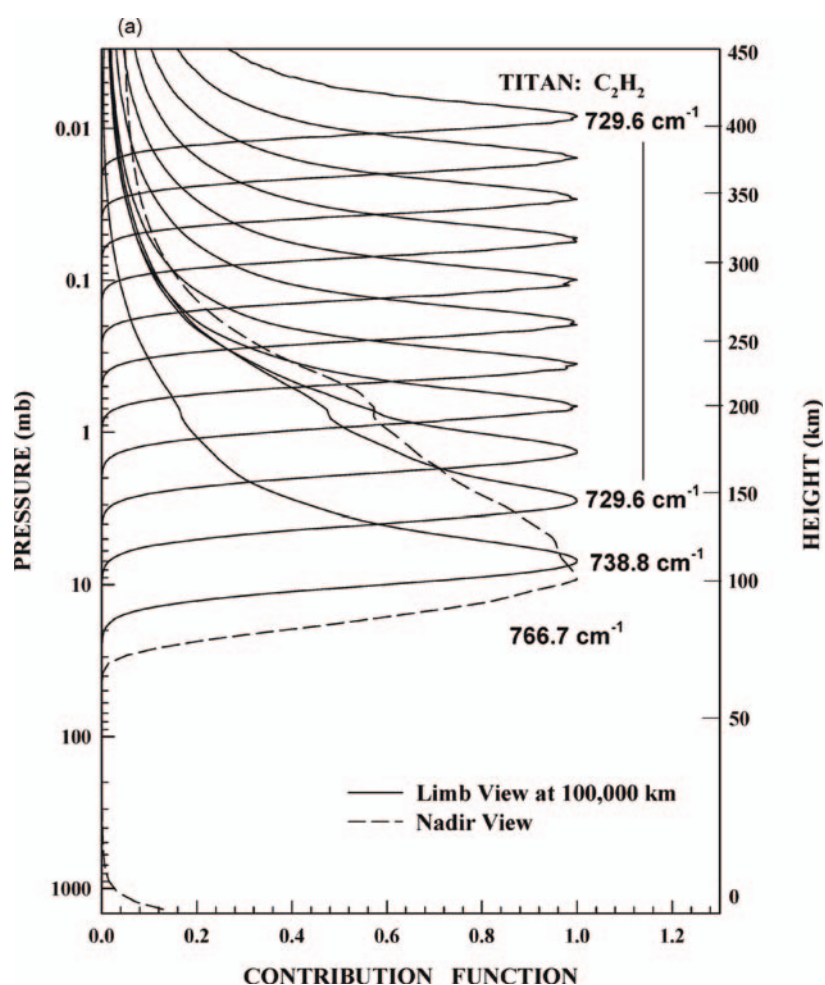


Figure 17. (a, b, c) Contribution functions for  $\text{C}_2\text{H}_2$ ,  $\text{C}_2\text{H}_6$  and  $\text{HCN}$  for limb and nadir viewing of Titan. The limb contribution functions have been convolved with a finite FOV whose full width projected onto the horizon equals one scale height.

(Continued on next page)

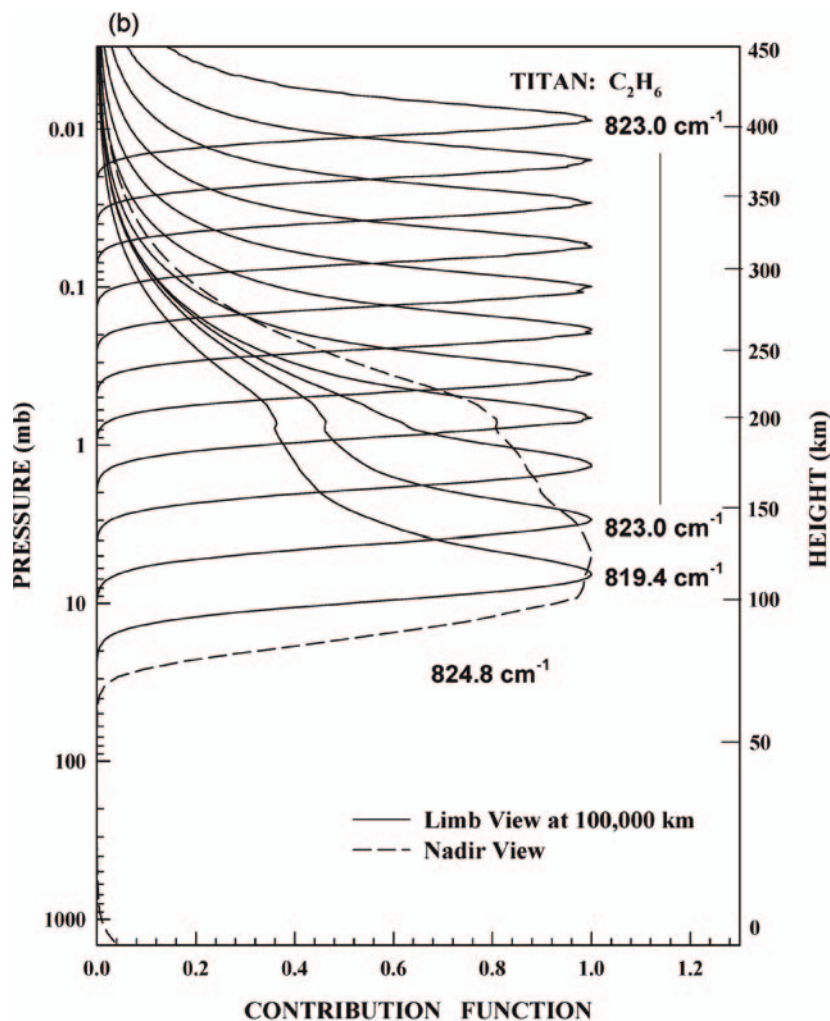


Figure 17. (Continued)

equilibrium and must experience continuous loss, reminiscent of  $CH_4$ . Replacement may come through cometary or interplanetary dust-particle impacts, or from internal sources. A depleted stratospheric abundance would suggest CO outgassing as the current source, although it would seem difficult to reconcile any nonuniformity with the fact that CO does not condense in Titan's atmosphere and dynamical overturning times that are much shorter than the timescales associated with photochemical destruction (Samuelson *et al.*, 1983). Alternatively, Samuelson *et al.* (1983) have suggested that the source of atmospheric CO is the influx of meteoric water that is photodissociated to form OH, which ultimately recombines with CO to form  $CO_2$  and escaping hydrogen atoms. In their model, the observed abundance

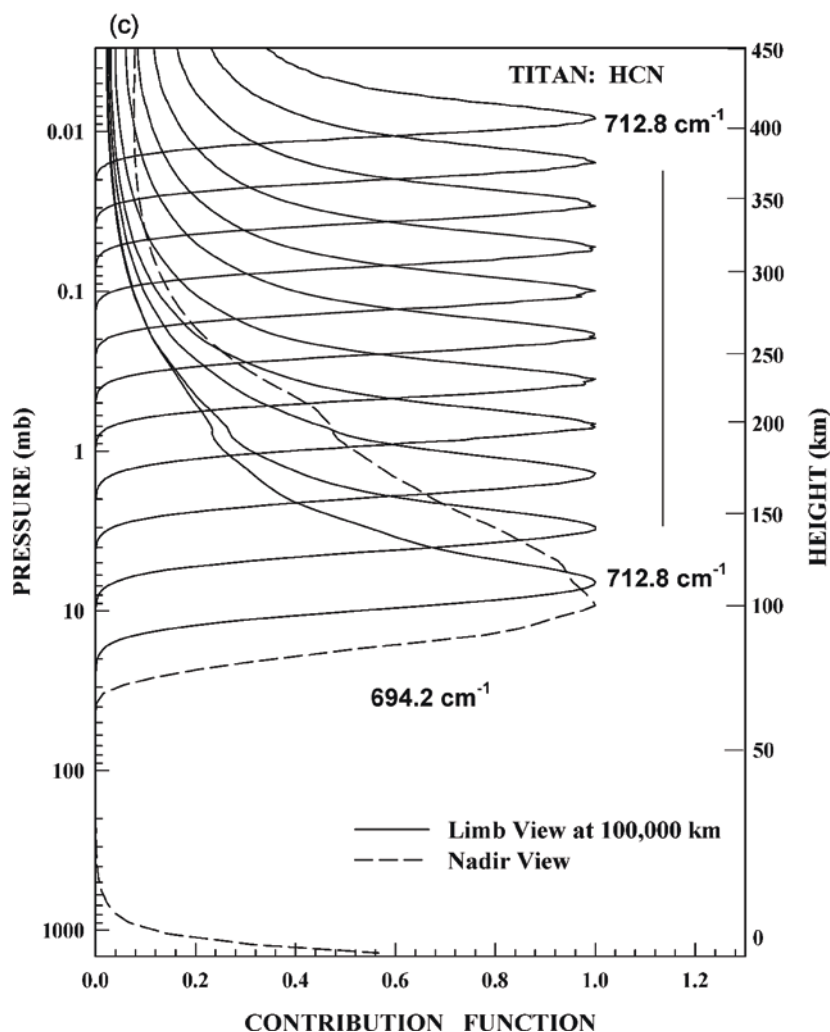


Figure 17. (Continued)

of CO<sub>2</sub> is regulated by condensation at the cold trap near the tropopause. Further progress in understanding the oxygen inventory of Titan requires better definition of the abundance and spatial distribution of the oxygen-bearing compounds in its atmosphere.

CIRS spectra in the far infrared can settle the issue of whether CO is depleted in the stratosphere. A synthetic limb spectrum for FP1 at 0.5 cm<sup>-1</sup> spectral resolution, shown in Figure 18, illustrates the rotational line emission of CO. This spectrum was computed for a limb tangent height of 125 km (~3 mbar), assuming 24 parts per million CO. The solid line is with CO emission, and the dotted line is without.

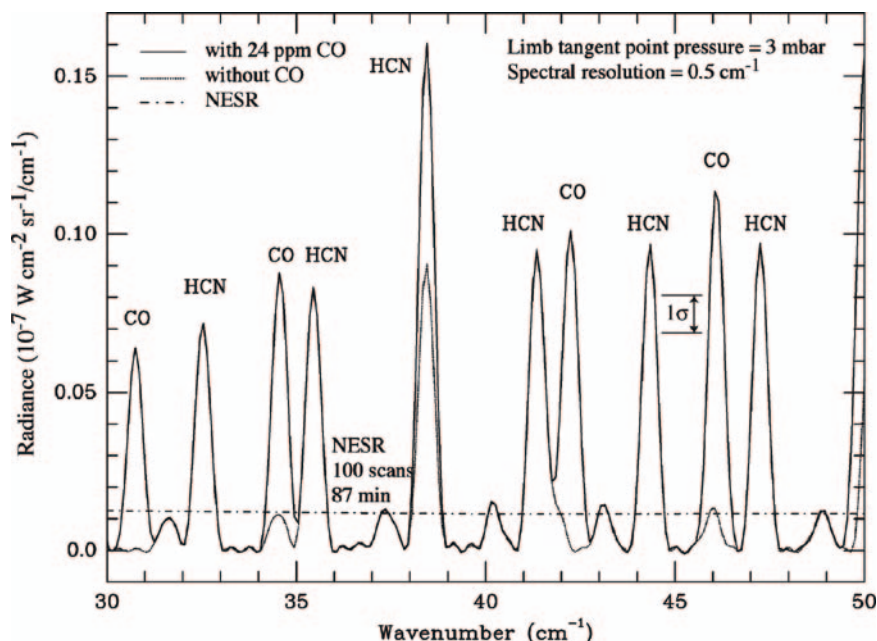


Figure 18. Synthetic far infrared spectrum ( $0.5 \text{ cm}^{-1}$ ) in FP1 for Titan limb viewing. The vertical profile of CO will be retrieved from the emission lines shown. Near  $38.5 \text{ cm}^{-1}$ , the CO and HCN emission are blended together, but all the emission lines can be used if both species are retrieved simultaneously.

The strongest relatively isolated CO lines are shown in the figure. The CO lines are intrinsically weak, and cannot be observed in an individual spectrum; an average of about 100 scans (87 min) at a specified altitude is needed to obtain the NESR and  $1\text{-}\sigma$  error shown. Limb viewing in the far-infrared must be done relatively close to Titan, within two hours of closest approach, for adequate vertical resolution. With the limited time available for this, the CO abundance will not be globally mapped in the limb mode, but at several latitudes from pole to pole. Nadir integrations, performed at greater distances, offer better horizontal coverage, although no vertical structure will be retrieved, only a column abundance down to the lower stratosphere. Although the line-to-continuum ratio is smaller than for limb-viewing, a 90-min integration at 1.5–2 air masses is sufficient to detect the CO lines.

$\text{CO}_2$  was first detected in Voyager IRIS nadir-viewing spectra from emission in the  $\nu_2$  Q branch at  $667 \text{ cm}^{-1}$ , (Samuelson *et al.*, 1983). The line-formation region is centered near 10 mbar (Coustenis *et al.*, 1989a), but otherwise the nadir-viewing observations provided little information on the vertical distribution. Depending on the vertical distribution assumed, estimates of the average mole fraction in the stratosphere range from  $1.5 \times 10^{-9}$  to  $1.4 \times 10^{-8}$  (Samuelson *et al.*, 1983; Coustenis *et al.*, 1989a). A value slightly higher than this range ( $2 \times 10^{-8}$ ) was derived from ISO high-resolution measurements, in which the  $\text{CO}_2$  contribution was separated

from  $\text{HC}_3\text{N}$  (Coustenis *et al.*, 2003; see also Table IV). This analysis assumed a stratospheric mixing ratio that was uniform with height. The IRIS spectra suggested that  $\text{CO}_2$  was depleted in the north polar region (Coustenis *et al.*, 1991). However, the retrieval was complicated by the blending of the  $667\text{ cm}^{-1}$   $\text{CO}_2$  emission with that from  $\text{HC}_3\text{N}$ , which was enhanced at high northern latitudes during the Voyager flybys. Because  $\text{CO}_2$  is photochemically active and condenses near the tropopause (Samuelson *et al.*, 1983), it can vary both vertically and laterally. CIRS observations will better characterize the spatial distribution of  $\text{CO}_2$ . The vertical distribution of  $\text{CO}_2$  can be determined from limb-viewing spectra. Figure 16a illustrates a spectrum characteristic of Titan's north polar region under Voyager conditions. The proximity of  $\text{HC}_3\text{N}$  and  $\text{CO}_2$  emission is evident. However, with 25 spectra averaged at  $3\text{ cm}^{-1}$  resolution (corresponding to a measurement time of 4.2 min), the SNR is adequate to separate the two features. Figure 16b illustrates that  $\text{CO}_2$  can also be detected in a nadir-viewing average of 16 spectra over the same wavenumber range, under equatorial conditions.

Recent ISO/SWS observations in the grating mode have identified water vapor (Coustenis *et al.*, 1998). The distribution of  $\text{H}_2\text{O}$  can be determined from its rotational lines in the FP1 spectrum. ISO measured the emission at two rotational lines at  $227.8$  and  $253.9\text{ cm}^{-1}$  to derive an  $\text{H}_2\text{O}$  mole fraction of  $8 \times 10^{-9}$  at the 400-km level in Titan's stratosphere. CIRS will use the stronger  $\text{H}_2\text{O}$  lines in the  $80\text{--}160\text{ cm}^{-1}$  range; some of these are shown in Figure 19. These lines are

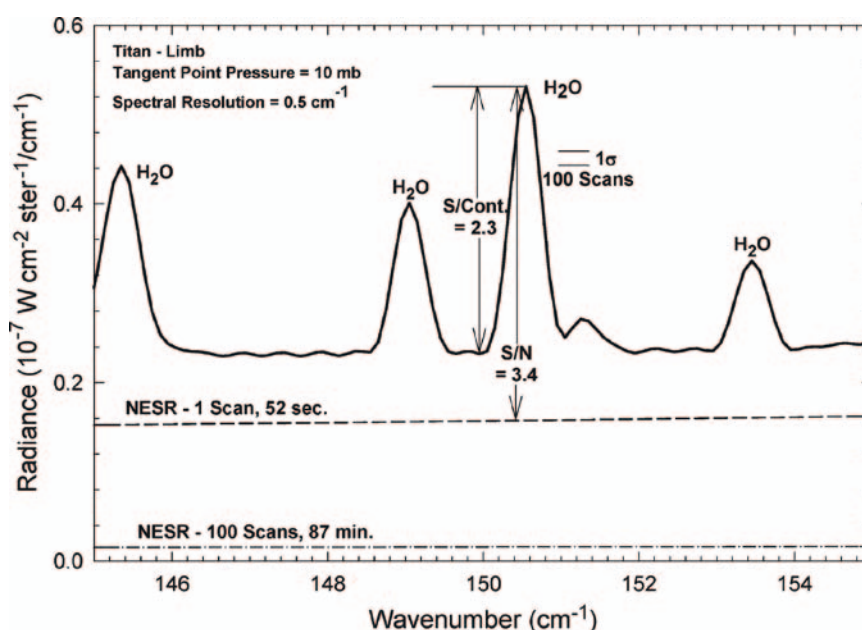


Figure 19. Synthetic mid infrared spectrum ( $0.5\text{ cm}^{-1}$ ) for FP1 for Titan limb viewing. The vertical profile of  $\text{H}_2\text{O}$  will be retrieved from the  $\text{H}_2\text{O}$  emission lines.



relatively weak, and cannot be observed in an individual spectrum; an average of about 100 scans (87 min) is needed to achieve the NESR and  $1-\sigma$  error bar shown in Figure 19.

*New Species.* With its unique combination of high spectral and spatial resolution, CIRS is uniquely qualified to search for compounds that were not detected in the Voyager or ISO spectra. Some of the more complex nitriles and hydrocarbons detected by Voyager, which had lower spectral resolution than ISO or CIRS, but better spatial resolution than ISO, were only found over a limited range of latitudes (the north polar region at the northern spring epoch of Voyager observations), and some were only seen at grazing incidence and high air mass.

For the possibility to detecting as yet unobserved molecules on Titan (Table VI) see the studies in Coustenis *et al.* (1993) and Coustenis *et al.* (2003). One important targeted species is the methyl radical,  $\text{CH}_3$ , discussed earlier for Saturn. This species has a strong emission band at  $606\text{ cm}^{-1}$  (in FP3); its location is given in Figure 16a. Although methyl acetylene ( $\text{CH}_3\text{C}_2\text{H}$ ) – propyne – has previously been observed on Titan (Table IV), the isomer allene ( $\text{CH}_2=\text{C}=\text{CH}_2$ ) has not. Allene has emission bands at  $353\text{ cm}^{-1}$  (in FP1) and  $845\text{ cm}^{-1}$  (in FP3). The  $353\text{ cm}^{-1}$  band is seven times weaker than the  $845\text{ cm}^{-1}$  band, but it is more easily detectable because it is more isolated, whereas the latter is blended with ethane features.

Extrapolation of the data from laboratory simulation experiments to conditions on Titan suggests that several organic compounds unstable at room temperature can be formed only at the low temperatures of Titan's stratosphere. Laboratory experiments simulating the gas phase synthesis of organic compounds indicate that quite complex nitrogen-containing organics are produced in a  $\text{N}_2$ – $\text{CH}_4$  atmosphere. A few of the most abundant (yet undetected on Titan) are propionitrile,  $\text{C}_2\text{H}_5\text{–CN}$ , acrylonitrile,  $\text{CH}_2=\text{CH–CN}$ , cyanopropyne,  $\text{CH}_3\text{–C}\equiv\text{C–CN}$ ; also polynes such as  $\text{C}_6\text{H}_2$  and  $\text{C}_8\text{H}_2$  and cyanopolynes, such as  $\text{HC}_5\text{N}$  (Thompson, *et al.*, 1991; de Vanssay *et al.*, 1995; Coll *et al.*, 1997). Other thermally unstable compounds such as  $\text{CH}_3\text{NC}$ ,  $\text{CH}_2\text{N}_2$  and  $\text{CH}_3\text{N}_2$  should also be present in Titan's atmosphere. All these compounds have relatively strong signatures in the spectral ranges of the three CIRS focal planes, including at low temperatures (Cerceanu *et al.*, 1985; Raulin *et al.*, 1990; Khlifi and Raulin, 1991, 1992; Delpech *et al.*, 1994; Nishio *et al.*, 1995; Shindo *et al.*, 2001a,b; Shindo, 2002) – see Table VI. Although some have IR bands interfering with those of other (known) constituents, the  $0.5\text{ cm}^{-1}$  resolution of CIRS will permit their separation, and allow their detection or the establishment of upper limits. Detection of even one of these compounds and/or the determination of reduced upper limits would be extremely important to establish key pathways in the synthesis of prebiotic compounds.

CIRS can also search for new oxygen-bearing compounds, such as formaldehyde ( $\text{CH}_2\text{O}$ ), or oxirane ( $\text{C}_2\text{H}_4\text{O}$ ), which is the most abundant o-organics produced in laboratory experiments simulating Titan's atmosphere chemistry (Coll *et al.*, 2003). The identification of these species can place constraints on evolutionary models of Titan and its atmosphere. Furthermore,  $\text{CH}_2\text{O}$  is a prebiotic organic, and its detection

TABLE VI

Some organics, as yet unobserved on Titan in the thermal IR, but potentially observable with CIRS and their deduced upper limits in Titan's atmosphere from previous observations.

Studied compounds	Strongest signatures		Upper limit of mean mixing ratio in Titan's stratosphere	
	Frequency (cm <sup>-1</sup> )	Band strength at 300 K (cm <sup>-2</sup> atm <sup>-1</sup> )	using Voyager IRIS spectra	using ISO disk-average data
Hydrocarbons				
CH <sub>2</sub> CCH <sub>2</sub>	356	65	5 × 10 <sup>-9a</sup>	2 × 10 <sup>-9b</sup>
	845	407		
C <sub>4</sub> H <sub>4</sub>	629	288	7 × 10 <sup>-10c</sup>	
C <sub>6</sub> H <sub>2</sub>	622	428	4.4 × 10 <sup>-10d</sup>	
C <sub>8</sub> H <sub>2</sub>	621.5	496	4 × 10 <sup>-10e</sup>	
Nitriles				
CH <sub>3</sub> CN	362 <sup>l</sup>	4.4		
CH <sub>2</sub> CHCN	230	10	8.4 × 10 <sup>-8g</sup>	< 5 × 10 <sup>-10b</sup>
	954	100		
CH <sub>3</sub> CH <sub>2</sub> CN	207	15	2.5 × 10 <sup>-7a</sup>	< 1 × 10 <sup>-10b</sup>
	1075	37		
CH <sub>3</sub> CH <sub>2</sub> CH <sub>2</sub> CN	728/742	3.5	5 × 10 <sup>-7a</sup>	
(CH <sub>3</sub> ) <sub>2</sub> CHCN	538	3.3	2 × 10 <sup>-7a</sup>	
ΔCN	726	19	1.5 × 10 <sup>-7a</sup>	
	818	34		
CH <sub>3</sub> CCCN	338	100	1.0 × 10 <sup>-8a</sup>	
	499	91		
CH <sub>3</sub> CHCHCN	728	230	2.5 × 10 <sup>-7a</sup>	< 5 × 10 <sup>-10b</sup>
CH <sub>2</sub> CHCH <sub>2</sub> CN	557	64	4 × 10 <sup>-8h</sup>	< 5 × 10 <sup>-10b</sup>
	942	110		
CH <sub>2</sub> C(CH <sub>3</sub> )CN	535	33	7.5 × 10 <sup>-8h</sup>	< 5 × 10 <sup>-10b</sup>
	928	130		
C <sub>4</sub> N <sub>2</sub>	614	34.4	5.6 × 10 <sup>-9i</sup>	
NCCHCHCN (trans)	947	178	1 × 10 <sup>-8j</sup>	
Other N organics				
CH <sub>3</sub> NC	526	8.8	1.3 × 10 <sup>-9k</sup>	
CH <sub>2</sub> N <sub>2</sub>	419	144	5.0 × 10 <sup>-9k</sup>	
CH <sub>3</sub> N <sub>3</sub>	250	9	5.4 × 10 <sup>-9k</sup>	

<sup>a</sup>Coustenis *et al.* (1993).

<sup>b</sup>Coustenis *et al.* (2003).

<sup>c</sup>Shindo *et al.* (2001a).

<sup>d</sup>Shindo *et al.* (2003).

<sup>e</sup>Shindo *et al.* (2001b).

<sup>f</sup>Nishio *et al.* (1995).

<sup>g</sup>Khelifi *et al.* (1999).

<sup>h</sup>Cerceau *et al.* (1985).

<sup>i</sup>Khelifi *et al.* (1997).

<sup>j</sup>Shindo (2002).

<sup>k</sup>Khelifi *et al.* (1996).

<sup>l</sup>Feature not yet observed. CH<sub>3</sub>CN detected in millimeter observations (Bézard *et al.*, 1993; Marten *et al.*, 2002).

would suggest the importance of oxygen compounds and indicate new pathways in prebiotic chemistry on Titan.

### 3.2.3. *Particulates*

*Aerosols.* A brownish haze of aerosol particles dominates the visible appearance of Titan. These particles are thought to be organic refractories that consist of a complex mix of polyacetylenes, aromatic compounds, and amino acid precursors (McKay *et al.*, 2001). They are first formed in a photochemically active zone at an altitude of about 400 km, from where they are dispersed by gravity, diffusion, and planetary scale circulations. Initially the particles are roughly spherical monomers that grow one molecule at a time. Once they reach regions where the pressure exceeds 0.1 mbar they grow by coagulation into highly nonspherical aggregates (Cabane *et al.*, 1992; Tomasko *et al.*, 2002). These aggregates then become rapidly larger through cluster-cluster ballistic growth.

Vertical and horizontal distributions of haze particles depend strongly on the relative importance of the rates of atmospheric diffusion and circulation. Because meridional velocities are about three to four orders of magnitude smaller in the stratosphere than those associated with zonal winds (Flasar *et al.*, 1981a), variations of aerosol densities with latitude are likely to dominate along constant altitude surfaces. Rannou *et al.* (2002) have suggested that Titan's detached haze at ~400 km is traced out by the meridional motion of small monomers that participate in a cross-equatorial Hadley cell circulation. The small size of the monomers precludes significant diffusive settling during a single season. However, the expected circulation pattern, moving from summer to winter hemisphere at high altitudes and returning at low altitudes, causes the monomers to descend rapidly in altitude at the winter pole. The attendant increase in ambient density associated with these monomers converts them into fractal aggregates that in turn settle relatively quickly when the circulation pattern reverses half a Titan year later, leaving a 50-km clear gap between the haze formed by these aggregates and the monomer haze higher up.

This circulation pattern also gives rise to an accumulation of haze at the winter pole, as suggested by Voyager 1 images (Smith *et al.*, 1981). In the absence of sources and sinks, a uniformly mixed atmosphere should give rise to a density scale height for an aerosol haze equal to that for the ambient atmosphere, provided only that the mixing rate is rapid compared with particle fall rates, a criterion that should be valid for Titan. When such sources and sinks are present, however, the relative scale heights will be different. In the case of Titan, the initial photochemical production zone near 400 km lies at a greater altitude than the aerosol sink; the latter is thought to be located in the lower stratosphere near 100 km where condensation of volatiles is expected. A subsequent precipitation of these condensates (hydrocarbons and nitriles) is expected to cleanse the atmosphere of aerosols below this level. Thus the aerosol scale height should exceed that of the gaseous atmosphere,

a characteristic found to be true for the north polar stratosphere at the time of the Voyager 1 encounter (Samuelson and Mayo, 1991).

Far-IR CIRS limb spectra covering the continuum between  $250\text{ cm}^{-1}$  and  $600\text{ cm}^{-1}$  will provide the vertical distribution of haze with a resolution of about two scale heights. From the work of Samuelson and Mayo (1991) this will determine the aerosol-to-gas scale height ratio to about 20%. Unlike the situation with Voyager IRIS, several limb locations can be sampled, permitting a determination of aerosol abundance with latitude. Measured vertical and latitudinal distributions of haze in turn can provide tests of seasonally-dependent dynamical models.

*Condensates.* The discussion in Sections 3.2.1 and 3.2.2 has already touched on the  $\text{CH}_4$  cycle in Titan's atmosphere. Methane is transported from surface and/or subsurface reservoirs into the upper mesosphere and thermosphere, where it and molecular nitrogen are decomposed by solar EUV radiation and high energy electrons originating from Saturn's magnetosphere. The ensuing products are responsible for initiating the chemistry from which all the observed higher hydrocarbons ( $\text{C}_2\text{H}_2$ ,  $\text{C}_2\text{H}_4$ ,  $\text{C}_2\text{H}_6$ ,  $\text{C}_3\text{H}_4$ ,  $\text{C}_3\text{H}_8$ ,  $\text{C}_4\text{H}_2$ ) and nitriles ( $\text{HCN}$ ,  $\text{HC}_3\text{N}$ ,  $\text{C}_2\text{N}_2$ ,  $\text{C}_4\text{N}_2$ ,  $\text{CH}_3\text{CN}$ ) are derived.

Atmospheric motions are also responsible for transporting these organic vapors down into the cold regions of the lower stratosphere where – almost without exception – their partial pressures exceed saturation vapor pressures (Maguire *et al.*, 1981). Whether or not they condense depends on the availability of condensation sites. Courtin *et al.* (1995) have suggested that aerosol particles may be immiscible in methane and ethane, making it unlikely that such particles can act as viable seed nuclei for at least some non-polar hydrocarbons. However, Titan aerosols may be slightly soluble in condensed nitriles (Raulin, 1987). In this case nitrile particles might in turn act as seed nuclei for hydrocarbons in the lower stratosphere. Condensate features of  $\text{C}_4\text{N}_2$  at  $478\text{ cm}^{-1}$  and possibly  $\text{HC}_3\text{N}$  at  $503\text{ cm}^{-1}$  were found in Titan's north polar stratosphere by Voyager1 IRIS near the time of northern spring equinox. A  $\text{C}_4\text{N}_2$  mean particle radius of about  $5\text{ }\mu\text{m}$  was inferred from its band shape by Samuelson *et al.* (1997a). Other unidentified features at  $225\text{ cm}^{-1}$ ,  $700\text{ cm}^{-1}$ , and  $765\text{ cm}^{-1}$ , tentatively attributed to condensates, were also found (Coustenis *et al.*, 1999). At this time the north polar region was both relatively cold and contained relatively high abundances of several organic vapors, implying that the probability for condensate formation was especially high at this season and location.

Once formed, stratospheric ice particles will begin to precipitate. Their rates of precipitation depend on growth rates, which in turn are strong functions of the degrees of supersaturation prevailing at the time. Particles with radii of  $5\text{ }\mu\text{m}$  will fall through the lower stratosphere in times short compared with a Titan season, and stratospheric clouds may be restricted to polar regions during late winter and early spring. Upon reaching the troposphere, precipitating ice particles can serve as nucleation sites for methane condensation. Thus high densities of stratospheric ice particles lead to low degrees of methane supersaturation in the troposphere. Because

particle growth rates are proportional to  $S - 1$ , the degree of supersaturation ( $S = 1$  is saturation), it follows that stable clouds can form and persist only near saturation. If  $S$  is substantially greater than unity, any particles that form should grow rapidly and fall out immediately, leaving nothing to form a cloud (Toon *et al.*, 1988).

Still, there is some evidence from ground-based near-IR spectra and images for the presence of occasional tropospheric cloud activity (Griffith *et al.*, 1998, 2000; Roe *et al.*, 2002; Brown *et al.*, 2002). It will be very important to compare near-infrared VIMS and far-infrared CIRS Cassini spectra in an effort to correlate the presence of clouds in space and time with the appearance of condensate spectral features and degrees of methane supersaturation close to unity.

### 3.2.4. Atmospheric Structure and Circulation

*Temperatures.* Atmospheric temperatures on Titan have been most extensively determined below 200 km altitude ( $\sim 1$  mbar). The vertical profiles of temperature retrieved from the Voyager radio occultation (Lindal *et al.*, 1983) indicate an atmosphere with a well defined tropopause and stratosphere, separated by a broad tropopause region (Figure 20). Radiative equilibrium studies (Yelle, 1991) suggest a mesosphere between 300 and 600 km altitude. To date, the only temperature retrievals in this region are from light curves that were obtained during the occultation

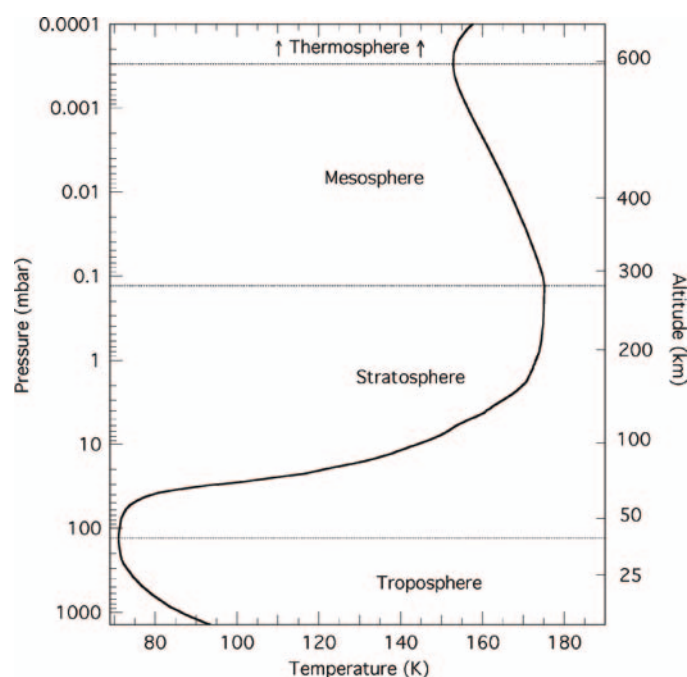


Figure 20. Representative Titan atmospheric temperature profile from the surface to 650 km altitude. The lowest 200 km is the nominal model derived by Lellouch *et al.* (1989) from Voyager radio-occultation and IRIS measurements. Above 200 km the profile is Yelle's (1991) model J.

of the bright K giant star 28 Sgr by Titan in 1989 (Hubbard *et al.*, 1993). These retrievals exhibit large variations that may be attributable more to uncertainties in the retrieval process itself than to spatial variability on Titan. As there was only one radio occultation with Voyager, with the ingress and egress located at equatorial latitudes, the horizontal variation in temperature below 200 km was determined mainly from IRIS spectra. IRIS generally acquired spectra in the nadir-viewing mode, and its coverage did not include the far-infrared portion corresponding to the N<sub>2</sub> inversion kernels in Figure 12. Hence, direct temperature retrieval was restricted to the range of the nadir-viewing CH<sub>4</sub> inversion kernels in the left panel of the figure: 0.3–3 mbar. Because of the limited sensitivity in this spectral region, the IRIS spectra of Titan were also spectrally averaged before the inversion, which effectively reduced the vertical resolution from that indicated in the figure (Flasar and Conrath, 1990). The unambiguous retrieval of temperature at other altitudes was impracticable, because aerosols, which vary heterogeneously, dominate the opacity in most of the IRIS spectra away from the  $\nu_4$  band of CH<sub>4</sub>. Nonetheless, it was possible to use the brightness temperatures at 520–540 cm<sup>-1</sup> and 200 cm<sup>-1</sup> to infer the variation of temperature with latitude at the surface and in the tropopause region, respectively (Samuelson *et al.*, 1981; Flasar *et al.*, 1981a; Courtin and Kim, 2002). Figure 21 illustrates the derived meridional variation of atmospheric temperature at these altitudes. The latitude range of each point is 10–20°, and it is partially indicative of the spatial resolution of the IRIS FOV, but it also results from the need to bin and average spectra to achieve an acceptable noise error. The meridional profiles suggest that the polar regions are colder than the equator by ~3 K at the surface and ~20 K in the upper stratosphere (0.4 mbar). Longitude coverage was limited to two bands, one on the day side, the other separated by ~180° on the night side (Flasar and Conrath, 1992). The ability to establish zonal variations was limited, but the available data suggested variations <1 K at the surface, and <3 K in the upper stratosphere (Flasar *et al.*, 1981a).

The repeated targeted flybys of Titan will enable CIRS to provide a much more complete latitude-longitude mapping of its temperature field (Section 4.3). Its far-infrared coverage allows the use of radiances where pressure-induced N<sub>2</sub> absorption dominates to retrieve atmospheric temperatures. It also can observe Titan's atmosphere in the limb-viewing mode. Hence, atmospheric temperatures can be retrieved from approximately the 400-mbar level up to the 10- $\mu$ bar level (Figure 12), providing much more continuous coverage with high vertical resolution than previous observations. This will provide the first complete mapping of Titan's mesosphere. There is a gap in the lower troposphere, slightly larger than a scale height, over which CIRS spectra cannot be used for unambiguous temperature retrieval. Recourse will have to be made to temperatures retrieved from radio occultation soundings, and from the onboard probe temperature sensors over a single descent trajectory.

The atmospheric opacity is small at 520–540 cm<sup>-1</sup>, and the radiances there are indicative of surface temperature (Samuelson *et al.*, 1981, 1997; Flasar *et al.*, 1981a; Courtin and Kim, 2002). Although the surface emission dominates, the



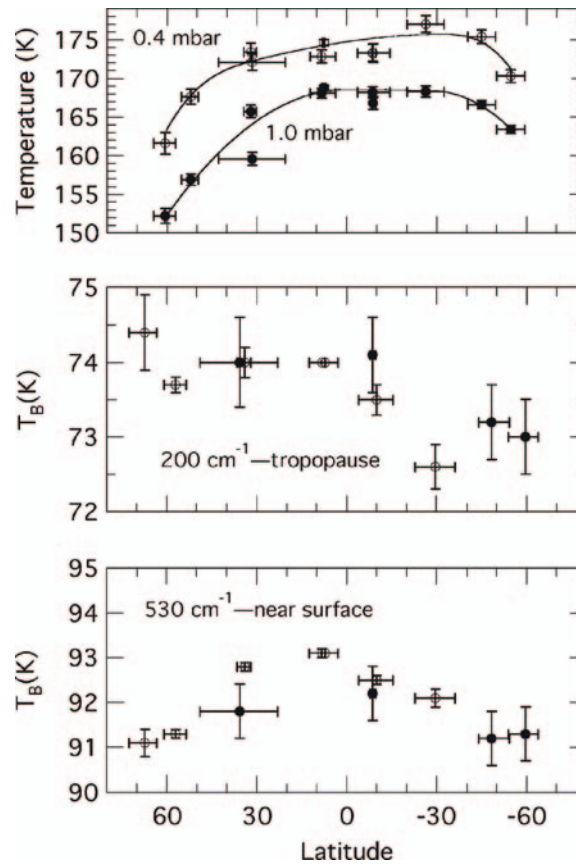


Figure 21. Top panel. Titan stratospheric temperatures retrieved from radiances at  $1260\text{--}1307\text{ cm}^{-1}$  in the  $\nu_4$  band of  $\text{CH}_4$ . The vertical bars denote errors attributable to instrument noise; the horizontal bars give the range of latitudes of the binned and averaged spectra used in the inversions (Flasar and Conrath, 1990). Lower panels. Brightness temperatures renormalized to a constant emission angle at  $200\text{ cm}^{-1}$  and  $530\text{ cm}^{-1}$ , representative of tropopause and surface temperatures, respectively. In these panels solid points are at night, open circles are during the day. The vertical bars include uncertainties from noise, calibration, and emission angle corrections; the horizontal bars give the latitude range of the binned and averaged spectra (Flasar *et al.*, 1981a).

contribution from the warm stratosphere is not negligible (Figure 21; Samuelson *et al.*, 1981; Toon *et al.*, 1988). Samuelson *et al.* (1981) constructed a two-level model to account for possible effects of stratospheric hazes, using IRIS equatorial spectra obtained at near normal viewing (emission angle =  $7^\circ$ ) and high emission angle ( $53^\circ$ ). The ability of CIRS to observe Titan's stratosphere on the limb, with deep space as the background, will enable one to separate the effects of stratospheric emission more cleanly from that of the surface.

*Zonal winds.* The equatorial pressure bulge implied by the meridional temperature gradients retrieved from Voyager IRIS spectra requires stratospheric zonal

winds with velocities up to 10 times the equatorial surface rotation velocity, or  $\sim 100 \text{ m s}^{-1}$ , to maintain the dynamical balance (see Equation (1)). Subsequent analysis of central-flash data from the 28 Sgr occultation in 1989 indicated an equatorial bulge in the isodensity contours that was consistent with zonal winds of comparable magnitude (Hubbard *et al.*, 1990; Sicardy *et al.*, 1990; Hubbard *et al.*, 1993). Thus Titan has a global cyclostrophic wind system analogous to Venus'. Titan's atmosphere exhibits a very interesting radiative-dynamical transition, in that the radiative response time in the troposphere is long compared to the seasonal modulation, whereas it is much shorter than the seasonal timescale in the upper stratosphere. Tropospheric temperatures therefore should exhibit little seasonal variation, but stratospheric temperatures should vary markedly (Flasar *et al.*, 1981a). As the zonal winds and temperature field are tightly coupled by the constraint of the thermal wind relation, the stratospheric winds should also vary seasonally. Observing this seasonal variation should provide clues to the maintenance of cyclostrophic wind systems, which is poorly understood. Venus, with its small obliquity, has little seasonal driving.

Detailed study of Titan's cyclostrophic zonal winds has been hampered by the lack of adequate spatial coverage and resolution, both horizontally and vertically, in the temperatures, as discussed above. The ability of CIRS to provide the needed temperature maps several times over the Cassini tour will go a long way toward rectifying this, but information from other experiments is needed. With cyclostrophic flows, the quadratic term dominates the left-hand side of the thermal wind Equation (1), and the direction of the zonal wind is ambiguous. If the temperature field is known down to the surface, where the winds are weak (from surface friction) and the linear geostrophic term dominates the left-hand side of (1), then the integration in principal can remove the ambiguity at higher altitudes where the cyclostrophic winds dominate. The radio-occultation soundings and the probe descent measurements should provide information on the temperature and pressure fields in the lower troposphere, but not the degree of mapping that CIRS can provide above the 400-mbar level. Direct measurements of the wind velocity will also be needed. The probe Doppler Wind Experiment (Bird *et al.*, 2002) will provide a valuable profile of the zonal wind along the descent trajectory. Tracking of discrete cloud or haze features, should they be discernible, by the imaging (ISS; Porco *et al.*, 2003) and near infrared mapping (VIMS; Brown *et al.*, 2003) experiments on the orbiter would also be useful.

*Meridional Circulations.* Gaseous and particulate tracers, the temperature field, and potential vorticity all probe residual meridional circulations, as they do for Saturn. Potential vorticity conservation does not have the complication of lagged ortho-para  $\text{H}_2$  conversion, as on Saturn. Even though the flow is cyclostrophic, the Ertel potential vorticity is conserved on time scales over which dissipative and radiative effects can be neglected.

Deviations of the observed meridional variation of atmospheric temperature (Figure 21) from that expected from a purely radiative response have led to estimates of the heat transport by zonally symmetric meridional circulations. The derived

meridional velocities are quite sluggish by terrestrial standards, centimeters per second or smaller (Flasar *et al.*, 1981a; Flasar and Conrath, 1990; Flasar, 1998b). Stratospheric temperatures retrieved from the IRIS spectra indicated a cross-equatorial asymmetry of several degrees, that was not initially expected at the Voyager season (northern spring equinox), given the small radiative response time (Flasar and Conrath, 1990; Coustenis and Bézard, 1995). Flasar and Conrath (1990) suggested that the asymmetry resulted from the additional dynamical inertia caused by the seasonal cross-equatorial transport of angular momentum needed to maintain the thermal wind balance. The adiabatic heat and cooling associated with the vertical motion produces the hemispheric asymmetry in temperature. An asymmetric distribution of solar and infrared opacities (Bézard *et al.*, 1995) and the lag associated with the (albeit small) radiative time constant in a temperature field with a large seasonal amplitude (Hourdin *et al.*, 1995), have also been invoked to explain this asymmetry. Observing Titan at a different season than Voyager will help to differentiate among these models.

The distribution of photochemical species is a promising indicator of dynamical transport on Titan. An interesting example of this is the circumpolar vortex that was observed on Titan by the Voyager spacecraft in 1980–1981. Voyager 2 images showed a thin dark circumpolar ring at 70°N. Voyager IRIS spectra showed that high northern latitudes were enriched in several hydrocarbons and nitriles (Coustenis and Bézard, 1995). The IRIS spectra also indicated cold temperatures in the polar stratosphere (Figure 21) and, from the thermal wind Equation (1), a circumpolar vortex, with winds  $\sim 80 \text{ m s}^{-1}$  (Flasar and Conrath, 1990). The 28 Sgr occultation data, obtained during Titan northern summer, indicated winds double this at high southern latitudes, again implying a strong vortex about the winter pole. On Earth, circumpolar vortices are known to inhibit meridional flow across the vortex, where the vortical winds are strong (Schoeberl and Hartmann, 1991). The large meridional gradient in hydrocarbons and nitriles retrieved from the IRIS spectra at high latitudes is likely indicative of this barrier effect, coupled with the photochemistry. (Flasar (1998a) discusses several of these issues further.) To understand these complex systems, it is important to be able to map the three-dimensional structure of such vortices. With its ability to map temperatures and composition in both the nadir- and limb-viewing modes, CIRS can provide much of the critical information. CIRS's ability to map several different atmospheric variables simultaneously should also provide a better conceptual understanding of the variability of Titan's stratospheric hazes. Several models have been developed, and we have already discussed the study by Rannou *et al.* (2002) in Section 3.2.3.

*Eddies and waves.* The transports of heat and angular momentum by eddies and waves must be important players maintaining Titan's global wind system, but little is known about them, except inferentially. No direct sign of waves and eddies has been seen in visible images. The only evidence of thermal waves is from scintillations in the Voyager radio-occultation soundings that seem to be consistent with the signature of vertically propagating gravity waves in the tropopause region and the

stratosphere (Hinson and Tyler, 1983). Temperatures retrieved from IRIS soundings only placed crude upper limits to the variation of temperature with longitude – which, if detected, could have indicated the presence of waves or eddies – but these sampled longitude rather sparsely (Flasar and Conrath, 1992). The capability of CIRS to map both the vertical and horizontal variation of temperature – and of composition – with high sensitivity, will provide an effective probe of wave and eddy structure. CIRS should be capable of defining the phase tilts of any vertically propagating waves over its vertical range of retrieval (Figure 12), which should aid in their identification.

### 3.3. ICY SATELLITES

Cassini's orbital tour of the Saturn system includes multiple near and distant flybys of Saturn's satellites (Figure 22), permitting CIRS to address many of the basic goals for satellite investigations, including composition, temperature, thermal properties, and delineation of geologically distinct structures. CIRS will map the satellite surfaces and provide their thermophysical characteristics to understand the differences from satellite to satellite better. The long wavelength data from CIRS provide essential information on the surface and near-surface compositions of the airless satellites. CIRS can probe several millimeters into the regolith, where temperature gradients associated with possible solid-state greenhouse enhancements can be observed. The details of surface thermal, thermophysical and compositional characteristics will allow greater insight into the evolution of these objects. Particular attention will be paid to the unique aspects of Enceladus, where current endogenic activity may be revealed by surface thermal anomalies and by gases and particulate material in associated plumes. Joint investigations with VIMS will strengthen the determination of surface and near-surface compositions. CIRS data, combined with radiometry data from the RADAR experiment, will provide information on the porosity and scattering characteristics of the regoliths to depths of several centimeters. Overall, the extended spectral range of the CIRS instrument, combined with the 4-year orbital mission of the Cassini spacecraft and collaborative investigations, will provide a great increase in the quality and quantity of data returned on satellite surfaces compared to that obtained from the IRIS and other instruments on the Voyager spacecraft.

Saturn's airless icy satellites are intermediate in size between massive haze-shrouded Titan and the myriad small particles of the rings. These range from long-known Iapetus, Rhea, Dione and Tethys, discovered in the 17th century by Giovanni Cassini, to the small, irregularly shaped F-ring shepherds, Pandora and Prometheus, discovered in 20th century Voyager images by Collins *et al.* (1980). In this section we describe the capabilities of CIRS for investigating these objects.

The infrared energy available to CIRS from the icy satellites originates within a centimeter of the surface. Consequently, the instrument senses only satellite

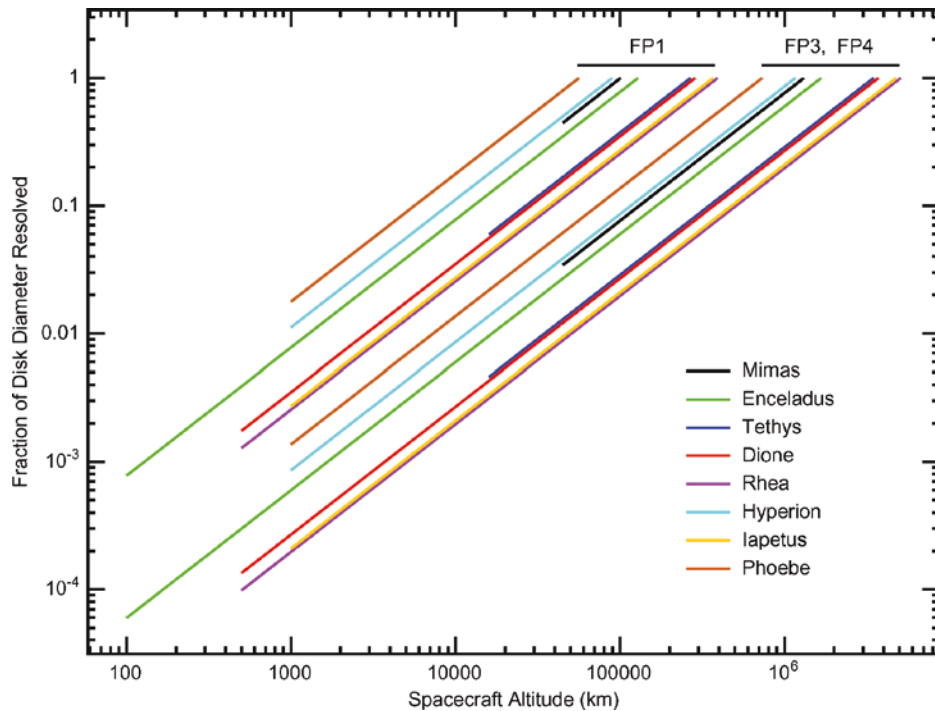


Figure 22. The spatial resolution of CIRS pixels projected onto the disks of various satellites as a function of altitude. The left ends of the curves are for the planned closest approaches during the tour. The right ends of the curves provide the altitudes at which the target objects just fill the pixel. The best Cassini encounters with all but Mimas (45,000 km) and Tethys (15,000 km) will be within 1,000 km of the surface (though for altitudes below  $\sim 2000$  km, the spacecraft cannot track the target, so that footprints will be smeared). A resolution of 10% of the disk diameter represents about 12 degrees of latitude at the sub-spacecraft point. The FP1 angular diameter ( $AD = 3.9$  mrad) resolution can be compared with Voyager IRIS resolution ( $AD = 4.4$  mrad), where the altitude for all encounters exceeded 70,000 km. At a given altitude, CIRS FP3 and FP4 resolution will exceed FP1 resolution by more than an order of magnitude.

regoliths or active surface sources. The information derived from such observations must then be related to the satellite interior and to its evolutionary history.

Evolutionary models that consider primordial composition, and heating and transport from accretional, gravitational (differentiation) and radioactive energy have been constructed in order to follow the development of the satellites (Ellsworth and Schubert, 1983; Schubert *et al.*, 1986). Except in the unlikely case that little of the accretional energy is lost during formation through radiation or through convection into the local nebula, the melting point of water would not have been reached. Thus, if the objects accreted as homogeneous ice-rock mixtures, they remained so. The possible presence of ammonia hydrate at the 20% level (Lewis,

1972) does not alter this conclusion, though melting of this fraction in the outer layers could have a profound effect on surface evolution, both through its influence on tectonics, and by providing a solvent for transport of subsurface salts.

Although one to two orders of magnitude less massive than poorly evolved Callisto, these saturnian satellites display considerable endogenic surface modification, both by tectonic and effusive processes. In many instances, two or more episodes of surface modification are recorded by the presence of extensive regions of vastly different crater ages. Superimposed on features from endogenic processes and major bombardment events will be modifications due to subsequent gardening by micrometeorites and implantation and alteration by magnetospheric interactions (e.g., Delitsky and Lane, 1998; Delitsky and Lane, 2002; Delitsky *et al.*, 2003).

Two groups of bodies can be recognized: the large icy satellites and the small, mostly irregularly-shaped objects.

*The large icy satellites* After Titan, the six largest satellites in the Saturn system are, in order of distance from Saturn: Mimas, Enceladus, Tethys, Dione, Rhea, and Iapetus. The first five can be considered regular satellites, having circular and prograde orbits lying very close to Saturn's equatorial plane with semi-major axes smaller than 10 saturnian radii. The sixth, Iapetus, moves at a larger distance (about 60 saturnian radii) on an orbit inclined  $14.7^\circ$ . The density of these satellites is only slightly greater than that of water, and all show the spectroscopic signature of water ice. Albedos have been determined from Voyager images (Buratti *et al.*, 1990; Cruikshank *et al.*, 1998).

*Mimas* ( $r = 197 \pm 3$  km;  $p_V = 0.8$ ) has an ancient, heavily cratered surface ( $r$  denotes radius,  $p_V$  visual geometric albedo). Herschel, the largest crater, is 130 km in diameter, and basically unmodified. However, evidence of limited surface modification early in Mimas' history is provided by small differences in crater counts. Brightness variations across its surface are small, with the leading side possibly a few percent brighter than the trailing side.

*Enceladus* ( $r = 251 \pm 5$  km;  $p_V = 1.0$ ) has the highest albedo among solar system objects, reflecting about 90% of incident sunlight. This, with a flat spectrum between 0.35 and  $0.59 \mu\text{m}$  indicates that the surface ice is relatively uncontaminated and unmodified by radiation. The surface is characterized by at least four distinct terrains, ranging from heavily cratered to featureless plains (Smith *et al.*, 1982; Kargel and Pozio, 1996). Even in the cratered areas the crater size distribution indicates a relatively young crust. The maximum density of Saturn's E ring is at the radius of Enceladus' orbit and may be related to possible endogenic activity on the satellite, though other mechanisms have been proposed (Haff *et al.*, 1983; Pang *et al.*, 1984; Hamilton and Burns, 1994). Albedo variations are very small.

*Tethys* ( $r = 530 \pm 10$  km;  $p_V = 0.8$ ) is densely cratered. A plains unit, with relatively few small and intermediate sized craters, indicates a period of internal activity that produced partial resurfacing of older terrain early in the satellite's history. The satellite is strikingly marked by Ithaca Chasma, a deep trench that



spans nearly three quarters of its circumference. The leading hemisphere is 10–15% brighter than the trailing hemisphere.

*Dione* ( $r = 560 \pm 5$  km;  $p_V = 0.55$  – leading;  $p_V = 0.4$  – trailing) is characterized by at least five terrains that differ in crater density (Plescia, 1983). Bright wispy terrain (linea) dominates the relatively dark trailing hemisphere. Ozone, the only material other than water ice so far identified on Saturn's icy satellites, is found on its surface (Noll *et al.*, 1997). It is believed to be the product of exposure to magnetospheric ion radiation.

*Rhea* ( $r = 765 \pm 5$  km;  $p_V = 0.65$  – leading;  $p_V = 0.55$  – trailing), the most heavily cratered satellite of Saturn, is characterized by at least three different terrains. Like Dione, its trailing hemisphere is also marked by linea, and ozone has been identified as well.

*Iapetus* ( $r = 718 \pm 18$  km;  $p_V = 0.04$  – leading;  $p_V = 0.5$  – trailing) is most notable for the extreme difference in albedo between its leading and trailing hemispheres. The leading hemisphere is covered with extremely dark material, while its trailing hemisphere is icy. Some bright-side craters have dark floors, suggesting flooding, but the dark hemisphere still needs explanation (Wilson and Sagan, 1995; 1996; Owen *et al.*, 2001; Buratti *et al.*, 2002). Comparison of the leading side with that of Phoebe indicates different compositions. The dark material is believed to be a complex organic solid (e.g., Bell *et al.*, 1985; Wilson and Sagan, 1995). Owen *et al.* (2001) found that the best match to the spectrum of the dark material over the range 0.3 to 3.8  $\mu\text{m}$  is provided by a mixture of water ice, amorphous carbon, and a nitrogen-rich organic compound. The latter is required to fit the strong absorption found at 3.0  $\mu\text{m}$ ; water ice alone will not suffice. Non-biogenic nitrogen-rich organics are rare, leading to the suggestion that the dark material might have been formed on Titan and transported to Iapetus by impact. If so, the surface of Hyperion may be contaminated with the same material.

The presence of  $\text{H}_2\text{O}$  ice on the surfaces of the six larger satellites, the recent detection (Noll *et al.*, 1997) of  $\text{O}_3$  on Dione and Rhea, plus the presence of unidentified UV absorption on Iapetus, suggest that further close analysis of the spectra of Saturn's satellites may reveal additional species (see Cruikshank *et al.* (1998) for a complete review). Recent results on the Galilean satellites from the Galileo spacecraft's NIMS (Near Infrared Mapping Spectrometer; McCord *et al.*, 1997) seem to indicate the presence of materials containing  $\text{CO}_2$ , C-N, C-H,  $\text{SO}_2$  and all the S-H bearing groups. It is extremely probable that similar kinds of materials, even if in very different proportions, will be found on the Saturn satellite surfaces. Recent studies of tholins have shown that the diagnostic region for organic materials extends far beyond the 5- $\mu\text{m}$  region (see, e.g., Khare *et al.*, 1994; Colthup *et al.*, 1975), where CIRS can give fundamental information.

*The small icy satellites.* Eleven satellites belong to an inner group, of which several will be observed by CIRS. Encounter geometries during the Cassini tour are not favorable for CIRS to view the smallest of these, or the recently discovered

outer irregular satellites (Gladman *et al.*, 2001). However, the first satellite we encounter will be a distant, irregular one – Pheobe.

*Phoebe* ( $r = 110 \pm 10$  km;  $p_V = 0.06$ ) is small and dark. It possesses a retrograde orbit. The spectrum of its dark material differs from that of Iapetus and Hyperion. As a likely captured satellite, its dark component may be unrelated to that of the satellites that were formed *in situ* with Saturn. Pheobe's photometric characteristics and albedo identify it as a C-type object (Simonelli *et al.*, 1999). Recently, water ice has been detected on its surface by Owen *et al.* (1999b), by Brown (2000), and by de Bergh *et al.* (2003), supporting the hypothesis of a captured primitive body related to the Centaurs or the trans-Neptunians objects.

*Hyperion* ( $164 \times 130 \times 107$  km;  $p_V = 0.3$ ) The rotation of Hyperion is chaotic; its rotation period is therefore indeterminate, though at the time of the Voyager 2 encounter it was 0.5 days (Thomas *et al.*, 1995); it is certainly nonsynchronous. The satellite's highly irregular shape indicates an intense collisional history. The dark component of its surface is as yet unidentified, but it is similar to that of Iapetus at visual wavelengths.

*Janus* ( $110 \times 95 \times 80$  km;  $p_V = 0.6$ ) and *Epimetheus* ( $70 \times 58 \times 50$  km;  $p_V = 0.5$ ) are co-orbital satellites somewhat outside the F-ring. Unexpectedly low masses are believed due to unusually low densities (Yoder *et al.*, 1989; Nicholson *et al.*, 1992). No compositional information is available, but ice is suspected to be the major component of both bodies.

An overview of CIRS's capabilities for observing the icy satellites can be obtained from Figure 23. The NESR levels for the instrument are presented for the workhorse low spectral resolution mode that will be used for surface temperature observations (4.75 s scan time,  $15.5 \text{ cm}^{-1}$  spectral resolution). Also indicated are labels for the blackbody curves corresponding to the maximum temperatures expected on each of the primary satellites. Spatial resolution will be  $<10$  km with FP1, and  $<0.3$  km with FP3 and FP4 for close flybys (Figure 22), although the ultimate spatial resolution will be limited by the ability of the spacecraft to track the rapidly passing target. The improvements over Voyager IRIS in long wavelength coverage, and in the higher sensitivity and spatial resolution in the mid-infrared ( $600\text{--}1400 \text{ cm}^{-1}$ ) have already been discussed in Section 2. From  $200$  to  $10 \text{ cm}^{-1}$  ( $50$  to  $1000 \text{ }\mu\text{m}$ ), the absorption coefficient of water ice at  $100 \text{ K}$  decreases by over two orders of magnitude, making the material progressively more transparent. In this wavelength range, the unit optical depth in pure ice moves from a physical depth of  $\sim 10 \text{ }\mu\text{m}$  to  $\sim 1 \text{ cm}$ . These values are somewhat dependent on water ice structure and temperature (Warren, 1984; Hudgins *et al.*, 1993; Matzler, 1998).

To date, information on surface composition has come from ultraviolet, visible, and near infrared spectroscopy (Cruikshank *et al.*, 1998). Water ice has been identified on all eight classical icy satellites and Titan. As noted above, ozone produced from the interaction of surface ice with magnetospheric charged particle and ultraviolet radiation, has been discovered on Dione and Rhea (Noll *et al.*, 1997). The

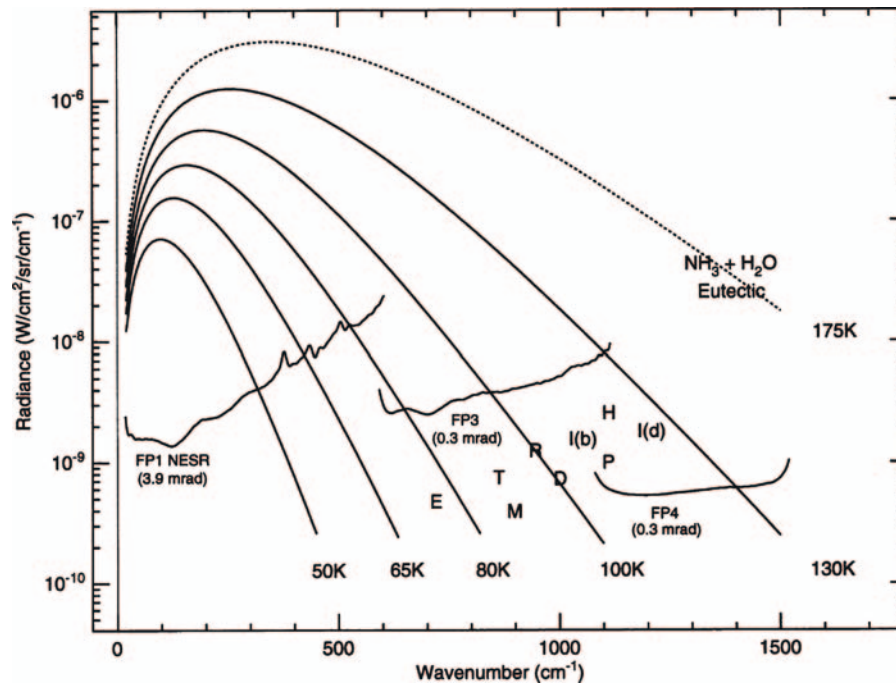


Figure 23. An overview of CIRS's capability for temperature sensing on the icy satellites. The irregular curves represent the NESR of the three CIRS focal planes (and their pixel sizes) for low spectral resolution short scans ( $15.5 \text{ cm}^{-1}$ , 4.75 sec). Blackbody curves are shown for reference. Letter symbols in the lower center of the figure lie on blackbody curves corresponding to maximum expected surface temperatures for the icy satellites; all temperatures are calculated using a thermal inertia of  $3 \times 10^4 \text{ erg cm}^{-2} \text{ s}^{-1/2} \text{ K}^{-1}$ . Temperatures are Mimas = M: 88 K; Enceladus = E: 73 K; Tethys = T: 91 K; Dione = D: 101 K; Rhea = R: 100 K; Hyperion = H: 118 K; Iapetus' (bright) = I(b): 109 K; Iapetus (dark) = I(d): 126 K; Phoebe = P: 112 K. The freezing temperature of a eutectic mixture of ammonia and water is approximately 175 K; in the event of current endogenic activity, material of this temperature might be observed.

visible spectrum of Phoebe is distinctly flatter than that of the dark side of Iapetus and of Hyperion; this puts to rest the hypothesis that the dark material on Iapetus results from the infall of dust from Phoebe (Cruikshank and Brown, 1982; Tholen and Zellner, 1983; Brown, 1983). Radar observations from Earth have revealed that the subsurface scattering properties of the bright hemisphere of Iapetus are remarkably similar to those of Titan, and very different from Ganymede, Europa and Callisto (S. Ostro, personal communication).

### 3.3.1. Regolith Properties

Information on Saturn's icy satellites from thermal infrared studies is limited (Cruikshank *et al.*, 1984). Early broadband observations were combined with photometric data to estimate satellite sizes and albedos for Rhea and Iapetus

(Murphy, *et al.*, 1972; Morrison, 1974; Morrison *et al.*, 1975), and for Hyperion (Cruikshank, 1979; Cruikshank and Brown, 1982).

The most extensive thermal infrared data on these icy satellites were obtained by the Voyager IRIS experiment (Hanel *et al.*, 1981; Hanel *et al.*, 1982; see also the summary by Cruikshank *et al.*, 1984). Useful results were obtained for Enceladus, Tethys, Rhea and Iapetus. The large flyby distances and relatively large IRIS FOV (4.4 mrad) precluded useful measurements of other satellites, and restricted the above observations to full disk or modest spatial resolution.

Only Rhea was resolved at better than disk resolution, the footprint at best covering  $25^\circ$  of latitude. At a solar phase angle of  $15^\circ$  the brightness temperature near the subsolar point was observed to be  $99 \pm 2$  K. A small correction for phase angle led to an estimate of  $100 \pm 2$  K for the subsolar temperature.

The temperature distribution across the disk was measured at low and intermediate phase angles. At  $15^\circ$  phase, the central disk brightness temperature was observed as  $99 \pm 2$  K with a gradual decrease to  $93 \pm 2$  K at the limb. Seen at phase angle  $77^\circ$ , the variation was from  $90 \pm 4$  K to  $83 \pm 4$  K. This suggests that thermal emission is peaked in the backward direction, in a manner similar to that of the Moon. Such an effect has been ascribed to macroscopic roughness (Spencer, 1990; Hapke, 1996a). It therefore appears that the large and small scale roughness of the Moon and of Rhea are similar, despite their different compositions and albedos; at Voyager resolution images suggest that this is also true on the topographic scale of a few kilometers (Smith *et al.*, 1981).

A disk observation of a solar eclipse of Rhea by Saturn was obtained. Relative to an observation made before eclipse entry, the pre-emergence flux dropped by roughly 75%, with a strong dependence on wavenumber (Figure 24). The nearly wavenumber-independent pre-eclipse brightness temperature of  $96 \pm 2$  K

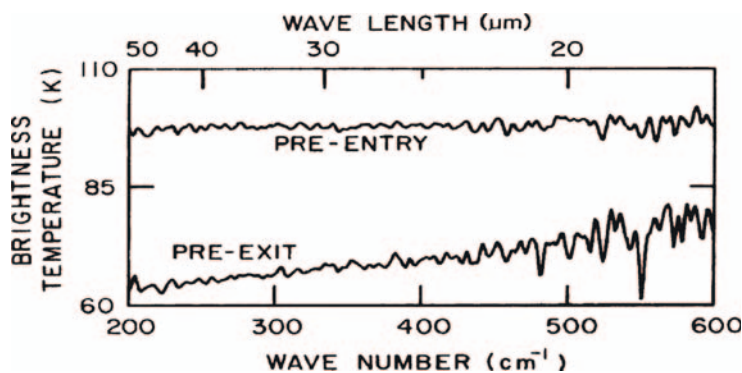


Figure 24. A solar eclipse of Rhea observed by Voyager IRIS. Before entry, the disk brightness temperature spectrum is nearly wavenumber independent; after roughly two hours in eclipse, the spectrum shows wavenumber dependent cooling, which indicates that materials with different thermal inertias are present (Hanel *et al.*, 1981).

is consistent with the spatially resolved measurements discussed above. By decomposing the spectrum in eclipse into two blackbody components, it is concluded that roughly half of the surface cools to  $\sim 75$  K, while the remainder cools to  $< 55$  K. This indicates the presence of components having different thermal inertias: a high inertia fraction of solid material with block size equal to or greater than the thermal skin depth, and a low inertia fraction, possibly frosty or fine-grained.

Striking diurnal deviations from blackbody behavior were also seen by Voyager IRIS on the icy Galilean satellites of Jupiter (Spencer, 1987). Subsolar spectra on Callisto are close to blackbodies, but those taken near the terminator show a large increase in brightness temperature with increasing wavenumber, probably due to temperature contrasts caused by uneven illumination of rough topography. Ganymede is quite different: spectra show a small increase in brightness temperature with increasing wavenumber regardless of time of day, probably due to spatial segregation of surface materials.

Full disk measurements at modest phase angles were used to infer subsolar temperatures for Enceladus, Tethys and Iapetus. To adjust for phase angle, a model for the surface temperature distribution must be used. A simple model for a slowly rotating satellite is  $T(\phi) = T_{ss} \cos^{1/n}(\phi)$ , where  $T_{ss}$  and  $\phi$  are the subsolar temperature and zenith angle of the sun, respectively. For a nonrotating Lambert sphere,  $n = 4$ ; for the Moon,  $n \approx 6$ ; a fit to the IRIS data for Rhea gives  $n \approx 7$ . Adopting the value derived for Rhea, disk measurements of Enceladus at phase angles between  $36^\circ$  and  $39^\circ$  indicate a subsolar point temperature of  $75 \pm 3$  K (including a 1 K adjustment for thermal beaming), while measurements of Tethys at phase angles between  $14^\circ$  and  $19^\circ$  indicate  $T_{ss} = 93 \pm 4$  K. Measurements of Iapetus from  $48^\circ$  and  $80^\circ$  were not corrected for the strong albedo variations across the satellite surface, and were only interpreted to indicate a temperature for the dark component in excess of 110 K.

From the derived subsolar temperatures, the bolometric Bond albedo,  $A$ , was estimated by using the equilibrium relation for absorbed solar and thermally emitted radiation for a Lambert surface with unit emissivity, on the assumption of instantaneous equilibrium with sunlight (i.e., no significant radiation of heat from the night side):

$$T_{ss}^4 = T_0^4(1 - A)/R^2, \quad (4)$$

where  $T_0$  is the equilibrium temperature for a black surface at 1 AU, taken as  $401 \pm 6$  K, and  $R$  is the distance to the sun in AU. The results:  $A_{En} = 0.89 \pm 0.02$ ,  $A_{Te} = 0.73 \pm 0.05$ , and  $A_{Rh} = 0.67 \pm 0.03$ , can be compared with values obtained from analysis of Voyager images:  $A_{En} = 0.9 \pm 0.1$ ,  $A_{Te} = 0.60 \pm 0.1$ , and  $A_{Rh} = 0.45 \pm 0.1$  (Cruikshank *et al.*, 1984). The large discrepancies for Tethys and Rhea probably result from the fact that significant heat is radiated from the night-side of these bodies, invalidating the above equation. The good agreement for Enceladus is consistent with a very bright friable surface layer that cools rapidly at night, i.e., radiates little from the night side. This is also consistent with the high single

scattering albedo, low compaction factor, and large scattering asymmetry factor derived for Enceladus from Hapke analysis (Buratti, 1985).

*Physical structure.* CIRS will combine observations of eclipses, and measurements of diurnal (orbital) and annual temperature variations to establish the vertical and horizontal structure of surface thermal inertia. From these data and the assumption of an icy regolith, the vertical profile of surface thermal conductivity can be established.

The temporal response of a passively heated surface is related to the period,  $P$ , of the radiative forcing through the thermal skin depth,  $\lambda$ :

$$\lambda^2 = Pk/(\pi\rho c), \quad (5)$$

where  $k$  is thermal conductivity,  $\rho$  is density, and  $c$  is specific heat. Thermal skin depths are shown in Table VII for typical time scales and expected densities.

At wavenumbers greater than  $200 \text{ cm}^{-1}$ , thermal radiation observed by CIRS will be emitted only from the upper few microns of the surface. Qualitatively, the mean level of the diurnal cycle of surface temperature depends on albedo, while the amplitude is a measure of the thermal inertia,  $\sqrt{k\rho c}$  (Figure 25). The spectrum of a satellite in eclipse (Hanel *et al.*, 1981; Figure 24) or at night will show significant deviations from blackbody behavior, principally due to differential cooling across a lateral distribution of materials having various thermal inertias. Spatially resolved measurements will enable these differences to be located and quantified. Remarkable spatial variations in thermal inertia have been mapped using nighttime temperatures on Mars (Mellon *et al.*, 2000), and on the icy Galilean satellites Europa (Spencer *et al.*, 1999), and Ganymede (Pappalardo *et al.*, 2004). On Europa, Galileo observations show striking and unexplained variations in thermal inertia with latitude and terrain type (Figure 26). On Ganymede, the temperature contrasts between bright and dark terrain reverse at night (dark terrain is warmer during the day, bright terrain is warmer at night), suggesting that the bright terrain contains more spatially-segregated, bright, high thermal inertia, ice than the dark terrain (Pappalardo *et al.*, 2004). On Earth's Moon, fresh craters are warmer at night than their surroundings due to the large abundance of high thermal inertia blocks on their rims (Saari and Shorthill, 1963).

TABLE VII  
Thermal skin depths associated with several natural heating periods.

Cycle	Period	$\lambda$
Eclipse	$\sim 2 \text{ h}$	$\sim 0.2 \text{ cm}$
Diurnal	$\sim 2 \text{ days}$	$\sim 1 \text{ cm}$
Annual	30 years	$\sim 70 \text{ cm}$



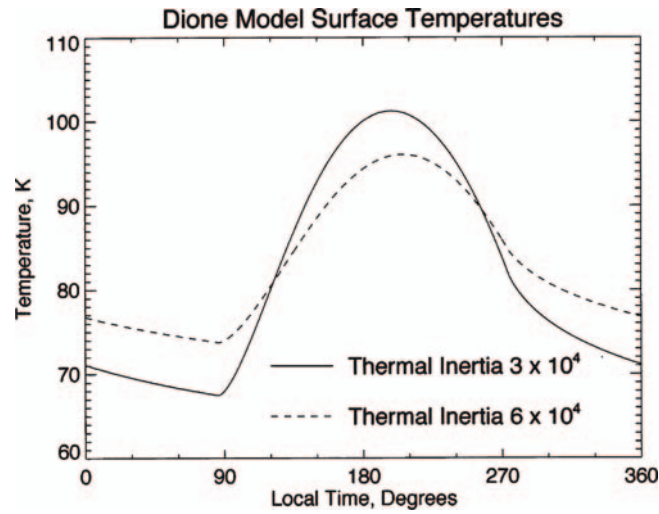


Figure 25. Example model diurnal temperatures for Dione at latitude 15 S, with the subsolar point also at 15 S. Two different but plausible thermal inertias are used to show the sensitivity of temperature to thermal inertia. Thermal inertia units are  $\text{erg cm}^{-2} \text{s}^{-1/2} \text{K}^{-1}$ . A bolometric albedo of 0.47 is assumed.

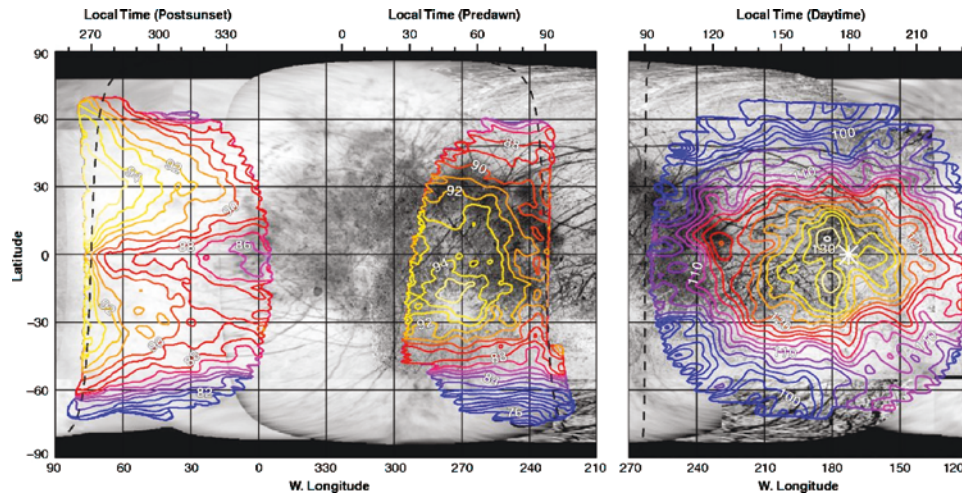


Figure 26. Contours of brightness temperature distributions on Europa. Contour interval is 1 K for the nighttime map, and 2 K for the daytime map; the color scheme is different for the two maps. Local time (top abscissa) is given in degrees of rotation past midnight. The terminator is shown by dashed black lines, and the subsolar point is indicated by a white star (Spencer *et al.*, 1999).

CIRS will obtain both full disk and spatially resolved measurements of the satellites Mimas through Phoebe (Figure 27). Observations of the dark winter north polar regions of Enceladus and Tethys will be obtained to determine the annual minimum temperatures in these regions.

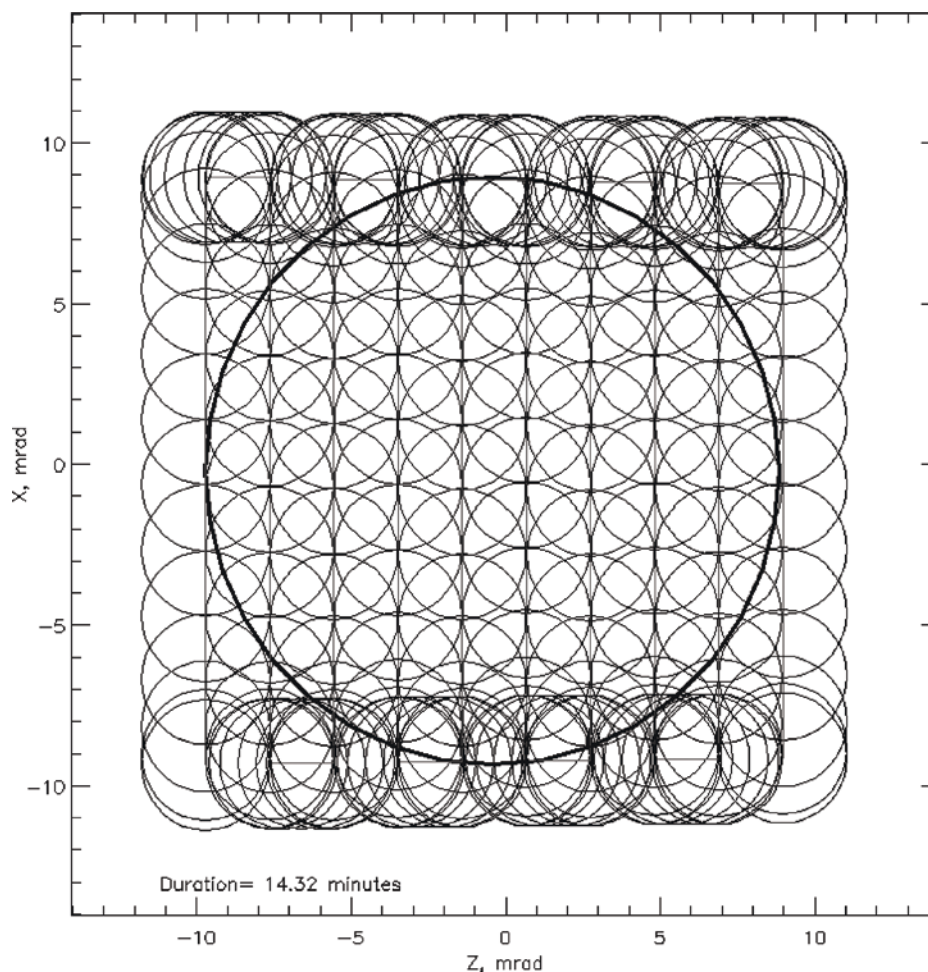


Figure 27. Idealized Nyquist-sampled FP1 map of an 18-mrad diameter disk. For frame time of 4.75 s (low spectral resolution mode) the execution time is 14.3 min. Designs of this type will be employed to map the cold dark sides of satellites to identify and quantify thermal inertia anomalies.

*Composition.* The utility of the thermal infrared region of the spectrum for determining surface composition has become increasingly well known, e.g., in the study of asteroids (see review by Sprague, 2000) and of Mars (Christensen *et al.*, 2000a,b; Bandfield, 2002; Christensen *et al.*, 2003; Hoefen *et al.*, 2003). Of special interest to Cassini will be signatures of ices and processed organics, e.g., kerogen- and tholin-like materials. In addition to fundamental and lattice modes, e.g., of  $\text{H}_2\text{O}$ , a number of group frequencies involving stretching and bending modes of C, N, O, and H in various configurations are available to CIRS below  $600\text{ cm}^{-1}$  (Socrates, 1980). The icy Galilean satellites are spectrally featureless from  $\sim 8$  to 50 microns (Spencer *et al.*, 2004), but the saturnian satellites may be different, or may show features at longer wavelengths. No useful compositional information on the

saturnian satellites was obtained from Voyager IRIS data, due to low signal to noise and to limited spectral coverage. In addition, no adequate spectral database existed at thermal wavelengths. We are now implementing laboratory studies of ices and refractory materials that will cover the spectral range from 10 to  $4000\text{ cm}^{-1}$  (1000 to  $2.5\text{ }\mu\text{m}$ ). The activity will be focused on studying the influence of mixtures of refractory material (silicates, oxides, amorphous carbon) and ice(s) ( $\text{H}_2\text{O}$ ,  $\text{CO}_2$ ,  $\text{CO}$ ,  $\text{NH}_3$ , etc.) on the reflectance and emittance spectroscopic behavior. Another important aim is to improve the knowledge on the temperature dependence of optical properties of refractory and icy materials and their mixtures (Mennella *et al.*, 1998). In the spectroscopic range above approximately  $50\text{ cm}^{-1}$  the fundamental diagnostic spectral structures (Christiansen, reststrahlen, and transparency features) are present. Moreover, at longer wavelengths spectral information on deeper layers of the surface is obtained. Detailed laboratory studies are needed to increase the database on the optical properties of different components useful for the interpretation of icy satellite spectra. Of particular interest to CIRS is the spectral range from 200 to  $10\text{ cm}^{-1}$ , where water ice becomes increasingly transparent. This offers the possibility of recording increased thermal contrast, which would accentuate the spectral signatures of minor constituents with long wavelength features such as low frequency fundamentals and lattice modes. The associated thermal gradients with depth should have much the same effect as atmospheric gradients in increasing the contrast of spectral features due to components of the medium. To exploit this, CIRS will make extensive FP1 observations at local times at which vertical thermal gradients are at their maximum. In addition, observations will be made with FP3 at very high signal to noise to accentuate subtle reststrahlen features that might be present in the  $600\text{--}1100\text{ cm}^{-1}$  (15 to  $9\text{ }\mu\text{m}$ ) region.

*Thermal structure (solid state greenhouse).* The concept of a solid state greenhouse was first considered for Io and the other Galilean satellites (Matson and Nash, 1983; Brown and Matson, 1987; Matson and Brown, 1989).

It accounts for the fact that sunlight is absorbed over a significant range of depths below an icy surface, while the opacity of ices in the thermal infrared means that thermal emission occurs only from the uppermost surface. As with an atmospheric greenhouse, mean temperature at depth may thus be higher than mean surface temperatures. CIRS can exploit the wavelength-dependent transparency of water ice beyond  $50\text{ }\mu\text{m}$  to measure vertical thermal gradients at different local times, using principles analogous to atmospheric thermal sounding. The depth to unit optical depth as a function of wavelength can be estimated using ice optical properties and regolith densities inferred from derived thermal inertias. Solid-state greenhouse effects can thus be identified or constrained.

### 3.3.2. Current Endogenic Activity

Several of Saturn's icy satellites may show evidence of recent activity unknown in other satellite systems. These include the "wispy terrain" deposits of Dione and Rhea, and the uniquely bright surface of Enceladus together with the satellite's

location in the most concentrated part of the diffuse E-ring. Each of these could be interpreted as the result of effusive or eruptive activity (though other possibilities have been considered for the relationship between Endeladus and the E-ring, e.g., Haff *et al.* (1983) or Hamilton and Burns (1994)). CIRS will search for thermal anomalies and unusual spectral signatures as evidence of current activity.

Cosmogonic arguments suggest that the saturnian satellites may have formed with up to 20% ammonia hydrate (Lewis, 1972). While evolution subsequent to accretion may have been inadequate to melt the water ice component of these bodies, it is very likely that the melting point of  $\text{NH}_3 \cdot \text{H}_2\text{O}$  ice ( $\sim 175\text{K}$ ) was exceeded (Ellsworth and Schubert, 1983). If current activity involves the liquid eutectic mixture, its thermal signature will be unmistakable in both FP3 and FP4 (Figure 23). Further, effusion or eruption of this material will be accompanied by an evaporative or ejected plume as material is released to the vacuum of space. CIRS will then be able to detect possible spectral signatures of gases and condensates in the plume, as was done with IRIS data for a plume on Io (Pearl *et al.*, 1979).  $\text{NH}_3$  has a strong broad band centered near  $1100\text{ cm}^{-1}$ . CIRS will make repeated observations of Enceladus throughout the tour. Emphasis will be on mapping the disk with FP3 and FP4, both to establish ongoing activity, and to follow its temporal behavior.

### 3.4. SATURN'S RINGS

Saturn has the most massive, extended and diverse planetary ring system in the solar system. Its three main rings (A, B, and C) span a radial distance of almost 70,000 km. A large population of particles orbits Saturn in intricate patterns with recognizable structure on all scales down to the Voyager observational limit of less than 100 m. A number of gaps fall within the main rings, some of which contain narrow ringlets. The total mass of the main rings is equivalent to the mass of the small Saturnian satellite Mimas. Four additional, much fainter rings (D, E, F and G) have been discovered thus far using ground-based or interplanetary spacecraft observations. Cuzzi *et al.* (1984) and Esposito *et al.* (1984) give comprehensive overviews.

Saturn's rings circle the planet in a region where the planet's gravitational tidal force is greater than the attractive forces between individual particles. Here the particles cannot accrete to form satellites. The origin and evolution of Saturn's rings are not well understood. Detailed measurements by the Voyager and Pioneer spacecraft provide evidence that Saturn's rings may evolve rapidly under the action of physical processes that may reduce their lifetime to less than 100 million years, a small fraction of the age of the solar system. The most efficient mechanisms for ring particle removal are erosion by meteoritic bombardment or ultraviolet radiation on ring particles, and the gravitational interactions with nearby satellites that finally drive the ring system toward the planet. However, the evolution of the rings relies on poorly known fluxes of impactors, which set the rate of erosion, and

on poorly understood physical properties of particles, which govern the outcome of interparticle collisions. If the rings are recent, a parent body would have to be destroyed in the neighborhood of the planet within the last few hundred million years, but the probability of having a close satellite disrupted on this timescale is small. Another possibility is that a comet may have been captured and destroyed by tides. However, the water ice on the surface of particles in Saturn's rings appears to be too pure to be of cometary origin, so a different parent may be needed.

Saturn's rings can be observed from Earth only over a narrow range of phase angles ( $0^\circ$ – $6^\circ$ ), which limits probing their properties. The two Voyager spacecraft did better, in that they observed Saturn's rings at phase angles ranging from  $6^\circ$  to  $155^\circ$ , two different solar elevations ( $3.8^\circ$  and  $8^\circ$ ), and over a broad range of opening angles on both the illuminated and unilluminated sides. IRIS recorded the ring's spectra between  $180$  and  $2500\text{ cm}^{-1}$  ( $55.5 - 4\text{ }\mu\text{m}$ ) with a spectral resolution of  $4.3\text{ cm}^{-1}$  and a  $4.4\text{-mrad}$  FOV on the sky. IRIS also had a single channel radiometer with a common FOV operating in the visible and near infrared,  $0.8$ – $2.5\text{ }\mu\text{m}$ .

CIRS will provide major advances over previous spacecraft infrared observations of the Saturn's rings in two respects: the extension of the spectral range to submillimeter wavelengths and the use of a linear array with much finer spatial resolution in the mid-infrared. With these new capabilities, CIRS can address many of the ring objectives of the Cassini mission, particularly those pertaining to composition, ring particle thermal properties, vertical dynamics, rotation states, and radial thermal structure. The properties of faint rings will be also explored. Cuzzi *et al.* (2002) provide a more detailed discussion of Saturn's rings and of the integrated ring measurements planned with the Cassini orbiter instruments.

#### 3.4.1. Particle Composition

Ring particle composition is a key parameter in determining scenarios for the formation of the rings and their dynamical and chemical evolution. The bulk of the ring material appears to be water ice (Pilcher *et al.*, 1970; Puetter and Russell, 1977; Epstein *et al.*, 1984). Its relatively red color at visual wavelengths requires small amounts of unidentified impurities in the surface layer of ring particles (Cuzzi and Estrada, 1998). The nature of the non-icy constituents, their link with the composition of close satellites, comets or meteoroids, and their degree of mixture with water ice all provide clues to the origin of the rings.

Voyager spacecraft images showed radial color and albedo variations across the rings (Smith *et al.*, 1982; Dones *et al.*, 1993; Doyle *et al.*, 1989; Estrada and Cuzzi, 1996). The A and B rings appear redder than the C ring and the Cassini division. The radial color variations likely indicate variations in composition (Estrada and Cuzzi, 1996). The most probable candidates are silicates, iron oxides or organics, which may account for the features in the observed spectrum not attributable to water ice (Clark and McCord, 1980). Recent modeling of the visual and near-infrared composite spectrum has favored a surface composed of an intimate mixture of water ice with a few percent of organic tholins, with the adjunction of traces of



segregated amorphous carbon grains (Poulet and Cuzzi, 2002). This supports the studies by Cuzzi and Estrada (1998), which showed that the radial color variations of main rings were consistent with the pollution of this same kind of intimate mixture from carbonaceous material brought in by interplanetary debris. While this intrinsic composition is supported by observations, the organic contaminants have not been unequivocally identified (Poulet and Cuzzi, 2002). The ability of organics to explain observations further in the infrared or in the radio wavelength domain has yet to be tested. Finally, ground-based thermal infrared spectroscopy in the 8–13  $\mu\text{m}$  window seems to rule out the presence of silicates in Saturn's rings (Lynch *et al.*, 2000). Voyager IRIS saw no spectral structure out to 50  $\mu\text{m}$  (Hanel *et al.*, 1981, 1982). Future measurements by the CIRS instrument will produce additional submillimeter temperatures at a variety of geometries.

At 100 K the absorption coefficient of water ice decreases by over two orders of magnitude from  $200\text{ cm}^{-1}$  to  $10\text{ cm}^{-1}$  (50 to 1000  $\mu\text{m}$ ), making the material progressively more transparent (Section 3.3). This decrease is primarily responsible for the dramatic variation in the long-wavelength spectrum of Saturn's rings, which changes from nearly blackbody emission at 20  $\mu\text{m}$  to essentially reflected planetary radiation by 1 cm (Figure 28). The ring emissivity is therefore very dependent on the fraction of other non-transparent materials. Ring particles have low emissivity

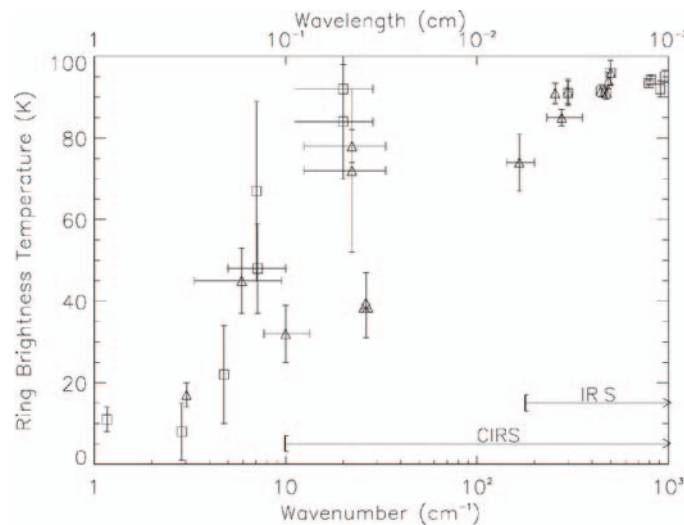


Figure 28. Brightness temperatures of Saturn's B ring for ring tilt angles  $\phi > 25^\circ$  (squares) and  $\phi$  between  $20^\circ$  and  $25^\circ$  (triangles) relative to the sun. Between wavelengths of 50  $\mu\text{m}$  and 1 mm ( $200\text{ cm}^{-1}$  and  $10\text{ cm}^{-1}$ ), the absorption coefficient for water ice at 100 K decreases by a factor  $\sim 10^4$ , making the material progressively more transparent. This gives CIRS the ability to probe icy material to various depths, providing a powerful tool for the investigation of the composition and physical properties of this material. The open symbol data can be found tabulated in Esposito *et al.* (1984). The triangle with the embedded asterisk is from Roellig *et al.* (1988).



and high reflectivity in the radio wavelength range and essentially scatter planetary radiation (De Pater and Dickel, 1991). Interpretation of microwave observations, which also sample the bulk of the ring mass by this effect, constrain the mass fraction of the non-icy silicate material to be less than 10% (Epstein *et al.*, 1984); it could be as low as 1% if uniformly mixed (Grossman *et al.*, 1989). Ground-based observations in the 100- $\mu\text{m}$  to 1-mm region are sparse and difficult because of the absorption of water vapor in the Earth's atmosphere. Very broad beam observations, which also suffer from a blending of planetary and ring signals, show that the ring brightness temperature rolls off somewhere in this wavelength region. For example, the B ring brightness temperature changes from 90 K at 20  $\mu\text{m}$  to near 10 K at centimeter wavelengths (Esposito *et al.*, 1984; Cuzzi *et al.*, 1984; Haas *et al.*, 1982). Exactly where the spectrum turns over is not known. Some broadband observations (Courtin *et al.*, 1979; Whitcomb *et al.*, 1980; Cunningham *et al.*, 1981) seem to imply that the spectrum remains flat out to  $\sim 400 \mu\text{m}$ , before particle-size-related effects decrease the emissivity. However, later work by Roellig *et al.* (1988) at 380  $\mu\text{m}$  ( $26 \text{ cm}^{-1}$ ) seems to indicate that there may be a gradual decrease in observed ring brightness temperature from the infrared into the radio. Roellig's values are about a factor of two smaller than values determined by the authors listed above.

Thanks to its unique sensitivity in a broad spectral range (Table I) and its good spatial resolution throughout the Cassini tour, CIRS will have the ability to probe icy ring particles to various depths, thus providing a powerful tool for the investigation of their composition and the way it varies with distance to the planet. Although the spectral signatures of C-H-N-rich organic material are mostly located in the near-infrared domain, some are still detectable in the mid-infrared, by the signature of stretch vibrations of N-H single bonds at  $750 \text{ cm}^{-1}$  (13  $\mu\text{m}$ ) for example. Silicate features, if any, may also be detected near 10  $\mu\text{m}$  and 20  $\mu\text{m}$ . The ring material may contain clathrate hydrates of ammonia and methane. The current observations in the near infrared cannot rule them out, because their spectral signatures are masked by water bands (Puetter and Russell, 1977). Identification of clathrate hydrates is only possible in the mid and far infrared where specific features can be distinguished from water and guest molecule signatures (Hudson and Moore, 1993). But laboratory determinations of optical constants in the far infrared of possible constituents (ammonia, methane clathrate hydrates) are required to identify them accurately. Any detection of clathrate hydrates in the mid and far infrared would imply a recent resurfacing of ring particles, as the lifetime of these volatiles should be strongly reduced by sputtering. Cubic crystalline water ice has been identified at the surface of Saturn's ring particles (Grundy *et al.*, 1999). The presence of amorphous ice is not ruled out yet. Condensing at low pressure and temperature (between 40 and 70 K), water ice adopts an amorphous state. If warmed gradually, it is irreversibly transformed into cubic crystalline ice above 110 K and then into hexagonal ice above 150 K (Smith *et al.*, 1994). If formed at a temperature greater than 110 K, solid structure of water ice particles remain crystalline despite their

actual lower temperature (90 K). Absorption features of crystalline water ice at 44 ( $227\text{ cm}^{-1}$ ) and  $62\text{ }\mu\text{m}$  ( $161\text{ cm}^{-1}$ ), which disappear in the amorphous state, may be then strong indicators of possible scenarios of ring particle formation. They may be detected in the CIRS spectrum if the regolith particle size is small enough.

### 3.4.2. *Thermal Properties of Ring Particle Surfaces*

The dynamics and evolution of rings strongly depend on the outcome of interparticle collisions and on the self-gravity of the rings. Energy loss, mass transfer, and sticking probability for relevant impact velocities will favor either aggregation or disruption and erosion of particles, modifying the size distribution and velocity dispersion, and thus the dynamics and structure of the rings. Saturn's rings consist of a vast array of irregular centimeter-sized to house-sized particles, the bulk of the ring mass concentrated in particles with radii of a few meters (Marouf *et al.*, 1983). A single ring particle has never been observed because of the limited spatial resolution of spacecraft instruments (e.g., a few kilometers for Voyager). Surface properties that largely constrain the result of a collision can therefore only be inferred from indirect observations. Reflectance models applied to visible and near-infrared spectra of Saturn's rings support the idea of particles covered by a regolith of  $50\text{ }\mu\text{m}$ -sized grains on average (Pollack *et al.*, 1973; Pilcher *et al.*, 1970; Clark and McCord, 1980; Poulet and Cuzzi, 2002). Recent analysis of the phase function of Saturn's rings near opposition suggests that A and B ring particles are significantly rougher than those in the thin C ring, maybe lumpy particles, still covered with micron-sized particles (Poulet *et al.*, 2002).

Measuring the thermal inertia of ring particles is an indirect and independent method to explore the structure of the ring particle surface. The thermal inertia can be obtained from observations of transient changes in temperature as ring particles cross the planetary shadow boundaries or at their surfaces as they rotate. This experiment has been proposed initially by Aumann and Kieffer (1973) to measure the ring particle sizes. Ground-based observations at  $20\text{ }\mu\text{m}$  in the early 1980's of the heating rate of B ring particles after eclipse behind Saturn (Froidevaux *et al.*, 1981) have constrained their thermal inertia to be very low, as low as the thermal inertia of Galilean satellites, if the particles are centimeter-sized. Pioneer measured a 15-K drop in temperature of the C ring during eclipse and less than 12 K for the A ring (Froidevaux and Ingersoll, 1980) confirming this qualitative estimate. From the observed heating curves at  $20\text{ }\mu\text{m}$ , Ferrari *et al.* (2003) have quantitatively estimated the thermal inertia for the B and C rings to be  $3.5 \pm 1.2\text{ Jm}^{-2}\text{K}^{-1}\text{s}^{-1/2}$  and  $6.3 \pm 3.0\text{ Jm}^{-2}\text{K}^{-1}\text{s}^{-1/2}$ , respectively. They are very similar to the thermal inertia of Centaur objects like Chiron or Asbolus. They correspond to very low thermal conductivities, of the order of  $10^{-5}$ – $10^{-4}\text{ W m}^{-1}\text{ K}^{-1}$ , depending on the actual porosity of the layer. These thermal properties are consistent with a frosty regolith, fractured by cracks from collisions or thermal stresses, or alternatively with very porous particle aggregates. The estimates have assumed an energy balance typical of slowly spinning particles, but did not account for the anisotropy of the heating

on their surfaces along their orbits. In general the particle surface temperature and thermal emission vary on the surface along the rotation axis (“latitude”) and azimuthally (“longitude”). A new model is being developed to use the crossing of the shadow and the day/night anisotropic emission to recover both the spin and thermal inertia of spherical particles from observations at different phase angles (Leyrat *et al.*, 2003).

Ground-based observations are limited to phase angles smaller than about  $6^\circ$ , but observations by the Voyager 1 IRIS spectrometer cover both low and high phase angles. The new model has recently been applied to IRIS observations of the C-ring particles passing into Saturn’s shadow (Spilker *et al.*, 2003; Leyrat *et al.*, 2003). However, the data are limited in the azimuthal sampling of the cooling and heating curves, and in phase-angle coverage. This makes it difficult to derive spin and thermal properties of the ring particle surface unambiguously. The 4-year-long Cassini tour will provide the geometries, azimuthal and radial sampling necessary to address these problems. The first minutes of both the cooling and heating curves will be observable. Measurements just at the entry and exit from the eclipse allow one to test the heterogeneity of the individual particles, i.e., whether the thermal conductivity changes between the first few millimeters below their surface and their interior. A change in the cooling/heating rates in these periods may appear depending on the thickness of a low-thermal-inertia surface layer on an eventually more compact core. Energy transport in regoliths depends on the compactness of the layer and the possible existence of fractures that prevent heat propagation, and also on the size, optical and thermal properties of the regolith grains (Hapke, 1996a,b; Snyder-Hale and Hapke, 2002). CIRS will also address the question of the regolith grains by studying their emission as a function of wavelength for the main rings.

### 3.4.3. Ring Vertical Dynamics and Particle Spins

The Voyager observations in the early 1980’s revealed numerous radial and azimuthal structures in the disk of Saturn’s rings that are the fingerprints of the physical processes at play. Known gravitational interactions with nearby satellites can explain fine to medium scale structures in the rings, e.g., spiral density waves (horizontal perturbations), bending waves (vertical perturbations), satellite wakes, or eccentric ringlets. The observation of these phenomena helps both in understanding local dynamical properties, such as viscosity, random velocities, and vertical height, of the ring layer, and in understanding the physics and efficiency of the processes involved. The scale height is directly related to the particle size, particle spin, and Keplerian velocity (Cuzzi *et al.*, 1984).

*Vertical structure.* Voyager radio and stellar occultation measurements place upper limits of 150–200 m on ring thickness in the main rings (Tyler *et al.*, 1981; Lane *et al.*, 1982). Locally this may be caused by waves excited by outer satellites. Studies of bending waves give smaller estimates, with a local thickness of about 30 m in the A and B rings (Shu *et al.*, 1982) and perhaps as low as 1 m in the C ring (Rosen, 1989). The A and B rings may thus be many-particles thick, whereas the

thin C ring appears to be a monolayer. The compatibility of the multilayer structure with Voyager observations at high phase angle is questionable (Dones *et al.*, 1993). Cuzzi *et al.* (2002) use HST observations to show that vertical structure may vary with location and the multilayer structure may not always be applicable.

The vertical thermal structure in the rings can constrain the typical ring scale height, as the temperature depends on the mutual shadowing and penetration of the sun's rays into the ring layer(s). A thermal gradient between the lit and unlit face of the rings should exist across a many-particle-thick ring. The brightness temperature of the unlit face of Saturn's rings at  $45\ \mu\text{m}$  was first measured by Pioneer (Froidevaux and Ingersoll, 1980). The determined value of  $54 \pm 3\ \text{K}$  was confirmed by Tokunaga *et al.* (1980) from ground-based observations at  $20\ \mu\text{m}$  with a brightness temperature of  $56 \pm 1\ \text{K}$  for the B ring. Tokunaga *et al.*, suggest that this temperature may originate solely from Saturn's visual and thermal illumination and does not require a supplementary heating by scattered solar light. How this gradient varies from the thin C ring or the optically thick A ring is unknown. Several ground-based observations at mid-infrared wavelengths in the 70s and 80s have shown that the lit face temperature increases with solar elevation for the optically thick A and B rings but decreases weakly for the less opaque C ring. Many thermal models have been elaborated to reproduce these observations, including alternatively mono- or many-particle-thick layers, and vertical inhomogeneity (Froidevaux, 1981; Kawata, 1983), but nothing definitive can be concluded. The objections about a possible monolayer structure for the C ring (Esposito *et al.*, 1984) have been overturned by recent ground-based observations in the thermal infrared (Ferrari *et al.*, 2003). In brief, the actual vertical structure of Saturn's main rings is uncertain. Viewing geometries have to be diversified to separate both types of vertical structures, most particularly how the brightness temperature varies with the elevation of the observer at fixed solar elevation and phase angle.

*Vertical Dynamics.* Ring particles, as they collide, are tumbling around the mid ring plane with a vertical excursion governed by the local dynamics. The ring scale height is one measure of this maximum dispersion. The thermal history of a particle along its orbit is also a marker of vertical dynamics. It is conditioned by the time it spends under sunlight and in the planetary shadow. Its ability to warm up at the exit of the shadow is a function of the average time it spends in the shadow of its neighbors, which is controlled by its vertical dynamics. Any difference in the heating curve between faces will reveal asymmetry in the time spent on each face by particles.

*Particle spins.* The actual distribution of particle spins in Saturn's rings is unknown. Most of the numerical simulations which have been developed to study this aspect are limited to monodispersed size distributions. The spin is prograde in the planet-fixed frame. The average spin value in the direction perpendicular to the ring plane and in a frame rotating with the particle at mean motion  $\Omega$  is  $\omega/\Omega \sim 0.3$  (Araki, 1991; Salo, 1995; Richardson, 1994). This number is fixed by the spatial distribution of impacts on the particle. The dispersion around this value is highly

dependent on friction, energy loss or on the optical depth. When gravitational scattering is taken into account,  $\omega/\Omega \sim 0.66$  in regions when particle clusters can form, in the A ring for example (Salo, 1995). If small particles are added to the simulation, they spin faster and have a wider distribution of spins (Richardson, 1994). The spinning rate of ring particles can be estimated qualitatively from observations with a simple energy balance equation. Both monolayer and multilayer thermal models of Saturn's rings suggest slow rotators for the main rings (Froidevaux, 1981, Kawata and Irvine, 1975; Ferrari *et al.*, 2003; Spilker *et al.*, 2003). Slowly rotating particles means that particles are essentially emitting over just one hemisphere, so that the day/night temperature contrast is important. A thermal model is currently being developed to determine whether results of numerical simulations are compatible with current observations in the thermal infrared (Leyrat *et al.*, 2003).

#### 3.4.4. Radial Thermal Structure

Ring opacity and temperature as a function of wavelength and radial distance from Saturn are important CIRS ring objectives. The radial and angular distributions of thermal flux from the rings provide a measure of ring opacity as a function of wavelength for various regions in the rings. Except for the C-ring, only crude estimates of ring opacity were derived from Voyager infrared data (Hanel *et al.*, 1981; Hanel *et al.*, 1982). CIRS will be able to determine ring opacity for all of the rings at high spatial resolution and over a broader range of wavelengths. These observations will provide the missing data on ring opacity from UV to radio wavelengths from which a detailed particle size distribution will be finally derived. The radial dependence of the size distribution in the disk is a key parameter to predict its reaction to perturbations and then its dynamical evolution.

The ring particles reveal their true physical temperatures at wavelengths of 10 to 30  $\mu\text{m}$ ; at 20  $\mu\text{m}$  their emission (and measured brightness temperature) is very close to blackbody emission. The physical temperatures of the A and B rings are similar while the C ring and Cassini Division temperatures can be slightly higher. This behavior is consistent with lower visible albedoes observed for the C ring and Cassini Division (Smith *et al.*, 1981; Cooke, 1991). The lit sides of the A and B rings exhibit a pronounced decrease in temperature with decreasing solar inclination. As the solar inclination decreases, the densely packed ring particles in these higher optical depth rings begin to shadow one another, resulting in a decrease in overall ring temperature. Temperatures range from 90 K near maximum solar inclination to less than 60 K as the solar inclination approaches zero. On the other hand, the C ring brightness temperature increases slightly with decreasing solar inclination as a result of its low optical depth and increased filling factor. Temperatures range from 80 K to almost 90 K when the solar inclination is near its minimum. The temperatures on the unlit sides of the A and B rings are typically less than 60 K. With its low optical depth, the C ring temperature is similar on both the lit and unlit sides of the ring. Figure 29 shows the CIRS NESR per minute of integration time for spectral resolutions of 0.53, 3.0 10.0 and 15.53  $\text{cm}^{-1}$ . CIRS can easily

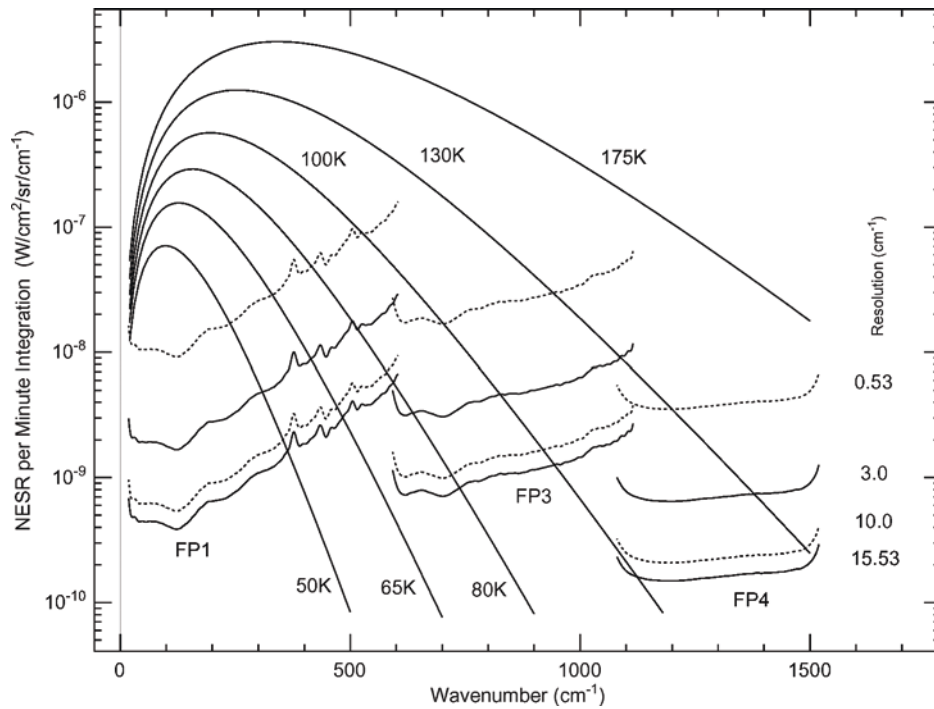


Figure 29. Planck radiances over the full CIRS spectral range for various temperatures. Superposed is the CIRS NESR for several spectral resolutions, assuming one minute of integration time. Ring temperatures vary from 60 K to 90 K, as a function of the solar illumination angle and of the lit or unlit sides of the rings. Comparison with the brightness temperatures of the rings shown in Figure 28 indicates that CIRS has the sensitivity to adequately probe the sub-millimeter portion of the rings' spectra.

measure the brightness temperatures of the main rings. Decreasing temperatures in the submillimeter region will make measurements in this region more challenging (see Figure 28 for submillimeter temperatures).

Brightness temperatures and optical depths were obtained from the IRIS spectra for the A, B and C rings (Hanel *et al.*, 1982). The ring was modeled as a simple, homogeneous, non-backscattering slab (multilayer) that radiates as a blackbody. For the unlit C ring the derived brightness temperature was  $85 \pm 1$  K, and the optical depth was  $0.09 \pm 0.01$ , consistent with the values obtained by Froidevaux and Ingersoll (1980) from Pioneer data. Brightness temperatures for the A and B rings are 50 K to 60 K for the unlit A ring, <50 K for the unlit B ring and 70 K to 75 K for the lit B ring. These data are uncorrected for optical depth and geometry, so they represent lower limits on temperature. Normal optical depths for the Cassini Division, A and C rings were in agreement with Voyager and ground-based values at shorter wavelengths (Smith *et al.*, 1981; Froidevaux and Ingersoll, 1980; Sandel *et al.*, 1982). The higher temperatures of the C ring and Cassini Division particles



are consistent with their lower visible albedos. Esposito *et al.* (1984) and Cuzzi *et al.* (1984) review in greater detail the observations of thermal radiation at wavelengths  $\sim 10\ \mu\text{m}$  to  $\sim 1\ \text{cm}$  from Saturn's ring particles.

More recent work on the radial thermal structure of the C ring has been done by Spilker *et al.* (2003) assuming that the ring particles are in a monolayer. Temperatures were found to decrease with increasing radial distance in the inner C ring, flatten somewhat in the middle of the unlit C ring and then decrease further in the outer C ring. For an albedo of 0.24 the slight decrease in temperature in the C ring can be mostly explained by including the Saturn visible and thermal contributions. Using this same albedo (0.24), the inner C ring is slightly warmer and the outer C ring is slightly cooler than the model. This implies either that the albedo is not constant throughout the C ring or some other geometric factor must be considered. The downward trend in temperature with increasing radial distance is consistent with previous measurements: temperatures decrease and albedoes increase from the inner to the outer C ring (Cooke 1991). It is also consistent with the optical depth trend since the innermost particles are least shaded and are the warmest.

#### 3.4.5. *Faint Rings*

In addition to the main A, B and C rings, Saturn has four much fainter rings, designated D, E, F and G. All are composed primarily of micron-sized dust and have optical depths  $\tau$  ranging from 0.1 down to  $\sim 10^{-6}$ , compared to  $\sim 1$  for the main rings. Dust grains in the Saturn system are expected to have very short lifetimes, due to a variety of removal and destruction mechanisms including solar radiation pressure, electromagnetic perturbations and drag forces, micrometeoroid erosion, and sputtering. Hence, the dust in these rings must be continuously replenished from (often unseen) embedded populations of "parent" bodies. See Burns *et al.* (2001) for a thorough review of the physical processes at work in these rings.

The D ring occupies the region interior to the C ring. It consists of two narrow ringlets surrounded by broad belts of fainter material with  $\tau \sim 10^{-5}$  (Showalter, 1996). The F ring comprises a set of narrow strands orbiting 3000 km outside the A ring. In the finest-resolution images from Voyager, this ring showed peculiar structures variously described as kinks, clumps and braids (Smith *et al.*, 1981). These structures are probably related to gravitational perturbations from the nearby "shepherding" moons Prometheus and Pandora, although the details remain mysterious. This ring shows peak  $\tau \sim 1$  but only over very narrow strands of  $\sim 1\ \text{km}$  width; more typical  $\tau$  values range from 0.1 to 0.01 (Showalter *et al.*, 1992). Next outward, the G ring is an isolated, 6000-km-wide band centered 168,000 km from the center of Saturn. It is the faintest ring component, with  $\tau \sim 10^{-6}$  (Showalter and Cuzzi, 1993). It was discovered in charged particle absorption signatures by Pioneer 11 (Van Allen, 1983) and imaged briefly during the Voyager encounters (Smith *et al.*, 1981). Finally, Ring E is the largest ring in this (or any) system, extending from inside Mimas's orbit to beyond the orbit of Dione. It is also vertically extended, with

a thickness varying from 6,000 km to 40,000 km at its outermost edge (Showalter *et al.*, 1991). Its  $\tau$  is very low,  $10^{-5}$ – $10^{-6}$ , with a distinct maximum near the orbit of Enceladus, which probably serves as its major source body (Horanyi *et al.*, 1992; Hamilton and Burns, 1994).

All of the aforementioned physical processes at work in these rings depend strongly on the sizes of the dust particles (and on the charge-to-mass ratio, which itself varies with size). For this reason, the distribution of dust sizes in faint rings is a critical parameter for understanding these rings' origin and dynamics. To date, our understanding of the particle sizes is based on photometric modeling of the (typically very limited) visual and near-IR observations from Earth and Voyager. Thermal emission from these rings has never been detected.

Most visual photometry is difficult to interpret for particle sizes because additional particle properties (most significantly, shape) can substantially alter the light-scattering properties of a ring population. Cassini CIRS has a distinct advantage over visual and near-IR observations in that it will be observing the faint rings at wavelengths comparable to or greater than the sizes of the constituent particles. In this regime, the effects of particle shape are negligible, simplifying the interpretation of the data. The thermal emission from these rings is expected to drop off at longer wavelengths, owing to the diminishing thermal emissivity of grains as the wavelength approaches and exceeds the particle size. This dropoff should be readily observed in the data, so CIRS holds out the possibility of providing unique and important new constraints on the dust in Saturn's faint rings.

## 4. CIRS Observations

### 4.1. OBSERVING STRATEGY

CIRS is versatile and complex. It has a commandable spectral resolution, the ability to view in both nadir and limb modes, and different fields of view in the mid and far infrared. This requires careful planning of observations. The angular sizes of the mid- and far-infrared fields of view dictate the distances particular measurements are made of the target body. The mid-infrared array pixels, being smaller, can be the drivers for useful observations further out than the larger far-infrared focal plane. For nadir observations, useful mapping can be achieved on a planet or satellite when the FOV subtends a few degrees of latitude. When limb sounding an atmosphere, best results are obtained when the FOV subtends a pressure scale height or less. Thus, for example, limb sounding of Titan can be usefully executed 5–9 h from closest approach in the mid-infrared (FP3 & FP4), but only within 2 h of closest approach in the far-infrared (FP1). Nadir maps in the mid-infrared will usually be done 12–28 h from closest approach (see below).

There is a tradeoff between spectral resolution and integration time that must be optimized by considering the scientific objective. The instrument noise, or the

Noise Equivalent Spectral Radiance (see Section 5.6.1), varies as

$$NESR \propto \frac{1}{\Delta\nu\sqrt{t}} \quad (6)$$

where  $\Delta\nu$  is the spectral-resolution element in  $\text{cm}^{-1}$  determined by the interferogram scan length, and  $t$  is the integration time (Hanel *et al.*, 2003). Observations to retrieve the abundances of trace atmospheric constituents generally require the highest available spectral resolution, because the targeted features are unresolved, and the signal (line – continuum) scales as  $1/\Delta\nu$ . Although the NESR is greater for a given integration time (because  $\Delta\nu$  is smaller), the SNR scales simply as  $\sqrt{t}$ . Hence, the search for new species entails long integrations. These tend to be done at larger distances from the target body, when there is more time available and fewer conflicts with other scientific objectives. However, other observations, for example the retrieval of vertical profiles of atmospheric temperature and aerosols, can be done with lower- resolution spectra and shorter integration times, allowing more extensive spatial mapping closer to the target body. In this case, the spectral features are either resolved (e.g., the pressure-induced lines of  $\text{H}_2$  on Saturn, for tropospheric temperature sounding) or resolved sufficiently for the retrieval (e.g., the manifolds of the P, Q, and R branches of the  $\nu_4$  band of  $\text{CH}_4$ , for sounding the stratospheric temperatures of Saturn and Titan). In this case the signal is just the Planck radiance at the effective emission level, and it is independent of the spectral resolution. The SNR then scales as  $1/\text{NESR}$ . One could in principle still use only the longest interferometric scans corresponding to the highest-resolution spectra, and then average adjacent wavenumbers in these spectra to achieve a higher SNR. However, there is a penalty in doing this. The gain in SNR is  $\sqrt{\Delta\nu_L/\Delta\nu_H}$ , where  $\Delta\nu_H$  denotes the spectral resolution of the original spectrum and  $\Delta\nu_L$  that for the spectrally averaged one. If shorter scans corresponding to  $\Delta\nu_L$  are used instead, the gain in SNR is greater,  $\Delta\nu_L/\Delta\nu_H$  from (6), because in this case no information from the scans has been discarded. Hence, it is generally more efficient for the interferometric scan lengths to be tailored to the spectral resolution required for the retrieval problem at hand.

#### 4.2. SATURN

The 4-year Cassini tour has 74 orbits of Saturn, and it provides the opportunity to map Saturn's atmosphere globally, including looking for time variations over the life-span of the mission. This is aided by the varying geometry. For example, the inclinations of the orbits range from near equatorial to almost  $78^\circ$  near the end of the nominal tour. The bulk of the orbits have apoapses in the range  $20\text{--}70 R_S$ , and periapses in the range  $2.4\text{--}16 R_S$ . Figure 30 depicts typical CIRS observations of Saturn at different ranges from the planet. These correspond to the entries in the last column of Table II, which are linked to the major scientific objectives

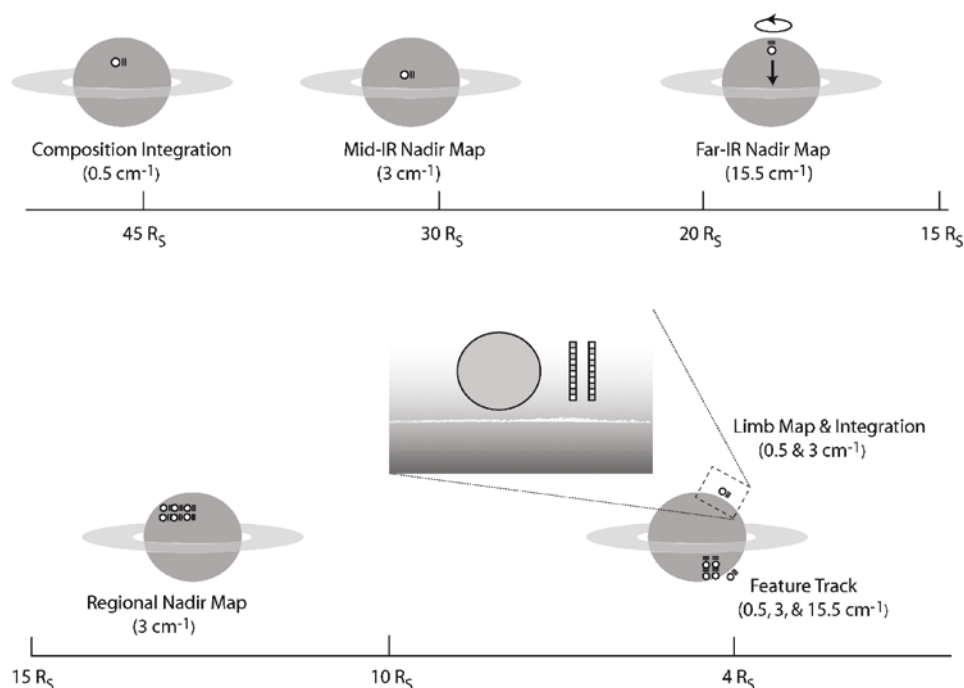


Figure 30. CIRS observations of Saturn at different ranges from the planet. Within a range of  $32 R_S$  the CIRS fields of view are smaller than indicated, relative to Saturn's disk.

and measurement targets. The measurement objectives dictate the required spatial resolution (hence range to Saturn) and the spectral resolution used. Moving toward the planet, the observations are:

- *Composition integrations.* Typically done  $\sim 45 R_S$  from Saturn, the individual mid-infrared pixels (FP3, FP4) subtend  $0.8^\circ$  of planetocentric arc on Saturn at the subspacescraft point. The arrays are aligned north-south, so they span 10 times that arc, or  $8^\circ$  of latitude at the subspacescraft point. The far-infrared focal plane, FP1, covers approximately  $10^\circ$  of latitude. The arrays are held fixed over one or more Saturn rotations. The spectral resolution is  $0.5$  or  $1.0 \text{ cm}^{-1}$ , and generally spectra will be averaged over longitude. The resulting long integrations will map the latitude distribution of the oxygen compounds  $\text{H}_2\text{O}$  (in FP1) and  $\text{CO}_2$  (in FP3) and of stratospheric hydrocarbons (in FP3), such as  $\text{C}_3\text{H}_4$  and  $\text{C}_4\text{H}_2$ . The integrations will also be used to search for new tropospheric species (in FP1), such as  $\text{HCP}$ ,  $\text{H}_2\text{S}$ ,  $\text{H}_2\text{Se}$ , and the halides.  $\text{PH}_3$  can be mapped both in the far- and mid-infrared (FP1 and FP3). Isotopic ratios, such as  $[\text{HD}]/[\text{H}_2]$ ,  $[\text{CH}_3\text{D}]/[\text{CH}_4]$ ,  $[\text{C}^{13}\text{CH}_4]/[\text{C}^{12}\text{CH}_4]$ ,  $[\text{C}^{13}\text{C}^{12}\text{CH}_6]/[\text{C}_2\text{H}_6]$  can be simultaneously retrieved from the

integrations. Because the fields of view do not cover Saturn's disk, latitude distribution must be composited from several integrations made over the tour.

- *Mid-IR nadir maps.* Executed  $\sim 30 R_S$  from Saturn, these have somewhat higher resolution than the composition integrations, but the attitude of the fields of view is identical. In this case the arrays span a  $5^\circ$ -latitude band (pixel resolution  $0.5^\circ$ ) as Saturn rotates. The spectral resolution of the maps is  $3 \text{ cm}^{-1}$ , and there is sufficient signal-to-noise to provide longitude-latitude maps of temperatures in the tropopause region and in the upper stratosphere, using the FP3 and FP4 radiances. The latitude mapping must be composited from latitude bands acquired during the tour. Most latitudes will be observed at least two times during the tour to obtain median-term temporal variations. Individual bands will be observed for two successive rotations or longer to characterize short-term variations and also to determine the zonal phase velocities of coherent structures, such as waves. In addition to temperatures, the more abundant hydrocarbons, such as  $\text{C}_2\text{H}_6$  and  $\text{C}_2\text{H}_2$ , and tropospheric compounds, such as  $\text{PH}_3$ , will be mapped.
- *Far-IR nadir maps.* These are driven by temperature mapping of the troposphere in the far infrared, down to approximately the 1-bar level (Figure 4). A spectral resolution,  $15.5 \text{ cm}^{-1}$ , is adequate for this purpose. This and the fact that the far-infrared portion of the spectrum is closer to the peak of the Planck function than the mid infrared means that shorter integration times are required. As a result, the fields of view can be scanned across Saturn. The scans are north-to-south scans (or vice versa) with flybacks. A scan rate of  $0.25 \text{ mrad s}^{-1}$  ensures a precision in the brightness temperature of 0.3 K. The requirement that successive scans be adjacent in longitude implies that they can only cover one hemisphere (northern or southern) as the planet rotates. Scanning over two or more rotations will provide information on short-term temporal variability and on the velocities of propagating waves. The mapping sequences are typically centered at  $16\text{--}20 R_S$ , where FP1 subtends  $4^\circ\text{--}5^\circ$  of planetocentric arc at the subspacecraft point. Although FP1 is the driver in these maps, temperatures in the upper troposphere and tropopause region can also be retrieved using the  $\text{H}_2 \text{ S}(1)$  line over the  $600\text{--}670 \text{ cm}^{-1}$  portion of FP3 (the spectral resolution is too coarse to resolve the Q-branch of the  $\nu_4$  band of  $\text{CH}_4$  in FP4). Hence the arrays are aligned east-west for the north-south scans. Averaging the FP3 pixels provide both a good SNR and spatial resolution comparable to that afforded by FP1.
- *Regional nadir maps.* Similar to the mid-IR nadir maps described earlier but limited in time, these are executed at higher spatial resolution for select regions, e.g., a portion of the ribbon wave near  $40^\circ\text{N}$ . Typically done at a range of  $12\text{--}15 R_S$ , the individual FP3 and FP4 array pixels subtend  $0.2^\circ\text{--}0.3^\circ$  and FP1  $3^\circ$  of planetocentric arc at the subspacecraft point. At  $3 \text{ cm}^{-1}$  spectral resolution, stratospheric and tropospheric temperatures can be retrieved, as well as information on the spatial distribution of  $\text{PH}_3$ ,  $\text{NH}_3$ , and major stratospheric hydrocarbons. At  $0.5 \text{ cm}^{-1}$ ,

better determinations of these gaseous constituents can be made, as well as of trace constituents and new species.

- *Limb maps.* Only the FP3 and FP4 pixel arrays have the spatial resolution to observe Saturn in the limb mode with approximately one scale-height resolution (60 km), and this must be done near periapsis. For these the arrays are aligned normal to the limb. A spectral resolution of  $15.5\text{ cm}^{-1}$  is sufficient for retrieving temperatures over the altitude range 10–0.01 mbar (Figure 4). Given the spacecraft attitude-control uncertainty for pointing ( $\pm 2\text{ mrad}$ ) two vertical positions are used at each location. Twenty minutes ensure a precision in retrieved temperatures better than 1 K. Eighteen locations can be measured over a 6-h period. The observations will cover a series of latitudes, and in some cases, held fixed at a given latitude, with Saturn's rotation providing a succession of different longitudes for the soundings. In addition to temperature profiles, the limb maps will allow the retrieval of stratospheric  $\text{CH}_4$  (Section 3.1.1).
- *Limb integrations.* These are similar to the limb maps, except that the fields of view remain at a single location. A spectral resolution of 0.5 or  $1.0\text{ cm}^{-1}$  is used to obtain vertical profiles of  $\text{CO}_2$  and various stratospheric hydrocarbons.
- *Feature tracks.* This is a  $\sim 5\text{-h}$  template for coordinated observations by CIRS, the imaging science experiment (ISS, Porco *et al.*, 2004), the visual and infrared mapping spectrometer experiment (VIMS, Brown *et al.*, 2004), and the ultraviolet spectrometer experiment (UVIS, Esposito *et al.*, 2004). The feature, or some specified area on Saturn, is tracked from limb to limb, as Saturn rotates. As the feature moves across the disk, an area equivalent to the  $6^\circ \times 6^\circ$  ISS wide-angle FOV (corresponding to a latitude span of  $17^\circ$  at the sub-spacecraft point) is mapped by a series of scans. The nadir mapping will measure tropospheric temperature perturbations with a precision of 0.2 K, which, for example, can be correlated with motions and features in ISS images. The observations will also determine heat fluxes associated with the motion of the temperature anomalies. When the feature is on both limbs, limb soundings will retrieve stratospheric temperatures with a vertical resolution of about a scale height. These may show evidence of vertically propagating disturbances associated with the feature that transport momentum and energy to the stratosphere. For the temperature-sounding flavor just given, the spectral resolution is  $15.5\text{ cm}^{-1}$ . An alternative, composition-driven, version is executed in similar fashion, except that the spectral resolution is higher (3, 1,  $0.5\text{ cm}^{-1}$ ). Because of the SNR requirements, a smaller area is mapped,  $\sim 5^\circ$  latitude. Specific targets are the spatial distribution of  $\text{NH}_3$  (with a SNR of 3–12),  $\text{PH}_3$  (SNR  $\sim 4\text{--}17$ ), and stratospheric hydrocarbons. An important objective is to determine whether meteorologically “interesting” local regions, e.g., with strong vertical motions, are characterized by subtle differences in atmospheric composition.

There are other observations that can fit into the previously listed categories, but which have specific measurement targets. Among these is:



- *Radio-occultation-point observations.* Nearly simultaneous observations by CIRS and RSS exploit synergies of the two types of data. For example, the combination of CIRS and RSS data can provide a better determination of the He abundance (Section 3.1.1). Moreover, higher vertical resolution of temperature profiles retrieved from radio-occultation soundings can help in the analysis of temperature perturbations seen in CIRS temperature maps and cross sections. By the nature of the geometry of the occultation, which is observed on Saturn's limb, and also the relative orientation of the spacecraft high-gain antenna (used by RSS) relative to the CIRS boresight ( $90^\circ$  apart in the sky), it is usually not feasible to do near-simultaneous observations, and the CIRS observations often must be done one or two Saturnian rotations away from the actual occultation. The targeted CIRS observation has two parts, nadir and limb. The nadir observation is similar to the MIR nadir maps and regional nadir maps, with the mid-infrared (FP3, FP4) arrays aligned north-south at a location so that the planetary rotation sweeps the occultation location through all three focal planes. Spectral resolution is  $3\text{ cm}^{-1}$ . The limb observation is similar to the mid-IR limb map, described above (spectral resolution  $15.5\text{ cm}^{-1}$ ), except profiles are retrieved only in the vicinity of the occultation. When the competing demands of other activities preclude observing the occultation point, a fallback position is to observe the occultation latitude close in time to the actual event.

#### 4.3. TITAN

There are 44-targeted flybys of Titan during the 4-year nominal Cassini tour. The most distant targeted flyby has a closest-approach altitude of 10,630 km, but virtually all the rest are within 3000 km, with over half around 950 km. Figure 31 provides a generic timeline for a close Titan pass (less than few thousand kilometers altitude at closest approach), and schematically depicts the various types of CIRS observations. These correspond to the entries in the last column of Table V.

The temperature-mapping sequences illustrate well the considerations that come into play for limb and nadir viewing when the different fields of view are the drivers. Moving closer in range to Titan, these sequences are (Figure 31):

- *Mid-IR nadir maps.* These use the radiances in the  $\nu_4$  band of  $\text{CH}_4$  to map temperatures in the upper stratosphere (Figure 12). They are nominally 7-h sequences, ideally executed within a range of 380,000 km from Titan ( $\sim 19$  h from closest approach), where the mid-infrared array pixels each resolve  $2.5^\circ$  of body-centric arc at the sub-spacecraft point. With a fixed remote-sensing pallet, it is more efficient to articulate the spacecraft in a series of continuous slews, rather than discrete steps, across the disk in a push-broom fashion. A spectral resolution of  $3\text{ cm}^{-1}$  (10-s interferometric scans) ensures adequate resolution of the P, Q, and R branches of the  $\nu_4$  band of  $\text{CH}_4$ . A slew rate of  $4\text{ }\mu\text{rad s}^{-1}$  means that the 0.3 mrad pixels will move half their width in 40 s, or 4 interferometric scans.

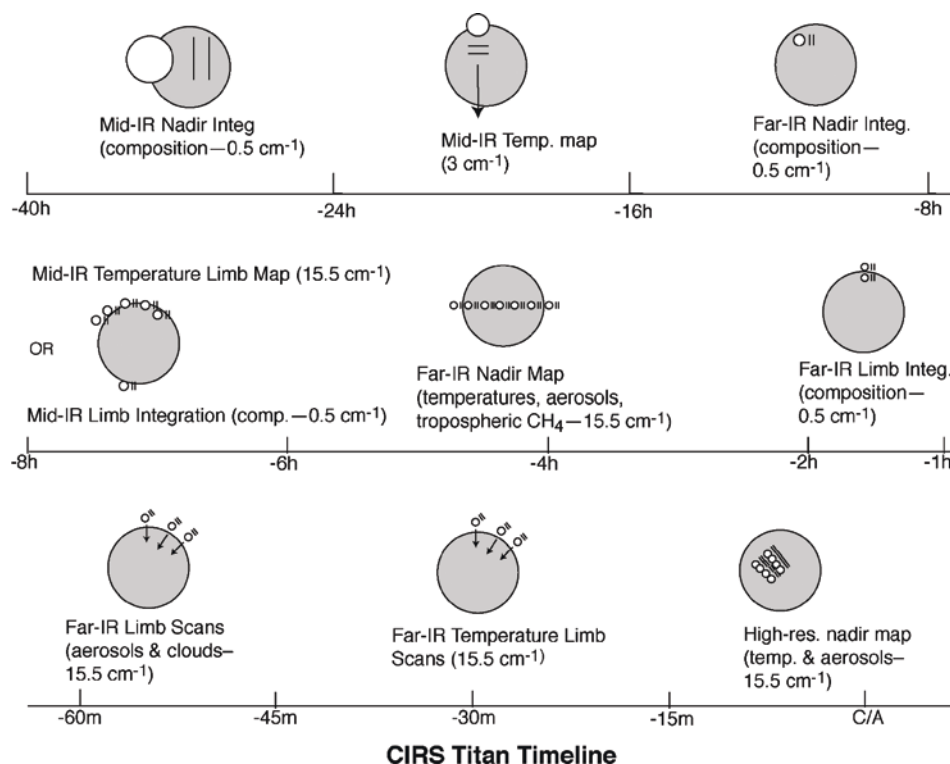


Figure 31. Generic Titan flyby timeline with CIRS observations. Time from closest approach can be converted to range by noting that the spacecraft velocity relative to Titan is typically  $5.5\text{--}6.1\text{ km s}^{-1}$ . The relative size of the CIRS fields of view is smaller than indicated within 4 h of Titan closest approach.

Averaging these would ensure a precision of 0.25 K in the retrieved temperatures in the upper stratosphere.

- *Mid-IR limb maps.* These provide better vertical resolution in the upper stratosphere and mesosphere (Figure 12). At 6 h from Titan closest approach, or a range of 120,000 km, the mid-infrared pixels resolve 36 km on the limb, comparable to the scale height (42 km) in the upper stratosphere. In the limb mode,  $15.5\text{ cm}^{-1}$  is sufficient to resolve the  $\nu_4$  band of  $\text{CH}_4$  for temperature retrieval. The mid-infrared arrays are held steady on the horizon, normal to the limb. Twenty interferometric scans can be acquired in approximately one minute, sufficient for a retrieved temperature with a precision of 0.25 K. After one location is observed, the arrays are moved to the next position, a few degrees along the limb relative to Titan's center.
- *Far-IR nadir maps.* The 4-mrad FP1 FOV is the driver here. At 3 h from Titan closest approach, the range is 60,000 km, and the FOV subtends  $5^\circ$  of body-centric arc at the subspacescraft point (Figure 31). As with the mid-IR nadir maps,

the FOVs slew across the disk. To retrieve temperatures in the upper troposphere and tropopause region, a spectral resolution of  $15.5\text{ cm}^{-1}$  requires a slew rate of  $40\text{ }\mu\text{rad s}^{-1}$ . However, if surface temperatures are simultaneously retrieved from the radiances in the window near  $520\text{ cm}^{-1}$  (which will usually be the case), much slower slew rates are needed (see below). An additional complication arises in using lower-resolution spectra below  $150\text{ cm}^{-1}$  for temperature retrieval, because of the superposition of several optically thin rotational lines of  $\text{CH}_4$ ,  $\text{HCN}$ ,  $\text{H}_2\text{O}$ , and other molecules, discussed earlier, on top of the underlying broader spectrum associated with  $\text{N}_2$  pressure-induced absorption. Adequate resolution of these lines requires a spectral resolution of at least  $1\text{ cm}^{-1}$ . To avoid a systematic bias in tropospheric and tropopause temperatures retrieved from the lower-resolution spectra, an empirical correction will be applied as a function of latitude. This will be based on the far-IR nadir composition integrations described below, which will be done at  $0.5\text{ cm}^{-1}$  resolution and at 160,000–270,000 km from Titan. As a check, a few of the far-IR nadir map scans closer in will be executed at  $1\text{ cm}^{-1}$  resolution.

- *Far-IR limb temperature and aerosol scans.* Done within 75 min of closest approach (Figure 31), the best resolution for temperature sounding occurs inside of 45 min. At 30 min out the FP1 FOV resolves 40 km altitude on Titan's limb, about one scale height in the upper stratosphere. Spectra with  $15.5\text{ cm}^{-1}$  spectral resolution will be acquired during vertical scans of  $40\text{ }\mu\text{rad s}^{-1}$ . From these, vertical profiles of temperature between 8 and 100 mbar will be retrieved. As with the nadir-viewing spectra, the low-resolution limb spectra will require the effects of unresolved rotational lines to be corrected before temperatures are retrieved. This is possible through the use of far-infrared limb integrations, acquired at one to two hours from closest approach at full spectral resolution.
- *Surface-temperatures mapping.* As noted in Section 3.2.4, both nadir and limb observations in the far-infrared are required to separate surface and stratospheric emission. The requisite limb spectra will be obtained in the dedicated aerosol limb and temperature scans, taken within 75 min of Titan closest approach (range 25,000 km), which were described above. The far-infrared nadir mapping can be done during the sequences described for mapping the troposphere and tropopause temperatures. However, the scan rates must be very slow,  $\sim 6\text{ }\mu\text{rad s}^{-1}$ ; this is equivalent to an integration time of 5 min in the 4-mrad FP1 FOV.

The sequences described above can also be used for compositional studies. However, there are other observations dedicated to longer integration and high spectral resolution,  $0.5\text{--}1.0\text{ cm}^{-1}$ . Moving toward Titan closest approach, they are:

- *Mid-IR nadir integrations.* These are typically done 500,000–1,000,000 km from Titan; for targeted flybys, this occurs one day or greater from closest approach. At this point the arrays span 60% or more of Titan's radius. When the arrays are oriented north-south, the integrations will the latitude distribution of hydrocarbons

(CH<sub>4</sub>, CH<sub>3</sub>D, C<sub>2</sub>H<sub>2</sub>, C<sub>2</sub>H<sub>4</sub>, C<sub>2</sub>H<sub>6</sub>, C<sub>3</sub>H<sub>8</sub>, C<sub>4</sub>H<sub>2</sub>, C<sub>3</sub>H<sub>4</sub>), nitriles (HCN, HC<sub>3</sub>N and CH<sub>3</sub>CN), the oxygen compound CO<sub>2</sub>, and new species (e.g., the CH<sub>3</sub> radical, C<sub>6</sub>H<sub>6</sub>, CH<sub>2</sub>=C=CH<sub>2</sub>, etc.).

- *Far-IR nadir integrations.* These integrations are executed closer in to Titan, at a range of 160,000 to 270,000 km (8–13 h from closest approach). They will measure the stratospheric emission from the rotational lines of CH<sub>4</sub>, HCN, CO, and H<sub>2</sub>O, as well as providing a basis for detecting new compounds. For better spectral contrast of the stratospheric emission, the integrations are at 1.5–2 airmasses. Generally, only one location will be observed during an integration. Spatial mapping must be composited from multiple flybys during the tour.
- *Mid-IR limb integrations.* Done 5–9 h from Titan closest approach, these are similar to the mid-IR limb maps described above, except in the execution. Instead of repositioning at successive locations on the limb, the arrays are centered at two altitudes – 125 km and 225 km – on the limb at a single location. The targeted species are identical to those for the mid-IR nadir integrations, above, but the limb-viewing geometry provides better vertical resolution with the arrays.
- *Far-IR limb integrations.* These occur between ~one and two hours from closest approach. The FP1 focal plane is centered at 225 km and 125 km, for coarse vertical profiles of CH<sub>4</sub>, HCN, CO, and H<sub>2</sub>O. The latter two require the longest integrations, about 90 min for each position. Typically this cannot be accommodated during a single flyby, and the vertical profiles and latitude mapping must be composited from several Titan flybys.

Nadir observations are typically done further from closest approach than the corresponding limb observations. The former therefore have more time afforded to them and thus offer better horizontal coverage, although the information on vertical structure is more limited than with limb sounding. Repeated observations at the same location, separated well in time during the Cassini tour, will define temporal variability on seasonal time scales.

#### 4.4. ICY SATELLITES

During the Cassini tour, there are eight flybys of the classical icy satellites targeted at 1000 km or less, as well as a number of “Voyager-class” (<300,000 km) encounters. There are also flybys of several much smaller satellites, such as Janus and Epimetheus, at various distances. The dimensions of these objects range from less than 100 km to as much as 1530 km (Rhea). Consequently, it is most useful to discuss CIRS observations in terms of the angular diameter of the object, rather than its distance from the spacecraft (see Figure 22).

Normally the spacecraft orientation is controlled by momentum wheels, which provide pointing accuracy and precision of ~2 mrad and ~0.04 mrad, respectively. Consequently, the full spatial resolution of the FP3 and FP4 pixels (0.3 mrad) cannot be utilized with reasonable confidence until the target exceeds 1 mrad in

diameter. At that point, the separation between focal planes 3 and 4 (0.9 mrad), and the large size of FP1 (nominally 3.9 mrad) offer reasonable assurance of obtaining useful data in either FP1 or at least one of FP3 and FP4. As with the planet and the rings, the order of magnitude difference in FOV scale between FP1 and the other focal planes plays heavily in the design of the icy satellite observations. Approaching from a distance, CIRS observations might proceed roughly in the following order.

- *Compositional integrations.* These are typically performed at ranges where the target angular diameter (AD) is 1–3 mrad. Because spectral features of solid materials are generally broader than those of molecular lines, these observations are made at 1–3  $\text{cm}^{-1}$  resolution. Conducted in staring mode, using FP1 and the center detectors of FP3 and FP4, these are concentrated in geometries with low phase angles, so as to view the icy satellite surfaces at their warmest and maximize the SNR. Due to the nature of the Planck function, there is a steep rolloff of thermal intensity with increasing wavenumber. This requires increasing integration time to extend the range of the spectrum. For a 100 K surface and a spectral resolution of 3  $\text{cm}^{-1}$ , a SNR of 10 at 600  $\text{cm}^{-1}$  can be obtained with one minute of integration, but extending the spectrum to 800  $\text{cm}^{-1}$  with the same SNR requires integration of 100 min (Figure 29). Therefore, extending the spectrum to the highest wavenumbers will involve coadding spectra over the entire tour.
- *Eclipse observations.* Several passages of the satellites through Saturn's shadow will be observed at entry and exit. Typically  $\text{AD} > 1$  mrad, phase angle  $\phi < 100^\circ$ ,  $\Delta\nu = 15.5 \text{ cm}^{-1}$ , and the eclipse duration is  $\sim 2$  h. The high sensitivity of FP1 permits observations of objects even when the FOV is incompletely filled, or when the phase angle is moderately high. At low phase angles, even FP3 can be used to follow the initial portion of the cooling curve for relatively dark objects (Figure 23); this allows observations with body-centric spatial resolution better than  $10^\circ$  to be made when the apparent target size exceeds  $\sim 3$  mrad. Eclipses provide the thermal inertia of the upper mm or so of the surface, as well as estimates of surface coverage by relatively large fragments of consolidated material (Figure 24).
- *Phase/longitude (diurnal cycle) coverage* ( $\text{AD} > 1$  mrad,  $\Delta\nu = 15.5 \text{ cm}^{-1}$ , 10–20 min). Focal plane 1 will be utilized to determine the disk-averaged temperature of the satellites. From the resulting diurnal behavior, mean thermal inertias in the upper cm or so of the surface will be derived.
- *Global thermal inertia mapping and/or hot spot monitoring* ( $\text{AD} > 3$  mrad,  $\Delta\nu = 15.5 \text{ cm}^{-1}$ ). Maps are made by slewing and rastering FP3 and FP4 across the disk at rates not to exceed that for Nyquist sampling (16  $\mu\text{rad/s}$  in blinking mode); observation durations will typically be 10–30 min. These maps will be successful for varying portions of a satellite, depending on its albedo, thermal inertia and phase angle. The exception is Enceladus, which is so cold that even the subsolar regions will be barely detectable in an individual measurement. In this case, mapping will serve to monitor the satellite for ongoing endogenic activity;

e.g., active sources at or above the  $\text{NH}_3\cdot\text{H}_2\text{O}$  eutectic temperature will be easily observed if they fill more than a few percent of an FP3 or FP4 pixel (Figure 23).

- *Search for a solid state greenhouse* ( $\text{AD} > 10$  mrad,  $\phi < 40^\circ$ ,  $\Delta\nu = 15.5\text{ cm}^{-1}$ , 15 min). In the far-IR the decreasing absorption coefficient of water ice with decreasing wavenumber permits detection of radiation from increasingly far below the surface, reaching as deep as 1 cm at  $10\text{ cm}^{-1}$ . Slow east-west slews using FP1 allow following the gradual penetration of the thermal wave into the regolith throughout the day.
- *Polar night (annual cycle) coverage* ( $\text{AD} > 10$  mrad,  $\Delta\nu = 15.5\text{ cm}^{-1}$ , 15 min). FP1 observations of the dark winter polar region from high latitude permit determination of the seasonal cooling curve. This enables an estimate of thermal inertia in the upper tens of centimeters of the polar regolith.
- *High-resolution hemispheric FP1 mapping*, near closest approach ( $\text{AD} > 10$  mrad,  $\Delta\nu = 15.5\text{ cm}^{-1}$ ). The high sensitivity of FP1 permits rapid mapping of satellite disks near closest approach, where time is at a premium. Nyquist-sampled maps at low spectral resolution (slew rate  $420\text{ }\mu\text{rad/s}$ ) will typically take 10–30 min. These permit identification of minor thermal anomalies, even on the night hemisphere, as for example, revealed for Europa from Galileo Photopolarimeter measurements (Figure 26).

#### 4.5. SATURN'S RINGS

The 4-year Cassini tour has three distinct intervals of inclined orbits which are of primary interest for ring science (Cuzzi *et al.*, 2002; Matson *et al.*, 2002; Wolf, 2002). The early inclined sequence, which begins about 9 months into the tour, catches the rings close to their maximum opening angle, and near their warmest. These orbits reach a maximum inclination of about  $20^\circ$ . This sequence is followed by almost a year with the spacecraft orbiting in Saturn's equatorial plane. This time is good for edge-on ring measurements, primarily of the faint rings. The Titan  $180^\circ$  transfer sequence begins about two years into the tour. This sequence has two stages, an "up-leg" where the orbit inclination is increasing, and a "down-leg", where the orbit inclination is decreasing. The maximum inclination in this sequence is about  $50^\circ$ . A few months later the final, high inclination sequence begins. The spacecraft ends the 4-year tour in a high-inclination orbit (about  $75^\circ$ ) with periapse on the lit side of the rings. This time provides a unique, high-inclination view of the rings.

*SOI.* The short period of time immediately following the Saturn Orbit insertion burn is of key interest for CIRS ring science. The spacecraft soars over the unilluminated side of the main rings and is nearly an order of magnitude closer to the rings than it will be at any other time in the mission. A single scan of a portion of the main rings will be obtained at  $15.5\text{ cm}^{-1}$  resolution. CIRS FP1 resolution will range from 100 to 250 km, and FP3/4 resolution will range from 8 to 19 km, with the highest resolution over the A ring.



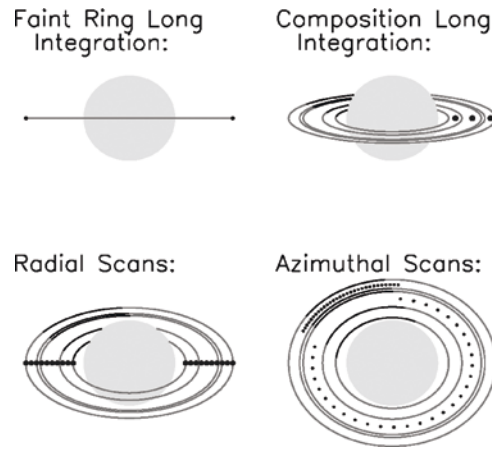


Figure 32. CIRS observations of Saturn's rings as a function of spacecraft elevation. Typical CIRS ring observations are depicted as a function of the observed ring opening angle.

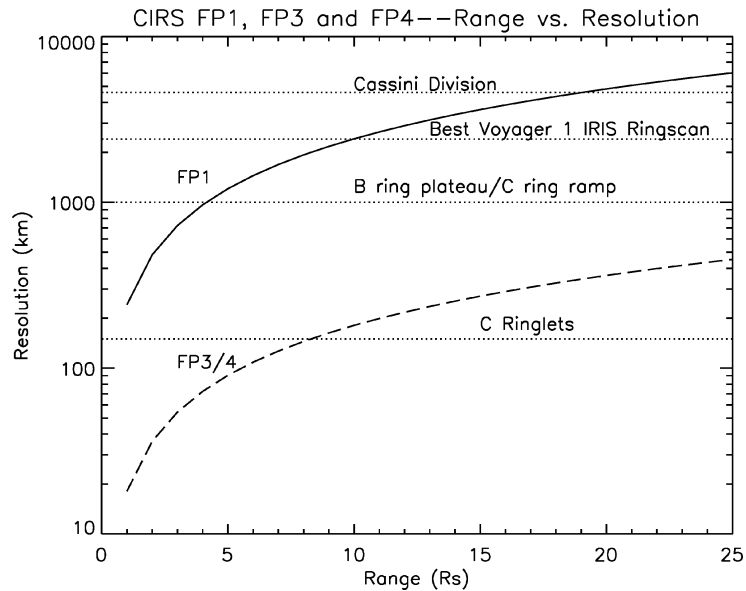


Figure 33. CIRS FP1 and FP3/4 spatial resolution as a function of distance from the rings. The spatial resolution for FP1 and a single pixel in FP3 or FP4 are shown as a function of the distance from the rings, for normal ring viewing. The curves above also depict the ring radial resolution when viewing the rings at either ansa. For comparison, the radial extent of ring features such as the Cassini Division, B ring plateau/C ring ramp, and C ringlets are indicated.

The main types of CIRS ring observations are listed below, in order of increasing spacecraft elevation. A schematic of these observations is shown in Figure 32. Typical ring radial resolution for focal planes FP1 and FP3/4 as a function of distance from the rings is shown in Figure 33.

- *Faint ring long integrations.* The low optical depths of the faint D, E, F and G rings will pose particular observing challenges for CIRS. These rings are best viewed edge-on because this geometry enhances the fill factor of the instrument field of view. Low spectral resolution of  $15.5 \text{ cm}^{-1}$  with FP1 provides the best signal-to-noise and should be sufficient for detecting the variations of emissivity with wavelength, which is our primary measurement goal. From close range ( $\sim 10 R_S$ ) and small opening angle, the FP1 filling factor will approach 1% when pointed at the F ring's ansa. Integrations of  $\sim 10$  min should yield usable signals. However, because the F ring is so clumpy, it needs to be sampled at many longitudes before a truly representative spectrum can be obtained. Observations will consist of alternating between both ring ansae every  $\sim 30$  min to achieve the most complete rotational coverage of this ring. The E ring will be observed by pointing FP1 near the orbit of Enceladus, where the long edge-on line of sight through the ring maximizes the fill factor. However, this fill factor will still remain quite low,  $\sim 10^{-4}$ , so, detecting the E ring will require many, perhaps 100 or more, hours of integration. On the other hand, because the ring is so thick vertically, the observing range can be quite large ( $30\text{--}40 R_S$ ). More observing time is available then during these apoapse periods of the tour. The VIMS and UVIS instruments will also require substantial integration on this ring, so E ring observations will be cooperative activities between all of Cassini's optical remote sensing instruments. Unfortunately, the best possible fill factors for the remaining rings, D and G, are still lower than for Ring E. It is unlikely that either will be detected with CIRS.
- *Composition integrations.* CIRS will determine with unique accuracy the ring spectrum between 50 and  $1000 \mu\text{m}$ . As intimately mixed contaminants significantly influence this part of the spectrum, mixtures derived from the visible and near-infrared spectra will be tested against this new spectrum. Spectra of the three main rings over the full CIRS wavelength range will be obtained to determine possible radial variations in the bulk composition. Two types of observations will be made: high spectral resolution ( $0.5 \text{ cm}^{-1}$ ) FP3 emission measurements of the A, B and C rings, and high spectral resolution transmission measurements of the rings with the rings against Saturn. The former can be obtained from large ranges  $20\text{--}40 R_S$  because of FP3's fine spatial resolution; long integrations of  $10\text{--}20$  h will be obtained on representative radial locations in each ring. The transmission measurements will be made from  $20 R_S$  at relatively low ring opening angles. This will allow a search for absorption features in the A and C rings, and the Cassini division. The same region of Saturn will be observed in at a similar spatial resolution when the rings are not present, to establish the background. The transmission spectra will be obtained over a series of emission angles.
- *Stellar occultations.* A handful of stellar occultations are observed by CIRS to directly obtain the ring opacity in the infrared. Only a limited number of targets are observable by CIRS, including CW Leo and Eta Carinae. Eta Carinae occultations are only observable during the final month of the tour. Occultations are observed

in one FP3 pixel (CW Leo) or one FP4 pixel (Eta Carinae) at  $15.5\text{ cm}^{-1}$  spectral resolution.

- *Radial scans.* These scans are typically executed between 5 and 20  $R_s$  over a range of spacecraft inclinations, from low ( $5^\circ$ ) to highest possible inclination ( $75^\circ$ ). Radial mapping (FP1, FP3) of the rings, on both lit and unlit sides, over a range of spacecraft elevations, local times and phase angles, is performed to obtain broadband radiometric measurements of the total flux and spectral shape in the CIRS wavelength range. Sets of observations are obtained in each of the inclined orbit intervals to map the temperature variation in the rings with changing solar illumination. Two types of scans are planned. Temperature scans will consist of spectra taken at  $15.5\text{ cm}^{-1}$  spectral resolution of the lit and unlit sides of the rings at many incidence and emission angles and provide prime information on the ring thermal gradient as a function of radial distance to Saturn. Submillimeter scans will be made of spectra at  $1\text{ cm}^{-1}$  spectral resolution of the lit and unlit sides of the rings to map the thermal characteristics and composition of the ring particles out to 1 mm.
- *Azimuthal scans.* These observations are executed between 5 and 20  $R_s$  at spacecraft inclinations greater than  $20^\circ$ . They will be used to study the surface properties, the vertical dynamics, and the spin of ring particles. Observations of the cooling and heating of the ring particles entering and emerging from the planetary shadow are planned to derive particle thermal inertias for all three main rings. Measurements at moderate radial resolution (typically 1000 km) across the shadow boundaries at low spectral resolution ( $15.5\text{ cm}^{-1}$ ) with the FP1 FOV. To constrain the vertical dynamics of ring particles, the temperatures of the main rings will be measured by CIRS along the azimuth of the main rings, from the exit of the shadow (morning) to the evening ansa, both on the unlit and unlit faces. This unique experiment will be realized with spectra at low spectral resolution ( $15.5\text{ cm}^{-1}$ ). Spins create both an azimuthal asymmetry in the ring temperature and a dependence of the temperature with the emission angle, due to day/night contrast. Circumferential scans at a variety of phase and emission angles will be executed to detect azimuthal asymmetries and the anisotropy in the ring particle emission function which are both function of particles spin and thermal inertia. Occasionally, when observing time is highly disputed, long azimuthal scans (8–20 h long depending on geometry and face) will be replaced by a series of radial scans at different azimuths.

There are other types of joint observations as well. Combined data from CIRS and VIMS, over a wide range of geometric and illumination conditions, will define the interior thermal distribution, from which a density distribution within the particles can be estimated. The thermal inertia and the infrared optical depth will be derived, which will provide information on regolith density, and possibly on collisional processes. The determination of the interior thermal distribution relies on the opportunities afforded by the orbiter and the semi-transparency of the ring

particles at submillimeter wavelengths. Information about the particle interiors will be obtained by long spectral averages at various locations in the rings with spatial resolutions from a few hundred to several thousand km. These observations will be taken at many incidence and emission angles over the mission.

## 5. Instrument Description

### 5.1. OVERVIEW

The CIRS instrument consists of the Optics Assembly (OA), Electronics Assembly (EA), and an interconnecting External Harness (EH). A photo of the CIRS Engineering Model (EM) on the Remote-Sensing Platform (RSP) is shown in Figure 34; the EM has the telescope cover off while undergoing ground optical boresight tests. The CIRS instrument evolved from the Voyager Infrared Interferometer Spectrometer (IRIS) (Hanel *et al.*, 1979), a single infrared interferometer covering the  $180\text{--}2000\text{ cm}^{-1}$  ( $56\text{--}5\text{ }\mu\text{m}$ ) region with an apodized spectral resolution of  $4.3\text{ cm}^{-1}$ . IRIS had a single thermopile detector with a 4.4-mrad diameter field of view (FOV). The CIRS instrument consists of two combined interferometers, operating in the far-infrared ( $10\text{--}600\text{ cm}^{-1}$ ) and mid-infrared ( $600\text{--}1400\text{ cm}^{-1}$ ) with a commandable apodized spectral resolution as high as  $0.5\text{ cm}^{-1}$ . The two interferometers share a common telescope and scan mechanism. The far-IR interferometer is a polarization interferometer, with a focal plane (labeled FP1) consisting of two thermopile detectors with a 3.9 mrad FOV. The mid-IR interferometer is a conventional Michelson interferometer with two focal plane arrays (FP3, FP4), each having 10 HgCdTe detectors, with 0.273 mrad FOV per pixel. (An additional focal plane, FP2, was eliminated in a Cassini downsizing). Table I summarizes the instrument characteristics. Kunde *et al.* (1996) provide a more complete engineering description of the instrument.

### 5.2. OPTICS ASSEMBLY

The OA consists of the beryllium telescope, relay optics, scan mechanism, two infrared interferometers, a reference and white-light interferometer, an 80 K passive radiator cooler, an instrument radiator, and detectors.

#### 5.2.1. Optical Design

Figure 35 illustrates the conceptual design of CIRS. Infrared radiation is focused by the telescope on a field splitting mirror, which divides the incident beam between the far-IR and mid-IR interferometers. In each interferometer, fore-optics collimate the beam and pass it through a beamsplitter and retroreflectors. In both interferometers, one retroreflector is fixed and the other is attached to the scan mechanism. After the beamsplitters, the recombined output beams go to the focal planes and are focused on the detectors. A reference interferometer provides servo signals for the

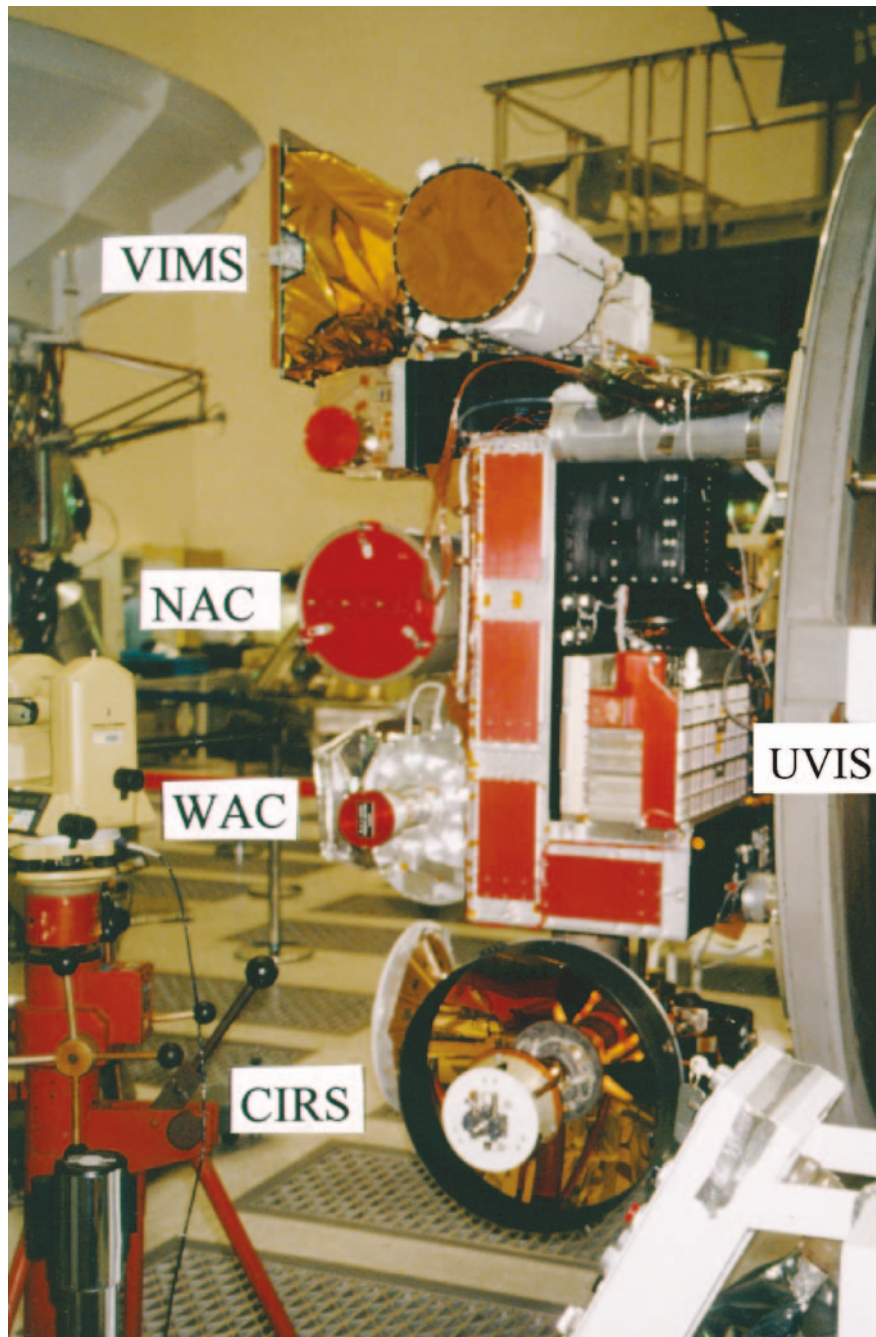


Figure 34. CIRS on the Cassini Optical Remote Sensing Pallet.



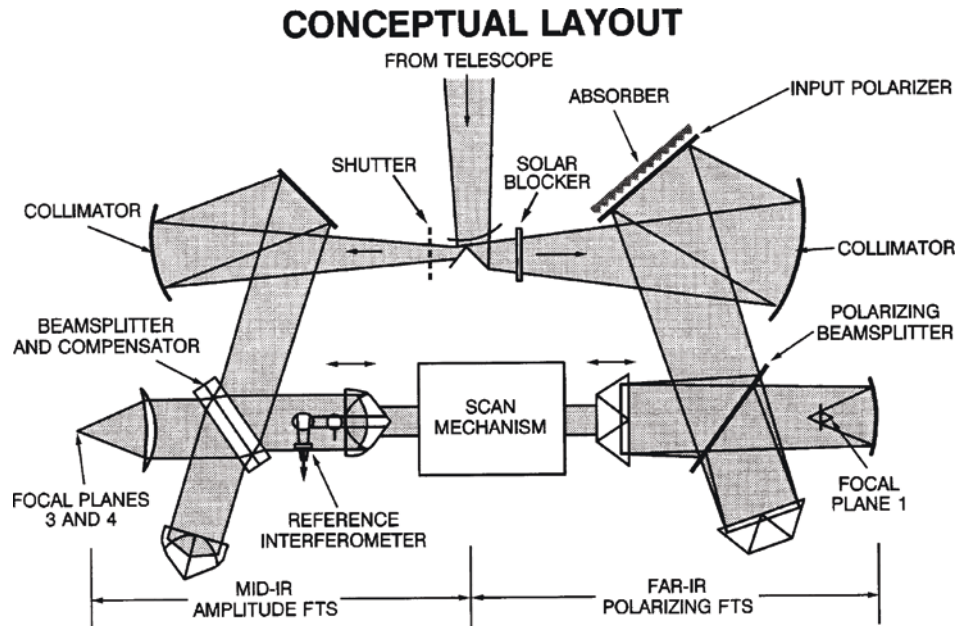


Figure 35. CIRS conceptual layout. Radiation from the telescope is field-split between the mid-IR and far-IR. interferometers. The moving retroreflectors share a common drive mechanism.

scan mechanism to maintain a constant velocity and to control data sampling. The reference interferometer uses the same moving retroreflector as the mid-IR interferometer in order to track the motion of the mechanism. The instrument, telescope and FP1 are operated at a temperature of 170 K. FP3 and FP4 are mounted on a passive cooler radiating to space, and are operated near 80 K (typically in the range 75–80 K).

A brief description of the major optical subsystems follows:

*Telescope.* The CIRS Cassegrain telescope is identical in size to the Voyager IRIS telescope, with an improved optical quality. It provides a large aperture, small field-of-view, and minimum volume. The telescope consists of a 50.8-cm F/6 paraboloidal primary mirror and 7.6 cm diameter hyperboloidal secondary mirror. A cylindrical tube extends from the central portion of the primary mirror to support the secondary mirror. The mid-IR FOV is centered on the telescope axis (see Figure 1) to provide good image quality for the FP3 and FP4 arrays. The central obscuration of the telescope is 41%. The primary and secondary each has its own sunshade/radiator.

*Fore-optics.* An entrance aperture plate, located at the telescope focus, directs the incoming radiation into the two infrared interferometers. There are two field stops at the exit focal plane of the telescope, corresponding to the fields-of-view of the two interferometers. The center of the mid-IR field stop is coincident with the telescope axis. The axis of each interferometer is aligned with its respective field stop. Between each field stop and its interferometer is a field splitting mirror,



a collimator, and a folding flat. The mid-IR fore-optics has a mechanical shutter which can be commanded to block the beam for calibration. The far-IR beam passes through a solar blocking filter, which rejects wavenumbers short of  $600\text{ cm}^{-1}$  to protect the thermopile detectors against accidental solar illumination. A polarizer acts as the folding flat in the far-IR. To minimize the sizes of beamsplitters and mirrors, the fore-optics are arranged to place the pupils (images of the primary telescope mirror) at the retroreflectors in the two interferometers.

*Infrared interferometers.* The far-IR and mid-IR interferometers provide complete coverage of the  $10\text{--}1400\text{ cm}^{-1}$  range, with an apodized resolution as high as  $0.5\text{ cm}^{-1}$ . The far-IR interferometer uses polarization modulation, produced by mylar mounted wire grid polarizers, to provide coverage of the  $10\text{--}600\text{ cm}^{-1}$  region. The mid-IR interferometer is a conventional Michelson using a KBr beamsplitter, covering the  $600\text{--}1400\text{ cm}^{-1}$  range. The far-IR and mid-IR interferometers use two types of retroreflectors. Cube corners are used in the mid-IR to provide tilt compensation during scanning and to minimize misalignment at 170 K. Dihedral mirrors are used in the far-IR to rotate the beam polarization by  $90^\circ$  before returning it to the beamsplitter (so that the transmitted/reflected incoming beam is reflected/transmitted toward the detector).

*Reference interferometer.* A reference interferometer, using a 785 nm (@170 K) diode laser, shares the mid-IR moving retroreflector and provides a servo signal for velocity control. The reference interferometer also produces a white-light fringe just before the start of scan to initiate sampling.

*Focal planes.* Radiation exiting the interferometers is focused on the detector focal planes with a germanium lens (FP3, FP4) and an on-axis mirror (FP1). The focal-plane detectors are discussed in detail below.

### 5.2.2. Fields of View

Figure 1 summarizes the locations of the CIRS focal planes in the plane of the sky. These were obtained from several scans of Jupiter and bright infrared stars, which were made in April to October, 2001, after the Jupiter swingby (closest approach: December, 2000). Over this period, Jupiter's diameter, viewed from the spacecraft, decreased from 1.24 mrad to 0.48 mrad. In May, 2002, another set of scans was made across Jupiter, when its angular diameter was 0.290 mrad, to determine the spatial response of FP1. This is discussed in Appendix B. A final set of scans will be made in May, 2004, when Jupiter subtends 0.114 mrad, to determine the spatial response of each pixel in FP3 and FP4.

### 5.2.3. Far-IR Interferometer

The far-IR interferometer operates on the principle of polarization modulation introduced by Martin and Puplett (1969), and Martin (1982). The interferometer operates by first polarizing the radiation and then modulating its polarization. The beam entering the interferometer is linearly polarized by an input polarizer. At the beamsplitter polarizer, which is oriented at  $45^\circ$  with respect to the input polarizer,

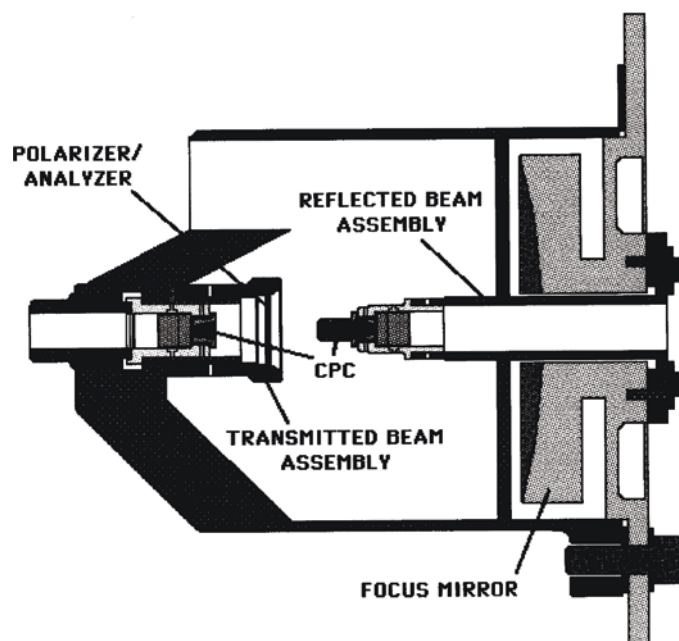
**CIRS FOCAL PLANE 1 ASSEMBLY**

Figure 36. CIRS far-IR FP1 assembly, consisting of the focusing mirror and mechanical structure supporting the thermopile detectors and polarizer/analyzer.

the beam is further split into two orthogonal components. These are sent to the two retroreflectors, rotated  $90^\circ$ , and returned to the beamsplitter. A phase difference between the two components is introduced by the path difference between the two arms. The beams are recombined at the beamsplitter and sent to the focal plane. The recombined beam is elliptically polarized and its instantaneous state of polarization switches between two orthogonal linear states as the moving mirror is scanned. These are selectively transmitted (and reflected) by the polarizer/analyzer, located in front of the detectors. The detector signals are therefore modulated, and the modulation frequency is proportional to the wavenumber ( $\text{cm}^{-1}$ ) of the radiation. The result is a conventional interferogram.

The beam from the interferometer is focused by an on-axis parabolic mirror ( $f/1$ ) at the entrance of a compound parabolic concentrator (CPC) located in front of each thermopile detector (see Figure 36). Prior to reaching the CPC's, the beam is split by the polarization analyzer. The transmitted polarization component is detected by one thermopile detector and the reflected polarization component is detected by the other thermopile detector. The use of two detectors gives a gain in signal, eliminates unmodulated intensity fluctuations, and provides redundancy.

The polarizing interferometer ( $10\text{--}600\text{ cm}^{-1}$ ) uses substrate-mounted wire-grid polarizers to split, recombine, and analyze the radiation. This technique takes

advantage of the existence of nearly ideal wire-grid polarizers for the far infrared to make an instrument with high efficiency and broad frequency response. The CIRS wire grids (input polarizer, beamsplitter, output analyzer) are  $1\text{-}\mu\text{m}$  diameter wire, with  $2\text{-}\mu\text{m}$  spacing, supported by a thin ( $1.25\text{ }\mu\text{m}$ ) film of Mylar. These grids give good efficiency from 10 to  $600\text{ cm}^{-1}$ . The grids were designed and developed at Queen Mary and Westfield College, London, England.

#### 5.2.4. *Mid-IR Interferometer*

The MIR interferometer ( $600\text{--}1400\text{ cm}^{-1}$ ) is a conventional Michelson design. The beamsplitter is a potassium bromide (KBr) substrate with a multiple-layer coating including a layer of germanium, an antireflection coating, and protective coatings. A matched compensator is placed adjacent to the beamsplitter to correct for refractive effects in the substrate. The beam coming from the collimator is divided equally at the beamsplitter, and the two halves are sent to the fixed and moving retroreflectors. The beams are reflected back to the beamsplitter, where they are recombined and sent to the focal planes. The beam is imaged by a Ge lens on the FP3 and FP4 HgCdTe detector arrays, which are mounted on the 80 K cold stage. As the moving mirror is scanned, the path difference between the two beams is varied, which modulates their interference and, therefore, the detected intensity. The modulation rate is proportional to the spectral wavenumber, and the total modulated signal at the detector creates the recorded interferogram. The detector arrays are mounted on a common carrier, and are rigidly mounted to the 80 K cooler using a tripod of titanium alloy supports. A cold shield limits out of field background radiation from the warm instrument onto the arrays.

#### 5.2.5. *Reference Interferometer*

The reference interferometer generates a signal for sampling the detector outputs from the far-IR and mid-IR interferometers. Sampling of the interferograms takes place at zero crossings of equally spaced reference fringes. This signal is also used in a phase-locked loop to control the velocity of the scan mechanism. The reference interferometer uses the central portion of the mid-IR optics and beamsplitter, and is constrained by the envelope of the central obscuration shadow of the mid-IR interferometer. The source for the reference interferometer is a solid state GaAlAs laser diode operating in the red region (811 nm at room temperature, 785 nm at 170 K). For redundancy, two laser diodes are available, selectable via command. Due to dependences on operating temperature and viewing geometries, the monochromatic emission source can provide only a short-term wavenumber calibration standard for the interferometer. The long-term standard is well-characterized molecular lines,  $\text{H}_2\text{O}$  and  $\text{NH}_3$  in FP1,  $\text{C}_2\text{H}_2$  and  $\text{C}_2\text{H}_6$  in FP3, and  $\text{CH}_4$  in FP4.

The zero path distance (ZPD) must be located in each interferogram to facilitate co-adding of interferograms in flight, in order to lower the CIRS telemetry data rate. For this purpose a white light interferogram must be produced so that the ZPD point can be located consistently from scan to scan. The source for the white light

interferometer is a Light Emitting Diode (LED), with a center wavelength of 870 nm, and a full width at half max of 70 nm. The white light shares the reference interferometer with the laser.

#### 5.2.6. Detectors

The detectors used in CIRS were chosen to maximize sensitivity in each wavelength range for the achievable operating temperatures. Thermopile detectors (FP1) give optimum performance in the far-infrared at 170 K. HgCdTe detectors (FP3 and FP4) can be tailored for highest performance near 80 K in the 7–16  $\mu\text{m}$  range.

*Far-IR: Thermal detectors.* The most important properties of a thermal detector are high sensitivity, a short response time and low excess noise. High sensitivity is achieved by having maximum absorptance in the absorbing element. The short response time is achieved by having a small heat capacity of the absorbing layer. Low excess noise is achieved by operating a thermoelectric detector without external bias. A thermopile detector consists of two elements, an absorber to convert infrared photons into heat, and a thermoelectric element that produces a voltage proportional to its internal temperature gradient. The cold side of the thermoelectric material is thermally sunk to a heat reservoir, and the hot side is attached to the radiation absorber.

*Mid-IR HgCdTe arrays.* The detectors for FP3 are a  $1 \times 10$  linear array of photoconductive (PC) HgCdTe elements operating near 80 K. The FP3 array was fabricated for a 15.7  $\mu\text{m}$  cut-off wavelength to optimize response in the 9–16  $\mu\text{m}$  range. The detectors for FP4 are a  $1 \times 10$  linear array of photovoltaic (PV) HgCdTe elements operating near 80 K. The FP4 array was fabricated for a 9.4  $\mu\text{m}$  cut-off wavelength to optimize response in the 7–9  $\mu\text{m}$  range. The use of a photovoltaic array allows a much lower bias-induced power dissipation, lessening the demand on the radiative cooler. The noise level for the photovoltaic array is also lower, due to its relative lack of  $1/f$  noise.

Five signal channels are available for each of the FP3 and FP4 10-element arrays. Therefore, only five detectors, or five paired detectors, are used in each observation. Four patterns of detectors – all even, all odd, center five or five pairs – are selected by scripted commands.

#### 5.2.7. Thermal Control

The CIRS optics assembly is passively cooled, and actively controlled to operate at  $170 \pm 0.1$  K for short time periods, with a maximum allowable drift of  $\pm 0.1$  K/day. This temperature is achieved by thermally isolating the instrument from the warmer spacecraft scan platform by a titanium mount, and by using thermal radiators to cool the instrument and FP1 detectors by radiating to deep space. Three control regions are monitored and controlled at 170 K: the telescope primary, telescope secondary, and instrument housing. The temperature at each of the control points is controlled by silicon diode thermistors. The temperature controller circuit power amplifies an

error signal and applies it to heater strips that warm the control point back up to 170 K. To minimize heater transient effects on the infrared signal, proportional heaters are used.

In addition to the thermal control heaters, the instrument also contains decontamination heaters. These high-powered heaters are command controlled, and are capable of increasing the instrument temperature to 270 K, and the cooler temperature to 300 K. They serve to drive off contaminants that might condense on the cooled optics and detectors.

### 5.3. ELECTRONICS ASSEMBLY

The analog and digital circuitry resides in a module outside the OA. Exceptions to this are preamplifier electronics, which must be close to detectors to minimize noise, and thermal-control sensors. The CIRS electronics assembly includes electronics for: (1) conditioning spacecraft power for electronics subassemblies; (2) communicating with the spacecraft, and processing of commands, science data and housekeeping data; (3) temperature control and temperature monitoring of the optics subassemblies; (4) operating and controlling the scan mechanism; (5) operating and controlling the science data sampling; and (6) processing the detector signals.

An instrument microprocessor provides instrument operation, on-board data processing, and communication with the spacecraft central computer. The signal handling and on-board processing are designed to minimize both the data rate and data volume. The data rate is minimized by tightly bandlimiting each signal by numerical filtering, and then resampling the numerical filter output at a reduced rate. The data volume is minimized by compressing the interferograms through efficient encoding. The dynamic range is high near zero path difference, and significantly lower in the wings of the interferogram. This allows the bits/word to be reduced in the wings. The on-board data processing for CIRS is performed under software control. CIRS is able to downlink individual interferograms, and summed pairs of sequential interferograms. The microprocessor carries out the functions of command and control, instrument operation, signal handling, and data compression/packetization.

### 5.4. 80 K COOLER

The FP3 and FP4 detector (HgCdTe) temperature is controlled with a single-stage passive cooler radiating to space. The temperature may be set via ground control to temperatures at discrete set points between 75 and 85 K, depending on the amount of backload present on the cooler from Saturn or its rings. The cooler is sized to drive the focal plane temperature below the selected set point, and control heat is supplied to stabilize the temperature at the set point. Temperature control is carried out with silicon diode sensors and thermostatic heaters. Calcutt *et al.* (1992) provide a preliminary discussion of the cooler design. The focal plane is rigidly

attached to the instrument, rather than to the cooler, which helps maintain optical alignment between the mid-infrared interferometer and the arrays through vibration and thermal cycling. The cooler cold stage supports the two HgCdTe arrays. The radiating cold panel is an aluminum honeycomb painted with electrically conductive black paint. The radiator panel is supported by a titanium cone-shaped housing. This is held by an aluminum tube, which surrounds the focal plane and forms the interface with the OA. The arrays are cooled via an aluminum alloy cold finger and a conductive strap from the cold finger to the arrays, which allows the cold finger to shift with respect to the instrument. A deployable aperture cover protected the cooler during launch and early cruise, and was jettisoned when the spacecraft was 2 AU from the sun.

### 5.5. INTERFEROGRAM PROCESSING

After the data are received on the ground, the interferograms are edited and transformed into calibrated spectra. Steps in this process include eliminating bad scans, removing predicted noise patterns, calibrating, apodizing, and Fourier transforming. Algorithms remove interferograms that have anomalous intensities and adjust interferogram lengths for uniformity. Known noise patterns are removed from the interferograms. Calibration is performed using deep space and internal shutter reference interferograms. The calibration uses untransformed interferograms and complex spectra, so that phase correction is an intrinsic part of the process. The interferograms are apodized (using a Hamming function) and Fourier transformed to produce calibrated spectra. A version of the spectra is also created without apodization.

### 5.6. IN-FLIGHT RADIOMETRIC CALIBRATION AND SENSITIVITY

The basic approach for the calibration of the CIRS measurements to absolute radiance units follows the calibration techniques developed previously for thermal emission interferometers (Hanel *et al.*, 2003; Hanel *et al.*, 1980; Revercomb *et al.*, 1988). Appendix C describes the calibration equations in detail. In-flight calibration of FP1 will be performed by periodically viewing deep space. FP3 and FP4 are calibrated by viewing deep space and an internal shutter at 170 K. The spectra amplitudes of the planetary spectra are scaled, at each wavenumber, to the amplitudes of the calibration targets. The detectors and electronics are designed to be linear at all wavenumbers with respect to the incoming radiance, a necessary condition for scaling the target spectra from the calibration spectra.

#### 5.6.1. In-Flight Sensitivity – NESRs

The NESR is the signal for which the SNR is unity (Hanel *et al.*, 2003). In-flight instrument responses and NESRs have been determined from in-flight calibration



data obtained during cruise. Detailed results will be reported elsewhere. The NESRs are calculated from noise changes observed in consecutive scan to scan interferograms. The standard deviation in response,  $\sigma$ , is calculated from the individual responses included in each average. This noise level includes random noise from detectors, scan-to-scan changes, and systematic noise from thermal drifts, etc. The NESR is calculated from:

$$NESR(\nu) = a \frac{\sigma[R(\nu)]}{R_{\text{Avg}}(\nu)} B_r(\nu) \quad (7)$$

where  $R_{\text{Avg}}(\nu)$  = the average of  $K$  measurements of the response,  $R(\nu)$ ;  $\sigma[R(\nu)]$  = the standard deviation of the response:

$$\sigma[R(\nu)] = \sqrt{\frac{\sum_{i=1}^K [R_i(\nu) - R_{\text{Avg}}(\nu)]^2}{K - 1}}. \quad (8)$$

$B_r$  is the Planck function at 170 K. FP1 is at the same temperature as the interferometer, so only deep space is required for the calibration (Appendix C).  $B_r$  corresponds to the instrument self-emission, and  $a = 1$  (Hanel *et al.*, 2003). For FP3 and FP4, the detectors are at a different temperature than the interferometer, and observations of a warm target (the detectors' view of the instrument with the shutter closed) and of deep space are both required for the calibration (Appendix C). In this case  $B_r$  corresponds to the 170-K warm target, and  $a = 1/\sqrt{2}$  (Hanel *et al.*, 1970).

The in-flight spectral responses and NESRs are shown in Figure 37. These responses cover the free spectral bandpass, which is the spectral region not affected by aliasing. Instrument "set points" are available to raise the FP3 and FP4 focal planes temperature above their nominal 76.4 K. These can be used to avoid calibration drifts that may result when the cooler is briefly exposed to the sun or Saturn during operations. However, an increase in focal plane temperature of 1 K causes an increase in the NESR of roughly 4%. The choice between sacrificing stability or SNR must be based on the objective of the observations affected.

### 5.6.2. Long-Term Stability

The CIRS temperature is maintained within 0.1 K (Section 5.2.7). Such a temperature excursion changes the uncalibrated detector signal due to changes in the instrument self-emission and also in the response term (Appendix C). The process of calibration removes these changes. Beyond these reversible short-term, temperature-driven changes, there remains the issue of possible long-term change or degradation, perhaps from contamination of optical surfaces, radiation damage, shift in optical alignment from stress relaxation, or detector degradation. In fact, CIRS appears to be quite stable once the short-term changes are accounted for. Observations of deep space made over two years, beginning with the telescope cover release in September, 2000, (3 months before the Jupiter swingby closest

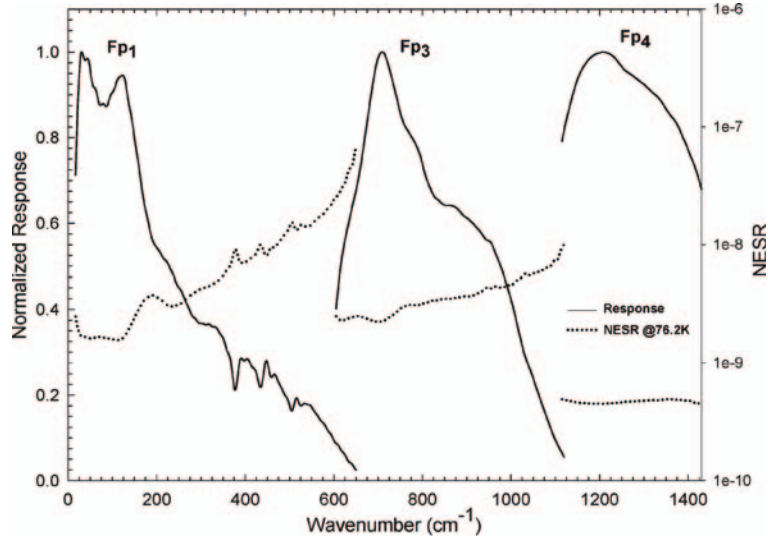


Figure 37. Spectral responses and NESRs for the three CIRS focal planes at a spectral resolution of  $15.5 \text{ cm}^{-1}$ . The FP3 and FP4 curves represent the average of the 10 detectors in each array, with each detector being within 20% of the average. The FP3 and FP4 NESRs correspond to a focal plane temperature of 76.2 K.

approach) show a cumulative decline in the mean FP1 signal level that is no larger than 0.5% (Brasunas and Lakew, 2003).

### Acknowledgments

We thank M. H. Elliot, J. S. Tingley, F. Carroll, S. Albright, S. Pilorz, and B. Wallis for their continuing support in the investigation science planning and operations, and P. J. Schinder for his assistance in setting up the CIRS database architecture.

### Appendix A: Retrieval of Atmospheric Parameters

Because CIRS measures thermal infrared emission, the measurements in a given spectral region will depend on both the atmospheric temperature and the abundances of the atmospheric constituents that are optically active in that region. The radiance  $I_\nu$  observed at wavenumber  $\nu$  is given by

$$I_\nu = \int_0^\infty B_\nu(T) \frac{\partial \tilde{T}}{\partial \mathbf{x}} \cdot d\mathbf{x}, \quad (\text{A.1})$$

where  $B_\nu$  is the Planck function at wavenumber  $\nu$ ,  $T$  is temperature,  $\tilde{T}$  is the transmissivity, and  $\mathbf{x}$  is the coordinate measured along the line of sight from the

observer to the portion of the atmosphere being observed. In the far- and mid-infrared,  $B_v$  is a strong function of temperature, while  $\tilde{T}$  primarily depends on the amount of absorber along the path length, with a weaker dependence on  $T$ . The retrieval of parameters within a given portion of the atmosphere requires the independent determination of temperature for that part of the atmosphere, either from the spectra or from an independent source.

Figure 2 illustrates the two types of observing geometry, nadir and limb viewing. In nadir viewing, atmospheric pressure and absorber mass increases along the line of sight until the surface is reached or else the local contribution to the observed radiance becomes negligible. In limb viewing the line of sight passes through the atmosphere, and deep space is the background; pressure increases along the line of sight to the tangent point and decreases beyond, while the absorber mass continues to increase monotonically. In nadir sounding there is no direct information on the dependence of the atmospheric parameters with the coordinate  $\mathbf{x}$ , and the optical depth is determined by the integrated number density of the absorber along the line of sight to a given pressure level. In this situation it is more straightforward to use pressure  $P$  as the vertical coordinate and rewrite (A.1) as

$$I_v = - \int_0^\infty B_v(T) \frac{\partial \tilde{T}}{\partial \ln P} d \ln P, \quad (\text{A.2})$$

The viewing geometry is implicitly contained in the transmissivity, which depends both on the vertical distribution of the absorber, and the viewing angle along the line of sight with respect to the local vertical direction. Equation (A.2) formally holds even when surface contributions matter, as they do over certain wavenumber intervals on Titan; one then includes delta functions at the surface pressure  $P_s$  within the integral. Alternatively, (A.2) can be expanded:

$$I_v = - \int_0^{P_s} B_v(T) \frac{\partial \tilde{T}}{\partial \ln P} d \ln P + B_v(T_s) \tilde{T}_s, \quad (\text{A.3})$$

where  $T_s$  is the surface temperature,  $\tilde{T}_s$  is the transmissivity along the line of sight to the surface, and the surface emissivity is assumed to be unity. The retrieval of temperature and composition profiles from (A.1) is generally an ill-posed problem, and solutions tend to be unstable unless structure at small spatial scales, which is dominated by instrument noise, is filtered out. Physically, this means that the profile information contained in the measurements is limited to relatively large vertical scales. Several general retrieval algorithms that introduce appropriate filtering, either explicitly or implicitly, are available (see, e.g., Craig and Brown, 1986; Hanel *et al.*, 2003; Rodgers, 2000).

Similar considerations apply to the inversion of limb-viewing spectra, but in this case one has additional information because of the viewing geometry, namely the dependence of the radiance on the tangent point altitude of the central ray within the FOV. Retrieval of both temperature and pressure at a given altitude is possible, because the spectrum typically has several wavelengths at which the optical depths

to the tangent point are  $\leq 1$ , but with different relative sensitivities to  $T$  and  $P$  (see, e.g., Gille and House, 1971). In practice, the absolute dependence of pressure on altitude is not precisely established, because of the inevitable errors associated with knowledge of the pointing of the instrument FOV during the measurements. However, the pressure-altitude relation is well determined relative to an arbitrary reference level, by application of the hydrostatic balance equation.

Conrath *et al.* (1998) and Conrath and Gautier (2000) discuss the retrievals of temperature (as well as the para fraction of  $H_2$  and the He abundance) for the outer planets from Voyager IRIS nadir-viewing spectra. Inversion of (A.2) typically entails the assumption that horizontal variations in atmospheric variables are small within the FOV. The sensitivity of the measured spectrum to the temperature at various atmospheric levels can be examined by assuming a reference temperature  $T^{(0)}(P)$  and computing the radiance spectrum  $I_v^{(0)}$ , assuming that the sources of opacity are known. Neglecting the temperature dependence of  $\tilde{T}$ , linearization of (A.2) gives

$$\delta I_v = - \int_0^\infty \frac{dB_v}{dT} \frac{\partial \tilde{T}}{\partial \ln P} \delta T d \ln P \equiv \int_0^\infty K \delta T d \ln P, \quad (\text{A.4})$$

where  $\delta I_v = I_v - I_v^{(0)}$  and  $\delta T = T - T^{(0)}$ ;  $K$  is the kernel for the retrieval problem, and it depends both on the derivative of the Planck function with respect to temperature and the derivative of the transmissivity with respect to  $\ln P$ . Similar considerations can be applied to the limb-viewing geometry.

The success of a temperature retrieval depends on the knowledge of opacity sources. For Saturn, the principal gaseous opacities used in temperature retrieval are  $H_2$  and  $CH_4$ . Figure 4 depicts the kernels, normalized to a maximum value of unity, with respect to absorption in the collision-induced S(0) and S(1) lines and the translational continuum of  $H_2$  ( $\nu < 600 \text{ cm}^{-1}$ ) and the  $\nu_4$  vibrational-rotational band of  $CH_4$  ( $\nu \sim 1300 \text{ cm}^{-1}$ ). Both nadir- and limb-viewing geometries are included. In the latter, the repetition of wavenumbers indicates that several tangent heights are being used. The Voyager IRIS observations were mostly done in the nadir-viewing mode, corresponding to the kernels on the left-hand side. In the spectral region dominated by collision-induced  $H_2$ , the opacity is a function of the height-dependent ratio of ortho to para hydrogen as well as the He/ $H_2$  ratio. Since both the temperature and ortho-para profiles are expected to vary with position on the planet, it is necessary to retrieve both parameters simultaneously. This is possible because there are multiple spectral intervals that sound the same atmospheric levels but have different relative sensitivities to temperature and the ortho-para ratio (Conrath *et al.*, 1998). In the initial analysis of Voyager data, IRIS spectra and radio occultation-derived profiles of the ratio of temperature to mean molecular weight were combined to obtain He/ $H_2$ . Temperature profiles for various mean molecular weights were used to calculate theoretical spectra, which were compared with the measured IRIS spectra at the occultation point. The molecular weight giving the best fit was then used to infer He/ $H_2$ . Subsequent comparisons with Galileo probe

results on Jupiter and a reanalysis of Saturn data in which only IRIS spectra were used indicate possible systematic errors in this technique (see Section 3.1.1). Both approaches will be used to obtain the Saturn He/H<sub>2</sub> ratio from the Cassini data.

Examination of the Saturn nadir kernels in Figure 4 reveals a gap in altitude coverage between  $\sim 3$  and 100 mbar. The addition of limb viewing helps to fill in this gap. Indeed the highest H<sub>2</sub> limb kernels, at 600 cm<sup>-1</sup>, overlap the nadir-viewing kernels corresponding to the  $\nu_4$  band of CH<sub>4</sub>, indicating that the CH<sub>4</sub> abundance of Saturn can unambiguously be determined. The additional air mass provided by limb viewing in the  $\nu_4$  band of CH<sub>4</sub> also permits one to obtain temperatures to higher altitudes, to  $\mu$  bar levels, although the retrieval at these levels is probably more complicated than discussed, because of non-LTE conditions.

Figure 12 depicts the normalized kernels for retrieval of atmospheric temperatures on Titan. Here collision-induced absorption of N<sub>2</sub> below 150 cm<sup>-1</sup> replaces collision-induced absorption by hydrogen as the dominant opacity source in the far-infrared. Again, limb viewing in the far infrared allows one to retrieve temperatures in the tropopause region and lower stratosphere that would otherwise be inaccessible from nadir viewing alone. The slight overlap between the inversion kernels from N<sub>2</sub> absorption and those from the  $\nu_4$  band of CH<sub>4</sub> will allow one to separate the effects of temperature and CH<sub>4</sub>, permitting the unambiguous retrieval of the distribution of CH<sub>4</sub> in Titan's stratosphere. The rotational lines of CH<sub>4</sub> near 100 cm<sup>-1</sup>, whose kernels (not shown) lie at lower altitudes in the stratosphere than those near 1300 cm<sup>-1</sup>, provide more overlap with the kernel from N<sub>2</sub>. Unlike the situation on Saturn, CH<sub>4</sub> on Titan is a condensable, and the stratospheric abundance potentially can vary with latitude. The direct retrieval of its spatial distribution is of great interest.

In addition to CH<sub>4</sub> on both Saturn and Titan and the Saturn hydrogen ortho-para ratio and He/H<sub>2</sub>, a number of other atmospheric parameters will be retrieved, including the abundances of hydrocarbons in the stratospheres of both Saturn and Titan. For these retrievals, the necessary independent constraint on the stratospheric thermal structure is provided by the retrievals from the  $\nu_4$  band of CH<sub>4</sub> band discussed above. Normalized nadir and limb contribution functions for spectral regions of C<sub>2</sub>H<sub>2</sub> and C<sub>2</sub>H<sub>6</sub> absorption are shown in Figure 9 for Saturn. Figure 17 depicts the contribution functions for spectral regions of C<sub>2</sub>H<sub>2</sub>, C<sub>2</sub>H<sub>6</sub>, and HCN absorption on Titan. Here, the contribution function is defined as the integrand in the first term on the right-hand side of (A3) and serves to indicate the portion of the atmosphere to which the measurement is sensitive. (Technically, the contribution function contains  $B(T)$  instead of  $dB(T)/dT$ .) In the case of the nadir measurements, the stratosphere is not completely opaque in these bands, and significant contributions to the measured radiances originate in the troposphere. Only mean abundances over relatively thick layers can be obtained; however, these retrievals can provide detailed horizontal mapping of these gases. In contrast, the limb-viewing measurements can provide significant vertical information on these gases when sufficiently near Saturn or Titan. The retrieval of the mole fraction profile of a gas from limb measurements is a highly non-linear problem, usually requiring considerable iteration. In addition, to

match the finite FOV of the instrument, contributions along several ray paths must be calculated for each limb foot print and each wavenumber. The problem is made computationally tractable by adopting the correlated-k approach for atmospheric transmittances (Goody and Yung, 1989). While  $C_2H_2$ ,  $C_2H_6$ , and HCN have been used as illustrations here, similar analyses will be applied to other constituents on Saturn and especially Titan. The inversion approach will provide a framework for assessing information content and analyzing error propagation even for gases that yield relatively weak spectral signals.

### Appendix B: FP1 FOV Response

CIRS is calibrated by viewing uniformly bright targets (the calibration shutter and/or deep space). This establishes the mean spatial response of the instrument FOV. For an ideal interferometer, the spatial response is uniform, so that the above procedure defines an adequate calibration protocol. However, the CIRS spatial response of FP1 is center-weighted. During the tour, many targets observed using FP1 will either not fill the field (such as satellites at large distances) or will be nonuniformly bright across the field (such as cloud structures on Saturn, or radial structure in the rings). To adequately calibrate such data it is therefore necessary to quantify the departure from the spatially uniform ideal. On 10–11 May 2002, we carefully executed two sets of orthogonal raster scans that covered an area  $8 \text{ mrad} \times 8 \text{ mrad}$  centered on the FP1 boresight. Jupiter was used as the target source. At the time of this measurement, the subtended angular diameter of Jupiter was  $0.290 \text{ mrad}$ , or  $0.075$  of the nominal  $3.9 \text{ mrad}$  FP1 diameter. This was chosen as a compromise between strong signal and fine spatial resolution. Pointing was verified against support images and against the reconstructed pointing files provided by the Cassini Project. Because the spacecraft was stabilized using reaction wheels, pointing was excellent, with jitter less than  $10\%$  of the apparent diameter of Jupiter.

Results of the test are illustrated in Figure 38. The FP1 response is greatest in the center and approximately follows a 2-D gaussian form, truncated in the wings. When viewing a spatially uniform source, a circle of  $2.54 \text{ mrad}$  diameter contains  $50\%$  of the total energy. The outer circle with diameter  $4.58 \text{ mrad}$  encircles  $95\%$  of the total energy (slightly more, actually, because the data have not yet had the finite size of Jupiter deconvolved). The nominal FOV diameter of  $3.9 \text{ mrad}$  contains  $83\%$  of the total.

Next, the signal from a uniform target disk, located at various distances from the FP1 center, was convolved with the spatial response function displayed in Figure 38. The ratio of the detected energy from a uniform target disk of a given radius, to the detected energy for a similar target that fills the FP1 FOV, was then calculated. The results, shown in Figure 39 enable calibration adjustments for imperfect pointing. Along the abscissa, the target is centered in FP1; the radii of contours, such as



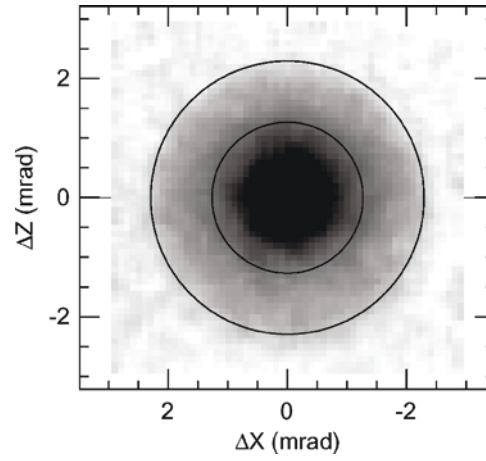


Figure 38. The spatial response of CIRS FP1 as derived from distant observations of Jupiter. The response is center-weighted, and approximately follows a 2-D gaussian form with truncated wings. Viewing a uniform target, the inner circle (radius 1.27 mrad) encloses 50% of the total signal. The outer circle (radius 2.29 mrad) encloses 95% of the total signal.

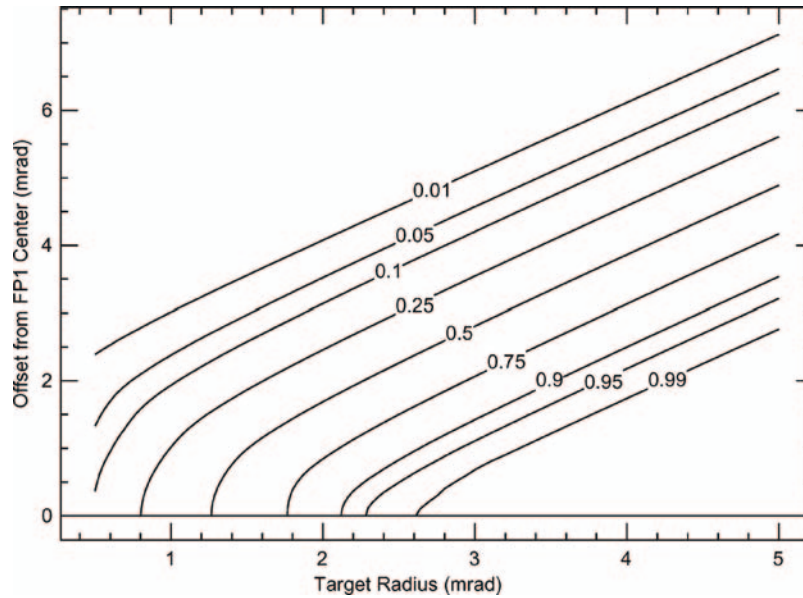


Figure 39. The fraction of a filled FP1 signal contributed by a finite circular target that is arbitrarily located within the FOV. The largest signal from such an unresolved target is obtained by centering it in the FOV where the spatial response is greatest.

shown in Figure 38, can be determined. The largest fractional encircled energy is obtained by placing the target in the center of FP1 where the spatial response is greatest.

### Appendix C: Radiometric Calibration Equations

The response of the instrument is one of the basic parameters describing the instrument and is monitored during flight to watch for any changes in instrument performance. The uncalibrated power spectrum ( $C_T$ ) of a thermal emission instrument is proportional to the difference between the spectral radiance of the instrument (self-emission) and the incoming target radiance:

$$C_T(\nu) = R(\nu)[B_I(\nu) - I_T(\nu)] \quad (\text{C.1})$$

where  $\nu$  = the frequency in wavenumbers ( $\text{cm}^{-1}$ ),  $C_T(\nu)$  = the amplitude of the observed uncalibrated power spectrum when viewing a target at temperature  $T_T$ ,  $R(\nu)$  = the spectral response of the interferometer in digital counts/spectral radiance,  $I_T(\nu)$  = the spectral radiance of the target in  $\text{W cm}^{-2} \text{ster}^{-1}/\text{cm}^{-1}$  at temperature  $T_T$ , and  $B_I(\nu)$  = the spectral radiance of the instrument (self-emission) in  $\text{W cm}^{-2} \text{ster}^{-1}/\text{cm}^{-1}$ .

The instrument self-emission is the dominant source of signal in any observation.

*Far-Infrared Interferometer.* The far infrared polarizing interferometer uses detectors at the same temperature as the instrument and telescope (170 K). Consequently, we only have one calibration parameter ( $R(\nu)$ ) to determine, and need only one calibration target, which is deep space. We may assume that  $B_I(\nu) = B_{170K}(\nu)$ . Then, from Equation (C.1) the applicable calibration equations are:

$$C_T(\nu) = R(\nu)[B_{170K}(\nu) - I_T(\nu)] \quad (\text{C.2})$$

$$C_C(\nu) = R(\nu)[B_{170K}(\nu) - B_C(\nu)] \quad (\text{C.3})$$

where  $C_C(\nu)$  = the amplitude of the observed uncalibrated power spectrum when viewing a target at temperature  $= T_C = 3 \text{ K}$ ,  $B_C(\nu)$  = the spectral radiance of the cold blackbody calibration target (deep space) at temperature  $= T_C$ ,  $B_{170K}(\nu)$  = the Planck function in  $\text{W cm}^{-2} \text{ster}^{-1}/\text{cm}^{-1}$  at temperature  $T_I = 170 \text{ K}$ .

Equations (C.2) and (C.3) may be solved for  $I_T(\nu)$  and  $R(\nu)$ :

$$I_T(\nu) = B_{170K}(\nu) - \frac{C_T(\nu)}{C_C(\nu)}[B_{170K}(\nu) - B_C(\nu)] \quad (\text{C.4})$$

$$R(\nu) = \frac{C_C(\nu)}{B_{170K}(\nu) - B_C(\nu)} \quad (\text{C.5})$$

*Mid-Infrared Interferometer.* The mid-infrared interferometer has two sets of detectors cooled to  $\sim 80 \text{ K}$ , quite different from that of the interferometer at 170 K. Consequently, the instrument emission term is due to a unknown combination of 80 K and 170 K radiation from the different optical components in the optical

train. Thus we need to determine two calibration parameters ( $R(\nu)$  and  $B_I(\nu)$ ) and need two calibration targets. For the mid-infrared interferometer, two blackbody reference sources will be viewed to establish the calibration: deep space at  $T_C \sim 3\text{K}$ , and a warm blackbody (via the shutter) at  $T_W = T_I = 170\text{ K}$ . In addition to Equation (C1) the applicable calibration equations are:

$$C_C(\nu) = R(\nu)[B_I(\nu) - B_C(\nu)] \quad (\text{C.6})$$

$$C_W(\nu) = R(\nu)[B_I(\nu) - B_W(\nu)] \quad (\text{C.7})$$

where  $B_C(\nu)$  = the Planck function at temperature  $T_C = 3\text{ K}$ ;  $B_W(\nu)$  = the Planck function at temperature  $T_W = 170\text{ K}$ .

Assuming that the spectral response is independent of the target radiance, and that the signal processing chain and detectors are linear, the three equations may be solved for  $I_T(\nu)$ ,  $R(\nu)$ , and  $B_I(\nu)$ :

$$I_T(\nu) = \frac{(C_T(\nu) - C_C(\nu))B_W(\nu) + (C_W(\nu) - C_T(\nu))B_C(\nu)}{C_W(\nu) - C_C(\nu)} \quad (\text{C.8})$$

$$R(\nu) = \frac{C_C(\nu) - C_W(\nu)}{B_W(\nu) - B_C(\nu)} \quad (\text{C.9})$$

$$B_I(\nu) = \frac{C_C(\nu)B_W(\nu) - B_C(\nu)C_W(\nu)}{C_C(\nu) - C_W(\nu)} \quad (\text{C.10})$$

The above formalism has assumed that the combined optical and electrical phase characteristics of the instrument are the same for all target radiances and for the internal instrument emission. This assumption is correct for FP1, because it is isothermal (Brasunas, 2002), but it only approximately holds for FP3 and FP4. For these, the above formalism will have to include complex Fourier transforms, using the complex power spectra and not just their amplitudes (Revercomb *et al.* 1988). A more detailed discussion of the CIRS calibration procedure will be given elsewhere.

## References

- Abbas, M. M., LeClair, A., Owen, T., Conrath, B. J., Flasar, F. M., Kunde, V. G., *et al.*: 2004, *Astrophys. J.* **602**, 1063–1074.
- Achterberg, R. K., Conrath, B. J., Gierasch, P. J., and Flasar, F. M.: 2003, *Bull. Amer. Astron. Soc.* **35**, 997.
- Achterberg, R. K. and Flasar, F. M.: 1996, *Icarus* **119**, 350–369.
- Allison, M., Godfrey, D. A., and Beebe, R. F.: 1990, *Science* **247**, 1061–1063.
- Andrews, D. G., Holton, J. R., and Leovy, C. B.: 1987, *Middle Atmosphere Dynamics*, Academic Press, Orlando, U.S.A., 489 pp.
- Araki, S.: 1991, *Icarus* **90**, 139–171.
- Atreya, S. K., Edgington, S. G., Trafton, L. M., Caldwell, J. J., Noll, K. S., and Weaver, H. A.: 1995, *Geophys. Res. Let.* **22**, 1625–1628.

- Atreya, S. K., Mahaffy, P. R., Niemann, H. B., Wong, M. H., and Owen, T. C.: 2003, *Planet. Space Sci.* **51**, 105–112.
- Atreya, S. K., Wong, M. H., Owen, T. C., Mahaffy, P. R., Niemann, H. B., de Pater, I., *et al.*: 1999, *Planet. Space Sci.* **47**, 1243–1262.
- Aumann, H.H. and Kieffer, H. H.: 1973, *Astrophys. J.* **186**, 305–311.
- Awal, M. and Lunine, J. I.: 1994, *Geophys. Res. Lett.* **21**, 2491–2494.
- Baines, K. H. and Bergstralh, J. T.: 1986, *Icarus* **109**, 20–39.
- Baines, K. H., Michelson, M. E., Larson, L. E., and Ferguson, D. W.: 1995, *Icarus* **114**, 328–340.
- Bandfield, J.L.: 2002, *J. Geophys. Res. (Planets)* **107** (E6), CiteID 5042.
- Barnet, C. D., Westphal, J. A., Beebe, R. F., and Huber, L. F.: 1992, *Icarus* **100**, 499–511.
- Beebe, R. F., Barnet, C., Sada, P. V., and Murrell, A. S.: 1992, *Icarus* **95**, 163–172.
- Bell, J. F., Cruikshank, D. P., and Gaffey, M. J.: 1985, *Icarus* **61**, 192–207.
- de Bergh, C., Schmitt, B., Binzel, R. P., and Bus, S. J.: 2003, *Bull. Amer. Astron. Soc.* **35**, 940.
- Bézard, B., Coustenis, A., and McKay, C. P.: 1995, *Icarus* **113**, 267–276.
- Bézard, B., Drossart, P., Lellouch, E., Tarrago, G., and Maillard, J. P.: 1989, *Astrophys. J.* **346**, 509–513.
- Bézard, B., Feuchtgruber, H., Moses, J. I., and Encrenaz, T.: 1998, *Astron. Astroph.* **334**, L41–L44.
- Bézard, B., Gautier, D., and Conrath, B.: 1984, *Icarus* **60**, 274–288.
- Bézard, B., Gautier, D., and Marten, A.: 1986, *Astron. Astrophys.* **161**, 387–402.
- Bézard, B., Marten, A., and Paubert, G.: 1993, *Bull. Amer. Astron. Soc.* **25**, 1100.
- Bézard, B., Moses, J. I., Lacy, J., Greathouse, T., Richter, M., and Griffith, C.: 2001a, *Bull. Amer. Astron. Soc.* **33**, 1079–1080.
- Bézard, B., Drossart, P., Encrenaz, T., and Feuchtgruber, H.: 2001b, *Icarus* **155**, 492–500.
- Bird, M. K., Dutta-Roy, R., Heyl, M., Allison, M., Asmar, S. W., Folkner, W. M., Preston, R. A., Atkinson, D. H., Edenhoffer, P., Plettemeier, D., Wohlmuth, R., Iess, L., and Tyler, G. L.: 2002, *Space Sci. Rev.* **104**, 613–640.
- Bossard, A., Kamga, R., and Raulin, F.: 1986, *Icarus* **67**, 305–324.
- Brasunas, J. C.: 2002, *Appl. Optics* **41**, 2481–2487.
- Brasunas, J. C. and Lakew, B.: 2004, Long-term stability of the Cassini Fourier transform spectrometer en route to Saturn, in *Recent Res. Devel. Optics*, **4**, 95–113.
- Bregman, J. D., Lester, D. F., Rank, D. M.: 1975, *Astrophys. J. (Lett.)* **202**, L55–L56.
- Briggs, F.H. and Sacket, P. D.: 1989, *Icarus* **80**, 77–103.
- Broadfoot, A. L., Sandel, B. R., Shemansky, D. E., Holberg, J. B., Smith, G. R., Strobel, *et al.*: 1981, *Science* **204**, 979–983.
- Brown, M. E.: 2000, *Astron. J.* **119**, 977–983.
- Brown, M. E., Bouchez, A. H., and Griffith, C. A.: 2002, *Nature* **420**, 797–797.
- Brown, R. H.: 1983, *Icarus* **56**, 414–425.
- Brown, R. H. and Matson, D. L.: 1987, *Icarus* **72**, 84–94.
- Brown, R. H., Baines, K. H., Bellucci, G., Bibring, J.-P., Buratti, B.J., Capaccioni, F., *et al.*: 2004, ‘Cassini Visible and Infrared Mapping Spectrometer experiment’, *Space Sci. Rev.*, this issue.
- Buratti, B. J.: 1985, *Icarus* **61**, 208–217.
- Buratti, B. J., Hicks, M. D., Tryka, K. A., Sittig, M. S., Newburn, R. L.: 2002, *Icarus* **155**, 375–381.
- Buratti, B. J., Mosher, J. A., and Johnson, T. V.: 1990, *Icarus* **87**, 339–357.
- Burns, J. A., Hamilton, D. P., and Showalter, M. R.: 2001, Dusty rings and circumplanetary dust: Observations and simple physics, in: Grün, E., Gustafson, B. A. S., Dermott, S. F., and Fechtig, H. (eds.), *Interplanetary Dust*, Springer-Verlag, Berlin, pp. 641–725.
- Cabane, M., Chassefière, E., and Israel, G.: 1992, *Icarus* **96**, 176–189.
- Calcutt, S. B., Taylor, F. W., Ade, P., Kunde, V. G., and Jennings, D.: 1992, *J. Brit. Interplanetary Soc.* **45**, 811–816.
- Caldwell, J., Hua, X.-M., Turgeon, B., Westphal, J. A., and Barnet, C. D.: 1993, *Science* **260**, 326–329.

- Carlson, B. E., Rossow, W. B., and Orton, G. S.: 1988, *J. Atmos. Sci.* **45**, 2066–2081.
- Carlson, B. E., Lacis, A. A., and Rossow, W. B.: 1992, *Astrophys. J.* **393**, 357–372.
- Cerceau, F., Raulin, F., Courtin, R., and Gautier, D.: 1985, *Icarus* **62**, 207–220.
- Charney, J. G. and Drazin, P. G.: 1961, *J. Geophys. Res.* **66**, 83–109.
- Christensen, P. R., Bandfield, J. L., Bell, J. F., Gorelick, N., Hamilton, V. E., Ivanov, A., *et al.*: 2003, *Science* **300**, 2056–2061.
- Christensen, P. R., Bandfield, J. L., Smith, M. D., Hamilton, V. E., and Clark, R. N.: 2000a, *J. Geophys. Res.* **105**, 9609–9621.
- Christensen, P. R., Bandfield, J. L., Clark, R. N., Edgett, K. S., Hamilton, V. E., Hoefen, T., *et al.*: 2000b, *J. Geophys. Res.* **105**, 9623–9642.
- Clark, R. N. and McCord, T. B.: 1980, *Icarus* **43**, 161–168.
- Clarke, D. W. and Ferris, J. P.: 1997, *Origins of Life and Evol. Biosphere* **27**, 225–248.
- Coll, P., Bernard, J.-M., Navarro-González, R., and Raulin, F.: 2003, *Astrophys. J.* **598**, 700–703.
- Coll, P., Coscia, D., Gazeau, M.-C., and Raulin, F.: 1997, *Adv. Space Res.* **19** (7), 1113–1119.
- Collins, S. A., Cook, A. F. II, Cuzzi, J. N., Danielson, G. E., Hunt, G. E., Johnson, T. V., Morrison, D., Owen, T., Pollack, J. B., Smith, B. A., and Terrile, R. J.: 1980, *Nature* **288**, 439–443.
- Colthup, N. B., Daley, L. H., and Wiberley, S. E.: 1975, *Introduction to Infrared and Raman Spectroscopy*, Academic Press, New York, 523 pp.
- Comas Sola, J.: 1908, *Astron. Nachr.* **179**, 289–290.
- Combes, M., Vapillon, L., Gendron, E., Coustenis, A., Lai, O., Wittenberg, R., and Sirdey, R.: 1997, *Icarus* **129**, 482–497.
- Connerney, J. E. C. and Waite, J. H.: 1984, *Nature* **312**, 136–138.
- Conrath, B. J., Flasar, F. M., Pirraglia, J. A., Gierasch, P. J., and Hunt, G. E.: 1981, *J. Geophys. Res.* **86**, 8679–8775.
- Conrath, B. J. and Gierasch, P. J.: 1983, *Nature* **306**, 571–572.
- Conrath, B. J. and Gierasch, P. J.: 1984, *Icarus* **57**, 184–204.
- Conrath, B. J. and Pirraglia, J. A.: 1983, *Icarus* **53**, 286–291.
- Conrath, B. J. and Gautier, D.: 2000, *Icarus* **144**, 124–134.
- Conrath, B. J., Gautier, D., Hanel, R. A., and Hornstein, J. S.: 1984, *Astrophys. J.* **282**, 807–815.
- Conrath, B. J., Gierasch, and Ustinov, E. A.: 1998, *Icarus* **135**, 501–517.
- Cooke, Maren: 1991, *Saturn's Rings: Photometric Studies of the C Ring and Radial Variation in the Keeler Gap*. PhD Thesis, Cornell University, p. 65.
- Courtin, R., Léna, P., De Muizon, M., Rouan, D., Nicollier, C., and Wijnbergen, J.: 1979, *Icarus* **38**, 411–419.
- Courtin, R., Gautier, D., Marten, A., and Kunde, V.: 1983, *Icarus* **53**, 121–132.
- Courtin, R., Gautier, D., Marten, A., Bézard, B., and Hanel, R.: 1984, *Astrophys. J.* **287**, 899–916.
- Courtin, R., Gautier, D., and McKay, C. P.: 1995, *Icarus* **114**, 144–162.
- Courtin, R., and Kim, S. J.: 2002, *Planet. Space Sci.* **50**, 309–321.
- Coustenis, A. and Bézard, B.: 1995, *Icarus* **115**, 126–140.
- Coustenis, A., Bézard, B., and Gautier, D.: 1989a, *Icarus* **113**, 267–276.
- Coustenis, A., Bézard, B. and Gautier, D.: 1989b, *Icarus* **82**, 67–80.
- Coustenis, A., Bézard, B., Gautier, D., Marten, A., and Samuelson, R.: 1991, *Icarus* **89**, 152–167.
- Coustenis, A., Encrenaz, Th., Bézard, B., Bjoraker, G., Graner, G., Dang-Nhu, M., and Arié, E.: 1993, *Icarus* **102**, 240–260.
- Coustenis, A., Gendron, E., Lai, O., Veran, J.-P. Woillez, J., Combes, M., *et al.*: 2001, *Icarus* **154**, 501–515.
- Coustenis, A., Salama, A., Lellouch, E., Encrenaz, Th., Bjoraker, G. L., Samuelson, R. E., de Graauw, Th., Feuchtgruber, H., and Kessler, M. F.: 1998, *Astron. Astrophys.* **336**, L85–L89.
- Coustenis, A., Salama, A., Schulz, B., Ott, S., Lellouch, E., Encrenaz, Th., Gautier, D., and Feuchtgruber, H.: 2003, *Icarus* **161**, 383–403.

- Coustonis, A., Schmitt, B., Khanna, R. K., and Trotta, F.: 1999, *Planet. Space Sci.* **47**, 1305–1329.
- Craig, I. J. D. and Brown, J. C.: 1986, *Inverse Problems in Astronomy*, Adam Hilger Ltd., Boston.
- Cruikshank, D. P.: 1979, *Icarus* **37**, 307–309.
- Cruikshank, D. P. and Brown, R. H.: 1982, *Icarus* **50**, 82–87.
- Cruikshank, D. P., Brown, R. H., Calvin, W. M., Roush, T. L., and Bartholomew, M. J.: 1998, in Schmitt, B. de Bergh, C., and Festou, M. (eds.), *Solar System Ices*, Kluwer Academic Publishers, Kluwer, Dordrecht, pp. 579–606.
- Cruikshank, D. P., Veverka, J., and Lebofsky, L. A.: 1984, Satellites of Saturn: Optical properties, in Gehrels, T., and Matthews, M. S. (eds.), *Saturn*, University of Arizona Press, Tucson, pp. 640–667.
- Cunningham, C. T., Ade, P. A. R., Robson, E. I., Nolt, I. G., and Radostitz, J. V.: 1981, *Icarus* **48**, 127–139.
- Cuzzi, J. N., Lissauer, J. J., Esposito, L. W., Holberg, J. B., Marouf, E. A., Tyler, G. L., and Boischot, A.: 1984, Saturn's rings: Properties and processes, in Greenberg, R. and Brahic, A. (eds.), *Planetary Rings*, University of Arizona Press, Tucson, pp. 72–198.
- Cuzzi, J. N., Colwell, J. E., Esposito, L. W., Porco, C. C., Murray, C. D., Nicholson, P. D., Spilker, L. J., Marouf, E. A., French, R. C., Rappaport, N., and Muhleman, D.: 2002, *Space Sci. Rev.* **118**, 209–251.
- Cuzzi, J. N. and Estrada, P. R.: 1998, *Icarus* **132**, 1–35.
- Delitsky, M. L. and Lane, A. L.: 1998, *J. Geophys. Res.* **103**, 31,391–31,403.
- Delitsky, M. L. and Lane, A. L.: 2002, *J. Geophys. Res.* **107**, 3.1–3.17.
- Delitsky, M. L., Lane, A. L., Henry-Riyad, H., and Tidwell, T. T.: 2003, *Bull. Amer. Astron. Soc.* **35**, 914.
- Delpech, C., Guillemin, J.-C., Paillous, P., Khelifi, M., Bruston, P., and Raulin, F.: 1994, *Spectrochimica Acta* **50A**, 1095–1100.
- Desch, M. D. and Kaiser, M. L.: 1981, *Geophys. Res. Lett.* **8**, 253–256.
- De Pater, I. and Dickel, J. R.: 1991, *Icarus* **94**, 474–492.
- Dermott, S. F. and Sagan, C.: 1995, *Nature* **374**, 238–240.
- Dones, L., Cuzzi, J. N., and Showalter, M. R.: 1993, *Icarus* **105**, 184–215.
- Doyle, L. R., Dones, L., and Cuzzi, J. N.: 1989, *Icarus* **80**, 104–135.
- Drossart, P., Lellouch, E., Bézard, B., Maillard, J. P., and Tarrago, G.: 1990, *Icarus* **83**, 248–253.
- Dubouloz, N., Raulin, F., Lellouch, E., and Gautier, D.: 1989, *Icarus* **82**, 81–96.
- Dunkerton, T.: 1978, *J. Atmos. Sci.* **35**, 2325–2333.
- Eliassen, A. and Palm, E.: 1961, *Geophys. Publ.* **22**(3), 1–23.
- Ellsworth, K. and Schubert, G.: 1983, *Icarus* **54**, 490–510.
- Epstein, E. E., Janssen, M. A., and Cuzzi, J. N.: 1984, *Icarus* **58**, 403–411.
- Esposito, L. W., Cuzzi, J. N., Holberg, J. H., Marouf, E. A., Tyler, G. L., and Porco, C. C.: 1984, 'Saturn's rings: Structure, dynamics, and particle properties', in Gehrels, T., and Matthews, M. S. (eds.), *Saturn*, University of Arizona Press, Tucson, pp. 463–545.
- Esposito, L. W., Barth, C. A., Colwell, J. E., Lawrence, G. M., McClintock, W. E., Stewart, A. I. F., et al.: 2004, *Space Sci. Rev.*, this issue.
- Estrada, P. R. and Cuzzi, J. N.: 1996, *Icarus* **122**, 251–272.
- Ferrari, C., Galdemard, P., Lagage, P. O., Pantin, E., and Quoirin, C.: 2003, Imaging Saturn's rings with CAMIRAS: Thermal inertia of B and C rings. Preprint.
- Feuchtgruber, H., Lellouch, E., De Graauw, T., Bézard, B., Encrenaz, Th., and Griffin, M.: 1997, *Nature* **389**, 159–162.
- Flasar, F. M.: 1983, *Science* **221**, 55–57.
- Flasar, F. M.: 1998a, *Planet. Space Sci.* **46**, 1109–1124.
- Flasar, F. M.: 1998b, *Planet. Space Sci.* **46**, 1125–1147.
- Flasar, F. M. and Conrath, B. J.: 1990, *Icarus* **85**, 346–354.



- Flasar, F. M. and Conrath, B. J.: 1992, 'The meteorology of Titan', in *Proceedings Symposium on Titan*, European Space Agency SP-338, pp. 89–99.
- Flasar, F. M., Conrath, B. J., Pirraglia, J. A., Clark, P. C., French, R. G., and Gierasch, P. J.: 1981b, *J. Geophys. Res.* **86**, 8759–8767.
- Flasar, F. M., Kunde, V. G., Achterberg, R. K., Conrath, B. J., Simon-Miller, A. A., Nixon, C. A., *et al.*: 2004, *Nature* **427**, 132–135.
- Flasar, F. M., Samuelson, R. E., and Conrath, B. J.: 1981a, *Nature* **292**, 693–698.
- Fortney, J. I. and Hubbard, W. B.: 2003, *Icarus* **164**, 228–243.
- Fouchet, T., Lellouch, E., and Feuchtgruber, H.: 2003, *Icarus* **161**, 127–143.
- Fouchet, T., Orton, G. S., Irwin, P. G. J., and Calcutt, S. B.: 2004a, *Icarus* **170**, 237–241.
- Fouchet, T., Irwin, P. G. J., Parrish, P., Calcutt, S. B., Taylor, F. W., Nixon, C., and Owen, T.: in press 2003b, *Icarus*. **172**, 50–58.
- Fouchet, T., Prangé, R., Connerney, J.E.C., Courtin, R., Ben Jaffel, L., Noll, K., and McConnell, J. C.: 1996, *Bull. Amer. Astron. Soc.* **28**, 1129.
- Friedson, A. J., West, R. A., Hronek, A. K., Larsen, N. A., and Dalal, N.: 1999, *Icarus* **138**, 141–156.
- Froidevaux, L.: 1981, *Icarus* **46**, 4–17.
- Froidevaux, L. and Ingersoll, A. P.: 1980, *J. Geophys. Res.* **85**, 5929–5936.
- Froidevaux, L., Matthews, K., and Neugebauer, G.: 1981, *Icarus* **46**, 18–26.
- Gautier, D., Conrath, B., Flasar, M., Hanel, R., Kunde, V., Chedin, A., and Scott, N.: 1981, *J. Geophys. Res.* **86**, 8713–8720.
- Gautier, D. and Grossman, K.: 1972, *J. Atmos. Sci.* **29**, 788–792.
- Gautier, D. and Owen, T.: 1983, *Nature* **304**, 691–694.
- Gautier, D. and Owen, T.: 1989, The composition of the outer planets' atmospheres, in Atreya, S. K., Pollack, J. B., and Matthews, M. S. (eds.) *Origins and Evolution of Planetary and Satellite Atmospheres*, to The University of Arizona Press, Tucson, pp. 487–512.
- Gendron, E., Coustenis, A., Drossart, P., Combes, M., Hirtzig, M., Lacombe, F., Rouan, D., Collin, C., Pau, S., Lagrange, A.-M.: in press, *Astron. Astroph.* **417**, L21–L24.
- Gierasch, P. J. and Conrath, B. J.: 1987, *J. Geophys. Res.* **92**, 15019–15029.
- Gierasch, P. J., Conrath, B. J., and Magalhães, J. A.: 1986, *Icarus* **67**, 456–483.
- Gierasch, P. J., Conrath, B. J., and Read, P. L.: 2004, *J. Atmos. Sci.* **61**, 1953–1965.
- Gierasch, P. J. and Goody, R. M.: 1969, *J. Atmos. Sci.* **26**, 979–980.
- Gille, J. C. and House, F. B.: 1971, *J. Atmos. Sci.* **28**, 1427–1442.
- Gillett, F. C., Forrest, W. J., and Merrill, K. M.: 1973, *Astrophys. J.* **184**, L93–L95.
- Gillett, F. C.: 1975, *Astrophys. J.* **201**, L41–L43.
- Gladman, B., Kavelaars, J. J., Holman, M., Nicholson, P. D., Burns, J. A., Hergenrother, C. W., *et al.*: 2001, *Nature* **412**, 163–166.
- Godfrey, D. A.: 1990, *Science* **247**, 1206–1208.
- Godfrey, D. A.: 1988, *Icarus* **76**, 335–356.
- Goody, R. M. and Yung, Y. L.: 1989, *Atmospheric Radiation: Theoretical Basis*, 2nd ed., Clarendon Press, Oxford.
- de Graauw, T., Feuchtgruber, H., Bézard, B., Drossart, P., Encrenaz, T., Beintema, D. A., *et al.*: 1997, *Astron. Astrophys.* **321**, L13–16.
- Greathouse, T., Moses, J., Bézard, B., Griffith, C., Lacy, J., Knez, C., and Richter, M.: 2003, *Bull. Amer. Astron. Soc.* **35**, 1019.
- Griffin, M. J., Naylor, D. A., Davis, G. R., Ade, P. A. R., Oldman, P. G., Swinyard, B. M., *et al.*: 1996, *Astron. Astrophys.* **315**, L389–L392.
- Griffith, C. A., Owen, T., Geballe, T. R., Rayner, J., Rannou, P.: 2003, *Science* **300**, 628–630.
- Griffith, C. A., Owen, T., Miller, G. A., and Geballe, T.: 1998, *Nature* **395**, 575–578.
- Griffith, C. A., Hall, J. L., and Geballe, T. R.: 2000, *Science* **290**, 509–513.
- Grossman, A. W., Muhleman, D. O., and Berge, G. L.: 1989, *Science* **245**, 1211–1215.

- Grundy, W. M., Buie, M. W., Stansberry, J. A., and Spencer, J. R.: 1999, *Icarus* **142**, 536–549.
- Guillot, T.: 1999, *Planet. Space Sci.* **47**, 1183–1200.
- Gurwell, M. A. and Muhleman, D. O.: 1995, *Icarus* **117**, 375–382.
- Haas, M. R., Erickson, E. F., McKibbin, D. D., Goorvitch, D., and Caroff, L. M.: 1982, *Icarus* **51**, 476–490.
- Haff, P. K., Siscoe, G. L., and Eviatar, A.: 1983, *Icarus* **56**, 426–438.
- Hamilton, D. P. and Burns, J. A.: 1994, *Science* **264**, 550–553.
- Hanel, R., Conrath, B., Flasar, M., Kunde, V., Lowman, P., Maguire, W., Pearl, J., Pirraglia, J., and Samuelson, R.: 1979, *Science* **204**, 972–976.
- Hanel, R., Crosby, D., Herath, L., Vanous, D., Collins, D., Creswick, H., Harris, C., and Rhodes, M.: 1980, *Applied Optics* **19**, 1391–1400.
- Hanel, R., Conrath, B., Flasar, F. M., Kunde, V., Maguire, W., Pearl, J. C., *et al.*: 1981, *Science* **212**, 192–200.
- Hanel, R. A., Conrath, B. J., Flasar, F. M., Kunde, V. G., Maguire, W., Pearl, J. C., *et al.*: 1982, *Science* **215**, 544–548.
- Hanel, R. A., Conrath, B. J., Jennings, D. E., and Samuelson, R. E.: 2003, *Exploration of the Solar System by Infrared Remote Sensing*, 2nd ed., Cambridge University Press.
- Hanel, R. A., Conrath, B. J., Kunde, V. G., Pearl, J. C., and Pirraglia, J. A.: 1983, *Icarus* **53**, 262–285.
- Hanel, R. A., Schlachman, B., Clark, F. D., Prokesh, C. H., Taylor, J. B., Wilson, W. M., and Chaney, L.: 1970, *Appl. Optics* **9**, 1767–1774.
- Hapke, B.: 1996a, *J. Geophys. Res.* **101**, 16,833–16,840.
- Hapke, B.: 1996b, *J. Geophys. Res.* **101**, 16,817–16,832.
- Held, I. M. and Hou, A. Y.: 1980, *J. Atmos. Sci.* **37**, 515–533.
- Hidayat, T., Marten, A., Bézard, B., Gautier, D., Owen, T., Matthews, H. E., and Paubert, G.: 1997, *Icarus* **126**, 170–182.
- Hidayat, T., Marten, A., Bézard, B., and Gautier, D.: 1998, *Icarus* **133**, 109–133.
- Hinson, D. P. and Tyler, G. L.: 1983, *Icarus* **54**, 337–352.
- Hoefen, T. M., Clark, R. N., Bandfield, J. L., Smith, J. C., and Christensen, P. R.: in press., *Science*.
- Holton, J. R.: 1979, *An Introduction to Dynamic Meteorology*, 2nd ed., Academic Press, New York.
- Horanyi, M., Burns, J. A., and Hamilton, D. P.: 1992, *Icarus* **97**, 248–259.
- Hoskins, B. J., McIntyre, M. E., and Robertson, A. W.: 1985, *Quart. J. Royal Met. Soc.* **111**, 877–404.
- Hourdin, F., Talagrand, O., Sadourny, R., Courtin, R., Gautier, D., and McKay, C. P.: 1995, *Icarus* **117**, 358–374.
- Hubbard, W. B.: 1980, *Rev. Geophys. Space Phys.* **18**, 1–9.
- Hubbard, W. B., Sicardy, B., Miles, R., Hollis, A. J., Forrest, R. W., Nicolson, I. K. M., *et al.*: 1993, *Astron. Astrophys.* **269**, 541–563.
- Hubbard, W. B., Hunten, D. M., Reitsema, D. M., Brosch, N., Nevo, Y., Carreira, E., *et al.*: 1990, *Nature* **343**, 353–355.
- Hudgins, D. M., Sandford, S. A., Allamandola, L. J., and Tielens, A. G.: 1993, *Astrophys J. Suppl.* **86**, 713–870.
- Hudson, B. L. and Moore, M. H.: 1993, *Astrophys. J.* **404**, L29–L32.
- Hunten, D. M., Tomasko, M. G., Flasar, F. M., Samuelson, R. E., Strobel, D. F., and Stevenson, D. J.: 1984, Titan, in Gehrels, T., and Matthews, M. (eds.), *Saturn*, University of Arizona Press, pp. 671–759.
- Ingersoll, A. P., Beebe, R. F., Conrath, B. J., and Hunt, G. E.: 1984, ‘Structure and dynamics of Saturn’s atmosphere’, in Gehrels, T., and Matthews, M. (eds.), *Saturn*, University of Arizona Press, pp. 195–238.
- Ingersoll, A., Orton, G. S., Münch, G., Neugebauer, G., and Chase, S. C.: 1980, *Science* **207**, 439–443.
- Ingersoll, A. P. and Porco, C. C.: 1978, *Icarus* **35**, 27–43.

- Irwin, P. G. J., Parrish, P., Fouchet, T., Calcutt, S. B., Taylor, F. W., Simon-Miller, A. A., *et al.*: 2004, *Icarus* **172**, 37–49.
- Kargel, J. S., Pozio, S.: 1996, *Icarus* **119**, 385–404.
- Karkoschka, E. and Tomasko, M.G.: 1992, *Icarus* **97**, 161–181.
- Kaye, J. A. and Strobel, D. F.: 1984, *Icarus* **59**, 314–335.
- Kawata, Y.: 1983, *Icarus* **56**, 453–464.
- Kawata, Y. and Irvine, W.M.: 1975, *Icarus* **24**, 472–482.
- Khanna, R. K., Perera-Jarmer, M. A., and Ospina, M. J.: 1987, *Spectrochim. Acta* **43A**, 421–425.
- Khare, B. N., Sagan, C., Thompson, W. R., Arakawa, E. T., Meissen, C., and Tuminello, P. S.: 1994, *Canad. J. Chem.* **72**, 678–694.
- Khelifi, M., Nollet, M., Paillous, P., Bruston, P., Raulin, F., Benilan, Y., *et al.*: 1999, *J. Mol. Spectrosc.* **194**, 206–210.
- Khelifi, M., Paillous, P., Bruston, P., Raulin, F., and Guillemin, J.-C.: 1996, *Icarus* **124**, 318–328.
- Khelifi, M., Paillous, P., Bruston, P., Guillemin, J.-C., Bénilan, Y., Daoudi, A., *et al.*: 1997, *Spectrochimica Acta* **53A**, 707–712.
- Khelifi, M. and Raulin, F.: 1991, *Spectrochim. Acta* **47A**, 171–176.
- Khelifi, M., Raulin, F., and Dang-Nhu, M.: 1992, *v. Mol. Spectrosc.* **154**, 235–239.
- Kliore, A. J., Anderson, J. D., Armstrong, J. W., Asmar, S. W., Hamilton, C. L., Rappaport, N. J., *et al.*: 2003, ‘Cassini radio science’, *Space Sci. Rev.*, this issue.
- Kliore, A., Patel, I. R., Lindal, G. F., Sweetnam, D. N., Hotz, H. B., Waite, J. H., and McDonough, T. R.: 1980, *J. Geophys. Res.* **85**, 5857–5870.
- Kuiper, G.: 1944, *Astrophys. J.* **100**, 378–383.
- Kunde, V. G., Aikin, A. C., Hanel, R. A., Jennings, D. E., Maguire, W. C., and Samuelson, R. E.: 1981, *Nature* **292**, 686–688.
- Kunde, V. G., Ade, P., Barney, R., Bergman, D., Borelli, R., Boyd, D., *et al.*: 1996, *SPIE* **2803**, 162–177.
- Kunde, V. G., Flasar, F. M., Jennings, D. E., Bézard, B., Strobel, D. F., Conrath, B.J., *et al.*: 2004, ‘Jupiter’s atmospheric composition from thermal-infrared observations at high spectral and spatial resolution’, *in preparation*.
- Lammer, H. and Bauer, S. J.: 2003, *Space Sci. Rev.* **186**, 281–291.
- Lammer, H., Stumptner, W., Molina-Cuberos, G. J., Bauer, S. J., and Owen, T.: 2000, *Planet. Space Sci.* **48**, 529–543.
- Lane, A. L., Hord, C. W., West, R. A., Esposito, L. W., Coffeen, D. L., Sato, M., *et al.*: 1982, *Science* **215**, 537–543.
- Lara, L., Lellouch, E., Lopez-Moreno, J. J., and Rodrigo, R.: 1996, *J. Geophys. Res.* **101**, 23261–23283.
- Lara, L. M., Bézard, B., Griffith, C. A., Lacy, J. H., and Owen, T.: 1998, *Icarus* **131**, 317–333.
- Lecluse, C., Robert, F., Gautier, D., and Guiraud, M.: 1996, *Planet. Space Sci.* **44**, 1579–1592.
- Lellouch, E., Bézard, B., Fouchet, T., Feuchtgruber, H., Encrenaz, T., and de Graauw, T.: 2001, *Astron. Astrophys.* **370**, 610–622.
- Lellouch, E., Bézard, B., Moses, J. I., Davis, G. R., Drossart, P., Feuchtgruber, H., *et al.*: 2002, *Icarus* **159**, 112–131.
- Lellouch, E., Coustenis, A., Gautier, D., Raulin, F., Dubouloz, N., and Frère, C.: 1989, *Icarus* **79**, 328–349.
- Lellouch, E., Coustenis, A., Sebag, B., Cuby, J.-G., López-Valverde, M., Schmitt, B., *et al.*: 2003, *Icarus* **162**, 125–142.
- Lemmon, M., Karkoschka, E., and Tomasko, M.: 1993, *Icarus* **103**, 329–332.
- Lemmon, M. T., Smith, P. H., Lorenz, R. D.: 2002, *Icarus* **160**, 365–375.
- Leovy, C. B., Friedson, A. J., and Orton, G. S.: 1991, *Nature* **354**, 380–382.

- Lewis, J. S.: 1972, *Icarus* **16**, 241–252.
- Leyrat, C., Ferrari, C., Spilker, L., and Charnoz, S.: 2003, *Bull. Amer. Astron. Soc.* **35**, 951.
- Lindal, G. F., Wood, G. E., Hotz, H. B., Sweetnam, D. N., Eshleman, V., and Tyler, G. L.: 1983, *Icarus* **53**, 348–363.
- Lindal, G. F., Sweetnam, D. N., and Eshleman, V. R.: 1984, *Astron. J.* **90**, 1136–1146.
- Linsky, J. L.: 1998, *Space Sci. Rev.* **84**, 285–296.
- Lorenz, E. N.: 1967, *The Nature and Theory of the General Circulation of the Atmosphere*, World Meteorological Organization, 161 pp.
- Lorenz, R. D., McKay, C. P., and Lunine, J. I.: 1997, *Science* **275**, 642–644.
- Low, F. J. and Rieke, G. H.: 1974, *Astrophys. J.* **190**, L143–L145.
- Lunine, J. I.: 1993, *Rev. Geophys.* **31**, 133–149.
- Lunine, J. I., Stevenson, D. J., and Yung, Y. L.: 1983, *Science* **222**, 1229–1230.
- Lunine, J. I., Yung, Y. L., and Lorenz, R. D.: 1999, *Planet. Space Sci.* **47**, 1291–1303.
- Lutz, B. L., De Bergh, C., and Owen, T.: 1983, *Science* **220**, 1374–1375.
- Lynch, D. K., Mazuk, A. L., Russell, R. W., and Hackwell, J. A.: 2000, *Icarus* **146**, 43–47.
- Magni, G. and Coradini, A.: 2004, *Planet. Space Sci.* **52**, 343–360.
- Maguire, W. C., Hanel, R. A., Jennings, D. E., Kunde, V. G., and Samuelson, R. E.: 1981, *Nature* **292**, 683–686.
- Mahaffy, P. R., Donahue, T. M., Atreya, S. K., Owen, T. C., and Niemann, H. B.: 1998, *Space Science Rev.* **84**, 251–263.
- Marouf, E. A., Tyler, G. L., Zebker, H. A., Simpson, R. A., and Eschelman, V. R., 1983, *Icarus* **54**, 189–211.
- Marten, A., Gautier, D., Tanguy, L., Lecacheux, A., Rosolen, C., and Paubert, G.: 1988, *Icarus* **76**, 558–562.
- Marten, A., Hidayat, T., Biraud, Y., and Moreno, R.: 2002, *Icarus* **158**, 532–540.
- Marten, A., Hidayat, T., Moreno, R., Paubert, G., Bézard, B., Gautier, D., Matthews, H., and Owen, T.: 1997, *IAU Circular* **6702**, July 19.
- Martin, D. H.: 1982, Polarizing (Martin-Puplett) interferometric spectrometers for the near- and submillimeter spectra, in Button, K.J. (ed.), *Infrared and Millimeter Waves, Vol. 6, Systems and Components*, Ch. 2, Academic Press, New York.
- Martin, D. H. and Puplett, E.: 1969, *Infrared Phys.* **10**, 105–109.
- Massie, S. T. and Huntten, D. M.: 1982, *Icarus* **49**, 213–226.
- Matson, D. L. and Brown, R.H.: 1989, *Icarus* **77**, 67–81.
- Matson, D. L. and Nash, D.: 1983, *J. Geophys. Res.* **88**, 4,771–4,783.
- Matson, D. L., Spilker, L. J., and Lebreton, J.-P.: 2002, *Space Sci. Rev.* **104**, 1–58.
- Matzler, C.: 1998, ‘Microwave properties of ice and snow’, in Schmitt, B., De Bergh, C., and Festou, M. (eds.), *Solar System Ices*, Kluwer, Dordrecht, pp. 241–257.
- McCord, T., Carlson, R. W., Smythe, W. D., Hansen, G. B., Clark, R. N., Hibbitts, C. A., et al.: 1997, *Science* **278**, 271–275.
- McKay, C. P., Coustenis, A., Samuelson, R. E., Lemmon, M. T., Lorenz, R. D., Cabane, M., Rannou, P., and Drossart, P.: 2001, *Planet. Space Sci.* **49**, 79–99.
- Meier, R., Smith, B.-A., Owen, T.-C., Terrile, R.-J.: 2000, *Icarus* **145**, 462–473.
- Meier, R., Owen, T., Matthews, H., and Marten, A.: 1997, JCMT observations of the HCN 4–3 transition, unpublished.
- Mellon, M. T., Jakosky, B. M., Kieffer, H. H., and Christensen: 2000, *Icarus* **148**, 437–455.
- Mennella, V., Brucato, J. R., Colangeli, L., Palumbo, P., Rotundi, A., and Bussolletti, E.: 1998, *Astroph. J.* **496**, 1058–1066.
- Morrison, D.: 1974, *Icarus* **22**, 51–56.
- Morrison, D., Jones, T. J., Cruikshank, D. P., and Murphy, R. E.: 1975, *Icarus* **24**, 157–171.

- Moses, J. I., Bézard, B., Lellouch, E., Gladstone, G. R., Feuchtgruber, H., and Allen, M.: 2000a, *Icarus* **143**, 244–298.
- Moses, J. I., Lellouch, E., Bézard, B., Gladstone, G. R., Feuchtgruber, H., and Allen, M.: 2000b, *Icarus* **145**, 166–202.
- Mousis, O., Gautier, D., and Coustenis, A.: 2002, *Icarus* **159**, 156–165.
- Muhleman, D.O., Grossman, A. W., Butler, B. J., and Slade, M. A.: 1990, *Science* **248**, 975–980.
- Murphy, R. E., Cruikshank, D. P., and Morrison, D.: 1972, *Astrophys. J.* **177**, L93–L96.
- Nicholson, P. D., Hamilton, D. P., Matthews, K., and Yoder, C.F.: 1992, *Icarus* **100**, 464–484.
- Niemann, H. B., Atreya, S. K., Carignan, G. R., Donahue, Haberman, T. M., Harpold, D. N., *et al.*: 1996, *Science* **272**, 846–849.
- Niemann, H. B., Atreya, S. K., Carignan, G. R., Donahue, T. M., Haberman, J. A., Harpold, D. N., *et al.*: 1998, *J. Geophys. Res.* **103**, 22831–22845.
- Nishio, M., Paillous, P., Khelifi, M., Bruston, P., and Raulin, F.: 1995, *Spectrochim. Acta* **51A**, 617–622.
- Nixon, C. A., Achterberg, R. K., Conrath, B. J., Irwin, P. G. J., Fouchet, T., Parrish, P. D., *et al.*: 2004, ‘Meridional variations of C<sub>2</sub>H<sub>2</sub> and C<sub>2</sub>H<sub>6</sub> in Jupiter’s atmosphere from Cassini CIRS infrared spectra’, preprint.
- Noll, K., Knacke, R. F., Geballe, T. R., Tokunaga, A. T.: 1986, *Astrophys. J. (Lett.)* **309**, L91–L94.
- Noll, K. S. and Larson, H. P.: 1990, *Icarus* **89**, 168–189.
- Noll, K. S., Roush, T. L., Cruikshank, D. P., Pendleton, Y. J., and Johnson, R. E.: 1997, *Nature* **388**, 45–47.
- Orsolini, Y. and Leovy, C. B.: 1989, *Geophys. Res. Lett.* **16**, 1245–1248.
- Orsolini, Y. and Leovy, C. B.: 1993a, *Icarus* **106**, 392–405.
- Orsolini, Y. and Leovy, C. B.: 1993b, *Icarus* **106**, 406–418.
- Orton, G. S.: 1992, ‘Ground-based observations of Titan’s thermal spectrum’, in *Proceedings Symposium on Titan*, European Space Agency SP-338, pp. 81–85.
- Orton, G. S. and Ingersoll, A. P.: 1980, *J. Geophys. Res.* **85**, 5871–5881.
- Orton, G., Fisher, B., Yanamandra-Fisher, P., Baines, K., Ressler, M., Beach-Kimball, B., *et al.*: 2003, *Bull. Amer. Astron. Soc.* **35**, 1018.
- Orton, G., Fisher, B., Yanamandra-Fisher, P., Baines, K. H., Momary, T. W., and Fox, O. D.: 2002, *Bull. Amer. Astron. Soc.* **34**, 855–856.
- Orton, G. S., Friedson, A. J., Caldwell, J., Hammel, H. B., Baines, K. H., Bergstralh, J. T., *et al.*: 1991, *Science* **252**, 537–542.
- Orton, G. S., Friedson, A. J., Huie, M., Malcom, M., Anthony, D., Caldwell, J., Tokunaga, A., and Klavetter, J.: 1989, *Bull. Amer. Astron. Soc.* **21**, 953–954.
- Orton, G.S., Serabyn, E., and Lee, Y.T.: 2001, *Icarus* **149**, 489–490.
- Owen, T.: 1982, *Planet. Space Sci.* **30**, 833.
- Owen, T., Biver, N., Marten, A., Matthews, H. E., and Meier, R.: 1999a, *IAU Circ.* 7306, Nov. 11. Please check a.
- Owen, T. C., Cruikshank, D. P., Dalle Ore, C. M., Geballe, T. R., Roush, T. L., and de Bergh, C.: 1999b, *Icarus* **139**, 379–382. Please check b.
- Owen, T. C., Cruikshank, D. P., Dalle Ore, C. M., Geballe, T. R., Roush, T. L., de Bergh, C., *et al.*: 2001, *Icarus* **149**, 160–172.
- Pang, K. D., Voge, C. C., Rhoads, J. W., Ajello, J. M.: 1984, *J. Geophys. Res.* **89**, 9,459–9,470.
- Pappalardo, R., Collins, G., Helfenstein, P., McCord, T., Prockter, L., Schenk, P., and Spencer, J.: 2004, Ganymede, in Bagenal, F., (eds.), *Jupiter*, Cambridge University Press, pp. 363–396.
- Pearl, J., Hanel, R., Kunde, V., Maguire, W., Fox, K., Gupta, S., Ponnampereuma, C., and Raulin, F.: 1979 *Nature* **280**, 757–758.
- Pilcher, C. B., Chapman, C., Lebofsky, L. A., and Kieffer, A. A.: 1970, *Science* **167**, 1372–1373.
- Pirraglia, J. A.: 1989, *Icarus* **79**, 196–207.

- Plescia, J. B.: 1983, *Icarus* **56**, 255–277.
- Pollack, J. B., Hubickyi, O., Bodenheimer, P., Lissauer, J. J., Podolak, M., and Greenzweig, Y.: 1966, *Icarus* **124**, 62–85.
- Pollack, J. B., Summers, A., and Baldwin, B.: 1973, *Icarus* **20**, 263–278.
- Poulet, F. and Cuzzi, J. N.: 2002, *Icarus* **160**, 350–358.
- Poulet, F., Cuzzi, J. N., French, R. G., and Dones, L.: 2002, *Icarus* **158**, 224–248.
- Porco, C. C., West, R. A., Squyres, S., McEwen, A., Thomas, P., Murray, C. D., *et al.*: 2004, *Space Sci. Rev.*, this issue.
- Prangé, R., Fouchet, T., Connerney, J. E. P., and Courtin, R.: 1999, ‘FUV diagnostic of Saturn’s stratosphere with the HST: Search for water influx from the rings, in *Planetary Systems: The Long View*, Proc. IXème Conférence de Blois, J. Tran Than Van et L. Celnikier (ed.), Editions Frontières, Paris, pp. 309–312.
- Prinn, R. G., Larson, H. P., Caldwell, J. J., and Gautier, D.: 1984, Composition and Chemistry of Saturn’s Atmosphere, in Gehrels, T., and Matthews, M. S. (eds.), *Saturn*, University of Arizona Press, Tucson, pp. 88–149.
- Puetter, R. C. and Russell, R. W.: 1977, *Icarus* **32**, 37–40.
- Rannou, P., Hourdin, F., and McKay, C. P.: 2002, *Nature* **418**, 853–856.
- Raulin, F.: 1987, *Adv. Space Res.* **7**, 71–81.
- Raulin, F., Accaoui, B., Razaghi, A., Dang-Nhu, M., Coustenis, A., and Gautier, D.: 1990, *Spectrochim. Acta* **46A**, 671–683.
- Raulin, F. and Owen, T. C.: 2003, *Space Sci. Rev.* **104**, 377–394.
- Revercomb, H. E., Buijs, H., Howell, H. B., LaPorte, D. D., Smith, W. L., and Sromovsky, L. A.: 1988, *Applied Optics* **27**, 3210–3218.
- Richardson, D.: 1994, *Mon. Not. R. Astron. Soc.* **269**, 493–511.
- Rodgers, C. D.: 2000, *Inverse Methods for Atmospheric Sounding: Theory and Practice*, London, World Scientific Publishing.
- Roe, H. G., de Pater, I., Macintosh, B. A., McKay, C. P.: 2002, *Icarus* **157**, 254–258.
- Roellig, T. L., Werner, M. W., Becklin, E. E.: 1988, *Icarus* **73**, 574–583.
- Romani, P. N.: 1989, *B.A.A.S.* **21**, 953.
- Rosen, P. A.: 1989, Waves in Saturn’s rings probed by radio occultation. Scientific Report No D845-1989-1, Jet Propulsion Laboratory.
- Saari, J. M. and Shorthill, R. W.: 1963, *Icarus* **2**, 115–136.
- Salo, H.: 1995, *Icarus* **117**, 287–312.
- Samuelson, R. E. and Mayo, L. A.: 1991, *Icarus* **91**, 207–219.
- Samuelson, R. E. and Mayo, L. A.: 1997, *Planet. Space Sci.* **45**, 949–958.
- Samuelson, R. E., Hanel, R. A., Kunde, V. G., and Maguire, W. C.: 1981, *Nature* **292**, 688–693.
- Samuelson, R. E., Maguire, W. C., Hanel, R. A., Kunde, V. G., Jennings, D. E., Yung, Y. L., and Aikin, A. C.: 1983, *J. Geophys. Res.* **88**, 8709–8715.
- Samuelson, R. E., Mayo, L. A., Knuckles, M. A., and Khanna, R. J.: 1997a, *Planet. Space Sci.* **45**, 941–948.
- Samuelson, R. E., Nath, N. R., and Borysow, A.: 1997b, *Planet. Space Sci.* **45**, 959–980.
- Sánchez-Lavega, A., Lecacheux, J., Colas, F., and Laques, P.: 1993, *Science* **260**, 329–332.
- Sánchez-Lavega, A., Pérez-Hoyos, S., Acarreta, J. R., and French, R. G.: 2002, *Icarus* **160**, 216–219.
- Sánchez-Lavega, A., Pérez-Hoyos, S., Rojas, J. F., Hues, R., and French, R. G.: 2003, *Nature* **423**, 623–625.
- Sandel, B. R., Shemansky, D. E., Broadfoot, A. L., Holberg, J. B., Smith, G. R., McConnell, J. C., *et al.*: 1982, *Science* **215**, 548–553.
- Schoeberl, M. R. and Hartmann, D. L.: 1991, *Science* **251**, 46–52.



- Schubert, G., Spohn, T., and Reynolds, R. T.: 1986, 'Thermal histories, compositions and internal structures of the moons of the solar system', in Burns, J. A. and Matthews, M. S. (eds.), *Satellites*, University of Arizona Press, Tucson, pp. 224–292.
- Sears, W. D.: 1995, *Icarus* **113**, 39–56.
- Shindo, F.: 2002, *Spectroscopie IR et UV expérimentale de composés intéressant l'atmosphère de Titan*, Thèse de Doctorat de l'Université Paris 7, Spécialité Astrophysique et Techniques Spatiales.
- Shindo, F., Bénilan, Y., Guillemin, J.-C., Chaquin, P., Jolly, A., and Raulin, F.: 2001a, *BAAS*, **33**(3), 1109.
- Shindo, F., Bénilan, Y., Chaquin, P., Guillemin, J.-C., Jolly, A., and Raulin, F.: 2001b, *J. Mol. Spectrosc.* **210**(2), 191–195.
- Shindo, F., Bénilan, Y., Guillemin, J.-C., Chaquin, P., Jolly, A., and Raulin, F.: 2003, *Planet. Space Sci.* **51**, 9–17.
- Showman, A. P.: 2001, *Icarus* **152**, 140–150.
- Showalter, M. R.: 1996, *Icarus* **124**, 677–689.
- Showalter, M. R. and Cuzzi, J. N.: 1993, *Icarus* **103**, 124–143.
- Showalter, M. R., Cuzzi, J. N., and Larson, S. M.: 1991, *Icarus* **94**, 451–473.
- Showalter, M. R., Pollack, J. B., Ockert, M. E., Doyle, L., and Dalton, J. B.: 1992, *Icarus* **100**, 394–411.
- Shu, F. H., Cuzzi, J. N., and Lissauer, J. J.: 1982, *Icarus* **53**, 185–206.
- Sicardy, B., Brahic, A., Ferrari, C., Gautier, D., Lecacheux, J., Lellouch, E., *et al.*: 1990, *Nature* **343**, 350–353.
- Simonelli, D. P., Kay, J., Adinolfi, D., Veverka, J., Thomas, P. C., and Helfenstein, P.: 1999, *Icarus* **138**, 249–258.
- Smith, B. A., Soderblom, L., Beebe, R., Boyce, J., Briggs, G., Bunker, A., *et al.*: 1981, *Science* **212**, 163–191.
- Smith, B. A., Soderblom, L., Batson, R., Bridges, P., Inge, J., Masursky, H., *et al.*: 1982, *Science* **215**, 504–537.
- Smith, M. D., Conrath, B. J., and Gautier, D.: 1996a, *Icarus* **124**, 598–607. Please check a.
- Smith, M. D. and Gierasch, P. J.: 1995, *Icarus* **116**, 159–179.
- Smith, P. H., Lemmon, M. T., Lorenz, R. D., Sromovsky, L. A., Caldwell, J. J., and Allison, M. D.: 1996b, *Icarus* **119**, 336–349. Please check b.
- Smith, R. G., Robinson, G., Hyland, A. R., and Carpenter, G. L.: 1994, *Month. Not. Roy. Astron. Soc.* **271**, 481–489.
- Smith, W. H. and Baines, K. H.: 1990, *Icarus* **85**, 109–119.
- Snyder-Hale, A. and Hapke, B.: 2002, *Icarus* **156**, 318–334.
- Socrates, G.: 1980, *Infrared Characteristic Group Frequencies*, Wiley-Interscience, New York.
- Spencer, J. R.: 1987, 'The surfaces of Europa, Ganymede, and Callisto: An investigation using Voyager IRIS thermal infrared spectra. Ph.D. Thesis, University of Arizona, Tucson.
- Spencer, J.: 1990, *Icarus* **83**, 27–38.
- Spencer, J. R., Carlson, R. W., Becker, T. L., and Blue, J. S.: 2004, Maps and spectra of Jupiter and the Galilean satellites, In *Jupiter: Planet, Satellites, and magnetosphere*, Bagenal, F., McKinnon, W. B., and Dowling, T. (eds.), Cambridge University Press, pp. 689–698.
- Spencer, J. R., Tamppari, L. K., Martin, T. Z., and Travis, L. D.: 1999, *Science* **284**, 1514–1516.
- Spilker, L., Pilorz, S., Ferrari, C., Pearl, J., and Wallis, B.: 2003, *Bull. Amer. Astron. Soc.* **35**, 929.
- Sprague, A. L.: 2000, 'Thermal emission spectroscopy and data analysis of solar system regoliths', in Sitko, M. L., Sprague, A. L., and Lynch, D. K. (eds.), *Thermal Emission Spectroscopy and Analysis of Dust, Disks and Regoliths*; Lunar and Planetary Institute, Houston, 167–186 pp.

- Sromovsky, L. A., Revercomb, H. E., Krauss, R. J., and Suomi, V. E.: 1983, *J. Geophys. Res.* **88**, 8650–8666.
- Strobel, D.: 1982, *Planet. Space Sci.* **30**, 839–848.
- Tholen, D. J. and Zellner, B.: 1983, *Icarus* **53**, 341–347.
- Thomas, P. C., Black, G. J., and Nicholson, P. D.: 1995, *Icarus* **117**, 128–148.
- Thompson, W. R., Todd, H., Schwartz, J., Khare, B. N., and Sagan, C.: 1991, *Icarus* **90**, 57–73.
- Tokunaga, A. T.: 1980, *Bull. Amer. Astron. Soc.* **12**, 669.
- Tokunaga, A. T., Caldwell, J., and Nolt, I. G.: 1980, *Nature* **287**, 212–214.
- Tomasko, M. G., West, R. A., Orton, G. S., and Tieffell, V. G.: 1984, Clouds and aerosols in Saturn's atmosphere, in *Saturn* (T. Gehrels and M. S. Matthews, Eds.) pp. 150–194. Univ. of Arizona Press, Tucson.
- Tomasko, M. G., *et al.*: 2002, *Space Sci. Rev.* **104**, 469–551.
- Toon, O. B., McKay, C., Courtin, R., and Ackerman, T.: 1988, *Icarus* **75**, 255–284.
- Tyler, G. L., Eshleman, V. R., Anderson, J. D., Levy, G. S., Lindal, G. F., Wood, G. E., *et al.*: 1981, *Science* **212**, 201–206.
- Van Allen, J. A.: 1983, *J. Geophys. Res.* **88**, 6911–6918.
- de Vanssay, E., Gazeau, M. C., Guillemin, J. C., and Raulin, F.: 1995, *Planet. Space Sci.* **43**, 25–31.
- Warren, S. G.: 1984, *App. Opt.* **23**, 1206–1225.
- Weisstein, E. W. and Serabyn, E.: 1996, *Icarus* **123**, 23–36.
- West, R. A., Strobel, D. F., and Tomasko, M. G.: 1986, *Icarus* **65**, 161–217.
- Whitcomb, S. E., Hildebrand, R. H., and Keene, J.: 1980, *Science* **210**, 788–789.
- Wilson, P. D. and Sagan, C.: 1995, *J. Geophys. Res.* **100**, 7,531–7,537.
- Wilson, P. D. and Sagan, C.: 1996, *Icarus* **122**, 92–106.
- Wolf, A. A.: 2002, *Space Sci. Rev.* **104**, 101–128.
- Wong, A.-S., Morgan, C. G., Yang, Y. L., and Owen, T.: 2002, *Icarus* **155**, 382–397.
- Wong, M. H., Bjoraker, G. L., Smith, M. D., Flasar, F. M., and Nixon, C. A.: 2004, *Planet. Space Sci.* **52**, 385–395.
- Yanamandra-Fisher, P. A., Orton, G. S., Fisher, B. M., and Sánchez-Lavega, A.: 2001, *Icarus* **150**, 189–193.
- Yelle, R. V.: 1991, *Astrophys. J.* **383**, 380–400.
- Yelle, R. V. and McGrath, M. A.: 1996, *Icarus* **119**, 90–111.
- Yoder, C. F., Synnott, S. P., and Salo, H.: 1989, *Astron. J.* **98**, 1875–1889.
- von Zahn, U. and Hunten, D.: 1996, *Science* **272**, 849–851.

# THE CASSINI ULTRAVIOLET IMAGING SPECTROGRAPH INVESTIGATION

LARRY W. ESPOSITO<sup>1,\*</sup>, CHARLES A. BARTH<sup>1</sup>, JOSHUA E. COLWELL<sup>1</sup>, GEORGE M. LAWRENCE<sup>1</sup>, WILLIAM E. McCLINTOCK<sup>1</sup>, A. IAN F. STEWART<sup>1</sup>, H. UWE KELLER<sup>2</sup>, AXEL KORTH<sup>2</sup>, HANS LAUCHE<sup>2</sup>, MICHEL C. FESTOU<sup>3</sup>, ARTHUR L. LANE<sup>4</sup>, CANDICE J. HANSEN<sup>4</sup>, JUSTIN N. MAKI<sup>4</sup>, ROBERT A. WEST<sup>4</sup>, HERBERT JAHN<sup>5</sup>, RALF REULKE<sup>5</sup>, KERSTIN WARLICH<sup>5</sup>, DONALD E. SHEMANSKY<sup>6</sup> and YUK L. YUNG<sup>7</sup>

<sup>1</sup>University of Colorado, Laboratory for Atmospheric and Space Physics, 1234 Innovation Drive, Boulder, CO 80303, U.S.A.

<sup>2</sup>Max-Planck-Institut für Aeronomie, Max-Planck-Strasse 2, 37191 Katlenburg-Lindau, Germany

<sup>3</sup>Observatoire Midi-Pyrénées, 14 avenue E. Belin, F31400 Toulouse, France

<sup>4</sup>Jet Propulsion Laboratory, 4800 Oak Grove Drive, Pasadena, CA 91109, U.S.A.

<sup>5</sup>Deutsches Zentrum für Luft und Raumfahrt, Institut für Weltraumsensorik und Planetenerkundung, Rutherford Strasse 2, 12489 Berlin, Germany

<sup>6</sup>University of Southern California, Department of Aerospace Engineering, 854 W. 36th Place, Los Angeles, CA 90089, U.S.A.

<sup>7</sup>California Institute of Technology, Division of Geological and Planetary Sciences, MS 150-21, Pasadena, CA 91125, U.S.A.

(\*Author for correspondence: E-mail: larry.esposito@lasp.colorado.edu)

(Received 8 July 1999; Accepted in final form 18 October 2000)

**Abstract.** The Cassini Ultraviolet Imaging Spectrograph (UVIS) is part of the remote sensing payload of the Cassini orbiter spacecraft. UVIS has two spectrographic channels that provide images and spectra covering the ranges from 56 to 118 nm and 110 to 190 nm. A third optical path with a solar blind CsI photocathode is used for high signal-to-noise-ratio stellar occultations by rings and atmospheres. A separate Hydrogen Deuterium Absorption Cell measures the relative abundance of deuterium and hydrogen from their Lyman- $\alpha$  emission. The UVIS science objectives include investigation of the chemistry, aerosols, clouds, and energy balance of the Titan and Saturn atmospheres; neutrals in the Saturn magnetosphere; the deuterium-to-hydrogen (D/H) ratio for Titan and Saturn; icy satellite surface properties; and the structure and evolution of Saturn's rings.

**Keywords:** Cassini, rings, Saturn, spectroscopy on Titan and on Saturn

## Nomenclature

CASPER	Cassini Sequence Planner
CDS	Command and Data Handling Subsystem
CEM	Channel Electron Multiplier
CIRS	Composite Infrared Spectrometer
CODACON	Coded Anode Array Converter (see Lawrence and McClintock, 1996)
D/H	Deuterium/hydrogen (ratio)
DISR	Descent Imager/Spectral Radiometer
EUV	Extreme ultraviolet
EUVE	Extreme Ultraviolet Explorer
FOV	Field of view



*Space Science Reviews* **115**: 299–361, 2004.

© 2004 Kluwer Academic Publishers. Printed in the Netherlands.

FUV	Far ultraviolet
HDAC	Hydrogen-Deuterium Absorption Cell
HSP	High Speed Photometer
HST	Hubble Space Telescope
HUT	Hopkins Ultraviolet Telescope
HV	High voltage
HVPS	High Voltage Power Supply
IR	Infrared
IRIS	Infrared Interferometer Spectrometer
ISM	Interstellar medium
ISO	Infrared Science Observatory
ISS	Imaging Science Subsystem
IUE	International Ultraviolet Explorer
LISM	Local interstellar medium
MAPS	Magnetosphere and plasma science
MPAe	Max-Planck-Institut für Aeronomie
NIST	National Institute for Standards and Technology
PAD	Pulse Amplifier Discriminator
PPS	Voyager Photo-Polarimeter Subsystem
RTG	Radioisotope Thermoelectric Generator
RSP	Remote Sensing Platform
SIRTF	Space Infrared Telescope Facility
SMOW	Standard mean ocean water
SOHO	Solar and Heliospheric Observatory
SSR	Solid state recorders
STIS	Space Telescope Imaging Spectrometer
UV	Ultraviolet
UVIS	Ultraviolet Imaging Spectrograph
UVS	Voyager or Galileo Ultraviolet Spectrometer
VIMS	Visual and Infrared Mapping Spectrometer
WFPC2	Wide Field and Planetary Camera 2

## 1. Introduction

As part of the Cassini orbiter remote sensing payload, the Ultraviolet Imaging Spectrograph (UVIS) is coaligned with the cameras (ISS) and the infrared spectrometers (CIRS and VIMS; see their chapters in this volume). The spectrograph design draws on the University of Colorado experience of building UV spectrometers for the Mariner, Pioneer, and Galileo missions and extends the previous capabilities by using two-dimensional CODACON detectors and adding separate channels for high speed photometry and for measuring the deuterium-to-hydrogen ratio with a Hydrogen Deuterium Absorption Cell. The spectrographic channels cover the wavelength range from 56 to 190 nm. A special pickoff mirror allows solar occultation observations in the extreme UV. All parts of the experiment are housed in a rectangular case that is rigidly attached to the spacecraft's Remote Sensing

Platform (RSP). The instrument has its own microprocessor for storing and executing commands, and a limited memory to buffer and store observational data. Sequences of commands in the instrument memory are initiated by ‘trigger’ commands from the spacecraft’s Command and Data Handling Subsystem (CDS). The UVIS microprocessor compresses, formats, and packetizes data for pickup and storage in the spacecraft’s solid-state recorders (SSR) before eventual telemetry to Earth.

### 1.1. UVIS OBSERVATIONS

The Cassini orbital tour of Saturn consists of more than 70 orbits of Saturn and 44 close passes to Titan (see chapter by Wolf in Vol. 1). Each orbit of Saturn contains a number of phases: apoapsis, Titan flyby, Saturn periapse, and possible icy satellite flybys. Table I shows the planned UVIS observations in each of these phases. Detailed descriptions of each observation can be found in the internal document, *UVIS Observation Description Handbook* (ODH), latest revision 6/99, available from the Principal Investigator.

### 1.2. UVIS ANTICIPATED RESULTS

We include in this introduction a brief summary of anticipated results. More details can be found in the body of our chapter.

#### 1.2.1. Titan

- (1) *Atmospheric abundances.* UVIS will determine the altitudinal and latitudinal distribution and mixing ratios of CH<sub>4</sub>, C<sub>2</sub>H<sub>6</sub>, and C<sub>2</sub>H<sub>2</sub> via the detection of well-defined absorption features. Vertical profiles of these molecules will be determined from limb observations and solar and stellar occultations. Solar and stellar occultations will yield measurements of H, and H<sub>2</sub> as well as N, N<sub>2</sub>, C<sub>2</sub>H<sub>4</sub>, C<sub>4</sub>H<sub>2</sub>, Ar, CO, and C<sub>2</sub>N<sub>2</sub>. The deuterium/hydrogen ratio will be determined. It may be possible to differentiate argon from nitrogen with UVIS in its high spectral resolution mode.
- (2) *Atmospheric chemistry and distribution of species; aerosols.* Horizontal and vertical distribution of active species will be detected. The photochemistry of the atmosphere of Titan displays a rich interaction between hydrocarbons, oxygen, and nitrogen species. The overall chemical composition can be understood in terms of a small number of chemical cycles that generate more complex compounds from the simple parent molecules (N<sub>2</sub>, CH<sub>4</sub>, and H<sub>2</sub>). UVIS will make a systematic survey of all the hydrocarbon species from which sources and sinks may be deduced.

The UVIS instrument will map the global distribution of UV-absorbing aerosols in Titan’s atmosphere in the spectral range 160 to 190 nm. Vertical profiles of high-altitude aerosols

TABLE I  
Observations by orbit period

Apoapsis	
USYSCAN	Scans of the Saturn system
USTARE	Long integrations of Saturn, Titan
UMAP	Inner magnetosphere maps
UFPSCAN	Whole sky scans during downlink
Titan	
UHIGHSN	High signal-to-noise spectroscopy of atmospheric constituents
UMAP	Maps of poles, equator, terminator, darkside, etc.
ULIMDRFT	Bright and dark limb drifts
UHDAC	Measure D/H ratio
UCSTAR	Atmospheric occultations by cool stars
UHSTAR	Atmospheric occultations by hot stars
USUN	Solar occultation
Periapse	
UHIGHSN	Spectra of rings, atmospheric features, limb, phase coverage
UMAP	Saturn N-S hemispheres, poles, etc.
URSTAR	Ring star occultation
UCSTAR	Atmospheric occultations by cool stars
UHSTAR	Atmospheric occultations by hot stars
UHDAC	Measure D/H ratio
ULIMDRFT	Limb drifts
USUN	Solar occultation
Icy Satellite	
UHIGHSN	Surface spectra
UMAP	Latitude-longitude maps
ULIMDRFT	Satellite limb drifts
UISTAR	Star occultation
USUN	Solar occultation

were seen in Titan's atmosphere by the Voyager UVS while observing a solar occultation. This type of measurement, as well as stellar occultations, will allow detailed vertical profiling of Titan's high-altitude aerosols at a variety of latitudes.

- (3) *Atmospheric circulation and physics.* Atmospheric transport processes may be inferred from the spatial distribution of chemical species. UVIS will search for polar vortices via the observed gradients of chemical species. The exact variation of species abundances between the tropopause and the mesosphere depends sensitively on the nature of the vertical transport (advection and diffusion), so a precise determination of the vertical distribution of the photochemically produced species will greatly constrain models. UVIS mapping of the distribution



of hydrocarbons will reveal the dynamics of the curious seasonal behavior of Titan's atmosphere—the asymmetry between the northern and the southern hemisphere at the time of the Voyager encounter, and the polar hood.

- (4) *Upper atmosphere and relation to magnetosphere.* Spectral images of UV thermospheric emission of the major nitrogen and hydrogen atmospheric species on Titan on Saturn will allow partitioning of excitation processes, determination of energy deposition (heating) rates, and ionospheric structure. The peak in emission brightness at the exobase may or may not be due to interaction with the magnetosphere, and the high spectral resolution of the UVIS EUV channel will help to answer this question: the spectral resolution of UVIS can provide a definitive separation of  $\text{H}_2\text{C}_4$  bands and  $\text{N}^+$  emissions, giving direct diagnostic information on excitation processes.

#### 1.2.2. Saturn

- (1) *Atmospheric and cloud properties and composition.* UVIS will map the global distribution of UV-absorbing aerosols in Saturn's atmosphere in the spectral range 160 to 190 nm. UVIS will determine the altitude-latitude distribution of the chemical species H,  $\text{H}_2$ ,  $\text{CH}_4$ ,  $\text{C}_2\text{H}_6$ ,  $\text{C}_2\text{H}_4$ , and  $\text{C}_2\text{H}_2$ .
- (2) *Synoptic features and processes; winds and eddies.* UVIS mapping of the hydrocarbon species will provide a basis for constructing two-dimensional models of the photochemistry, radiation and dynamics of Saturn's atmosphere. Upwelling brings the parent molecule  $\text{CH}_4$  from the troposphere into the upper atmosphere, where it undergoes photolytic decomposition. The products will descend into the lower stratosphere, and may be partially converted into photochemical aerosols. The distribution of aerosols will be affected by the meridional circulation, which in turn is caused by radiative heating due to the hydrocarbons and the aerosols.
- (3) *Ionospheric diurnal variations and magnetic control.* The aurorae on Saturn show two distinctly different morphological characteristics. Most of the Voyager observations show a high-altitude emission from  $80^\circ$  latitude in the north and south polar regions with an  $\text{H}_2$ -band spectrum that is remarkably similar to the emission for the sunlit equatorial region. The spectra appear to contain additional features that are compatible with transitions in  $\text{N}^+$ . Much brighter spectra from deep in the thermosphere are also observed, showing the same periodicity in apparition as the planetary rotation period. These spectra show the effects of  $\text{CH}_4$  absorption, strong self absorption and a very weak H Lyman- $\alpha$  line, characteristic of excitation of  $\text{H}_2$  with a very low  $[\text{H}]/[\text{H}_2]$  mixing ratio. This behavior and the connection to the magnetosphere are not clear, and the better resolution of the Cassini UVIS (as compared to Voyager's UVS) will yield more insight into the primary processes.
- (4) *Physical and compositional properties and evolution.* In bulk composition, Saturn is a typical Jovian planet with reducing chemistry. The dominant chemistry in the upper atmosphere is the hydrocarbon chemistry initiated by the photolysis

of  $\text{CH}_4$  and leading to the production of  $\text{C}_2\text{H}_6$ ,  $\text{C}_2\text{H}_4$ , and  $\text{C}_2\text{H}_2$ . UVIS will make a systematic survey of these major carbon species as well as H atoms. Limb observations and solar stellar occultations will yield vertical profiles. Sources, sinks, and atmospheric transport processes may also be inferred from the spatial distribution of these chemical species.

- (5) *Lightning*. Optical searches will be made for lightning in the FUV, in concert with other remote-sensing instruments.

### 1.2.3. Rings

- (1) *Configuration and processes*. UVIS will provide high spatial resolution, low-noise stellar occultations, spectroscopy, photometry, and limited imaging of the rings. Several high-resolution (10 to 40 m), low-noise occultation opportunities at multiple azimuths will be available during each Cassini orbit. Measurement of these occultations will reveal ring structures with spatial variability on the scale of the larger abundant ring particles. The true sharpness, shape, and azimuthal variability of the many sharp edges in Saturn's rings will be measured with a spatial resolution of approximately 20 m. Ring thickness will be measured directly from oblique occultations of sharp edges. Closely spaced occultations will show the time development of spiral waves, wakes, and edge waves.
- (2) *Composition and particle size*. With UVIS operating as a spectrograph, scans and drifts will yield the areal variation of UV brightness across the rings, showing compositional or age differences and the presence of submicron particles as postulated to form the spokes. Variations in reflectance can be interpreted in terms of the individual particle properties like albedo and phase function, because the radial profile of extinction optical depth will be known from the occultations.
- (3) *Interrelation with satellites*. The presence or absence of phase shifts in edge waves will be determined from closely spaced occultations. The effects of imbedded or nearby moonlets will be detected in the F ring and in the similar rings in the gaps and the C ring region.
- (4) *Dust and meteoroid distribution*. Photometric and spectroscopic studies will identify the emissions of H and O near the rings. Since the rings are mostly water ice, this provides a constraint on ring erosion rates. Submicron dust will be visible in the UV: the spectral variation of reflected sunlight will establish the number and size of dust particles near the rings.
- (5) *Interactions with Saturn magnetosphere, ionosphere, and atmosphere*. Saturn receives oxygen and nitrogen species from the magnetosphere and the rings; thus, CO and HCN are predicted to exist in the upper atmosphere.

### 1.2.4. Icy Satellites

- (1) *Characteristics and geological histories*. Regional units may be differentiated by their UV reflectance. Darkening in the UV may be an indicator of surface age and exposure to radiation.

- (2) *Mechanisms of modification.* UVIS limb drifts and stellar occultations will be used to detect the existence of tenuous, possibly transient atmosphere, whose source may be surface activity, sputtering, or seasonal sublimation.
- (3) *Composition and distribution of surface materials, especially dark, organic-rich condensates.* UV reflectivity will be used to identify and/or constrain possible composition of surface materials. The overall phase function of surface materials, including the UV, is important in determining the fine structure and degree of compaction of surface materials.
- (4) *Interactions with magnetosphere and rings.* UVIS will map H Lyman- $\alpha$  throughout the Saturnian system as well as emissions from neutrals and ions, by acquiring data during downlink rolls. A full sky map will identify the sources of particles being detected *in situ* by the MAPS (magnetosphere and plasma science) instruments. Heavy atomic species are known to be present in the magnetosphere. It has been argued that the heavy ions are mainly  $O^+$ , derived from sputtering of the icy satellite surfaces and subsequent  $H_2O$  chemistry.

#### 1.2.5. Magnetosphere

The mass content of the Saturn magnetosphere is determined almost entirely by sources internal to the Saturn system. The magnetosphere reflects the dynamic processes in the atmospheres and surfaces of the planet and satellites, which in turn are influenced by interaction with the magnetosphere in a partially closed system. Measurement of the content of neutrals and ions in the magnetosphere can provide critical information on basic atmospheric evolutionary processes as well as definition of magnetospheric structure. An understanding of this complex interactive system will clearly require knowledge of the composition, distribution, and dynamics of the magnetospheric particles. Because of the sensitivity to very weak emissions and ability to observe the entire magnetosphere remotely, UVIS will make a unique contribution to this understanding.

- (1) *Configuration of magnetic field and relation to Saturn kilometric radiation.* UVIS will map H Lyman- $\alpha$  throughout the Saturnian system as well as emissions from neutrals and ions by acquiring data during downlink rolls. A full sky map will identify the sources of particles being detected *in situ* by the MAPS instruments.
- (2) *Charged particle currents, compositions, sources and sinks.* Atomic H, which is present in significant quantities in Saturn's magnetosphere, has a complex three-dimensional distribution. Lyman- $\alpha$  mapping by UVIS will establish the relative dominance of the hydrogen sources (e.g., Saturn exosphere, Titan, satellites, rings). UVIS will be able to detect emissions from  $N^+$ ,  $N^{++}$ ,  $O^+$ , and  $O^{++}$ .
- (3) *Wave-particle interactions and dynamics.* None identified.
- (4) *Interactions of Titan's atmosphere and exosphere with surrounding plasmas.* Spectral images of UV thermospheric emission of the major nitrogen and hydrogen atmospheric species on Titan and Saturn will allow partitioning of

excitation processes, determination of energy deposition (heating) rates, and ionospheric structure. The peak in emission brightness at the exobase may or may not be due to interaction with the magnetosphere, and the high spectral resolution of the UVIS EUV channel will help to answer this question: the spectral resolution of UVIS can provide a definitive separation of  $\text{H}_2\text{C}_4$  bands and  $\text{N}^+$  emissions, giving direct diagnostic information on excitation processes.

### 1.3. SUMMARY

In summary, the UVIS investigation has a broad range of scientific objectives encompassing the origin and evolution of the planets and their atmospheres, clouds and aerosols, magnetospheres, thermospheres and exospheres, satellite surfaces and their tenuous atmospheres, and ring structure, composition, and histories. These various objectives overlap—Titan, the rings, and satellites are sources of magnetospheric neutrals; lost atmospheric gases may be retained in the Saturn system; and magnetospheric constituents bombard and modify the rings and satellites. Furthermore, UVIS provides just one segment of the broad range of new scientific information to come from the orbiter's complement of *in situ* and remote measurements and from the Titan measurements by the Huygens probe. A major result of the UVIS investigation will be to contribute to the advance of knowledge of the Saturn system from the Cassini-Huygens mission through collaborative studies.

This paper gives a brief description of the UVIS experiment, its science objectives, and its planned observations.

## 2. Instrument Description

In this section, we describe the optical configuration and performance of the UVIS that enables the scientific investigation (McClintock *et al.*, 1992, 1993). The UVIS design represents a balance between the science objectives and the constraints of mass, power, volume, and operability for a spacecraft instrument. Figures 1 and 2 and Table II summarize the optical and mechanical characteristics of the instrument. UVIS consists of two moderate-resolution telescope-spectrographs covering the wavelength ranges 56 to 118 nm (extreme ultraviolet, or EUV) and 110 to 190 nm (far ultraviolet, or FUV), a sensitive High Speed Photometer (HSP), and a Hydrogen Deuterium Absorption Cell (HDAC). The four separate channels are aligned for simultaneous observation.

To meet the breadth of science objectives, UVIS uses a variety of observation techniques. These include producing maps and images by moving the slit to a sequence of locations through rastering, slewing, and drifting the spacecraft optical axis. Limb drifts provide high spatial resolution at the target's limb. Occultations of the sun are observed with the EUV channel; the HSP can observe stellar occultations in concert with the EUV and FUV channel spectrographs.

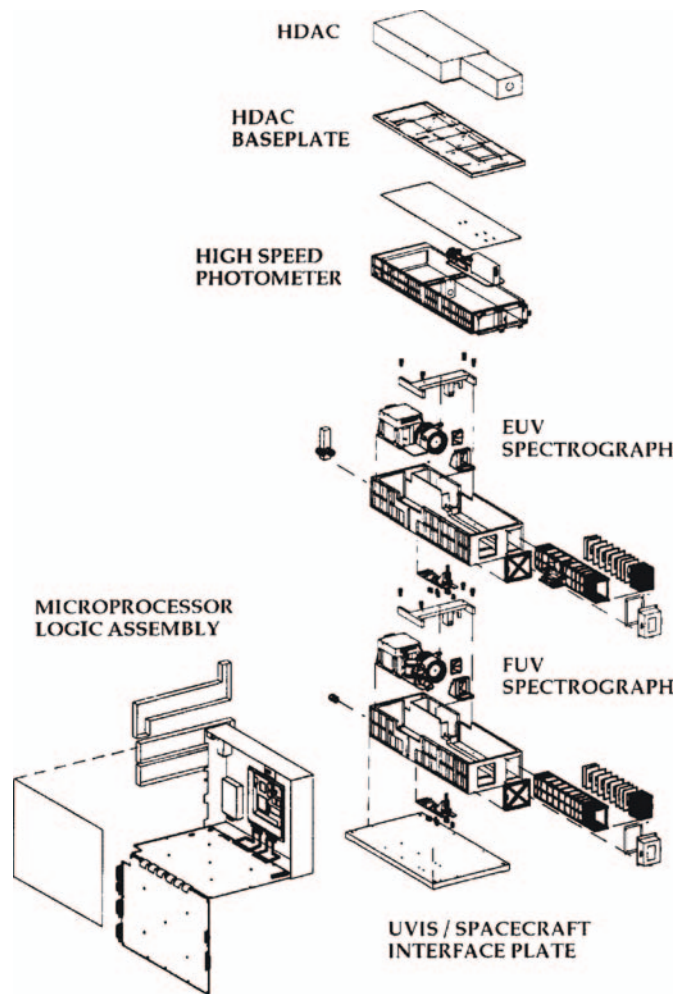


Figure 1. UVIS instrument: two spectrographs, a high speed photometer, and a hydrogen absorption cell.

UVIS will encounter a wide range of signal strengths. Saturn system atmospheric and magnetospheric emissions at wavelengths shorter than 200 nm are very faint, with radiances of the order of 0.1 to 10 Rayleighs in individual emission lines. In contrast, sunlight scattered from the disk of Saturn and its icy satellites produces radiance in the range of 1 to 10 kR/nm.

## 2.1. SPECTROGRAPHIC CHANNELS

The basic instrument design adapts proven design concepts using a grating spectrometer followed by a multi-element detector. We chose to use imaging,

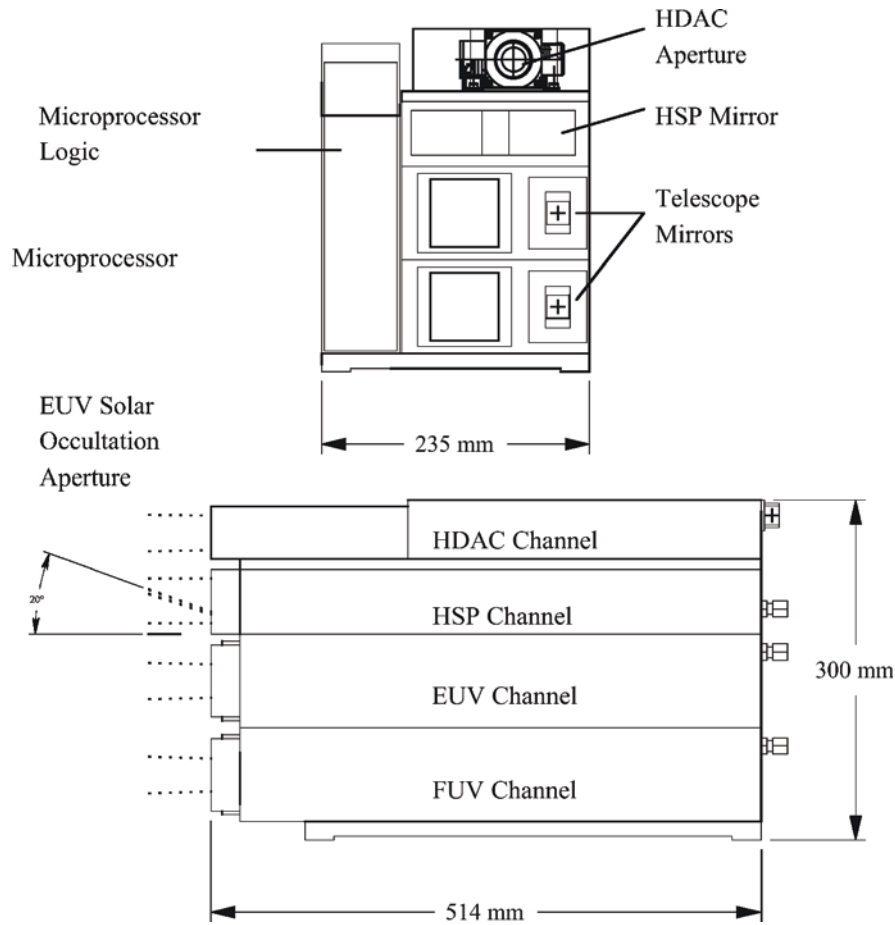


Figure 2. UVIS optical-mechanical configuration. The four channels share the same boresight. In solar occultation mode, a pick-off mirror allows sunlight to enter the EUV channel without striking the primary.

pulse-counting microchannel plate detectors because of more than a decade of experience using this kind of detector equipped with a CODACON readout anode.

#### 2.1.1. CODACON Detector

The CODACON (Coded Anode Array Converter) acts as a photon locator. For  $2^M \times 2^N$  pixels on the anode array, the output electronics generate a logic compatible  $M + N$  bit address for each detected photon. The located photon counts are accumulated in an external memory to build a picture that is periodically read out for transfer to the spacecraft memory and eventually, the ground. The spectrograph detectors have a count rate limit of  $10^5/\text{s}$ , set by the speed of the detection electronics. Details of the CODACON operation are described by McClintock *et al.* (1992) and Lawrence and McClintock (1996).



TABLE II  
UVIS spectrographic channels and HSP

	FUV (1115–1912 Å)	EUV (563–1182 Å)	HSP
Telescope			
Focal length size (mm)	100	100	200
Entrance pupil size (mm)	20 × 20	20 × 20	135 × 30
Reflecting surface	Al + MgF <sub>2</sub>	Boron carbide	Al + MgF <sub>2</sub>
Toroidal gratings			
Size (mm)	60 × 60	60 × 60	
Grating radii (mm)	300, 296.1	300, 296.8	
Grating surface	Al + MgF <sub>2</sub>	Boron carbide	1068 1371
Grooves/mm	1068	1371	
Input angle $\alpha$ (degrees)	9.22	8.03	
Out angles $\beta$ (degrees)	±2.9	−4.08 + 1.72	
3-Position slits			
Slit widths (microns)	75, 150, 800	100, 200, 800	6 × 6
$\Delta\lambda$ (Å) (Extended source)	2.75, 4.8, 24.9	2.75, 4.8, 19.4	
Field of view (mrad)	(.75, 1.5, 8) × 60	(1, 2, 8) × 59	
Detectors			
Photocathode	CsI	KBr	CsI
% Maximum QE	8	25	10
Detector window	MgF <sub>2</sub>	none	MgF <sub>2</sub>
Detector size (mm)	25.6 × 6.4	25.6 × 6.4	11.0 dia
Pixel format ( $\lambda \times \theta$ )	1024 × 64	1024 × 64	
Pixel size ( $\mu$ )	25 × 100	25 × 100	
Pulse resolution	10 $\mu$ sec	10 $\mu$ sec	50 $n$ sec
UVIS characteristics			
Mass	15.6 kg		
Volume (L × W × H)	50.8 cm × 23.5 cm × 30.5 cm		
Power	8 W (average), 12 W (peak)		

The two-dimensional format for the CODACON detectors allows simultaneous spectral and one-dimensional spatial coverage. The detector format is 1024 × 64 (spectral by spatial) with a pixel size of 25 × 100 mm. Two separate detectors span the instrument's wavelength range, as follows. A windowless detector is required for the EUV wavelength range 56 to 118 nm. We chose KBr as the photocathode material for this detector because of its ability to withstand a moderate amount of exposure to atmospheric water vapor. CsI was also considered as the EUV photocathode, but it requires a door with a hermetic seal to protect it before launch. CsI is the photocathode material for the FUV wavelength range, 110 to 190 nm. This detector is enclosed in a separate vacuum housing with a MgF<sub>2</sub> window.

Although other materials such as CsTe are more efficient photocathodes than CsI for wavelengths longer than 130 nm, we use CsI for the FUV because it is much less sensitive to longer wavelength scattered light within the spectrograph. This scattered light usually dominates and can often obliterate weak planetary FUV emissions when a CsTe or a more red-sensitive photocathode is used.

### 2.1.2. Optical Design

The optical requirements for EUV channel spectrometers are unique because the low reflectivity of optical materials at these wavelengths requires that the number of optical elements in the system be as small as possible. Our design is a single-mirror telescope followed by an entrance slit and a concave grating used in a Rowland circle mount.

We found that the EUV channel configuration also provides satisfactory spatial and spectral resolution in the FUV channel. The two channels are identical except for the optical coatings, diffraction grating rulings, and detector photocathodes. To achieve the desired spectral resolution, the optics must provide image quality in the spectrograph dispersion direction that is comparable to the CODACON spatial resolution limit of 2 pixels (0.05 mm). Toroidal gratings used with the angle of diffraction equal to zero in the center of the detector have the best imaging properties because, for a given angle of incidence, they produce stigmatic images at two wavelengths in the focal plane.

The FUV channel is shown in Figure 3. This design represents the best compromise for spectral resolution, image quality, and instrument size. The EUV channel is identical to the FUV except that the detector window and ion pump are not present. Each telescope consists of an off-axis section of a parabolic mirror with a 100 mm focal length. A  $20 \times 20$  mm aperture, which is 133 mm in front of the telescope mirror, acts as a Lyot stop conjugate to the grating. We have equipped the telescope

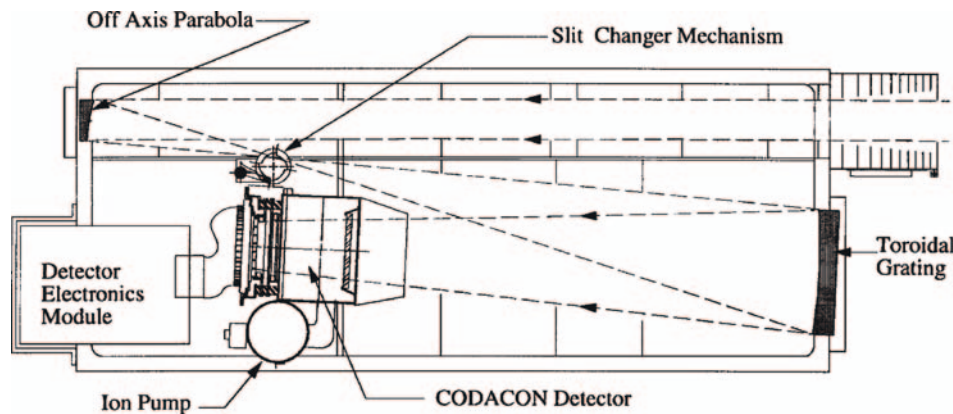


Figure 3. FUV optical configuration optimizes the trade-off between imaging and spectral resolution in the available volume.

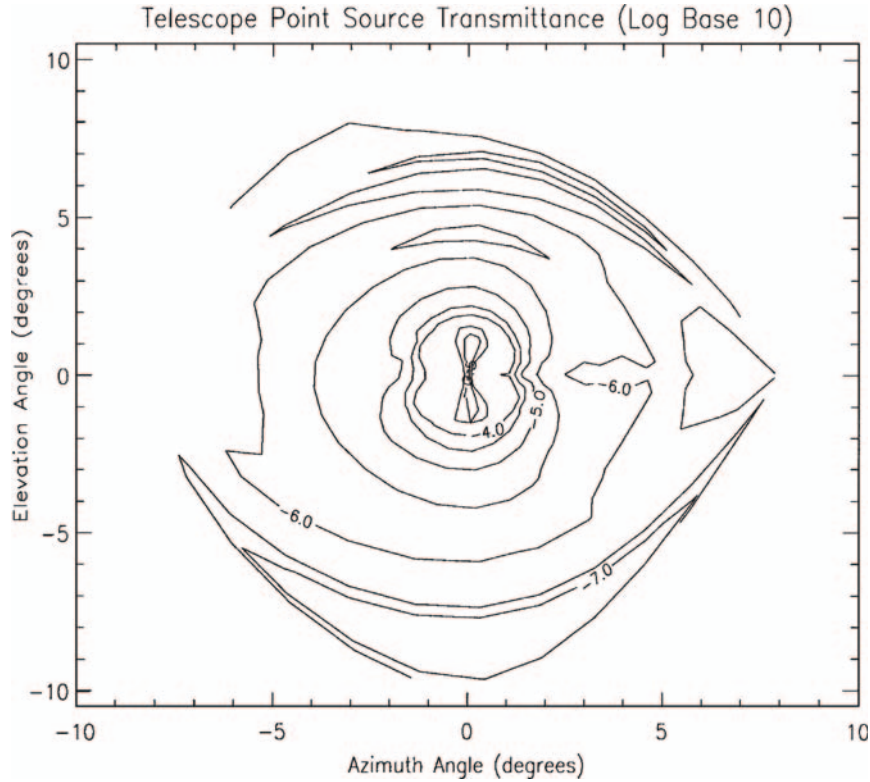


Figure 4. Contour plots of the logarithm of the telescope point source transmittance of the FUV and EUV channels.

with a sunshade and baffle system to minimize scattered light background during limb scan measurements. The point source rejection ratio, which was measured using a laboratory collimator to simulate a star, is  $10^6$  for sources located  $1^\circ$  or more away from the field of view (Figure 4).

Each spectrograph consists of a set of three interchangeable entrance slits (0.075 to 0.8 mm wide  $\times$  6.4 mm tall, see Table II) and a toroidal grating with a 300 mm horizontal radius of curvature used in a Rowland circle mount. The spectrum is thus formed on a cylinder of radius 300 mm. The detector lies on a chord of the Rowland circle to minimize average defocus over its planar  $25.6 \times 6.4$  mm sensitive area. The grating ruling spacing is set to meet the spectral coverage requirement for each channel.

Mechanical constraints require the spectrograph housings to have the angle  $\alpha - \beta = 9.2^\circ$  identical for both channels ( $\alpha$  and  $\beta$  are the angles of incidence and diffraction, respectively). This configuration results in  $\beta = 0^\circ$  at the center of the detector for the FUV channel. The detector then subtends angles  $\Delta\beta = \pm 2.45^\circ$  along the Rowland circle. The grating radii yield the stigmatic wavelengths at  $\beta_s = \pm 1.23^\circ$ , with the detector plane also intersecting the Rowland circle at these

wavelengths. This configuration thus yields the best average imaging over the entire detector.

### 2.1.3. Spectrometer Sensitivity

The following equations relate the signal and noise output of the UVIS spectrometer channels to their design parameters. For viewing extended sources,

$$S(\lambda) = I(\lambda) * A_T(\lambda)/F_T^2 * A_{\text{pix}} * \tau(\lambda) * QE(\lambda)T \quad (1)$$

$$N^2(\lambda) = S(\lambda) + BT \quad (2)$$

where  $S$  is the signal in counts per pixel,  $\lambda$  the wavelength,  $I$  the source radiance in kR ( $10^9$  emitted photons per square centimeter per  $4\pi$  steradian per second),  $A_T/F_T^2$  the square of the optical system focal ratio,  $A_{\text{pix}}$  the area of a single detector pixel in square centimeters,  $\tau$  the optical system transmission,  $QE$  the detector quantum efficiency;  $T$  the observation time in seconds;  $N$  the noise in counts per pixel, and  $B$  the detector background or ‘dark count’ in counts per pixel per second.

Figure 5 shows the system sensitivity of UVIS for each channel and for the high-resolution and low-resolution slit widths (each labeled by its width in  $\mu\text{m}$ ) and spectral resolution in nm. Curves for the occultation slits (not shown) are a factor of 10.7 higher than the curves for a  $75 \mu\text{m}$  slit. In limb scan mode, we orient the entrance slit parallel to the planet limb and slew the spacecraft to obtain vertical profiles, summing all 64 spatial pixels into a  $1024 \times 1$  spectrum. Mapping mode uses the full 2-dimensional capability of the detector, and we generate a spectral-by-spatial map of  $1024 \times 64$  pixels.

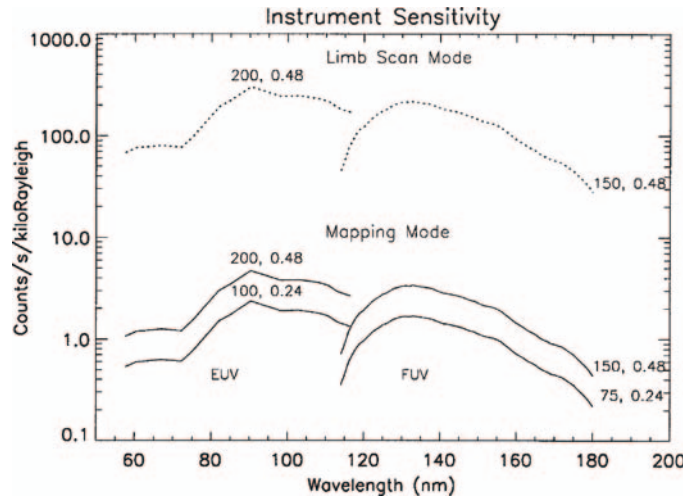


Figure 5. UVIS sensitivity in counts/second/kiloRayleigh. Each curve is labeled by the slit width ( $\mu\text{m}$ ) and the resolution (nm). Higher sensitivity is available in limb scan mode from adding all the 64 picture elements along the slit.

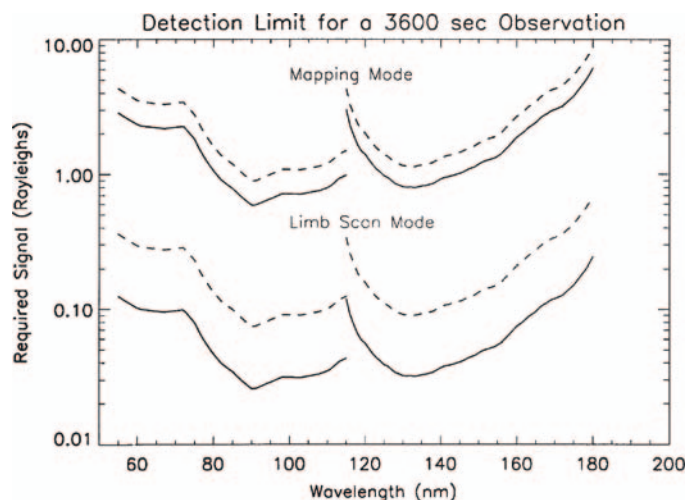


Figure 6. UVIS sensitivity limits for an integration period of one hour. Solid lines indicate low resolution and high resolution slits. Dashed lines indicate summing of all spatial information along slit.

In Figure 6, we plot the detection limit (i.e., the signal required to produce a signal-to-noise ratio of 3.0) for a 3600 s observation in limb scan and mapping modes. Solid lines are for typical observed CODACON backgrounds of 2 counts per detector (65,536 pixels) per second. The dashed lines in Figure 6 show detection limits for the total expected background, including the three Radioisotope Thermoelectric Generators (RTGs) that provide the spacecraft with electrical power. We estimate that the gamma rays emitted by the RTGs will increase the background by an additional 20 counts per detector per second. Observations during instrument check-out in 1999 gave a preliminary estimate of 35 counts.

#### 2.1.4. Example Spectroscopic Observations

An example of mapping is as follows. Titan's disk has an angular diameter of  $2.6^\circ$  (45 mrad) at 5.2 h before closest approach (at a distance of about  $1.2 \times 10^5$  km), and a single detector pixel subtends  $2.5^\circ$  of latitude at the sub-spacecraft point. The satellite just fills the length of the spectrograph entrance slit at  $T-3.7$  h. Thus  $T-5.2$  h to  $T-3.7$  h is an ideal time to make maps to provide data for photochemical models and aerosol studies (see Sections 3 and 4 below).

Limb scans and atmospheric occultation measurements provide higher spatial resolution nearer to closest approach. We have good off-axis rejection of the bright disk for weak emissions if it is  $5^\circ$  from the optical axis. For thermosphere measurements at an altitude of 1000 km, this requires that the range must be less than  $11 \times 10^3$  km. This occurs at about  $T-0.5$  h when the high resolution, 75- $\mu\text{m}$ -wide entrance slit subtends about 9 km at the limb and the spacecraft drifts about 1 scale height (50 km) every 8 s. Occultation measurements of the atmosphere can be made

at larger ranges, especially on Titan's night side, when there is minimal scattered light from the sunlit disk.

## 2.2. STELLAR AND SOLAR OCCULTATION MODES

The UVIS spectroscopic channels will view stars that are occulted by the atmospheres of Saturn and Titan and by Saturn's rings. Because spacecraft pointing accuracy is estimated at  $\pm 2$  mrad, we have set each telescope field of view to be 8 mrad wide (using the occultation slit: 'Occ') for stellar occultation experiments. The field of view is selected by a three-position slit mechanism in each channel (Figure 2). Two other slit positions are provided: one that is 0.75 mrad wide (FUV) or 1.0 mrad wide (EUV) to give the highest spectral resolution requirements for extended sources ('Hi-Res'), and one that is 1.5 mrad (FUV) or 2.0 mrad (EUV) wide to provide a larger signal at less resolution ('Lo-Res').

We also added a solar occultation capability to the EUV channel; more distant stars are generally not useful at wavelengths shorter than 91.2 nm because interstellar atomic hydrogen blocks their radiation. In this observing mode (see Figure 2), light enters the EUV channel through a small aperture located  $20^\circ$  away from the normal viewing direction, and it is directed toward the telescope mirror by a small grazing incidence mirror. A two-position mechanism is used to block the light path when the solar viewing mode is not used.

## 2.3. HIGH SPEED PHOTOMETER

UVIS contains a High Speed Photometer (HSP) with an integration time of 2.0 ms to observe stars occulted by the rings of Saturn. Figure 7 shows the HSP configuration, which consists of a telescope mirror that is approximately 10 times as large as those used in the spectroscopic channels, followed by an aperture to

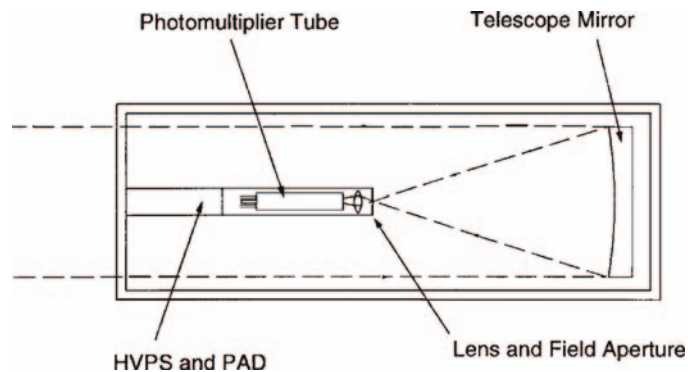


Figure 7. High Speed Photometer (HSP) layout showing High Voltage Power Supply (HVPS) and Pulse Amplifier/Discriminator (PAD).



limit the field of view to 6 mrad, a  $\text{MgF}_2$  lens, and a Hamamatsu model R1081 photomultiplier tube with a CsI photocathode used in pulse-counting mode. The lens images the telescope mirror onto the photocathode of the photomultiplier. Without this lens, small changes in spacecraft pointing would cause the image of the star to move around on the nonuniform detector photocathode, resulting in unwanted signal variations. Figure 7 also shows the detector electronics location, which includes a High-Voltage Power Supply (HVPS) and a Pulse Amplifier Discriminator (PAD).

The spectral response of the HSP is limited at short wavelengths to about 115 nm by the  $\text{MgF}_2$  detector window and at long wavelengths to about 190 nm by the work function of the CsI photocathode. We chose CsI for its low sensitivity to solar light, because the spacecraft orbit geometry requires that many of the occultation observations be made while looking through the sunlit rings. The photometer field of view must be at least 6 mrad to account for pointing errors of  $\pm 2$  mrad. If we used a photomultiplier with either a CsTe or a Bi-alkali photocathode with this large a field of view, sunlight reflected from the rings would produce a background at least 100 times larger than the signal from the brightest stars. Figure 8 is a contour plot of the off-axis response of the HSP. The off-axis response is roughly symmetric around the HSP boresight and drops off to  $10^{-5}$  at  $10^\circ$  off axis. Using a CsI photocathode, we are limited to stars with spectral class O and B (effective temperatures in the range 10,000–40,000 K), but the background from reflected sunlight is equal to the signal from a B5 star with a visual magnitude  $M_v$  of 4.5. During the Saturn orbital mission, we expect over 350 stellar occultation opportunities for the rings with stars that are at least 10 times brighter than  $M_v$  of 4.5.

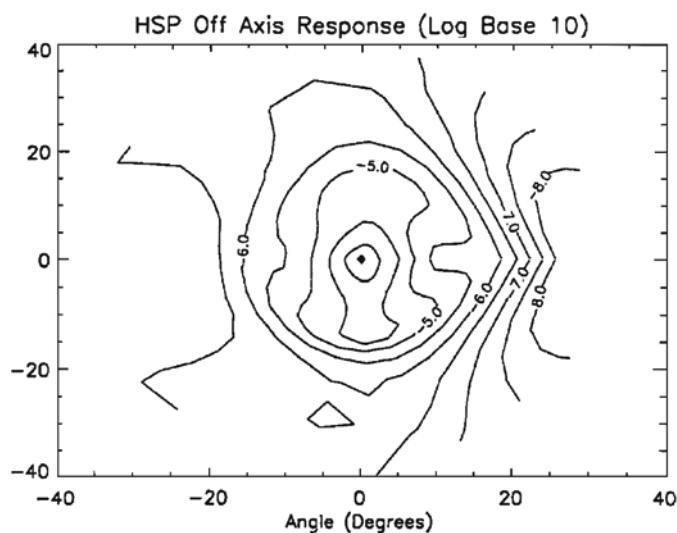


Figure 8. HSP off-axis response (contours:  $\log_{10}$  of sensitivity relative to maximum signal).

## 2.4. HDAC DESCRIPTION

The first use of a hydrogen absorption cell for spaceborne remote sensing was by Morton and Purcell (1961). They used the cell as a broadband blocking filter to prove that hydrogen Lyman- $\alpha$  emission was present in the night sky of the Earth. Winter and Chubb (1967) used a hydrogen cell to observe the night-sky hydrogen Lyman- $\alpha$  line shape. In the 1970s, Bertaux flew hydrogen cells to study the line shape of hydrogen Lyman- $\alpha$  in planetary coronae and the local interstellar medium (LISM). These experiments included OGO-5 at Earth (Bertaux, 1978), the Soviet Venera missions at Venus (Bertaux *et al.*, 1978), the Soviet Mars missions (Babichenko *et al.*, 1977), and the Soviet Earth orbiters Prognoz 5 and 6 (Bertaux, 1977).

The only successful use of a hydrogen deuterium absorption cell to measure the deuterium-hydrogen ratio (D/H) in the Earth's atmosphere is by Bertaux *et al.* (1984) aboard Spacelab-1. Unsuccessful attempts to measure atomic D/H include Mars (Babichenko *et al.*, 1977) and Venus (Bertaux *et al.*, 1978). The cells mentioned above were made of glass. The Japanese Nozomi mission to Mars has hydrogen deuterium absorption cells similar to the Bertaux cells (Kawahara *et al.*, 1993). For information on this experiment, also see Kawahara (1994). The forerunners of the HDAC (stainless steel hydrogen cells) were developed by Hans Lauche and Wilhelm Barke of the Max-Planck-Institut für Aeronomie (MPAe) in Katlenburg-Lindau, Germany, as part of the Interzodiac program. The Teflon coating of the HDAC cells allows lighter weight and lower power, since recombination times are longer.

The Cassini HDAC channel (Figures 9 and 10), which was built at the MPAe, consists of a Channel Electron Multiplier (CEM) photodetector equipped with 3 absorption cell filters: a hydrogen cell, a deuterium cell, and an oxygen cell. The cells are separated by MgF<sub>2</sub> windows. The oxygen cell was designed to be a static

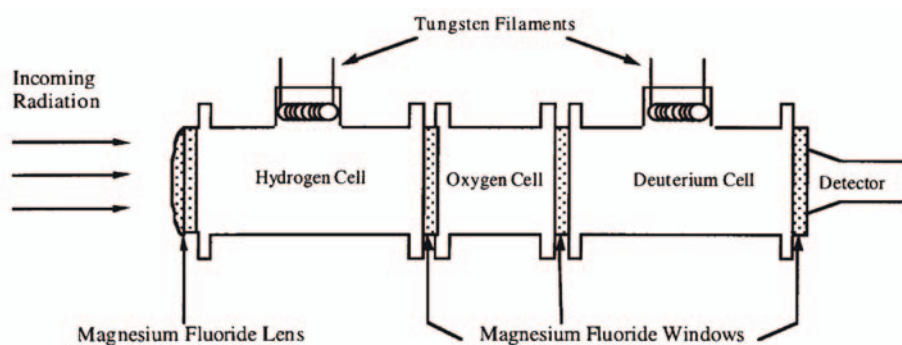


Figure 9. Conceptual diagram of the Cassini Hydrogen Deuterium Absorption Cell (HDAC). The tungsten filaments dissociate molecular hydrogen and deuterium inside the cells. The dissociated atoms resonantly absorb hydrogen and deuterium Lyman- $\alpha$ . Cycling the filament currents in both the hydrogen and deuterium cells gives a direct measurement of the hydrogen and deuterium Lyman- $\alpha$  intensities.

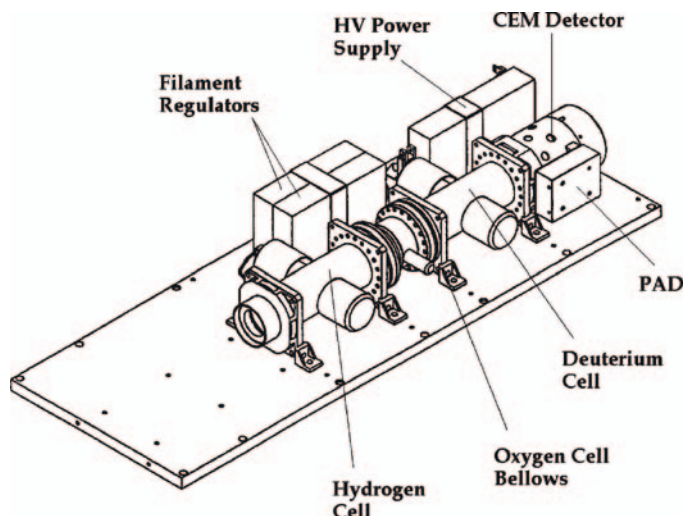


Figure 10. The Cassini HDAC without baffle and cover.

broadband filter from 1150 to 1800 Å but was unfortunately vented prior to flight due to contamination caused by water vapor accumulating in the O<sub>2</sub> cell. The hydrogen and deuterium cells function as adjustable absorption filters, as described below.

In each cell, a hot tungsten filament dissociates the H<sub>2</sub> and D<sub>2</sub> molecules into atoms, producing an atomic density dependent on the filament temperature. These atoms resonantly absorb the hydrogen and deuterium Lyman- $\alpha$  lines (located at 1215.67 Å and 1215.34 Å) passing through the cells. Cycling the filaments on and off and comparing the differences in signal gives a direct measurement of the relative hydrogen and deuterium signals. For an analysis and calibration of the Cassini HDAC absorption cell, see Maki (1996).

The cells are mounted on an anodized aluminum baseplate along with a baffle attached to the front of the hydrogen cell. At the entrance to the HDAC, a single MgF<sub>2</sub> lens focuses the incoming light. The lens and windows are laser-welded into the ends of the cell bodies, and the cells are connected by flanges. The cells are filled to approximately 1.2 mbar pressure. Each cell has two filaments controlled by separate filament current regulators for each cell. The two regulators are essentially low-voltage power supplies that set and regulate the power into the filaments. Only one filament at a time per cell is used during flight. A Pulse Amplifier Discriminator detects photoelectrons from the CEM and sends pulses to the UVIS instrument logic.

## 2.5. MEASURING D/H WITH THE HDAC

The optical depth  $\tau$  of an HDAC cell at line center is  $\tau = \sigma n_H L$ , where  $\sigma$  is the photoabsorption cross section,  $n_H$  is the number density of the atoms, and  $L$  is the

TABLE III

Hydrogen atom density and the corresponding number of atoms in a 300 K hydrogen absorption cell for various values of optical depth.

Optical depth	Atomic hydrogen density (atoms/cm <sup>3</sup> )	Number of dissociated hydrogen atoms in a single HDAC absorption cell
0.5	$1.7 \times 10^{11}$	$7.5 \times 10^{12}$
1	$3.5 \times 10^{11}$	$1.5 \times 10^{13}$
5	$1.7 \times 10^{12}$	$7.5 \times 10^{13}$
10	$3.5 \times 10^{12}$	$1.5 \times 10^{14}$

*Note.* The number of dissociated atoms is much smaller than the total number of molecules in the cell ( $10^{18}$ ). The maximum optical depth of the HDAC is less than 20 (see Section 2.4).

TABLE IV

Measured HDAC flight unit optical depths for the hydrogen and deuterium cells (Maki, 1996)

Step	Hydrogen cell		Deuterium cell	
	$\tau_H$	$\tau_D$	$\tau_H$	$\tau_D$
1	0.15	0.0	0.3	0.02
2	0.8	0.0	1.5	0.16
3	1.4	0.0	2.7	0.25
4	2.1	0.0	4.3	0.37
5	4.8	0.0	10.0	0.87
6	6.0	0.0	11.0	1.06
7	7.0	0.0	13.0	1.28

path length (8.5 cm). For the HDAC hydrogen cell at 300 K,  $\sigma = 3.4 \times 10^{-13}$  cm<sup>2</sup>. Table III shows the hydrogen atom density for selected values of optical depth. The transmission of the cell at line center is given by  $T = e^{-\tau}$ . See Table IV for the measured values of the flight HDAC optical depth as a function of filament step. Transmission as a function of wavelength is given by

$$T(\lambda) = e^{-\tau\phi(\lambda)}, \quad \text{where } \phi(\lambda) = e^{-\frac{x^2}{\Delta\lambda_D^2}} \quad (3)$$

where  $\Delta\lambda_D$  is the Doppler width.

Because the HDAC is sensitive to electromagnetic radiation over a wide spectral range, the signal generated by the HDAC is directly proportional to the integrated intensity of the incoming radiation over this region. The total signal is expressed as

$$I = \int_{-\infty}^{\infty} S(\lambda)H(\lambda)T(\lambda) d\lambda \quad (4)$$

where  $I$  is the signal from the photometer,  $H(\lambda)$  is the intensity of the radiation as a function of wavelength,  $S(\lambda)$  is the sensitivity of the photometer, and  $T(\lambda)$  is the transmission of the filter as a function of wavelength. The ratio of the modulated intensity  $I$  to the unmodulated intensity  $I_0$  (assuming no background) is given by the reduction factor  $R$ :

$$R = \frac{I}{I_0} = \frac{\int_{-\infty}^{\infty} S(\lambda)H(\lambda)T(\lambda) d\lambda}{\int_{-\infty}^{\infty} S(\lambda)H(\lambda) d\lambda} \quad (5)$$

When no power is applied to the filament, the absorption cells contain only molecules, and the cells are transparent to incoming radiation at Lyman- $\alpha$ . When power is applied to the filament in the cell, the molecules dissociate into absorbing atoms, which block incoming radiation at Lyman- $\alpha$ . This process defines a negative filter; subtracting this filter profile from unity gives an effective filter,  $I_0 - I$ , which is:

$$I_0 - I = \int S(\lambda)H(\lambda)(1 - T(\lambda)) d\lambda \quad (6)$$

Note that in general, the background level will be unknown and will be determined by taking the differences between the modulated and unmodulated signals.

In addition to measuring the ratios of the deuterium and hydrogen Lyman- $\alpha$  lines, the Cassini HDAC, as a high resolution spectrometer, has the ability to measure the Lyman- $\alpha$  line shapes. Because instrument filter functions have different shapes for each filament level, a full cycle through the filament settings produces a set of filters that probes the line shape of the incoming radiation. Additionally, the range of spacecraft Doppler velocities scans these filter functions through the line.

## 2.6. HDAC CALIBRATION

### 2.6.1. Lyman- $\alpha$ Sensitivity

The sensitivity  $S_{Ly\alpha}$  of the instrument is the count rate per input flux:

$$S_{Ly\alpha} = \frac{10^6}{4\pi} \cdot QE \cdot \Omega \cdot T_W^3 \cdot T_L \quad (7)$$

where  $S_{Ly\alpha}$  is in units of counts/sec/Rayleigh,  $QE$  is the quantum efficiency of the detector in units of counts/photon,  $\Omega$  is the solid angle subtended by the HDAC FOV in units of steradians,  $T_W^3 \cdot T_L$  is the transmission of the three windows and the single lens, and  $A$  is the area of the front lens in units of  $\text{cm}^2$ . The value of  $S_{Ly\alpha}$  (as measured in the laboratory using a calibrated NIST windowed UV photodiode) is  $(30 \pm 10)$  counts/sec/Rayleigh.

### 2.6.2. Broadband Sensitivity

The red tail of the HDAC is the sensitivity of the instrument to electromagnetic radiation redder than 1216 Å. The broadband spectral sensitivity of the HDAC is

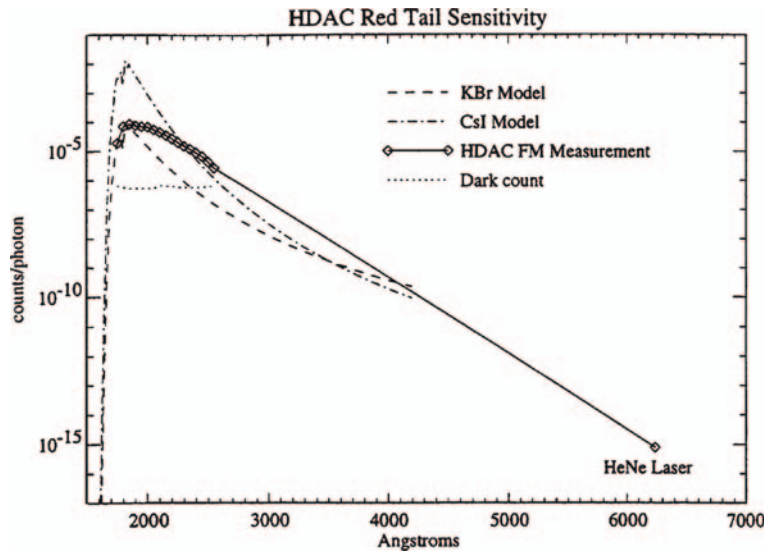


Figure 11. HDAC on-axis red tail sensitivity. Because detector red tails typically decrease with time, this value for the sensitivity is an upper limit. The dash dot and dashed lines represent the modeled sensitivity for an HDAC with a CsI and KBr detector, respectively. The detector in the HDAC Flight Model (FM) has a KBr photocathode, implying that the FM red tail curve may eventually fall on the modeled curve for KBr. The dotted line at  $10^{-6}$  counts/photon is the dark count of the detector divided by the number of photons in the beam, the lowest sensitivity value that could be measured in this particular experiment.

bracketed on the blue side by the  $\text{MgF}_2$  windows, which absorb radiation below  $1150 \text{ \AA}$ . The value for the sensitivity of the instrument from  $1750 \text{ \AA}$  to  $2400 \text{ \AA}$  is important, because at this point the UV output of the sun begins to increase rapidly with wavelength. Because the signal from the reflected solar background radiation is an important component in the determination of the signal-to-noise ratio of HDAC data, a KBr (potassium bromide) detector was chosen because it possesses the combination of low detector sensitivity to solar radiation and high sensitivity to Lyman- $\alpha$ . When making observations of planetary atmospheres, the background signal in the red tail region is determined by a competition between the increasing solar output and the decreasing photocathode sensitivity. If the photocathode efficiency decreases fast enough relative to the solar output, the solar contribution to the background will be minimal. If however, the photocathode efficiency decreases too slowly, the background from the sun can dominate and Lyman- $\alpha$  observations will be difficult due to the low signal-to-background ratio. Measurements of the HDAC red tail are shown in Figure 11. The red-tail sensitivity of CEM detectors of this type has been known to increase over the timescale of several years (Hans Lauche, personal communication). We are monitoring possible changes in the red tail by performing in-flight calibrations. The measurements are above the predicted KBr response, but may decay to the model curve with use.



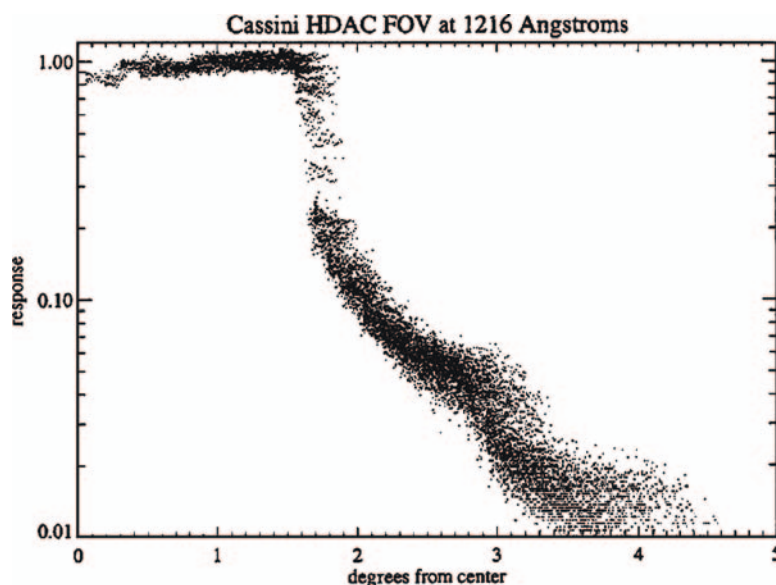


Figure 12. The HDAC off-axis radiometric response at 1216 Å.

#### 2.6.3. Off-Axis Response

The HDAC off-axis response was measured at two wavelengths (1216 Å and 2537 Å) using a pan/tilt calibration fixture. See Figure 12 for a plot of the HDAC off-axis response at 1216 Å.

#### 2.6.4. In-flight HDAC Performance

To date, HDAC has had several checkout and calibration activities in flight. Unfortunately, these activities were dissimilar to those we plan during the Saturn tour, and some behavior was unexplained. Thus, we are engaged in further testing and HDAC observations of the interstellar medium, Jupiter, and stellar sources to better define the HDAC performance and confirm its capability to meet the science measurement objectives for D/H at Titan.

### 3. Chemical Composition in the Atmospheres of Titan and Saturn

A unifying theme that relates our atmosphere to all planetary atmospheres in the solar system is to understand their origin, composition, and evolution. All planets share a common origin about 4.6 billion years ago. The subsequent divergence in the solar system may be attributed to initial conditions and subsequent evolution. A comprehensive survey of the chemical composition of all planetary atmospheres, including that of the Earth, has recently been carried out by Yung and DeMore (1999). Unfortunately, most of the evidence for atmospheric

evolution in the solar system has not been preserved. Since Saturn and Titan were derived from materials in the same region of the solar nebula, and the two atmospheres were subjected to the same solar radiation over the age of the solar system, the comparative study of the chemical composition of the atmospheres of Saturn and Titan offers a unique opportunity to explain planetary composition.

### 3.1. COMPARISON OF SATURN AND TITAN

The atmosphere of Saturn is composed primarily of the lightest elements, hydrogen and helium, which were captured from the solar nebula during formation. The planet has a rocky core made of heavier elements. However, the mass of the gas greatly exceeds that of the core. Due to the enormous gravity of the giant planet, little mass has escaped from its atmosphere. Hence, the bulk composition is expected to provide a good measure of the initial composition of the solar nebula. Recently, significant departures (by factors of 2 to 3) from the solar values for the heavy elements C, N, P, and S have been observed for Jupiter and presumably for Saturn (Owen *et al.*, 1999; Atreya *et al.*, 1999; Orton *et al.*, 2000). The enhancement of O is not confirmed because the Galileo probe entered an unusually dry part of the atmosphere of Jupiter (Showman and Ingersoll, 1998). An influx of icy planetesimals formed at low temperature ( $T < 30$  K) might have been responsible for the enrichment of heavy elements.

Titan was formed in the Saturnian sub-nebula at the time of the formation of Saturn. Due to the lower temperatures in this region of the solar nebula, ices were common, and Titan (like Saturn) accreted material that is rich in ices. As the atmospheric constituents are photochemically processed and converted into condensable material, the ices on the surface or outgassing from the interior must maintain the supply of gas to the atmosphere. Titan possesses a thick, mildly reducing atmosphere that is different from the atmosphere of Saturn in at least two aspects. First, there is little  $H_2$  in the atmosphere of Titan relative to the most abundant gas,  $N_2$ . The gravity is low enough that light gases like H and  $H_2$  did not accumulate at formation. In contrast, the composition of Saturn is dominated by  $H_2$ . Second, unlike Saturn, Titan has a cold, solid surface. Organic compounds that are synthesized in the atmosphere are deposited on the surface, resulting in their permanent sequestration. This implies an irreversible chemical evolution of the atmosphere and the surface. Titan has no recycling of organic species as in Saturn. The atmosphere is being gradually destroyed by photolysis and must be resupplied by primordial ice on the surface or outgassing from the interior.

The net result of the photochemical destruction of  $CH_4$  is its conversion to higher hydrocarbons. Ultimately the product species gain molecular weight and become heavy enough to condense, giving rise to a ubiquitous aerosol layer in the atmosphere known as Axel-Danielson dust. The Titan aerosol chemistry

is augmented by the coupled chemistry of  $\text{CH}_4$  and  $\text{N}_2$ , resulting in the formation of nitrile compounds. The presence of an aerosol layer in the atmospheres of Saturn and Titan has profound consequences for the thermal budget of the upper atmosphere. Indeed, aerosol heating is a primary cause of the thermal inversion in the atmospheres of Saturn and Titan above the tropopause. The aerosols may also present a surface for possible heterogeneous chemical reactions.

The previous major advance in our knowledge of Saturn and Titan is from the Voyager encounters, summarized in special issues of *Science* (Voyager 1, 1981, Voyager 2, 1982) and the *Journal of Geophysical Research* (Voyager 2, 1983). The Cassini mission offers a unique opportunity to expand the base of knowledge from previous missions and Earth-based observations and to make new fundamental discoveries. One of the most important contributions of the Cassini observations is a comparison of the thermal structure and photochemistry of Titan and Saturn. There are at least three important aspects of the chemistry of Saturn and Titan: the hydrocarbon chemistry, the oxygen chemistry, and the nitrogen chemistry.

### 3.2. THERMAL STRUCTURE

Figures 13a and b show the temperature and bulk number density of the atmospheres of Saturn and Titan as a function of altitude. Unless otherwise stated, all Saturn and Titan data in the figures are from Moses *et al.* (2000) and Yung *et al.* (1984). The temperature at the top of the Saturn atmosphere is uncertain; two values have been reported: 420 K (Smith *et al.*, 1983) and 700 to 800 K (Atreya *et al.*, 1988). The results based on Voyager (see special issues referenced above) reveal several prominent common features of the thermal structure that are so distinctive as to be the basis for dividing the atmosphere into regions. The region from the reference level to the temperature minimum is known as the troposphere, where the temperature decreases with altitude. The troposphere is characterized by vigorous convective activities. Above the tropopause is the stratosphere, where the temperature increases to a maximum around 400 km. The inversion is caused by the absorption of sunlight by aerosols and has the effect of inhibiting mass exchange between the stratosphere and other parts of the atmosphere. Above this, the temperature decreases again in the mesosphere to a second minimum near the mesopause (around 800 km). Above the mesopause, the temperature rises again in the thermosphere.

The most interesting aspects of the thermal structure of Saturn and Titan are the thermal inversions in the stratosphere and the thermosphere. The principal heat absorbers in the stratosphere are  $\text{CH}_4$  and the Danielson-Axel aerosols. Titan has more aerosols, and its stratosphere is therefore warmer. A quantitative relation between the composition and the heat budget remains to be established from more precise measurements.

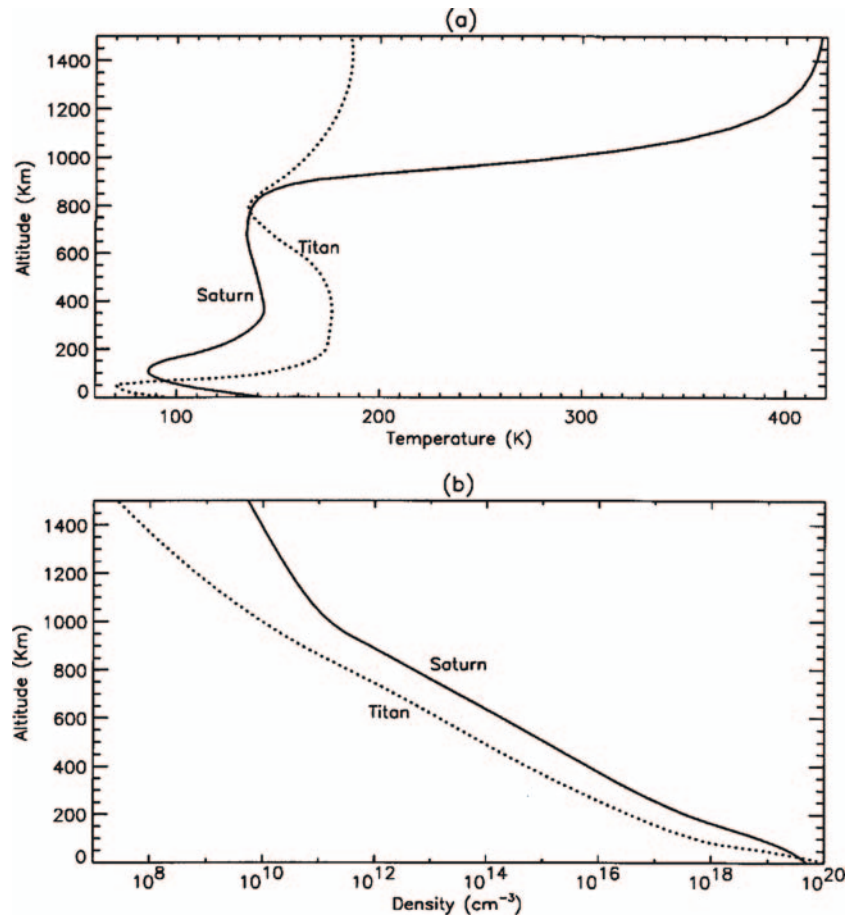


Figure 13. (a, b) Temperature profiles in the atmospheres of Saturn and Titan. Zero km refers to the 1 bar level on Saturn and 1.5 bar (the surface) for Titan. A possible higher temperature of Saturn's upper atmosphere of 700 K to 800 K (Atreya *et al.*, 1988) is not shown.

The hot thermosphere of Saturn is a puzzle (Festou and Atreya, 1982). In the terrestrial atmosphere, the high temperature can be explained by solar heating balanced by cooling due to conduction. This appears to be an adequate explanation for the thermospheric temperature on Titan, but not for Saturn, because it implies a very large eddy diffusion coefficient. An additional heating mechanism, such as that associated with the viscous damping of upward propagating waves from the troposphere, may be needed to account for the hot thermosphere of Saturn (Young *et al.*, 1997). To quantify this mechanism, we need observations of gravity waves, as manifested in the vertical structure of temperature and the vertical profiles of chemical species in the mesosphere and lower thermosphere. This can best be accomplished by UVIS solar or stellar occultations.

### 3.3. PHOTOCHEMISTRY

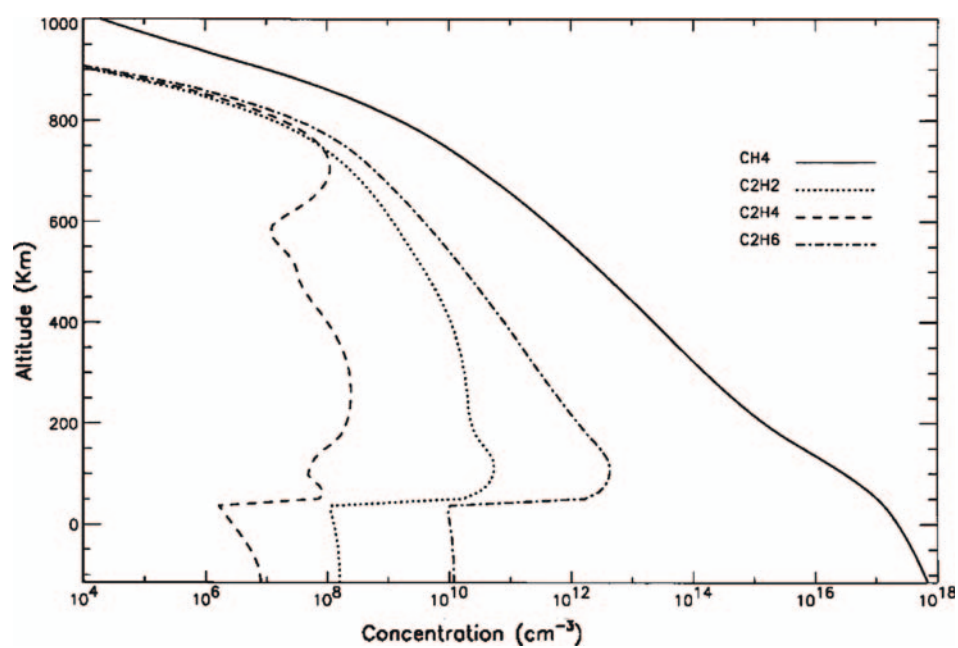
The photochemistry of hydrocarbons in the atmosphere of Jupiter has been studied in a comprehensive model that includes all the relevant chemistry up to 8 carbon atoms and vertical transport by eddy diffusion (Gladstone *et al.*, 1996). As one of the four giant planets, Saturn's photochemistry should be similar to that of Jupiter. The chemical model for Jupiter has recently been extended to Saturn by Moses *et al.* (2000). The major changes in the model include the new chemistry of oxygen species that have been detected by the Infrared Space Observatory (ISO) (Degraauw *et al.*, 1997). The photochemistry of hydrocarbon, oxygen, and nitrogen species on Titan was modeled by Yung *et al.* (1984) in a comprehensive chemical model that incorporated all the observations of the Voyager available at that time. Since then, there have been updates and extensions of that model based on subsequent Voyager analysis (Coustenis and Bezard, 1995; Coustenis *et al.*, 1989, 1991), and further analysis of data (Lara *et al.*, 1996), as well as laboratory kinetic studies (e.g., Zwier and Allen, 1996). These results will be briefly discussed in their relation to a comparative study of Saturn and Titan by Cassini.

#### 3.3.1. Hydrocarbon Chemistry

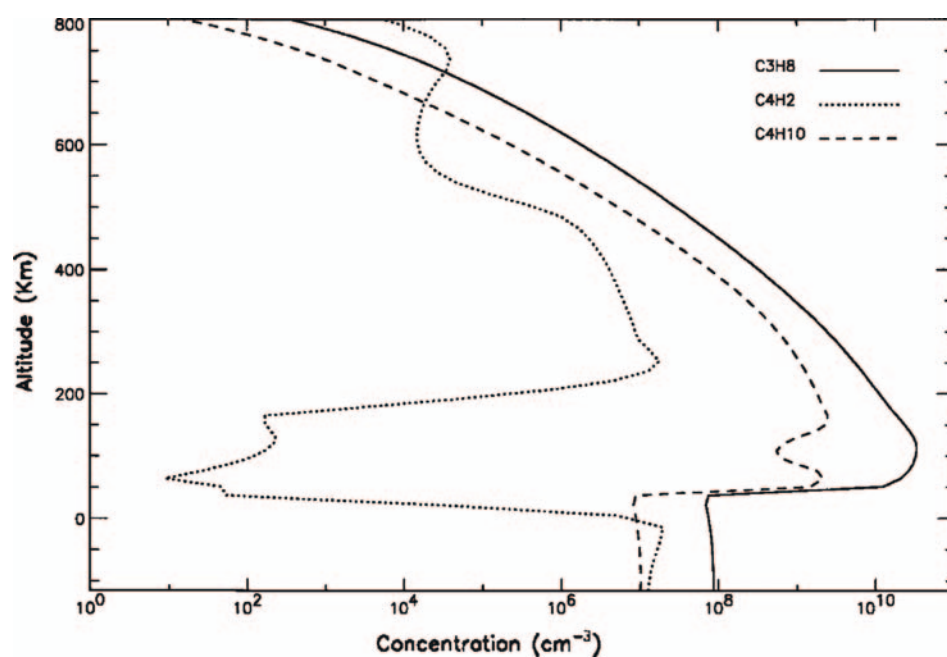
Figures 14a and b show the principal hydrocarbon species in the atmosphere of Saturn. Methane is the parent molecule of all hydrocarbons in the model. Its mixing follows the bulk density of the atmosphere (see Figure 14a). Rapid destruction occurs around and above the homopause, which is at an altitude of 1110 km (Atreya, 1982). The destruction of CH<sub>4</sub> gives rise to the production of radical species, which eventually recombine to form C<sub>2</sub>H<sub>6</sub>, C<sub>2</sub>H<sub>4</sub>, C<sub>2</sub>H<sub>2</sub> (Figure 14a) and heavier species C<sub>3</sub>H<sub>8</sub>, C<sub>4</sub>H<sub>2</sub> and C<sub>4</sub>H<sub>10</sub> (Figure 14b). We note that the alkanes (C<sub>2</sub>H<sub>6</sub>, C<sub>3</sub>H<sub>8</sub>, C<sub>4</sub>H<sub>10</sub>), once formed, are stable; their concentrations are high in the stratosphere. But the unsaturated hydrocarbons (C<sub>2</sub>H<sub>2</sub>, C<sub>2</sub>H<sub>4</sub>, C<sub>4</sub>H<sub>2</sub>) are less stable. They are destroyed before they reach the lower stratosphere. All higher hydrocarbon species are rapidly removed below the tropopause by rapid transport to the interior of the planet, where they are recycled back to the thermodynamically most stable product, CH<sub>4</sub>. Since CH<sub>4</sub> is originally derived from the deep atmosphere, this constitutes a closed loop; there is negligible loss of even the lightest molecules.

Figures 15a and b show the principal hydrocarbon species in the atmosphere of Titan. Comparing with Saturn, we note that the efficiency of organic synthesis is much higher in Titan, even though the total rate of CH<sub>4</sub> photolysis (the primary driver of photochemistry) is the same. The main reason is that Saturn's atmosphere is dominated by H<sub>2</sub>, whereas Titan's atmosphere is dominated by N<sub>2</sub>. This will become clear if we examine the comparison between atomic hydrogen profiles in the atmospheres of Saturn and Titan (Figure 16). The lower concentration of H atoms on Titan is due to their escape from Titan. As a result, the back reaction:





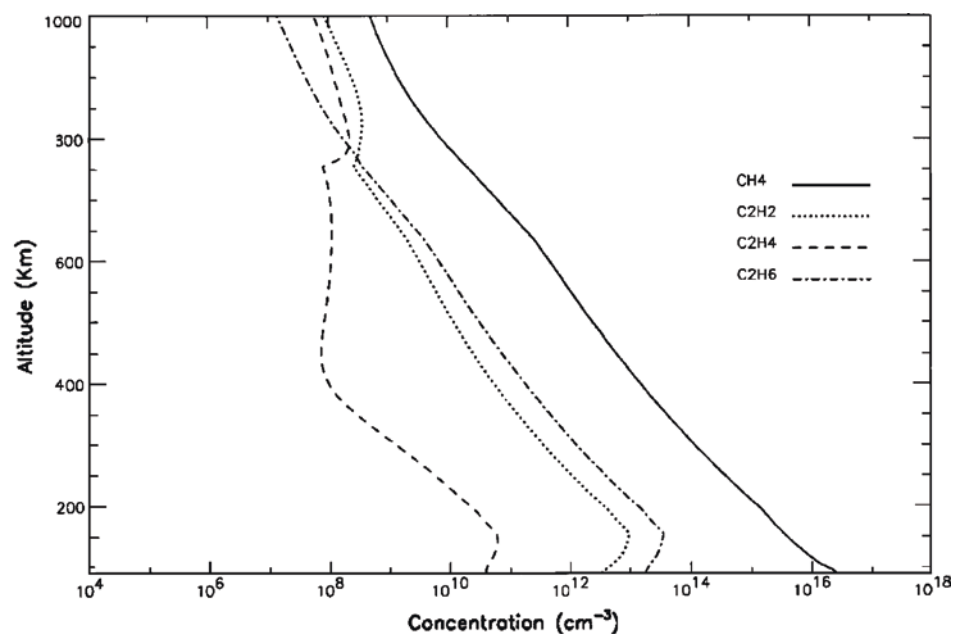
(a)



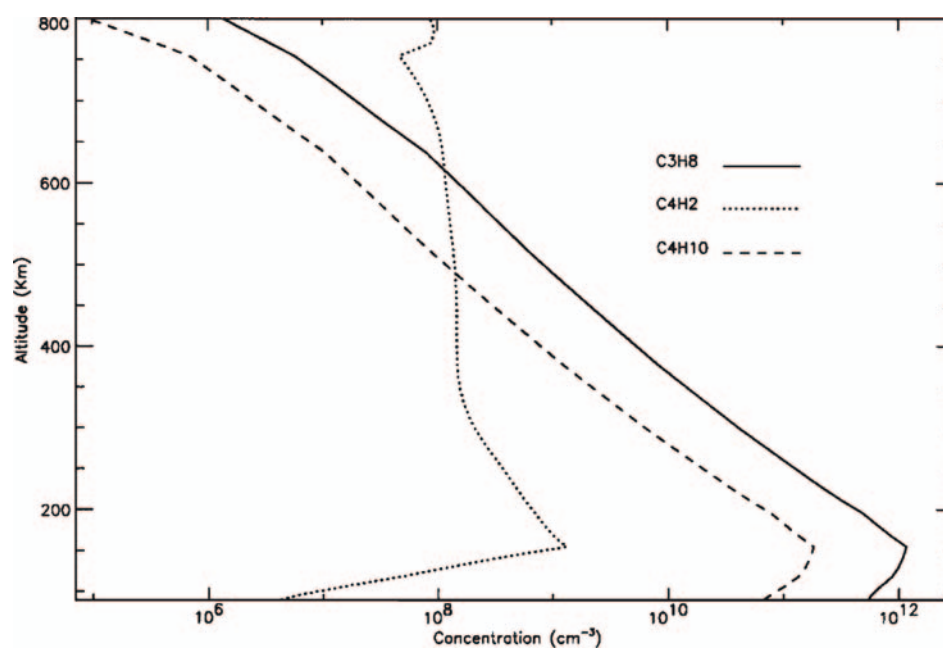
(b)

Figure 14. (a) Number density profiles for the major hydrocarbons in the atmosphere of Saturn:  $\text{CH}_4$ ,  $\text{C}_2\text{H}_6$ ,  $\text{C}_2\text{H}_4$ ,  $\text{C}_2\text{H}_2$ . (b) Number density profiles for the major hydrocarbons in the atmosphere of Saturn:  $\text{C}_3\text{H}_8$ ,  $\text{C}_4\text{H}_2$ ,  $\text{C}_4\text{H}_{10}$ .





(a)



(b)

Figure 15. (a) Number density profiles for the major hydrocarbons in the atmosphere of Titan:  $\text{CH}_4$ ,  $\text{C}_2\text{H}_6$ ,  $\text{C}_2\text{H}_4$ ,  $\text{C}_2\text{H}_2$ . (b) Number density profiles for the major hydrocarbons in the atmosphere of Titan:  $\text{C}_3\text{H}_8$ ,  $\text{C}_4\text{H}_2$ ,  $\text{C}_4\text{H}_{10}$ .

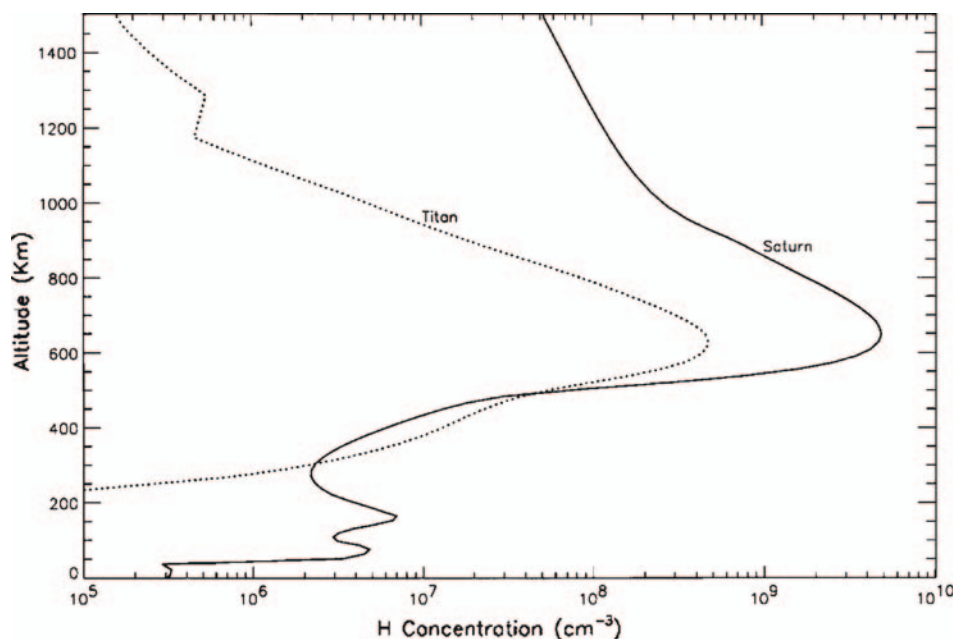


Figure 16. Number density profiles of H atoms in the atmospheres of Saturn and Titan.

is less important on Titan than on Saturn, and the methyl radicals can proceed to form higher hydrocarbons more efficiently. A careful quantitative comparison between the hydrocarbons and hydrogen from the Cassini mission is expected to reveal major new insights on the carbon chemistry in the outer solar system and to confirm or disprove some of the current models. A major puzzle is the model's failure to account for the formation of  $\text{CH}_3\text{C}_2\text{H}$  (not shown), which requires a new chemical pathway for forming this molecule. Although some of the heavy hydrocarbons are not expected to be observable by the UVIS experiment, the model provides a reference for future experiments. Also, in polar regions, the hydrocarbon concentrations may be enhanced due to auroral processes, and the model might have underestimated their concentrations.

### 3.3.2. Oxygen Chemistry

The composition of Saturn and Titan is reducing. The oxygen chemistry is entirely driven by an exogenic source, the ablation of micrometeoroids in the upper atmosphere. Figures 17 and 18 show the concentration profiles of the major oxygen species in the atmosphere of Saturn and Titan, respectively. UVIS measures O and CO directly; other species can be inferred indirectly or measured by CIRS. Although all the oxygen species are initially derived from a meteoric source, the most abundant oxygen species is not  $\text{H}_2\text{O}$  but CO. The reason is that  $\text{H}_2\text{O}$  condenses in the stratosphere and is removed from the middle atmosphere. The ultimate loss

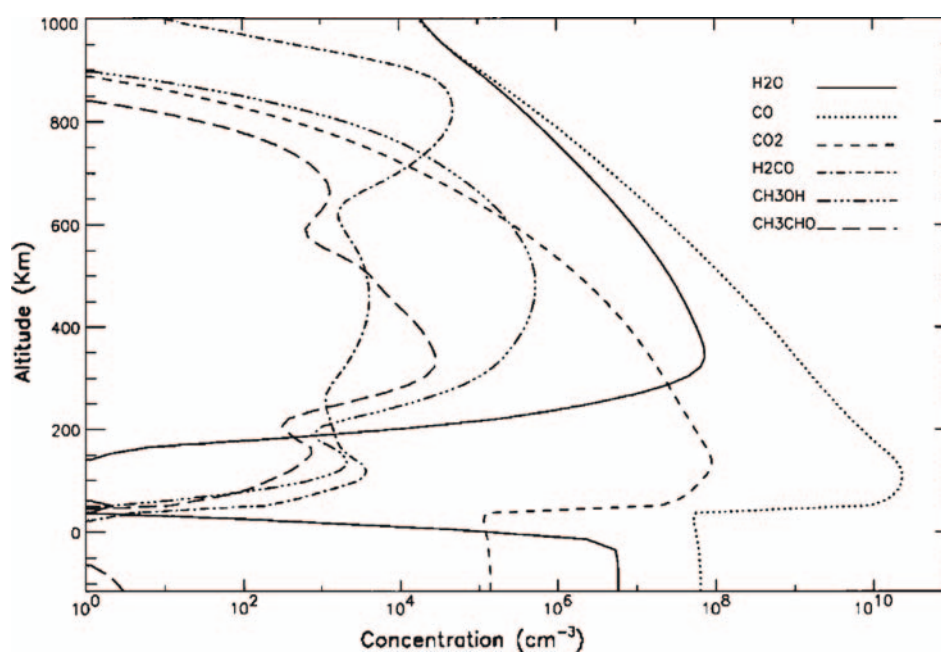


Figure 17. Number density profiles for the major oxygen species in the atmosphere of Saturn.

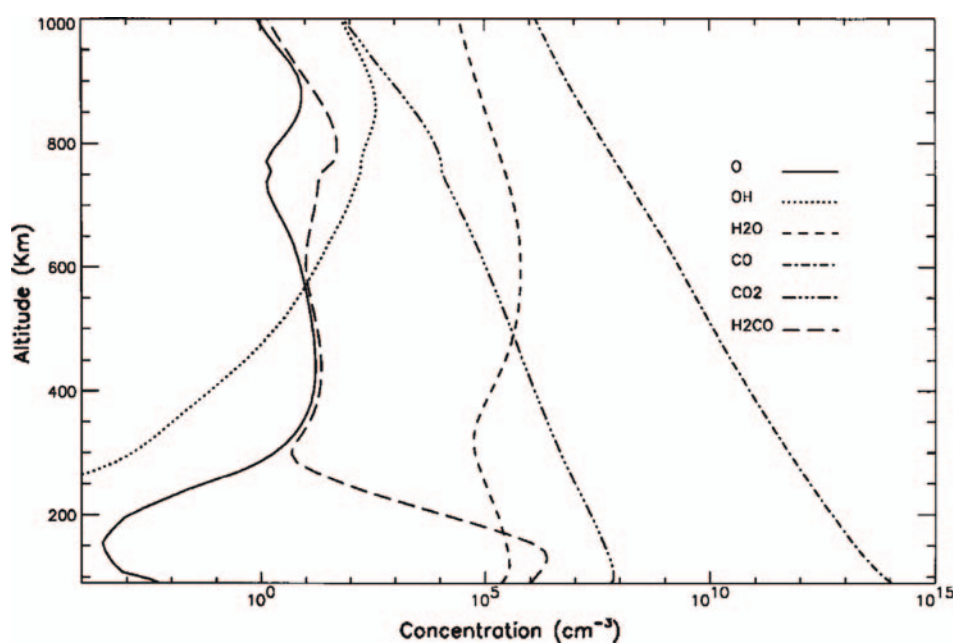


Figure 18. Number density profiles for the major oxygen species in the atmosphere of Titan.

mechanism of CO is formation of  $\text{CO}_2$ , followed by condensation at the tropopause. There is an interior sink for CO on Saturn, where CO is eventually converted to the thermodynamically stable molecules,  $\text{CH}_4$  and  $\text{H}_2\text{O}$ . On Titan, CO is stable on the surface (like  $\text{N}_2$ ). This explains the main difference between the vertical profiles of CO on Saturn and Titan. Our CO concentration for Titan is consistent with the measurements of Lutz *et al.* (1983), Muhleman *et al.* (1984), and Gurwell and Muhleman (1995). However, Marten *et al.* (1988), Hidayat *et al.* (1997), and Noll *et al.* (1996a) found significantly lower values. Since the chemical lifetime of CO on Titan is on the order of  $10^9$  years, we expect CO to be well mixed in the atmosphere, and there should be little change from year to year. Thus, the discrepancies between the observations are puzzling and must be resolved by future measurements. The most interesting question concerning the oxygen species on Saturn and Titan is the origin of the micrometeoroids. Are these interplanetary dust particles from the Asteroid Belt, the Kuiper Belt, the rings of Saturn; or is debris from the icy satellites transformed to exotic molecules in the atmosphere of Saturn and Titan?

### 3.3.3. Nitrile Chemistry

Figure 19 shows the nitrile compounds in the atmosphere of Titan. No nitrile compounds have been discovered on Saturn. These compounds are of great interest to

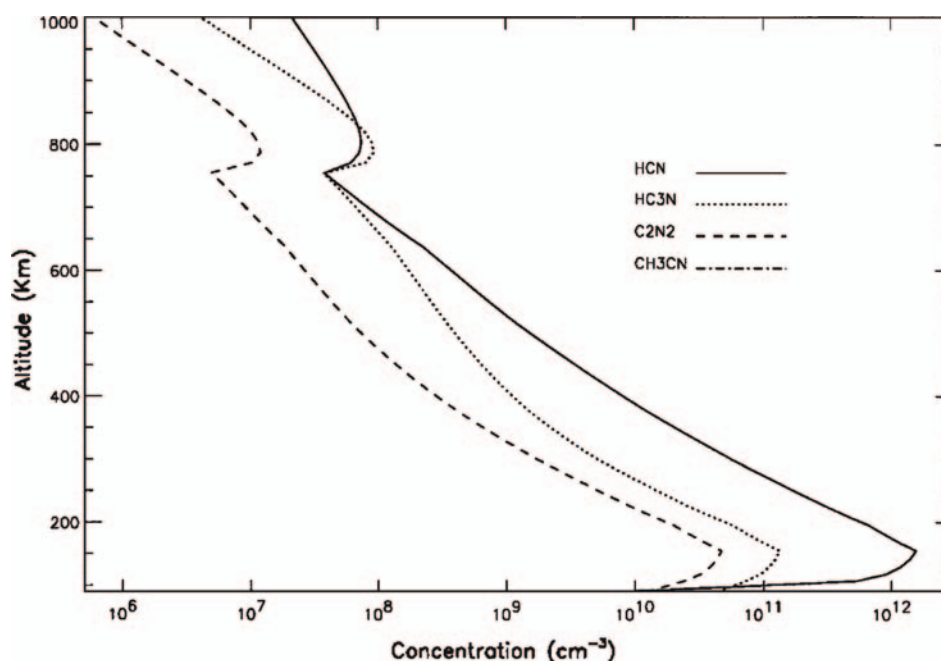


Figure 19. Number density profiles for the major nitrogen species in the atmosphere of Titan.

the origin of life as the basic constituents of amino acids and precursors to life. They are produced as a result of the photochemistry of nitrogen and hydrocarbons. Both the energy source that drives the nitrogen photochemistry and the chemical kinetics that generate and recycle these compounds are poorly understood from previous observations. For example, the abundance of  $\text{CH}_3\text{CN}$  cannot be explained by chemistry based on measured kinetics.

The model of Lara *et al.* (1996) is based on the reaction:



While branch (9) is well known, branch (10) has never been measured. Detailed observations of the altitude profile of  $\text{CH}_3\text{CN}$  in the future would provide a test of this hypothesis.

In summary, the Cassini UVIS observations will result in major advances in our understanding of the upper atmospheres of Saturn and Titan:

- (1) The temperature of the thermosphere and the heating mechanism responsible for maintaining the high temperature on Saturn.
- (2) The eddy mixing in the atmospheres of Saturn and Titan; comparison of an atmosphere without a surface and a thick satellite atmosphere with surface and possibly ocean.
- (3) The efficiency of organic synthesis in an  $\text{H}_2$  dominated atmosphere versus that in an  $\text{N}_2$  dominated atmosphere.
- (4) The impact of hydrogen escape at the upper boundary on atmospheric chemistry.
- (5) The magnitude and fate of the influx of oxygen in the ablation of micrometeoroids in the atmospheres of Saturn and Titan.
- (6) The chemical pathways leading to the formation of Danielson-Axel aerosols in the atmospheres of Saturn and Titan.

## 4. Clouds and Aerosols

### 4.1. STRATOSPHERIC AEROSOLS

The study of aerosols touches on many facets of atmospheric science. Aerosols are one of the end products of chemistry in the high atmosphere initiated by the breakup of molecules by photolysis and by charged particle bombardment. Charged particle bombardment is thought to be especially important in auroral regions. Aerosols absorb solar radiation and thereby play a role in the energy balance and meridional circulation of the stratosphere. UV wavelengths are more sensitive than longer wavelengths to small particles, which have a long residence time in the stratosphere and can serve as tracers of the circulation and horizontal eddy transport. Observations by UVIS will lead to detailed knowledge of their UV optical properties

and vertical distribution, which are necessary to estimate solar heating, and can be used along with observations of infrared cooling and heating to derive the mean meridional circulation, as West *et al.* (1992) have done for Jupiter's stratosphere. These observations are also necessary to derive aerosol number density, size, shape, and refractive index, which in turn serve to constrain aerosol/chemical life-cycle and microphysical models.

Ultraviolet wavelengths remotely sense the stratospheres of Saturn and Titan. Molecular scattering by H<sub>2</sub> and He provides enough opacity to establish vertical optical depth 1 at 37 mbar at 190 nm wavelength, decreasing to lower pressure approximately as  $\lambda^{-4}$ . Additional opacity due to gas (mostly hydrocarbons, see Section 3) and aerosol constituents will push this level to even lower pressures, especially near the poles, which are considerably darkened. In Titan's stratosphere, an optically thick aerosol haze dominates the opacity at wavelengths down to 180 nm and causes Titan's geometric albedo to be remarkably low (0.02 from 180 to 220 nm, McGrath *et al.*, 1998).

#### 4.2. SATURN

Saturn's banded appearance is the result of cloud and aerosol particles, which are transported by the zonal wind structure. As on Jupiter, the polar and low-latitude regions are distinctly different. Equatorward of the transition region, the atmosphere is moderately absorbing, but at higher latitudes the concentration of absorbers is much greater. This difference may be attributable to the strong contribution that auroral energy deposition makes to aerosol formation in the auroral zones, coupled with a dynamical confining mechanism (such as a zonal jet at the transition latitude), which inhibits particle transport to lower latitudes. Auroral processes have been implicated for aerosol formation on Saturn ever since the Voyager 2 photopolarimeter experiment showed UV absorbers to be concentrated at high latitude (Lane *et al.*, 1982; Pryor and Hord, 1991). Jaffel *et al.* (1995) discovered an auroral dark oval in the northern polar region. They considered this to be strong evidence for an auroral connection to UV haze production.

Previous work on Saturn's aerosols and their connection to auroral processes leaves us with a number of questions. What is the nature of the dark feature associated with the aurora? Does it serve as a tracer for recent (within hours) aerosol formation, or does it reflect processes operating over longer time scales? At what altitudes do the aerosols begin to form? What dynamical process produces the sharp transition region? Can we see longitudinal contrasts over short spatial scales, and can they be exploited to reveal the nature of the zonal wind field at mbar pressures in the polar stratosphere? Are there variations over short or long time scales, and what do they imply? What are the sizes and shapes of the particles, and what is the nature of the microphysical processes that govern these parameters? What are the compositions of the particles at high and low latitude?



The UVIS instrument will provide information uniquely suited to addressing these questions. It will supply images of Saturn at many wavelengths between about 150 and 190 nm, which will be used to study the morphology of the banded structure and of the illuminated polar region. These images will have several advantages compared to what is obtainable from earth orbit, including better viewing angles during high-inclination orbits, better signal-to-noise ratio, frequent temporal coverage over a 4-year period, and phase angle coverage. Phase angle coverage provides information on the scattering phase function of the particles, which is diagnostic of the particle size distribution. Together with information at other wavelengths from other instruments, it will help constrain particle shape and the imaginary part of the refractive index (which is diagnostic of composition).

Solar and stellar occultations will be used to measure the vertical profile of aerosol and gas opacity at the highest altitudes (pressure less than about 0.2 mbar). Solar occultations (with EUV only) provide EUV signal but are rare (at most a few during the mission), and the spatial resolution is limited by the angular size of the sun's disk as projected on the limb. These provide direct measurements of the atomic hydrogen density and the thermospheric temperature. One or more stellar occultation events (primarily FUV) are expected for every orbit, providing modest latitudinal coverage and high spatial resolution in the vertical. Opportunities to do vertical profiling in and near the auroral region will be particularly interesting, since the altitudes probed coincide with the location of auroral energy deposition. In addition to aerosol and gas-opacity profiles, these occultation measurements will provide temperature information over one or two scale heights. An estimate of zonal winds at low pressure is possible within a limited latitude range if the latitudinal density of occultations is sufficient to derive isobaric slopes.

#### 4.3. TITAN

The importance of aerosols to atmospheric physics and chemistry is nowhere more evident than on Titan, and many papers in recent scientific literature have concerned themselves with Titan aerosols. Titan's atmosphere contains mostly nitrogen with trace amounts of hydrocarbons, mostly methane. Destruction of methane by photolysis (Yung *et al.*, 1984) and by charged particle bombardment from Saturn's magnetosphere, the solar wind, and high-energy cosmic rays leads to the production of a plethora of hydrocarbons and nitriles (see Section 3). Through a process as yet too complex to model accurately, these molecules lead to the formation of small haze particles high above the surface (in the altitude range 350 to 600 km). Several laboratory studies and theoretical treatments have revealed likely chemical pathways and products in this process (Yung *et al.*, 1984; Thompson *et al.*, 1994; Devanssay *et al.*, 1995; Zweir and Allen, 1996; McKay, 1996; Clarke and Ferris, 1997).

Refractive indices of the particles derived from studies of Titan's geometric albedo are within a factor of 2 of those produced in the laboratory work of Khare *et al.* (1984). The particles do not absorb much at red wavelengths but absorb strongly at UV wavelengths. The particles that formed in several of the laboratory studies were aggregates of small spheres (Bar-Nun *et al.*, 1988; Scattergood *et al.*, 1992). Aggregate particles can account for the combination of modest forward scattering (near 160° phase angle) and high linear polarization (near 90° phase angle) produced by Titan's haze (West and Smith, 1991; Lemmon, 1994; Rannou *et al.*, 1997).

Conventional aerosol microphysical models for Titan assumed that the particles are spheres (e.g., Toon *et al.*, 1992). Tomasko and Smith (1982) proposed a vertically inhomogeneous model with an optically thin layer of larger particles at the top of the atmosphere to account for the combination of forward scattering and linear polarization. Toon *et al.* (1992) showed how that scenario could be supported with a microphysical model having upwelling at some latitudes. They simultaneously account for the detached haze layer seen in Voyager images (Rages and Pollack, 1983). Haze morphology in the polar region as seen in Voyager images has considerable structure, indicating the importance of atmospheric dynamics in aerosol formation and transport.

More recent models of haze microphysics have emphasized the aggregation process. This work has been carried out mostly by Cabane *et al.* (1993), Chassefiere and Cabane (1995), and Rannou *et al.* (1997). These models have become more sophisticated with time, attempting to account for details of the haze vertical structure as well as the fractal dimension of the particles.

Yet another important facet of Titan aerosol science is the observed north/south contrast and seasonal variation. Karkoschka and Lorenz (1997) used images of Titan's shadow on Saturn to derive a north/south difference in altitude of the optical limb of the planet, which is close to zero at 337 nm wavelength but is 130 km at 954 nm. This implies a hemispheric asymmetry in aerosol size (0.3  $\mu\text{m}$  mean radius in the north compared to 0.1  $\mu\text{m}$  mean radius in the south). We still don't have a good understanding of the highly coupled chemical/microphysical/ radiative/dynamical processes that produce the observed asymmetries and their variations with time.

Observations by the UVIS instrument will provide unique and important information to help sort out current questions about Titan aerosols. Maps of Titan's reflectivity at many latitudes and phase angles at UV wavelengths will put new constraints on the size distributions and shapes of particles as a function of latitude. At close range (within 20,000 km of Titan), imaging along the limb will resolve structure whose scale height is much smaller (20 km or less) than the scale height of the gas. Because ultraviolet wavelengths are sensitive to small particles, the UVIS experiment will provide critical information on the aerosol formation region (300 to 600 km altitude). Solar occultations at Titan can resolve subscale-height structure and provide important information on gas and aerosol opacity at high altitude. Multiple stellar occultations will allow detailed vertical profiling of gas and aerosols at many latitudes down to an altitude of approximately 350 km.

In concert with Cassini images and IR spectroscopy, this will allow a complete picture of Titan's stratosphere, which can be linked to the Huygens probe results at lower altitudes from the Descent Imager/Spectral Radiometer (DISR) experiment.

## 5. Thermospheres and Exospheres

### 5.1. INTRODUCTION

The unexpectedly high thermospheric temperatures of the giant planets are an unsolved puzzle. Unlike the terrestrial planets, we cannot explain their high temperatures (see Figure 20). UVIS can measure the various heating mechanisms by their direct and indirect effects on UV thermospheric emissions.

### 5.2. SATURN

#### 5.2.1. *Saturn's Aurora*

The Voyager UVS obtained limited information on Saturn's aurora, which showed strong intensity variations in both north and south ovals (Sandel and Broadfoot, 1981; cf. Broadfoot *et al.*, 1981; Sandel *et al.*, 1982). More recent measurements

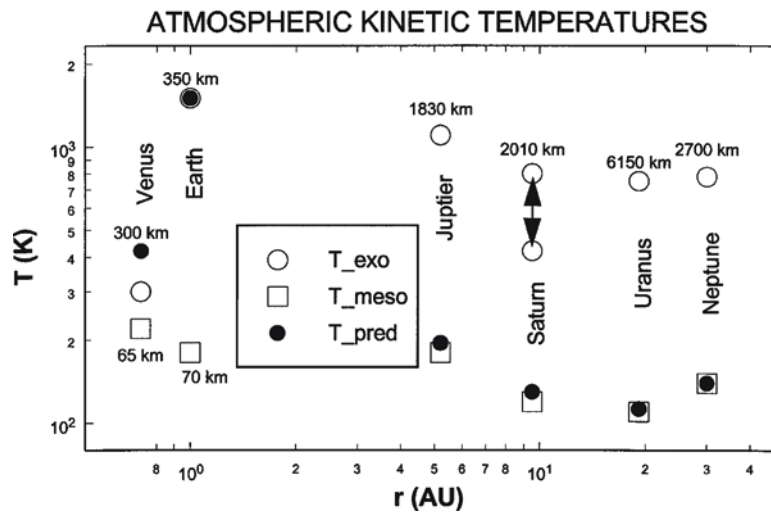


Figure 20. Kinetic temperatures of the atmospheres of the giant outer planets compared to the Earth and Venus. Open circles are the temperatures measured at the tops of the thermospheres (exobase; note range for Saturn). Filled circles are the temperatures predicted through model calculations. The modeled exobase temperatures for the outer planets are based on solar radiation input and the known thermal transfer properties of  $H_2$ . Open squares are the mesospheric temperatures. Altitudes of the exobase are indicated on the plot.

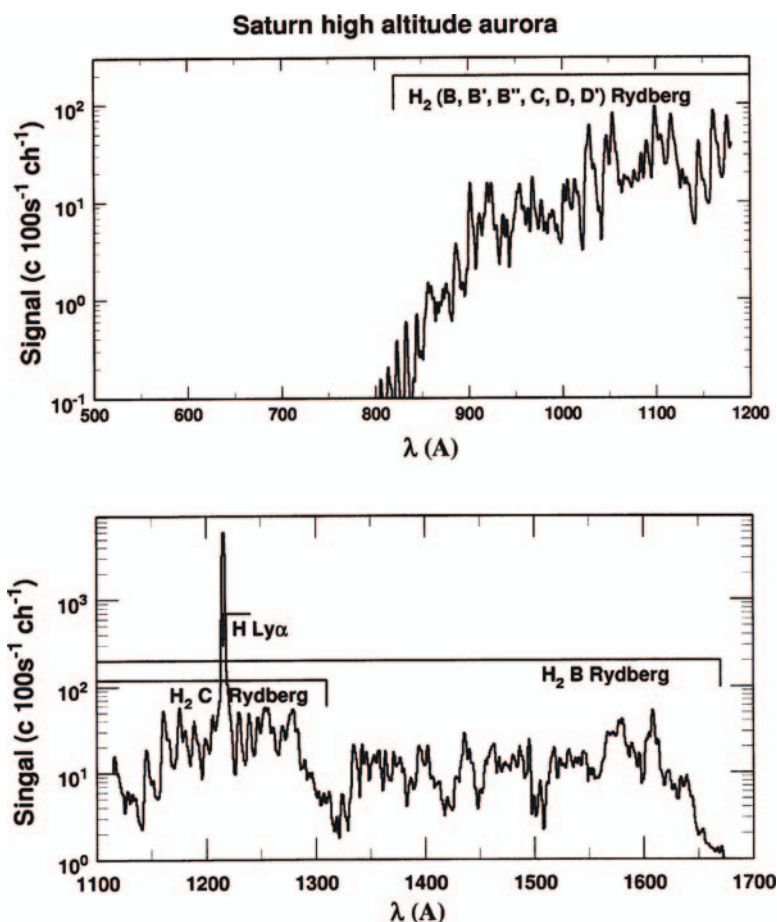


Figure 21. Model synthesis of high altitude Saturn auroral spectra in the UVIS EUV and FUV channels, showing  $\text{H}_2$  bands and H emissions excited by soft electron precipitation. A brightness of 10 kR is assumed.

with the HST's WFPC2 and STIS (Trauger *et al.*, 1998) show temporal, longitudinal, and local time effects. The UVS data showed that much of the emissions come from the high thermosphere, implying very soft primary particles together with brighter, spatially confined 'hot spots' whose spectra are similar to those of Jovian aurorae and therefore imply primaries with sufficient energy to penetrate to the hydrocarbon homopause. The variations, the differences from Jovian aurorae, and the evidence that neutral gases dominate Saturn's magnetosphere indicate very significant dissimilarities between Saturnian and Jovian processes. The study of Saturn's aurora by UVIS will further explore these differences and should greatly advance our understanding of the Saturnian phenomena. A model of the UVIS response to a 10 kR aurora is shown in Figure 21.

### 5.2.2. *Saturn's Airglow*

The H<sub>2</sub> emissions in Saturn's dayglow show a spectrum very similar to that of its high-altitude 'soft' aurora (and to that of Jupiter's dayglow (Sandel *et al.*, 1982; Shemansky, 1985; Shemansky and Ajello, 1983)). The H emissions are relatively stronger than in the aurora, suggesting a larger H/H<sub>2</sub> ratio or a substantial difference in source function. Although the Voyager UVS observations were affected by the weaker signal and the presence of the rings and their shadow, the Saturnian dayglow clearly differs from the Jupiter dayglow. Dawn is twice as bright as dusk, and the H Lyman- $\alpha$  and H<sub>2</sub> bands show limb-brightening at dawn, whereas Jupiter shows limb-darkening in H Lyman- $\alpha$  and H<sub>2</sub> emissions at both dawn and dusk. Saturn does not show Jupiter's Lyman- $\alpha$  'bulge' in longitude. Limb profiles at Saturn showed airglow scale heights five times larger than that of neutral H<sub>2</sub>, indicating a high-altitude source for the airglow other than solar radiation. Precipitation of soft electrons could explain the airglow and, by dissociating H<sub>2</sub>, provide both a source of thermospheric heating and a source of the observed magnetospheric H. A model of the UVIS response to the dayglow is shown in Figure 22.

### 5.2.3. *Occultation Measurements of Thermospheric Structure*

Solar and stellar occultations provide composition and temperature information throughout the thermosphere. Solar occultations below 912 Å yield exospheric temperature and both H and H<sub>2</sub> profiles in the upper thermosphere. At lower altitudes, where the angular size of the Sun exceeds the relevant scale heights, stellar occultations yield temperature and the identity and vertical distribution of absorbing hydrocarbons around the homopause. Analysis of Voyager occultation data also yielded the vertical flux of H and the eddy diffusion coefficient (Smith *et al.*, 1983; Festou and Atreya, 1982).

## 5.3. TITAN

Titan, like Triton and Pluto, has an atmosphere dominated by N<sub>2</sub>, and CH<sub>4</sub> is the most abundant trace gas. Their atmospheres derive from the slow release of CH<sub>4</sub> and NH<sub>3</sub> from clathrates in the interior, with the NH<sub>3</sub> photolyzing to produce N<sub>2</sub> (Atreya *et al.*, 1978), and the delivery of volatiles by cometary impact (Zahnle and Dones, 1992).

### 5.3.1. *Thermospheric Emissions and Structure*

Titan's atmosphere shows FUV and EUV emissions from N<sub>2</sub>, N, N<sup>+</sup>, and H, which are detectable on the night side and much brighter in sunlight. The excitation mechanisms involve magnetospheric-particle precipitation and photoelectrons, perhaps accelerated by internal processes (Hall *et al.*, 1992). The particle deposition may also produce both heating in and atom escape from the exobase region. Voyager spectra of the N<sub>2</sub>C'4-X system are unaffected by predissociation, implying generation at the exobase (Shemansky *et al.*, 1995) and hence a flux of soft electrons.

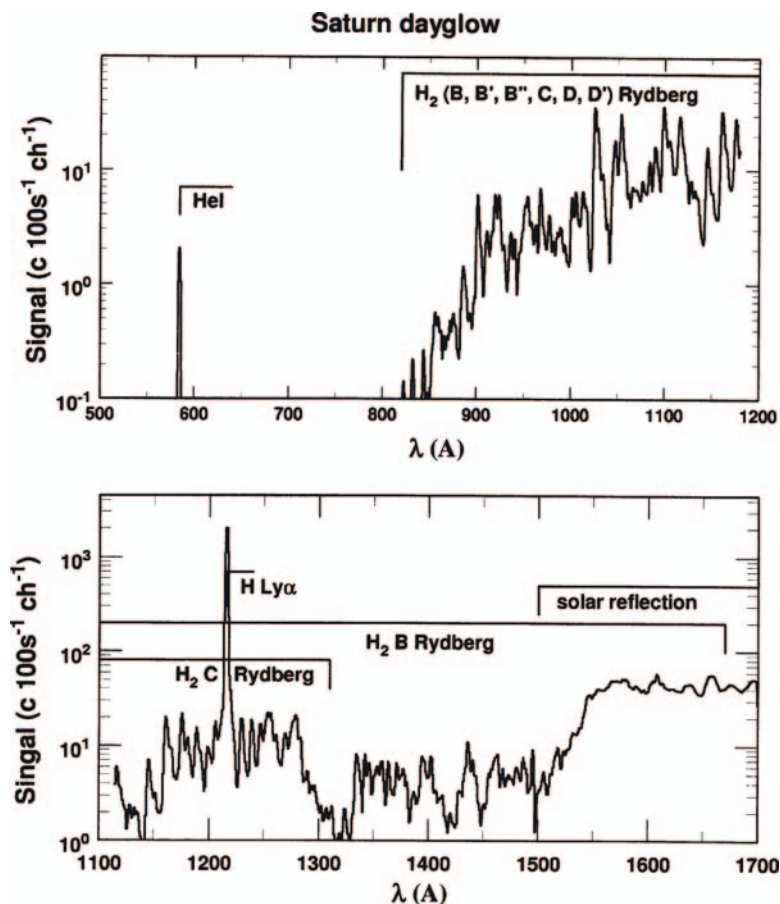


Figure 22. Model synthesis of Saturn dayglow spectra in the UVIS EUV and FUV channels showing soft-electron excited  $\text{H}_2$  and H. The long wavelength region is dominated by the reflection of solar radiation. A brightness of 1.0 kR for the  $\text{H}_2$  bands is assumed, matching the value obtained by the Voyager UVS experiment.

These electrons would also dissociate  $\text{N}_2$  and any  $\text{H}_2$  present; heating and escaping atoms would result.

### 5.3.2. Occultation Measurements of Thermospheric Structure

Voyager UVS occultation data analyzed by Smith *et al.* (1982) at several wavelengths (Figure 23) yielded temperature and composition information for altitudes between 400 and 1200 km. At dusk near the equator, the exospheric temperature was 186 K. Photolytic conversion of  $\text{CH}_4$  to  $\text{C}_2\text{H}_2$  was seen above 800 km, and two absorbing haze layers were seen. The lower layer (at 375 km) appeared uniform, which was confirmed by the Voyager cameras (Rages and Pollack, 1983). The upper layer (700 to 1100 km), presumably composed of polyacetylenes, differed



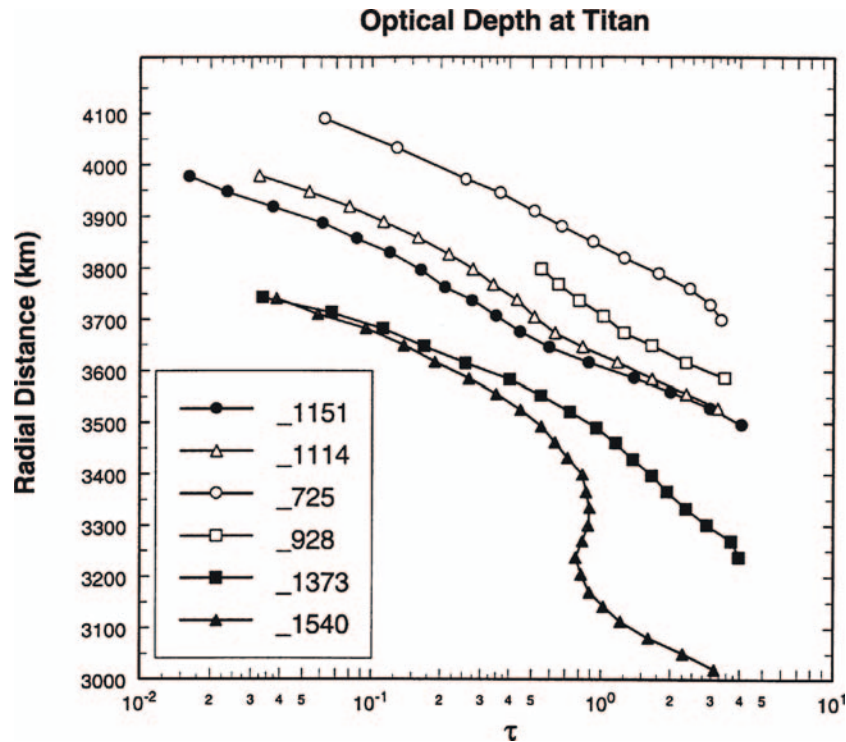


Figure 23. Voyager 1 UVS ingress ( $2.74^\circ\text{N}$ ) occultation measurements of optical depth at various indicated wavelengths as a function of radial distance from the center of Titan (after Smith, *et al.*, 1982).

between ingress and egress. Other nonuniformities in temperature and composition have been reported by the Voyager IRIS (Coustenis, 1992). The Cassini UVIS, with much better resolution and sensitivity than the Voyager UVS, should provide information to within 100 km of the radio occultation limit of 200 km.

#### 5.4. MAGNETOSPHERE

Both Saturn and Titan may supply neutrals to the magnetosphere. In any case, there is compelling evidence that considerable amounts of water are supplied by sputtering from ices in the system. The Voyager UVS detected H at out to 20 Rs, with a peak density of  $100\text{ cm}^{-3}$  and extending 8 Rs above and below the equatorial plane. HST has detected OH at 4.5 and 6 Rs, with a null result at 8 Rs. There are theoretical grounds for expecting O in amounts similar to OH. Other sputtering products may be present in quantities detectable by UVIS, in addition to the H and O. The large neutral/ion ratios will have a large effect on magnetospheric energetics and structure.

## 5.5. JUPITER

Cassini will fly past Jupiter in December 2000, presenting the opportunity to examine questions raised by earlier observations at similar wavelengths (the Voyager UVS, the Galileo UVS and EUV, the IUE, the HUT, and the EUVE). The UVIS combination of sensitivity, resolution, wavelength coverage, imaging capability, and potential for extended synoptic coverage in many ways exceeds the sum of these earlier instruments.

### 5.5.1. *Jupiter's Aurora*

The auroral spectrum consists of emissions from  $H_2$  and H showing the effects of self-absorption by  $H_2$  and of absorption by  $CH_4$ ,  $C_2H_2$ , and perhaps  $C_2H_6$ . X-rays have been detected (Waite *et al.*, 1994), perhaps originating from the precipitation of heavy magnetospheric ions (Cravens *et al.*, 1995; Gladstone *et al.*, 1998). Information on the energy of the precipitating particles can be obtained from the absorption features and the relative strengths of the Lyman series of H. Galileo and HST images have shown the auroral oval to be narrow (200 km) and structured, with variable emissions from inside the oval in the dusk sector. System III longitudinal dependence is well studied.

### 5.5.2. *Jupiter's Airglow*

Airglow emissions from H,  $H_2$ , and He have been detected (Shemansky, 1985; Feldman *et al.*, 1993). They are all limb-darkened, as is the reflected solar continuum at 166 Å. X-rays from an unknown excitation process have been measured at low latitudes (Gladstone *et al.*, 1998). UVIS, with its superior resolution and its spectral coverage, is well suited to throw light on the excitation and absorption mechanisms. It may also provide a resolution of the controversy surrounding the interpretation of the  $H_2$  emissions.

### 5.5.3. *Io's Plasma Torus*

Detailed observations of the torus's radiant output (90% of which falls within UVIS's range), ion composition, electron temperature, and structure will provide new information on its energy budget to elucidate its energy sources. UVIS may also detect the O and S atoms escaping from the torus and the Jovian system. Figure 24 compares a Galileo UVS/EUV spectrum at 35 to 40 Å resolution with a model of the UVIS EUV response to torus emission at 2.4 Å resolution.

## 5.6. SUMMARY

The Cassini UVIS will bring to bear on the Saturn system considerably greater capabilities than possessed by the Voyager and Galileo UVS/EUV instruments. The long time scale of the Cassini tour will provide opportunities for multiple spectral images and solar and stellar occultations. These will provide the data to

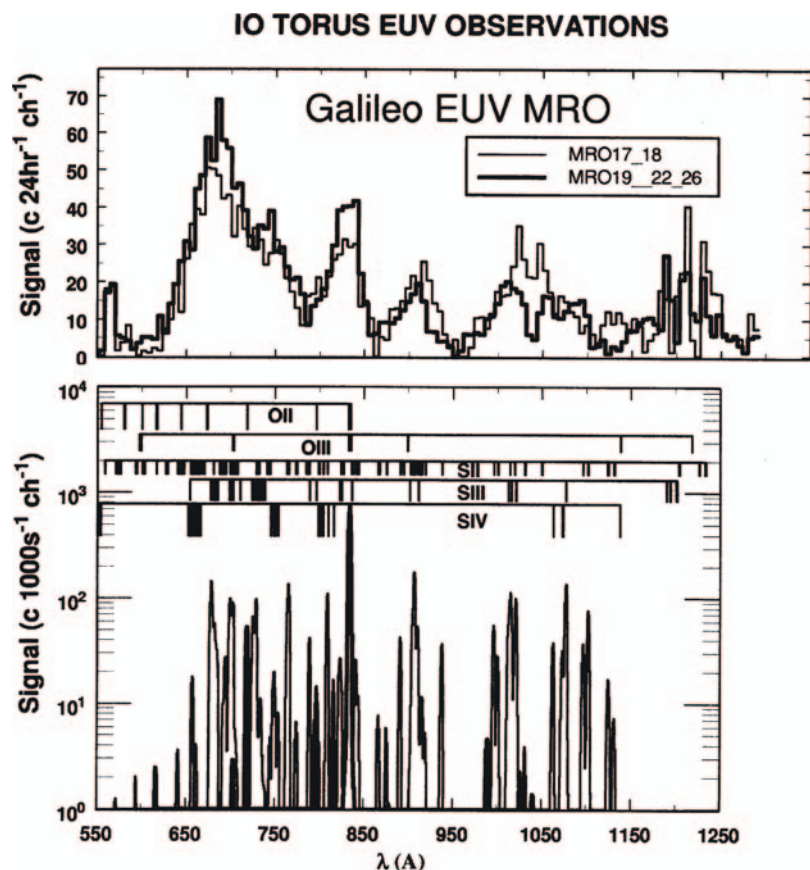


Figure 24. Comparison of modeled UVIS spectrum of Io plasma torus with Galileo observation. The predicted UVIS spectrum at  $2.4 \text{ \AA}$  resolution obtains higher total signal counts in 1000 s than those obtained by the Galileo EUV instrument in 24 h, at a resolution of  $40 \text{ \AA}$ .

examine and explain the thermospheric energy balance and to elucidate the supply of neutrals to Saturn's unique magnetosphere.

## 6. Icy Satellite Surfaces and Exospheres

Saturn's entourage of icy satellites is an important target for the Cassini mission. Most of what we know about Phoebe, Iapetus, Hyperion, Rhea, Dione, Tethys, Enceladus, Mimas, Janus, and Epimetheus (to name just the larger moons) dates from the Voyager mission. The distance of the flybys and limited capability of the Voyager ultraviolet spectrometer leave much for the Cassini UVIS to discover.

The moons of Saturn, whose orbits are within Titan's orbit (except Hyperion, Iapetus, and Phoebe), are embedded in Saturn's magnetosphere. Composed primarily of water ice, they are too small to retain the thick atmosphere of their large sibling,

Titan. Their surfaces bear the signature, both in terms of radiation damage and evolved chemistry, of long exposure to Saturn's charged particle environment. New discoveries on the Galilean satellites of oxygen chemistry driven by charged-particle bombardment and UV photolysis of water ice are relevant to Saturn's moons, also. Molecules sputtered from the icy satellite surfaces may form tenuous atmospheres, and they are a source of matter to Saturn's magnetosphere.

With UVIS we will use the interaction between the satellite surface and its magnetospheric environs to study three key areas of icy satellite science: (1) surface age and evolution, (2) surface composition and chemistry, and (3) tenuous atmospheres/exospheres.

### 6.1. SURFACE AGE AND EVOLUTION

Voyager images suggest complex thermal and geologic histories: for example, clear regional differences in surface age are visible in the Voyager images of Enceladus. Enceladus is speculated to be the source of Saturn's E ring, possibly implying the existence of some sort of geologic activity supplying particles. Intriguing low-resolution images of 'wispy terrain' on Rhea and Dione also suggest regional units that have experienced very different thermal histories than are visible in high-resolution images of cratered regions of their surfaces (Smith *et al.*, 1982). Our goal with UVIS will be to establish the exposure history of surface units by measuring their UV albedo, thus addressing regional age.

Saturn's icy satellites, which orbit within Saturn's magnetosphere, experience the impact of energetic particles onto their surfaces; this bombardment can eject atoms and molecules from the surfaces, affect surface microstructure, and cause chemical alteration (e.g., Cheng *et al.*, 1986; Johnson and Quickenden, 1997; Delitsy and Lane, 1998). Surface UV albedo is affected by radiation darkening and surface chemistry and thus will vary with the amount of time; a unit has been exposed to the magnetosphere's radiation and high energy particles.

Leading-side versus trailing-side asymmetries are to be expected. Bound magnetospheric plasma orbits faster than the satellites and thus impacts their surface on the trailing side. The leading sides of Dione and Rhea are indeed brighter than their trailing sides (Nelson and Lane, 1987).

The Galileo discovery at Jupiter that Ganymede certainly, and possibly Europa and Callisto, have internally generated fields and possess their own magnetospheres (Kivelson *et al.*, 1997) is also relevant to our investigation of Saturn's icy satellites. A magnetosphere will protect the satellite surface from Saturn's plasma bombardment. The structure of the satellite's magnetosphere may affect the geographic distribution of radiation damage by focusing radiation along open field lines (Johnson, 1997). In this case, rather than being able to determine relative surface ages, we may be able to study the structure of the moon's own magnetosphere.

The fact that the orbits of Hyperion, Iapetus, and Phoebe are well outside Saturn's magnetosphere, except when they are in the portion of their orbits that carries them through Saturn's magnetotail, gives us the opportunity to compare surfaces with quite different exposure levels.

The Cassini UVIS will acquire full disk albedo maps of each of the Saturnian satellites and spatially resolved spectra for most of the satellites. We will assemble the albedo map from observations acquired every  $15^\circ$  of longitude and  $10^\circ$  of latitude, resolution permitting, for each of the major moons. Three factors determine exposure history: the existence of an internal magnetosphere, the structure of the Saturn magnetosphere (e.g., leading- vs. trailing side bombardment), and the amount of time a surface unit has been exposed (which depends on the geologic history). In order to separate these causes, UVIS data maps will be correlated with imaging data to quantify the relationship between UV darkening and surface age. Cassini magnetometer data for close flybys may determine the existence of internal magnetospheres. Disk-resolved UV spectra have been used quite successfully by the Galileo Ultraviolet Spectrometer (UVS) Team to carry out similar investigations (Hendrix *et al.*, 1998).

In addition to relative age, surface evolution can be investigated by looking at surface microstructure via the phase function. Surface scattering properties are determined by the surface microstructure and large-scale roughness. The phase function will be different depending on whether the surface is smooth or structured at the scale of the wavelength being investigated, providing insight into the evolution of the regolith. One fascinating Voyager result is that in spite of the very different ages and appearance of different regions on Enceladus, the albedo, color, and photometric function properties are uniform, suggesting the possibility of a thin, ubiquitous layer of geologically fresh frost (Buratti and Veverka, 1984; Veverka *et al.*, 1986; Buratti, 1988).

Cassini will view Enceladus at  $\pm 0.01^\circ$  phase angle, allowing us to measure the opposition effect, which in turn yields surface porosity. We will acquire phase curves for all of the Saturnian satellites, from  $0^\circ$  (Enceladus only) or  $5^\circ$  (most of the other satellites) to  $160^\circ$ .

## 6.2. SURFACE COMPOSITION AND CHEMISTRY

The bulk composition of the Saturnian satellites is predominantly water ice. Their surfaces are nearly pure water ice (Clark *et al.*, 1984), but with enough compositional or morphological differences to cause their spectra and UV/IR color ratios to be significantly different (Clark *et al.*, 1986; Nelson and Lane, 1987) from each other and from the Jovian and Uranian satellite families. In spite of these differences, we use the Jovian satellites as predictors of phenomena we may expect to find in the Saturnian system, adjusted for the colder temperatures.

Investigation of photolysis and radiolysis of water ice is currently a very active area of research, propelled by recent Galileo results, earth-based observations,

and laboratory work. UV radiation dissociates  $\text{H}_2\text{O}$  into H and OH, and  $\text{H}_2$ .  $\text{H}_2$ , O, and  $\text{O}_2$  are produced from H and OH. H and  $\text{H}_2$  are quickly lost to thermal escape. The flux of atomic hydrogen escaping from Ganymede has been measured by the Galileo UVS (Barth *et al.*, 1997). O and  $\text{O}_2$  have been detected at Europa and Ganymede (Hall *et al.*, 1995; Spencer *et al.*, 1995; Calvin *et al.*, 1996; Saur *et al.*, 1998); thus, we might expect to detect these species at the Saturnian satellites. Reactions powered by solar UV ice photolysis have significant energy available but only affect the top tens of monolayers of the satellite surface. Plasma bombardment penetrates deeper, and the products may stay in the solid surface long enough to participate in other reactions, for example, providing the possibility for  $\text{O}_2$  to form  $\text{O}_3$ . Spectral absorption suggestive of ozone has been detected by the Galileo UVS on Ganymede (Hendrix *et al.*, 1999) and by the Hubble Space Telescope on Ganymede, Rhea, and Dione (Noll *et al.*, 1996b; Noll *et al.*, 1997). Laboratory results are not entirely consistent with Galilean satellite observations, however (Vidal *et al.*, 1997 and Baragiola and Bahr, 1998), so being able to compare oxygen chemistry at a variety of temperatures and radiation environments will help in understanding the processes.

Use of the ultraviolet portion of the spectrum for compositional studies of a surface is difficult, since few solids have features in the UV. If, however, component atoms and molecules are sputtered or sublimated from the surface, vapor phase spectral features may be detectable. With UVIS, we will look in particular for the spectral signature of O, N,  $\text{N}_2$ , and CO as indicators of  $\text{CH}_4$ , acetylene, ammonia ice, and water ice-oxygen chemistry. An ammonia-water ice composition that would have a lower melting point than pure water has been proposed to explain the young geology on Enceladus (Stevenson, 1982; Squyres *et al.*, 1983). UVIS compositional data may give us insight into whether endogenic or exogenic processes have been responsible for the state of the surfaces of Iapetus and Phoebe. Comparison of compositional differences from one Saturnian satellite to the next may provide additional perspective on the formation of the Saturnian satellite system.

### 6.3. TENUOUS ATMOSPHERES AND EXOSPHERES

It is known that molecules are being sputtered from the surfaces of the Saturnian satellites from the distribution of neutrals and ions in Saturn's magnetosphere (Shemansky *et al.*, 1993). It is possible that vapor pressure atmospheres of constituents more volatile than water ice exist. Regardless of how these tenuous atmospheres are produced, they are more properly regarded as exospheres, since the atmospheric density is expected to be extremely low. In the following paragraphs *atmosphere* and *exosphere* are used interchangeably.

UVIS objectives are to address the following questions:

- (1) Do Saturn's icy satellites possess extremely tenuous atmospheres due to sputtering or seasonal sublimation?



- (2) What is the composition of these atmospheres? Can we identify trace constituents in their vapor phase, which would support the hypothesis that the satellites' water ice surfaces contain some amount of methane clathrates or  $\text{NH}_3$  hydrate?
- (3) Do we see any evidence of seasonal volatile transport? Can we detect and measure the flux of escaping atomic H produced by photolysis and sputtering of water ice?
- (4) Can we identify (on Enceladus, in particular) evidence for transient or localized volatiles in the atmosphere associated with eruptive activity such as geysers? Are the constituents of these plumes particulate or gas?

We will employ three different observational techniques to address these questions: limb drifts to search for scattered light, stellar occultations to detect atmospheric absorptions, and integrations on the night sides to see atmospheric emission.

Given the low surface temperatures of the Saturnian satellites, a vapor pressure equilibrium water atmosphere is not to be expected at detectable levels using limb drifts. A sputtered water atmosphere may be detectable (see Cheng *et al.*, 1986 for an excellent description of sputtering- vs. sublimation-produced atmospheres). A primary goal is to search for more volatile trace constituents such as  $\text{NH}_3$  or  $\text{CH}_4$ , implicated to exist in Saturnian satellite surface ices, or  $\text{N}_2$ , the product of photolyzed  $\text{NH}_3$ . On Titan, the temperature and pressure of the solar nebula at Saturn could have allowed as much as 15%  $\text{NH}_3$  or  $\text{CH}_4$  to be trapped in water ice as hydrates or clathrates during satellite formation (Lunine and Stevenson, 1985; Stevenson, 1991). Clathrates would end up primarily near the surface by subsequent differentiation of the satellite. Massive Titan, with its substantial gravity relative to the icy satellites, is able to retain its volatiles as a substantial atmosphere. With the same source surface ices but the much lower gravitational fields of the icy satellites, we may find very much thinner atmospheres. Rough use of Raoult's law predicts that  $\text{N}_2$  produced by photolysis of  $\text{NH}_3$  will be easily detectable by UVIS at the surface ice temperatures of the Saturnian satellites, with  $\text{CH}_4$  almost as easily detectable.

Stellar occultations provide a powerful technique for the study of planetary atmospheres (e.g., Smith and Hunten, 1990). The Voyager UVS was able to place an upper limit on the surface pressure of a hypothetical Ganymede atmosphere of  $10^{-11}$  bar by observing the occultation of Kappa Centauri, a moderately bright UV star (Broadfoot *et al.*, 1979) and assuming that a 10% extinction of the starlight would have been detectable by UVS. With the higher sensitivity of the Cassini UVIS instrument, and given adequate stellar occultation opportunities (i.e., star type, brightness), UVIS will be able to do at least as well at the Saturnian satellites.

The signature of oxygen emission excited by electron impact has been detected at Europa (Hall *et al.*, 1995) at 130.4 and 135.6 nm. Since we expect similar processes of photolysis and radiolysis of ice to produce O and  $\text{O}_2$  on Saturn's other satellites, we will search their night sides for this airglow.

## 7. Deuterium in the Saturn System

### 7.1. SCIENTIFIC BACKGROUND: THE SIGNIFICANCE OF D/H IN THE SOLAR SYSTEM

Most (perhaps all) of the deuterium in the universe was produced shortly after the big bang, when temperatures were high enough to allow its formation. As deuterium finds its way into stars, it is destroyed in the second step of the proton-proton chain ( ${}^2_1\text{H} + {}^1_1\text{H} \rightarrow {}^3_2\text{He} + \gamma$ ). This process, called astration, depletes the universe of deuterium as it cycles its way through star formation, astration, and interstellar injection. As a consequence, the ratio of deuterium to hydrogen in the interstellar medium (ISM) has been decreasing since the universe began and currently has a value of  $2 \times 10^{-5}$  (McCullough, 1992). The mass difference between the two atoms causes different vibrational and rotational energies in  $\text{H}_2$  and  $\text{D}_2$  molecules, different diffusion rates, different thermodynamic characteristics, and slightly different electronic energies. For these reasons, the measurement and interpretation of these isotopic effects yield important clues to understanding the processes involved in the formation and evolution of the planets.

Measurements of the deuterium-to-hydrogen ratio (D/H) in the solar system reveal two distinct reservoirs of deuterium, both of which are believed to predate the solar system itself (Owen *et al.*, 1986). The first reservoir is deuterium enriched relative to the second and includes the Earth, Mars, Uranus, Neptune, Titan, and cometary material. The second reservoir consists of Jupiter, Saturn, and the Sun. The general explanation for the differences in D/H between these two reservoirs lies in the theory of their formation (Owen, 1994). During the formation of the solar system, the cold, deuterium-enriched ( $\text{D/H} \sim 2 \times 10^{-4}$ ) molecular clouds (Geiss and Reeves, 1981) in the interstellar medium accreted to form the cores of the planets and other solid bodies. These icy/rocky cores outgassed deuterium (generally in the form of deuterated methane) in a process that preserved the deuterium enrichment (Owen, 1994).

The D/H ratio of the second reservoir (Jupiter, Saturn, and the Sun,  $\text{D/H} \sim 2 \times 10^{-5}$ ) closely matches that of the interstellar medium and the solar nebula (Owen, 1994). If the cores of the accreting material became large enough, they captured gas from the solar nebula and assumed the corresponding D/H ratio. Because Jupiter and Saturn have a low ratio of core mass to total mass (around 0.03 to 0.06 for Jupiter and 0.11 to 0.22 for Saturn (Owen, 1994)), they are believed to be primarily derived from the main reservoir of gas in the proto-solar nebula. Measurements of Jovian and Saturnian D/H support this theory.

To date, measurements of D/H in the atmospheres of the outer planets have been made by measuring deuterated molecules from Earth-based telescopes and by direct measurements of Jupiter by the Galileo probe mass spectrometer (Mahaffy *et al.*, 1998) (Table V). A comparison of Saturn hydrogen Lyman- $\alpha$  intensities from Voyager 1 and 2 with IUE measurements on nearly the same dates show a

TABLE V

D/H values and measurement techniques. The majority of these methods utilize deuterated molecules for the D/H measurement.

Location	D/H value	Method	Spectral range	Reference
Solar wind	$2 \times 10^{-5}$	He <sup>3</sup>	<i>in situ</i> (solar wind)	a
Earth	$1.6 \times 10^{-4}$	Standard mean ocean water (SMOW)	<i>in situ</i>	b
Interstellar medium (ISM)	$2 \times 10^{-5}$	Absorption of stellar D and H Ly- $\alpha$ lines in the ISM	1216 Å	c
Interstellar clouds	$>10^{-4}$	HCO <sup>+</sup> , HCN, H <sub>2</sub> O	Thermal radio emission	b
Meteorites	$1.6 \times 10^{-4}$	Hydrated silicates and organic material	<i>in situ</i>	b
Venus	$2 \times 10^{-2}$	Pioneer Venus LNMS HDO	<i>in situ</i> 2.3 $\mu\text{m}$	d e
Mars	$9 \times 10^{-4}$	HDO	3.7 $\mu\text{m}$	f
Jupiter	$2 \times 10^{-5}$	CH <sub>3</sub> D HD, Galileo probe	1.55–1.95 $\mu\text{m}$ 6063.88 Å, 56 $\mu\text{m}$ , <i>in situ</i>	g, h, n, r, s
Saturn	$2 \times 10^{-5}$	CH <sub>3</sub> D, HD	1.55–1.95 $\mu\text{m}$ 56 $\mu\text{m}$	i, n, o
Uranus	$9 \times 10^{-5}$ $5.5 \times 10^{-5}$	CH <sub>3</sub> D HD	1.55–1.95 $\mu\text{m}$ 56 $\mu\text{m}$	j, u
Neptune	$1.2 \times 10^{-4}$ $6.5 \times 10^{-5}$	CH <sub>3</sub> D HD	1.55–1.95 $\mu\text{m}$ 56 $\mu\text{m}$	k, u
Titan	$1.6 \times 10^{-4}$ $1 \times 10^{-4}$	CH <sub>3</sub> D	1.55–1.95 $\mu\text{m}$ 8.7 $\mu\text{m}$	l, p, q, t
Halley	$2 \times 10^{-4}$	HDO (Giotto NMS)	<i>in situ</i>	m

Note. (a) Geiss and Reeves, 1972, (b) Geiss and Reeves, 1981, (c) McCullough, 1992, (d) Donahue *et al.*, 1982, (e) de Bergh *et al.*, 1991, (f) Owen *et al.*, 1988, (g) Beer and Taylor, 1978, (h) Smith *et al.*, 1989, (i) Fink and Larson, 1978, (j) de Bergh, *et al.*, 1986, (k) de Bergh, *et al.*, 1990, (l) de Bergh *et al.*, 1988, (m) Eberhardt, *et al.*, 1987, (n) Encrenaz *et al.*, 1999, (o) Griffin *et al.*, 1996, (p) Orton, 1992, (q) Coustenis *et al.*, 2000, (r) Mahaffy *et al.*, 1998, (s) Lellouch *et al.*, 1997, (t) Taylor and Coustenis, 1998, (u) Feuchtgruber *et al.*, 1999.

discrepancy of a factor of 2 (McGrath and Clarke, 1992). They note that this discrepancy may be due to an incorrect value for the interplanetary hydrogen density. These discrepancies, along with the limited Hubble Space Telescope (HST) time dedicated to Saturn in the UV, make the observations of D/H at Saturn and Titan an important goal for the Cassini UVIS.

The first observations of the D/H ratio of Titan showed values considerably higher than those of Saturn (Table VI). Immediately, the question arose how

TABLE VI  
Measured and corrected D/H for Titan

	de Bergh <i>et al.</i> (1986)	Coustenis <i>et al.</i> (1989)	Orton (1992)
Observed D/H [ $10^{-5}$ ]	$11.1 \leq \text{D/H} \leq 32.6$	$10.0 \leq \text{D/H} \leq 30.0$	$5.50 \leq \text{D/H} \leq 10.0$
Corrected D/H [ $10^{-5}$ ]	$4.0 \leq \text{D/H} \leq 19.5$	$3.2 \leq \text{D/H} \leq 18.7$	$2.5 \leq \text{D/H} \leq 5.9$

the enrichment in the moon's atmosphere relative to that of Saturn itself could be explained. The early values were close to the SMOW value of  $1.56 \times 10^{-4}$  (Hagemann *et al.*, 1970). A popular scenario was to form the atmosphere of Titan and the earth by in-falling comets (Zahnle and Dones, 1992; Griffith and Zahnle, 1995; Owen and Bar-Nun, 1995, 1996). The most recent determination of the D/H ratio (relating to  $\text{H}_2\text{O}$ ) of comet Halley (Eberhardt and Krankowsky, 1995) and the observations of comets Hyakutake (Bockl  e-Morvan *et al.*, 1998) and Hale-Bopp (Meier *et al.*, 1998) yield consistent D/H ratios around  $30 \times 10^{-5}$ , well above the SMOW value. Cometary ices could have contributed to the atmosphere, but obviously neither the earth's ocean nor Titan's atmosphere reflect the deuterium enrichment of the cometary icy grains.

Values were derived from ground-based, near-IR observation (de Bergh *et al.*, 1986) of the deuterated methane from the Voyager spacecraft (Coustenis *et al.*, 1989) and by observations in the middle (thermal) infrared (see Orton, 1992). Pinto *et al.* (1986) calculated the enrichment factor over the lifetime of Titan to be between 1.7 and 2.2. Titan's history and formation are quite different from that of the giant planets. Titan was formed from the ices of the early Saturnian nebula. It could not retain molecular hydrogen, and fractionation by atmospheric-loss processes is strong.

It is interesting to note that the most precise determination of the original D/H ratio agrees within the error margin with the proto-solar value, and it cannot be ruled out that there is no (or very little) deuterium enrichment in Titan. It is obvious that a precise determination of the D/H ratio is of high interest and could be a major clue to the formation and history of Titan and of the whole Saturnian system.

## 7.2. HDAC USAGE AT TITAN

There are two methods for probing the Titan deuterium and hydrogen line profiles during a Titan flyby: (1) modulating the cell optical depth when Titan fills the HDAC field of view, and (2) measuring the HDAC count rate during the Doppler shifts caused by the relative motion between the Cassini orbiter and Titan. During a Titan flyby, the spacecraft Doppler velocity shifts the Lyman- $\alpha$  lines through the absorption profile of the cell. This Doppler effect allows the HDAC to probe the line in wavelength (while simultaneously probing it at different optical depth settings) as the spacecraft flies by Titan. Flybys with the furthest flyby altitudes (less than

90,000 km, the point at which Titan begins to fill the HDAC field of view), are best for HDAC observations because these flybys allow the spacecraft to spend more time near 0 km/s Doppler velocity (where the HDAC absorbs most efficiently).

### 7.3. LYMAN- $\alpha$ OBSERVATIONS AT SATURN

All measurements of HDAC include observations of the normal atomic hydrogen, either in photometer mode where the total brightness is registered, or with the absorption switched on when the Lyman- $\alpha$  emission line profile is scanned. Both the variation of the optical depth within the cell or the change in radial velocity component relative to the emitting atoms (or a combination of both methods) will yield information on the emission-line profiles and hence on the temperature and velocity distribution of the hydrogen atoms in the Saturn upper atmosphere.

### 7.4. INTERPLANETARY/INTERSTELLAR HYDROGEN

The solar system is moving through interstellar gas at about  $20 \text{ km s}^{-1}$ , and neutral hydrogen sweeps through the planetary system as interstellar wind. The sun ionizes hydrogen atoms by its EUV radiation and by charge-exchange with the solar wind. The solar emission in the resonance line at Lyman- $\alpha$  exerts a strong radiation pressure force that approximately balances solar gravity. The flow of hydrogen atoms causes an asymmetry of the (interstellar) hydrogen atom density and distribution in the inner planetary system. Lyman- $\alpha$  observations show that the strongest contributions upstream come from a distance of about 5 AU, while downstream the cavity extends to about 20 AU. The variation of solar-wind flux and speed with heliocentric latitude studied in detail by SOHO (Bertaux *et al.*, 1997) leads to deviation from the cylinder symmetry. These effects can be most easily observed at a distance of about 10 AU, the heliocentric distance of Saturn (Lallement *et al.*, 1995).

The density and velocity distribution (temperature) of interstellar hydrogen are influenced by the interaction with the Sun and its radiation. The solar wind expands into the interstellar plasma until its pressure is balanced by the plasma pressure and interstellar magnetic field defining the heliospheric boundary at around 200 AU. When the interstellar protons try to cross this boundary, they are slowed down, compressed in their density, and heated at the same time (Wallis and Ong, 1975). These processes influence the velocity and density distribution of the hydrogen atoms passing through the inner solar system.

Observations of interplanetary Lyman- $\alpha$  emission have two goals: (1) to determine the physical parameters of the interstellar hydrogen, such as its density, flow velocity, and temperature, and (2) to learn about the properties of the solar wind, such as its latitudinal dependence of its flux and speed, as well as its EUV emission. Elaborate models of the interaction predict the brightness distribution

of interplanetary Lyman- $\alpha$  as a function of the looking direction and position of the observer. A multitude of parameters and their variation with solar cycle can be derived if the observational set is extensive enough. A recent example is provided by the UV spectrometer onboard the Galileo spacecraft (Ajello *et al.*, 1994).

The HDAC can take advantage of a common spacecraft mode in which the Cassini spacecraft slowly rotates during cruise and at Saturn during periods when data are transmitted to earth. These observations will map the Lyman- $\alpha$  brightness consistently over many years. In addition, the absorption of the hydrogen cell can be used to scan through the emission-line profile whenever the radial velocity component of the atoms along the line of sight relative to the Cassini spacecraft is near zero.

### 7.5. SUMMARY

Information about the D/H and hydrogen line shapes will be extracted from a collection of HDAC count rates at the various optical depths, Doppler velocities, and viewing geometries. These results will provide a comparison to the infrared measurements from ISO and SIRTf for Titan, a key piece of information for theories of the origin and evolution of the Saturn system, the Saturn Lyman- $\alpha$  line shape, and the emissions from the local interstellar medium. Long-term observations and appropriate modeling will allow us to determine the Lyman- $\alpha$  background signal with good accuracy. This is essential in order to measure the foreground contributions of features within the Saturnian system (e.g., Titan's exosphere and torus) with confidence.

## 8. UVIS Ring Observations

Planetary rings, which just two decades ago were thought unique to the planet Saturn, have now been observed around all the giant planets (for a recent review, see Esposito, 1993). These rings are composed of many particles with a broad range in size. The observed rings systems are quite diverse. Jupiter's ring is optically thin and composed of dustlike small particles (Showalter *et al.*, 1987). Saturn's rings are broad, bright, and opaque (Cuzzi *et al.*, 1984; Esposito *et al.*, 1984). Uranus has narrow, dark rings among broad lanes of dust that are invisible from Earth (French *et al.*, 1991; Esposito *et al.*, 1991). Neptune's rings include incomplete arcs restricted to a small range of the circumference (Porco *et al.*, 1995). All rings lie predominantly within their planet's Roche limit, where tidal forces would destroy a self-gravitating body (Nicholson and Dones, 1991). They are also within the planet's magnetosphere, and in the case of Uranus, they are within the upper reaches of the planetary atmosphere. Saturn's rings are the largest of any planet's, and show all the diverse phenomena seen in other ring systems.



### 8.1. VOYAGER RESULTS AND CASSINI CAPABILITIES

Voyager 1 and 2 made the closest investigations of Saturn's rings in 1980 and 1981. These missions provided images, spectra, and radio and stellar occultations as well as information on the ring environment. Reviews are provided by Cuzzi *et al.* (1984) and Esposito *et al.* (1984). The radio occultation, stellar occultation, and sequences of images each provided complete radial coverage of the ring system (Figure 25). Conversely, the azimuthal coverage is more sketchy. As to temporal coverage, the data encompass only a few weeks around each encounter, with the best resolution data for each from a period of less than a day. The images are all from the Voyager Reticon cameras: the spectral sensitivity of their silicon detectors explains why we have no pictures in the UV or IR. This information is now supplemented by data from the ground, HST, and IUE, which all lack the radial, azimuthal, and temporal resolution provided briefly by the spacecraft encounters. A new data set from the spectacular 1995 ring-plane crossing (see Nicholson *et al.*, 1996; Showalter, 1997) provides information on the more transparent rings. The thickest parts of Saturn's rings were not penetrated by either the radio or stellar occultations.

The Cassini mission provides the opportunity to measure the rings at high resolution in the radial, azimuthal, and vertical dimensions over a period of 4 years.

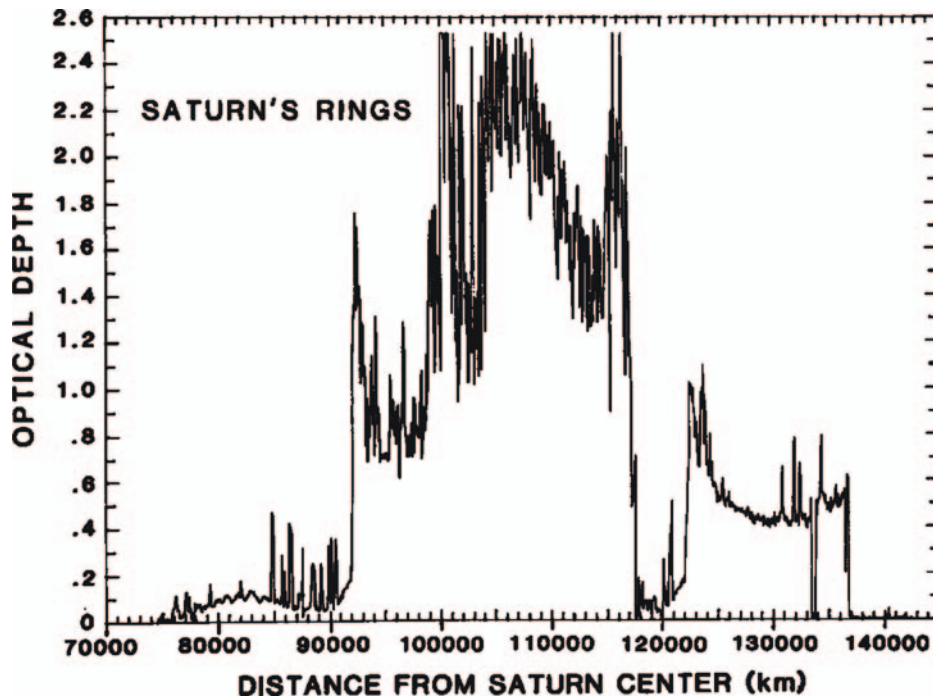


Figure 25. Saturn's rings from the Voyager 2 PPS  $\delta$  Scorpii stellar occultation showing ring radial structure (Esposito *et al.*, 1983a).

Observations of the ring environment, magnetosphere, and small nearby satellites will determine the interactions of the various parts of the Saturn system with its rings. The UVIS experiment has the capability for imaging, spectroscopy, and high speed photometry that can contribute to these scientific objectives.

## 8.2. RING STRUCTURE

Figure 26 shows observations of density waves in Saturn's rings from the Voyager PPS occultation (Esposito *et al.*, 1983a,b). These features are but one of a number of dynamic phenomena evident in the ring radial profile. The UVIS High Speed Photometer (HSP) channel has been optimized to follow up on the Voyager investigations. The HSP field of view is  $6 \text{ mrad} \times 6 \text{ mrad}$ , large enough that no brightness modulations are expected from pointing variations. The CsI photocathode is essentially solar-blind, allowing high signal-to-noise occultations of both sunlit and shadowed rings. The HSP is bore-sighted with the spectroscopic channels, allowing concurrent spectroscopy of the transmitted starlight from 91 to 190 nm. Simultaneously, we can obtain a long slit image

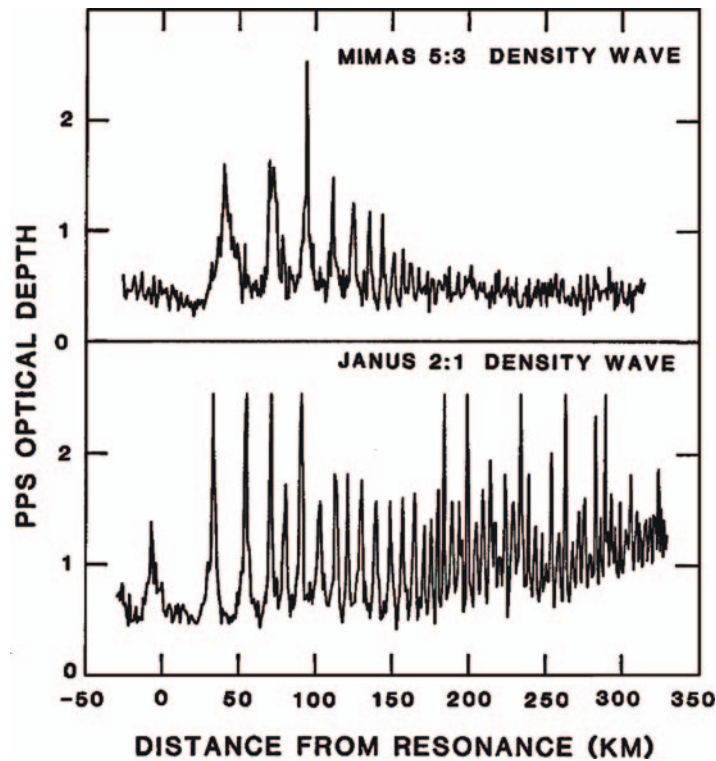


Figure 26. Density waves seen in the PPS occultation (Esposito *et al.*, 1983b). Compare the resolution with Figure 25.

of the occultation point up to a distance  $\pm 30$  mrad, allowing the observation of diffracted light in the stellar aureole. The time resolution of 2 ms can give spatial resolution of 20 m or better on the rings, comparable to the diffraction limit.

The large mirror and amplifiers in the HSP allow very high counting rates. We expect 2000 counts in 2 ms for the occultation star  $\delta$  Sco. This compares to the Voyager PPS observation of  $\delta$  Sco of 39 counts every 10 ms (Esposito *et al.*, 1983a). Thus the Cassini UVIS HSP can probe structures five times narrower than Voyager, with 50 times the signal in each integration period. This high sensitivity and resolution will be used to probe wakes, waves, and ring edges.

Occultation tracks at multiple ring longitudes will likely reveal azimuthal asymmetries in the rings, as was seen by the Voyager PPS at Uranus (Colwell *et al.*, 1990) and ground-based stellar occultation observations of Neptune's rings (Elliot *et al.*, 1985; Covault *et al.*, 1986; French *et al.*, 1993). These asymmetries may provide clues to the origin of the ring features and imply the presence of nearby perturbing satellites. These data will be used to constrain physical models of their origin and evolution.

Radial optical depth profiles will be generated from stellar occultation measurements (Colwell and Esposito, 1990a,b). Accurate absolute determinations of the locations of edges, gaps, and wave features in the data will allow the identification of new ring-satellite resonances, and quite possibly the indirect detection of new, small satellites within the ring system (e.g., Horn *et al.*, 1990). Such satellites are linked to the evolution and the origin of the rings. Their number and distribution within the rings will help constrain theories of ring origin (Colwell, 1994; Sicardy and Lissauer, 1992).

During HSP observations of stellar occultations, the UVIS Far Ultraviolet channel (FUV) will measure ring background brightness. These measurements will also provide information on the size distribution of small (micrometer-sized) dust particles in the rings during occultations by the shadowed rings. Dust in Saturn's rings will produce a diffraction aureole detectable by the FUV channel of UVIS. This diffraction signature is sensitive to the characteristic dust particle size. Size distributions based on different physical models of the creation, transport, and destruction of dust will be tested against the observations. The abundance, size, and distribution of dust in the rings are useful diagnostics for the size distribution, velocity distribution, and surface properties of the larger ring particles, which act as sources and sinks of dust in the rings (Colwell and Esposito, 1990a,b). Data on these larger particles will be obtained from stellar occultations and combining UVIS reflectance data with images from the Cassini Imaging Science Subsystem (ISS) and Visual and Infrared Mapping Spectrometer (VIMS). The FUV data will also be used to determine the magnitude of the ring background signal to be removed from the HSP occultation data. Figures 27 and 28 show the multitude of available opportunities and the progress of a stellar occultation from Cassini tour T18-5.

Thu Sep 18 13:38:19 1997

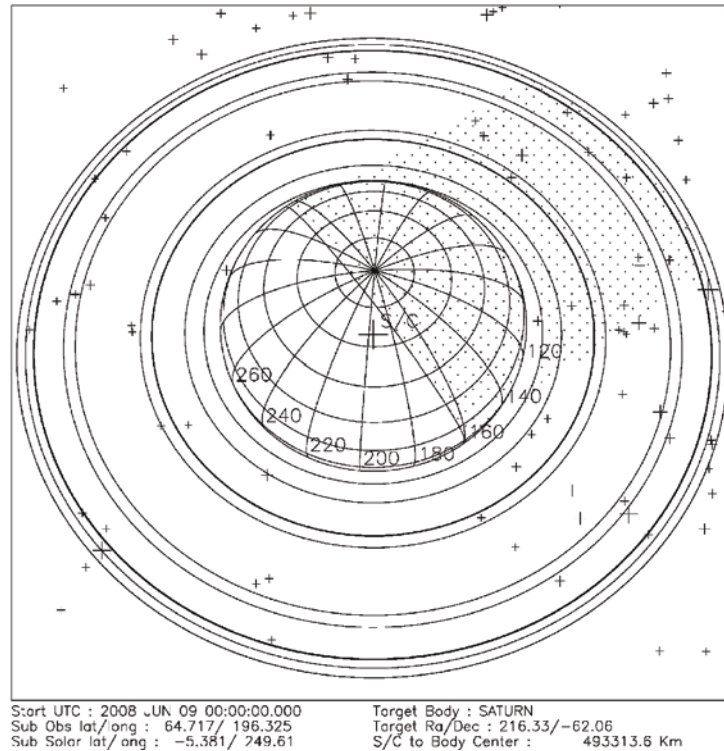


Figure 27. Numerous ring stellar occultation opportunities are shown with CASPER (Cassini Sequence Planner) software in this near-polar view of Saturn and its ring system. Plus symbols indicate stars; larger symbols are brighter stars. The stippled region indicates Saturn's shadow. The sub-spacecraft point is indicated by a cross on the planet.

### 8.3. UVIS IMAGES

During remote-sensing ring observations, UVIS will slew its slit to make images of the rings. At a range of  $10^6$  km, the UVIS resolution of 1 mrad gives a picture element of 1000 km width. Typical images will be 64 elements tall (along the slit), with the image width determined by the total slew duration. Because UVIS has the shortest wavelength of any of the remote sensing instruments, it will be more sensitive to the smallest particles in the rings, with sizes as small as  $0.01$  to  $0.1\mu$ . The images at different UV wavelengths can be compared to camera images to determine the dust contribution and extend the size distribution. The ring 'spokes' are one natural target. By combining the UV observations with CIRS spectra, ISS, VIMS images, and radio occultations, the size distribution of the ring particles can be measured from submicron to meter sizes.

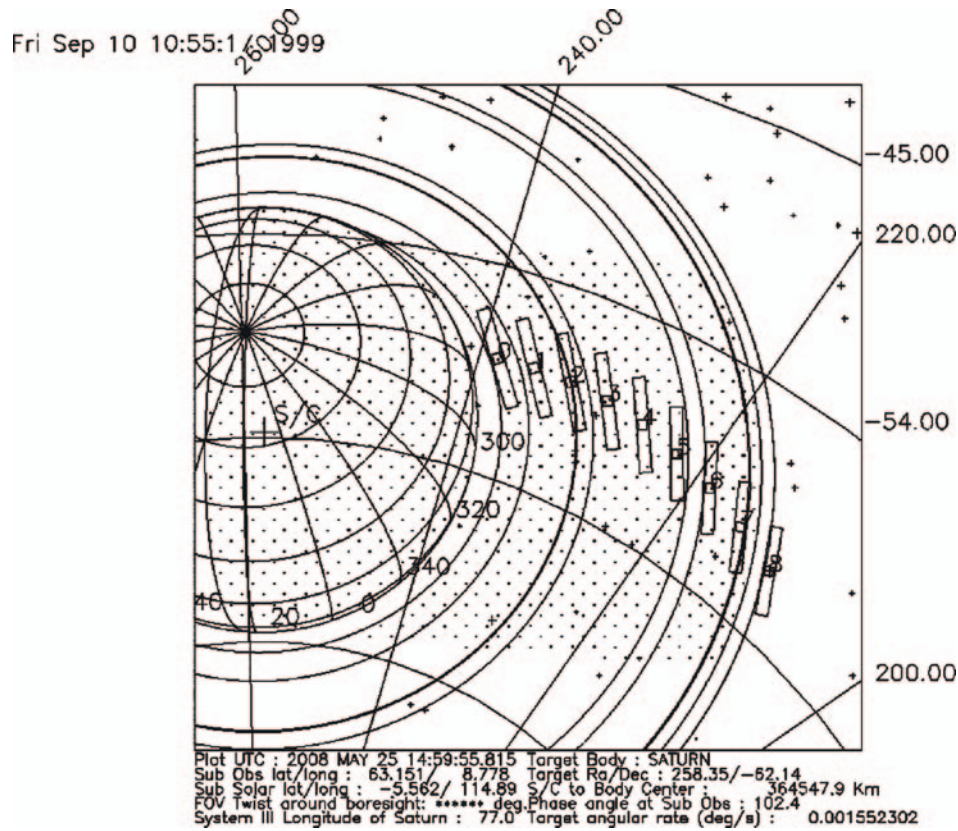


Figure 28. The star  $\beta$  Cen is occulted by the shadowed rings of Saturn. The FUV occultation slit and the HSP aperture are shown around the star.

#### 8.4. RING COMPOSITION

The reflectance spectrum of Saturn's rings from IUE and Voyager clearly shows the water absorption edge at 1650 Å. We will map the depth and wavelength of this feature across the rings to determine compositional and age variations. At wavelengths of 1800 to 2000 Å, water ice is transparent, and the non-icy ring component may be studied.

During systematic spectroscopy of the Saturn system, UVIS will map the emissions from neutral hydrogen (1216 Å) and oxygen (1304 Å and 1356 Å). Emissions near the rings will define the ring atmosphere (Broadfoot *et al.*, 1981; Hall, 1996) and the interactions of the ring with its local environment. This will constrain the long-term evolution of the ring particles. UVIS will also measure remotely a number of magnetospheric constituents (particularly H, O, N, and D) that will define the broader ring-magnetosphere interactions.



### 8.5. RING HISTORY

The UVIS and the other remote-sensing and *in situ* Cassini experiments will provide a rich data set on the current state of the rings and their present interactions with other parts of the Saturn system.

A comprehensive model of the origin and large-scale evolution of Saturn's rings will be developed based on the ensemble of Cassini observations at Saturn. Crater statistics on the larger satellites and the anticipated discovery of smaller ring moons will allow development of an accurate model of the time-dependent interplanetary impacting flux at intermediate and large sizes. This flux, when combined with theoretical and experimental results on catastrophic fragmentation, drives the global evolution of the ring system. Disruption of satellites or 'rubble piles' creates new ring particles. These then undergo orbital evolution, influenced by gravitational perturbations from other satellites, and partial accretion (Canup and Esposito, 1995). Dust is produced within the ring from interparticle collisions and micrometeoroid bombardment. These processes can be combined into a single global Markov chain simulation of the ring system (Colwell and Esposito, 1993) for time scales of the age of the solar system. Monte Carlo simulations can be conducted using the same transition probabilities in order to create simulated histories of the rings system for direct comparison with Cassini observations.

Variations of the abundance of dust between different ring features will provide additional information on ring particle characteristics, including collision velocities and regolith properties. Dynamically active regions may exhibit different dust abundances than quiescent regions in the rings. Features such as arcs, kinks, braids, and other azimuthal asymmetries may indicate a mode of origin from satellite disruption or complex gravitational interactions with nearby satellites. The distribution of small moons, their resonances, and density waves and gaps within the rings will be used to characterize the large-scale transport of angular momentum through the system for use in global evolution models of the rings.

### 8.6. SUMMARY

The UVIS ring studies will provide (1) a comprehensive study of features in Saturn's rings, including their dynamical links to embedded satellites, (2) a determination of the abundance and size distribution of dust within the rings as a function of location within the rings, (3) modeling of ring processes and system interactions at short time scales, and (8) models of the global evolution of the rings over the age of the solar system.

## 9. Conclusions

The UVIS investigation aboard the Cassini orbiter will provide key new information on the chemistry of the Titan and Saturn atmospheres; their clouds and aerosols;



exospheres, thermospheres, and magnetospheres in the Saturn system; satellite surfaces and atmospheres; Titan's atomic D/H ratio; and the physics and history of rings. These results are enabled by the spectroscopic and imaging capabilities of UVIS, the long-time coverage allowed by the Cassini orbit, stellar and solar occultations, multiple phase angles, close-up maps, limb scans, and synergistic investigations with other Cassini experiments.

### Acknowledgement

This work was supported by the National Aeronautics and Space Administration under JPL Contract 961196. The Hydrogen Deuterium Absorption Cell (HDAC) was designed and constructed with support from the Max-Planck-Gesellschaft zur Foerderung der Wissenschaften. Grants were received from the DLR under FKZ 50 OH 9201 7. The authors thank Sushil Atreya and an anonymous reviewer for their helpful comments.

### References

- Ajello, J. M., Pryor, W. R., Barth, C. A., Hord, C. W., Stewart, A. I. F., Simmons, K. E., *et al.*: 1994, *Astron. Astrophys.* **289**, 283.
- Atreya, S. K.: 1982, *Plan. Space Sci.* **30**, 849.
- Atreya, S. K., Donahue, T. M., and Kuhn, W. R.: 1978, *Science* **201**, 611.
- Atreya, S. K., Waite, J. H., Jr., Donahue, T. M., Nagy, A. F., and McConnell, J. C.: 1988, 'Theory, measurements, and models of the upper atmosphere and ionosphere of Saturn', in Gehrels, T. and Matthews, M. S. (eds.), *Saturn*, University of Arizona Press, Tucson, p. 239.
- Atreya, S. K., Wong, M. H., Owen, T. C., Mahaffy, P. R., Niemann, H. B., de Pater, I., *et al.*: 1999, *Planet. Space Sci.* **47**, 1243.
- Babichenko, S. I., Derigusov, E. V., Kurt, V. G., Romanova, N. N., Skljankin, V. A., Smirnov, A. S., *et al.*: 1977, *Space Sci. Instr.* **3**, 271.
- Baragiola, R. A. and Bahr, D. A.: 1998, *J. Geophys. Res.* **103**, 25865.
- Bar-Nun, A., Kleinfeld, I., and Ganor, E.: 1988, *J. Geophys. Res. (Atmospheres)* **93**, 8383.
- Barth, C. A., Hord, C. W., Stewart, A. I. F., Pryor, W. R., Simmons, K. E., McClintock, W. E., Ajello, J. M., Naviaux, K. L., and Aiello, J. J.: 1997, *Geophys. Res. Lett.* **24**, 2147.
- Bertaux, J. L.: 1977, *Nature* **270**, 156.
- Bertaux, J. L.: 1978, *Planet. Space Sci.* **26**, 431.
- Bertaux, J. L., Blamont, J. E., Lepine, V. M., Kurt, V. G., Romanova, N. N., and Smirnov, A. S.: 1978, *Planet. Space Sci.* **26**, 817.
- Bertaux, J. L., Goutail, F., Dimarellis, E., Kockarts, G., and Van Ransbeeck, E.: 1984, *Nature* **309**, 771.
- Bertaux, J. L., Quémerais, E., Lallement, R., Kyrölä, E., Schmidt, W., Summanen, T., Goutail, J. P., *et al.*: 1997, *Solar Phys.* **175**, 737.
- Bockelée-Morvan, D., Gautier, D., Lis, D. C., Young, K., Keene, J., Phillips, T. G., *et al.*: 1998, *Icarus* **133**, 147.
- Broadfoot, A. L., Belton, M. J. S., Takacs, P. Z., Sandel, B. R., Shemansky, D. E., Holberg, J. B., *et al.*: 1979, *Science* **204**, 979.
- Broadfoot, A. L., Sandel, B. R., Shemansky, D. E., Holberg, J. B., Smith, G. R., Strobel, D. F., *et al.*: 1981, *Science* **212**, 206.
- Buratti, B. J.: 1988, *Icarus* **75**, 113.

- Buratti, B. and Veverka, J.: 1984, *Icarus* **58**, 254.
- Cabane, M., Rannou, P., Chassefiere, E., and Israel, G.: 1993, *Planet. Space Sci.* **41**, 257.
- Calvin, W. M., Johnson, R. E., and Spencer, J. R.: 1996, *Geophys. Res. Lett.* **23**, 673.
- Canup, R. M. and Esposito, L. W.: 1995, *Icarus* **113**, 331.
- Chassefiere, E. and Cabane, M.: 1995, *Planet. Space Sci.* **43**, 91.
- Cheng, A. F., Haff, P. K., Johnson, R. E., and Lanzerotti, L. J.: 1986, 'Interactions of planetary magnetospheres with icy satellite surfaces', in Burns, J. A., and Matthews, M. S. (eds.), *Satellites*, University of Arizona Press, Tucson, p. 403.
- Clark, R. N., Brown, R. H., Owensby, P. D., and Steele, A.: 1984, *Icarus* **58**, 265.
- Clark, R. N., Fanale, F. P., and Gaffey, M. J.: 1986, 'Surface composition of natural satellites', in Burns, J. A., and Matthews, M. S. (eds.), *Satellites*, Univ. Ariz. Press, Tucson, p. 437.
- Clarke, D. W. and Ferris, J. P.: 1997, *Icarus* **127**, 158.
- Colwell, J. E.: 1994, *Planet. Space Sci.* **42**, 1139.
- Colwell, J. E. and Esposito, L. W.: 1990a, *Icarus* **86**, 530.
- Colwell, J. E. and Esposito, L. W.: 1990b, *J. Geophys. Res.* **17**, 1741.
- Colwell, J. E. and Esposito, L. W.: 1993, *J. Geophys. Res. (Planets)* **98**, 7387.
- Colwell, J. E., Horn, L. J., Lane, A. L., Esposito, L. W., Yanamandra-Fisher, P. A., Pilorz, S. H., *et al.*: 1990, *Icarus* **83**, 102.
- Coustonis, A.: 1992, 'Titan's atmosphere: Latitudinal variations in temperature and composition', in *Symposium on Titan*, Conf. Proc. ESA, SP 338, 53.
- Coustonis, A., and Bezard, B.: 1995, *Icarus* **115**, 126.
- Coustonis, A., Bezard, B., and Gautier, D.: 1989, *Icarus* **80**, 54.
- Coustonis, A., Bezard, B., Gautier, D., Marten, A., and Samuelson, R.: 1991, *Icarus* **89**, 152.
- Covault, C. E., Glass, I. S., French, R. G., and Elliot, J. L.: 1986, *Icarus* **67**, 126.
- Cravens, T. E., Howell, E., Waite, J. H., and Gladstone, G. R.: 1995, *J. Geophys. Res.* **100**, 17153.
- Cuzzi, J. N., Lissauer, J. J., Esposito, L. W., Holberg, J. B., Marouf, E. A., Tyler, G. L., *et al.*: 1984, 'Saturn's rings: Properties and processes', in Greenberg, R. and Brahic, A. (eds.), *Planetary Rings*, University of Arizona Press, Tucson, p. 73.
- de Bergh, C., Bézard, B., Owen, T., Crisp, D., Maillard, J. P., and Lutz, B. L.: 1991, *Science* **251**, 547.
- de Bergh, C., Lutz, B. L., Owen, T., Brault, J., and Chauville, J.: 1986, *Astrophys. J.* **311**, 501.
- de Bergh, C., Lutz, B. L., Owen, T., and Chauville, J.: 1988, *Astrophys. J.* **329**, 951.
- de Bergh, C., Lutz, B. L., Owen, T., and Maillard, J. P.: 1990, *Astrophys. J.* **355**, 661.
- Degraauw, T., Feuchtgruber, H., Bezard, B., Drossart, P., and Encrenaz, T.: 1997, *Astron. Astrophys.* **321**, L-13.
- Delitsy, M. L., and Lane, A. L.: 1998, *J. Geophys. Res.* **103**, 31391.
- Dessler, A. J.: 1981, *Planet. Space Sci.* **29**, 215.
- Devanssay, E., Gazeau, M. C., Guillemin, J. C., and Raulin, F.: 1995, *Planet. Space Sci.* **43**, 25.
- Donahue, T. M., Hoffman, J. H., Hodges, R. R., Jr., and Watson, A. J.: 1982, *Science* **216**, 712.
- Eberhardt, P., Dolder, U., Schutte, W., Krankowsky, D., Lammerzähl, P., Hoffman, J. H., *et al.*: 1987, *Astron. Astrophys.* **187**, 435.
- Eberhardt, P., and Krankowsky, D.: 1995, *Astron. Astrophys.* **295**, 795.
- Elliot, J. L., Baron, R. L., Dunham, E. D., French, R. G., and Meech, K. J.: 1985, *Astron. J.* **90**, 2615.
- Encrenaz, T., Drossart, P., Feuchtgruber, H., Lellouch, E., Bézard, B., Fouchet, T., *et al.*: 1999, *Planet. Space Sci.* **47**, 1223–1240.
- Esposito, L. W.: 1993, *Ann. Rev. Earth Planet. Sci.* **21**, 487.
- Esposito, L. W., Brahic, A., Burns, J. A., and Marouf, E. A.: 1991, 'Particle properties and processes in uranus' rings', in Bergstralh, J. T., Miner, E. D., and Matthews, M. S. (eds.), *Uranus*, University of Arizona Press, Tucson, p. 410.

- Esposito, L. W., Cuzzi, J. N., Holberg, J. B., Marouf, E. A., Tyler, G. L., and Porco, C. C.: 1984, 'Saturn's rings: Structure, dynamics and particle properties', in Gehrels, T. and Matthews, M. S. (eds.), *Saturn*, University of Arizona Press, Tucson, p. 463.
- Esposito, L. W., O'Callaghan, M., Simmons, K. E., Hord, C. W., West, R. A., Lane, A. L., *et al.*: 1983a, *J. Geophys. Res.* **88**, 8643.
- Esposito, L. W., O'Callaghan, M., and West, R. A.: 1983b, *Icarus* **56**, 439.
- Feldman, P. D., McGrath, M. A., Moos, H. W., Durrance, S. T., Strobel, D. F., and Davidsen, A. F.: 1993, *Astrophys. J.*, **406**, 279.
- Festou, M. C. and Atreya, S. K.: 1982, *Geophys. Res. Lett.* **9**, 1147.
- Feuchtgruber, H., Lellouch, E., Bézard, B., Encrenaz, T., deGraauw, T., and Davis, G.: 1999, *Astron. Astrophys.* **341**, L17–L21.
- Fink, U. and Larson, H. P.: 1978, *Science* **201**, 343.
- French, R. G., Maeue, S., Mason, E. C., McGhee, C. A., Nicholson, P. D., Matthews, K., and Roques, F.: 1993, *Bull. Amer. Astron. Soc.* **25**, 1110.
- French, R. G., Nicholson, P. D., Porco, C. C., and Marouf, E. A.: 1991, 'Dynamics and structure of the uranian rings', in Bergstrahl, J. T., Miner, E. D., and Matthews, M. S. (eds.), *Uranus*, University of Arizona Press, Tucson, p. 327.
- Geiss, J. and Reeves, H.: 1972, *Astron. Astrophys.* **18**, 126.
- Geiss, J. and Reeves, H.: 1981, *Astron. Astrophys.* **93**, 189.
- Gladstone, G. R., Allen, M., and Yung, Y. L.: 1996, *Icarus* **119**, 1.
- Gladstone, G. R., Waite, J. H., and Lewis, W. S.: 1998, *J. Geophys. Res.* **103**, 20083.
- Griffin, M. J., Naylor, D. A., Davis, G. R., Ade, P. A. R., Oldham, P. G., Swinyard, B. M., *et al.*: 1996, *Astron. Astrophys.* **315**, L389–L392.
- Griffith, C. A. and Zahnle, K. Z.: 1995, *J. Geophys. Res.* **100**, 16,907.
- Gurwell, M. A. and Muhleman, D. O.: 1995, *Icarus* **117**, 375.
- Hagemann, R., Nief, G., and Roth, E.: 1970, *Tellus* **22**, 712.
- Hall, D. T.: 1996, *Science* **272**, 516.
- Hall, D. T., Shemansky, D. E. and Tripp, T. M.: 1992, 'A reanalysis of Voyager UVS observations of Titan', in *Symposium on Titan*, Conf. Proc. ESA, SP-338, p. 69.
- Hall, D. T., Strobel, D. F., Feldmann, P. D., McGrath, M. A. and Weaver, H. A.: 1995, *Nature* **373**, 677.
- Hendrix, A. R., Barth, C. A., and Hord, C. W.: 1999, *J. Geophys. Res. (Planets)* **104**, 14169.
- Hendrix, A. R., Barth, C. A., Hord, C. W., and Lane, A. L.: 1998, *Icarus* **135**, 79.
- Hidayat, T., Marten, A., Bézard, B., Gautier, D., Owen, T., Matthews, H. E., *et al.*: 1997, *Icarus* **126**, 170.
- Horn, L. J., Yanamandra-Fisher, P. A., and Esposito, L. W.: 1990, *Icarus* **76**, 485.
- Jaffel, L. B., V'eronique, L., and Sandel, B. R.: 1995, *Science* **269**, 951.
- Johnson, R. E.: 1997, *Icarus* **128**, 469.
- Johnson, R. E., and Quickenden, T. I.: 1997, *J. Geophys. Res. (Planets)* **102**, 10985.
- Karkoschka, E., and Lorenz, R. D.: 1997, *Icarus* **125**, 369.
- Kawahara, T.: 1994, 'A Study on Hydrogen/Deuterium Absorption Cell Technique for Spacecraft Observations of Planetary Atmospheres', Ph.D. dissertation, Tohoku University, Japan.
- Kawahara, T., Okano, S., Abe, T., and Fukunishi, H.: 1993, *Tohoku Geophys. J. Sci. Rep.*, ser. 51, **34**, 35.
- Khare, B. N., Sagan, C., Arakawa, E. T., Suits, F., Callcott, T. A., and Williams, M. W.: 1984, *Icarus* **60**, 127.
- Kivelson, M. G., Warnecke, J., Bennett, L., Joy, S., Khurana, K. K., Linker, J. A., *et al.*: 1997, *J. Geophys. Res. (Planets)* **103**, 19963.
- Lallement, R., Kyroelae, E., and Summanen, T.: 1995, *Space Sci. Rev.* **72**, 455.
- Lane, A. L., Hord, C. W., West, R. A., Esposito, L. W., Coffeen, D. L., Sato, M., *et al.*: 1982, *Science* **215**, 537.

- Lara, L. M., Lellouch, E., Lopezmoreno, J. J., and Rodrigo, R.: 1996, *J. Geophys. Res.* **101**, 23261.
- Lawrence, G. M. and McClintock, W. E.: 1996, *Proc. SPIE* **2831**, 104.
- Lellouch, E., Feuchtgruber, H., de Graauw, T., Encrenaz, T., Bézard, B., and Griffin, M.: 1997, 'Deuterium and oxygen in the giant planets', in Kessler, M (ed.), *Proceedings of the First ISO Workshop on Analytical Spectroscopy*, ESA SP-419, Madrid, 6–8 October, p. 131.
- Lemmon, M. T.: 1994, Ph.D. dissertation, University of Arizona, Tucson.
- Lunine J. I. and Stevenson, D. J.: 1985, *Astrophys. J. Supp. Ser.* **58**, 493.
- Lutz, B. L., de Bergh, C., and Owen, T.: 1983, *Icarus* **220**, 1274.
- Mahaffy, P. R., Donahue, T. M., Atreya, S. K., Owen, T. C., and Niemann, H. B.: 1998, *Space Sci. Rev.* **84**, 251.
- Maki, J. N.: 1996, 'The hydrogen deuterium absorption cell on the sCassini spacecraft: A remote sensing instrument for atomic D/H measurements on Saturn and Titan', Ph.D. dissertation, University of Colorado, Boulder.
- Marten, A., Gautier, D., Tanguy, L., Lecacheux, A., Rosolen, C., and Paubert, G.: 1988, *Icarus* **76**, 558.
- McClintock, W. E., Lawrence, G. M., Kohnert, R. A., and Esposito, L. W.: 1992, *Proc. SPIE* **1745**, 26.
- McClintock, W. E., Lawrence, G. M., Kohnert, R. A., and Esposito, L. W.: 1993, *Opt. Eng.* **32**, 3038.
- McCullough, P.: 1992, *Astrophys. J.* **390**, 213.
- McGrath, M. and Clarke, J. T.: 1992, *J. Geophys. Res.* **97** (A9), 13691.
- McGrath, M. A., Courtin, R., Smith, T. E., Feldman, P. D., and Strobel, D. F.: 1998, *Icarus* **131**, 382.
- McKay, C. P.: 1996, *Planet. Space Sci.* **44**, 741.
- Meier, R., Owen, T. C., Matthews, H. E., Jewitt, D. C., Bockelée-Morvan, D., Biver, N., *et al.*: 1998, *Science* **279**, 842.
- Morton, D., and Purcell, J.: 1961, 'Rocket Observations of Lyman- $\alpha$  in the Night Sky', *Report of NRL Progress*, June 1961.
- Moses, J. I., Bézard, B., Lellouch, E., Gladstone, G. R., Feuchtgruber, H., and Allen, M.: 2000, *Icarus* **143**, 244.
- Muhleman, D. O., Berge, G. L., and Clancy, R. T.: 1984, *Science* **223**, 393.
- Nelson, R. M., and Lane, A. L.: 1987, 'Planetary satellites', in Kondo, Y. (ed.), *Scientific Accomplishments of the IUE*, p. 67.
- Nicholson, P. D., and Dones, L.: 1991, *Rev. Geophys.* **29**, 313.
- Nicholson, P. D., Showalter, M. R., Dones, L., French, R. G., Larson, S. M., Lissauer, J. J., *et al.*: 1996, *Science* **272**, 509.
- Noll, K. S., Geballe, T. R., Knacke, R. F., and Pendleton, Y. J.: 1996a, *Icarus* **124**, 625.
- Noll, K. S., Johnson, R. E., Lane, A. L., Dominique, D. L., and Weaver, H. A.: 1996b, *Science* **273**, 341.
- Noll, K. S., Roush, T. L., Cruikshank, D. P., Johnson, R. E., and Pendleton, Y. J.: 1997, *Nature* **388**, 45.
- Orton, G.: 1992, 'Ground-based observations of Titan's thermal spectrum', in *Symposium on Titan*, Conf. Proc. ESA, SP-338, 81.
- Orton, G. L., Serabyn, E., and Lee, Y. T.: 2000, *Icarus* **146**, 48–59.
- Owen, T.: 1994, *Astrophys. Space Sci.* **212**, 1.
- Owen, T. and Bar-Nun, A.: 1995, *Icarus* **116**, 215.
- Owen, T. and Bar-Nun, A.: 1996, *Earth, Moon, Planets* **72**, 425.
- Owen, T., Lutz, B. L., and de Bergh, C.: 1986, *Nature* **320**, 245.
- Owen, T., Mahaffy, P., Niemann, H. B., Atreya, S., Donahue, T., Bar-Nun, A., *et al.*: 1999, *Nature* **402**, 269.
- Owen, T., Maillard, J., de Bergh, C., and Lutz, B.: 1988, *Science* **240**, 1767.
- Pinto, J. P., Lunine, J. I., Kim, S. J., and Yung, Y. L.: 1986, *Nature* **319**, 388.
- Porco, C. C., Cuzzi, J. N., Esposito, L. W., Lissauer, J. J., and Nicholson, P. O.: 1995, 'Neptune's ring system', in Bergstrahl, J., Miner, E. D., and Matthews, M. S. (eds.) *Neptune and Triton*, University Arizona Press, Tucson.
- Pryor, W. R. and Hord, C. W.: 1991, *Icarus* **91**, 161.

- Rages, K. and Pollack, J. B.: 1983, *Icarus* **55**, 50.
- Rannou, P., Cabane, M., Botet, R., and Chassefiere, E.: 1997, *J. Geophys. Res.* **102**, 10997.
- Sandel, B. R. and Broadfoot, A. L.: 1981, *Nature* **292**, 679.
- Sandel, B. R., Shemansky, D. E., Broadfoot, A. L., Holberg, J. B., Smith, G. R., McConnell, J. C., *et al.*: 1982, *Science* **215**, 548.
- Saur, J., Strobel, D. F., and Neubauer, F. M.: 1998, *J. Geophys. Res. (Planets)* **103**, 19947.
- Scattergood, T. W., Lau, E. Y., and Stone, B. M.: 1992, *Icarus* **99**, 98.
- Shemansky, D. E.: 1985, *J. Geophys. Res.* **90**, 2673.
- Shemansky, D. E. and Ajello, J. M.: 1983, *J. Geophys. Res.* **88**, 459.
- Shemansky, D. E., Kanik, I., and Ajello, J. M.: 1995, *Astrophys. J.* **452**, 480.
- Shemansky, D. E., Matheson, P., Hall, D. T., Hu, H. Y., and Tripp, T. M.: 1993, *Nature* **363**, 329.
- Showalter, M. R.: 1997, Paper presented at Ring-Plane Crossing Workshop, Wellesley, Massachusetts, abstracted in *Bull. Am. Astron. Soc.* **29**, 999.
- Showalter, M. R., Burns, J. A., Cuzzi, J. N., and Pollack, J. B.: 1987, *Icarus* **69**, 458.
- Showman, A. P. and Ingersoll, A. P.: 1998, *Icarus* **132**, 205.
- Sicardy, B. and Lissauer, J. J.: 1992, *Adv. Space Res.* **12**, 97.
- Smith, B. A., Soderblom, L., Batson, R., Bridges, P., Inge, J., Masursky, H., *et al.*: 1982, *Science* **215**, 504.
- Smith, G. R. and Hunten, D. M.: 1990, *Rev. Geophys.* **28**, 117.
- Smith, G. R., McConnell, J. C., Shemansky, D. E., Holberg, J. B., Broadfoot, A. L., and Sandel, B. R.: 1983, *J. Geophys. Res.* **88**, 8667.
- Smith, W. H., Schempp, W. V., and Baines, K.: 1989, *Astrophys. J.* **336**, 967.
- Spencer, J. R., Calvin, W. M., and Person, M. J.: 1995, *J. Geophys. Res.* **100**, 19049.
- Squyres, S. W., Reynolds, R. T., Cassen, P. M., and Peale, S. J.: 1983, *Icarus* **53**, 319.
- Stevenson, D. J.: 1982, *Nature* **298**, 142.
- Stevenson, D. J.: 1991, 'Interior of Titan', in *Symposium on Titan*, Conf. Proc. ESA, SP-338, p. 29.
- Taylor, F. W. and Coustenis, A.: 1998, *Planet. Space Sci.* **46**, 1085–1097.
- Thompson, W. R., McDonald, G. D., and Sagan, C.: 1994, *Icarus* **112**, 376.
- Tomasko, M. G. and Smith, P. H.: 1982, *Icarus* **51**, 65.
- Toon, O. B., McKay, C. P., Griffith, C. A., and Turco, R. P.: 1992, *Icarus* **95**, 24.
- Trauger, J. T., Clarke, J., Bellester, G., Evans, R., Burrows, C., Crisp, D., *et al.*: 1998, *J. Geophys. Res.* **103**, 20237.
- Veverka, J. P., Thomas, P., Johnson, T. V., Matson, D., and Housen, K.: 1986, in Burns, J. A., and Matthews, M. S. (eds.), *Satellites*, University of Arizona Press, Tucson, p. 342.
- Vidal, R. A., Bahr, D., Baragiola, R. A., and Peters, M.: 1997, *Science* **276**, 1839.
- Waite, J. H., Bagenal, F., Seward, F., Na, C., Gladstone, G., Cravens, T., *et al.*: 1994, *J. Geophys. Res.* **99**, 14799.
- Wallis, M. K. and Ong, R. S. B.: 1975, *Planet. Space Sci.* **23**, 713.
- West, R. A., Friedson, A. J. and Appleby, J. F.: 1992, *Icarus* **100**, 245.
- West, R. A. and Smith, P. H.: 1991, *Icarus* **90**, 330.
- Winter, T. C. and Chubb, T. A.: 1967, *J. Geophys. Res.* **72**, 4405.
- Yelle, R. V., Sandel, B. R., Shemansky, D. E., and Kumar, S.: 1986, *J. Geophys. Res.* **91**, 8756.
- Young, L. A., Yelle, R. V., and Young, R. E.: 1998, *Bull. Am. Astron. Soc.* **30**, 1075.
- Young, L. A., Yelle, R. V., Young, R., Seiff, A., and Kirk, D. B.: 1997, *Science* **276**, 108.
- Yung, Y. L., Allen, M., and Pinto, J. P.: 1984, *Astrophys. J. Supp. Ser.* **55**, 465.
- Yung, Y. L. and DeMore, W. B.: 1999, *Photochemistry of Planetary Atmospheres*, Oxford University Press, New York.
- Zahnle, K. and Dones, L.: 1992, 'Impact Origin of Titan's Atmosphere', in *Symposium on Titan*, Conf. Proc. ESA, SP-338, 19.
- Zwier, T. S. and Allen, M.: 1996, *Icarus* **123**, 578.

## CASSINI IMAGING SCIENCE: INSTRUMENT CHARACTERISTICS AND ANTICIPATED SCIENTIFIC INVESTIGATIONS AT SATURN

CAROLYN C. PORCO<sup>1,\*</sup>, ROBERT A. WEST<sup>2</sup>, STEVEN SQUYRES<sup>3</sup>, ALFRED McEWEN<sup>4</sup>, PETER THOMAS<sup>3</sup>, CARL D. MURRAY<sup>5</sup>, ANTHONY DELGENIO<sup>6</sup>, ANDREW P. INGERSOLL<sup>7</sup>, TORRENCE V. JOHNSON<sup>2</sup>, GERHARD NEUKUM<sup>8</sup>, JOSEPH VEVERKA<sup>3</sup>, LUKE DONES<sup>9</sup>, ANDRE BRAHIC<sup>10</sup>, JOSEPH A. BURNS<sup>3</sup>, VANCE HAEMMERLE<sup>2</sup>, BENJAMIN KNOWLES<sup>1</sup>, DOUGLAS DAWSON<sup>4</sup>, THOMAS ROATSCH<sup>11</sup>, KEVIN BEURLE<sup>5</sup> and WILLIAM OWEN<sup>2</sup>

<sup>1</sup>*CICLOPS/Space Science Institute, Boulder, CO, U.S.A.*

<sup>2</sup>*Jet Propulsion Laboratory, Pasadena, CA, U.S.A.*

<sup>3</sup>*Cornell University, Ithaca, New York, U.S.A.*

<sup>4</sup>*University of Arizona, Tucson, AZ, U.S.A.*

<sup>5</sup>*Queen Mary, University of London, London, England*

<sup>6</sup>*NASA Goddard Institute for Space Studies, New York, New York, U.S.A.*

<sup>7</sup>*California Institute of Technology, Pasadena, CA, U.S.A.*

<sup>8</sup>*Freie Universität, Berlin, Germany*

<sup>9</sup>*Southwest Research Institute, Boulder, CO, U.S.A.*

<sup>10</sup>*Université Paris 7-Denis Diderot, Paris, France*

<sup>11</sup>*DLR, Berlin, Germany*

(\*Author for correspondence: E-mail: carolyn@ciclops.org)

(Received 8 January 2004; Accepted in final form 18 May 2004)

**Abstract.** The Cassini Imaging Science Subsystem (ISS) is the highest-resolution two-dimensional imaging device on the Cassini Orbiter and has been designed for investigations of the bodies and phenomena found within the Saturnian planetary system. It consists of two framing cameras: a narrow angle, reflecting telescope with a 2-m focal length and a square field of view (FOV) 0.35° across, and a wide-angle refractor with a 0.2-m focal length and a FOV 3.5° across. At the heart of each camera is a charged coupled device (CCD) detector consisting of a 1024 square array of pixels, each 12  $\mu$  on a side. The data system allows many options for data collection, including choices for on-chip summing, rapid imaging and data compression. Each camera is outfitted with a large number of spectral filters which, taken together, span the electromagnetic spectrum from 200 to 1100 nm. These were chosen to address a multitude of Saturn-system scientific objectives: sounding the three-dimensional cloud structure and meteorology of the Saturn and Titan atmospheres, capturing lightning on both bodies, imaging the surfaces of Saturn's many icy satellites, determining the structure of its enormous ring system, searching for previously undiscovered Saturnian moons (within and exterior to the rings), peering through the hazy Titan atmosphere to its yet-unexplored surface, and in general searching for temporal variability throughout the system on a variety of time scales. The ISS is also the optical navigation instrument for the Cassini mission. We describe here the capabilities and characteristics of the Cassini ISS, determined from both ground calibration data and in-flight data taken during cruise, and the Saturn-system investigations that will be conducted with it. At the time of writing, Cassini is approaching Saturn and the images returned to Earth thus far are both breathtaking and promising.

**Keywords:** Cassini, Saturn, Imaging, Rings, Moons



*Space Science Reviews* **115**: 363–497, 2004.

© 2004 Kluwer Academic Publishers. Printed in the Netherlands.



## 1. Introduction

On October 15, 1997, the Cassini spacecraft was launched to the planet Saturn from Cape Canaveral Launch Pad 40. When it reaches and begins orbiting Saturn on July 1, 2004, UTC it will become, at 10 AU from the Sun, the farthest robotic orbiter that humankind has ever established in the solar system. The nominal mission duration of 4 years and the variable orbit design will allow an unprecedented exploration of the Saturn system tour over an extended period from a variety of illumination and viewing geometries. Saturn's atmosphere, rings, icy satellites, Titan, and their mutual interactions will all be monitored for temporal changes in a way not previously possible during the Pioneer and Voyager flyby missions.

The Cassini Imaging Science Subsystem (ISS), the most sophisticated, highest-resolution two-dimensional imaging device ever carried into the outer solar system, has been specifically designed to image bodies in the Saturn system. In its photometric sensitivity, linearity and dynamic range, its spectral range and filter complement, resolving power and variety of data collection and compression modes, it represents a significant advance over its predecessor carried on Voyager, as demonstrated by the images obtained during the Cassini Jupiter flyby (Porco *et al.*, 2003). As on other Saturn-bound spacecraft, the ISS is also the instrument used for optical navigation of the spacecraft.

The cruise to Saturn entailed gravity assist flybys of Venus (one in 1998 and another in 1999), Earth (1999) and Jupiter (2000/2001), and a relatively close (1.5 million km) serendipitous flyby of the asteroid Masursky (2000). Aside from the usual periodic in-flight instrument checkouts during which images were collected of stars (Spica, Fomalhaut, Pleiades) for spectral and geometric calibration and for assessing instrument performance, the ISS acquired imaging data only during the Earth, Masursky, and Jupiter flybys. Earth flyby provided the first opportunity to take scientific data on planetary targets – in that case, the Moon – as well as to test in flight the stray light rejection capabilities of the ISS instrument by imaging very near the limb of the Moon. The Masursky flyby saw the first use of the autonomous target-tracking capability of the Cassini spacecraft, and the promise of future success in steady imaging during periods of rapidly changing geometry during the Cassini orbital tour. Finally, the Jupiter flyby was the first attempt to operate the spacecraft as it would be used at Saturn, using simple pointing mosaics and modules, data management in the solid-state recorder (SSR), etc., and indicated (as have subsequent observations) accurate absolute and relative pointing and a steady spacecraft. These results, as well as images collected on approach to Saturn in early 2004 (Figures 1 and 2), open up the exciting possibility of extremely high-quality, sharp, high signal-to-noise (S/N) images of all Saturn targets, bright and dark, and promise the opening of a new era in outer planet studies.

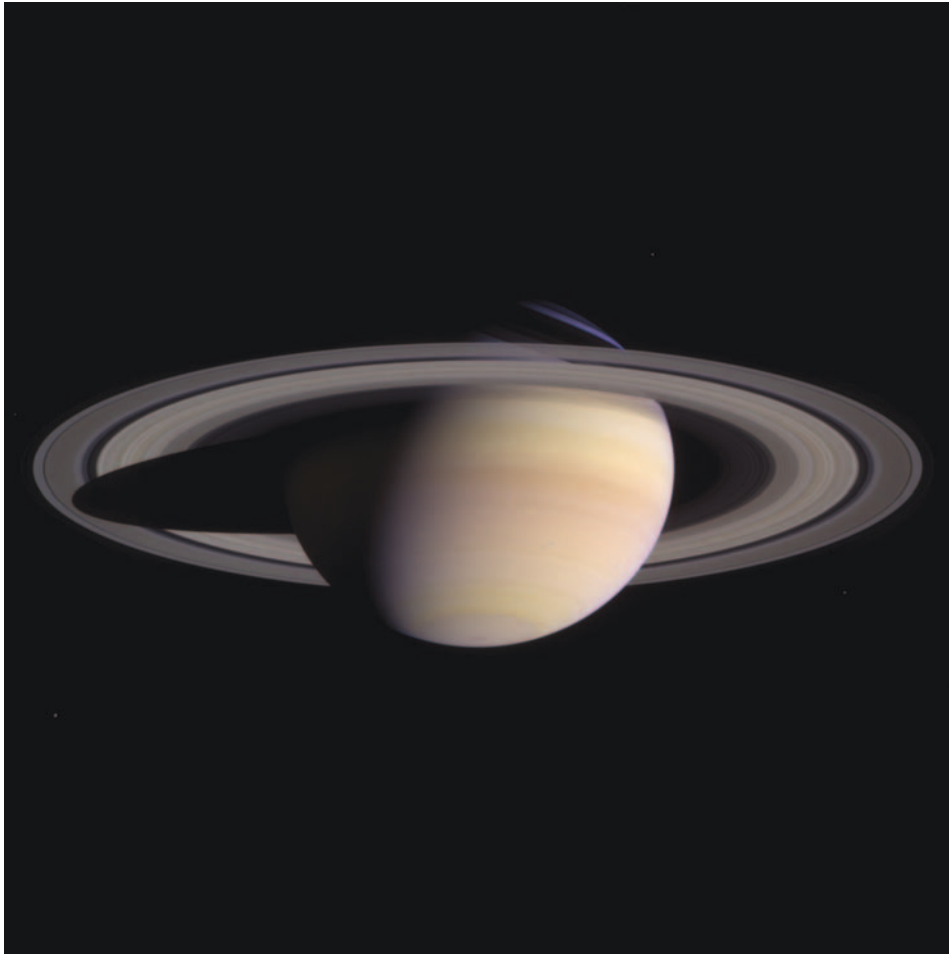


*Figure 1.* Saturn and its rings completely fill the field of view of Cassini's narrow-angle camera in this natural color image taken on March 27, 2004. This was the last single 'eyeful' of Saturn and its rings achievable with the narrow-angle camera on approach to the planet. The image shown here is a composite of three exposures in red, green, and blue, taken when the spacecraft was 47.7 million km (29.7 million miles) from the planet. The image scale is 286 km (178 miles) per pixel. Color variations between atmospheric bands and features in the southern hemisphere of the planet, as well as subtle color differences across Saturn's middle B ring, are evident.

In this article, we describe the scientific investigations that the Cassini Imaging Team (Table I) intends to conduct at Saturn (Section 2), and the characteristics of the Cassini Imaging Science Subsystem that make these investigations possible (Section 3). We also present the results of the instrument calibrations that have been performed thus far using both ground calibration data taken before launch and data taken in flight.

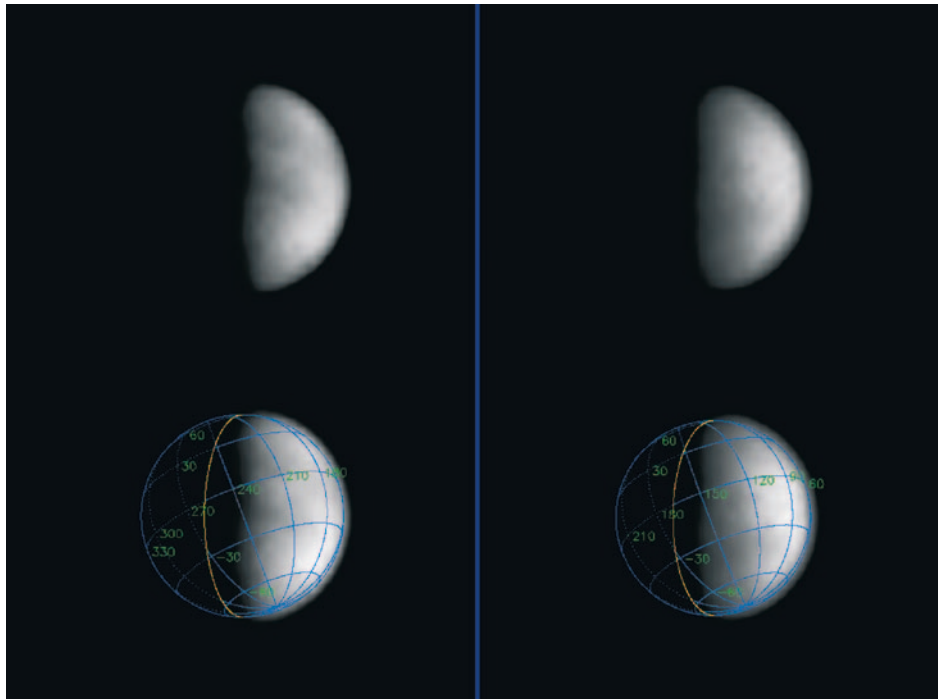


*Figure 2.* Two narrow-angle camera Titan images, each 38 s exposure, taken 4 days apart in mid-April, 2004, through the CB3 (938 nm) filter at an image scale of  $\sim 230$  km/pixel. The images have been magnified and smoothly interpolated by a factor of ten from the original images. Large-scale variations in brightness across the disk are real and can be correlated with features seen by Earth-based observers. The bottom images are the same two Titan images above, overlain with a Western longitude coordinate grid. The bright feature between  $-30^\circ$  latitude and the equator, and extending from  $\sim 60$  to  $120^\circ$  West longitude is Xanadu, the brightest feature on Titan.

## 2. Anticipated Imaging Science Investigations at Saturn

In this section, we describe the major outstanding questions concerning Saturn and its rings and moons that will be addressed by the Imaging Science experiment over the course of Cassini's multi-year orbital tour. In brief, the Cassini 4-year tour calls for:

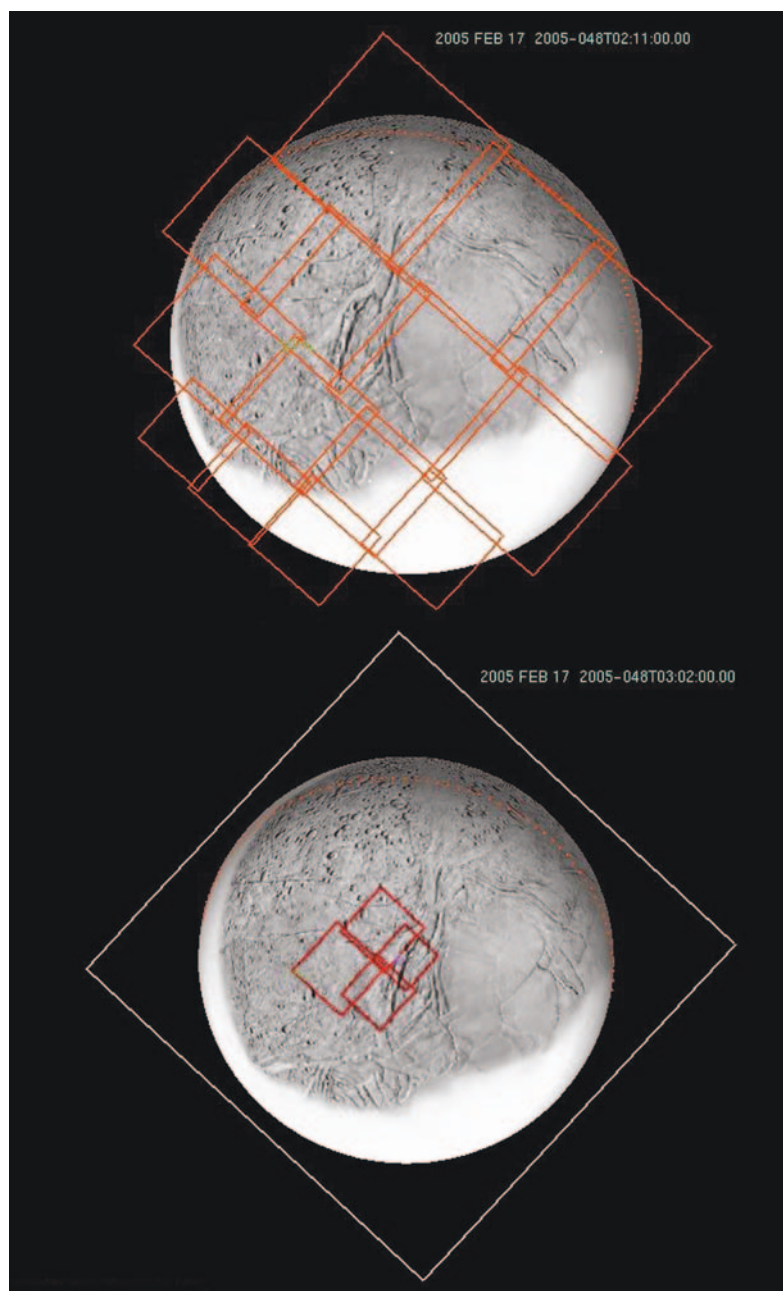
- repeated synoptic imaging of the planet and rings and Titan on approach to Saturn;
- a very close flyby of Phoebe on approach on June 11, 2004;
- extremely high-resolution imaging of the rings during the Saturn Orbit Insertion (SOI) maneuver when the spacecraft is skimming over the rings by only several tens of thousands of kilometers;

TABLE I  
Imaging team.

Carolyn Porco, Team Leader	Space Science Institute, Boulder, CO
Andre Brahic	Université Paris 7-Denis Diderot, Saclay, Paris
Joseph Burns	Cornell University, Ithaca, NY
Anthony DelGenio	NASA Goddard Institute for Space Studies, NY, NY
Henry Dones	Southwest Research Institute, Boulder, CO
Andrew Ingersoll	Caltech, Pasadena, CA
Torrence Johnson	Jet Propulsion Laboratory, Pasadena, CA
Alfred McEwen	University of Arizona, Tucson, AZ
Carl Murray	Queen Mary, University of London, London
Gerhard Neukum	Freie Universität, Berlin
Steven Squyres	Cornell University, Ithaca, NY
Peter Thomas	Cornell University, Ithaca, NY
Joseph Veverka	Cornell University, Ithaca, NY
Robert West	Jet Propulsion Laboratory, Pasadena, CA

- forty-five (45) close ‘targeted’ flybys of Titan (40 of which approach within 2500 km of the surface, and 24 of these within 1000 km of the surface);
- very close ‘targeted’ flybys of Enceladus (4) (Figure 3), Dione, Rhea, Iapetus, and Hyperion, all approaching within  $\sim 1500$  km of the surface;
- thirty-one (31) non-targeted but still close (within 100,000 km of the surface) flybys of Iapetus and the five major icy satellites Mimas, Enceladus, Tethys, Dione and Rhea;
- three (3) extended periods of inclined and low-periapse orbits (May–August 2005, September 2006–June 2007, and December 2007–June 2008) for high-resolution, high-latitude ring and Saturn observing;
- a dozen orbits with sufficiently distant apoapses to permit atmospheric movie making.

Imaging sequences planned for the nominal 4-year tour call for the acquisition of hundreds of thousands of images of known Saturn targets, as well as sequences designed to search for new satellites and faint ring material. Imaging scales on the targeted satellites will be as small as a few tens of meters/pixels; on the rings and atmosphere,  $\sim 1$  km/pixel. In comparison, the best Voyager resolution obtained on the Saturnian satellites was  $\sim 2$  km/pixel; on the rings and atmosphere,  $\sim 4$  km/pixel. The sophisticated capabilities of the ISS, together with Cassini’s upcoming variable and extended tour of the Saturn system, portend dramatic advances in our knowledge of this rich planetary system from the investigations described herein.



*Figure 3.* Example imaging sequence during part of an early 2005 close targeted flyby of Enceladus. Upper image shows the sequence of some frames at a range of about 29,000 km. Lower shows frames at about 9000 km range. Small boxes are narrow-angle images; large box in bottom example is the wide-angle field of view. Features mapped by Voyager are shown; white areas were not adequately imaged by Voyager. Best Voyager image is in Figure 7.

## 2.1. SATURN'S ICY SATELLITES

The Saturn satellite system, like that of the other giant planets, has several distinct components. The most distant outer population extends from 10 to 20 million km (out to the dynamical limit known as the ‘Hill’s sphere’), and is growing rapidly in number owing to successful ongoing ground-based telescopic searches for new Saturnian moons (Gladman *et al.*, 2001). At last count, this group contains 14 satellites, including Phoebe at a semi-major axis of 12.9 million km; none are believed to be bigger than  $\sim 20$  km across (except Phoebe at  $\sim 220$  km diameter), and about half (including Phoebe) are on retrograde orbits. With the exception of the close Phoebe flyby on approach to Saturn, no Cassini observations of this group of objects have been planned.

The inner population is a collection of bodies, from ring-embedded Pan at  $\sim 20$  km across to Mercury-sized Titan (Table II). It is arguably the most complex

TABLE II  
Saturnian satellite characteristics.

Satellite	$a$ ( $\times 10^3$ km)	Period (days)	Axes (km)			Radius (km)	Density ( $\text{g cm}^{-3}$ )	References
Pan	133.59	0.5751				10		1
Atlas	137.64	0.6019	18		13	$16 \pm 4$		2
Prometheus	139.35	0.6129	70	50	37	$51 \pm 7$		2
Pandora	141.70	0.6288	55	43	32	$42 \pm 5$		2
Epimetheus	151.42	0.6946	70.2	54.1	51.9	$58.2 \pm 3$	$0.63 \pm 0.11$	3
Janus	151.42	0.6946	101.5	94.9	76.8	$90.5 \pm 3$	$0.65 \pm 0.08$	3
Mimas	185.52	0.9424	209.1	195.8	192.2	$198.9 \pm 0.5$	$1.12 \pm 0.03$	5, 4
Enceladus	238.02	1.3702	256.3	247.3	244.6	$249.4 \pm 0.3$	$1.00 \pm 0.03$	4
Tethys	294.66	1.8878	535.6	528.2	525.8	$529.8 \pm 1.5$	$0.98 \pm 0.02$	5
Calypso	294.66	1.8878	15	12	7	$11 \pm 3$		2
Telesto	294.66	1.8878	–	12	11	$12 \pm 3$		2
Dione	377.40	2.7369				$559 \pm 5$	$1.49 \pm 0.05$	6, 8
Helene	377.40	2.7369	17	–	14	$16 \pm 3$		2
Rhea	527.04	4.5175				$764 \pm 4$	$1.24 \pm 0.04$	7, 9
Titan	1221.85	15.9454				$2575 \pm 2$	$1.88 \pm 0.01$	10
Hyperion	1481.1	21.2766	164	130	107	$133 \pm 8$		11
Iapetus	3561.3	79.3302				$718 \pm 8$	$1.03 \pm 0.1$	9
Phoebe	12952.	550.48R	115	110	105	$110 \pm 3$		2

1: Showalter (1991); 2: Thomas *et al.* (1983); 3: Nicholson *et al.* (1992); 4: Dermott and Thomas (1994); 5: Thomas and Dermott (1991); 6: Davies and Katayama (1983a); 7: Davies and Katayama (1983b); 8: Harper and Taylor (1993); 9: Campbell and Anderson (1989); 10: Lindal *et al.* (1983); 11: Thomas *et al.* (1995).



collection of satellites in the solar system and exhibits an enormous variety in shape, size, planetocentric distance and surface characteristics. It contains 1430 km wide Iapetus, whose orbit is the most distant at 3.6 million km and somewhat inclined ( $\sim 15^\circ$ ) to Saturn's equator; the small ( $\sim 300$  km wide) chaotic rotator Hyperion; haze-enshrouded Titan (5100 km across); the five major icy satellites Rhea, Dione, Tethys, Enceladus and Mimas (ranging linearly in size with distance from the planet from 1528 km Rhea to 396 km Mimas); the small (20–30 km) Trojans, Helene, Telesto and Calypso, of Tethys and Dione; and finally the remaining 'ring region' satellites Janus and Epimetheus (the 'co-orbitals'), the F ring shepherds Pandora and Prometheus, Atlas orbiting immediately outside the main rings, and Pan,  $\sim 20$  km across and orbiting within the main rings where we expect to find other small gap-clearing moons. It is this population that Cassini will investigate in depth.

The present-day physical, compositional and orbital characteristics of each of these bodies result from a combination of original formation conditions and subsequent surface and (possibly) orbit modification by external and internal processes operating over geologic time. Consequently, the ISS investigations of these bodies are focused on developing as complete and accurate a picture as possible of the visual properties of each satellite. Most of these inner satellites are tidally locked and synchronously rotating with their orbital periods. As a consequence, the Voyager spacecraft, each of which spent only a brief period of time in the Saturn system, imaged only one hemisphere of some of these moons at reasonably high ( $\sim 2$  km) resolution. Cassini's multi-year tour of the Saturn system, which includes global imaging of almost all these bodies, will in part be an initial reconnaissance of the other 'half' of the Saturnian system. Global spectral images at Voyager and better resolution, very high, sub-kilometer resolution images of localized regions, and repeated long distance images over the orbital tour for positional measurements are all part of the imaging sequences planned for the inner Saturnian satellites.

The diversity within the Saturnian satellite system, and its placement ten times farther from the Sun than that of Jupiter – the only other outer planet satellite system for which we have a moderately detailed view – provide an unusual opportunity to evaluate and disentangle the contributions of initial conditions and subsequent modifications to the satellites' present day attributes. With Cassini observations in hand, fundamental questions will be addressed, such as: How did heliocentric distance affect the composition of the original proto-Saturnian nebula materials and how did planetocentric distance affect their subsequent incorporation into the satellites? What have been the thermal and geologic histories of the Saturnian satellites? Which satellites have undergone tidal heating and do any have present-day subsurface oceans? How did the flux and chronology of impacts vary across the Saturnian system? How did the impactor populations and chronology vary across the outer solar system?

The ultimate goal of all Cassini satellite imaging investigations is to develop a more comprehensive view of the origin and evolution of the Saturnian system as

a whole, and that of outer giant planet satellite systems in general. Moreover, as a collection of bodies, all orbiting in the same plane, in the same direction, around the same massive central body, and nearly all formed from the same protoplanetary nebula, the inner Saturnian system resembles the assemblage of planets in orbit around the Sun. Consequently, the study of the Saturnian satellites will have direct impact on our understanding of the processes that were in play during the formation and subsequent differentiation and evolution of the planets. The multiplicity of satellite phenotypes around Saturn, and their distinctive characteristics when compared with the satellites of the other giant planets, offer an eagerly awaited chance to understand many fundamental aspects of planetary evolution.

The investigations of Titan, whose surface, and therefore geologic history, remain unknown, may well yield the single greatest scientific advance from the Cassini mission. Because the exploration of Titan by Cassini is special, and because the ISS has been especially equipped to penetrate the haze that obscured the surface to the Voyager cameras, we reserve a separate subsection to describe the pressing scientific questions surrounding it and our intended investigations.

#### 2.1.1. *Geomorphology*

Many of the fundamental questions about the composition, origin and evolution of the Saturnian satellites can be addressed by global and high-resolution imaging of surface morphology. The array of geological and photometric features on each satellite surface – such as crater densities, tectonic patterns, and albedo markings – tells not only the body's individual history, but may be used, in concert with other information, like mean density, to ascertain the trends across the system in composition, the physical conditions at time of formation, and other important factors that are relevant to the workings of the system as a whole.

Most morphological investigations to be addressed by imaging are relevant for all satellites. Determination of surface ages from crater density statistics is one such investigation, and is best accomplished with imaging at low solar elevation angles, where shadows are longest, and at resolutions as high as possible. The Galileo experience (Bierhaus *et al.*, 2001) has shown the usefulness of crater density measurements of sub-kilometer craters in revealing the order of geological events (stratigraphy) on satellite surfaces and in examining the mechanical properties of the substrate, although interpretations may be controversial. Many problems of general geologic evolution, such as crater degradation, tectonic faulting, cryovolcanism, viscous relaxation, isostatic rebound, and mass movements require accurate measurements of topography, including slopes. Slope information can be extracted from photometric and stereogrammetric measurements. The relative accuracy and utility of stereo imaging depend upon lighting conditions and the convergence angles and pixel scales of different images. For example, 50-m stereo images taken at a convergence angle of 20° (under similar lighting conditions) yield elevation accuracies of 13–26 m, depending on image contrast. The rapid flybys and slow maneuverability of the Cassini spacecraft require careful planning, use of both WA

and NA cameras, and combination of imaging from different satellite flybys to maximize high-resolution stereo data. Additionally, in some areas photoclinometry – the determination of slopes from the light scattering behavior of a surface whose photometric function is known – can be used to map relative topographic patterns. Photoclinometry can be used to measure slopes at higher spatial resolution with poorer control of regional slopes, than can stereogrammetry, so the two techniques are best combined (Giese *et al.*, 1996; Kirk *et al.*, 2003).

One geological example where critical topographic measurements are required is that of the ridged units on Enceladus, which are less than a few kilometers across and a few hundred meters high. Testing hypotheses for the formation of these ridges requires relative height determinations of a few tens of meters down to a few meters. Imaging resolutions of meter scale are also vital for the geologic mapping of ridge characteristics, a lesson learned in detail from Galileo's imaging of ridges on Europa (Figure 4; Carr *et al.*, 1998; Nimmo *et al.*, 2003). Another critical use of accurate local topographic measurements lies in mass wasting studies where measures of the filling of craters and other depressions, and the burial of otherwise positive relief features, are needed. The surprising findings of significant surface filling and erosion on Callisto from Galileo images (Moore *et al.*, 1998) show the need for these volume measures with vertical precision of tens of meters. Current tour scenarios allow for measurement of vertical displacements on some regions of Enceladus, Dione, Iapetus, Hyperion, Phoebe and possibly Rhea and Titan to a precision of a few tens of meter; areas on Mimas and Tethys may be imaged with lower resolution stereo.

Individual satellites present geological features that appear unique, and high-resolution imaging can address the question: what makes them so different? Iapetus is a prime example. The question of internal/external controls of its large albedo asymmetry has significance for both models of icy satellite interiors as well as orbital dynamics (Section 2.1.2). One requirement in imaging Iapetus is that both light and dark areas and the boundary between them be seen at favorable resolution and lighting. This requirement is met in the currently planned targeted flyby over the boundary. The low flyby speed allows high resolution ( $<50$  m/pixel) over many areas within the dark region, over brighter areas nearer the trailing side of Iapetus, and in several areas near the boundary where stratigraphic relations are sought. Planned imaging sequences include stereoscopic data and monoscopic mapping at high resolution to determine morphology and topography (as well as color and photometric sampling), much of this at much better than 1 km/pixel.

*2.1.1.1. Geodesy and Cartography.* High-resolution imaging is also required for the production of geometrically accurate maps. Correct maps are important tools for the planning of imaging activities when the objective is to point the camera precisely to specific targets. They also form the contextual basis for further geologic, geophysical and photometric studies of the satellites.

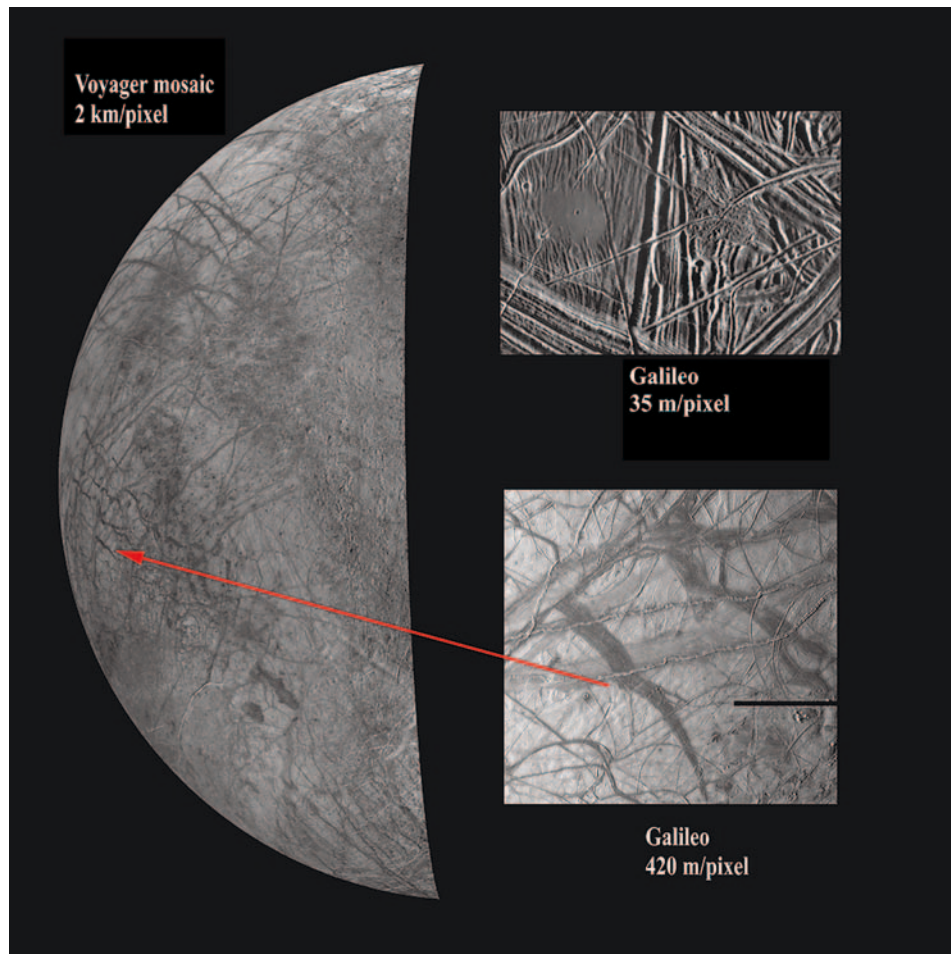


Figure 4. Voyager image of Jupiter's satellite, Europa, at 2 km/pixel, and two Galileo images at 420 and 35 m/pixel. The improvement in resolution from hundreds of meters/pixel to tens of meters/pixel altered the view of the morphology of Europa's 'bands' from one of crossing linear features to one of specific tectonic features of changing morphology, for which a robust chronology and morphology have been developed (see Carr *et al.*, 1998). The morphological relations revealed by high resolution are those between tectonic forms, and also between tectonics and craters and their ejecta. Image prepared by C. Philips, SETI.

The production of such maps begins with laying out networks of "control points", typically small craters, for which the coordinates in the satellite-fixed coordinate system must be determined. These are generally determined from large numbers of line/sample measurements of the control points in large numbers of images by "bundle block adjustment techniques", a dedicated inversion procedure used in photogrammetry (Davies *et al.*, 1998; Zeitler and Oberst, 1998; Oberst and Schuster, 2004). Solutions of the bundle block adjustment include latitudes, longitudes, radii

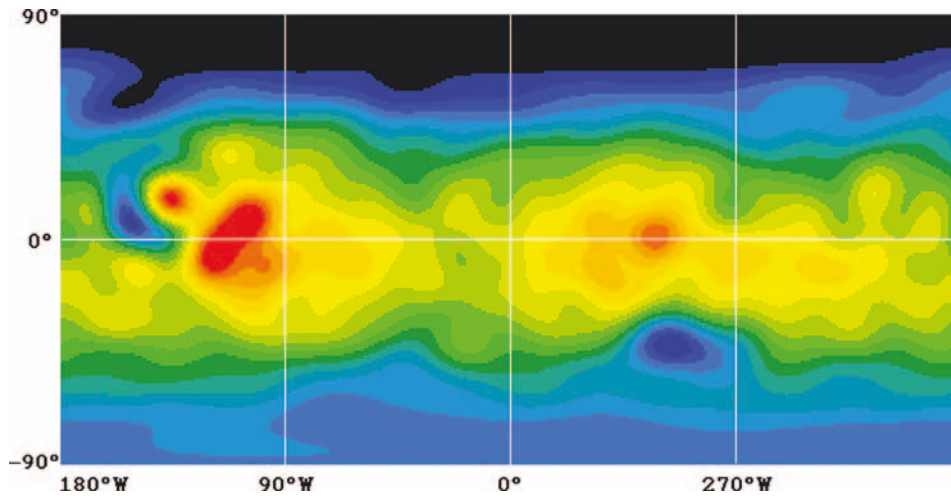


Figure 5. Spherical harmonics shape model of degree and order 16 for Mars. Parameters of this function were determined as the best fits to 3739 three-dimensional control point coordinates, obtained by photogrammetric analysis of Viking Orbiter images (Zeitler and Oberst, 1998b). Elevations with respect to a best-fit sphere range from  $-17$  km (black) to  $+21$  km (red). Similar global shape models will be obtained for the satellites of Saturn.

of the control points, pointing data for each image involved, and possibly, rotational parameters of the satellite as well. Assuming that at least 10 images with global coverage and surface resolutions of  $3\text{--}5$  km/pixel are available, three-dimensional coordinates for several hundreds of control points will be determined with precisions of one standard deviation equal to  $1\text{--}3$  km (Oberst *et al.*, 1998; Oberst and Schuster, 2004). The precision will increase as more images or images at higher resolution are available. The radius components of the control points may be used to study the global shape of the satellite, as has recently been demonstrated for Mars (Figure 5) and for Galileo control points on Io (Oberst and Schuster, 2004).

Librations are a minor uncertainty in these solutions, except for Hyperion where the departure from synchronous rotation is extreme, and possibly Enceladus (see Section 2.1.1.3). Detection of libration, which is a necessary part of the overall geodetic process, is accomplished by measuring the rotational position of landmarks on the surface in comparison to predicted rotational models, such as simple synchronous. Its success depends upon accurate stereogrammetric measurements of parts of the satellite's surface at two different points in the orbit relative to periapse.

**2.1.1.2. Topography.** Virtually all studies of geological processes require knowledge of surface topography. Topographic mapping can be carried out using stereo image analysis and "shape-from-shading" modeling.

**Stereo imaging:** Stereo image analysis will be carried out in different stages. First, as described above, control point measurements and block adjustment



techniques are used to improve the nominal pointing of the images. Next, “digital image matching” is carried out to find large numbers ( $>10,000$ ) of conjugate points in image pairs. Object coordinates (latitude, longitude, radius) of these points are computed from the improved camera pointing data. Interpolation in between these points is used to form a contiguous grid. Points from several stereo pairs can be combined to form terrain mosaics covering large areas.

The accuracies of the control point coordinates depend on lighting conditions and the specifics of the imaging geometry. For single points of interest, precisions of object coordinates on the order of one pixel can be obtained if stereo images have reasonable convergence (stereo) angles, near  $20^\circ$ . However, terrain models of large, contiguous areas typically have reliable spatial scales of three to five times larger than the image pixel size: i.e., a map resolution three to five times lower than the inherent image resolution. Coordinates are difficult to reference to absolute heights if no additional data (e.g. extra images) are available. However, relative elevation information is generally sufficient to support geological studies of the terrain.

The methods for analysis have been developed and applied using Galileo images of the Moon obtained during the Earth – Moon flyby in 1992 (Oberst *et al.*, 1997) (Figure 6) and during encounters with Ganymede and Europa (Giese *et al.*, 1998; Oberst *et al.*, 1998). However, owing to the low data rate of the Galileo spacecraft

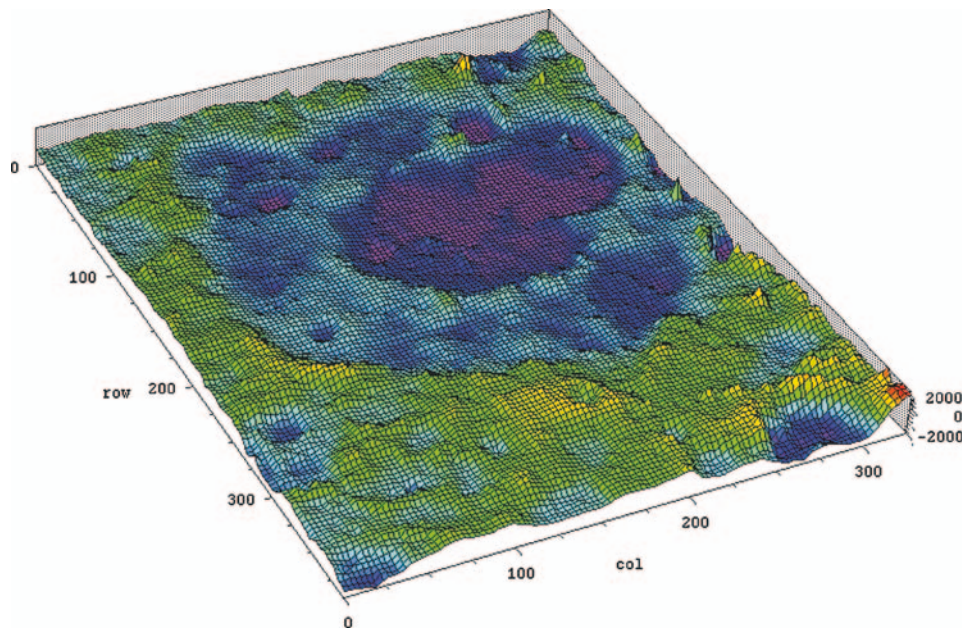


Figure 6. Digital Terrain Model of the 600 km diameter Lunar Humboldtianum Basin, derived from Galileo ( $\sim 1$  km/pixel) stereo images of the Moon obtained during the second Earth–Moon flyby in December 1992. Terrain models of this type will be obtained for selected regions on the Saturnian satellites.



at Jupiter, only a small number of stereo images were returned. We expect better results from Cassini.

*Shape-from-shading (or photoclinometry):* In this technique, which is used when stereo is not available and/or the highest possible resolution is needed, surface slopes are determined from the apparent brightness of the image. However, the photometric function (the function that describes the variation of surface brightness with illumination and viewing angles) must be known. One-dimension profiles and two-dimension grids of relative heights can be obtained by integration. The chief limitations on this technique can be the lack of knowledge of the albedo variations and photometric function across the surface. These conditions are frequently not met – in fact, the technique may be impossible on Titan due to atmospheric scattering that washes out topographic shading – but a uniformly bright satellite like Enceladus may be ideal. Photoclinometry has successfully been applied to various planetary surfaces (Figueredo *et al.*, 2002; Schenk *et al.*, 2004). Terrain models for asteroid Ida, derived from shape-from-shading and stereo image analysis show good agreement (Giese *et al.*, 1996).

*2.1.1.3. Geophysics and Internal Structure.* Important geophysical parameters such as rotational moments of inertia may be inferred from the shapes and masses of relaxed ellipsoidal satellites, and from observations of amplitudes of librations, all of which can be derived from imaging observations. The mass distribution within a satellite, inferred from the moment of inertia, can help refine interior models that constrain the composition of the originally accreted materials as well as define past and present differentiation of those materials. The primary parameter sought is the moment of inertia factor,  $C = I/MR^2$  ( $I$  is the rotational moment of inertia;  $M$  the mass,  $R$  the mean radius;  $C = 0.4$  for homogeneous sphere). The moment factor is detected with imaging by measurement of the satellite's shape parameter,  $(a-c)/R$ , where  $a$  and  $c$  are the long and short ellipsoidal axes. The  $(a-c)$  for a satellite is proportional to  $H_m$ , where  $H$  is the measure of the internal mass distribution relatable to  $C$ , and  $m$  is inversely proportional to mean density and directly proportional to rotational speed. Thus, the low density ( $<2.0$  g/cm<sup>3</sup>) and high rotational frequency of many of the Saturnian satellites means they have relatively large shape parameters,  $(a-c)/R$ , even with differentiation ( $H < 1$ ). Measurement of the shape is done with full-disk imaging, capturing the limbs. These data can be obtained with a CCD to a precision of about 0.1–0.15 pixels, so images a few hundred pixels in diameter can be measured to levels that allow useful resolution of the  $(a-c)$  values. Appropriate spacecraft satellite (NAC) imaging ranges vary between 75,000 km for Mimas and 285,000 km for Rhea – often achievable during the Cassini orbital tour – with discrimination of  $C$  likely to be better than 7% for Rhea and 1% for Mimas and Enceladus.

Limb profiles provide the most direct route to overall characterization of an ellipsoidal shape of a satellite. For restricted sections of a large satellite, or for the entire shape of smaller, irregularly shaped ones, the stereoscopic geodetic measurements

of control points provide the basic data and can be used in conjunction with limb measurements for testing high-order departures from ellipsoidal shapes (see Section 2.1.1.1). Best-fit ellipsoid parameters determined from a grid of control points, or local elevation models can address many geophysical issues (Zeitler and Oberst, 1998; Oberst and Schuster, 2004).

Moments of inertia can also be constrained by measurements of a satellite's forced libration, if the libration is large enough to be measured. The strongest result will be for Mimas, where the predicted libration amplitude of about  $0.5^\circ$  is 1.7 km on the equator (Dermott and Thomas, 1988), a quantity that should be easily observed in the planned imaging sequences. And Enceladus presents a special case in which a measure of its libration, if present, holds great significance for its internal structure and interpretation of the tectonic features seen on its surface (see below). However, in most other cases, it is more likely that the shapes will provide more accurate estimates of moments of inertia.

How might the satellites have reached different stages of differentiation? Accretional heat is believed to have been important very early in the satellites' history (Ellsworth and Schubert, 1983; Federico and Lanciano, 1983; Squyres *et al.*, 1988). Accretion for these satellites has been modeled to be quite rapid (Safronov, 1972; Safronov and Ruskol, 1977; Safronov *et al.*, 1986), and impactor kinetic energy is largely deposited as heat at and below a satellite's surface. At the end of accretion, a satellite's temperature profile is cool at the center, rises to a maximum several tens of kilometers below the surface, and drops sharply at the surface. The maximum temperature can approach or exceed the  $\text{NH}_3\text{--H}_2\text{O}$  eutectic temperature for Tethys, Dione, and Rhea even if the satellites accreted in a gas-free environment, and also for Mimas and Enceladus if a warm nebula was present (Squyres *et al.*, 1988). Following accretion then, some satellites will have had a region of relatively warm, mobile, and buoyant material a few tens of kilometers beneath the surface. An exception is Iapetus, which accretes more slowly, and is able to radiate its accretional heat effectively (Squyres *et al.*, 1988).

Continued evolution takes place by radiation, warming by radionuclides, and heat transport by conduction and (in some cases) convection. Rapid post-accretion cooling of the outer layers can produce extensional thermal stresses as large as  $\sim 200$  bars, even accounting for a viscoelastic crust (Hillier and Squyres, 1989). Such stresses should cause failure, producing extensional tectonism and perhaps enabling extrusion of buoyant subsurface materials. Deep warming can cause further extension (Ellsworth and Schubert, 1983). The magnitude of warming is limited by solid-state convection which removes heat rapidly. For Rhea and Iapetus, which can contain ice II (and for Iapetus only if it is largely undifferentiated), warming can also cause expansion via the ice II–ice I phase change. As heating diminishes and heat loss by conduction becomes dominant, the satellites cool and contract, albeit at a rate slow enough that tectonism may not result.

There are some hints on internal structures from Voyager data. The shape of Mimas is consistent with a central increase in density if the surface is in hydrostatic

equilibrium (Dermott and Thomas, 1988). However, this observation might also imply a silicate core, an increase with depth in the compaction of rubble, or just a rigid, non-hydrostatic surface layer (Ross and Schubert, 1988). On Tethys, if Ithaca Chasma is the result of relaxation of Odysseus, the flow implied places an upper limit on the size of its core of  $\sim 20\%$  of the satellite's radius (Thomas and Squyres, 1988). The shape of Enceladus, combined with reasonable assumptions on possible materials, suggests a denser core within a deep water ice mantle (Dermott and Thomas, 1994).

Enceladus is unusual in two important ways. A 2:1 orbital resonance with Dione forces its eccentricity and produces some degree of tidal heating (Yoder, 1979; Squyres *et al.*, 1983; Ross and Schubert, 1989). A simple model suggests that the present eccentricity is several times too small to maintain a partially molten interior if the thermal conductivity of the crust is that of solid ice, but perhaps sufficient if a low-conductivity regolith is present (Squyres *et al.*, 1983). A more sophisticated treatment using a viscoelastic rheology suggests that melting is somewhat more likely (Ross and Schubert, 1989), though there is still the question of why Enceladus would have melted due to this mechanism and not similarly-sized Mimas.

Also, it has been recently shown that Enceladus may be in a 3:1 secondary spin-orbit resonance capable of increasing its tidal heating over previous estimates by 100- to 1000-fold, depending on physical parameters like the rigidity of ice and the moon's oblateness (Wisdom, 2004). If Enceladus is indeed in this resonance, the model predicts a large forced libration amplitude – up to  $10^\circ$ – $20^\circ$ –which would be easily measured in Cassini images and would suggest a degree of tidal heating possibly large enough to produce a subsurface liquid mantle and hence present-day geologic activity on Enceladus. The implications for surface expressions such as geysers, chaotic 'ice flow' terrain as seen on Europa, and other morphological indicators are obvious. Enceladus could be the Europa of the Saturn system.

Hyperion's chaotic rotation presents challenges in observation and modeling. Imaging at ranges less than  $10^6$  km is sufficient to refine the shape and track rotation. Indications from Voyager data are that much of the time the rotation consists of two components that can remain fairly uniform for long periods. The combination of the close flyby imaging for geology, mass, and other compositional information, combined with rotational monitoring, should allow for excellent modeling of variations in density distribution and overall geologic history, better than for any other irregularly shaped icy object.

*2.1.1.4. Surface Processes: Resurfacing and Tectonism.* Voyager results indicate that resurfacing has occurred on several Saturnian satellites, but the mechanisms are not obvious due to the lack of very-high-resolution images of these bodies. Resurfacing is expected to occur by volcanic or "cryovolcanic" extrusion of material from below, by impacts, or by faulting and fracturing of the surface by tectonic stresses. Water (H<sub>2</sub>O)-rich material was probably extruded to the surface of these bodies, but it is not known if it was liquid, slush, or solid ice. Predominantly

liquid resurfacing is favored on theoretical grounds (Stevenson, 1982; Squyres and Croft, 1986). However, ice is difficult to melt in such small, cold satellites. Moreover, liquid water is denser than ice, so achieving melt buoyancy is difficult if the satellites have silicate-poor outer regions. Ammonia ( $\text{NH}_3$ ), which is cosmochemically plausible (Lewis, 1972; Prinn and Fegley, 1981), could help on both counts (Stevenson, 1982; Squyres *et al.*, 1983; Ellsworth and Schubert, 1983), since it lowers the melting point by 100 K, and leads to eutectic melt that is less dense than pure  $\text{H}_2\text{O}$  liquid (Croft *et al.*, 1988).

The Voyager images are inconclusive on the matter of cryo-volcanism. No lobate flow fronts are observed at Voyager resolution. This situation probably rules out solid-state flow, since plausible ice rheology should lead to thick, and therefore Voyager-observable, flows on these satellites (Jankowski and Squyres, 1988; Schenk, 1989), as seen on the Uranian moon Ariel. However, slush, which may have something like a Bingham rheology (Melosh and Janes, 1989; Schenk, 1989; Thomas and Squyres, 1989), may have properties (Kargel and Croft, 1989) such that a significant solid fraction could still yield flows too thin to be seen at Voyager resolution. (Bingham fluids have yield strengths which are independent of viscosity, and so flow characteristics – thick or thin – are not solely determined by viscosity.) High-resolution images of resurfaced (sparsely cratered) regions will place better limits on flow rheology.

Recent resurfacing on Enceladus may be indicated by its high, nearly uniform albedo (Smith *et al.*, 1981, 1982; Buratti, 1984, 1988) that ignores geological boundaries. Its physical association with Saturn's E ring (Baum *et al.*, 1981; Larson *et al.*, 1981; Pang, 1984), which consists of small particles of short lifetimes ( $10^2$ – $10^4$  years; Morfill *et al.*, 1983; Haff *et al.*, 1983; Burns, 1984) suggests Enceladus as the source of the E ring, and one possible mechanism is liquid-rich resurfacing events. Alternatively, Hamilton and Burns (1994) concluded that the ring may be self-sustaining, with meteoroid impacts on Enceladus as the originator of ring particles. High-resolution images may refute this model if small craters are rare, as seen on the Galilean satellites (Bierhaus *et al.*, 2001). Also, cryo-volcanism cannot be ruled out as a source for some ring particles and for the uniform albedo since volcanic constructs have been interpreted on its surface (Schenk and Moore, 1995).

Evidence for tectonic activity on the Saturnian satellites generally takes the form of troughs or grooves that may represent graben or other faulting, generally of an extensional nature. Evidence of compressional features on the icy Saturnian satellites is sparse from Voyager images. Investigating the tectonics on these bodies requires global mapping of fault patterns and determination of the geometry of the surface expressions of these patterns in order to work out the nature and history of events recorded in the tectonic features. Low-sun imaging to reveal very low-amplitude folding as seen on Europa (Proctor and Pappalardo, 2003) is also needed.

Enceladus shows widespread evidence for tectonism (Smith *et al.*, 1981, 1982; Squyres, 1983; Kargel and Pozio, 1996; Gomez *et al.*, 1996). While the boundaries of some resurfaced regions are diffuse, there is one band of resurfaced terrain with

sharp margins cutting through cratered terrain (Figure 7). This relationship may indicate that a structural rift has been filled with extruded material, but the contact has not been characterized in detail. Grooves concentrated within resurfaced regions are a few kilometers wide, a few hundred meters deep, and in some cases more than 100 km long. Their geometry correlates with the apparent age (crater density) of

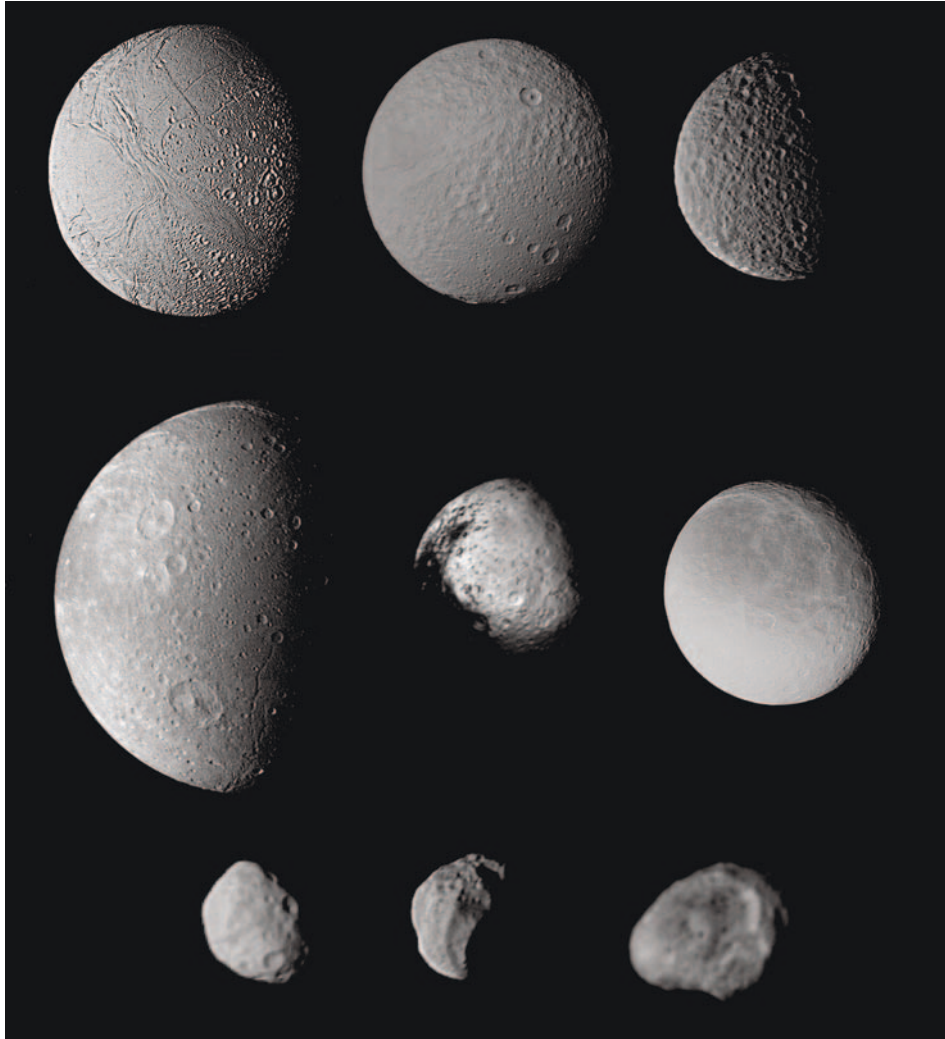


*Figure 7.* Voyager global images of icy satellites of Saturn, not to scale. Left to right, top to bottom: Enceladus: linear tectonic features, craters with variable morphology are visible. Tethys: linear marking from middle left to upper right is part of Ithaca Chasma. Mimas: non-circular outline is real: this high latitude view shows the 10% elongation due to rotational and tidal effects. Dione: bright markings, craters, and sinuous troughs. Iapetus: greatly varying albedo pattern. Rhea: heavily cratered. Janus: irregular shape and shallow craters. Epimetheus: heavily cratered and a ring shadow. Hyperion: scalloped topography suggests spallation of large amounts of material.



the terrain: in the youngest terrains, grooves are common and occur in curvilinear sub-parallel sets; in older terrains they tend to be straighter and to occur singly. The oldest terrains generally lack grooves. The details of groove morphology are poorly known, and their underlying structural nature is an open question. They may be grabens, modified extension fractures, or ductile necking features.

Several other Saturnian satellites show evidence of tectonism (Smith *et al.*, 1981, 1982; Plescia, 1983; Moore and A'Hearn, 1983; Moore, 1984; Moore *et al.*, 1985; Thomas, 1988; Gomez *et al.*, 1996; Kargel and Pozio, 1996). Mimas, Tethys, Dione, and Rhea all have narrow, shallow troughs on their surfaces. The troughs' origins are unknown. Mimas has a series of topographic troughs which show no clear association either to the largest impact crater, Herschel, or to tidal stress orientations. The surface of Tethys is also cut by an enormous trough, Ithaca Chasma (Figure 7), that extends at least 270° around the satellite. It is up to 100 km wide and perhaps ~3 km deep. The walls show evidence of complex structure, including internal terraces and grooves. Ithaca Chasma may be a large graben. It roughly traces a rough great circle across Tethys, and the large crater Odysseus lies at one pole of this great circle, suggesting a genetic link (Smith *et al.*, 1982; Moore and A'Hearn, 1983; McKinnon, 1985; Thomas and Squyres, 1988).

Dione has a few very subdued ridges that may be compressional (Moore, 1984). They are at most a few hundred kilometer long, and have very gentle slopes and low relief. They are only visible near the terminator in Voyager 1 images (Moore, 1984), so their global distribution, like their topography, is unknown.

*2.1.1.5. Crater Studies. Geomorphology.* Impact craters are ubiquitous geologic features throughout the solar system and the Saturnian satellites are no exception (Smith *et al.*, 1981, 1982). The study of craters is vital for determining material properties as well as establishing the chronology of geologic events in the satellites' histories. Crater depths are poorly determined on the basis of Voyager images, but simple craters appear to be a few tens of percent shallower than those of equivalent size on silicate bodies (Schenk, 1989). This observation may reflect a difference in the strength properties of icy material, but is not well understood. Ejecta deposits are difficult to identify in the Voyager images of the Saturnian moons. Secondary crater fields have not yet been identified but must be present. The diameter of the transition from simple to complex craters seems to scale roughly with gravity among the satellites, but there are deviations from this trend (Chapman and McKinnon, 1986; Schenk, 1989). The transition takes place at a diameter far smaller than expected by extrapolation from silicate bodies, and may indicate lower cohesion for icy materials.

Observations of large craters are severely hampered by inadequate Voyager coverage, resolution, and viewing geometry. Multi-ringed structures should form most readily on high-gravity bodies, and the clearest multi-ringed structure in the Saturn system is indeed on the second largest satellite: Tirawa, on Rhea, with a diameter of 350 km. (The presence or absence of impact basins on Titan is



presently unknown.) Tirawa lies on the terminator in Voyager images, however, so its morphology is poorly known. There may be another multi-ring structure on Rhea, seen on the limb at very low resolution by Voyager (Moore *et al.*, 1985). The largest known crater in the Saturn system is Odysseus, on Tethys, with a diameter of 430 km. It seems to have a complex central peak structure, but no clear rings.

Craters with polygonal rims are observed, and are common on Rhea (Smith *et al.*, 1981). The shapes probably indicate exploitation of trends of structural weakness during excavation (Shoemaker, 1960). Rim segments on some areas of Rhea show preferred orientations (Moore *et al.*, 1985; Thomas, 1988). This observation probably reflects an underlying structural stress pattern, but the pattern's global nature is not known.

Viscous relaxation of craters in the Saturn system appears rare, apparently due to the low gravity and cold temperatures of the satellites. Exceptions seem to be the large craters Tirawa and Odysseus (Schenk, 1989), although their degree of relaxation is poorly known. Relatively small craters on Enceladus also appear to be relaxed (Passey, 1985), probably because that satellite has undergone tidal warming. The morphology of craters on Enceladus could enable estimation of depth to a possible liquid water mantle, as has been possible on Europa (Turtle and Pierazzo, 2001; Schenk, 2003).

*Impact history:* The cratering records of the satellites are diverse (Smith *et al.*, 1981, 1982; Strom, 1981; Plescia and Boyce, 1982, 1983, 1985; Hartmann, 1984; Neukum, 1985; Lissauer *et al.*, 1988). Crater density variations are largest on Enceladus, where some areas are nearly as cratered as any in the Saturn system, and others show no craters at the best Voyager resolution. Only an upper limit may be placed on the age of the most recent resurfacing on Enceladus, due to the lack of information about the density of unresolved craters in the youngest areas. Tethys and Dione are generally more cratered than Enceladus, with a smaller variation in ages. Nevertheless, there is clear evidence on Dione and good evidence on Tethys for local resurfacing. The global pattern of resurfacing on all three satellites is poorly known due to coverage limitations. The most densely cratered surfaces on some of the moons, e.g. Mimas, might date back to a period of heavy post-accretional bombardment (Neukum, 1985).

On Mimas and Rhea the distribution of large craters is also spatially inhomogeneous (Smith *et al.*, 1981; Plescia and Boyce, 1982). However, statistical analyses (albeit based on limited numbers of craters) suggest that this degree of inhomogeneity is expected from spatially random cratering (Lissauer *et al.*, 1988). More complete coverage of the satellites' surfaces is needed to confirm this conclusion. Some areas on Rhea also show an apparent shortage of small craters (Plescia and Boyce, 1982)—an observation that could indicate local surface mantling or a paucity of small comets in the outer solar system (Zahnle *et al.*, 2003). However, there is a correlation of small crater density with illumination geometry (small craters appear scarcest where the sun is overhead (Lissauer *et al.*, 1988), so the observation is

inconclusive. Images with different illumination geometries and higher resolution are needed.

The crater density on Iapetus is large (Smith *et al.*, 1982; Plescia and Boyce, 1983; Lissauer *et al.*, 1988), but poorly known due to Voyager resolution limitations: the highest resolution Voyager image had a scale of 8.5 km/pixel. Craters on Iapetus are mainly observed in bright terrain. Only recently were craters also detected and counted in Voyager images of the northwestern edge of the dark terrain under photometrically favorable (low-sun) conditions (Denk *et al.*, 2000), indicating that the crater size – frequency distribution is similar in the measured parts of the dark and bright terrain. Interestingly, Rhea and Mimas, which lie deeper in Saturn’s gravity than Iapetus, appear to have crater densities lower than that of Iapetus by a factor of about 1.5 (Smith *et al.*, 1981, 1982; Plescia and Boyce, 1982, 1983; Lissauer *et al.*, 1988). Either Iapetus preserves a record of impacts by planetocentric debris that did not cross Rhea’s orbit (unlikely according to Zahnle *et al.*, 2003), or the surfaces of Mimas and Rhea are younger than that of Iapetus. We can potentially use the density of craters on Iapetus to calculate the probability that the other satellites have been collisionally disrupted since formation of Iapetus’ surface. One such calculation suggests multiple disruptions and reaccretions of most satellites inside Rhea (Smith *et al.*, 1982). Another hypothesis suggests that disruption is only probable for the small satellites – Atlas, Prometheus, Pandora, Janus, Telesto, and Calypso – whose irregular shapes suggest they are collisional remnants (Lissauer *et al.*, 1988).

Old surfaces in the system have, in general, less “steep” crater size – frequency distributions than young ones (Smith *et al.*, 1981, 1982; Plescia and Boyce, 1982; Lissauer *et al.*, 1988). A “steep” distribution indicates a rapid increase in the cumulative number of craters larger than a given diameter as that diameter decreases. One interpretation is that there were two impactor populations: an early Population I, with a “normal” amount of large impactors, and a later Population II with fewer large impactors (Smith *et al.*, 1981, 1982). In this scenario, young regions were cratered primarily by Population II. Another interpretation is that there was a single “steep” impactor population. Under this interpretation, young surfaces retain the shape of the production distribution, while old surfaces have had their curves “flattened” at large diameters by saturation-equilibrium effects. For the Galilean satellites, the high-resolution image data returned by the SSI camera onboard the Galileo Orbiter has not resolved this issue (Neukum, 1997; Neukum *et al.*, 1998; Chapman *et al.*, 1998; Zahnle *et al.*, 2003; Schenk *et al.*, 2004). Neukum (1985) and Wagner and Neukum (1996) found similarities between crater distributions in the inner solar system, the Galilean satellites of Jupiter, and the satellites of Saturn. This similarity, if real, suggests a similar projectile population, derived from collisionally evolved bodies, such as Main Belt asteroids, and a lunar-like impact cratering scenario with (1) a heavy bombardment period prior to about 3.3 Gyr and (2) a constant cratering rate ever since (Neukum, 1997; Neukum *et al.*, 1998).

Other investigators (Zahnle *et al.*, 1998, 2003; Schenk *et al.*, 2004; Chapman *et al.*, 1998; Bierhaus *et al.*, 2001), have presented evidence that comets play the

major role in impacting the jovian satellites. Zahnle *et al.* (1998, 2003) summarize observations and calculations showing that comets dominate the present-day cratering in the outer solar system. They note that while there is a paucity of small primary impacts on the Galilean satellites (Chapman *et al.*, 1998; Bierhaus *et al.*, 2001; Schenk *et al.*, 2004), the small craters on Triton, if primary rather than secondary craters, imply a population rich in small bodies. Small craters on Triton may be of heliocentric or planetocentric origin. Zahnle and colleagues considered two cases for Saturn, one in which the size – frequency distribution is like that at Jupiter, and the second in which small objects obey a collisional distribution. Resulting surface ages for the Saturnian moons are much younger in the second case. For example, average surface ages for Tethys, Dione, and Rhea may be as young as 1 Gyr or as old as 4 Gyr. Iapetus should have experienced little planeocentric cratering and must be very old.

Both global coverage and high-resolution images of the Saturnian satellites will help to extend the database of crater distributions at all sizes to another satellite system, crucial to interpreting the cratering record of these bodies and others in the outer solar system.

#### 2.1.2. Spectrophotometry

Multi-spectral imaging is a powerful tool for understanding the relationships between satellite compositions, geology, and surface modification processes, both endogenic and exogenic. In general, multi-spectral imaging can be used to attempt the difficult task of specific compositional identifications or to identify color units that have specific geologic associations. In particular, the nature and origin of the dark material in the Saturn satellite system, which as a collection of bodies is unusually bright, is of special interest (Owen *et al.*, 2001), both because dark material is rare in the Saturnian system and because of the inferred presence of organics on Iapetus and Titan. Variations in the scattering of light as a function of viewing and illumination geometry may also provide information on surface texture that can be associated with either local geology or with patterns expected from exogenic effects.

The geometric albedoes of many of the satellites are very high: the inner five major satellites, Mimas, Enceladus, Tethys, Dione, and Rhea, all have albedoes as high as, or higher than, the brightest icy satellite of Jupiter, Europa. Enceladus is extraordinarily bright, with a geometric albedo of  $\sim 1.0$  (Smith *et al.*, 1981; Buratti and Veverka, 1984; Buratti, 1988). There is little variability of albedo, and essentially no correlation of albedo with underlying geology. These observations are consistent with recent deposition of surface frost. Most of the other satellites are also bright, with Bond albedos of 0.45–0.6, and phase integrals of 0.7–0.9 (Buratti and Veverka, 1984).

Dione and Rhea both have bright leading and darker trailing hemispheres (Noland *et al.*, 1974; Franz and Millis, 1975; Smith *et al.*, 1981, 1982; Buratti and Veverka, 1984), and Rhea's normal reflectance is strikingly bimodal (Verbiscer and

Veverka, 1989). Tethys has a broad, darker north – south “stripe,” observed only at very low resolution, centered on its trailing hemisphere (Smith *et al.*, 1981; Buratti and Veverka, 1984). Dione and Rhea also have bright “wispy” markings transecting their trailing hemispheres (Smith *et al.*, 1981, 1982), and on part of Dione these appear to correlate roughly with some poorly observed tectonic features. However, the wispy markings have not been observed with favorable geometry or resolution, and their origin is unknown.

Current knowledge of the spectral properties of the major icy Saturnian satellites comes from a combination of ground-based telescopic and Voyager data. Telescopic near-infrared spectra ( $\sim 1\text{--}3.5\ \mu\text{m}$ ) show that essentially all of these objects are rich in water ice or frost on their surfaces (Johnson *et al.*, 1975). Color data from ultraviolet to near-infrared wavelengths ( $\sim 0.35\text{--}1.0\ \mu\text{m}$ ) give evidence for varying amounts of non-water ice constituents mixed with the ices and frosts on the surface (McCord *et al.*, 1971; Noland *et al.*, 1974; Morrison *et al.*, 1984; Cruikshank *et al.*, 1984; Cruikshank, 1981, 1999). (The low mean densities of the satellites for which we have mass estimates are consistent with a dominance of water ice. Densities of about  $1.0\text{--}1.5\ \text{g/cm}^3$  suggest that the satellites overall are predominately ice mixed with tens of percent of non-ice material: i.e., rock plus carbonaceous material.)

The satellites also have relatively bland colors in the visible and ultraviolet and are redder than expected for pure ice models but much less so than the Galilean satellites (McCord *et al.*, 1971; Noland *et al.*, 1974; Smith, *et al.*, 1981; Buratti *et al.*, 1990). (Interestingly, the ring colors are significantly redder than the inner satellites and comparable to the Galilean satellites (Lebofsky, *et al.*, 1971; Smith, *et al.*, 1981) in spite of also being primarily pure water ice.) Buratti *et al.* (1990) found broad-scale patterns of spectral variation without a high degree of correlation to geologic structures. The major exception is the so-called “wispy” terrain which appears as a distinct “bluish” unit, possibly indicating that it is a deposit of fresher frost of some type. The dark material on Iapetus is both dark and red, and it has been suggested that this material is similar to very dark red asteroids (so-called D-class) and to complex organic material produced in laboratory experiments (“Tholins” – Bell *et al.*, 1985; Wilson and Sagan, 1995). Hyperion, inward of Iapetus, appears to also be abnormally red, while Phoebe, probably a captured object, is representative of another class of dark, more spectrally neutral material.

Among the observational goals of the Cassini ISS team will be searching for spectral correlations with geologic units at high resolution. Spectral imaging of the Galilean satellites by Galileo has demonstrated the utility of such studies, and Cassini ISS has many more spectral bandpasses. On Jupiter’s satellite Europa, for instance, the near-infrared range of the CCD allows the separation of units with differing ice particle sizes that led to the discovery of “IR-bright” units not visible at shorter wavelengths; these results allowed the relative ages of the surface units to be determined (Geissler *et al.*, 1998). Comparisons of visible and near-infrared spectral units with those seen at longer wavelength by NIMS (whose improved Cassini counterpart is VIMS) have proven vital to understanding the geologic setting

of non-ice materials identified as hydrated salts by the NIMS experiment. Galileo found that dark, non-ice materials are concentrated in low areas on Europa and Ganymede (Oberst *et al.*, 1999).

Exogenic modification may mask local variations in composition or texture. Concentration of non-ice material by preferential removal of volatiles through evaporation, impact or sputtering has been considered as an important process, but its relative importance compared with collection of material from infalling meteoritic and ring material is unknown at present. The ambiguity concerning the origin of the unusually uniform spectral and photometric properties of Enceladus, mentioned in Section 2.1.1.3, is an example. Exogenic modification by the E ring on several other satellites besides Enceladus is suggested by near-IR photometry (Buratti *et al.*, 1998). Additionally, the hemispheric dichotomies exhibited by some of the other satellites has been suggested as arising from preferential bombardment of the leading sides of the satellites by cometary and meteoritic material (see Buratti *et al.*, 1990). The effects of radiation on the surface materials is another potential source of spectral modification. The identification of O<sub>3</sub> on Dione and Rhea (Noll *et al.*, 1996), probably in gas inclusions in the surface ices, is a piece of evidence suggesting radiation modification of the near surface.

Iapetus has perhaps the strangest photometric properties in the solar system. At low Voyager resolutions, the color properties across the hemispheres appear to vary as a smooth mixture of ice with the dark red material (Buratti and Mosher, 1995), but there are also hints that at high resolution, material might be very localized. Normal reflectance ranges from  $\sim 0.03$  near the apex of orbital motion to  $\sim 0.6$  near the poles (Squyres and Sagan, 1983; Goguen *et al.*, 1983; Squyres *et al.*, 1984). The dark material is reddish in color (Cruikshank *et al.*, 1983; Squyres *et al.*, 1984). The albedo pattern is symmetric about the apex, and photometric contours nearly parallel calculated impact flux contours. Along the boundary between bright and dark terrain there is evidence for topographic control of albedo, including dark-floored craters and bright slopes facing toward the antapex. Evaluation of the spectrum of dark components on Iapetus and Hyperion suggest similar materials on both bodies (Jarvis *et al.*, 2000).

Hypotheses proposed to explain the pattern of Iapetus' albedo (Cook and Franklin, 1970; Soter, 1974; Smith *et al.*, 1982; Squyres and Sagan, 1983; Bell *et al.*, 1985) include coating of the leading hemisphere with debris from Phoebe, and volcanic eruption or exposure by impact erosion of dark material indigenous to Iapetus. A case can be made that the varying impact flux has influenced the albedo pattern, but present poor resolution and signal-to-noise ratio make it impossible to evaluate confidently the relative roles of endogenic and exogenic processes. While debris from Phoebe (which is in a retrograde orbit) may add to the asymmetric impactor flux, it is unlikely that coating of Iapetus' surface with this material is the answer. Phoebe has a low normal reflectance of  $\sim 0.05$  (Simonelli *et al.*, 2000), but is spectrally neutral except for a slope in the 0.3–0.4  $\mu\text{m}$  range (Degawij *et al.*, 1980; Tholen and Zellner, 1983; Thomas *et al.*, 1983a) and a turndown from 0.9



to  $1.1\ \mu\text{m}$  (Tholen and Zellner, 1983). It shows some spatial variations in albedo, though little is known of their detail or origin, or about spatial variations in color.

Description of the satellites' photometric properties is limited by phase-angle coverage, which is spotty and in only a few cases extends past  $70^\circ$ . The fitting of Hapke's photometric function (Hapke, 1981, 1984, 1986) suggests high single-scattering albedos, regolith compaction similar to Moon's, and particle phase functions somewhat more backscattering than Moon's (Buratti, 1985). Estimation of surface roughness is virtually precluded by a shortage of high phase angle data.

### 2.1.3. *Determination and Refinement of Satellite Orbits and Masses*

Before the advent of spacecraft flybys, ground-based astrometric observations of orbital variations were the only means of determining satellite masses. Doppler tracking of the Cassini spacecraft during close satellite flybys will yield mass determinations for some of the satellites, but detailed analysis of satellite orbits and their variation over the Cassini tour from ISS images will be an invaluable complement. In addition to the mutual perturbations of all the satellites, there are three resonant relationships in the Saturnian satellite system that induce significant orbital variation between pairs of satellites: (i) Mimas and Tethys are involved in 2:1 resonance that modulates the inclination of both satellites; (ii) Enceladus and Dione are locked in a 2:1 resonance which leads to a significant forced component on the eccentricity of each satellite; and (iii) the 4:3 resonance between Titan and Hyperion has no effect on Titan but causes a large forced eccentricity (0.1042) on Hyperion. These resonant relationships are important because they can be used to determine the masses of some of the satellites involved.

Detailed knowledge of the orbits of the satellites and their variation derived from ISS observations is essential for the success of the Cassini mission. This is because the optical navigation of the spacecraft utilizes ISS images of distant satellites against the background stars to determine the position of the spacecraft. Such images are also used, in turn, to improve the orbits of the satellites and thereby help in targeting close flybys. The best ground-based astrometric observations of Saturn's larger satellites (such as Titan, Rhea, Tethys and Dione) have 1-sigma residuals of  $\sim 0.08$  arcsec, corresponding to positional errors of  $\sim 500$  km. For the smaller satellites (such as Mimas, Enceladus and Iapetus) the errors are  $\sim 1200$  km. Because Phoebe is so distant it is difficult to obtain plates or CCD frames of it with other satellites and so its positional error is currently  $\sim 6000$  km. The limits of ground-based astrometry will be overcome and the positional errors reduced by using the Cassini ISS data as they become available throughout the mission. Therefore, one of the end products of the mission will be sets of orbital elements for the satellites that can be used as starting values for long-term numerical simulations of the dynamical evolution of the system.

Accurate orbit determinations of the Trojan satellites can be used as independent checks on the masses of Tethys and Dione, and indeed any satellite that is found to have a co-orbital companion. This is because for small amplitude librations about



the equilibrium points,  $T \propto (M/m)^{1/2}$ , where  $T$  is the period of libration of the Trojan satellite,  $m$  the mass of the parent satellite and  $M$  the mass of Saturn. For Tethys and Dione the respective libration periods of their Trojan should be close to 660 and 775 days, respectively; Cassini should be able to observe several libration cycles.

The Janus and Epimetheus pair is unique in the solar system. Both satellites are in near-circular, near-equatorial orbits with an orbital separation of 50 km, which is less than or comparable to the smallest physical dimension of either object. However, rather than collide, a study of the three-body problem shows that although they come close to one another every 4 years, they cannot pass even though they affect each other's orbits. The resulting configuration is called a horseshoe orbit. At closest approach, the radial displacements of each satellite ( $\pm 10$  and  $\pm 40$  km from the mean semi-major axis for Janus and Epimetheus, respectively) are functions of their mass ratio and their separation in longitude is a function of the sum of their masses (Yoder *et al.*, 1983). Given that the Voyager spacecraft obtained resolved images of both Janus and Epimetheus, their volumes are known and astrometric observations have led to estimates of their densities of  $0.65 \pm 0.08$  and  $0.63 \pm 0.11$  g/cm<sup>3</sup>, respectively (Nicholson *et al.*, 1992). Therefore, these icy objects are significantly underdense and may be typical of the material of which the small satellites and rings are composed. A major goal for ISS will be to derive improved shape models and volumes for these satellites to combine with improved orbits in order to get better estimates for their densities. During the nominal tour, an orbital switch of Janus and Epimetheus is due to occur in February 2006 when, over the course of a few days, Janus will move inwards by  $\sim 20$  km while Epimetheus moves outwards by  $\sim 80$  km. Observations of the switch have a particular importance for satellite and ring studies (see Section 2.3.1.2).

#### 2.1.4. *Summary of Satellite Imaging Objectives*

With these fundamental scientific questions in mind, the satellite science objectives for the Cassini ISS experiment include the following.

*All satellites:* Complete high-resolution global coverage to make geodetic maps, characterize the surface, and identify geologic resurfacing and tectonic mechanisms on all satellites; Acquire high-resolution and multiple-geometry images of cratered terrains for crater formation, size–frequency, and spatial distribution studies; Establish the spectrophotometric properties of surface units over a broader and more complete range of viewing and illumination geometries than currently available; Determine the nature of the dark material in the Saturn system; Establish the details of satellite shape to draw inferences about internal structure; Measure librations, where present.

Utilize the information gathered on all the satellites on tectonic patterns, albedo patterns, projectile populations, resurfacing events, composition, masses, densities, etc. to formulate a history (i.e., origin scenarios and evolution) of the entire Saturnian satellite system; Determine what is unique about this system's origin

and evolution, and how it differs from the satellite systems of Jupiter, Uranus, and Neptune.

Some satellite-specific objectives are given as follows.

- Mimas, Enceladus, Tethys, Dione, Rhea: Establish detailed morphology of topographic grooves to investigate their formation mechanism.
- Enceladus, Tethys, Dione: Examine resurfaced regions at high resolution, to investigate the resurfacing mechanism.
- Enceladus, Tethys, Rhea: Determine topography of relaxed craters, to infer rheology.
- Tethys, Dione, Rhea, Iapetus: Characterize global-scale photometric variations.
- Dione, Rhea: Obtain coverage at high resolution and a range of illumination and viewing geometries of “wispy” markings.
- Enceladus: Determine crater densities in youngest regions. Perform regular monitoring to search for eruptive events. Measure libration amplitudes as evidence of spin-orbit resonance and tidal heating. Use crater morphologies and dimensions to constrain the depth to a potential water mantle (or “subsurface ocean”).
- Tethys: Establish the morphologic details of Ithaca Chasma.
- Dione: Obtain high-incidence-angle coverage of ridges to confirm topography and global distribution.
- Rhea: Characterize the global distribution and orientations of polygonal crater rims.
- Hyperion: Investigate the details of color and albedo variations to help constrain the nature and origin of the dark material.
- Iapetus: Establish the details of the distribution of dark material at much higher resolution, particularly at the dark/light boundary. Establish the details of photometric properties and topography on the leading hemisphere, using images with high signal/noise ratio.
- Phoebe: Investigate the details of color and albedo variations to help constrain the nature and origin of surface material.
- All small irregular satellites: Globally characterize these bodies – cratering statistics, surface topography and morphology, shapes, colors, etc. – at high resolution. Search for evidence for collisional fragmentation and evidence of unique surface processes. Determine color variations among satellite terrains and differences or similarities to ring colors.
- Tethys/Mimas, Enceladus/Dione, Titan/Hyperion, Janus/Epimetheus: Use refined measures of their orbital elements and evolution to determine accurate masses and densities.

Observational plans to accomplish these goals are as follows.

- Global, low-resolution (few km/pixel, or better) observations covering as wide a range of longitudes as possible at approximately regular phase-angle increments, in concert with other remote sensing instruments, to characterize the global spectrophotometric properties of the satellites.
- At those times when satellites fill a substantial fraction of the NAC FOV, imaging from different viewing geometries throughout the ‘encounter’ allows for high-resolution morphology and color, as well as stereo observations for topography, and limb observations for shape.
- During those times outside of the ‘targeted’ flybys, when the satellite still subtends more than a NAC FOV, specific targets on the surface are selected on the basis of the low-resolution views obtained by Voyager. Many of these mosaics are in areas where there is essentially no useful Voyager coverage and thus are purely exploratory. The speed of the flybys determines roughly how many images can be obtained at these close ranges. The target characteristics influence whether stereo or color is sought at very high resolution over limited areas.
- ‘Targeted’ flyby imaging, to give very high-resolution (tens of meters per pixel) morphology of specific features (e.g., Figure 4) in those instances where Voyager data indicate potentially diagnostic features, such as structural forms, and to make surveys at high resolution where we currently have no specific geologic expectations. Color and stereo are important parts of these sequences, although the high angular rates restrict the amount of such coverage. Wide-angle images are also taken during close passes, as they can provide context and obtain more regional views at specific geometries than can be done solely with the NAC.
- Some very high-phase observations of Enceladus are planned to seek any associated particles or venting phenomena. Some of these are obtained while the moon is in the shadow of Saturn.

### 2.1.5. *Combined Studies with Other Cassini Instruments*

Many instruments on the Cassini Orbiter in addition to ISS will observe icy satellite surfaces. These include the Composite Infrared Spectrometer (CIRS), the VIMS, the Ultraviolet Imaging Spectrograph (UVIS), and RADAR. Coordinated observations and scientific analyses of satellites are planned utilizing data from all instruments. ISS–VIMS coordination is important since the two instruments are functionally complimentary and co-analysis is scientifically powerful. (Co-analysis between comparable experiments on Galileo (SSI and NIMS) has proven fruitful (e.g., Lopes-Gautier *et al.*, 1998; Fanale *et al.*, 1998).) The spectrometer is limited to covering relatively small areas at moderate spatial resolution ( $\sim 1$  km/pixel or better) because of the high data volume produced by hyperspectral imaging and short period at close range to targets. The imaging experiment is limited with respect to compositional interpretations by the spectral range ( $0.25\text{--}1.1\ \mu\text{m}$  for ISS versus  $0.35\text{--}5.1\ \mu\text{m}$  for VIMS) and spectral resolution (even though ISS has many color filters). With a coordinated ISS–VIMS observation plan it is possible to achieve (1)

global mapping of color units with ISS (via wide-angle camera (WAC) when close and NAC when distant); (2) VIMS spectra that sample all color units at moderate resolution, to enable more definitive compositional interpretations of the ISS color units, and (3) high-resolution and stereo images of surface features for interpretation of processes (impact, tectonic, etc.). RADAR should be synergistic with ISS images and VIMS spectra of icy satellite surfaces, providing very different information (such as subsurface structure). CIRS and UVIS spectra, giving temperature and composition, can be related to the geologic context of ISS images.

## 2.2. SATURN'S ATMOSPHERE

The state of our knowledge of Saturn's atmosphere is immature in comparison with that of Jupiter's. As a starter, the colder temperatures of the Saturnian atmosphere result in a visible cloud deck being lower in the atmosphere, and overlain by a greater abundance of haze, than for Jupiter, so contrasts are intrinsically lower. Moreover, the jovian atmosphere has been more extensively studied – both from spacecraft and from Hubble Space Telescope (HST) – than Saturn's. For example, in the derivation of cloud-tracked winds, the Voyager imaging team gathered 10 times more wind vectors from Jupiter than from Saturn, owing entirely to the poor visibility of cloud features on the latter. The latest advances in jovian atmospheric science were made, in fact, by the Cassini ISS during the Cassini December 2000 Jupiter flyby (Porco *et al.*, 2003).

Nonetheless, what we do know about Saturn is that, unlike the apparent stability of the jovian jets, Saturn's atmosphere is remarkably changeable. HST images during 1990–1991 captured the eruption of a giant equatorial storm (Sanchez-Lavega *et al.*, 1991), and other similar disturbances in 1994–1997 (Sanchez-Lavega *et al.*, 1996, 1999). And recent observations (Sanchez-Lavega *et al.*, 2003) have suggested that the equatorial jet on Saturn has decreased in speed by a factor of two from 1996 to 2002, although it is not clear whether or not these recent observations sample the same level in the vertical wind profile as earlier measurements.

Cassini ISS goals are focused on using the unique spectral and photopolarimetric capabilities of the instrument to derive the observational quantities necessary for estimating the cloud and aerosol structure and energy balance in the atmosphere, to search for previously unseen atmospheric phenomena, to measure and understand the three-dimensional general circulation of the atmosphere, including indirect inferences about conditions below the visible cloud tops, and to measure the spatial, spectral, and temporal properties of Saturn's auroral and lightning emissions, the latter being especially important as tracers of atmospheric convection.

### 2.2.1. Photometric and Polarimetric Studies of Saturn

The spectrophotometric capabilities of the ISS, and its photometric precision and linearity, will be used to singular advantage in the study of the processes energizing the Saturn atmosphere. Accurate knowledge of the intensity, spectral variation, and

linear polarization state of light reflected from Saturn can be used to address a variety of atmospheric objectives, listed as follows.

1. Deriving the optical properties and vertical distribution of aerosols to develop quantitative models of radiative forcing, and investigate the coupled dynamical, radiative, chemical and aerosol microphysical processes that determine the state of the upper troposphere and stratosphere. This objective addresses the mean meridional circulation, vertical and latitudinal transports and seasonal effects.
2. Improving our understanding of the formation mechanisms and composition of aerosols in the stratosphere and upper troposphere by comparing their spatial distribution with models of their source regions, and by interpreting diagnostic photometric and polarimetric signatures such as halo features at specific scattering angles.

Radiative balance calculations for meridional circulation models require knowledge of methane absorption, particle distribution, particle single scattering albedo, optical depth, and scattering phase function throughout the entire spectrum. No single instrument can provide these quantities over the whole spectrum. The ISS can (with its suite of filters and observing strategy) provide information on methane absorption, aerosol distributions and optical properties from about 250 to 1000 nm. Knowledge of aerosol optical properties can be used to infer aerosol physical properties (size, shape, imaginary refractive index) which can be used to constrain aerosol microphysical models.

Aerosol single-scattering albedo, scattering phase function and linear polarization can be deduced from the types of measurements ISS will make, as summarized in Table III. The measurements listed in Table III are compared with multiple-scattering models to derive the phase function, polarization and single-scattering albedo. For Saturn the derivation of particle polarization at visible wavelengths relies on knowledge of the vertical structure as molecular scattering is strongly polarized. The vertical structure and aerosol properties must be modeled simultaneously.

TABLE III  
ISS diagnostics for aerosol optical properties.

Aerosol property	Measurement
Single-scattering albedo	Intensity at disk center at low phase angles at continuum wavelengths
Derivative of single-scattering albedo with depth	Limb darkening at low phase angles at continuum wavelengths
Phase Function	Behavior of intensity with phase angle
Polarization	Behavior of polarization with phase angle
Derivative of single-scattering polarization with depth	Center-to-limb behavior of the polarization

Aerosol optical properties lead to an estimate of aerosol physical properties. It is unlikely that particles are spherically shaped because the particles are most likely in the solid phase. Particles produced photochemically or as a result of auroral bombardment in Saturn's upper atmosphere may be aggregates of small ( $r \ll 1 \mu\text{m}$ ) particles (West and Smith, 1991). Unlike spheres, these types of particles can have phase functions that are forward scattering while at the same time producing strong positive linear polarization near  $90^\circ$  scattering angle. Table IV summarizes how optical properties will be used to infer physical properties.

Information on the vertical structure of the aerosols is carried by the same intensity and polarization data used for aerosol optical properties. The ISS has available four types of measurements for studies of vertical structure, listed in Table V.

The suite of measurements listed in Tables III and V will be combined to yield information on the vertical structure and optical properties of atmospheric aerosols. Images in each of the three short-wave (400–700 nm) polarizing filters on the NAC will be combined to produce linear polarization images. The orientations of the

TABLE IV  
ISS diagnostics for aerosol physical properties.

Aerosol optical property	Derived physical property
Phase function in forward scattering ( $\sim 20^\circ$ to $40^\circ$ scattering angle)	Particle effective radius
Single scattering albedo	Imaginary part of refractive index, particle composition
Halo feature	Crystal shape, refractive index, and composition
Polarization	Particle shape and effective radius (contingent on available laboratory or theoretical results)
Dependence of extinction cross-section on wavelength	Particle shape, after radius and imaginary refractive index are determined

TABLE V  
ISS diagnostics for aerosol vertical structure.

Measurement technique	Comments
Limb images	Vertical profiling (6 km/pixel at $16R_S$ in the NAC); Stratospheric vertical coverage to 150 mb at $1 \mu\text{m}$
Methane band photometry	ISS has three methane filters that probe to different depths
Polarimetry near $0.4 \mu\text{m}$ wavelength	Rayleigh scattering is highly polarized near $90^\circ$ scattering angle
UV center-to-limb photometry	Probes altitudes of UV-absorbers



polarization axes of these filters are offset by  $0^\circ$ ,  $60^\circ$  and  $120^\circ$  from the line in the image plane perpendicular to the Z-axis of the spacecraft. We estimate an uncertainty of  $\pm 0.5\%$  in the magnitude of linear polarization if  $5 \times 5$  pixel regions are summed. Two orthogonally oriented near-IR (700–1100 nm) polarizers are mounted in the WAC filter wheel. These give a good measure of the linear polarization, provided the spacecraft Z-axis is approximately parallel or perpendicular to the plane of scattering. Both short- and long-wave polarizers can be combined with passband filters, including methane filters to measure the wavelength dependence of the polarization. The NAC filter wheel contains a single near-IR polarizer which can be used to filter polarized light and provides deeper penetration of the atmosphere at intermediate phase angles.

Our measurement strategy for Saturn calls for images at many wavelengths, over the globe, and at many solar incidence, emission and phase angles. Of the spacecraft encounters with Saturn thus far, only the Pioneer imagers obtained good phase-angle coverage, but only at two wavelengths and not sufficiently dense in phase-angle coverage to look for halo features. During the Saturn tour, we will obtain images of Saturn at many wavelengths from the near-UV to near-IR, in three methane bands, and with polarization filters. The requirement to orient the spacecraft in order to align the axes of the polarizers with the scattering plane posed real but manageable operational constraints on observation planning.

Global views with the NAC are possible only if the spacecraft is greater than about  $60 R_s$  from Saturn; at closer range, the required number of images and observing time to cover the planet is prohibitive. Therefore, the Saturn approach period and the apoapses of the most distant orbits are the best times for global coverage in the UV and in the short-wave polarizing filters. Phase-angle coverage will be built up gradually over the tour. We will take advantage of special circumstances during the orbit. The orbital characteristics of the tour will permit good coverage in both hemispheres, especially at high latitudes on inclined orbits. We will make use of opportunities to photograph stars near the limb in order to establish accurate altitudes for limb hazes.

### 2.2.2. *Atmospheric Dynamics and Thermodynamic Structure*

The first-order science objective for the ISS atmospheric dynamics investigation is to determine the processes responsible for maintaining the banded alternating jet and cloud structure on Saturn. The only direct information comes from visible cloud levels and above, while the relevant driving mechanisms have their roots below. Thus, the challenge for Cassini ISS is to use imaging to infer as much as possible about conditions at depth. Voyager satisfactorily observed the cloud-top mean zonal wind field on Saturn (cf. Ingersoll *et al.*, 1984), and Cassini ISS will do the same, with the specific objective of verifying recent suggestions of weakening of the equatorial jet. We will document such changes at much higher resolution than is possible from HST, increasing confidence that the changes are associated with actual winds rather than wave motions. Multi-spectral imaging will offer the

possibility of detecting vertical shears in these winds and will allow us to determine whether the observed changes in the mean zonal wind of the equatorial jet are due primarily to changes in the wind at a given pressure level or to an upward shift of the visible cloud top after the disturbances of the 1990s. Observations of high latitudes in both hemispheres will allow us to extend our knowledge of the jet structure on Saturn farther poleward than was possible with Voyager, just as we did on Jupiter (Porco *et al.*, 2003), though observations of the north pole will not take place until after the nominal 4-year mission when that pole is finally illuminated by sunlight. Accurate observations of flow curvature can be combined with potential vorticity conservation and mixing concepts to learn more about the state of the atmosphere below the visible cloud level (cf. Dowling and Ingersoll, 1989; Allison *et al.*, 1995; Allison, 2000). However, observations of mean zonal winds alone are not sufficient to constrain the responsible dynamical mechanisms.

To understand jovian planet dynamics at the process level, additional information is required.

- (a) Voyager imagery indicates a variety of eddies on the jovian planets. Do these eddies maintain or deplete the jets (Ingersoll *et al.*, 2000), or is their role only secondary to that of other processes? Are the important drivers tied to deep-seated convection or do they originate in a shallower “weather layer” near and below the visible cloud tops? To understand Saturn’s heat and momentum budgets, we must observe eddy fluxes and eddy-mean kinetic energy conversions. Estimates from Voyager cloud-tracked winds exist, but the sampling is inadequate and perhaps biased. Over a period of three Saturn rotations (1.25 days) of useful imaging for cloud tracking (at resolutions of 50–100 km/pixel), Voyager obtained about 800 wind vectors, about 10% of that observed by Voyager at Jupiter because of Saturn’s lower contrast at visible wavelengths. RMS deviations from the mean wind speeds at different latitudes varied inversely as the square root of the number of observations, indicating that real eddy motions were not being measured, i.e., a  $S/N \leq 1$ . For Cassini to diagnose eddy motions reliably, a 10:1  $S/N$  is required, necessitating a wind vector inventory 2 orders of magnitude larger than that acquired by Voyager.
- (b) Mean meridional motions are diagnostic of deviations from geostrophic balance and hence provide clues about either thermally forced overturning circulations or mechanically driven (i.e., by eddy momentum flux convergences) cells. The sign of the convergence of the meridional wind indicates the global pattern of upwelling and downwelling and thus gives insights into cloud formation and dissipation processes as well as observed spatial variations in condensable gas concentrations. Meridional winds are anticipated to be several orders of magnitude weaker than mean zonal winds and perhaps comparable to the eddy wind components. Thus, the observational requirements are similar to those described in (a). In addition, since pointing errors can alias a small fraction of the zonal wind into a spurious first-order meridional wind, monitoring of

meridional motions requires that NAC cloud-tracking mosaics be accompanied by single-frame WAC images of the entire planet (or at least a large fraction that includes much of the bright limb) for the most accurate navigation possible.

- (c) The objective information acquired from circulation statistics is only one of the two complementary ways of observing jovian planet dynamics. By creating movies of the Saturn atmosphere in motion, we can observe the life cycle of vortices as they merge, split, or oscillate (Ingersoll, 1990; Polvani *et al.*, 1990; Li *et al.*, 2004; see movies of the Jupiter atmosphere at <http://ciclops.org>). The nature and time scales of these nonlinear interactions provide information about the vertical structure and depth of the layer in which they occur and hence constrain candidate theories for their formation. Movies also allow us to visually observe the eddy–jet interactions responsible for the eddy fluxes described earlier. They can be used to determine propagation characteristics of planetary-scale and mesoscale waves, which in turn constrain the unknown deep vertical stratification (cf. Allison *et al.*, 1990). Finally, movies can capture the rapid evolution of small-scale clouds typically interpreted as being the visible evidence of outflow at the tops of deep convective updrafts and hence diagnostic of Saturn’s deep water abundance and stability. The presence of near-infrared continuum, weak methane, and strong methane band filters on the NAC allows us to determine the optical thickness and top heights of such clouds and more confidently identify them as the products of moist convection (Banfield *et al.*, 1998; Gierasch *et al.*, 2000; Porco *et al.*, 2003). The observational strategy for Saturn movies is repeated multi-spectral global and regional imaging; a proper imaging sequence design can satisfy the requirements for both movies and cloud-tracking simultaneously (Porco *et al.*, 2003).
- (d) All the strategies described earlier infer information about the deep Saturn atmosphere indirectly from cloud-level signals. An opportunity for more direct sensing of deeper levels arises if Saturn has a sufficient inventory of water to experience deep moist convection (cf. Del Genio and McGrattan, 1990; Hueso and Sanchez-Lavega, 2001). If the lapse rate above the condensation level exceeds the moist adiabatic lapse rate, cloud-scale updrafts may be vigorous enough in some places to mix supercooled liquid water above the freezing level into regions of ice formation, and the resulting interaction can be expected to generate lightning. Jupiter lightning and moist convection detection by Galileo and Cassini (Little *et al.*, 1999; Porco *et al.*, 2003) has shown that convective storms occur only on the poleward sides of the eastward jets, i.e., in the cyclonic shear zones. This observation has broad implications because it implies that the belts are regions of net upwelling motion and convergence at depth, just the opposite of the traditional picture (Ingersoll *et al.*, 2000; Porco *et al.*, 2003). ISS results at Jupiter also confirmed that convection and lightning have different latitudinal distributions, implying cooler temperatures at higher latitudes above the condensation level. Finally, differences in lightning frequency on Jupiter seen through a narrow-band Cassini ISS filter and a

broad-band Galileo filter can be interpreted as an indicator of super-solar water abundance (Dyudina *et al.*, 2004). Thus, our goals at Saturn are to detect both moist convection and lightning, map their latitudinal distributions, and define the spectral characteristics.

The science objectives described earlier can be met with the following observational strategies.

On day-side apoapsis orbits.

- The majority of imaging for atmospheric dynamics will take place on orbits with distant day-side apoapses (of order  $60 R_s$  or greater, ideally) at low phase angles. This allows for maximum contrast in cloud features formed in reflected sunlight (a priority on Saturn, whose overlying haze reduces feature contrast relative to Jupiter), and allows global coverage to be obtained at resolutions comparable to that of Voyager with reasonably sized NAC mosaics plus single WAC frames of the globe for navigation. The best opportunities occur on orbits 49–52, when we will acquire repeated near-global mosaics near apoapsis (Fig-

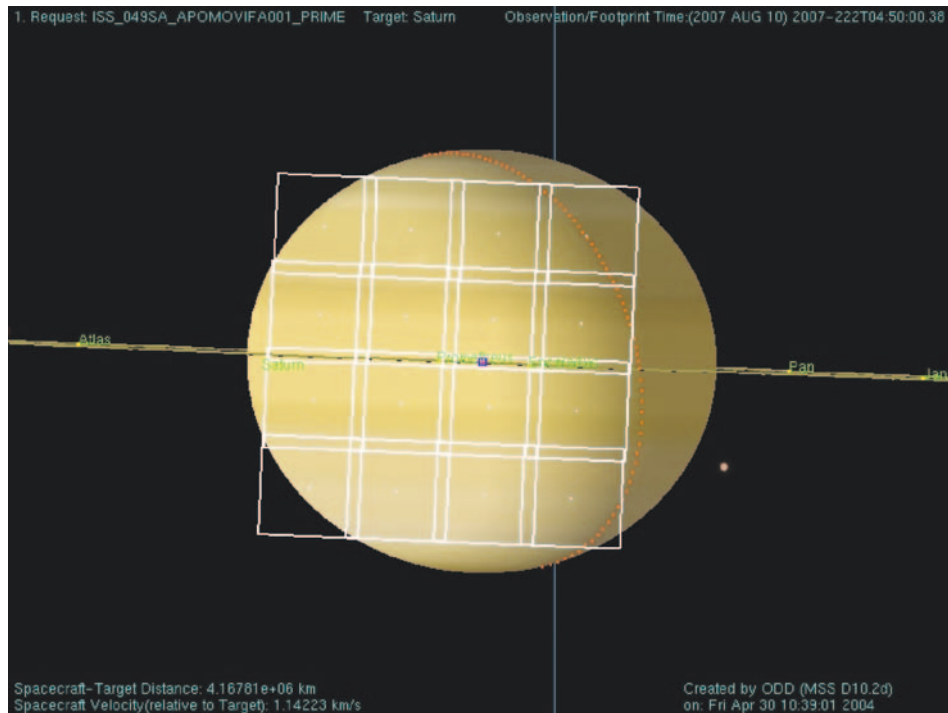


Figure 8. Typical mosaic of NAC frames of Saturn from the apoapsis of Rev 49, one of the most distant in the tour, which constitutes a single ‘picket’ or snapshot of the planet as it rotates. Mosaics like these are repeated every 1.75 h over a Saturn rotation, and then again over weeks (minus downlink periods), to form movie sequences for studying atmospheric dynamics.

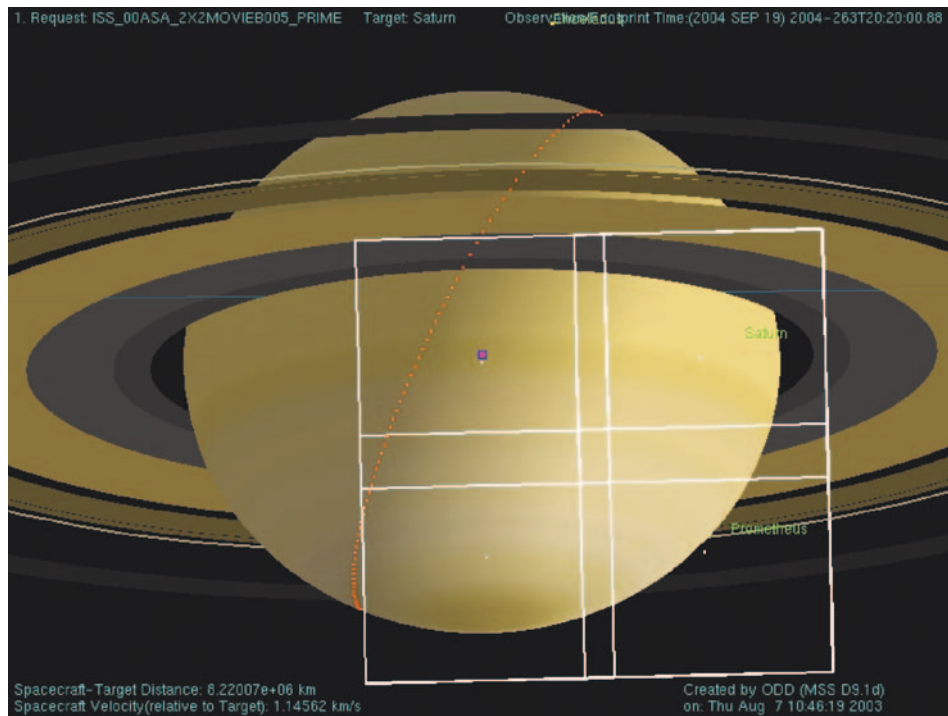


Figure 9. Typical ISS NAC mosaic of Saturn in 13 spectral filters early in the tour on Rev A for the study of atmospheric dynamics and spectrophotometry.

ure 8) in two filters (methane band and continuum) and higher-resolution strip mosaics along specific latitude bands outbound and inbound near  $40 R_s$  in six filters.

- Similar opportunities occur to a lesser extent during 96 days on approach to Saturn at lower spatial resolution and intermediate phase angles (Figure 1) but with better spectral coverage (generally, five or more visible and near-IR filters) and in orbit A, when moderate phase angles are sampled at very large distances (Figure 9).
- During orbits 4–20, when apoapses are close to  $40 R_s$  and phase angles moderate, two-color mosaics will be acquired in high-resolution longitudinal strips at different latitudes.

Each mosaic usefully observes only about a  $70^\circ$  wide swath on Saturn centered on nadir (outside this range, foreshortening and contrast loss due to the increasing slant path limit feature discrimination), and it is necessary to observe each meridian once per Saturn rotation to detect motions at all longitudes. To accomplish this, we will acquire mosaic sequences every 1.7–2.13 h as often as possible while the spacecraft is at least  $60 R_s$  distant from Saturn.

On night-side apoapsis orbits.

- Lightning storms flash once every few seconds, and the camera shutter must be open at least that long to reliably see the flashes. However, a day-side image saturates at these long exposures, so the lightning search must be conducted on the night side. At Saturn, reflected light from the rings illuminates much of the night side and tends to saturate the long-exposure images, though the rings will become fainter and this effect will be diminished as the tour progresses and the Sun descends towards Saturn's equator plane. During the Cassini tour, the best place to avoid both ring shine and direct sunlight is the north polar region, because the rings are over the horizon at latitudes greater than  $\sim 65^\circ$  and the north pole is in darkness during this season. Orbits 27–36 offer the best opportunities, because apoapse is over the north pole.
- We will also search for lightning on the large-apoapsis, high phase angle orbits 21–28, which offer better spatial coverage albeit with the potential for more ring-shine contamination. We will use a mix of exposure times and filters (broad-band clear, broad-band red, and narrow-band  $H\alpha$ ) to determine the best lightning detection strategy and to define its spectral signature. The spatial distribution, spectral range, and temporal variation of the emissions all are of interest. Because the distribution of lightning is not known, sequences are designed to scan the night-side atmosphere. In some cases, the same terrain is viewed on the day and night sides so that lightning strikes can be associated with specific cloud structures. A multi-instrument auroral campaign occurs in orbits 70–74.

'Feature track' sequences target specific atmospheric regions with NAC or WAC mosaics during several periapsis portions of orbits, when the NAC FOV is smaller than Saturn. Multi-spectral, spatial mosaics are acquired at several time steps, following a particular feature from day side to night side as was done by Galileo and Cassini at Jupiter (Little *et al.*, 1999; Gierasch *et al.*, 2000; Porco *et al.*, 2003). The day-side images allow one to study motions, cloud heights, and radiative properties, and the night-side images allow one to look for lightning. Targets vary throughout the tour, but include the equatorial and polar regions.

### 2.2.3. Auroral Phenomena

Trauger *et al.* (1998) present images taken by the HST of Saturn's UV aurora. The observations show the bright auroral arc on the day side of the planet. In contrast, ISS can image the aurora in visible light on the night side of the planet, and with much higher spatial resolution, than HST; it did so at Jupiter (Porco *et al.*, 2003). These differences are important for several reasons. First, the visible emissions represent less energetic processes than the UV emissions, and may be occurring by different mechanisms. Second, the day/night differences may reflect differences in the magnetic field upstream and downstream of the planet in the solar wind flow.



Third, the higher spatial resolution yields edge-on views of the limb that give the altitude of the aurora. One can also study the relation of the aurora to magnetic field lines and the time-dependent behavior of small features within the aurora. Such features might be monitored by particles and fields instruments as the spacecraft flies through the magnetic field lines that connect to surface features seen by ISS.

Aurora observations were made at Jupiter by Galileo (Ingersoll *et al.*, 1998; Vasavada *et al.*, 1999), and have proved useful in all the above ways. Cassini repeated the Galileo observations 4 years later (Porco *et al.*, 2003), and observed changes in position over periods of 10 h, 12 days, and 4 years. Some changes are due to local time-of-day effects at points on the planet. Other changes are due to the dynamic nature of the aurora. The Galileo Jupiter observations also revealed auroral-type emissions at the base of the magnetic flux tube that connects to Io. It will be interesting to see if any of Saturn's satellites exhibit similar phenomena. As with the lightning observations, the best opportunities are on orbits 27–36 when the apoapse of Cassini's orbit is over Saturn's north pole.

#### 2.2.4. Combined Studies with Other Cassini Instruments

Eddy heat fluxes have never been measured on any planet except Earth. Detection of correlated wind and temperature fluctuations would be an interesting and fundamental contribution to our understanding of Saturn dynamics, indicating whether baroclinic conversion analogous to that which dominates terrestrial midlatitude storms occurs on jovian planets. CIRS will retrieve temperatures just above the ISS viewing altitudes, though at much lower spatial resolution. CIRS may also retrieve the H<sub>2</sub> *ortho/para* ratio and abundances of condensable gases like ammonia (NH<sub>3</sub>), which are sensitive measures of upwelling and downwelling. Thus, coordinated ISS – CIRS scans across the Saturn disk are planned. This is best done near periapse when CIRS resolution is <1000 km, which is sufficient to resolve the large-scale eddies. Having 10 to 12 of these so-called “feature tracks” would allow one to sample all latitudes and dynamical regions.

Similar comments apply to coordinated VIMS–ISS observations. Because VIMS can measure in the strong absorption bands of methane and ammonia, as well as in the window regions, it can discriminate both high and low clouds in the atmosphere. ISS has a similar capability with filters that are sensitive to methane absorptions between 700 and 1000 nm (Banfield *et al.*, 1998). ISS has better spatial resolution than VIMS, but VIMS has better spectral coverage. Together they provide outstanding information on cloud heights and vertical structure. One goal, not yet realized for any of the outer planets, is to directly measure vertical wind shear, e.g., the variation of horizontal wind with altitude.

UVIS is generally sensitive to higher altitudes than ISS and the other instruments. Coordinated observations might yield evidence that dynamical features extend from cloud top levels into the upper atmosphere.

The observational strategy for measuring cloud-tracked winds at periapse is similar to that employed at Jupiter by both Galileo (Vasavada *et al.*, 1998) and

Cassini (Porco *et al.*, 2003). The problem is that the planet more than fills the FOV of the Cassini WAC, and the limb cannot be used directly as a reference to determine camera pointing. The same problem occurs with Galileo, which has no WAC to determine pointing for the NAC. In both cases, camera pointing is determined either by mosaicing in from the limb or by referencing to the large-scale features and jets, which are nearly steady in time. The small-scale motions are then determined relative to the large-scale features. For measurements of eddy fluxes and the eddy life cycles, these methods work quite well (Vasavada *et al.*, 1998).

The ISS shares many aerosol/radiation science goals with UVIS and VIMS. The UVIS will probe to shorter wavelengths than ISS while VIMS will probe at longer wavelengths. The shorter UV wavelengths and VIMS data in strong methane bands will be more sensitive than ISS to aerosols high in the stratosphere. The combined wavelength coverage of all three instruments will more tightly constrain aerosol models than is possible with any single instrument. The net radiative heating, which can be inferred from measurements with all three instruments, can be combined with information on net radiative (thermal-infrared) cooling provided by the CIRS instrument to deduce net heating and cooling for studies of stratospheric dynamics (West *et al.*, 1992).

### 2.3. SATURN'S RINGS

Voyager observations from a variety of experiments (imaging, stellar occultations, radio occultations) revealed a remarkable architectural diversity within the rings of all four giant planets. Saturn's rings are representative of all rings in being home to many of the types of features found around Jupiter, Uranus and Neptune. There are eccentric, inclined narrow rings; non-axisymmetric and sharp ring edges; broad, tenuous rings; incomplete arc-like ring segments; small moons 'shepherding' nearby ring material; tightly wound spiral waves; axisymmetric but radially irregular features; azimuthally asymmetric ring brightness variations; and a great deal more. A collisional disk if left to itself should spread until it is featureless. But Saturn's main rings are far from featureless.

Characterizing ring structure at a spatial scale finer, and a spectral range wider, than previously possible, determining its root causes, and searching for secular changes in the rings both during the multi-year long Cassini mission and since the Voyager era are prime objectives of the ISS ring investigations at Saturn. The latter in particular, if successful, will provide a direct measure of ring evolution time scales – at the heart of which is the rate at which angular momentum is being exchanged within and/or removed from the ring – and could definitively replace current theoretical and poorly constrained estimates of ring age and lifetime.

Ring structure may either be externally or internally caused. In the case of the main Saturnian rings, consisting primarily of cm- to meter-sized

particles – external causes can vary from meteoroid impacts to the gravitational perturbations of nearby or distant satellites or the non-sphericity of the planet's gravity field (see Section 2.3.1). Internal causes have their origins in the free mechanical energy derived from the global Keplerian angular velocity shear across the rings balanced by the energy dissipation and viscosity that arises from highly inelastic particle collisions. Even in the absence of external forcing, radial variations in particle number density (i.e., the number of particles per unit volume) across the rings may develop and self-perpetuate from initial local radial gradients in particular characteristics of the particle distribution: e.g., viscosity or effective local velocity shear in the presence of finite-sized particles (see Section 2.3.2). In the case of non-collisional tenuous rings made of dust-sized particles, atmospheric drag, Poynting – Robertson drag, and electromagnetic effects are among the external causes that can have dramatic and observable effects (Section 2.3.5). In each of these processes, a torque is imposed on a local patch of ring, angular momentum, the lifeblood of a collisional ring system, is exchanged, and the ring system evolves.

### 2.3.1. *Ring Structure: External Perturbations*

The greatest success in explaining the origins and gross characteristics of the ring features that are composed of particles on longitudinally phased, eccentric and/or inclined orbits has been achieved by relying on the perturbations of satellites, either outside, or embedded within, the ring system. Most of the structure in the intermediate density A ring, for example, can be explained by the interactions with external satellites which force a sizable number of density and bending waves in the A ring at the location of their gravitational resonances, or by the presence of a tiny moon in the rings which opens and maintains a gap and also sculpts its wavy edges, such as the Encke gap. (The degree to which perturbations on ring particle orbits create visible disturbances in a featureless disk system depends on the ring's natural ability to distribute the change in angular momentum resulting from the imposed torque. If the angular momentum removed, deposited or exchanged is less than the ring's natural ability to carry the excess/deficit away from the excitation region, then the ring response (if any) will take the form of a wave. On the other hand, if the external torque is greater than this natural ring 'viscous' torque, then the ring will respond by opening a gap, presumably with sharp edges: the particles themselves must physically move to accommodate the external driving.)

However, despite the success in associating ring features with satellite perturbations, the detailed characteristics of most of these non-axisymmetric features are not completely understood.

**2.3.1.1. *Ring Edges.*** The origin and maintenance of extremely sharp edges ( $</\sim 1$  km) within the vast expanse of otherwise continuous ring material is of considerable interest. 'Flux reversal' – the phenomenon by which a resonantly perturbed ring may actually contribute to its own edge sharpening – has been predicted to occur in these locales (Borderies *et al.*, 1982, 1983). The two strongest resonant

perturbations in Saturn's rings are in fact responsible for the very sharp edges of the major rings A and B, as well as for their kinematics and non-axisymmetric shapes: i.e., the two-lobed rotating pattern of radial oscillations observed in the sharp outer edge of the B ring, and the seven-lobed rotating distortion observed in the outer A ring edge, are due to the Mimas 2:1 and the Janus/Epimetheus 7:6 Lindblad resonances, respectively (Porco *et al.*, 1984b).

In a simple model of resonant perturbations, the amplitude of a radial distortion is a function of the satellite's mass and other geometrical quantities. However, in both the outer A and B rings, the observed distortion amplitudes, and even the azimuthal shape, are not accurately described by the simple model. For the B ring, significant residuals ( $\sim$ several kilometers) in the fitted two-lobed model, the extension of the outer edge  $\sim 24$  km beyond the resonance position, and the fact that the distortion amplitude of  $\pm 75$  km is a factor of  $\sim 4$  larger than would be expected from the simple model indicate that other perturbations on the ring particle orbits are present. In an interplay of local and external influences, the rings' self-gravity and viscosity may play a role in enhancing the amplitude of the externally produced distortion (Porco *et al.*, 1984b); amplification of a standing density wave, excited at the Mimas resonance location and reflecting off the sharp outer B ring edge, may also help explain the amplitude enhancement as well as the extension of the ring beyond the resonance (Namouni and Porco, 2002). High-resolution imaging observations of this unusual region, taken over the course of the Cassini mission, will be critical in developing a full description of the rings' shape and behavior, which in turn will help constrain the region's surface mass density and viscosity, quantities that are presently unknown. The mass present in the outer B ring may also play a role in distorting the narrow Huygens ring 250 km beyond in the Cassini Division (Turtle *et al.*, 1991, 1992; Section 2.3.1.5), another reason why examination of this region is particularly interesting.

Understanding the confinement of the outer A ring edge offers a special challenge. Analysis of Voyager imaging and occultation data indicated that the shape and kinematics were consistent with a seven-lobed distortion rotating with the mean angular velocity of the co-orbital satellites. However, as with the B ring, the amplitude ( $\pm \sim 7$  km) is larger than predicted from simple resonant perturbations, and the latter are complicated by the presence of many potential components with slightly different pattern speeds. These arise from the frequency splittings associated with two fundamental frequencies: the mean orbital frequency of the two satellites and their libration frequency (Section 2.3.1; Porco *et al.*, 1984b). The 'side-band' resonances are spaced at  $\pm 3$  km on either side of the central resonance; the uncertainty in the A ring outer edge is  $\sim 8$  km, so it is unclear which, if any, is the dominating resonance and how the side resonances affect the observed behavior. (The satellites' eccentricities, and the uncertainty in the exact mass ratio of the co-orbitals, complicate this brew even further.)

Nonetheless, an interesting opportunity to examine this unusual configuration is presented by the swapping of orbits that the co-orbital satellites, Janus and

Epimetheus, will undergo in early 2006. Any resonances produced by these bodies should shift by measureable amounts as the outside moon moves to the inside track and the inside moon moves to the outside. This is a unique opportunity to see the rings respond to a very specific external stimulus. Although theory suggests that the edge region will take several months to settle into the new regime, valuable information on the physical properties of the rings will be gained by observing the switch and its consequences. High-resolution observations of this region, and adequate azimuthal coverage of the ring's edge, both prior to the switch and after, to monitor the response of the ring system, are required. The changing response of the rings at other resonances produced by these satellites (e.g., density waves throughout the A ring; see the following paragraphs) will also be examined. High-resolution radial scans of the entire ring region are planned to straddle the orbit switch.

**2.3.1.2. Waves.** The rings, particularly the outer A ring, contain dozens of density waves (Cuzzi *et al.*, 1981) and a few bending waves (Shu *et al.*, 1983). These tightly-wound spiral waves are excited by Saturn's moons Prometheus, Pandora, Janus, Epimetheus, and Mimas (Lissauer, 1985; Gresh *et al.*, 1986; Rosen *et al.*, 1991). The waves typically damp within  $\sim 100$  km of the resonance at which they are excited, and the wave region generally contains  $\sim 10$  cycles of the wave.

The forcing and damping of density and bending waves is a major and important problem in planetary ring dynamics. In principle, the observations of decaying waves provide a tool for probing the particles' physical properties and nature of the disk: the local ring surface mass density can be estimated through measurement of the variation in wavelength with distance from the resonance, and the damping rates inferred from the decrease in wave amplitude with distance can be used to derive an estimate for the local ring viscosity, and hence, the elastic ring particle properties. However, these results suffer from the fact that none of the theories of wave propagation, either linear or nonlinear, completely describe the observations as they presently stand. The strongest waves in Saturn's rings are all highly nonlinear, and radial profiles through the crests of the waves are generally noisy. Improved profiles of density waves, and improved measurements of the heights of bending waves from Cassini imaging and occultation observations, will aid this situation enormously. Also, as indicated earlier, the co-orbital satellites' swap and the consequent response of the ring to a changing external stimulus should help in independently ascertaining the A ring's internal properties, such as the ring's viscosity, in a perturbed region, a needed ingredient in interpreting density waves.

**2.3.1.3. Satellite Orbital Evolution.** The generation of spiral density waves at the location of a Lindblad resonance with a satellite leads to an exchange of orbital angular momentum. The net consequence is a secular evolution of the satellite orbit away from the rings. The exact rate of orbit expansion for a given satellite depends on parameters such as the surface density of the rings and the mass of the satellite.

Thus, in principle, if a satellite's mass is known, an observation of a secular change in its orbit can yield (i) a direct measure of the rate of ring evolution and (ii) a measure of the ring's surface mass density. However, with the exception of Janus and Epimetheus, the masses of the small satellites of Saturn are essentially unknown. Also, complications arise due to the mutual perturbations of the satellites on each other, which can also lead to changes in their orbital elements. The net drift rate of a satellite drawing angular momentum out of the rings at a Lindblad resonance will be slowed if it is in resonance with another satellite.

Prior to 1995, the best candidate for deducing the rate of angular momentum exchange between a satellite and the rings was Prometheus which drives a number of resonances within the A ring. Its orbit was expected to expand sufficiently rapidly that by 1995, over 14 years after the Voyager flybys, when the Sun and Earth passed through Saturn's ring plane as Saturn orbited the Sun, it should have lagged behind its expected Voyager-derived position by  $\sim 0.2^\circ$ . However, a lag that was 2 orders of magnitude larger than this was observed (Bosh and Rivkin, 1996; Nicholson *et al.*, 1996). Further, observations since 1995 using the HST indicated a similar problem with the orbit of Pandora. Both orbits changed again in late 2000 (French, 2003).

This is now known to be due to the chaotic environment in which the two moons reside – a circumstance initially pointed out by Borderies *et al.* (1984), subsequently detailed by Goldreich and Rappaport (2003a,b) – as well as the fact that every 6.2 years, the apsidal lines of Prometheus and Pandora become anti-aligned, bringing the satellites very close to each other. Other effects are certainly present in their orbits, such as a nearby Mimas 3:2 resonance.

One major objective of the ISS investigations at Saturn is refinement in the orbital elements of the known satellites, including Prometheus and Pandora, and a measure of their periodic and secular (if any) changes with time. An orbital integration of the whole satellite system will likely be needed to derive estimates of individual satellite masses from their mutual perturbations and to detect any secular changes due to these interactions or ring torques. Images are planned to capture all the known satellites at various points in their orbits and throughout the tour for just this purpose; many ring images will serendipitously capture the ring region satellites over the course of the mission. These measurements will be combined with observations of these bodies made by Voyager 25 years earlier and HST in the interim. Relative precisions in the orbital elements of the known small satellites of  $\Delta n/n \sim 10^{-9}$ , and  $\Delta e/e \sim \Delta i/i \sim 10^{-4}$  can be expected by the end of the nominal 4-year orbital tour.

For geophysical purposes as well, the satellite densities are of great interest. Janus, Epimetheus, Prometheus and Pandora are all believed to be very porous, with densities less than  $1 \text{ g/cm}^3$ . The fact that the densities of most of the small satellites and even of the ring material itself are unknown highlights the need to obtain masses of objects by observations of their gravitational effect on other bodies, since no targeted flybys from which mass might be determined from spacecraft tracking are planned. We require good size and shape models of the satellites in



order to determine their densities. Images to capture ring region satellites at high resolution are planned for this purpose.

*2.3.1.4. Planetary Acoustic Oscillations.* Traveling acoustic oscillations within the body of Saturn, in particular the low degree f-mode oscillations which have the potential to create the largest disturbances among all the modes, have been suggested (Marley and Porco, 1993) as a source of particular waves observed in the inner C and D rings (Rosen *et al.*, 1991). Present application of this idea is hampered by an incomplete description of the waves in question and the ambiguity in the assignments of particular waves to particular f-modes. Cassini observations are planned to ascertain the nature of these features and test the acoustic oscillation hypothesis.

*2.3.1.5. Gaps, Embedded Moons and Ringlets.* Saturn's rings contain about a dozen true gaps, defined as regions with  $\tau \ll 0.01$ , with widths ranging from  $\sim 20$  to 400. As stated earlier, gaps may be opened by very strong resonances; e.g., the Mimas 2:1 resonance that sculpts the outer B ring edge is also responsible for the Huygens gap in the inner Cassini Division (Goldreich and Tremaine, 1978). But gaps may also be opened by an embedded moon, and the requirement for doing so, and the size of the resulting gap, depend on the balance between the torque imposed by the satellite and the ring's natural viscous torque. In the only case known so far, the 10-km-radius moonlet Pan clears the 325-km wide Encke Gap in the outer A Ring (Showalter, 1991); this configuration is consistent with the density of Pan being similar to that for Janus and Epimetheus ( $\sim 0.6 \text{ g/cm}^3$ ) and a viscosity found for the A ring by the examination of density waves:  $\sim 100 \text{ cm}^2/\text{s}$ .

Pan also causes the Encke Gap to have wavy edges (Cuzzi and Scargle, 1985) with a wavelength of  $0.7^\circ$ , and causes quasi-periodic optical depth fluctuations ("moonlet wakes") in the surrounding A ring (Showalter *et al.*, 1986; Lewis and Stewart, 2000). In fact, the presence, mass and separation of a small satellite can be deduced by detections of edge waves and wakes in a gap's edges, owing to the gravitational impulse that the satellite imparts to passing ring particles and consequent excitation of orbital eccentricities in the ring particles. Pan was, in fact, discovered by its perturbations on the edges of the Encke gap.

The Encke gap also contains unusual arc-like and contorted ring segments, one of which appears to be the same orbit as Pan and may even be gravitationally confined by it. There are few images of these rings; they may have a similar relation to Pan that the Neptune ring arcs have to the moon Galatea (Porco, 1991). ISS will undertake a survey the Encke gap to catalogue all edge-wave phenomena and characterize the unusual rings within the gap.

Edge waves were also detected in the 35 km wide Keeler gap (Cooke, 1991) at the outer part of the A ring but Voyager provided limited azimuthal coverage and no satellite has been detected in the gap. The Keeler gap is also more puzzling than the Encke gap because the observed edge waves appear to have varying wavelength

and the observed amplitude implies the presence of a satellite that should have been detected by the Voyager cameras. One possibility is that more than one satellite is involved.

A number of genuine narrow gaps in the Cassini Division, the Keeler Gap in the outer A Ring and a few in the C ring are presumably caused by small moonlets, but the putative bodies have not been observed. Narrow (and frequently eccentric) ringlets are found in many of the gaps and are in some cases close analogs of the Uranian rings (Porco, 1990). Numerical simulations show that ringlets like the Huygens ringlet in the inner Cassini Division or those in the C ring can form at isolated Lindblad resonances (Hänninen and Salo, 1994, 1995; Goldreich *et al.*, 1995; Rappaport, 1998). The Colombo Gap in the C ring is associated with the relatively strong Titan 1:0 apsidal resonance. This resonance dominates the kinematics of a narrow eccentric ring within the gap and may be an example of a resonance that simultaneously maintains a gap and shepherds a narrow ring (Porco *et al.*, 1984a). On the other hand, the Maxwell gap in the C ring and the narrow eccentric ringlet that resides in it are not associated with any resonance. Presumably a small so-far-undetected moonlet is both creating this gap and shepherding the ring. Moonlets in these gaps in the C ring, where the viscous stresses are likely to be smaller, could be on the order of a few kilometers in radius and still clear their host gaps. Other gaps throughout the rings, similarly bereft of any definite cause, may also host small moons.

The non-axisymmetric structures detected at the edges of the A and B rings and the Encke and Keeler gaps, and the narrow eccentric rings in the Maxwell and Colombo gaps, are all regular in nature and reasonably well understood. In contrast, the chaotic-looking structure in the F ring system has yet to be satisfactorily explained. The two so-called “shepherding” satellites, Prometheus and Pandora, are expected to produce wave-like structures on the various components of the ring but the Voyager images show a more confused picture, with strong evidence of variability in the F ring region on a variety of time scales. Some of the F ring strands appear to be intertwined in Voyager 1 images and then to be a series of parallel strands in Voyager 2 images 9 months later. Clump-like structures were observed in Voyager and HST images that apparently persist for no longer than 9 months. The ring is seen to brighten locally, perhaps due to meteoroid impacts (Showalter, 1998) or tidal breakup (Nicholson *et al.*, 1996). Some of these phenomena, such as strand alignment and the unusual azimuthal structure, suggest the presence of small satellites undetected by Voyager. What is lacking is complete, high-resolution, azimuthal coverage of the ring and its surrounding region at different epochs in order to determine the structure and monitor its evolution.

A major objective of the ISS ring imaging investigation, and one for which a substantial number of images is planned, is a search for moonlets in gaps in the main rings and outside the A ring in the F ring region, a search for their gravitational effects on nearby ring material and the determination of their orbital elements. (In the absence of direct detections of a satellite, the observations of edge waves and other

perturbing effects on surrounding ring material can be used as a diagnostic tool to infer a satellite's existence and, with sufficiently good data, its orbital and physical parameters.) These will be conducted by imaging over  $360^\circ$  of longitude when the spacecraft is at reasonably high latitude and has a more-or-less uninterrupted view of the rings. (Other supplemental observations directed towards this end, which will be less taxing on spacecraft resources, are movie sequences of the ansa of a ring feature or gap, generally at lower resolution, to observe material and possibly moons moving through the FOV.) Selected targets for the high-resolution azimuthal scans and the ansa movies are the F ring, the Keeler gap (which will also capture the outer edge of the A ring), the Encke gap, the inner and outer Cassini Divisions, several gaps in the C ring, and the D ring. Because the structure expected in these regions – either edge waves or narrow, eccentric ringlets or complex F ring structure – is expected to evolve with time, and because precise orbits for embedded moonlets are desired for investigations of their dynamical interactions with surrounding ring material, these azimuthal scans and movies are repeated at various times over the 4-year mission. For the F and Encke ringlets, observations are planned when the spacecraft is close to the planet and at high phase, where these dusty rings are brightest.

The same data sets will be used to delineate the orbits, and investigate the kinematics, of any eccentric rings or ring edges within or forming the gap. As a general rule, the kinematic behavior of such features is predominantly influenced by the planet's non-spherical gravity field, perturbations by both distant and nearby satellites and rings, and by the self-gravity of the constituent ring particles (Porco *et al.*, 1984a; Porco and Nicholson, 1987). The greater the accuracy to which the kinematics are known, the greater the degree to which these individual contributions may be separated. The addition of data collected during the ground-based 28 Sgr occultation by Saturn's rings to the pool of Voyager imaging and occultation data on the behavior of the narrow Huygens ring outside the B ring confirmed that the ring consists of a freely precessing, simple elliptical component (commonly observed in narrow eccentric rings of Saturn and Uranus) as well as a double-lobed component apparently forced by both the nearby Mimas 2:1 resonance and the double-lobed shape of the outer edge of the B ring itself (Turtle *et al.*, 1991). Cassini observations, in concert with Voyager and previous ground-based occultation observations, will permit the search for additional modes in other narrow rings. Finally, a slight, but as yet unmeasured, inclination to the F ring may account for many of the properties displayed by the system as a whole during the 1995–1996 ring-plane crossing (Nicholson *et al.*, 1996). Developing accurate shape and kinematical models for all of Saturn's eccentric and inclined ringlets is a high priority of the Cassini ISS investigation.

The observations of satellites in gaps, and the accurate determination of their orbital elements, are key to understanding the fundamental dynamical interactions between a body and its host particle disk, whether it be a moon in Saturn's rings or a proto-planet carving out a gap in the exo-solar disk from which it has formed. It is not clear whether or not, in the case of Saturn's rings, the body's orbit will

be circular or eccentric, and the outcome will decide the nature of the ring–moon interaction as well as guide interpretation of astronomical observations of exosolar disks and their phenomenology. To improve on the high-resolution azimuthal scans and lower-resolution ansa movies targeted to gap regions where moons are expected to be, retargettable observations are planned in which the target can be decided shortly before uplink of commands to the spacecraft. Any moon discovered in a gap and whose orbital parameters are known well enough to predict its location at a future time will be imaged again using these ‘place-holder’ opportunities. Multiple observations at different positions in an orbit of an embedded moon are essential to detect the anticipated radial excursions of any eccentric orbit: i.e., no larger than half the gap’s width. Relative precisions in orbital elements of  $\Delta n/n \sim 10^{-8}$  to  $10^{-9}$ , and  $\Delta e/e \sim \Delta i/i \sim 10^{-3}$  from both planned searches of gaps and follow-on retargettable observations are expected by the end of the nominal 4-year orbital tour.

### 2.3.2. *Ring Structure: Internal Causes*

In marked contrast to many of the non-axisymmetric structures described earlier for which some degree of success has been achieved in devising an explanation, almost all the fine-scale structure that is observed throughout the optically thick B ring (Figure 10) is still unexplained and not even fully characterized. This ring region exhibits large, radially irregular, axisymmetric variations in brightness

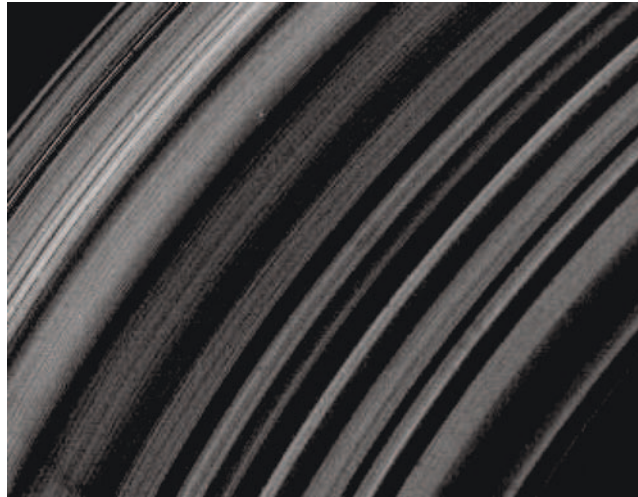


*Figure 10.* Voyager image of the lit face of Saturn’s B ring covering a region  $\sim 6000$  km across. The narrowest features here are 4 km wide. There are no gaps in this image: variations in brightness across the rings are due to a combination of differences in ring particle density and light scattering properties. All of the features in the image remain unexplained.

at the smallest scales observable in Voyager images (4 km), up to the dominant spatial scale of 100 km (Horn and Cuzzi, 1996); some of brightness variations appears to vary with ring longitude. There are few resonances in this region. There has been some suggestion that this structure represents not the usual radial variations in optical depth but in ring particle albedo, instead. The presence of this irregular structure, regardless of the cause, is surprising because the time scale on which such irregularities should be removed is shorter than the estimated age of the rings.

Various explanations for this irregular structure have been proposed since the early 1980's. Depending on the surface mass density of the ring, dynamical instabilities such as the diffusion instability (or 'viscous instability'; e.g., Ward, 1981), and the pulsation instability (or 'viscous overstability'; e.g., Schmit and Tscharnuter, 1999; Schmidt *et al.*, 2001) can be active and lead to the formation of axisymmetric structure. (The latter can also lead to non-axisymmetric structure.) A diffusion instability could occur in regions where the viscosity arises from the momentum transport associated with the random motions of the particles. A pulsation instability prevails when the viscosity is dominated instead by non-local momentum transport through a densely packed region of particles without particle transfer. In the case of the B ring, where the optical depth is large and the filling factor is high, the diffusion instability is unlikely to be a contender as the explanation of the irregular structure, and the pulsation instability apparently gives rise to sub-kilometer structure in dense rings, unlike the 100-km scale structure observed in the outer B ring (Schmit and Tscharnuter 1999; Salo *et al.*, 2001; Schmidt *et al.*, 2001). A third possibility is the presence of liquid–solid phase transitions in the B ring, and a suggestion has recently been made (Tremaine, 2002) that shear-dependent cohesive forces among the ring particles could lead to nested and narrow annuli of 'solid' and 'liquid' regions. In this case, the resulting irregular structure would depend on how the tensile strength responds to the Keplerian shearing motion.

Clearly, structure throughout the B ring has to be spatially and temporally characterized. The degree to which it is caused by albedo variations, perhaps due to random meteoroid impact events, needs to be determined. Radio and stellar occultations, together with high-resolution imaging observations, will be needed to determine the variation in optical depths across the region, as well as the character of the region at scales less than 4 km, the smallest that Voyager images were able to achieve. Models for the response of the ring to the Mimas 2:1 resonance and the effect of this ring region on the dynamics of the Huygens ring will also be valuable in providing an independent estimate of the surface mass density and viscosity in this region. Understanding how a dense ring, essentially left to itself, forms detailed structures like the one observed in the outer B ring will prove illuminating in understanding disk structures of much larger scale, like the proto-solar nebula, exo-solar disks around other stars and even the spiral galaxies.



### 2.3.3. Photometric Studies of Saturn's Rings:

#### *Particle Properties and Disk Structure*

The largest particles in Saturn's rings in any substantial number are of order 10 m in radius (Zebker *et al.*, 1985; French and Nicholson, 2000), and the ring thickness is likely to be of the same order. By contrast, even the images taken closest to the rings during SOI will have resolutions of  $\sim 100$  m/pixel. Thus, the ISS will not image the ring particles directly. In order to infer the nature and spatial distribution of the ring particles (e.g., the ring thickness), we must use indirect means.

One such method is to measure the reflected or transmitted brightness ( $I/F$ ) of the rings in different geometries. Such geometries include the sunlit and unlit faces of the rings, and in backscatter (nearly "full" phase, i.e., opposition, or near-zero solar phase angle) and forward scatter (nearly "new" phase, or near  $180^\circ$  phase angle). As measured by cross-sectional area, or optical depth, most particles in the main rings are much larger than the wavelength of visible light. Such particles are strongly backscattering. At visual wavelengths, the reflectivity of the main rings is dominated by singly scattered sunlight in backscatter, and by multiply scattered sunlight and singly scattered "Saturn-shine" in forward scatter.

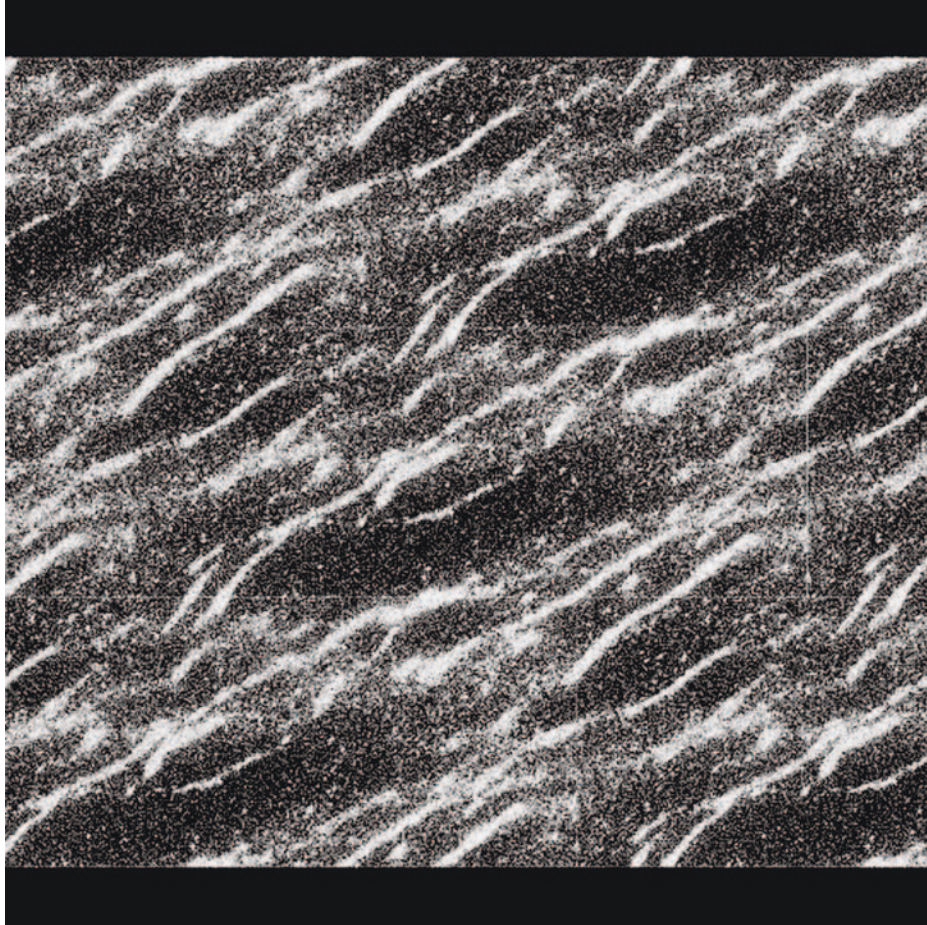
By contrast, the F ring and the tenuous D, E and G rings are dominated by microscopic "dust" particles, and these rings are brighter in forward-scattering geometries due to the diffraction of light by wavelength-sized particles. Multiple scattering is negligible for the D, E, and G rings (and generally for the F ring as well).

Many published photometric models of Saturn's rings (e.g. Cuzzi *et al.*, 1984; Dones *et al.*, 1993) use the formalism of classical radiative transfer, which in its simplest form assumes a vertically thick, horizontally homogeneous ring (Chandrasekhar, 1960). Such models are convenient because multiple scattering can easily be calculated using, for example, an adding-doubling code (Hansen and Travis, 1974). However, even if the rings were at first physically thick, collisions would rapidly flatten them until they were only a few particles thick (Jeffreys, 1947; Brahic, 1977; Wisdom and Tremaine, 1988). Dones *et al.* (1993) noted a number of discrepancies between classical models and the measured  $I/F$  of the A ring, such as its low brightness at large phase angles. More realistic models in which the rings are physically thin and/or clumpy have recently been formulated, and have gone a long way in resolving the disagreements between models and observations (Porco *et al.*, 2002; Salo and Karjalainen, 2002).

Specifically, the so-called "azimuthal asymmetry" in Saturn's A ring, a quadrupole variation of the ring's reflectivity seen in ground-based, Voyager, HST, and radar images (Thompson *et al.*, 1981; Smith *et al.*, 1981; Dones *et al.*, 1993; French *et al.*, 2000; Nicholson *et al.*, 2000) is thought to be caused by the presence of transient "wakes" of much-enhanced particle density in the rings that form due to local gravitational instabilities and then shear out (Figure 11; Colombo *et al.*, 1976; Franklin and Colombo, 1978; Dones and Porco, 1989; Salo, 1992, 1995; Richardson, 1994; for an animation, see <http://www.astro.umd.edu/~dcr/Research/ringpatch.mpg>).



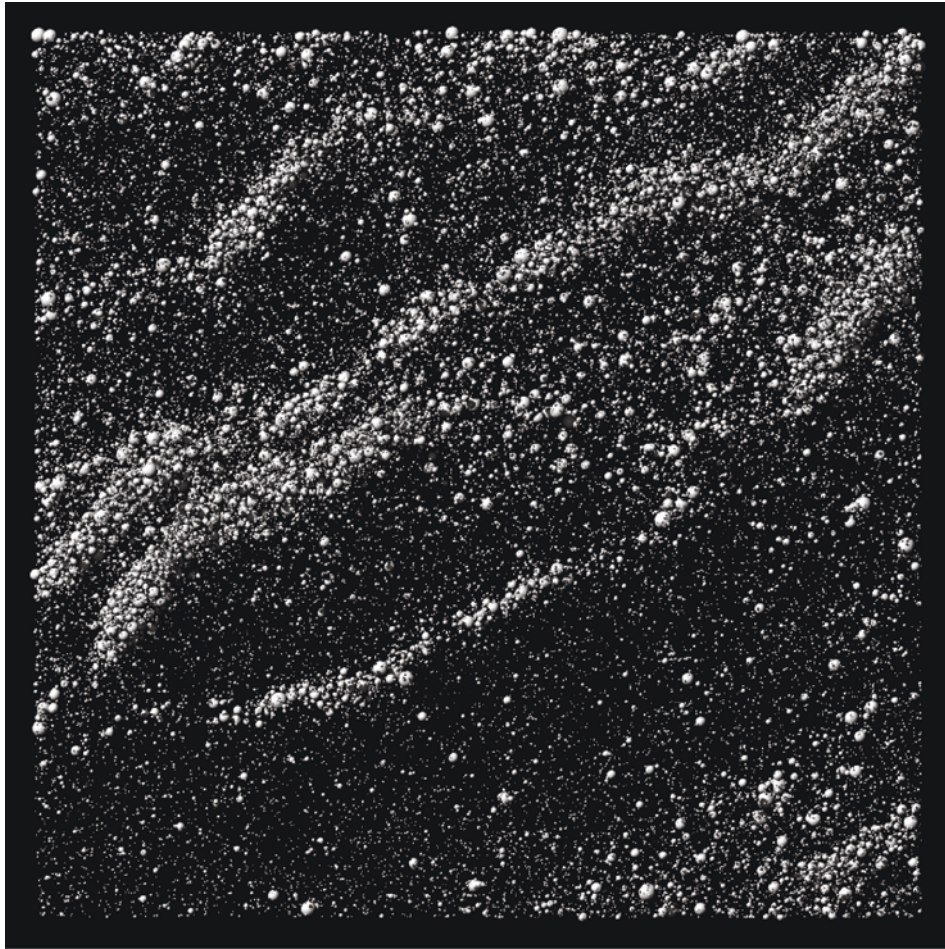
The separation and length of these wakes is of order 100 m; their long axis trails the direction of motion of the ring particles by some  $26^\circ$ . Because the number of particles contributing to the reflected light seen by an observer depends upon the orientation of the wake, the ring brightness has minima about  $26^\circ$  from the ring



(A)

*Figure 11.* (A) A snap-shot taken from a large-scale computer dynamical simulation (Porco *et al.*, 2005) showing 220,000 particles in Saturn's mid-A ring after 10 complete orbits. (The middle panel is  $230 \text{ m} \times 580 \text{ m}$ ; the panels above and below are the sliding patches which accomodate periodic boundary conditions.) Parameters for optical depth, particle size distribution, surface mass density and particle elastic properties characterizing the A ring were used in this simulation. The radial direction is up; orbital motion is to the left. At this stage, the evolution of the system is characterized by the rapid (one orbit) formation, dissolution and reformation of filamentary wake-like structures with a pitch angle of  $\sim 26^\circ$  to the azimuth and an average separation of 100 m, in agreement with theory. (B) The innermost  $190 \text{ m} \times 190 \text{ m}$  portion of (A) containing  $\sim 52,500$  particles, illustrating expected particle distribution. Figures courtesy D. Richardson, U. Maryland.

(Continued on next page)



(B)

*Figure 11. (Continued).*

ansae. Recently, two groups have performed realistic simulations of the asymmetry that incorporate both large-scale N-body simulations and ray-tracing photometric modeling (Porco *et al.*, 1999, 2001; Salo *et al.*, 1999, 2000). These simulations show broad agreement with the observed properties of the asymmetry, with the exception of the amplitude which has not yet been successfully modeled. The amplitude of the asymmetry depends upon several parameters, including the surface mass density of the rings and the coefficient of restitution, which measures the degree of elasticity during interparticle collisions. Further modeling of the asymmetry should provide an excellent probe of the properties of the rings, such as their viscosity (Daisaka *et al.*, 2001). By contrast, analysis of spiral density and bending waves, which thus far have provided much of our understanding of the rings' mass density and viscosity,



provides information on parts of the rings that have been strongly perturbed by external satellites. Wave regions typically have larger values of mass density and velocity dispersion, or viscosity, than unperturbed regions (Shu, 1984).

During SOI the putative wakes in the A ring may be marginally resolved by the NAC. Direct confirmation of their existence would provide an important test of dynamical models, as well as a measure of the surface mass density in the A ring (since the spatial scale of the wakes is determined by this quantity), and would help to remove ambiguities in modeling of the rings' reflectivity measured at grosser resolution throughout the main tour.

Ring color, in particular its variation across the rings, is also of interest as it may relate to ring origin and ongoing processes which alter ring particle surfaces like meteoroid bombardment and interaction with the magnetosphere. The particles in the C ring and Cassini Division are generally darker, less red, and smaller than those in the B and A rings (Cuzzi *et al.*, 1984; Esposito *et al.*, 1984; Estrada and Cuzzi, 1996; French and Nicholson, 2000). The significance of these differences and the presence of color differences on smaller spatial scales will be sought. Images taken on approach to Saturn in 2004 already show color variations across the B ring (Figure 1).

Another photometric phenomenon which is diagnostic of ring structure is the opposition effect in which the ring brightness increases dramatically very close to zero phase. This effect probably results from a combination of physical optics within the particle surfaces (coherent backscattering, Poulet *et al.*, 2002) and "shadow-hiding" between different particles. The angular width of the shadow-hiding effect depends on the thickness of the ring and the ring's particle size distribution, and provides one of our best diagnostics of the rings' vertical structure.

#### 2.3.4. *Spokes*

On approach to Saturn in 1980, Voyager 1 imaged faint, dark, nearly radial, wedge-shaped spoke-like features extending across Saturn's B rings. Observations of these features by both Voyager 1 and 2, taken over the course of each encounter and through a large range of phase angles and imaging resolutions (Smith *et al.*, 1980, 1981) indicated that spokes were typically 10,000–20,000 km long, ~2000–5000 km wide, occurred only in the B ring, and straddled the radial location where Keplerian ring particle motion is identical to the magnetic field motion. On short time scales (minutes), they orbit the planet with the Keplerian motion, resulting in shearing away from radial in the trailing sense. Spokes were most readily visible on the illuminated morning ansa of the rings, where ring particles have emerged from Saturn's shadow, and over long periods (many rotations) their appearance there was found to vary in contrast and areal coverage with the period of Saturn's magnetic field (Porco and Danielson, 1982). Also, greatest spoke activity occurred within the same northern magnetic field sector responsible for the emission of Saturn Kilometric Radiation. (There is a suggestion that spoke activity on the rings also varied with a period equal to that of the broad-band Saturn Electrostatic Discharges,

but this finding was less convincing (Porco and Danielson, 1984).) Spokes are likely composed of micron-sized particles elevated above the main ring particles (Smith *et al.*, 1981; Doyle and Grun, 1990), accounting for their reversal in contrast (with respect to the rings) between low- and high-phase viewing geometries. Only four spokes were observed to form by Voyager; the upper limit to the formation time was  $\sim 4$  min. Very few spokes have been observed from the ground (Colas *et al.*, 1995), and those observed by the HST (McGhee *et al.*, 2004) were visible only when the elevation angle of the Earth (Sun above or below the rings) was less than  $\sim 15^\circ$ . The latter authors attribute the difficulty in seeing spokes at other times to a photometric effect: low elevation angles producing long line-of-sight pathlengths through clouds of dust, making them more visible in those geometries. Others suggest that the appearance of spokes at some times and their absence at other times, and their observed orbital distribution, may be a seasonal effect related to the variable flux of meteors on the rings from heliocentric orbits during the Saturn year (Cuzzi and Durisen, 1990).

Models proposed for the origin of spokes have all invoked electromagnetic forces (which have their greatest effect on small, dust-sized particles) operating on clouds of dust debris generated by the impact of a meteoroid onto the rings (Goertz and Morfill, 1983; Goertz, 1984; Tagger *et al.*, 1991). Spoke formation times have been calculated under some of these scenarios to be as short as tens of seconds.

Cassini will provide the opportunity to gather far more information on these elusive and mysterious features. The hemisphere illuminated by the sun during the Voyager epoch was the northern Saturn hemisphere; the nominal Cassini orbital tour takes place during southern summer. If the appearance of spokes is related at all to seasonal effects, it should be discernible in Cassini data.

Ring imaging campaigns to capture spokes, either on the illuminated or unilluminated part of the rings, with imaging intervals of  $\sim 1.5$  h, are planned at various times throughout the orbital tour to confirm the periodicities and orbital phases observed by Voyager. Recent Cassini approach observations by the RPWS indicate an SKR period that is 1% longer than that observed in 1980–1981. Will the spoke periodicity also be longer? Will the SED period be confirmed? The capability of the ISS to acquire images with an interval as short as 11 s will be utilized in several observing sequences throughout the tour to capture spokes in the act of forming. As Voyager indicated significant modification in spoke activity when spokes pass through the shadow region, image sequences have been planned for observing ring material before and after shadow passage. Finally, to understand the details of the evolution of spoke morphology, spoke ‘tracking’ sequences are planned to follow spokes around the rings. As the spoke formation process is a stochastic one, there are no assurances that any of these observations will be successful. Spokes have not so far been observed on approach to Saturn from an spacecraft elevation angle of  $\sim -16^\circ$ , and a solar elevation angle of  $\sim -25^\circ$ .

### 2.3.5. Diffuse Rings

Diffuse, extensive clouds of dust encircle Saturn. These structures, reaching out as far as  $8 R_s$ , are of substantial scientific interest (Burns *et al.*, 2001) because, in some respects, the physics governing tenuous rings is simpler to understand than that of Saturn's more familiar rings where collisions are frequent. In addition, the widely separated particles comprising these rings concern some spacecraft engineers because Cassini will repeatedly traverse these diaphanous structures; the consequent impacts, occurring at high speeds, may jeopardize the entire spacecraft or its components (Burns *et al.*, 1989).

We define a diffuse ring as any with normal optical depth less than 0.001; this somewhat arbitrary separation means that collisional time scales in diffuse rings are less than orbital precession times. Saturn's diffuse rings then include the D ring, portions of the F ring, especially that lying radially interior to the main strands, the E ring, the G ring, and perhaps the contorted Encke ringlet (s).

Since the lifetimes of individual dust grains are brief, diffuse rings must be continually regenerated from source bodies (Burns *et al.*, 2001). General goals for the investigation of faint rings include (i) comprehensive photometric coverage to allow size distributions (indicative of dust origin and evolution) and particle shapes to be inferred; (ii) the search for sources (parent bodies, probably small moons) and sinks (satellite surfaces, Saturn's main rings and atmosphere, as well as particle destruction); and (iii) signatures of the symbiosis between the dusty rings and ambient plasma as well as the effects of circumplanetary dust on the coating of satellites through orbital photometry.

By their very nature, diffuse rings are difficult to study observationally: they are faint and often three-dimensional, meaning that lines of sight may pierce the structure in several places, confounding a simple interpretation. Long exposures, especially when taken along shallow slant paths through the ring in order to increase the signal, have proven effective. Unfortunately, light from nearby bright sources scattered into the optical imaging device has complicated interpretations (Throop *et al.*, 2004). Images taken at shallow elevations can be effective in determining ring thicknesses. The boundaries of the planet's shadow across these rings were used by Voyager scientists to selectively demarcate very faint rings from the blackness of the sky background; similar techniques will be used on Cassini, employing the shadows of the planet and perhaps large satellites.

Faint rings usually contain primarily small particles, which effectively forward-scatter optical light into narrow cones of a few degrees. Cassini observations of the jovian ring taken alone (Porco *et al.*, 2003) and in combination with other spacecraft and Earth-based observations of the ring (Throop *et al.*, 2004) have indicated that irregularly shaped, small ( $\mu\text{m}$ -sized) particles are more likely than spherical Mie scattering particles, at least for the rocky jovian ring particles. Because of the small particle size, diffuse rings are often most visible at high phase angles. Voyager images of Saturn's spokes and of abrupt brightness clumps in the F ring

(Showalter, 1998) indicate that features may be time-variable; charged-particle absorption signatures surrounding the F ring (Cuzzi and Burns, 1988) and ground-based images of transient events in the E ring (Roddier *et al.*, 1998) also imply that clouds may develop rapidly and then fade. To document and then to understand its causes, this time variability will require repeated imaging of some features throughout the mission.

Saturn's E ring, an extensive diaphanous cloud encircling Saturn and spanning the orbits of Mimas to Rhea, has two distinctive properties: its distinct brightness peak at Enceladus and its narrow size distribution, dominated by particles near a micron (Showalter *et al.*, 1991). Hamilton and Burns (1994) claim that, owing to resonance effects, E-ring particles move along elongated orbits; this hypothesis can be tested with measurements made by Cassini's dust detector. The same authors maintain that the resultant high-speed collisions into Enceladus sustain the ring. A corollary is that regions adjacent to other nearby moons should have enhanced ring intensity. The E ring's photometry and broad-band color need to be refined in order to tie down its unique and peculiar size distribution. Particles which are nearly spherical, mono-dispersed ice grains (as believed for the E ring constituents) will exhibit a strong polarimetric signature, which can be sought in images acquired through the ISS polarizing filters.

Saturn's G and D rings were discovered by Voyager but were the least studied by that mission. The former is tenuous, localized, and centered on orbital radius 168,000 km, far from any other known ring or moon. Its source is uncertain; small satellites in the vicinity will be sought. The particle size distribution is disputed (Showalter and Cuzzi, 1993; Throop and Esposito, 1998) and its firm identification will require broad phase coverage, with the diffraction lobe emphasized; polarimetry may also be useful. Saturn's innermost D ring was scarcely observed by Voyager (Showalter, 1996). The ring contains wave-like faint ringlets as well as two narrow rings. The ring's photometric properties are poorly constrained.

The band between the F ring and the outer edge of the A ring contains faint material whose optical properties vary with distance to Saturn (Murray *et al.*, 1997; Showalter, 1998), possibly giving clues to ring sources and sinks. Good photometry and color can clarify the causes. (Cuzzi and Burns, 1998) believe that the region immediately exterior to the F ring may have faint transient clumps, while others claim that it contains several small moons; it should be surveyed carefully. Cassini should target the region surrounding Atlas's orbit to seek a faint ring formed from the satellite's ejecta as Jupiter's gossamer rings seem to be (Burns *et al.*, 1999). Faint rings may also trail from the Lagrangian satellites of Tethys and Dione, especially following the controversial claim (Roddier *et al.*, 1998) of a time-variable cloud near one of Enceladus's triangular points.

Gaps in the main system, particularly across the Cassini Division and in the C ring, should be scrutinized to set upper bounds on the presence of any material, with the goal to understand the mechanism(s) that evacuate gaps.



### 2.3.6. *Proposed Observations*

Most investigations aimed at addressing these important issues require the highest imaging resolution possible. Outside the period of time immediately following the SOI, when Cassini is closest to the rings and cruising above them on the dark side at a distance only tens of thousands of kilometers (yielding a smear-limited resolution of  $\sim 100$  m), the highest imaging resolution obtainable on the rings anytime during the Cassini tour is  $\sim 1.0$  km. (For most of the tour, the NAC resolution on the rings ranges from  $\sim 1.0$  to  $15$  km/pixel; in the WAC, the range is  $10$ – $150$  km/pixel.) Imaging the entirety of Saturn's rings at this resolution would present an impossible task: the total surface area of the rings, including both illuminated and unilluminated sides, is  $\sim 1200$  times the surface area of Titan. Consequently, high-resolution imaging observations have been carefully chosen and focused on regions expected to yield the greatest fundamental science. (The highest-resolution "clear filter" images of the rings taken by Voyager had a pixel scale of  $4$  km.)

Other investigations that require variable lighting and viewing geometries and only modest resolution have been planned either with the NAC taken at larger distances, or the WAC taken in close. Though not significantly different than Voyager's best resolution color images, with a scale of  $25$ – $30$  km/pixel, Cassini's camera system has much broader spectral coverage, particularly in the UV and the near-IR, and its CCD is much more sensitive, with a larger dynamic range, than was Voyager's vidicon.

Thus, in all types of investigations – either those requiring relative or absolute, high-precision positional measurements or those requiring sensitive photometric and color measurements – we anticipate that Cassini images of Saturn's rings, with  $\sim 100,000$  planned over 4 years, will provide dramatic advances in our understanding of planetary rings.

Planned observations include the following:

- Approximately a dozen high-resolution ( $1$ – $2$  km/pixel) radial scans of the main rings taken at low-to-moderate solar phase angles will provide our best signal-to-noise imaging data on the finest-scale structure of the rings available to the ISS, including the irregular structure in the outer B ring.
- The radial variation of the amplitude of the opposition effect, a rapid brightening of the rings near zero phase angle, will be measured in several colors as the opposition spot passes diametrically across the rings.
- Observations taken during SOI may marginally resolve the "wakes" that are believed to produce the azimuthal asymmetry in the A ring (Figure 11) and will provide the highest resolution views of the rings during the whole tour.
- Moderate-resolution multicolor imaging of at least one complete ring ansa will be carried out in a wide range of viewing geometries in order to map out the way in which the rings' reflectivity ( $I/F$ ) varies with solar phase angle and with tilt angle (i.e., high or low elevation above the lit or unlit face of the rings). These observations, diagnostic of the nature of the particle surfaces and the particle

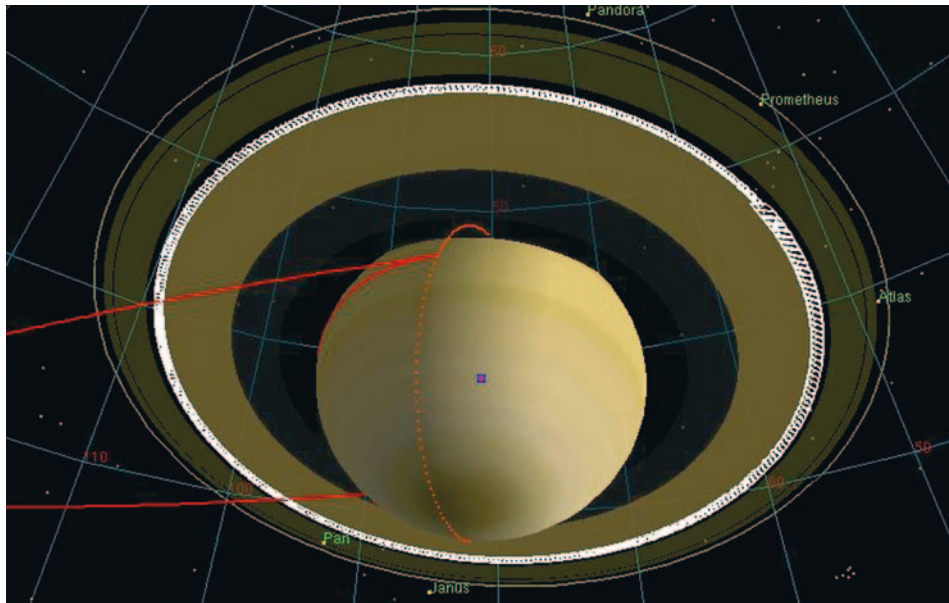


*Figure 12.* A typical azimuthal scan of a ring edge and gap (in this case, the outer B ring edge and inner Cassini Division) at moderate phase and high spacecraft latitude,  $-35^\circ$ . ISS will acquire observations like this on a dozen or so features in Saturn's rings for the purpose of searching for new moons, detecting edge waves and, in some cases, fully sampling the circumference and shape of eccentric rings.

disk characteristics, will also be used to characterize the azimuthal asymmetry in the A ring, search for its presence in other rings, and to probe the internal structure of the rings and the ring particle properties.

- Moderate-resolution radial scans using up to 15 filters to complement the higher spectral, but poorer spatial, capabilities of VIMS and CIRS in the composition of the ring particles, particularly the abundance and nature of the non-icy contaminants in different regions.
- Approximately a dozen or more high-resolution ( $\leq 3.5$  km/pixel)  $360^\circ$  scans of select features in the rings: the F ring, the Encke gap, the outer A and B rings edges, the Cassini Division, the major gaps in the C ring, the D ring, and select density waves in the rings to search for embedded moonlets and/or the small-scale signatures of their gravitational perturbations on surrounding ring material (Figure 12).
- Search for unseen satellites between the rings and the orbit of Hyperion.
- Imaging observations to measure the positions of, and refine the orbits of, satellites in the Saturnian system.
- Retargetable observations for orbit refinement and/or high-resolution morphology of newly discovered moons.

- Rapid ( $\sim 11$  s interval) time-lapse, moderate-resolution imaging sequences of the morning ansa of the rings in the hopes of capturing spoke formation; Movie sequences of the rings at low resolution to determine the periodicities in the appearance of spokes on the rings; Moderate-resolution spoke-tracking imaging campaigns to follow spokes to investigate spoke evolution.
- Imaging of the main rings at phase angles higher than those observed by Voyager will map out the abundance of sub-micron “dust” in the rings.
- Imaging of the diffuse rings (E, G and D), as well as some of the ring gaps (such as Encke) over a wide range of phase angle, including high phase, to constrain particle size and shape distributions.

### 2.3.7. *Combined Studies with Other Cassini Instruments*

Several dozen stellar (VIMS and UVIS) and radio (RSS) occultations by the rings will occur, spread over the 4-year mission, with a resulting radial resolution of 100 m. Many of these will penetrate and measure the optical thickness of the deepest portions of the B ring at these resolutions, something that Voyager was unable to do.

While occultations will provide the highest radial resolution available from Cassini at specific and limited longitudes on the rings, images can capture a continuous sweep of longitude. In this regard, these data sets are complementary. The combination of stellar/radio occultation data with imaging data will provide a powerful collection of information about the kinematical behavior of perturbed ring features, and their deviations from circularity, down to a precision of tens of meters for occultations, and down to  $\sim 1/4$  km for images.

Also, as with investigations of the surfaces of satellites, VIMS and ISS provide complementary results. Where VIMS can acquire high spectral resolution with low spatial resolution, determining far more precisely the composition of the material, ISS will provide the high-resolution context. Once the mapping of composition to ISS colors has been done by using the two instruments together, subsequent ISS color observations can be used to push compositional studies to higher resolution than is available with VIMS.

## 2.4. TITAN: SURFACE AND ATMOSPHERE

What we know of Titan today, on the threshold of Cassini’s orbital tour of Saturn, comes from more than a century of telescopic observations from the ground and low Earth orbit and from the Voyager encounters with Titan in the early 1980s. Owing to the ubiquitous haze enveloping the satellite and obscuring the surface and lower atmosphere to visible wavelength observations, most Voyager-era results were derived from the other spectroscopic and occultation experiments and not the imaging investigation.

Relevant to the Cassini ISS investigation are the facts that Titan has a thick, largely  $N_2$  atmosphere (mole fraction of  $\sim 95\%$ ) with a few percent  $CH_4$  and trace

amounts of other simple and some complex organics; surface temperature ( $\sim 94$  K), pressure ( $\sim 1.4$  bar) and near-surface lapse rate consistent with the presence of methane–ethane liquid surface reservoirs; a troposphere with a methane mixing ratio and lapse rate likely to produce methane clouds a few kilometers above the surface; a 200 km thick haze layer with a lower boundary in the stratosphere,  $\sim 100$  km above the surface; an upper atmosphere (with wind speeds  $\sim 100$  m/s which is believed to rotate faster than the surface, possibly giving it a super-rotator-like general circulation pattern like that of Venus; methane photolysis in the upper atmosphere likely to result in polymerized organics which rain down and coat the surface, collecting in depressions (such as craters). With such a complex environment, dominated by a thick atmosphere with a condensable material, it is possible that the Titan terrain exhibits geologic features produced by wind, rain, and fluvial erosion – channels, gullies, ‘waterfalls’, lakes, shorelines, etc. – as well as the usual tectonic and impact-produced morphologies seen on the other icy satellites.

Though Voyager images of Titan were unsuccessful in revealing the details of its surface – (however, see Richardson *et al.*, 2004) – we are hopeful that major and seminal scientific advances will result from the Cassini ISS investigation of Titan’s surface and lower atmosphere for two primary reasons. First, it has been demonstrated from both ground-based and HST imaging investigations, and now Cassini ISS approach observation of Titan (Figure 2), that the surface and troposphere of Titan can be remotely sensed in the near-IR spectral regions in between the methane absorption bands that dominate its spectrum (Lemmon, 1994; Smith *et al.*, 1996). In these inter-methane-band ‘windows’, the dominant source of opacity is scattering by stratospheric haze, which decreases in strength with increasing wavelength in the near-IR. Second, the Cassini ISS has been equipped with special capabilities for penetrating the hazy atmosphere, among them IR filters and filter combinations specially designed to match the inter-methane-band windows, and IR polarizers to cut down the light scattered by the overlying haze. Use of these polarizers will have the effect of increasing (in the relative sense) the percentage of photons reaching the cameras that were last reflected from the surface and unattenuated by the overlying atmosphere. None of these circumstances guarantees success in completing the imaging investigations that are described later (some of which are aimed at very high resolution of the Titan surface which may be hampered by overlying haze). But as Cassini makes it way towards Saturn, optimism remains high.

#### 2.4.1. Meteorology

Titan’s 16-day rotation period appears to place its atmosphere into the same slowly rotating dynamical regime that characterizes the general circulation of Venus (Del Genio *et al.*, 1993, 1996; Allison *et al.*, 1995). The dominant features of Venus’ atmospheric circulation are its surprising zonal super-rotation and extensive cloud-level Hadley circulation. Similar features are expected on Titan (Hourdin *et al.*, 1995), but no wind measurements exist to date because (a) prior to Huygens, Titan’s atmosphere has not been probed in situ; (b) to date, imaging of Titan’s clouds,

primarily at wavelengths sensing its stratospheric haze, has revealed no features suitable for tracking winds. Nonetheless, indirect evidence from Voyager IRIS brightness temperature profiles (Flasar *et al.*, 1981) and stellar occultation estimates of oblateness (Hubbard *et al.*, 1993; Sicardy, 1992) strongly suggest the presence of super-rotation at and above the tropopause.

A primary objective for Cassini ISS at Titan, therefore, is to map Titan's global wind field at the tropospheric levels where its atmosphere interacts with the surface angular momentum source. Such measurements would provide a global context for the local vertical profile of wind to be measured by the Huygens Probe Doppler Wind Experiment (Bird *et al.*, 2002), and if sufficiently extensive, might shed light on the mechanism(s) sustaining the super-rotation. On Venus, planetary-scale transient waves due to barotropic instability (Rossow and Williams, 1979), solar-fixed thermal tides (Ingersoll and Pechmann, 1984), and small-scale gravity waves (Young *et al.*, 1987) have all been hypothesized as significant contributors to the super-rotation; evidence for any of these processes operating on Titan would greatly advance our understanding of the slowly rotating regime. Specifically, knowledge of the latitudinal profile of zonal wind would constrain the efficiency of lateral angular momentum and potential vorticity mixing on Titan.

To track Titan cloud features, we must see below the featureless stratospheric haze into the troposphere, where methane clouds may exist in regions of rising motion. At the longest ISS wavelengths, we expect to see through the haze and view Titan's troposphere and surface (see Section 2.4.3). We therefore plan to image Titan in the near-IR using filters IR2/IR1 (827 nm), CB3 (938 nm), IR4 (1002LP nm), and IR5 (1028LP nm). To improve tropospheric visibility, the NAC carries an IR polarizer that can be used in combination with CB3 (938 nm), while the WAC carries two orthogonal IR polarizers that can be used with CB3 (938 nm), IR4 (1001LP nm), or IR5 (1028LP nm). We will image Titan, initially at intervals of a few hours, within 1 day of closest approaches to allow for detectable cloud displacements. In the event that small-scale features can be seen, we also plan to image at shorter time intervals to capture the evolution of these features.

Although there is uncertainty in Titan's methane abundance and the availability of condensation nuclei, ground-based observations have detected possible methane clouds (Griffith *et al.*, 1998) and transient clouds have been imaged in Titan's south polar region (Roe *et al.*, 2002; Brown *et al.*, 2002). Given sufficient methane abundance at the surface, Titan's temperature profile is steep enough to be unstable to moist convection and thus we anticipate that upper troposphere methane cirrus, created from the outflow of convective updrafts, might be the most common type of cloud feature, but visible only on the small spatial scales that ISS will be able to resolve. If convection does exist, its presence may be difficult to detect because infrequent convection is probably sufficient to remove the required energy from Titan's surface. Indirect evidence for methane convection might exist in the form of lightning. If lightning occurrence can be detected and mapped, it effectively will serve as a tracer for large-scale vertical motions such as the upwelling branch of the



Hadley cell. The H-alpha filter (HAL) on the NAC may be used to detect lightning flashes associated with methane ( $\text{CH}_4$ ) dissociation in long-exposure night-side images taken several hours before or after Titan closest approach; the clear filter may also be used to detect faint lightning flashes. In addition, we will seek lightning signatures of NII at 820 nm by overlapping the IR1 and IR2 filters.

#### 2.4.2. *Photometric and Polarimetric Studies of Titan's Atmosphere*

Deposition of solar radiation in the atmosphere and radiative interaction with tides or other wave phenomena is thought to be at the root of the mechanism that drives circulation. It is therefore important to understand radiative heating and cooling. The Descent Imager Spectral Radiometer (DISR) on the Huygens Probe will provide the sole Cassini direct measurement of the internal radiation field, but at only one location on the planet. The ISS can provide information on the radiation field at other locations on Titan in the same manner it will do for Saturn: by using photometry and polarimetry to infer the optical and physical properties, and the vertical and horizontal distributions, of aerosols, and using these parameters in studies of radiative energy balance. Photometry and polarimetry of Titan will also be important for understanding other microphysical processes at work in the stratosphere.

The measurements to be made to infer particle properties and distributions are listed in Tables III–V. Only the first two techniques (limb profiling and methane-band imaging) listed in Table V will be used at Titan. (The others techniques in Table V utilize the molecular Rayleigh scattering contribution to optical depth, which is negligible for Titan.)

Titan's disk nearly fills the NAC frame at a distance of  $10^6$  km, and that is approximately the range from which the ISS will image Titan for haze studies. The spatial resolution of the NAC at that distance is 6 km/pixel, which is significantly smaller than a scale height. Aerosol profiling can be done over the entire illuminated limb of Titan in a single image. Images at different wavelengths will yield the wavelength dependence of the haze as a function of location. As for Saturn we will target special opportunities such as times when a bright star is near the limb. Images of Titan in which the dark limb can be seen against the bright disk of Saturn can be used to profile optical depth on the night side. As for Saturn, images at many phase angles and many wavelengths and with polarizing filters will be used together to provide new and powerful constraints on particle size, shape, and distribution, and in turn on microphysical models of haze production and in studies of energy balance.

#### 2.4.3. *Visibility of the Surface*

It was long believed that Voyager ISS did not see the surface of Titan, but recent work (Richardson *et al.*, 2004) has shown that the surface was detected in the orange filter. The Voyager surface detection is very marginal, perhaps 2:1 SNR, but gives us reason for guarded optimism for the capabilities of Cassini ISS. The Voyager orange filter, centered at about 590 nm, covers the first (shortest wavelength) of nearly



six inter-methane-band windows from 600 to 1000 nm (Section 3). Optical depth in these windows, due to stratospheric haze scattering, decreases with increasing wavelength (Lemmon, 1994), so each of the other methane windows (accessible to Cassini ISS but not Voyager) should provide improved images of the surface. Furthermore, the total S/N of the Voyager image (at the top of Titan's atmosphere) is only  $\sim 50:1$  rather than  $\sim 200:1$  expected from Cassini ISS. Finally, Cassini ISS includes IR polarizer filters, which reduce the effects of haze at moderate phase angles. Based on the Voyager results and the spectrum of Titan, we expect to be able to detect the surface of Titan through the RED (650 nm), IR1 (752 nm), IR2 (862 nm), IR3 (930 nm), CB2 (750 nm), CB3 (938 nm), IR4 (1002LP nm), and IR5 (1028 nm) filters. However, major uncertainty persists as to the quality and resolution of these surface detections.

We are most optimistic that surface details will be visible to ISS in the continuum filter centered at 938 nm (filter CB3), especially since surface features on Titan have been seen on approach to Saturn with the Cassini ISS utilizing this particular filter (Figure 2). HST has shown that contrast from the surface of Titan can be seen through a broad-band filter similar to IR3 (Smith *et al.*, 1996), but CB3 is centered in the middle of the methane window and should be superior. Lemmon (1994) used constraints from observations of Titan's geometric albedo as well as spacecraft observations of reflected intensity and polarization to estimate haze optical depth at many wavelengths. In order to fit the weak methane bands in the near-infrared, he included a plane-parallel cloud in the lower atmosphere with optical depth 0.46, independent of wavelength. The overlying stratospheric haze in his model has an optical depth that decreases with wavelength. The sum of the two optical depths in the 938 nm methane window region is close to 1.0.

Although there are uncertainties associated with the model, it is reasonable to ask how well ISS can expect to see contrast features in the lower atmosphere or on the surface with an overlying cloud and haze optical depth of 1.0. We are most interested in features with small spatial scales (the NAC pixel spacing corresponds to about 6 m for the closest passes,  $\sim 950$  km above the surface. The contrast at large spatial scales seen in Voyager images and HST images (Smith *et al.*, 1996) can be carried by the diffuse radiation field. However, at small spatial scales (smaller than the vertical distance of the scattering layer from the surface, roughly 200 km), the contrast must be carried by photons that traverse the atmosphere without suffering a scattering event.

The fraction of the light leaving the surface which emerges at the top of the atmosphere without suffering a scattering is  $e^{-1/\mu}$ , ignoring atmospheric curvature, where  $\mu$  is the cosine of the emission angle. The critical question is: how much contrast is seen at the top of the atmosphere for a given surface contrast? Here, contrast is defined as (maximum intensity – minimum intensity)/maximum intensity. The problem is exceedingly difficult if one is trying to estimate contrast induced by topographic slopes. Here, we take the easier route and assess contrast at the top of the atmosphere for a given albedo contrast on the surface.

A plane-parallel model atmosphere would probably suffice for an estimate of contrast near the center of the disk. However, some of the close approaches to Titan will be near the terminator where the atmospheric curvature is important. Therefore, we have constructed multiple-scattering radiative transfer models with the appropriate curvature of Titan's atmosphere. The multiple-scattering model takes full account of multiple scattering in a spherical shell atmosphere containing particles with the asymmetric phase functions thought to be appropriate for Titan (from Lemmon, 1994). It does not take into account polarization except for single scattering. We were able to estimate the effects of Titan's strongly polarizing haze layer by calculating the radiation field carried by singly scattered photons that polarize the light in the way that fractal aggregates do: highly positively polarizing at  $90^\circ$  scattering angle (West and Smith, 1991; Lemmon, 1994). Our estimate of how much the contrast is improved by the use of a polarizing filter is conservative in the sense that light from photons scattered more than once is assumed to be unpolarized. We consider the surface to depolarize the light and to diffusely reflect according to Lambert's law.

In order to estimate contrast at the top of the atmosphere we performed two calculations, each having a spherically symmetric surface and atmosphere. The first calculation had a surface albedo of 0.1; the second, a surface albedo of 0.4. The emerging contrast for the small-scale features was then given by the contrast in the directly transmitted beam divided by the average of the total reflected light from the two runs.

The calculations can be summarized as follows. For nadir viewing near the sub-solar point a surface contrast of 30% at small spatial scales will produce top-of-atmosphere contrast of 6.3% for an average surface albedo of 0.1. The same surface contrast will produce a top-of-atmosphere contrast of 12% if the average surface albedo is 0.4. The light is unpolarized for nadir viewing of the sub-solar point so the contrasts reported above apply to the polarizing filters and non-polarizing filters equally. Near the terminator the top-of-atmosphere contrasts would be 2.6 and 7.1% for the non-polarizing filters and average surface albedos 0.1 and 0.4, respectively. With a polarizer filter the contrast increases to 3.3 and 8.4%. The signal/noise ratio in a single pixel exposed to 70% full well is expected to be 260. The Modulation Transfer Function of the Cassini ISS at the Nyquist frequency is approximately 15%, which reduces the contrast over a few pixels by a factor of 0.15. If the atmospheric model is correct, we expect to detect features at the Nyquist frequency (corresponding to two pixels or 20 m per cycle at the closest Titan flybys) with S/N greater than 10 if the top-of-the atmosphere contrast is 25%. The corresponding surface contrast would need to be near 100%. Features with larger scales or features near the top of the tropospheric cloud level can be detected at lower contrast. Features with horizontal scales larger than  $\sim 5$  pixels should be detectable at surface contrast levels near 30%.

Although Cassini provides an extremely stable platform for long-exposure images, smear remains a significant concern during the very close 'targeted' satellite

flybys, including the close flybys of Titan. Cassini's on-board Inertial Vector Propagation (IVP) system can precisely track a target on Titan from any range greater than  $\sim 1500$  km, but the changing range to Titan introduces significant smear in long exposures ( $> 10$  s) when the range is less than  $\sim 10,000$  km (within  $\sim 30$  min of closest approach). Long exposures are needed to ensure a high S/N at the top of the atmosphere, especially in the CB3 filter, in order to achieve an adequate S/N on the surface. Use of  $2 \times 2$  pixel binning and nearly four times shorter exposure times alleviates this problem, but with a halving of pixel scale. Given the low contrast expected on scales of a few pixels,  $2 \times 2$  binning should result in little loss of available information, and may provide our best imaging mode for Titan's surface. Another option is to image at shorter wavelengths where we can use shorter exposure times than with the CB3 filter. Most promising is the IR1/IR2 combination, which produces a medium-width band center on the 825-nm inter-methane-band window (Section 3). Exposure times for the IR1/IR2 filter combination can be a factor of  $\sim 10$  shorter than for the CB3/Clear combination. However, we cannot combine this two-filter bandpass with an IR polarizer filter. The IR1 filter covers several methane windows and could enable imaging of the surface with exposure times  $\sim 100$  times shorter than with CB3, but with even less contrast on small-scale surface features.

#### 2.4.4. Titan Surface Science

As for all the other satellites of Saturn, a major objective of the ISS for Titan is a determination of its geologic and thermal history. Titan may have initially been largely melted in its outer several hundred kilometers by accretional heat (Schubert *et al.*, 1981), producing a deep global ocean of water ( $\text{H}_2\text{O}$ ) or a water–ammonia mixture ( $\text{H}_2\text{O}$ – $\text{NH}_3$ ). The deep interior initially may have been a largely undifferentiated mass of ice and rock. With the cessation of accretion, an outer layer would have cooled and solidified. Simultaneously, the interior would have warmed due to radio nuclides in the silicates, and perhaps differentiated to form a rocky core and an icy mantle. Based on the evidence for subsurface water in the icy Galilean satellites (Kivelson *et al.*, 2004), most workers now expect a mantle of liquid  $\text{H}_2\text{O}$  to have persisted on all large icy satellites such as Titan (Schubert *et al.*, 2004).

If methane ( $\text{CH}_4$ ) clathrate was present initially, it could be expected to dissociate in the deep interior, releasing methane, which would subsequently tend to rise towards, and possibly extrude out onto, the surface, where it might have formed bodies of liquid and/or evaporate into the atmosphere. (The presence of ammonia ( $\text{NH}_3$ ) might provide a source of material that could also rise to the surface cryovolcanically (Kargel *et al.*, 1991).) A reasonable model for the present internal structure of Titan, then, has a silicate core, a deep mantle of water–ammonia ( $\text{H}_2\text{O}$ – $\text{NH}_3$ ) ice, a subsurface “ocean” of  $\text{H}_2\text{O}$ – $\text{NH}_3$  liquid, upper mantle of  $\text{H}_2\text{O}$  ice that may contain  $\text{CH}_4$  clathrate, and a thin uppermost layer that could be rich in liquid methane and other hydrocarbons (Stevenson, 1992; Lunine *et al.*, 1998; Grasset *et al.*, 2000).

Geologic activity seems likely on Titan. Ganymede shows evidence for tectonism and resurfacing and Callisto does not (Smith *et al.*, 1979a,b); Titan probably contains more volatile material than either and is correspondingly more likely to have been active. Evidence for geologic activity comparable to or more extensive than that on Ganymede would suggest significant tidal heating sometime in Titan's history. Indeed, many of Saturn's small inner satellites, which may contain lower concentrations of volatiles than Titan have been active (Smith *et al.*, 1981, 1982). On most icy satellites, extensional features appear to dominate the resurfacing (Squyres and Croft, 1986). The primary sources of stress are probably internal phase changes and solid-state convection – both likely on Titan.

Evidence for resurfacing on icy satellites ranges from flat, smooth, crater-poor regions (on Enceladus (Squyres *et al.*, 1993) and Ganymede (Parmentier *et al.*, 1982)) to thick, lobate flows indicating emplacement of fluid with a high viscosity or yield stress (on Ariel (Jankowski and Squyres, 1988) and Triton (Smith *et al.*, 1990)). This variety results from a range in the rheologic properties of materials, which may have been extruded in solid, partially molten, or liquid form. Liquid or slush is favored on the small Saturnian satellites because of their low gravity and small buoyant forces (Stevenson, 1982), but extrusion of warm ice on a satellite as large as Titan is possible. Constraints may be placed on the rheology and extrusion state of flows if their thickness can be determined (Jankowski and Squyres, 1988; Melosh *et al.*, 1989; Schenk, 1991), either by observation of topography or by measurement in subsurface profiles. Resurfacing on Titan could lead to unusual effects. For example, buoyancy caused by extrusion beneath liquid could lead to enhanced flow thicknesses. Also, extrusion in the presence of ongoing sedimentation could produce a sequence of interbedded ice and organic layers.

Of the many organics produced in Titan's atmosphere (Raulin and Owen, 2002), most are slightly to negligibly soluble in any surface liquid that may be present. Under the physical conditions present on Titan's surface, they are also generally solid, with the exception of propane ( $C_3H_8$ ), and more dense than a liquid mixture of ethane–methane–nitrogen ( $C_2H_6$ – $CH_4$ – $N_2$ ). One can therefore expect a slow accumulation of solid organic sediment at Titan's surface. If no liquid is present, this solid material will cover Titan's icy surface; if liquid is present, the material might accumulate as sediment in topographic basins. The most abundant insoluble molecules produced by atmospheric chemistry are acetylene ( $C_2H_2$ ), hydrogen cyanide (HCN), methyl acetylene ( $C_3H_4$ ), methyl cyanide ( $CH_3CN$ ), and other alkynes and nitriles. The  $C_2H_2$  alone should accumulate to form a layer  $\sim 100$  m thick (Yung *et al.*, 1984; Sagan and Thompson, 1984). Other solids expected include polyacetylene (Allen *et al.*, 1980; Yung *et al.*, 1984) and complex nitrogenous organic polymers.

Impact craters are probes of satellite crusts, indicators of surface ages and thermal history, and provide information on impactor populations and atmospheric properties over time. Titan's atmosphere should shield the surface from small projectiles and decelerate and ablate larger comets (Ivanov *et al.*, 1997; Engel *et al.*,

1995; Lorenz, 1997; Artemieva and Lunine, 2003). A first-order question to be answered by Cassini is whether Titan's surface is heavily cratered and old or whether there has been extensive resurfacing since an early period of heavy cratering. If Titan's surface is as old as that of Rhea and Hyperion, there should be  $\sim 200$  craters larger than 20 km diameter per  $10^6$  km<sup>2</sup>, close to a saturation density (Engel *et al.*, 1995; Lorenz, 1997). If all of Titan's surface has such a spatial density of large craters similar to Callisto's, then it may have experienced little differentiation and endogenic geologic activity. Observation of terrains with substantially fewer craters will be our first indication that Titan has experienced an extended period of geologic activity, perhaps similar to Ganymede or Triton. The morphologies of the large craters and multi-ring structures may provide clues to the presence or depth to subsurface water (Turtle and Pierazzo, 2001; Schenk, 2002).

Titan's cold temperatures would tend to inhibit the crater relaxation observed on Ganymede and Callisto, while NH<sub>3</sub> hydrate, if present, could soften the ice and enhance relaxation (Durham *et al.*, 1989). An impact regolith on Titan might be coarser grained than on other satellites because small impactors responsible for most near-surface comminution and mixing will be stopped by the atmosphere. With continuous deposition of organic solids, cratering could lead to a sequence of interbedded icy ejecta and organic sediment layers. If liquid is present on the surface, the effects on cratering could be substantial. Normal regolith formation would not be expected. A liquid layer with a depth more than about 40% of the depth of a normal transient cavity should be sufficient to inhibit formation of a crater on its floor (Gault and Sonett, 1982). Even much shallower liquid should be adequate to produce unusual crater forms, with shallow floors and little or no rim (Gault and Sonett, 1982).

If liquid is present on Titan, it could promote erosion. One possible mechanism arises from the solubility of H<sub>2</sub>O in liquid CH<sub>4</sub>–C<sub>2</sub>H<sub>6</sub>–N<sub>2</sub> (Rebiai, 1984). Dissolution of ice over long periods could alter immersed topography (Lunine, 1985b). Dissolution could, of course, be limited by saturation, so one would expect it to be most effective where there is flow of unsaturated fluid, perhaps as tidal currents (Sagan and Dermott, 1982). On the order of 100 m of erosion, could occur in 10<sup>9</sup> years if not inhibited by sediment accumulation. Patterns of erosion and deposition could be complex, influenced by circulation patterns, saturation conditions, and sediment distribution. Dissolution could be promoted by fracturing and zones of weakness in the ice, and it is even possible that caverns, like those formed by aqueous dissolution of carbonates on Earth, could develop. Also, if methane rain occurs (Toon *et al.*, 1988) and falls onto a dry surface we could see physical erosion, development of drainage systems, and even a true 'hydrological cycle'. A number of workers have speculated that the bright region on Titan's leading hemisphere may be a high-standing area of water ice washed clean of dark atmospheric sediment by methane rain. Multi-spectral observations suggest that the leading hemisphere has a purer and/or finer-grained ice surface than the darker hemisphere (Griffith *et al.*, 2003).

Evidence for smooth surfaces with specular reflections have been detected from Earth-based radar (Campbell *et al.*, 2003). If lakes or rivers of liquid organics are present on Titan's surface and if the overlying particle optical depth is not greater than about 2, ISS will be able to image the glint pattern in the specular direction. The size of the glint pattern is diagnostic of the amplitude of capillary waves driven by wind. The relationships between surface slope and wind velocity derived by Cox and Munk (1954) are often used for the Earth. The relationship between wind and surface slope will be different for Titan because of the differences in gravity and viscosity of the liquid and air. Glint reflection is typically much stronger than reflection from diffuse surfaces. Even very small bodies of water were easily detected as specular bright spots in Galileo images of the Earth's land surface. Polarization measurements of specularly reflected light may constrain the refractive index of the liquid. Information to be obtained in this way will depend on the surface coverage of liquid and on our ability to disentangle the effects of atmospheric scattering – a much more severe problem than for the earth.

Finally, even if no liquid is present on the surface, eolian redistribution of sediment or ice might occur. The wind regime at the surface of Titan is unknown. Calculated meridional winds are small, but zonal winds of 25 m/s have been estimated in the lower troposphere (Flasar *et al.*, 1981). Given the high atmospheric density, low gravity, and likely small size of sediment particles, eolian transport may be common. Eolian redistribution could result in an uneven surface distribution of organic sediment, perhaps like that produced by eolian transport of fine dust on Mars.

According to models by Tokono and Neubauer (2002), Saturn's gravitational tide on Titan's atmosphere has a large influence on the meteorology down to the surface. The surface pressure oscillates up to 1.5 Pa through the orbit, with strong temporal and spatial variation in the atmospheric flow near the surface. The superposition of annual thermal latitudinal pressure gradients produces a surface wind pattern of equatorward flow and high-latitude whirls. Meridional tidal winds can be as fast as 5 m/s, perhaps sufficient to produce streaks of fine-grained materials on the surface with a unique global pattern.

#### 2.4.5. *Strategy for Titan Imaging*

For planning purposes, we have placed Titan observations by ISS into the following seven categories:

- Movies or time sequences will be acquired when Titan fills from half to all of the FOV (NAC when distant; WAC at lesser range), to monitor atmospheric features. Low phase angles are favored.
- Photometry observations are planned to image Titan at a range of phase angles through many filter combinations to study atmospheric properties.
- Full-disk mosaics ( $3 \times 3$  to  $5 \times 5$  images) will be taken in several colors for surface and atmospheric studies.



- Global surface mapping at medium resolution (500–1000 m/pixel) is planned from many passes. We expect to achieve  $\sim 70\%$  global coverage at 500–1000 m/pixel, and can fill most gaps at resolutions of a few kilometers/pixel.
- Regional mapping (200–500 m/pixel) will cover areas of interest, including repeat coverage from different viewing angles for stereo imaging of the topography.
- High-resolution imaging will sample terrains at scales of 12–200 m/pixel, covering  $\sim 10\%$  of Titan's surface. Low phase and emission angles are favored for the global, regional, and high-resolution observations. Because the surface of Titan is almost unknown, we are planning 'retargetable' mosaics at regional and local scales to be repositioned after we have mapped the surface at scales of a few kilometers or better. A set of WAC images with filters for atmospheric studies will be acquired along with NAC surface observations to model and remove atmospheric effects.
- Night-time observations will be acquired to search for lightning and aurorae.

In addition to these categories, we will also have observations that ride along with other experiments such as VIMS, CIRS and UVIS.

#### 2.4.6. *Combined Studies with Other Instruments*

Synergistic studies of Titan by Cassini/Huygens experiments will be especially important for the study of Titan (Lunine and Lorenz, 1996; Lunine and Soderblom, 2002). Combined observations and analyses between the orbiter instruments ISS and VIMS, CIRS, UVIS, and RADAR, as described earlier for other satellites, will be especially important because of the challenges presented by the presence of a dense atmosphere. The atmospheric haze will limit ISS to imaging the surface and lower atmosphere in only a few bandpasses but its capabilities for high spatial resolution and global mapping dovetail nicely, for example, with those of VIMS which observes farther into the near-IR where stratospheric haze optical depth is less. Simultaneous imaging of Titan in regions of methane cloudiness should enhance both experiments' ability to place local cloud events on Titan into a large-scale perspective, as well as allow ISS to model the effects of the atmosphere on surface images through retrieval of atmospheric structure from VIMS data.

In surface imaging, ISS will provide primarily morphologic and albedo/contrast information, while VIMS will add compositional mapping of the surface. RADAR altimetry can help to control regional tilts in ISS stereo models. Imaging by ISS will be important to place the narrow RADAR imaging strips into regional context, and to image these locations at higher spatial resolution. The subsurface information returned by RADAR could be especially interesting, combined with the high-resolution ISS images and VIMS spectral image cubes. The most accurate maps of Titan will require a joint solution utilizing Radar (SAR) and ISS images.

We expect that ISS images of Titan will be important for the choice of targets by other experiments, especially VIMS. Likewise, observations by VIMS, RADAR,

and perhaps CIRS will influence targeting by ISS. There will be particular challenges if the lower atmosphere is patchy and variable, or if the surface is geologically active and temporally variable.

The DISR on the Huygens probe will make extensive and detailed measurements of a very small region on Titan as it descends through the atmosphere (Tomasko *et al.*, 2002). It will image the surface and atmosphere from near-nadir to above the horizon. Its solar aureole cameras will measure light scattered from the sun at forward angles to within a few degrees of the sun and in horizontal and vertical polarization states. Its visible and near-infrared spectrometers will provide information on the spectral content of the internal radiation field and surface. These measurements will be invaluable to ISS. The DISR observations can be used as ‘ground truth’ for ISS retrievals of surface features, aerosol optical depth and aerosol properties as a function of altitude. They will help the ISS team assess the information content and quality of the retrievals which will be carried out on a global scale with the help of other orbiter data as mentioned earlier. Orbital imaging at the highest possible spatial resolution of the region observed by DISR is a high priority.

### 3. Instrument Characteristics and Capabilities

#### 3.1. HISTORY OF THE CASSINI ISS DESIGN

The origin of the Cassini camera dates back to the NASA/JPL Mariner Mark II program that called for the development of a series of common spacecraft to explore the outer solar system in the post-Voyager era. One main feature of this design, relevant to imaging investigations, was a high-precision scan platform (HPSP) for supporting the optical remote sensing instruments. In the early 1980s, the now extinct Comet Rendezvous/Asteroid Flyby (CRAF) mission and Cassini were identified as the first two missions of this program.

In 1984, an Instrument Development Team (IDT), led by Dr Joseph Veverka of Cornell University, was appointed by NASA to help define an imaging system for CRAF and subsequent Mariner Mark II missions. In 1988, this task was expanded specifically to include Cassini and the emphasis of the IDT became the definition of an imaging system that would meet *all* of the scientific requirements of both missions. The IDT recommended the following system characteristics:

- Dual focal lengths: A NAC for high-resolution studies with a maximum focal length consistent with the projected pointing stability of the Mariner Mark II platform, and a WAC, like Voyager but unlike Galileo, for context and broad spatial coverage with a FOV six to eight times larger than the NAC.
- Broad and identical spectral range in *both* cameras from 1100 nm down to the near-UV at 200 nm (compared to 300–650 nm on Voyager, and 350–1100 nm on Galileo).

- Improved filter wheel design to accommodate more than the traditional (Voyager and Galileo) eight filter slots, in order to exploit the increased spectral range and the known richness of cometary emission spectra for CRAF, and compositional diagnostics of near-IR spectra of ices in comets and at Saturn.

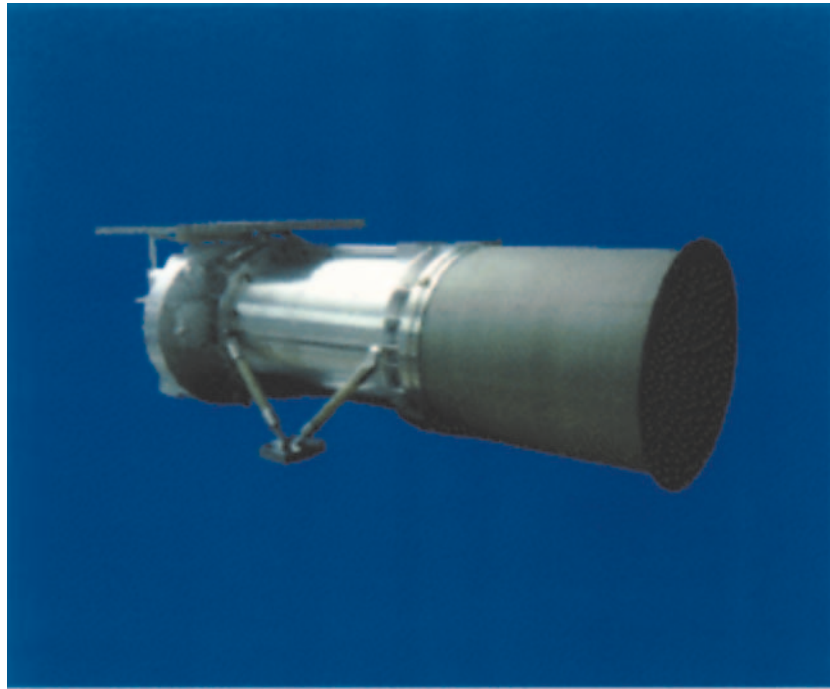
The narrow-angle design, essentially the Cassini NAC of today, evolved into a 2-m focal length,  $f/10.5$  Ritchey-Chretien telescope, extending from 200 to 1100 nm with a dual filter wheel system similar in design to that used in the HST's Wide Field Planetary Camera (WFPC) and capable of carrying 24 filters. To date, this is the longest focal length framing camera flown on a planetary mission. Both Voyager and Galileo had 1.5 m focal length cameras. The longest focal length to date (3.5 m) belongs to the MOC camera on Mars Global Surveyor (Malin *et al.*, 1992). MOC is a "push-broom" system with a single-line CCD, rather than a two-dimensional array, having a linear FOV that is 'pushed' along the target by the translational motion of the spacecraft.

The complementary wide-angle design initially developed for Mariner Mark II was to be a  $f/2.5$  Schmidt-Cassegrain reflector with a 0.3 m focal length, a  $2.3^\circ$  square FOV (compared to  $0.35^\circ$  for the NAC), and designed to utilize a dual filter wheel system carrying 14 filters covering the spectral range from 200 to 1100 nm. Although this original WAC design met *all* the scientific requirements of CRAF and Cassini, it was deemed too complex, heavy, and costly. By the time the Cassini Announcement of Opportunity was published in 1989, the Cassini WAC had evolved into a less expensive  $f/4$  refractor, with a 0.25 m focal length, a  $2.8^\circ$  FOV and a less desirable lower wavelength limit of 350 nm (unfortunately sacrificing the near-UV response).

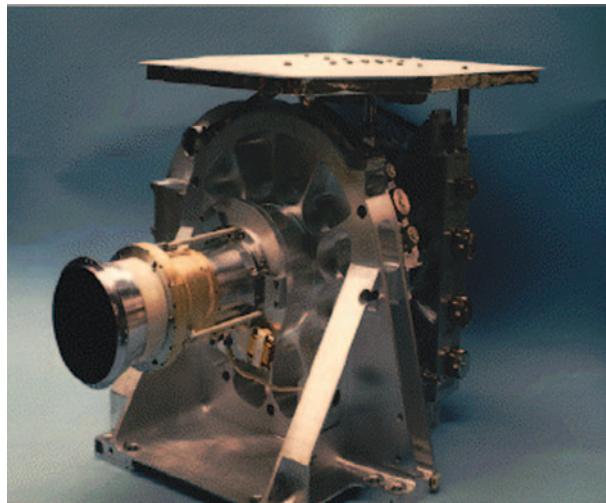
In November 1990, the Cassini Imaging Science team was selected (Table I) and it was left to this group to oversee and participate in the development of the ISS by JPL. As part of a serious cost reduction to the CRAF/Cassini program in 1992 that resulted in the termination of CRAF as well as the deletion of the Cassini HPSP and the placement of all Cassini remote sensing instruments directly onto the body of the spacecraft, the Imaging Team, in collaboration with the JPL instrument engineers, decided to abandon the WAC optical design to save money and replace it with spare Voyager-era wide-angle optics. The instrument, which is the present Cassini WAC, became an  $f/3.5$  color-corrected refractor, with a 200 mm focal length and a  $3.5^\circ$  square FOV, fronting a new dual filter-wheel assembly and focal plane. The spectral range was limited to 380–1100 nm, spanned by 18 filters.

### 3.2. GENERAL INTRODUCTION TO CAMERA CHARACTERISTICS

The Cassini ISS consists of two fixed focal length telescopes called 'cameras' (Figure 13). The NAC is 95 cm long and 40 cm  $\times$  33 cm wide; the WAC is 55 cm long and 35 cm  $\times$  33 cm wide. Both camera systems together have a mass of 56.9 kg. They sit on the Remote Sensing Palette (RSP) (Figure 14), fixed to the body



(A)



(B)

*Figure 13.* Photographs taken of the flight models of the Cassini (A) Narrow-Angle Camera Head Assembly and (B) Wide-angle Camera Head Assembly.

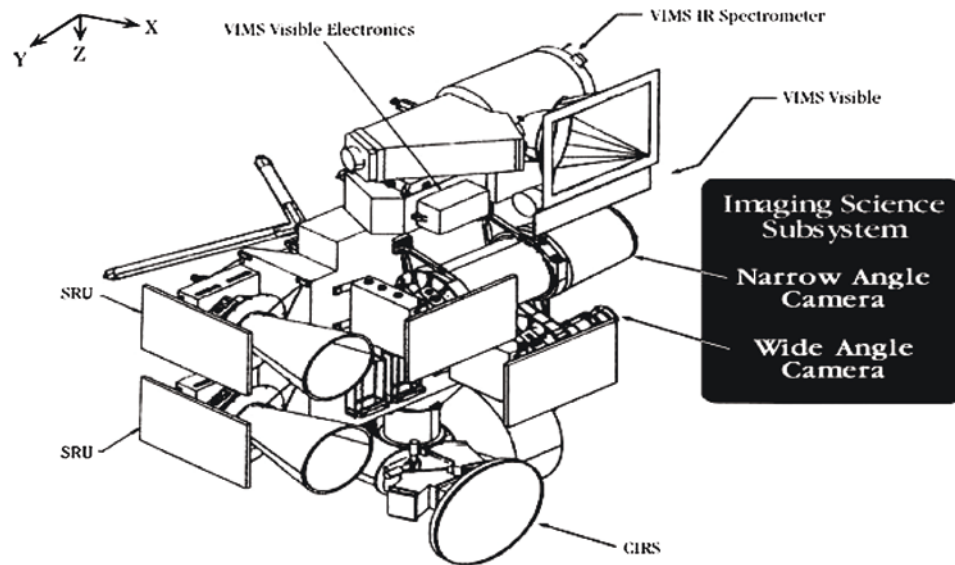


Figure 14. The layout of the optical remote sensing instruments, including the narrow and wide-angle cameras of the ISS and the Stellar Reference Units (SRU), on the Remote Sensing Palette of the Cassini Orbiter spacecraft. The spacecraft coordinate system ( $X$  s/c,  $Y$  s/c,  $Z$  s/c) is also indicated in the upper left (Section 3.6.1).

of the Cassini Orbiter, between the VIMS and the CIRS, and above the Ultraviolet Imaging Spectrometer. The apertures and radiators of both telescopes are parallel to each other. Figure 15 illustrates the FOVs of the NAC and WAC and those of the other remote sensing instruments on the palette.

The cameras are identical, except in the design of the optics and the number of filters. Each has its own set of optics, mechanical mountings, CCD, shutter, filter wheel assembly, temperature sensors, heaters, various control electronics, Engineering Flight Computer (EFC), and Bus Interface Unit (BIU) to the central spacecraft Command and Data System (CDS) (Figure 16). The electronics that control each camera consist of two parts: sensor head subassembly and the main electronics subassembly. The Sensor Head electronics supports the operation of the CCD detector and the preprocessing of the pixel data. The Main Electronics provide the power and perform all other ISS control functions, including generating and maintaining internal timing which is synchronized to the CDS timing of 8 Hz, control of heaters, and the two hardware data compressors. The Cassini EFC is a radiation-hardened version of IBM's standard, general purpose MIL-STD-1750A 16-bit computer and is the ISS processor that controls the timing, internal sequencing, mechanism control, engineering and status data acquisition, and data packetization.

The NAC is an  $f/10.5$  reflecting telescope with an image scale of  $\sim 6\mu$  rad/pixel, a  $0.35^\circ \times 0.35^\circ$  FOV, and a spectral range from 200 to 1100 nm. Its filter wheel

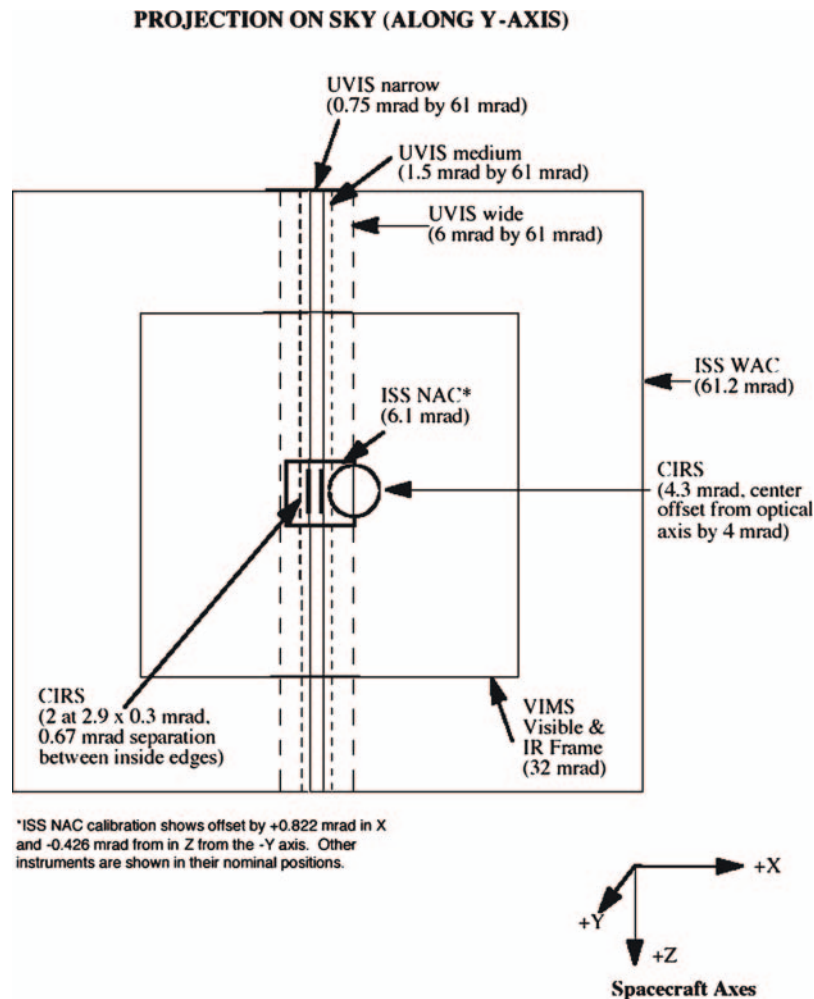
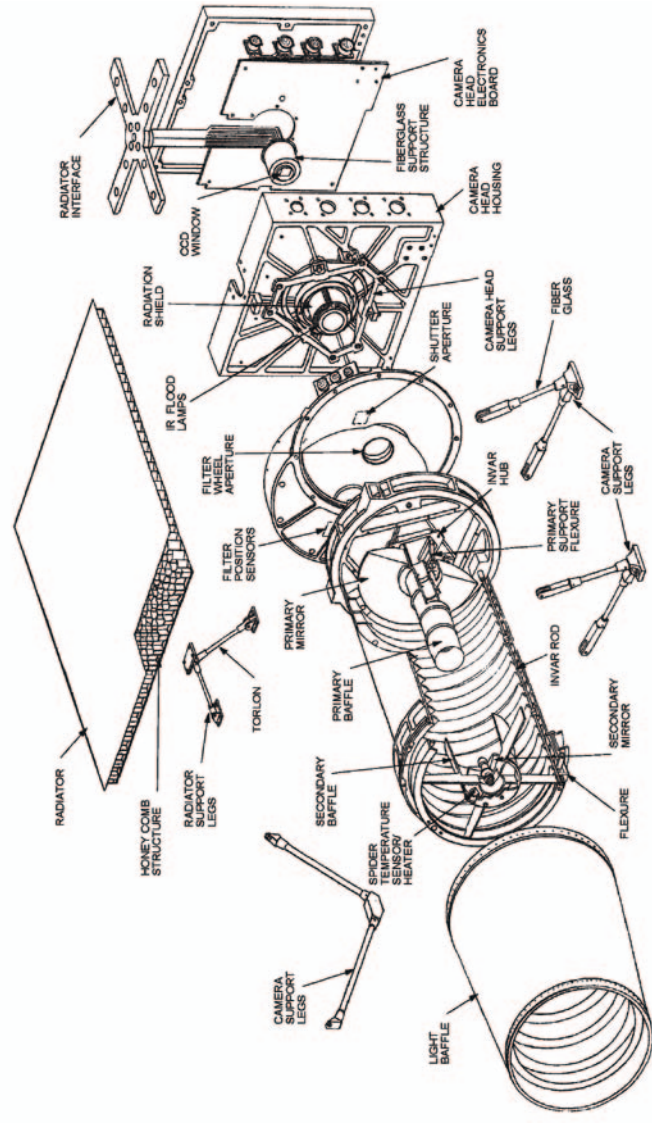


Figure 15. A diagram illustrating the fields of view of the optical remote sensing instruments (Ultra Violet Imaging Spectrometer (UVIS), Composite Infrared Spectrometer (CIRS), and Visual and Infrared Mapping Spectrometer (VIMS), Imaging Science Subsystem (ISS) narrow (NAC) and wide-angle (WAC) cameras.

subassembly carries 24 spectral filters: 12 filters on each of two wheels. The optical train of the WAC, a Voyager flight spare, is an  $f/3.5$  refractor with a  $\sim 60 \mu$  rad/pixel image scale and a  $3.5^\circ \times 3.5^\circ$  FOV. The refractor design limits the lower end of the spectral range on the WAC which is 380–1100 nm. The WAC filter subassembly carries nine filters in each of two filter wheels, for a total of 18 filters. In both cameras, images are acquired through two filters, one on each wheel, allowing in-line combinations of filters for greater flexibility: i.e., polarizers in line with other spectral filters, new bandpasses created by the overlap of two spectral filters, etc.



# Narrow Angle Camera

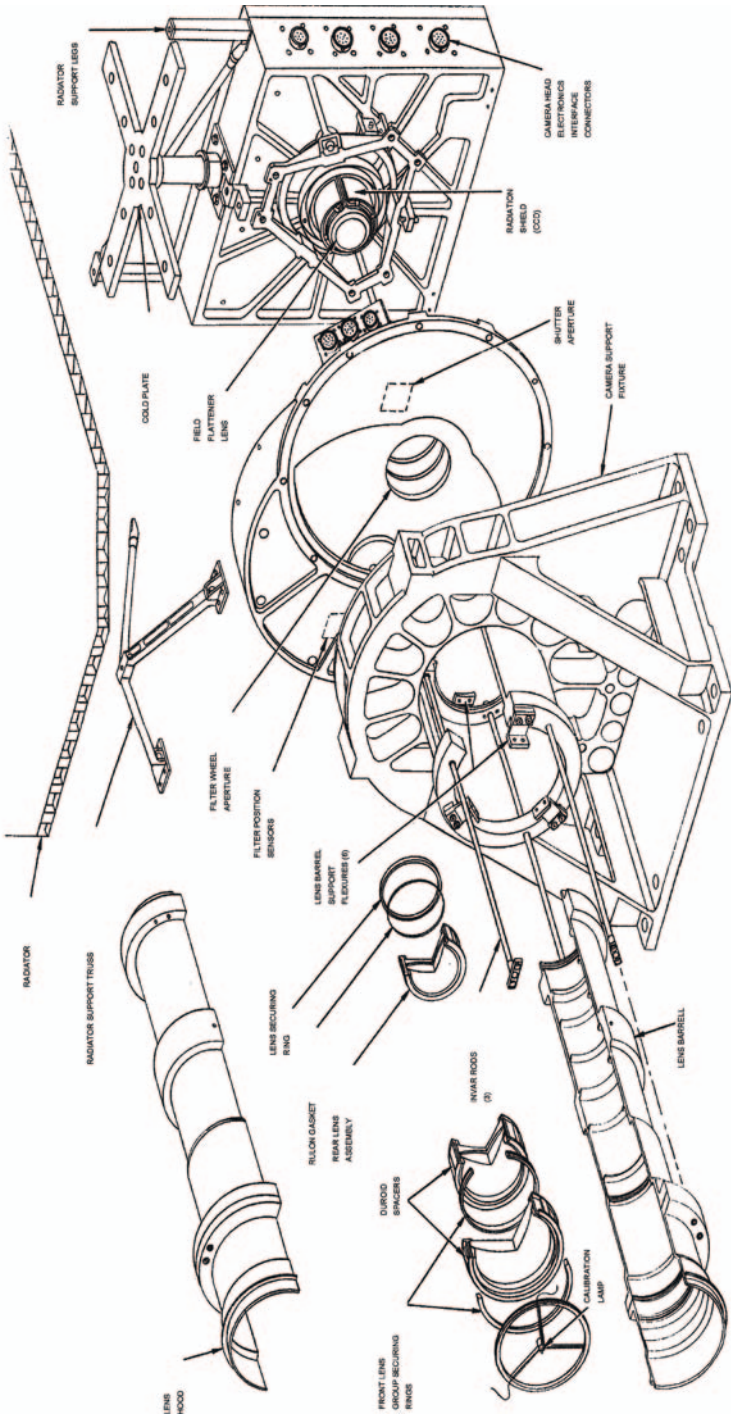


(A)

Figure 16. (A) A diagram showing the various components in the Cassini Narrow-Angle Camera Head Assembly. (B) Similar diagram for the Cassini Wide-angle Camera Head Assembly.

(Continued on next page)

Wide Angle Camera



(B)

Figure 16. (Continued).

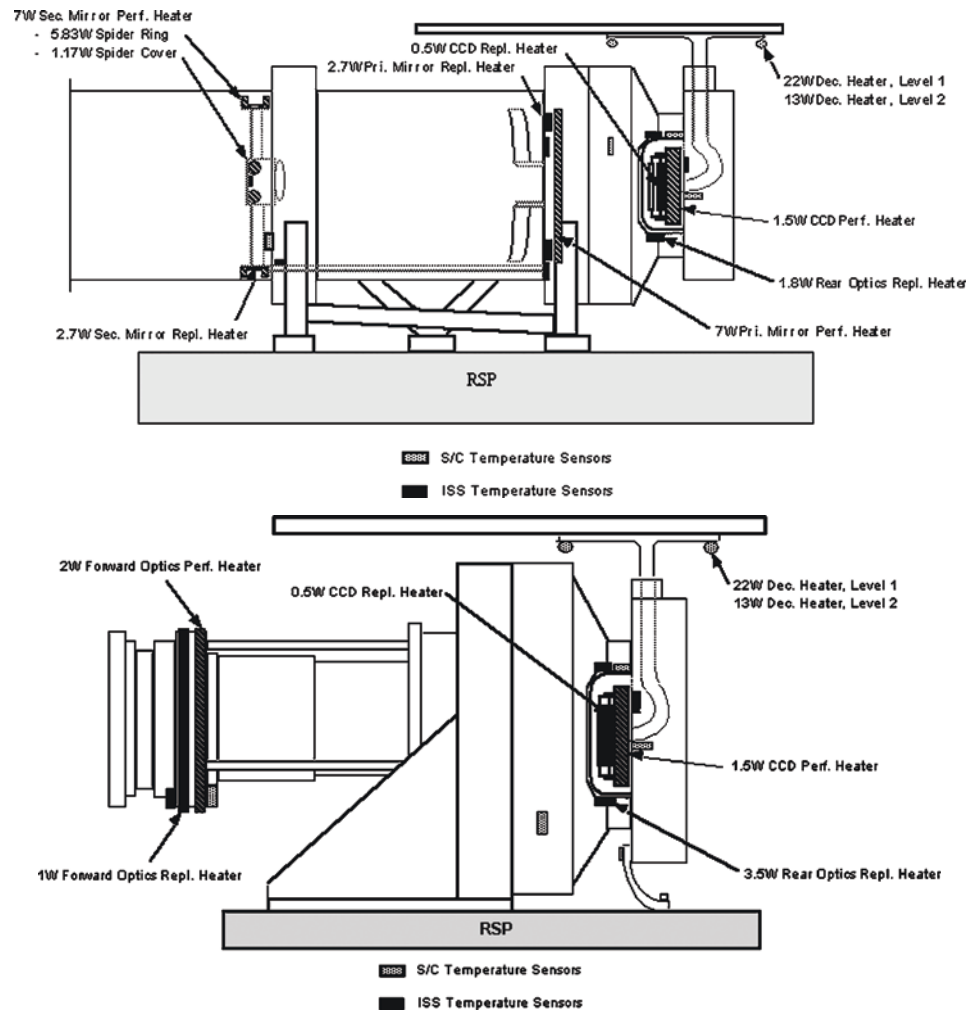


Figure 17. A diagram illustrating the placement of the ISS-controlled replacement and performance ('active') heaters and spacecraft-controlled heaters which thermally stabilize the ISS and keep it within flight-allowable operating limits.

The NAC is thermally isolated from the RSP in order to minimize the effects of RSP thermal transients on the NAC image quality. Unlike the NAC, the WAC has less stringent image quality requirements and its bulk temperature control is provided by the pallet. Figure 17 illustrates the placement of heaters within the ISS.

The temperature of the CCD is controlled by a passive radiator, directly connected to the focal plane, along with an active 'performance' heater on the CCD to adjust the temperature. The temperature of the optical elements is con-

trolled by active ‘performance’ heaters positioned along the optical path. The radiator subassembly also includes two sets of spacecraft-controlled decontamination heaters, which are used to minimize deposition of volatile contaminants on either the detector or radiator and to minimize radiation damage to the CCD. All heaters are commandable (On or Off) during flight.

The ISS has three operational power states: On, Sleep and Off. In the On state, the cameras are Active or Idle. In this state, both the spacecraft replacement heaters and ISS decontamination heaters are Off. The camera software has active control over the performance heaters to set appropriate operating temperatures for the optics and CCD detector. The Active sub-state is entered to collect science data as well as for calibration and maintenance activities. Command execution in the Active state includes science data readout, filter wheel movement, shutter movement, activation of light flood and calibration lamps, and other high power-consuming activities. Idle is a background state in which no commands are executing. When the camera is in Idle state, uploads can be processed, real-time and ‘trigger’ commands can be accepted from the CDS (Section 3.7), and macros can be stored. The execution of any command sends the camera into the Active state. The camera always returns to Idle state after completing a command sequence. Peak power consumption during active imaging is 26.2 W in the NAC and 19.4 W in the WAC (Table VI).

The ISS Sleep state is a non-data-taking low power state that is used when no activity is planned for an extended period. During this state, the sensor head and main ISS electronics are drawing power, and the optics and CCD heaters are On to maintain operating temperature limits. Spacecraft controlled replacement heaters are Off. The decontamination heaters may be used, if necessary. In Sleep, the NAC consumes 22.3 W, and the WAC consumes 16.4 W.

In Off, no power is drawn by the ISS in either the NAC or WAC. The spacecraft controlled replacement heaters and ISS decontamination heaters may be turned

TABLE VI  
Power states of the ISS.

Camera state	Estimated power for NAC (W)	Estimated power for WAC (W)
Off (includes replacement heat)	8.4	4.5
On/Sleep	22.3	16.4
On/Idle	22.3	16.4
On/Active	26.2	19.4
Off/Decon Level 1 (includes replacement heat)	25.7	21.4
Off/Decon Level 2 (includes replacement heat)	35.0	30.7

Currently, Decon 1 draws 20 W, and Decon 2 draws 10 W for both NAC and WAC. The average operating power is 45.6 W during Cruise when NAC and WAC are turned on.

On when necessary. The replacement heaters keep the ISS within allowable flight non-operating temperature limits and the decontamination heaters can be used to provide for CCD protection from the radiation environment and from the condensation of volatiles. In this state, the NAC consumes 8.4 W and the WAC, 4.5 W.

### 3.3. OPTICS

#### 3.3.1. *Design*

The essential difference between the narrow and wide angle camera lies in the design of the optical train. The NAC optics were specially designed to improve on the quality and resolution of images of the bodies in the Saturn system returned by Voyager. It is based on a Ritchey-Chretien reflector design. The focal plane fields of view for both cameras are limited by the size of the CCD. The NAC point spread function (PSF) was designed to be approximately the same physical size as a pixel in the near-IR. Because of the Voyager optics, the same is not true for the WAC, whose PSF is somewhat larger than the pixel size. The full width at half maximum (FWHM) of the PSFs of the NAC and WAC through the clear filters are 1.3 and 1.8 pixels, respectively. The in-flight measured characteristics of the optics of both the NAC and WAC as well as other characteristics are given in Table VII.

All the reflective optical elements within the NAC (the primary and secondary mirrors) are manufactured of fused silica; all refractive NAC elements (such as the field correctors and the window on the sealed CCD package) are made of either fused silica or single-crystal vacuum-UV-grade calcium fluoride. The optical elements in the WAC are composed of radiation-hardened optical glass (BK7 or lithium fluoride) or fused silica. Antireflection coatings consisting of single layer  $\text{MgF}_2$  were deposited on all optical elements (except the NAC mirrors) in both cameras, such as the field correctors in the NAC and the primary optics in the WAC; a multi-layer  $\text{MgF}_2$  coating was applied to the primary and secondary aluminum-coated mirrors in the NAC to enhance reflectivity. A fused silica quartz plug is placed immediately in front of each CCD package to protect the detector against radiation damage and to minimize radiation-induced noise in the images. The spectral transmissions of the NAC and WAC optics are shown in Figure 18.

#### 3.3.2. *Geometric Fidelity*

The use of a CCD ensures that the image geometry is not affected by the brightness, or gradients in brightness, across the scene as it is in a vidicon detector, like Voyager's, with a particle beam readout. Any departure from geometric fidelity in the Cassini cameras is expected to come from the optical elements and/or thermal effects thereon. The long focal length of the NAC makes optical image quality especially vulnerable to temperature changes and gradients along the barrel of the camera. Both cameras were designed to remain in focus without an active focus

TABLE VII  
Cassini ISS characteristics.

General		
CPU	IBM MIL-STD-1750A 16-bit processor	
CCD	Three-phase, front-side illuminated	
Pixel size	12 $\mu\text{m}$	
Format	1024 $\times$ 1024	
Available exposures	64 commandable settings, 5 msec–1200 s	
Minimum framing time	11 s (4 $\times$ 4 sum, highest CDS pickup rate)	
Signal digitization	12 bits, 4095 DN	
Summation modes	1 $\times$ 1, 2 $\times$ 2, 4 $\times$ 4	
Pixel full well	120,000 e <sup>−</sup> (normal); 1,000,000 e <sup>−</sup> (low gain, 4 $\times$ 4)	
Data conversion (12:8)	‘Square Root Encoding’ (LUT), Least-Significant 8 Bits (L58B)	
Data compression	Lossless; Lossy	
Read noise level	12 e <sup>−</sup> (high gain state)	
	NAC	WAC
Type	Reflector	Refractor
Mass	30.5 kg	26.4 kg
Dimensions	95 cm $\times$ 40 cm $\times$ 33 cm	55 cm $\times$ 35 $\times$ 33 cm
$F/N$	10.5	3.5
Focal length	2002.70 $\pm$ 0.07 mm	200.77 $\pm$ 0.02 mm
Pixel angular size	5.9907 $\mu\text{r}$ /pixel	59.749 $\mu\text{r}$ /pixel
FOV	6.134 mrad	61.18 mrad
FWHM of PSF	1.3 pixels	1.8 pixels
Peak power (active)	26.2 W	19.4 W
Spectral range	200–1050 nm	380–1050 nm
Filter positions	12 $\times$ 2 filter wheels	9 $\times$ 2 filter wheels
Gain state	0: 1: 2: 3	0: 1: 2: 3
Gain values (e-/DN)	233: 99: 30: 13	211: 85: 28: 12
Gain state factors	0.13: 0.31: 1.0: 2.36	0.13: 0.31: 1.0: 2.36
Limiting magnitudes (in $t_{\text{exp}}$ = 1 s, gain state 2, 12-bit data)	$M_v \sim 14$	$M_v \sim 11.6$

mechanism. Instead, heaters have been placed in both cameras at various locations (Figure 17) to (i) maintain the temperatures of the optical elements within 1 °C in the NAC and 5 °C in the WAC of the nominal temperature, and (ii) maintain the temperature difference along the barrel within 2 °C in the NAC and 10 °C in the WAC. Low expansion invar spacers help maintain focus in the NAC.



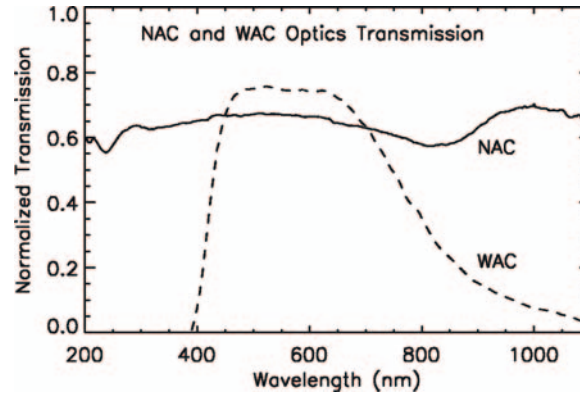


Figure 18. The transmission of the optics of the NAC and the WAC as measured pre-flight. The WAC optics are Voyager-era spare optics which were used in order to reduce costs.

In an ideal camera, the position of an object in the image plane is linearly proportional to its angular distance from the optical axis. Departure from this ideal is expressed as geometric distortion. The larger FOV of the WAC makes it more susceptible to such distortions. Measurements of distortion and its dependence on temperature and spectral bandpass in the NAC and WAC were made on the ground and in flight.

If  $R_{\text{obs}}$  is the observed radial distance of a point from the optic axis, and  $R_{\text{id}}$  the ideal radial distance, the relation can be expressed as  $R_{\text{obs}} = R_{\text{id}} \div (1 + k * R^2)$ . The ground-based measurements suggested distortions up to about  $R_{\text{obs}} - R_{\text{id}} \sim 3.6 \pm 0.2$  pixels in the corners of the CCD in the WAC, independent of spectral bandpass, over the optics temperature range of  $-10^\circ$  to  $+25^\circ\text{C}$ . (Nominal operating optics temperature is  $5^\circ\text{C}$ ). Ground-based measurements were not made on the NAC since analytical calculations indicated distortions less than 1 pixel.

During the cruise from launch to Jupiter, observations were made of the Pleiades and on the open cluster M35 in Gemini in both cameras to determine focal length and distortion, as these observations are capable of far greater accuracy than the ground measurements and also apply to the flight state of the cameras. These images demonstrated a consistent distortion parameter for the WAC of  $k = -6.27 \pm 0.25 \times 10^{-5} \text{ mm}^{-2}$ , and slight changes in focal length as a function of filter combination. The WAC focal length in the clear filter is  $200.77 \pm 0.02 \text{ mm}$ . Focal lengths in other filter combinations range from 200.71 to 201.22 mm, yielding a range in image radius of 1.27 pixels for a nominal 500-pixel radius object. Thus, individual filter combinations need to be fully calibrated to determine specific focal length. The distortion parameter remains essentially constant in the different filters. In-flight distortion measurements for the WAC are consistent with those taken from the ground: 3.36 pixels in the corners.

In the NAC, in-flight measurements from M35 yielded a distortion parameter of  $k = -8.26 \pm 0.23 \times 10^{-6} \text{ mm}^{-2}$ , 0.45 pixels of distortion in the corners, and a clear filter focal length of  $2002.70 \pm 0.07 \text{ mm}$ . NAC focal lengths in different filters range from 2002.13 to 2003.09 mm, yielding a range in radius of a nominal 500-pixel target of 0.24 pixels.

The resulting nominal pixel scale for the NAC is  $5.9907 \mu\text{rad/pixel}$ ; for the WAC it is  $59.749 \mu\text{rad/pixel}$ .

(It was found that the pixels are systematically rectangular, and not square, at a level  $9\times$  the measurement error in the NAC and the  $25\times$  the measurement error in the WAC, and that they are slightly smaller in the line direction, yielding a different scale in one direction than in the other. However, the difference from square is only 0.01% of the pixel size (or image scale) and is not likely to affect either spatial or photometric measurements in any significant way.)

#### 3.4. SPECTRAL FILTERS: SCIENCE JUSTIFICATION, CHARACTERISTICS AND PLACEMENT

The selection of filters for the Cassini ISS and their distribution between the two cameras were determined by the scientific objectives to be addressed by each camera, the cameras' spectral range and capabilities, and even the orbital tour itself. The fundamental nature of an outer planet orbiter mission like Cassini, which is required to examine many targets at close range at various distances from the planet and is therefore characterized by highly eccentric planet-centered orbits and very fast flybys, mandates coverage of a wide range of viewing and phase angles in very short time intervals. Viewing and phase angle coverage is required for all photometric science, including major Cassini objectives such as characterizing the nature of the icy satellites' terrains, the nature of the ring particles and their size and vertical distributions, and the scattering behavior and vertical distribution of hazes and clouds in the atmospheres of Saturn and Titan. It is during the periods nearest closest approach to Saturn, Titan and the icy satellites that the largest variation in viewing and phase angles occurs. These geometries are not, in general, duplicated at other times during the tour, yet these intervals around closest approach do not allow sufficient time to cover the necessary territory with the NAC. While the NAC will be used for spectrophotometric observations on approach to a target when sequencing time is generally not a contentious issue, this task will be handed over to the WAC during the times nearest closest approach.

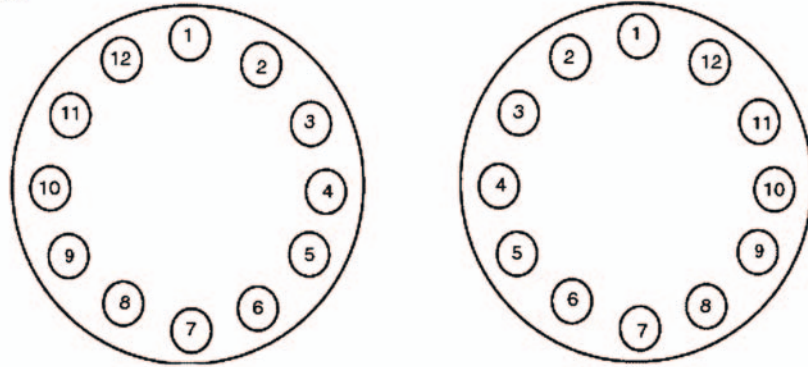
To this end, more than half of the NAC filters are duplicated in the WAC. Seven medium/broad-band filters from the blue to the near-IR for spectrophotometry, two methane and two continuum band filters for atmospheric vertical sounding, two clear filters, and a narrow band Ha filter for lightning observations are all carried on both cameras. For these common filters, the bandpasses are actually shifted a

little (up to 15 nm) because of the differing spectral transmissions of the WAC and NAC optics. These common filters will also enable a cross-check on radiometric calibrations.

The ISS filter assembly design – consisting of two filter wheels and a filter changing mechanism – is inherited from the HST WF/PC camera. Each wheel is designed to move independently, in either the forward or reverse direction, at a rate of two filter positions per second in the WAC and three positions per second in the NAC. A homing sensor on each wheel defines a home wheel position: wheel positioning can be commanded absolutely or relatively.

(The layout of the filters in each filter wheel in each camera is illustrated in Figure 19; filter characteristics are listed in Table VIII; the spectral transmissions are plotted in Figures 20–22.)

A. NAC:



#### NAC Filters

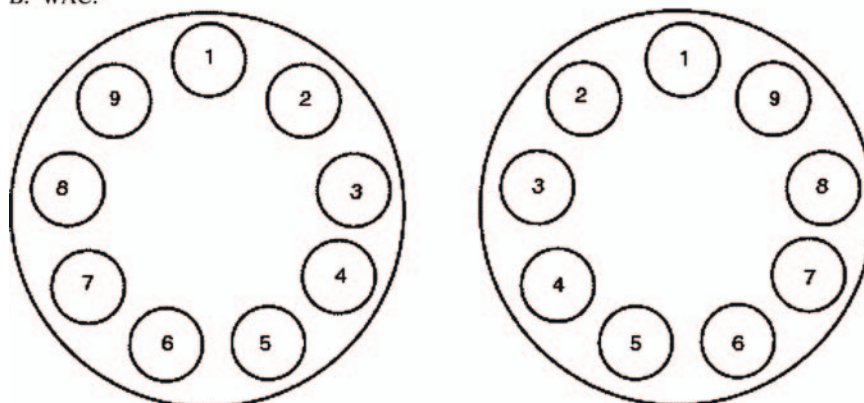
(Wavelengths, in nm, are central wavelengths computed using the full system transmission function.)

Filter Wheel #1	Filter Wheel #2
1) CL1 (611W)	1) CL2 (611W)
2) Red (650W)	2) GRN (568W)
3) BL1 (451W)	3) UV3 (338W)
4) UV2 (298W)	4) BL2 (440M)
5) UV1 (258W)	5) MT2 (727N)
6) IRP0 (746W)	6) CB2 (750N)
7) P120 (617W)	7) MT3 (889N)
8) P60 (617W)	8) CB3 (938N)
9) P0 (617W)	9) MT1 (619N)
10) HAL (656N)	10) CB1 (619N)
11) IR4 (1002LP)	11) IR3 (930W)
12) IR2 (862W)	12) IR1 (752W)

Figure 19. The distribution of the Cassini spectral filters in the two filter wheels in the NAC and WAC. The numerical values quoted for each filter are the central wavelengths computed using the full system transmission function (Table VIII) and are the numerical ‘names’ by which the filters are referenced.

(Continued on next page)

## B. WAC:

**WAC Filters**

(Wavelengths, in nm, are central wavelengths computed using the full system transmission function.)

**Filter Wheel #1**

- 1) CL1 (635W)
- 2) IR3 (918W)
- 3) IR4 (1001LP)
- 4) IR5 (1028LP)
- 5) CB3 (939N)
- 6) MT3 (890N)
- 7) CB2 (752N)
- 8) MT2 (728N)
- 9) IR2 (853W)

**Filter Wheel #2**

- 1) CL2 (635W)
- 2) RED (648W)
- 3) GRN (567W)
- 4) BL1 (460W)
- 5) VIO (420SP)
- 6) HAL (656N)
- 7) IRP90 (705W)
- 8) IRP0 (705W)
- 9) IR1 (742W)

*Figure 19. (Continued).*

Specific scientific considerations that dictated filter choices included the following.

1. Achieving the highest possible sensitivities for imaging faint targets as well as allowing short exposure times to minimize smear during close flybys. There are clear filters in each filter wheel, sensitive to the full spectral range of the CCDs. The clear filter is in the “home” slot of each filter wheel, since it was deemed that sticking of a filter wheel, should it occur, was most likely to occur in the home position. Typically, a clear filter in one wheel is combined with a color filter in the other wheel. Because of the use of Voyager refractive optics, the CL1 filter in the WAC is a special thin filter designed to improve focus across the entire spectral range of the WAC when used in combination with the filters on the second WAC filter wheel (Figure 19).
2. Covering the spectral range of the CCD for color imaging of a wide range of targets. These are a set of medium- and broad-band color filters and include the

TABLE VIII  
ISS filter characteristics.

Filter	$\lambda_{\text{cen,NAC}}$	$\lambda_{\text{eff,NAC}}$	$\lambda_{\text{cen,WAC}}$	$\lambda_{\text{eff,WAC}}$	Science justification
UV1	258W	264	–	–	Aerosols
UV2	298W	306	–	–	Aerosols, broad-band color
UV3	338W	343	–	–	Aerosols, broad-band color, polarization
VIO	–	–	420SP	420	Broad-band color
BL2	440M	441	–	–	Medium-band color, polarization
BL1	451W	455	460W	463	Broad-band color
GRN	568W	569	567W	568	Broad-band color
MT1	619N	619	–	–	Methane band, vertical sounding
CB1	619N	619	–	–	Two-lobed continuum for MT1
CB1a	635	635	–	–	
CB1b	603	603	–	–	
RED	650W	649	648W	647	Broad-band color
HAL	656N	656	656N	656	H-alpha/lightning
MT2	727N	727	728N	728	Methane band, vertical sounding
CB2	750N	750	752N	752	Continuum for MT2
IR1	752W	750	742W	740	Broad-band color
IR2	862W	861	853W	852	Broad-band color; ring absorption band
MT3	889N	889	890N	890	Methane band, vertical sounding
CB3	938N	938	939N	939	Continuum for MT3; see thru Titan haze
IR3	930W	928	918W	917	Broad-band color
IR4	1002LP	1001	1001LP	1000	Broad-band color
IR5	–	–	1028LP	1027	Broad-band color
CL1	611	651	635	634	Wide open, combine with wheel 2 filters
CL2	611	651	635	634	Wide open, combine with wheel 1 filters
P0	617	633	–	–	Visible polarization, 0°
P60	617	633	–	–	Visible polarization, 60°
P120	617	633	–	–	Visible polarization, 120°
IRP0	746	738	705	705	IR polarization; see through Titan haze
IRP90	–	–	705	705	IR polarization; see through Titan haze

All wavelengths in nm. Central wavelengths ('cen') are computed using the full system transmission function (i.e., item (12) given in Section 3.13.1). These numbers are taken to be the numerical name assigned to the filter. Effective wavelengths ('eff') are computed using the full system transmission function convolved with a solar spectrum (Figure 23). Bandpass types: SP: short wavelength cutoff; W: wide; N: narrow; LP: long wavelength cutoff.

BL1, GRN, RED, IR1, IR2, IR3, and IR4 filters on both cameras, and the UV1, UV2, and UV3 (NAC only) and VIO and IR5 (WAC only) (Figure 20).

Because of its reflecting optics and its unique ability to see in the UV, only the NAC carries filters for UV observations. The lumogen coating on the CCDs

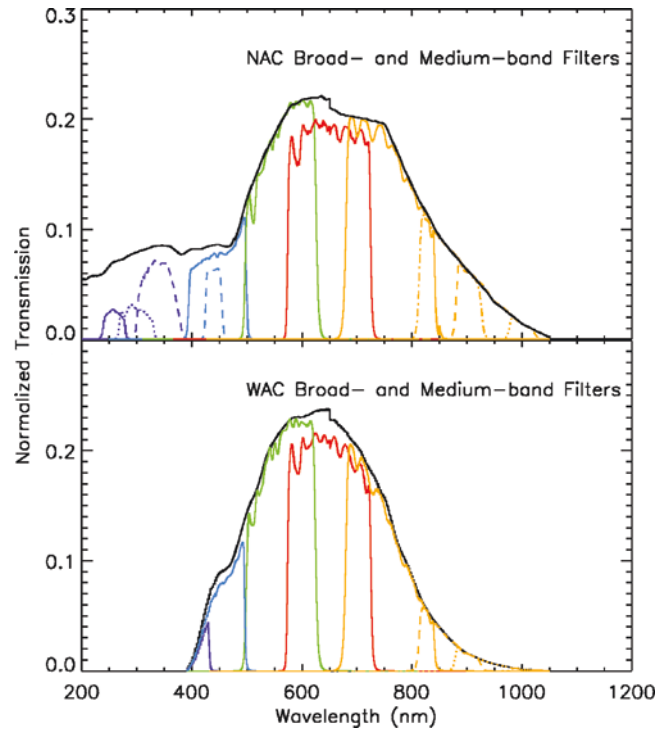


Figure 20. System transmission functions for NAC and WAC broad- and medium-band filters. Filters for the NAC are as follows: UV1, UV2, UV3 (purple: solid, dotted, and dashed); BL1, BL2 (blue: solid and dashed); GRN (green); RED, (red); IR1, IR2, IR3, and IR4 (orange: solid, dot-dash, dashed, and dotted). For the WAC: VIO (purple), BL1 (blue), GRN (green), RED (red), IR1, IR2, IR3, IR4 and IR5 (orange: solid, dashed, dotted, and the latter two not shown). The CL1/CL2 filter combination is given by the solid black line in both plots.

(Section 3.6) provides a unique spectral capability, unavailable on either the Voyager or Galileo imaging systems, which Cassini carries to the outer solar system for the first time. It enables spectral response down to 200 nm. To take advantage of this capability, the range from 230 to 390 nm is spanned by three UV filters: UV1, UV2, and UV3. These provide the best visibility of stratospheric aerosols and potential UV auroral phenomena (as observed at Jupiter; Porco *et al.* 2003), and may aid discrimination of satellite and ring surface materials of special interest such as carbonaceous materials (Wagner *et al.*, 1987). However, the solar spectral irradiance at Saturn is extremely low in the UV, especially at 255 nm (UV1) (Figure 23) so long exposure times will be needed and  $2 \times 2$  or  $4 \times 4$  summation modes may be used to increase the signal to noise ratio at these wavelengths. The demonstrated stability of the spacecraft on reaction wheels enables investigations of Saturn system targets in the UV not previously possible with Voyager.



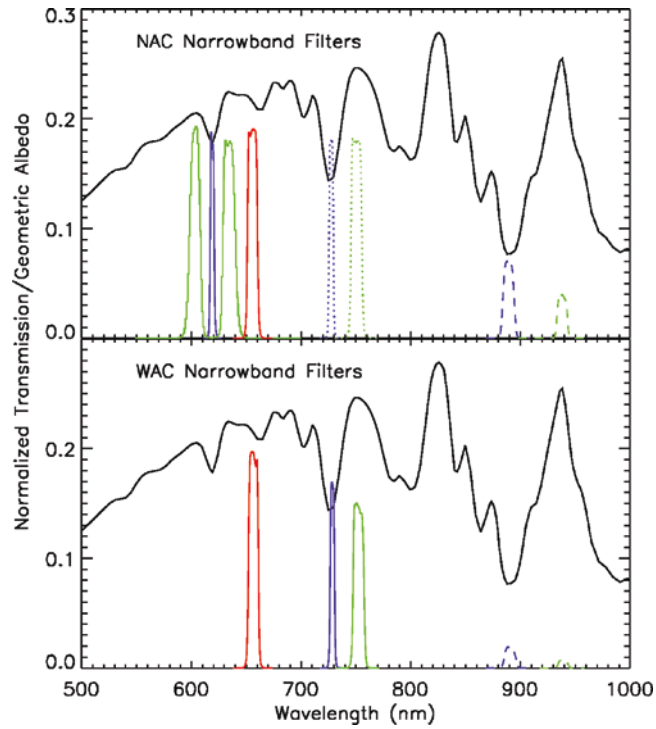


Figure 21. System transmission functions for the NAC and WAC narrow-band filters. NAC filters are as follows: MT1, MT2, MT3 (purple: solid, dotted, and dashed); CB1, CB2, CB3 (green: solid, dotted, and dashed); and HAL (red). WAC filters are HAL (red), MT2, MT3 (purple: solid and dashed); CB2 and CB3 (green: solid and dashed). The geometric albedo of Titan is also given (solid black) to illustrate the placement of the methane band and continuum filters relative to the methane features in the spectrum of Titan.

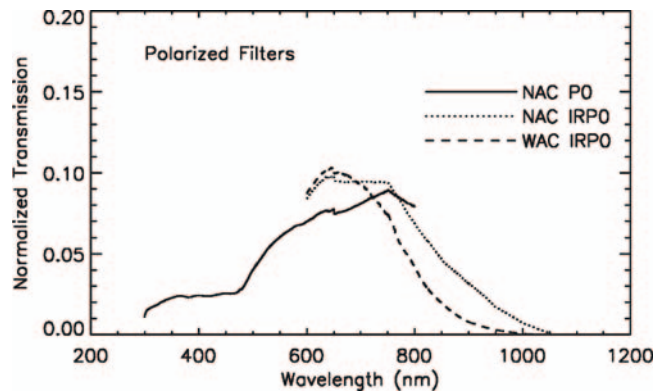


Figure 22. System transmission functions for the NAC visible and infrared, and the WAC infrared, polarizers.

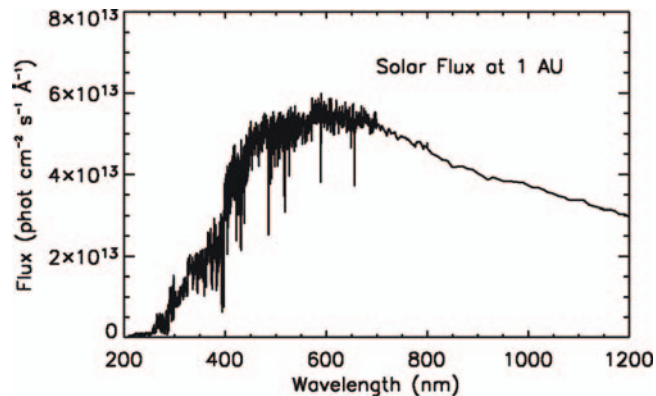


Figure 23. The solar spectrum that has been used in performing calibrations of the ISS (Tobiska *et al.*, 2000).

3. The need for narrow band filters for atmospheric studies. Methane absorption bands and continuum wavelengths are available for studying the vertical structure; these include MT1 and CB1 (NAC only), MT2 and CB2, and MT3 and CB3. (CB1 is a two-lobed continuum filter, with lobes on each side of the methane absorption band.) The HAL filter is included on both cameras for Ha emissions from lightning on Saturn (Figure 21).

Though both cameras are capable of seeing into the near-IR at  $\sim 1.0 \mu$ , the WAC is nine times faster for a given exposure than the NAC. It is consequently better equipped to sense this spectral region for either broad-band color imaging or atmospheric sounding where the CCD quantum efficiency and solar flux are declining and a large camera throughput is desired. (This benefit is reduced somewhat by the Voyager optical coatings.)

4. Polarization filters, for the study of the scattering properties of atmospheres, rings, and satellite surfaces. Three polarizers with principal transmission axes separated by  $60^\circ$  are sufficient to measure intensity and the degree and direction of linear polarization regardless of camera orientation, and so provide the greatest viewing versatility. Three such polarizers, useful only in the visible spectrum are carried in the NAC: P0, P60 and P120 (Figure 22). Given the reduced number of filter slots in the WAC, it does not include the visible polarizers. However, the WAC carries two orthogonal infrared polarizers, IRP0 and IRP90, which can provide intensity and the Stokes parameter,  $Q$ , referenced to the principal axes of the polarizers. If the polarizers are oriented parallel or perpendicular to the scattering plane, the information provided by  $Q$  is in most cases as informative as that provided by three polarizers because the polarized electric vector is usually aligned parallel or perpendicular to the scattering plane. Estimates of  $Q$  referenced to the scattering plane can be made for other orientations but with diminishing precision as the angle between the scattering plane and the polarizer axis approaches  $45^\circ$  at which point the measurement of  $Q$  is not useful.

TABLE IX  
Two-filter bandpasses.

Camera	Filters	$\lambda_{\text{cen}}$ (nm)	$\lambda_{\text{eff}}$ (nm)
NAC	UV2-UV3	316	318
NAC	RED-GRN	601	601
NAC	RED-IR1	702	702
BOTH	IR2-IR1	827	827 (NAC)
		826	826 (WAC)
NAC	IR2-IR3	902	902
NAC	IR4-IR3	996	996

The NAC has only one infrared polarizer, IRP0. By measuring the intensity in this polarizer and also in the clear filter, we can measure  $Q$  although with less accuracy than is achieved with two orthogonal polarizers.

The polarizers are, of course, to be used in combination with other spectral filters and so filter placement was important. In the NAC, the three visible polarizers and the one IR polarizer can all be used in conjunction with a suite of spectral filters on the opposite wheel covering the UV to the near-IR. In the WAC, two broad-band filters IR2 (853 nm) and IR4 (1002LP nm), and the four narrow-band filters – the two strong methane filters MT2 (728 nm) and MT3 (890 nm) and the accompanying continuum band filters CB2 (752 nm) and CB3 (939 nm) – are all placed in the same wheel opposite the wheel containing the two IR polarizers. The polarizers on both the NAC and WAC will be used to reduce contributions from scattering by atmospheric haze. In particular, the IR polarizers on both cameras will aid in imaging the surface and lower atmosphere of Titan, especially when used in combination with near-IR filters such as CB3. The ability to reduce scattering from haze is most effective near 90° solar phase angle.

5. The requirement to image in particular absorption bands. Although the common filter choices involve use of either a clear or polarizing filter in one filter wheel and a spectral filter in the other, we have designed spectral overlap into the broad-band color filters to create a series of two-filter bandpasses to be used primarily in the NAC (Figure 24; Table IX). The two-filter bandpasses were, when possible, designed to cover potential absorption bands of candidate materials, such as weak bands of ammonia (NH<sub>3</sub>), methane (CH<sub>4</sub>), and water (H<sub>2</sub>O) ices. There is also a weak band at 600 nm, of unknown origin, in the spectra of several satellites, which can be mapped out with the RED/GRN combination. The IR1/IR2 two-filter bandpass (available on both NAC and WAC) may permit detection of nitrogen emission lines on Titan. A reasonable job of identifying and mapping the 800–1100 nm region, where silicates and oxides containing Fe<sup>2+</sup> and Fe<sup>3+</sup> produce absorption bands, can be done via use of the following

filter combinations: CL1/CB2 (750 nm), IR2/IR1 (827 nm), IR2/IR3 (902 nm), CL1/CB3 (938 nm), IR4/IR3 (996 nm), IR4/CL2 (1002LP nm) or IR5/CL2 (1028LP nm).

On the WAC, with the spare Voyager refractive optics, we encountered difficulty in achieving a sharp focus in filter combinations that did not utilize the thin CL1 filter. As a result, the only useful two-filter bandpass in the WAC is IR1–IR2.

#### 3.4.1. Filter Fabrication

With the exception of the clear filters and the polarizers, the filters are all interference filters manufactured using an ion-aided deposition (IAD) process which makes the filters temperature and moisture tolerant and resistant to de-lamination. Conventional interference filters have passbands that shift with temperature. The shift can be significant for narrow-band filters such as those targeted to methane absorption bands or the H $\alpha$  line. Temperature shifts for IAD filters are typically an order of magnitude or more smaller than for conventional filters and are insignificant

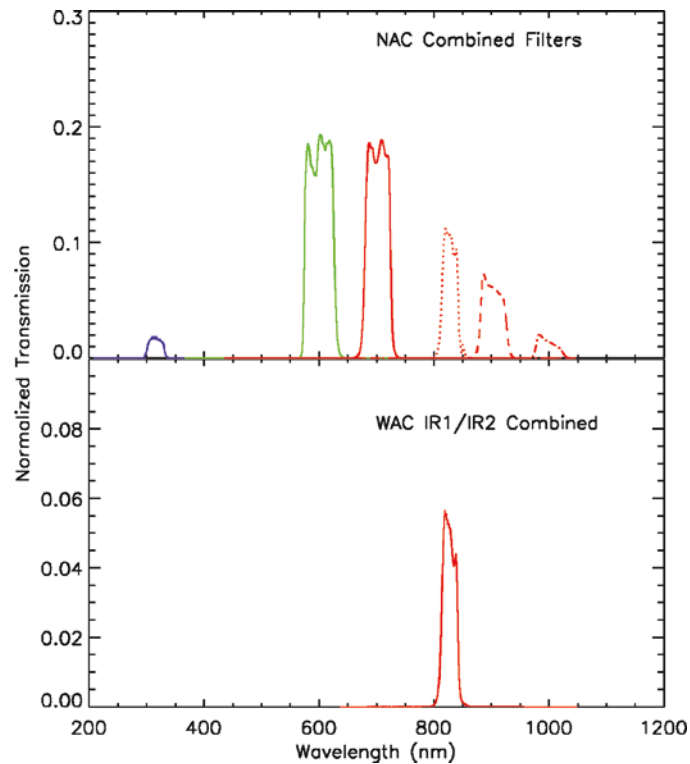


Figure 24. System transmission functions for selected filter combinations in the NAC and WAC. NAC filter combinations are as follows: UV2/UV3 (purple), RED/GRN (green), RED/IR1 (red: solid), IR1/IR2 (red: dotted), IR2/IR3 (red: dashed), and IR3/IR4 (red: dot-dashed).

over the temperature range (room temperature to 0° C) relevant to calibration and operation of the Cassini cameras.

The NAC visible polarizers consist of a thin film (less than 1  $\mu\text{m}$  thick) of a polarizing polymer deposited between two fused silica plates. Ideal polarizers block only photons whose electric vector is orthogonal to the principal axis of the polarizer. The visible polarizers fall short of this ideal behavior in two ways. They transmit too little of either polarization in the ultraviolet, and too much of the light polarized orthogonal to the principal axis in the near-infrared. Their performance is best between 450 and 650 nm, where the principal axis transmission is between 0.45 and 0.65 and the orthogonal transmission is less than 1%. The useable range of the visible polarizers extends from the UV3 filter near 350 nm to the CB2 filter at 750 nm.

The infrared polarizers have a 1 mm thick layer of Polarcor (trademark Corning) cemented between two slabs of BK7-G18 glass. Polarcor is a borosilicate glass impregnated with fine metallic wires. The infrared polarizers have much better performance over their range (700–1100 nm) where the principal transmission is greater than 0.9 and the orthogonal transmission is 0.001 or less.

### 3.5. SHUTTER

Between the filter wheel assembly and the CCD detector is the shutter assembly, a two-blade, focal plane electromechanical system derived from the one used on Voyager, Galileo and WFPC. To reduce scattered light, the shutter assembly was put in the optical train ‘backwards’, with the unreflective side towards the focal plane, unlike its positioning in the Voyager and Galileo cameras. Each blade moves independently, actuated by its own permanent magnet rotary solenoid, in the sample direction: i.e., keeping the blade edge parallel to the columns of the CCD (see Section 3.6.1). The shutter assembly is operated in three phases: open (one blade sweeps across the CCD), close (the other blade sweeps across the CCD to join the first), and reset (both blades simultaneously sweep across the CCD in the reverse direction to the start position).

There are 64 commandable exposure settings which can be updated during flight if so desired. These correspond to 63 different exposure times, ranging from 5 ms to 20 min, and one ‘No Operation’ setting. (The shortest non-zero exposure is 5 ms.) In the ISS flight software, the time tag on the image is the time of the close of the shutter. Because of mechanical imperfections in the shutter mechanism, there is a difference between the commanded exposure time and the actual exposure time, and a gradient in exposure time across the CCD columns. At an operating temperature of 0°C, the mean differences in the NAC for commanded exposure times of 5, 25 and 100 ms were measured to be 0.98, 1.52 and 0.97 ms, respectively. In the WAC, the differences are 0.15, 0.39 and 0.07 ms. In all cases, the actual exposure times

are less than the commanded times. There is also a small temperature dependence to these shutter offsets.

The 1024th column is illuminated first in both cameras. In the NAC, this column is illuminated for  $\sim 0.3$  ms longer than the first column; in the WAC, the 1024th column is illuminated  $\sim 0.1$  ms longer than the first. These values are independent of exposure time and reasonably independent of temperature. The expected precision or repeatability of an exposure (equal to the standard deviation of actual exposure durations measured at any one location on the CCD in ground tests) is  $\leq 0.03$  ms for the NAC and  $\leq 0.04$  ms for the WAC. Corrections for the mean and the spatially dependent shutter offsets are incorporated into Cassini ISS calibration software (CISSCAL). The shutters were tested for light leak. None was detectable in the NAC at a fluence level of 12,000 times full well exposure on the closed shutter. A small signal was detected in the WAC. It produced 1 DN (12 electrons) or less at a level of 10,000 times full well incident on the closed shutter.

### 3.6. DETECTOR

The CCD detector used in the Cassini ISS was manufactured by Loral, packaged by JPL, and employs three phase, front-side-illuminated architecture. The imaging area – the region on which light is focused – is a square array of  $1024 \times 1024$  pixels, each  $12 \mu$  on a side. The CCDs on both cameras were packaged, hermetically sealed and fronted by a fused silica window.

The CCD's response to light is determined by the spectral dependence of each pixel's quantum efficiency: i.e., the number of electrons released in the silicon layer for each photon incident on it. In front-side-illuminated CCDs (like that in the Cassini ISS), the overlying polysilicon gate structures do not transmit UV light. To achieve the required UV response, a UV-sensitive organic fluorescent material called lumogen was vacuum-deposited onto the CCD at  $+80^\circ$  C after it was bonded. In this  $0.6 \mu$  layer, UV photons are converted into visible photons in the range 540–580 nm that readily penetrate the silicon below. Under vacuum conditions, the lumogen layer would tend to evaporate when CCD temperatures reached  $+60^\circ$  C. For this reason, the CCD sealed packages were back-filled with inert argon gas to a half atmosphere pressure. All flight candidate CCDs were coated with lumogen before the two flight CCDs were chosen and assigned to each camera. Hence, despite the fact that the WAC optics do not transmit in the UV, the WAC CCD is also coated with lumogen.

The efficiency of a CCD in the near-IR depends on its thickness, or more precisely on the thickness of the very thin, high-purity silicon layer which is epitaxially grown over a thicker ( $\sim 500 \mu$ ) substrate. It is the photons absorbed in the epitaxial layer that are converted into the signal electrons that are subsequently collected and sampled. Nearly all of the near-IR photons actually penetrate beyond the 'epi' layer and create charge in the substrate. However, the purity contrast between the



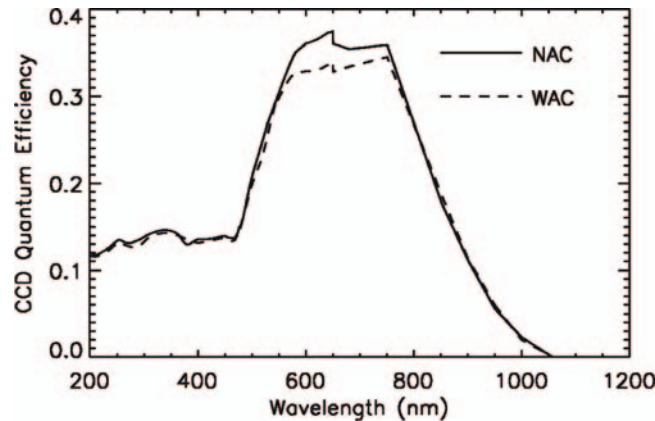


Figure 25. The quantum efficiency of the CCDs in the NAC and WAC, as measured during the ground calibration. Despite the fact that the WAC optics are opaque in the ultraviolet, the WAC CCD was also coated with lumogen and consequently has significant response in the UV.

substrate and the epi layer prevents substrate-generated charge from entering the epi layer and being collected. Thus, the 1100 nm quantum efficiency is essentially the fraction of incident flux which is absorbed in the thin layer of pure silicon: the thicker the 'epi' layer, the higher the infrared sensitivity.

However, the thicker this layer, the lower the spatial resolution. A compromise was made in the manufacture of the CCD to yield some response near 1100 nm while maintaining high spatial resolution. The 'epi' layer is 10–12  $\mu\text{m}$  thick on Cassini and results in a quantum efficiency (QE) of  $\sim 1\%$  at 1000 nm.

Figure 25 shows the quantum efficiency versus wavelength of the CCDs carried in Cassini ISS.

A compromise involving the near-IR response was also made in choosing the CCD operating temperature. At Saturn, this temperature is  $-90^\circ \pm 0.2^\circ \text{C}$  and is a compromise between yielding an acceptably low dark current ( $\leq 0.3 \text{ e}^-/\text{sec}/\text{pixel}$ ) and maintaining a reasonable near-IR response (which is diminished at low temperatures). CCD thermal control is achieved by means of balance between passive radiation to space, which alone would maintain the CCD below its operating temperature at Saturn, and active heater control. The radiator of each camera also supports a decontamination heater (35 W in all) that can heat the CCD to  $+35^\circ \text{C}$  to reduce the deposition of volatile contaminants on either the detector or the radiator. (Because damage to the CCD due to cosmic rays can be annealed at elevated temperatures, the CCD operating temperature during cruise, when data were not being collected, was maintained at  $0^\circ \text{C}$  to minimize such damage.)

The CCD has the capability of being commanded to operate in full mode (i.e.,  $1 \times 1$ ) or either  $2 \times 2$  or  $4 \times 4$  on-chip pixel summation modes. The latter two modes are used for either enhancing signal to noise and/or decreasing the data volume and/or readout time at the expense of spatial resolution. The full well of the

TABLE X

Gain values (electrons/DN) and Ratios (Relative to Gain 2) for the different gain States in the ISS.

Gain state		NAC (e-/DN)	Ratio	WAC (e-/DN)	Ratio
0	Designed for $4 \times 4$	$233 \pm 29$	0.134	$211 \pm 16$	0.134
1	Designed for $2 \times 2$	$99 \pm 13$	0.314	$85 \pm 7$	0.311
2	Used in $1 \times 1$	$30 \pm 3$	1.000	$28 \pm 1$	1.000
3	Used in $1 \times 1^*$	$13 \pm 2$	2.36	$12 \pm 1$	2.36

\*The highest gain state was chosen to match the read noise.

CCD is roughly  $120,000 \text{ e}^-/\text{pixel}$ . Four gain states are available: for imaging faint objects (high gain, Gain 3) and bright objects (normal gain, Gain 2), and to match the output of the  $2 \times 2$  (Gain 1) and  $4 \times 4$  (Gain 0) full wells. The summation well can hold only  $1.6 \times 10^6$  electrons; this corresponds to full well with  $4 \times 4$  summing. However, the relation between number of electrons in the signal and the digital data numbers (DN) into which the signal is encoded starts to become nonlinear above  $10^6$  electrons because at this signal level, the on-chip amplifier becomes nonlinear. For this reason, in the lowest gain state (Gain 0), the full-scale signal is set to correspond to  $\sim 10^6$  electrons at 4095 DN. The array of summation and gain state options as well as the uncertainties in each gain are given in Table X.

The capability also exists within the ISS to reduce the effect of blooming, the phenomenon whereby a highly overexposed pixel can spill electrons along an entire column of pixels, and sometimes along a row, when the full well of the CCD is exceeded. The default camera setup has anti-blooming On, with the option to turn it Off. Anti-blooming mode is achieved by applying an AC voltage to the chip, forcing excess electrons into the silicon substrate. An undesirable side effect of this action is to pump electrons into traps in the silicon at the expense of electrons in adjacent pixels. For long exposures (longer than about 20 s) this produces bright/dark pixel pairs. These were initially present in nearly all the NAC flat-field files obtained during calibration in the thermal vacuum chamber. Corrected flat-field files with these pixel pairs removed have been created.

### 3.6.1. *Coordinate System and Readout Scheme*

There are two ISS coordinate systems in use: the one officially used on the Cassini Project to describe camera orientation ( $X \text{ cm}$ ,  $Y \text{ cm}$ ), which is directly related to the readout directions of the CCD samples and lines, and another used in general by imaging scientists ( $X \text{ im}$ ,  $Y \text{ im}$ ) to describe images which are rotated from the target being imaged. There is also the spacecraft coordinate system ( $X \text{ s/c}$ ,  $Y \text{ s/c}$ ,  $Z \text{ s/c}$ ). Figure 26 indicates the relationships among all these systems.

The cameras and other instruments on the RSP are pointing in the  $-Y \text{ s/c}$  direction. The positive  $Z \text{ s/c}$  axis points towards the spacecraft's main engines; the

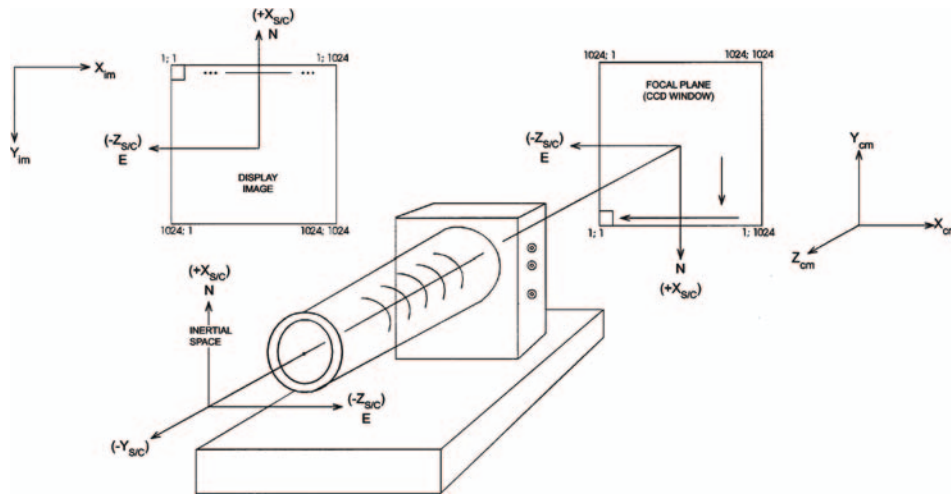


Figure 26. An illustration of the relationships among the three main coordinate systems involved in the analysis and interpretation of image geometry: the spacecraft coordinate system ( $X$  s/c,  $Y$  s/c,  $Z$  s/c), the JPL/ISS coordinate system ( $X$  cm,  $Y$  cm,  $Z$  cm) (which is determined by the readout of the CCD, indicated by arrows drawn in the CCD Window (ie, the physical sample and line directions,  $(s, l) = (X$  cm,  $Y$  cm))), and the coordinate system generally used in the display and examination of an image, ( $X$  im,  $Y$  im). In this diagram, the spacecraft  $+X$  s/c is aligned with inertial north; celestial (or astronomical) east is indicated. The optics rotates the image of the target, as well as the image of the spacecraft's orientation in inertial space,  $180^\circ$ , from their true inertial space orientations.

$-Z$  s/c points towards the High Gain Antenna; the  $+X$  s/c axis is up. In Figure 26, the CCD readout proceeds as follows.

The bottom line of the CCD is shifted down (i.e., toward the remote sensing palette, toward  $-X$  s/c)) into a vacant one-line serial register. This line is then shifted to the left (in the  $+Z$  s/c direction), pixel by pixel, to the signal chain until the entire line is readout. The pixels are numbered by the order in which they proceed to the signal chain. Thus, the first has sample =  $X$  cm = 1, the last has sample =  $X$  cm = 1024. That is, the readout proceeds in the  $-X$  cm direction. After this line is completely readout, the next line is shifted down into the serial register and readout, and so on until all 1024 lines have been shifted into the register and then along to the signal chain.

This results in the following relationship between the spacecraft and the physical ISS/CCD coordinate systems: (sample, line) =  $(+X$  cm,  $+Y$  cm) =  $(-Z$  s/c,  $+X$  s/c).

The images of celestial bodies taken by the ISS are inverted up/down and flipped left/right (i.e., rotated  $180^\circ$ ) by the optics in both cameras. The relationships between targets and inertial space, as well as the relationship between the target and the orientation of the Cassini spacecraft, are all maintained through this rotation. Thus, the *image* of a celestial target, as well as the *image* of the spacecraft coordinate system in the focal plane, are rotated from their physical orientations. A celestial

target with its North pole aligned with the spacecraft  $+X$  s/c axis would appear inverted and flipped on the CCD: that is, *in the focal plane and display image plane* (Figure 26), the North pole of the target and the  $+X$  s/c axis would point in the direction of decreasing line ( $-Y$  cm and  $-Y$  im); the target's western limb (or, astronomical East) and the  $-Z$  s/c axis would point towards decreasing sample ( $-X$  cm and  $-X$  im).

The Cassini C-Kernel contains information that is used by the Navigational Ancillary Information Facility (NAIF) SPICE toolkit to derive a matrix which transforms a vector in inertial coordinates into the spacecraft coordinate system ( $X$  s/c,  $Y$  s/c,  $Z$  s/c). The Cassini Frames kernel describes a transformation matrix that transforms a vector from the camera coordinate system ( $X$  cm,  $Y$  cm,  $Z$  cm) into the spacecraft frame. The proper combination of the two describes the orientation of the physical camera/CCD system relative to inertial space. To compute the correct orientation of inertial space, and the targets in it, in the image plane, which is where anyone handling an image will work, one must apply an additional  $180^\circ$  rotation about the center of the image.

The detector system includes an unilluminated region eight samples wide – the ‘extended pixel region’ – extending into the negative sample direction in the serial register. These pixels get readout first. Moreover, once an entire row of 1024 pixels is readup into the serial register and out to the signal chain, the readout continues for eight more clock cycles, or over-clocked ‘virtual’ pixels, to provide a measure of the offset bias, the DN value that corresponds to zero signal level. The extended pixel region and the over-clocked pixels in principle provide two independent measures of offset bias and a sample of the horizontal banding pattern (Section 3.11.1.1) that may be used to remove the pattern from images lacking dark sky.

In the NAC, the extended region of the readout register, and the first 13 columns into the serial register – i.e., samples 1–12 of the register – are corrupted by a grounding problem with the epoxy that bonds the pure silicon layer to the substrate. This causes spurious swings in the voltage during the initial ‘clockings’ of data out of the CCD into the signal chain. Consequently, the first 13 columns of NAC CCD data are unreliable, and the NAC's extended pixel region cannot be used to monitor the camera's bias or noise state (see Figure 27).

### 3.7. CAMERA COMMANDING AND TELEMETRY

The ISS accepts from the CDS blocks of commands which are then stored in camera memory to be executed at a later commanded ‘trigger’ time. Each block can be expanded in the ISS into commands to the camera electronics specifying camera modes, timings, and other data taking parameters. The internal ISS commands are executed within 5 ms of the start of the second following the arrival of a trigger command from CDS.

The acquisition of images can be accomplished in several ways. Individual NAC or WAC frames may be acquired, or the NAC and WAC can be used in simultaneous



Figure 27. The dark band on the left of this NAC dark frame illustrates the lack of response in the first ~13 columns of the NAC CCD due to a grounding problem caused by improper bonding of the silicon epitaxial layer to the substrate of the CCD.

N A C  W A C	Prepare Cycle							Read-out Cycle		
	Shutter Reset & 200 ms Pad	NAC Filter Wheel	Wait	Pad 325 ms	Wait	Flood & Erase	Exposure	NAC Read-out	Pad 262 ms	Wait
	Shutter Reset & 200 ms Pad	Wait	WAC Filter Wheel	Pad 325 ms	Wait	Flood & Erase	Exposure	Wait	WAC Read- out	Pad 262 ms

Figure 28. Diagram illustrating the breakdown of the ISS prepare and readout windows for a BOTSIM imaging mode into the various sub-windows and the activities that occur within each one. Note that the shutter close occurs at the same instance for the NAC and WAC, regardless of the exposure duration of each, and that the NAC is read out before the WAC. The NAC and WAC filter movement windows are also each segmented into sub-windows for separate movement of each of the two sets of filter wheels.



mode, called BOTSIM (for ‘both simultaneous’). The entire event, which is called a framing event and requires a total duration called a ‘framing time’, is broken down into two steps: the prepare cycle and the readout cycle.

The prepare cycle is used to alter the state of the ISS, step the filter wheels, perform heater operations, light flooding, and other functions required to prepare for an exposure. It also includes the exposure time. The prepare cycle is constructed from a series of quantized windows of time in which specific functions are assigned to occur. A simplified timing diagram is given in Figure 28.

During the prepare cycle, the shutter blades are reset from the previous exposure and the filter wheels are moved into position. Because simultaneous motion of each filter wheel requires more power than the ISS was allocated for peak operation, all filter wheels – NAC and WAC – are moved separately. Windows of quantized duration are set aside for the motion of each filter wheel. Next, the CCD is prepared for exposure to light. This preparation begins with a wait; the duration of the wait is chosen to ensure that the shutter will close exactly at the end of the quantized prepare window. After the wait, a light-flood fills the wells of the CCD to many (~50) times saturation, followed immediately by a readout. The entire light-flood/erase event takes 950 ms and has the effect of erasing any residual image of previous exposures from the CCD. Within 5 ms of the end of the light-flood/erase event, the shutter is opened for the commanded duration. (For dark frames, this duration is set to zero.) (Simultaneous imaging between NAC and WAC during a BOTSIM results in shutter close in each camera to within 10 ms of each other.) The image is tagged with the time of shutter close.

During the following readout window, the CCD is read out in the manner described in Section 3.6.1, the data are encoded and/or compressed, and the results are packetized.

(During a BOTSIM, the prepare cycle is lengthened to include time to prepare both NAC and WAC. The NAC is prepared first; then the WAC is prepared so as to avoid simultaneous movement of any of the four filter wheels. If the NAC and WAC exposure times are different, the exposures begin in a staggered fashion so that the NAC and WAC shutters are closed simultaneously. There are 63 discrete commandable exposure times which are accommodated within 13 discrete prepare cycle windows. This table is updatable in flight.)

For any of the six individual CDS pickup rates, there are four discrete readout windows for each camera. The readout window is scaled by the CDS pickup rate giving 24 actual readout windows per camera and 96 actual BOTSIM readout windows.

Prepare times and readout times are chosen before uplink. The prepare cycle is completely determinate; the readout time required to fully readout an image is not. The required readout time during the image event will depend on the amount of data being readout of the CCD, and the CDS pickup rate or on the line readout rate from the CCD, whichever is slowest (Section 3.9.4). If the data volume in the image was underestimated and the required readout time exceeds the commanded readout



time, the camera will cease reading out part way through an image and lines will be lost. For this reason, a great deal of effort has gone into estimating the amount of data returned for different scenes and choices of compression parameters. In-flight data, including data acquired during the Jupiter flyby, has proven essential in honing these estimates for Saturn tour planning.

The ISS can collect pixel (image) data, engineering data and status data, and packetize them with appropriate header information as either science telemetry packets (which include all types of data) or housekeeping packets (which only include engineering and status data). The latter are returned alone when ISS is in an ON power state but not actively taking images. The frequency with which housekeeping packets are collected is one packet per second and is programmable in flight. The amount of housekeeping data that gets sent to the ground is determined by the rate at which CDS picks up such packets and is currently one housekeeping packet every 64 s.

### 3.8. DATA PATHS

The analog-to-digital (A/D) conversion happens right as the analog signal is read-out from the chip, after it has passed through the on-chip amplifier. Data from the analog-to-digital converter (ADC) are encoded to 12-bit data numbers (DN), giving a dynamic range of 4096. However, they are stored as 16 bits: the upper 4 bits are all 1's. The ISS flight software masks the upper 4 bits when doing calculations. Compression and conversion functions are performed after the electrons are converted to DN. The next juncture is a choice of data conversion (from 12 to 8 bits) or no data conversion. Unconverted data can then proceed to a lossless compressor or undergo no compression at all. Converted data can undergo no compression or lossless or lossy compression. From there, the data are placed on the BIU, where they are ultimately picked up by the CDS and sent to the SSR where they are stored as 16-bit data. (Although each camera has its own BIU, CDS only listens to science packets from one address value for ISS. Thus, the ISS has the ability to switch the addresses between cameras so that the one being readout has the proper, CDS-recognizable value.)

### 3.9. DATA COMPRESSION

Serious constraints are imposed on imaging of the Saturn system by the limited data storage volume on the spacecraft's SSR, and by the limited communication bandwidth back to Earth. In order to make the most effective use of these resources, the Cassini imaging system includes the capability to convert the data from 12 to 8 bits (called data conversion), and also to perform either "lossless" or "lossy" image compression. Data conversion, and both lossless and lossy compression, are implemented in hardware.

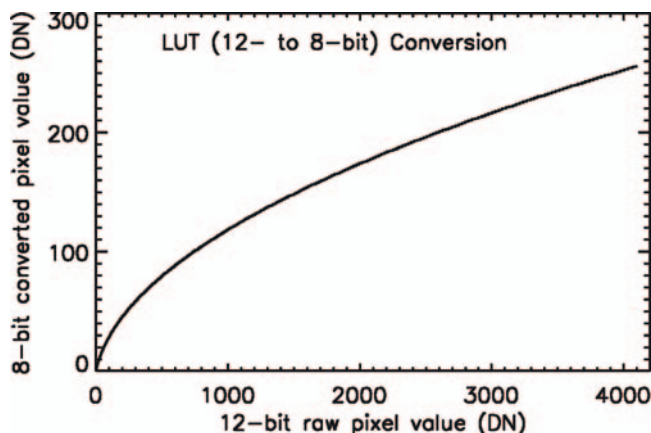


Figure 29. Diagram illustrating the function used to convert 12-bit data numbers into 8-bit values when the look-up table (LUT) conversion is used. The function is close to that of a square root function, and is often called the ‘square root encoder’.

### 3.9.1. Data Conversion to 8 Bits

Two sub-options are available for 8-bit conversion. One is a variant on conventional “square root” encoding. In such encoding, a look-up table (LUT) is used to convert the original data values to 8-bit values. The output 8-bit values are related to the input values in a nonlinear fashion, typically scaling with the square root of the 12-bit value. This nonlinear scaling more closely matches the quantization level to the photon shot noise so that the information content is spread more evenly among the 256 levels. The Cassini 12-to-8-bit conversion table is shown graphically in Figure 29. It differs somewhat from pure square root encoding, having been designed for the known noise properties of the Cassini cameras to distribute quantization-induced errors uniformly across the dynamic range of the system. The LUT is stored in ROM within the cameras’ memory and cannot be altered in flight; choice of ON or OFF is commandable in flight.

The other sub-option is conversion from 12 bits to the least-significant 8 bits (LS8B). This type of conversion is useful for reducing the data volume of images taken of very faint targets, such as diffuse rings or the dark side of Iapetus, which generally do not yield large signal levels and can be encoded to the lowest 8 bits. (This strategy is applicable only if there is no significant background or scattered light in the image.)

### 3.9.2. Lossless Compression

Both converted (8-bit) and unconverted (12-bit) data can be losslessly compressed. The ISS lossless hardware compressor is based on Huffman encoding, a high-efficiency, numerical encoding scheme in which the length of the bit sequence used to encode a given number is chosen based on the frequency of occurrence of that number. In ISS lossless compression, each compressed image can be reconstructed

on the ground with no loss to the information content of the image, provided the image entropy does not exceed the threshold where 2:1 compression is achieved. Scenes with low entropy will have compression ratios higher than 2:1; scenes with high entropy will never compress greater than 2:1, but the ends of lines will be truncated so that the total amount of data returned in a pair of lines of the image never exceeds the total number of bits for a single uncompressed line. The truncation scheme has been designed so that the truncation alternates – i.e., every other line – from one line to the next, on the right (large sample number) side of the image. If the data loss is great, it can in principle result in the complete loss of every other line. In either case, with this scheme information (though reduced in spatial resolution) can be retained across the image, even at the edges.

### 3.9.3. *Lossy Compression*

Imaging sequences requiring larger compression ratios than can be achieved with the lossless compressor may instead be more strongly compressed using the camera's lossy compression circuitry. This capability requires that the data have been converted to the 8-bit form. Consequently, data conversion must be employed first before the data are sent to the lossy compressor. Compression is implemented by a pair of specialized signal-processing chips manufactured by Matra Marconi Space and provided to Cassini by the French Centre Nationale D'Etude Spatiale (CNES). These chips perform a variation on the familiar Joint Photographic Experts Group (JPEG) compression algorithm used in many image transfer and storage applications.

The JPEG algorithm operates by selectively removing information from an image, particularly at high spatial frequencies, thus decreasing the amount of information that must be encoded, while retaining the most visually important details. The basic JPEG algorithm has four steps.

1. The image is subdivided into  $8 \times 8$  pixel blocks. Each pixel is "level shifted" by subtracting 128 from it.
2. The blocks are each subjected to a discrete cosine transform (DCT). This is analogous to the more familiar Fourier transform, in that it breaks the  $8 \times 8$  pixel block into spatial frequency components. The result is an  $8 \times 8$  array of cosine transform coefficients.
3. Information is selectively removed by dividing each array of transform coefficients by the values in a "quantization matrix". This is an integer divide operation, so the coefficients with the lowest values (usually at the highest spatial frequencies) tend to suffer the greatest information loss. The values in the matrix may be uniform, or may be weighted so as to preferentially eliminate information at chosen frequencies. An adjustable "scale factor" is used as a multiplier to the matrix. The scale factor determines the overall degree to which spatial frequency components are attenuated, and hence the compression ratio.

TABLE XI

The contents of the four Cassini compression parameter memory (PMEM) pages.

MALGO	TB	Page	Quantization Matrix	Huffman Table
0	0	0	Flat	Busy
1	0	1	Scaled	Busy
0	1	2	Flat	Sky
1	1	3	Flat	Atmospheric

The two parameters called MALGO and TB are single bits that are used in a camera command to specify the desired page.

4. The information remaining in the blocks is Huffman encoded and formatted for transmission. The overall reduction in data volume results from the very efficient Huffman coding that is possible for the requantized transform coefficients.

The Matra implementation of the JPEG algorithm makes use of four-parameter memory, or PMEM “pages”, numbered 0–3. Each PMEM page contains a quantization matrix, a table of scale factors, and a Huffman coding table. For any given image, a single page can be selected for image compression.

The four PMEM pages in the Cassini imaging system have been designed in the following fashion. In pages 0, 2, and 3, the quantization matrix is “flat”; i.e., each element has the same value. For page 1, the matrix is scaled to discard more high-frequency information. The table of scale factors is identical for pages 0, 1, and 3 but is different for page 2 (the ‘dark sky’ page). The Huffman tables for pages 0 and 1 are identical, and have been optimized for compression of “busy” images. This optimization was performed using a collection of real and synthetic CCD images of cratered surfaces and Saturn’s rings. The Huffman table for page 2 was optimized for images that are mostly black sky, and the Huffman table for page 3 was optimized for images of planetary atmospheres. Again, this optimization was performed using actual CCD images of black sky and atmospheric targets. Table XI summarizes the contents of the four Cassini PMEM pages.

In order to specify compression for a Cassini image, three choices must be made. The first is selection of the PMEM page, done by specifying two bits named MALGO and TB. The second is selection of the value of a parameter called  $B$ . The  $B$  values may range from 0 to 15, and are used to select the value from the scale factor table on the specified PMEM page. High  $B$  values yield higher compression ratios. A given  $B$  value generally selects a different scale factor when used with page 2 than it does with the other pages.

The final parameter that must be specified for compression is the “group of blocks”, or GOB, length. GOB length is a parameter that can range from 0 to 255, and that determines how frequently error correction headers are placed in the data

stream. If GOB length is 0, no headers are inserted. For other values, a GOB length  $L$  will cause error correction headers to be placed after each group of  $L$  image blocks. These headers allow an image to be largely recovered if there are noisy data but introduce some overhead in the bit stream, reducing the compression ratio with no improvement in image quality if no bit errors are present. Choice of GOB length must balance the desire for a high compression ratio against a desire for protection against bit errors. (In the event of transmission errors, all packets downstream of a lost packet are not recoverable in lossy compressed data.) GOB length is almost always chosen to be 41 for lossy-compressed Cassini images. Figure 30 illustrates the effect that lossy compression has on Cassini images.

#### 3.9.4. Readout Times

In the analysis of images, the time it takes the image data to be readout of the CCD is of interest because it relates to the buildup of dark current in the image. It is also of interest in the sequencing of images because, along with the duration of the prepare cycle, it determines the framing time, the time it takes to acquire an image and be ready for the next one.

The process of readout includes: (i) moving CCD lines into a 344,064 (16-bit) pixel image memory or buffer; (ii) moving CCD lines from image memory, converting them into science packets; (iii) moving science packets to the BIU memory; and (iv) CDS picks up packets at the BIU at the CDS pickup rate.

Imaging packets consist of 476 16-bit words or 7616 bits each, including headers. Twelve-bit (12-bit) pixels are placed in the least-significant end of a 16-bit word, so that each word represents a single pixel and a full-size ( $1 \times 1$ ), '12-bit' image consists of  $1024 \times 1024$  words = 2277 packets.

The CDS has various Science and Engineering Readout (S&ER) modes, each having a different rate of packet pickup by CDS. The cameras' rate of transmission of data to the CDS is synchronized to these rates. They can vary from 8 (S&ER2), 16 (S&ER1), 24 (S&ER3), 32 (S&ER6), 40 (S&ER5a) and 48 (S&ER5) data packets/s, defined by the CDS requirement for an integer number of packets during the unit of time, 1/8 s, employed by the CDS.

This translates into the following table of readout times, for *non-compressed images*, for the various summation and conversion modes in the cameras.

If CDS pickup rate were the sole factor in the CCD readout, Table XII would give accurate values of the readout times for uncompressed images; for compressed images, one could merely calculate the number of packets in the compressed image and divide by the CDS pickup rate to determine the readout time. However, there are other factors that come into play, making Table XII only partially correct.

In most cases – for example, a  $1 \times 1$  unconverted '12-bit' image – the CDS pickup rate is the rate-limiting factor in the data transfer to the spacecraft's SSR and the data must be buffered (or even wait on the chip before it is readout if the buffer is full) before the image is entirely picked up by the CDS. In such cases, the readout time from the buffer is merely the data volume divided by the CDS pickup rate.

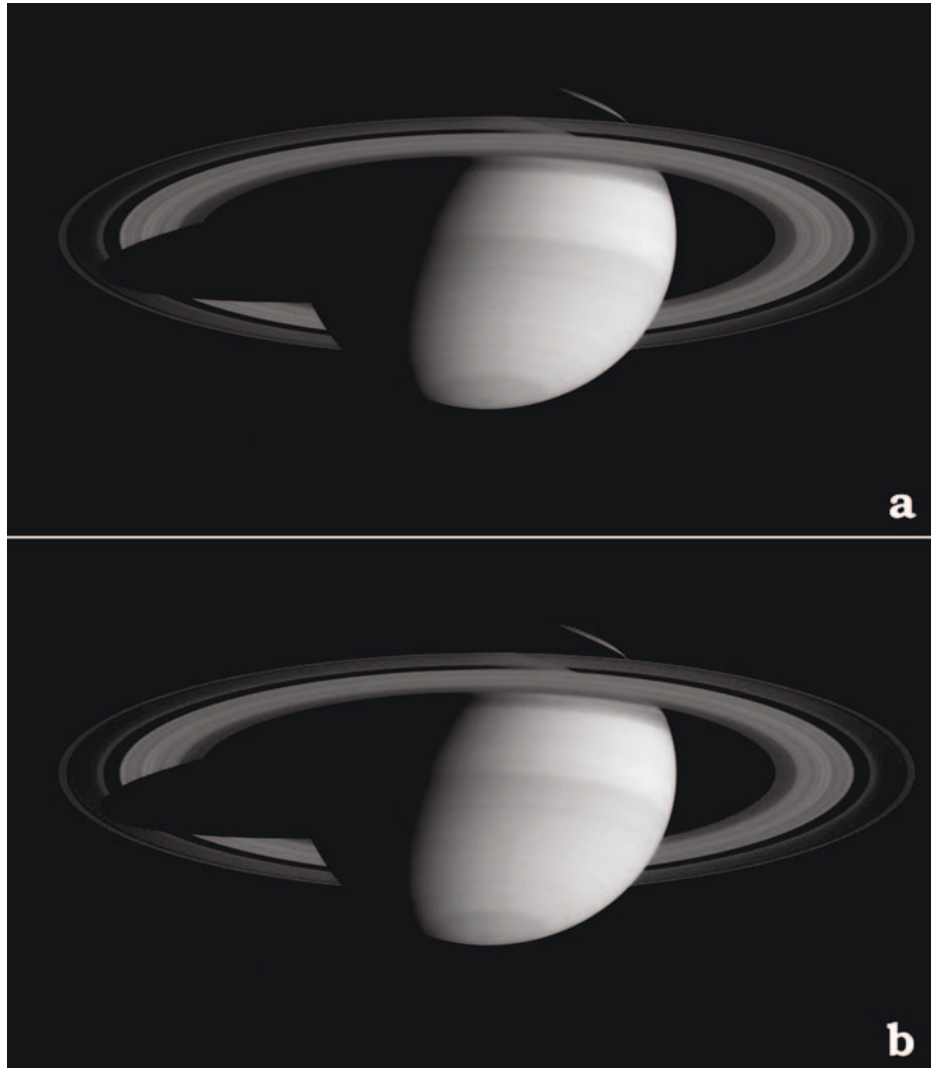


*Figure 30.* A set of two Saturn NAC images in the GRN filter showing both the planet and rings: (a) image acquired using lossless compression; (b) one taken with lossy compression. The lossy parameters chosen were  $B = 0$ , PMEM = 0, and GOB = 41. The  $B = 0$  setting produces the least amount of compression. The full-disk images are linearly stretched between 40 and 180 DN. There is little obvious difference in the full-disk images. The next two images are a close up of a region south of the equator, stretched between 100 and 160 DN, in (c) the lossless compressed image (a), and (d) the lossy image (b). Note the presence of a dark atmospheric spot or storm near the left edge and its degradation under compression. Compression significantly reduces the quality of the image when viewed at this scale, and most scientific objectives (photometry, cloud tracking) would be hampered by use of lossy compression. The final two images are a zoomed view of the right ring ansa, stretched between 20 and 110 DN: (e) the lossless version (a), and (f) the lossy version (b). Here the  $8 \times 8$  pixel boxes (artifacts) are obvious especially in the bland areas. The other filters show very similar artifacts.

(Continued on next page)



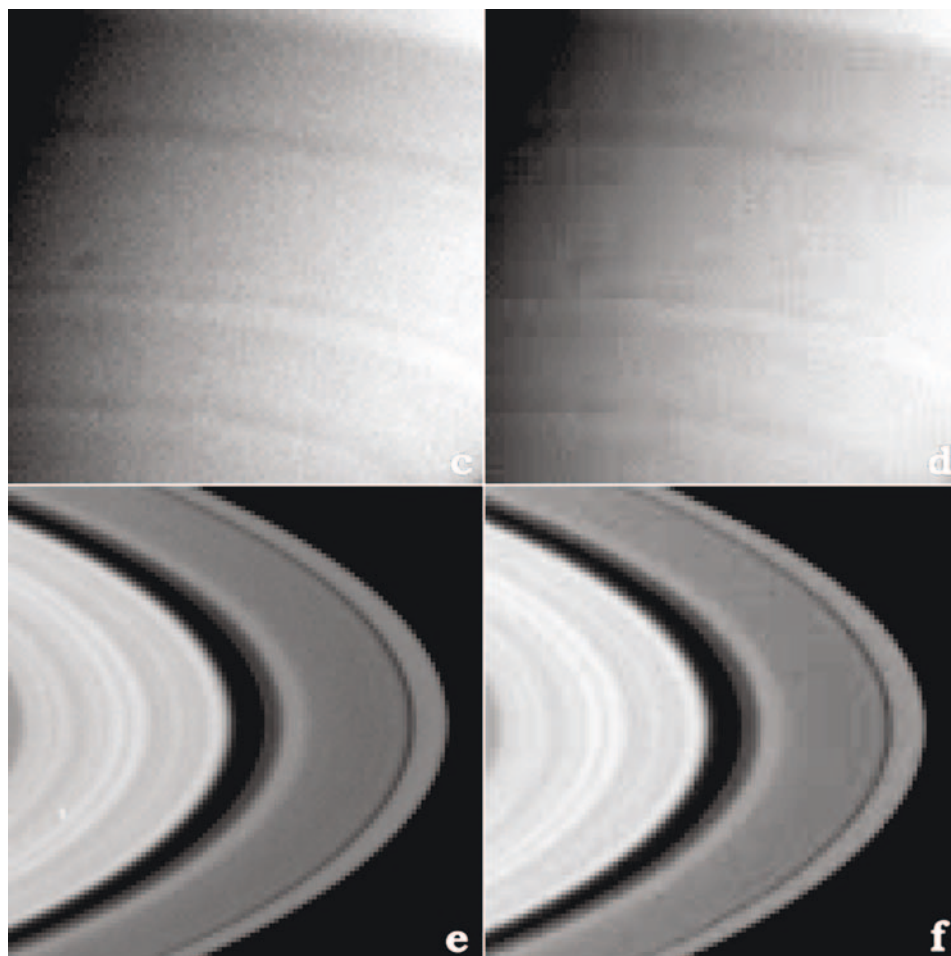


Figure 30. (Continued).

However, under certain circumstances, such as large compression factors (i.e., low data volume images) and fast pickup rate (48 packets/s), the CCD line readout rate into the camera buffer, which varies with summation, conversion, and compression modes, is the limiting factor in the data transfer and it is possible for the CDS data pickup to outrun the data stream from chip to buffer. For example, a  $1 \times 1$  losslessly compressed image cannot readout faster than approximately 12 s; a  $2 \times 2$  losslessly compressed image cannot readout faster than 6 s. In other words, the factor of 4 decrease in data volume in the latter case is not translated into a four times smaller readout time because of the limiting CCD line readout rate.

Finally, in the sequencing of images, a cardinal factor is the framing time: i.e., the sum of the prepare window duration plus the readout window duration. In the operation of the camera, both of these intervals come in quantized values. No matter

how fast the readout of the CCD, the shortest readout window available is 6.525 s. The shortest prepare cycle is 4.475 s. Thus, the shortest possible framing time in the Cassini ISS is 11 s (see Section 3.7).

### 3.9.5. Image Reconstitution

Once an image is telemetered back to the DSN and then sent on to JPL, it is reformatted from a series of data packets back into a two-dimensional image. In the reformatting process, the upper 1's in 16-bit unconverted, uncompressed data are converted to 0's. Images that had been compressed, either losslessly or lossily, are automatically decompressed in the reconstitution process before being sent to the Cassini Imaging Central Laboratory for Operations (CICLOPS) where they are ingested into the Archive Database (from which the Imaging Archive will be built). If they had been converted down to 8 bits by the LUT, a reverse LUT can be applied to them to restore them to their approximate full 12-bit values. (This will be an option in the Cassini ISS Calibration (CISSCAL) software that will be supplied to the PDS along with the Imaging Archive.) There is no way to restore an image previously converted to the eight lowest bits back to 12 bits unless one is confident of smooth gradients throughout the image. Further modifications can take place to clean them and convert them to physical units in the process of calibration (see Section 3.13).

### 3.10. RANDOM NOISE

There are several sources of noise in the ISS. Read noise is the electronic noise added to the signal as it is readout of the CCD and passes through the on-chip amplifier before it is converted to DN. In the Cassini ISS, great care was taken to

TABLE XII

The image readout times (in seconds) for uncompressed images and various choices of summation mode ( $1 \times 1$ ,  $2 \times 2$ , or  $4 \times 4$ ) and data conversion: i.e., no conversion or 12:8 conversion (either LUT or LS8B), under the assumption that the rate-limiting factor is the CDS pickup rate.

Summation	Conversion	Total no. of packets	Data pickup rate (kbits/s (packets/s))					
			365.6 (48)	304.6 (40)	203.1 (32)	182.8 (24)	121.9 (16)	60.9 (8)
$1 \times 1$	None	2277	47.44	56.93	71.16	94.88	142.31	284.63
$1 \times 1$	12:8	1143	23.81	28.58	35.72	47.63	71.44	142.88
$2 \times 2$	None	572	11.92	14.30	17.88	23.83	35.75	71.50
$2 \times 2$	12:8	288	6.00	7.20	9.00	12.00	18.00	36.00
$4 \times 4$	None	144	3.00	3.60	4.50	6.00	9.00	18.00
$4 \times 4$	12:8	74	1.54	1.85	2.31	3.08	4.63	9.25

minimize this noise. Its value is equal to  $\sim 12 \text{ e}^-/\text{pixel}$ , and in the highest gain state with  $13 \text{ e}^-/\text{DN}$ , is equal to 1 DN by design.

Shot noise, or Poisson or photon noise, is the noise in the photon stream hitting the detector and has the usual characteristics: the noise is equal to the square root of the signal. It is reduced to  $\sim 1 \text{ DN}$  in data converted with the LUT converter (Section 3.9.1), regardless of signal strength, because of the design of the LUT. The final outcome is that the bits that are lost in the conversion are the bits devoted to encoding the noise; the process is a lossless one.

### 3.11. DARK CURRENT

Dark current accumulates on the CCD in a manner that is dependent on many factors: readout rate, camera mode (BOTSIM versus single camera), summation mode, etc. Traditionally, dark current is thought to be the result of a defect in the sensor that produces a quasi-constant current which is sensitive to temperature but not to illumination. At the detector operating temperature of  $-90^\circ \text{ C}$ , most pixels have very low dark currents and so another source of electrons, called Residual Bulk Image (RBI), dominates the signal for dark (shutter-inhibited) frames. For practical reasons, we lump the electrons produced by both processes into a conceptual ‘dark current’ signal which must be subtracted before other calibration procedures can be applied.

RBI results from the leakage of trapped electrons. At the CCD operating temperature of  $-90^\circ \text{ C}$ , the time scale for the liberation of RBI electrons into the potential wells ranges from several seconds to several hundred seconds. This produces a latency effect. The chip has a memory of past illumination. To reduce the sensitivity to a negligible level of RBI to prior exposures, a procedure of light flood and erase is used whereby infrared LEDs ringing the CCD in each camera, centered in wavelength on 900 nm, saturate the CCD by approximately 50 times prior to every image to fill the traps. An erase cycle follows the light flood to remove any untrapped charge prior to the start of the next exposure. The light flood/erase cycle is the same for every exposure. By filling all traps, this procedure reduces sensitivity to prior exposures, but the RBI from the light flood itself must be removed. The resulting distribution of light-flood RBI electrons depends on many factors (including readout time) and this complicates the process of dark current removal.

The dark current (now defined to be the combination of the conventional dark current and RBI from light flood) will increase with the length of time that charge remains on the CCD. Because potential wells pickup charge as they are clocked down the chip, the dark current buildup is greater at large line (i.e.,  $y$ ) values than at smaller line values, resulting in a gradient across the chip. This is most important for pixels upstream of hot pixels or for short exposures when the charge leaking from RBI is greatest. If the data must be buffered (as in the  $1 \times 1$  mode), clocking is temporarily suspended, leaving the later lines of pixels on the chip. The result

is a discrete jump in dark current level at a particular line location, depending on the compressibility of the image (if compression was chosen). A much larger effect is the higher level of dark current in the potential wells that are halted at the two edges of the chip because of the large number of defects produced at those edges by the manufacturing process. Also, the number of hot pixels increases with time as cosmic ray damage increases so calibration dark frames need to be obtained and updated periodically.

This is sufficiently complex, and the various possibilities for dark current buildup and the number of different camera modes that determine dark current signal levels are sufficiently large, that it is impractical to do what many other imaging investigators have done and attempt to acquire dark current frames for every different scenario. Instead, an algorithm has been designed to estimate dark current buildup for every pixel on the CCD, using actual ground calibration and in-flight dark frames to determine, via standard least squares fitting, the parameters of the algorithm.

$$DN(t) = C + \alpha t + \sum \beta_I (1 - e^{-t/\tau_I}), \quad I = 1, 2, 3$$

where  $C$  is a constant which is negative for a few pixels at the left edge of the CCD,  $\alpha$  accounts for the true dark current, and the other six terms  $-\beta_I$  and  $\tau_I$ , with  $I = 1, 2$  and  $3$ —account for electrons produced by the light-flood which leak from traps during the readout. For the light-flood-trapped charge, three terms with different amplitudes and decay times are needed to simulate a distribution of trap sizes and decay rates. These eight terms must be determined separately for each pixel by a least-squares fit to dark images at a variety of exposure times.

This algorithm will be used to create a matrix of simulated dark frames that will be used to remove dark current buildup from real data.

### 3.11.1. Coherent Noise

*3.11.1.1. Horizontal Banding.* Both NAC and WAC images exhibit a low-amplitude, coherent noise characterized by horizontal banding with significant power concentrated in a few spatial frequencies (Figure 31). The spatial frequencies present in the images depend on the readout rate from the CCD. The cameras did not show this problem until they were connected to the spacecraft in the Spacecraft Assembly Facility. The pattern is not fixed on the chip and is highly correlated with the over-clocked pixel value, indicating a fluctuation in the video bias level of the CCD. The changing amplitude of the banding (measured in DN) in various gain states is consistent with a constant amplitude in electrons; the dependence of the frequency content on readout rate is consistent with a constant temporal frequency. The source is unknown but is likely a ground-loop somewhere on the spacecraft.

Measurements indicate that the banding in the NAC has an amplitude of  $\sim 2.5$  DN in the  $13 \text{ e}^-/\text{DN}$  gain state (Gain 3); Fourier analysis shows mainly two frequency components, with the secondary peak having  $1/3$  the power of the main peak. After correction for the CCD readout rate, the main peak occurs at  $2.1 \text{ Hz}$ ; the secondary

peak at 2.5 Hz. This produces a beating pattern with a combined frequency of 0.4 Hz. In the WAC, the amplitude is much smaller ( $\sim 0.5$  DN for the  $12\text{ e}^-/\text{DN}$  (Gain 3) state), with a dominant readout-corrected frequency of 4.0 Hz; two smaller peaks of 1/10th the power occur at 1.9 and 5.9 Hz.

Calibration software being developed by the Imaging Team and within the Cassini Imaging Central Laboratory for Operations will contain algorithms designed to reduce this coherent noise in Cassini images without unacceptable damage to the image data themselves.

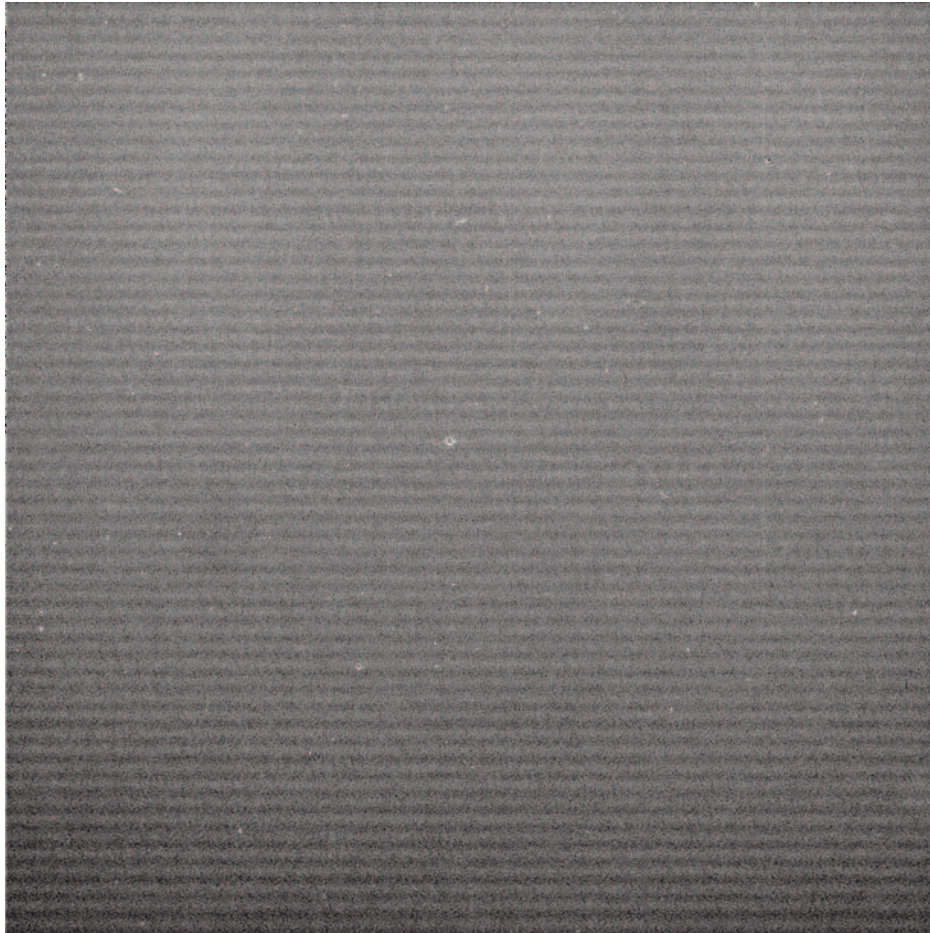


(A)

*Figure 31.* (A) Horizontal banding in the NAC is obvious at very low signal levels. The change in spatial frequency in this image is due to a change in readout rate from the CCD once the camera buffer is filled. Cosmic rays are evident. (B) The horizontal banding in the WAC.

*(Continued on next page)*





(B)

Figure 31. (Continued).

*3.11.1.2. Vertical Banding.* The ISS also exhibits other kinds of coherent noise and Figure 32 is an example of this. Irregular vertical banding of this type has been seen in many images; it seems to be absent in images that are readout in telemetry mode S&ER5. The source of the banding is presently unknown.

### 3.12. PERFORMANCE ON DIFFICULT TARGETS

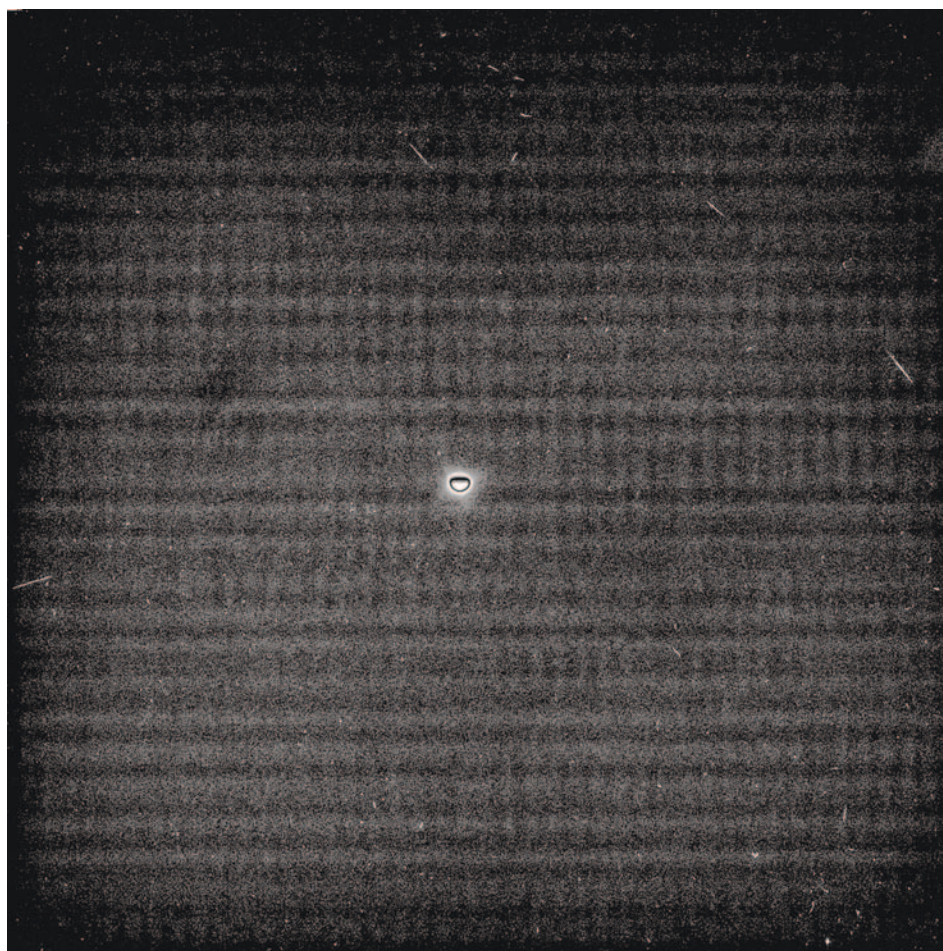
#### 3.12.1. *Spacecraft Pointing Accuracy and Stability*

As the highest resolution imager on the Cassini Orbiter, the ISS is especially vulnerable to spacecraft jitter and pointing inaccuracies. The number of images needed to construct a gore-less mosaic depends on the accuracy of the absolute and relative spacecraft pointing. The quality of images and the detectability, especially of



difficult targets like unresolved satellites and very dark terrains on icy satellites, depend sensitively on how stable the spacecraft is during an exposure.

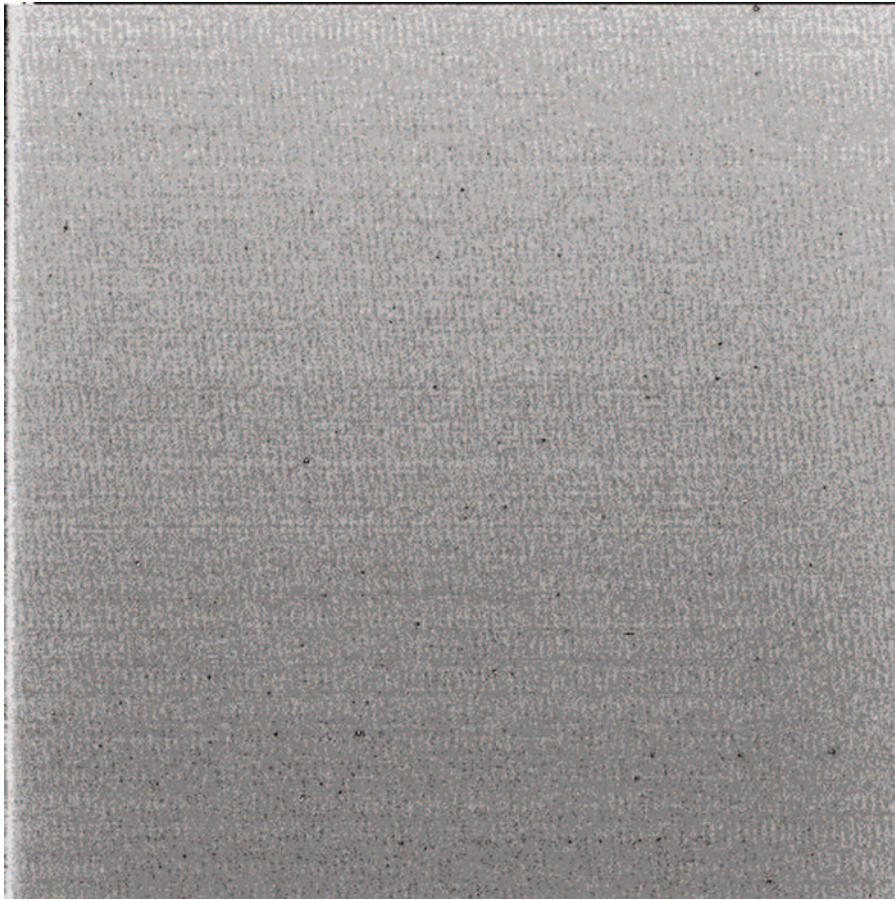
The absolute inertial attitude of the spacecraft is determined in flight by on-board algorithms which detect and measure the positions of stars observed in the Stellar Reference Units (SRU) or ‘star trackers’ on the RSP (Figure 14), and then calculate from star maps the orientation of the spacecraft. The SRU is deliberately out of focus so that the centroids of the stellar point response functions, which can be more precisely measured when de-focussed, can be determined to an ac-



(A)

*Figure 32.* Two examples of low-signal vertical banding. (A) A 38-s, gain state 2 (30 e-/DN),  $1 \times 1$ , unconverted, losslessly compressed narrow-angle camera image of Titan taken in April, 2004 and readout in S&ER3 pickup mode. (B) A 1-s, low gain state,  $2 \times 2$  summed, unconverted, uncompressed NAC image taken as part of a BOTSIM and readout in S&ER1 pickup mode.

*(Continued on next page)*



(B)

*Figure 32. (Continued).*

curacy of  $60 \mu\text{rad}$ , which in the SRU is 0.08 pixels. The FOV is  $15^\circ$ ; up to five stars are used in the navigation calculation. The boresight of the SRU is orthogonal to that of the ISS and pointed in the  $+X$  s/c direction. Rotation about the spacecraft  $Z$  s/c axis results in motion of objects in the line direction in the SRU and also in the line direction in the ISS. Thus, in the ISS line direction, inertial pointing can be controlled and determined to the SRU navigation quantization noise of  $</\sim 60 \mu\text{rad}$ .

However, motion of objects along the sample direction in the ISS is brought about by spacecraft rotation around the SRU boresight,  $+X$  s/c. Thus, to determine the boresight of the ISS in inertial space in the sample direction requires a measure of the twist of the SRU around its boresight. The accuracy and precision to which the latter can be determined depends sensitively on the distribution of the five stars used in the navigation calculation. If the five stars are clustered close to



the boresight and therefore provide a poor lever arm in the twist determination, the resulting angle will suffer greater uncertainty; the fact that the SRU exhibits barrel distortion, which when corrected can be as large as a pixel for stars near the edge of the field, means that even well-distributed stars can yield a relatively inaccurate value for the twist angle, and therefore for the sample location of the ISS boresight in inertial space. This systematic error will vary with the changing boresight position across the sky and with the orientation of the secondary axis around the boresight, since they determine the distribution of stars imaged by the square FOV of the SRU.

A further complication is that during long and continuous observing periods, when the spacecraft remains pointed at a single planetary target whose celestial coordinates as seen by the spacecraft are slowly changing, the star field imaged by the SRU will also change slowly. However, the discrete slippage of one star out of the SRU FOV and/or the entry of another can suddenly alter the *calculated* orientation of the spacecraft because of the effect mentioned earlier. This circumstance can masquerade as a delta function change in the inertial position of the ISS boresight. This was observed during Jupiter flyby.

The net result is that in absolute pointing, the differences between commanded and actual pointing of the Cassini orbiter can range up to 150 NAC pixels (or 900  $\mu\text{rad}$ ) in the sample direction – still an improvement over the 2 mrad pointing uncertainty for Voyager and for Cassini on thrusters – but is  $\leq 60 \mu\text{rad}$  in the line direction, equal to the quantization noise in the SRU calculation of orientation of the spacecraft. The relative pointing of the spacecraft is good in both directions:  $\sim \leq 50 \mu\text{rad}$ .

Once pointed, the orientation and direction of the spacecraft is remarkably steady when on reaction wheels. Exposures as long as 32 s on stars resulted in less than 6  $\mu\text{rad}$  (i.e., 1 NAC pixel) of smear. In images taken of the star Fomalhaut in September 2000, the pointing of the NAC over 50 min varied by only 18  $\mu\text{rad}$ , or three NAC pixels. Images of Saturn in the UV, taken on approach to orbit insertion, were acquired with 320-s exposure times and showed no noticeable smear.

Ironically, these values far exceed the initial advertised capability of the High-Precision Scan Platform on the original Mariner Mark II spacecraft, and are due to the large inertia of the Cassini spacecraft and the reaction wheels which maintain its orientation.

### 3.12.2. Point Spread Function

*3.12.2.1. In-Flight Calibrations.* The camera optics and filters cause some spreading of the images of point sources. The PSFs for both NAC and WAC were measured prior to flight; they were also measured in flight using the stars in the cluster M35 in the constellation Gemini. In 1-s images taken through the clear filters in both cameras, using unconverted (12-bit), unsummed data modes and a gain state of 29  $e^-/\text{DN}$ , images of stars were fitted by a two-dimensional

Gaussian function, with the height and width as adjustable parameters. (A Gaussian function is not an exact match to the shape of the PSF, but a least-squares fitting using one does an adequate job of measuring dimensions.) The FWHM of the fitted functions were 1.3 pixels through the NAC clear filter and 1.8 pixels through the WAC clear filter; the RMS residuals in the fits are below 0.06 pixels, with no sign of obvious trends in the results with changing position on the CCDs.

*3.12.2.2. NAC Haze Anomaly of 2001.* In May 2001 (Day 150), in NAC images taken of the Pleiades, a diffuse circular halo appeared around the central peak of the image of Maia; WAC images were not likewise degraded. The apparent cause of this anomaly was the resumption of normally scheduled decontamination cycles after a 13-month hiatus. Decontamination is a process by which the two heaters, attached to each of the radiators of the NAC and WAC cameras and specially placed for such activity, are turned On and heat the CCD. The purpose is to “bake off” any contamination that may have condensed on the cold parts of the instrument. The May cycle was the first in flight to cover a particularly large range in temperature – from the  $-90^{\circ}\text{C}$  operating temperature up to  $-30^{\circ}\text{C}$  for 16 h – and was the first after the Jupiter encounter. The halo size and intensity were wavelength dependent: the intensity of the brightest part of the halo was only 1–2% of the central peak, but because of its spatial extent, contained 30–70% of the light of the star. The properties of the PSF were consistent with contamination by very small particles on a transmissive surface causing a diffraction pattern in images of point source objects. The source of this contamination has not been identified but may have been something in the camera’s environment that outgassed during the May 2001 decontamination cycle and subsequently condensed on the CCD, either the window or the CCD itself.

The Instrument Operations team at JPL responsible for the health and safety of the ISS conducted additional conservative decontamination cycles, carefully designed to take small increments in temperature between test imaging. These occurred in October 2001 and January 2002, each for a week. A third began on March 5, 2002 and lasted 57 days, and a fourth began on May 9 and lasted for 60 days. After the third cycle, the haze disappeared leaving the point response function of the NAC within pre-anomaly limits; no significant improvement has been seen since then. The quoted values for the NAC point response function are those determined in flight after haze evaporation. Figure 33 shows images of stars taken before the anomaly appeared, during its presence, and then after it disappeared.

### *3.12.3. Detectivity of Point Sources*

The detectivity of point sources with a space-based imaging system depends critically on the photometric sensitivity of the detector, the throughput of the imaging

device, and the stability of the spacecraft. The noted stability of the Cassini spacecraft when stabilized on reaction wheels has translated into a surprisingly good capability to detect faint point sources. This is an important characteristic when the goal is to search for previously undetected satellites.

In NAC images of the open cluster M35 in Gemini, taken for purposes of calibrating the geometric fidelity and point response of the cameras, the limiting magnitude for losslessly compressed 12-bit images in gain state 2 was  $M_v \sim 14$  in 1 s through the clear filter. When the images were converted first to 8 bits and then sent through the lossless compressor, the limiting magnitude became  $M_v \sim 13$  in the NAC clear filter for a 1 s exposure. The brightest stars in these images were  $M_v = 6.3$  and were not saturated. In the WAC, the limiting magnitudes in 1 s in losslessly compressed 12- and 8-bit images were  $\sim 11.6$  and 10.6, respectively; the brightest unsaturated star was  $M_v = 3.4$ .

At Saturn, these numbers imply a detection limit for new unresolved satellites in unconverted images (12-bit) in the absence of a severe scattered light background given by  $I/F r^2/D^2 \sim 4.3 \times 10^{-15}/t$  (s) in the NAC, and  $\sim 3.9 \times 10^{-14}/t$  (s) in the WAC, where  $I/F$  is the phase-corrected reflectivity of the object,  $D$  the distance of Cassini from the object,  $r$  the object's radius, and  $t$  (in seconds) is the residence time of the object in a pixel or the exposure time, whichever is shorter. Given the remarkable stability of the spacecraft on reaction wheels – i.e., a variation of only three NAC pixels over 50 min – the detection limit for small unseen bodies would appear to be affected by the amount of time one has to observe, the relative motion of spacecraft and object, including its orbital motion, which will ultimately determine the residence time in a pixel, and the desire to keep the confusion of cosmic ray hits to a minimum (see Figure 34.) However, scattered light can be a serious limiting factor when observations are made close to Saturn (Figure 35). Detection limits for small satellites between the orbits of Rhea and Hyperion, a region being searched on approach to Saturn when the phase

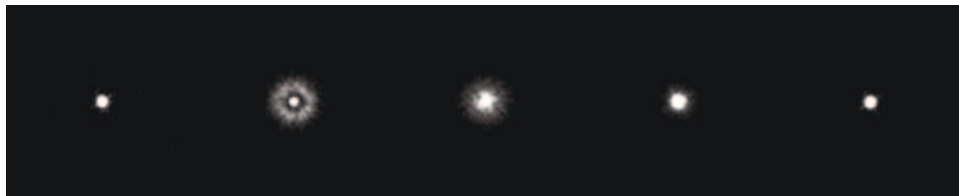


*Figure 33.* The figure above show stellar images taken before the anomaly, one image taken after the anomaly surfaced, and three taken after the decontamination sequences, all in the same BL1/CL2 filters and adjusted for total stellar brightness. The images are all contrast enhanced in the same manner to show the faint extended light. All images were taken at a CCD temperature of  $-90^\circ$  C. Calculations indicate that for this filter combination, approximately 68% of the light fell outside a radius of five pixels when the anomaly was at its maximum. After the first sequence (third image above), that fraction was reduced to 44%; after the second (fourth image above), 18%. It is now 5% (fifth image above). . . back to pre-anomaly values.

angle is  $\sim 70^\circ$ , are expected to be  $r \sim 3$  km in 82-s NAC exposures for objects with a geometric albedo equal to that of Hyperion (0.3). During observations designed to search for ring-embedded moonlets when the pixel residence time is limited by the rapid orbital motion, moons observed at low phase with  $r \sim 1$  km and a geometric albedo equal to that of typical ring particles should be easily detected.

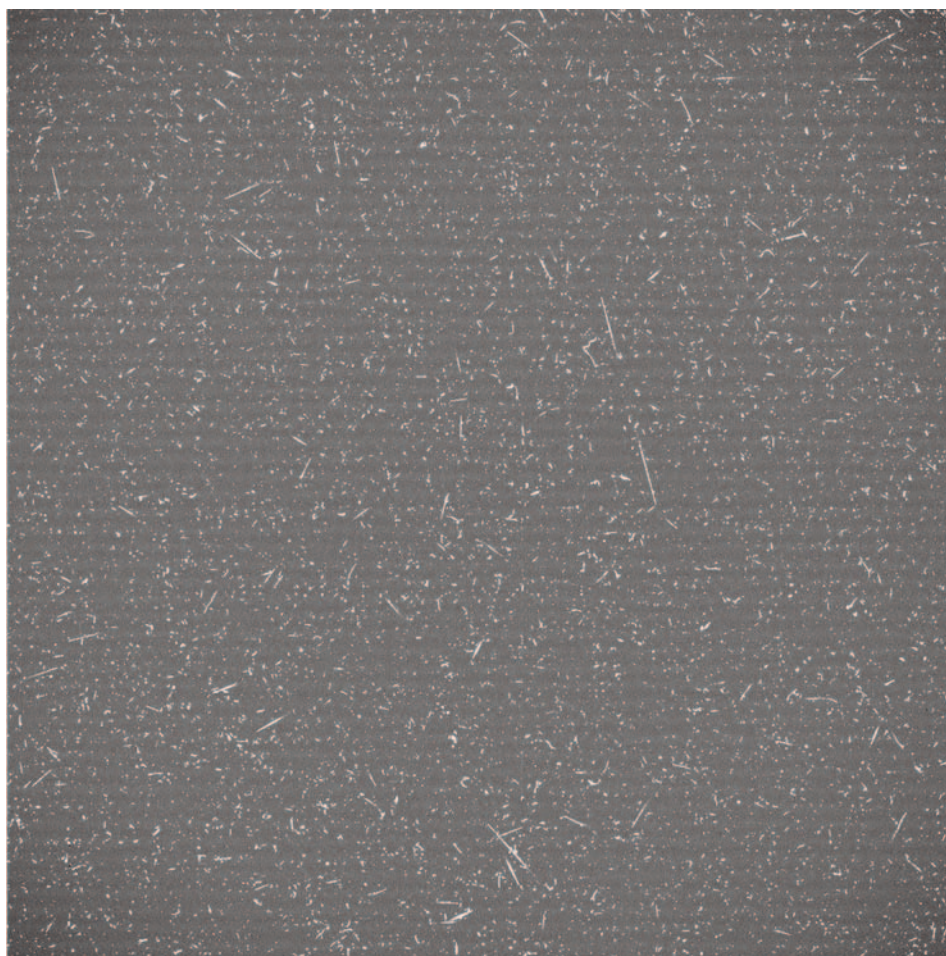


(A)

*Figure 34.* (A) A 560-s dark exposure in the WAC. (B) A 1200-s dark exposure in the WAC. In both, the 100-DN background and cosmic rays are evident.

*(Continued on next page)*





(B)

*Figure 34. (Continued).*

#### 3.12.4. *Expected Performance on Diffuse Sources*

The detectivity of diffuse sources, such as tenuous rings like the E and G rings of Saturn, depends less on spacecraft stability than on the CCD dynamic range, noise sources, photometric sensitivity, the light scattered from nearby bright sources (like Saturn's main rings) into the camera, and the desire to keep the number of cosmic rays in the image to a minimum. The latter can be a big problem for very long exposures (Figure 34), and the scattered light can be a big problem when the angular distance to a bright source is small (Figure 35). Because of these effects, typical exposures to search for new diffuse rings, and to characterize the ones already known to be there, will be a hundred seconds or less, and will generally utilize the summation mode for increasing signal to noise when the resolving capability

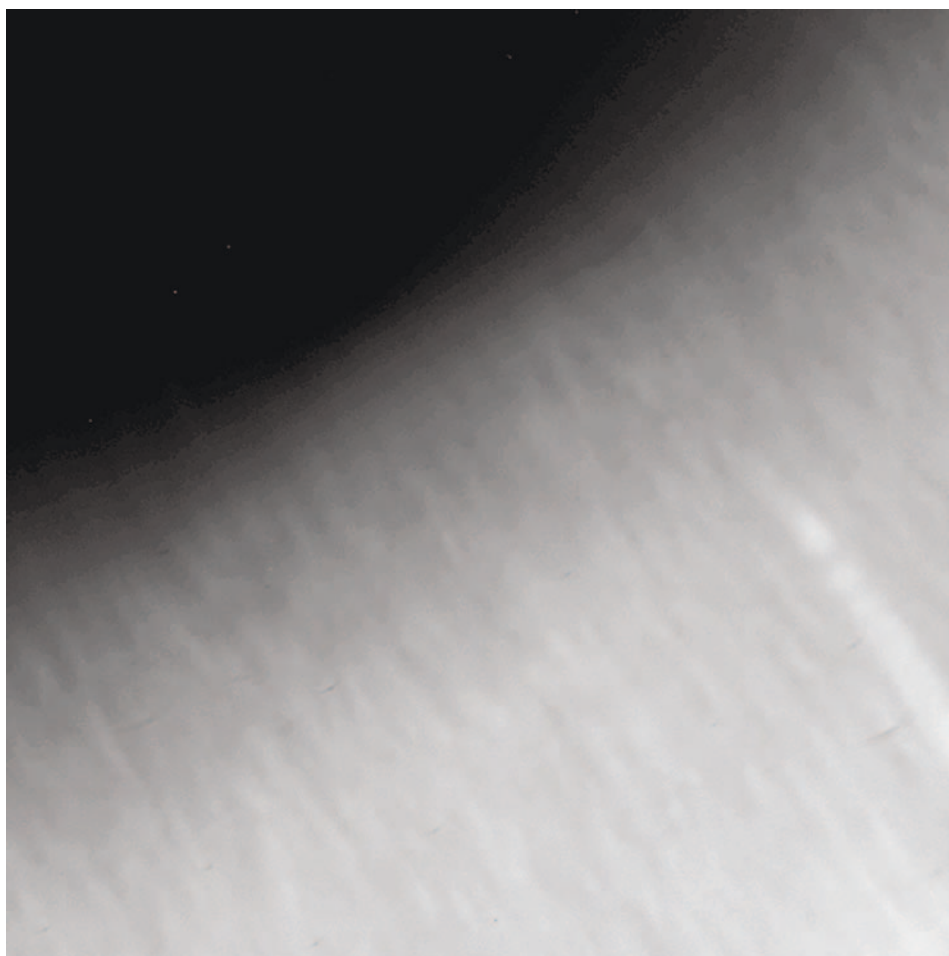
can tolerate it. Polarizers for potentially separating out generally polarized light reflected from natural ring particles from unpolarized light scattered in the optics will also be employed. Such exposure times may give a detection limit of better than  $I/F \sim 10^{-9}$  with a  $S/N \sim 10\text{--}30$  for those circumstances where scattered light is not a factor; i.e., when Cassini is in at close range and the angular distance to



(A)

*Figure 35.* (A) An 18-s narrow-angle camera image, one in a series of satellite search images taken close to the planet's rings (off the bottom of the frame) in the CLR filter, using lossless compression,  $1 \times 1$  mode, gain state 3 (i.e., high gain state). The 2-Hz pattern is apparent. The pattern at the bottom of the frame is light scattered off the NAC's secondary mirror and its supports. (B) A 320-msec WAC image taken through the BL1 filter, about  $20^\circ$  away from the Sun, illustrating the structure present in the image of the light scattered in the WAC optics.

*(Continued on next page)*



(B)

*Figure 35. (Continued).*

Saturn is large. We thus expect the Cassini ISS to have the ability to detect diffuse rings several hundred times fainter than G ring.

### 3.13. CALIBRATION

This section describes the relationship between measured signal,  $S$  ( $e^-/\text{pixel}$ ), the corresponding image values or data numbers (DN), and incident intensity  $I$ , and outlines the steps required to derive  $I$  from the DN values. (Most filters are not sensitive to the polarization state of the target, and so the methodology outlined later neglects polarization. Polarization must be taken into account when polarizing filters are used.) Definitions used in this section are given in Table XIII.

TABLE XIII  
Calibration definitions and units.

Quantity	Units	Definition
$\Omega$	Steradian	Solid angle sampled by one pixel
A	cm <sup>2</sup>	Collecting area of camera optics $0.25 \pi d^2$ , $d$ is the primary mirror or lens diameter
$C(f_1, f_2)$		Absolute sensitivity correction factor determined from in-flight calibration
$e_p(i, j)$	Electrons	Electrons produced by photons striking the CCD
$f_1, f_2$		Filter 1 in wheel 1, filter 2 in wheel 2
$FF(i, j, f_1, f_2)$		Flat field relative sensitivity
$g$	Electrons/DN	Gain constant (Table X)
$I(i, j, \lambda)$	Photons/(cm <sup>2</sup> s nm steradian)	Intensity at pixel $(i, j)$ and $\lambda$
Line		The vertical coordinate (1:1024) of the image. Index $j$ indicates line number
$QE(i, j, \lambda)$	Electrons/photon	CCD quantum efficiency
$RBI(i, j, \text{mode})$	DN	Residual bulk image
Sample		The horizontal coordinate (1:1024) of the image. Index $i$ is used in this document for sample number
$t(i)$	Seconds	Shutter open time, depends on sample number
$T_0(i, j, \lambda)$		Optics transmission. Accounts for beam obscuration as well as losses at lens and mirror surfaces
$T_1(i, j, \lambda)$		Filter 1 transmission
$T_2(i, j, \lambda)$		Filter 2 transmission

### 3.13.1. Methodology

To understand the processes involved in calibration, it is useful to follow the light as it travels through the optical system, is converted to an electric signal and a data number and then is processed by the digital electronics.

The light that hits the CCD first passes through the camera optics and two filters, and the shutter. As a result of this process, the number of photons incident on one pixel at location  $(i, j)$  is  $A\Omega t(i) I(i, j, \lambda) T_0(i, j, \lambda) T_1(i, j, \lambda) T_2(i, j, \lambda)$ . Note that the exposure time depends on sample number ( $i$ ) because the shutter velocity across the CCD is not uniform. Note also that the actual shutter open time differs significantly from the commanded time for one of the exposures on each camera (20 ms for the WAC and 25 ms for the NAC).

Some of the photons (a fraction  $QE(i, j, \lambda)$ ) that strike a pixel will be converted to electrons. The number of electrons generated by photons is given by

$$e_p(i, j) = A\Omega t(i) \int I(i, j, \lambda) T_0(i, j, \lambda) T_1(i, j, \lambda) T_2(i, j, \lambda) QE(i, j, \lambda) d\lambda \quad (1)$$

The optics and filter transmissions have spatial dependence because of low spatial frequency components (e.g. vignetting) and high spatial frequency components (dust particles). Calibration measurements are not able to determine the source of the spatial variations and so all spatial variations are combined and taken out of the wavelength integral. Henceforth, we will call this combined relative spatial dependency  $FF(i, j, f_1, f_2)$ . It is obtained with flat-field calibration measurements. It is a relative dependency because it is normalized to unity, i.e.  $(1/N^2) \sum_{j=1}^N \sum_{i=1}^N FF(i, j, f_1, f_2) = 1.0$ . The dependence on  $f_1$  and  $f_2$  reflects the fact that the FF depends on the filters 1 and 2. Then Equation (1) becomes

$$e_p(i, j) = C(f_1, f_2) A \Omega t(i) FF(i, j, f_1, f_2) \int I(i, j, \lambda) T_0(\lambda) T_1(\lambda) T_2(\lambda) \times QE(\lambda) d\lambda \quad (2)$$

In Equation (2),  $T_0(\lambda)$ ,  $T_1(\lambda)$ , and  $T_2(\lambda)$  refer to transmissions averaged over the focal plane. These were measured as part of the calibration procedure. A new term  $C(f_1, f_2)$  was introduced into Equation (2). It is a correction factor to account for the fact that there are errors in the calibration measurements of absolute sensitivity. This factor will be determined from in-flight absolute calibration of standard stars and other objects whose radiometric flux or intensity is independently calibrated. If the ground calibration measurements are accurate it should be close to unity.

Other processes add to or reduce the number of electrons in a pixel. Residual bulk image (RBI) from light flood/erase cycle, and (at a very low level) previous exposures, and dark current add electrons. If anti-blooming is on electrons can be shifted from one pixel to an adjacent pixel containing traps. The pixel with the traps will accumulate electrons at the expense of its neighbor. The neighbor is always the adjacent pixel in the line direction.

Dark current is usually negligible except at the edge of the image. However, an uncompressed unsummed ( $1 \times 1$ ) image will readout partially into memory and then wait since the camera memory cannot store an entire image. If the bus rate is low, the remaining image may sit on the CCD for many seconds. During this time, dark current at the edge of the frame builds up. Since the image is only partially readout, former line 337 waits at the edge of the CCD where dark current builds rapidly. Which line waits at the edge of the frame depends on the data rate and possibly also whether compression is used. Line 337 was observed to have bright pixels in uncompressed calibration frames taken in the laboratory, all at a rate of 60.9 kbits/s. All lines after 336 contain enhanced RBI electrons from the time spent waiting.

The RBI from the part of the image remaining on the chip also builds up. Therefore, the resulting dark current and RBI pattern has a complicated spatial structure and depends on how the chip was readout, which in turn depends on the data rate, the summation mode, exposure time, which camera was read first after simultaneous shuttering, and compression. To remove the unwanted signal,



one would either take a series of dark frames in each mode used during the image sequence (potentially requiring large data volumes and long observation times) or produce these from a model of the dark current as described earlier. We have chosen the latter. Here, mode refers to all the factors that influence the time spent on the chip and the read pattern. These factors include exposure time, summation mode, compression mode, framing time, readout rate, etc.

The CCD contains a summation well. On-chip summation of  $2 \times 2$  or  $4 \times 4$  pixels can be commanded. Data volumes in these summation modes are small enough that the entire chip can be read to memory.

Voltages on the chip are set so that the zero level (no electrons in the pixel) will produce a positive DN value. This is called the bias level. It should not change except over long periods or after a voltage reset. It can be measured for each frame from the over-clocked pixels. Calibration data taken in the thermal vacuum chamber revealed that the bias level, as revealed by over-clocked pixels, increases with increasing exposure time. The reason for this is unknown. For gain state 3, the bias level is a function also of the electronics temperature. To ensure that the correct bias level is subtracted, the bias level should be obtained from the over-clocked pixels for each frame. The best measure of the bias level is to average as many over-clocked pixels as possible.

The summation well is deep enough to accommodate  $2 \times 2$  summation moderately well, but is not adequate for  $4 \times 4$  summation in the lowest gain state. DN values above about 1600 in the lowest gain state depart from the linear coefficients derived from low DN levels. Nonlinearity is noticeable in other gain states as well. It is least severe for the highest gain state. A quadratic term was derived from linearity test data, and the calibration procedure applies a quadratic-term correction to extend the DN range over which the calibration is good to 1% or better. For  $1 \times 1$  and  $2 \times 2$  summation the entire range of the 12-bit readout can be corrected to better than 1%. In these modes all unsaturated pixels are calibrated. For  $4 \times 4$  summation with gain 0, a separate file containing maximum allowed DN needs to be checked to make sure the DN value for any pixel is not above the DN range over which calibration is accurate to 1% or better.

The electrons on the CCD are shifted to an output register and then to the ADC. The ADC introduces a slight error in the DN levels because of a process called uneven bit weighting. Instead of a one-to-one linear correspondence between input signal and output DN, some of the DN values are under-populated and some are over-populated. Four gain states are available. The uneven weighting is different for each of the gain states.

Data from the ADC are 12-bit numbers. These can be sent to memory or passed through one of the 12-to-8 tables. One of the tables approximates a square root function. The other takes the eight least-significant bits.

Eight-bit data can be passed through one of two compressors. One is a lossless Huffman compressor. The other is a lossy cosine transform compressor.



Radiometric calibration requires the following steps, which reverse the effects of each of the processes listed earlier.

1. Decompression if compression was used. (This step is performed at JPL before images are available to the Imaging Science team.)
2. Conversion from 8- to 12-bit words if a 12-to-8 table was used.
3. Correction for uneven bit weighting using a table appropriate for the gain state.
4. Bias subtraction using over-clocked pixel values (average of many to improve statistics).
5. Removal of the coherent horizontal banding using as a representative source of the noise signal, either the over-clocked pixel values for each line or some mean taken from the image itself. (The latter is used when there is black sky in the image with which to measure the banding signal.)
6. Subtraction of appropriate dark frame containing RBI and dark current corresponding to the exposure time, summation mode, gain state, and readout mode of the image. This frame has had its own bias value already subtracted and may contain some negative DN values.
7. Correction for bright/dark differences in anti-blooming mode.
8. Correction for nonlinearity for the appropriate gain state.
9. Correction of static blemishes on the CCD ('bad pixels').
10. Multiply by the gain constant  $g$ . The result will be  $e_p(i, j)$  as given by Equation (2).
11. Divide the frame by the factors  $C(f_1, f_2)A\Omega t(i)FF(i, j, f_1, f_2)$ .
12. Divide the image values by  $\int T_0(\lambda)T_1(\lambda)T_2(\lambda)QE(\lambda)d\lambda$ .  
The resulting image will be an array of intensities averaged over the passband of the filter with a weighting function  $T_0(\lambda)T_1(\lambda)T_2(\lambda)QE(\lambda)$ .
13. The quantity  $I/F$  is often desired for solar system objects, where  $\pi F$  is the incident solar flux. The appropriate value of  $F$  is the passband-averaged  $F$  weighted the same way as the intensity, namely

$$F = \frac{\int F_1(\lambda)T_0(\lambda)T_1(\lambda)T_2(\lambda)QE(\lambda)d\lambda}{\pi R^2 \int T_0(\lambda)T_1(\lambda)T_2(\lambda)QE(\lambda)d\lambda}$$

In the above equation  $F_1$  is the solar flux at 1 AU and  $R$  is the distance between the sun and target body in AU.

14. Interpolate over isolated saturated pixels or pixel-pairs from anti-blooming, if desired. All saturated pixels are identified and stored in a separate file.

### 3.13.2. *Calibrated Photometric Performance on Resolved Targets*

At the time of writing, the calibration of the ISS is not complete, and more in-flight data are required. However, we have preliminarily calibrated the most useful filters and filter combinations and the results have been cast in terms of a simple relation giving the signal,  $S$ , in  $e^-/\text{pixel}$ , as a function of the exposure time,  $t_{\text{exp}}$ , and the  $I/F$

TABLE XIV

The factor,  $\omega_0^{\text{NAC}}$ , relating the brightness of the target,  $I/F$ , to the signal,  $S$  (electrons/pixel), and exposure time in the NAC camera.

F1	F2	$\lambda_{\text{cen,NAC}}$	$\lambda_0^{\text{NAC}}$
UV1	CL2	258	3.54E+02
UV2	CL2	298	2.59E+03
UV2	UV3	316	1.43E+03
CL1	UV3	338	1.54E+04
P120	UV3	341	4.96E+03
P60	UV3	341	5.15E+03
P0	UV3	341	5.98E+03
CL1	BL2	440	1.74E+04
P120	BL2	440	5.89E+03
P60	BL2	440	5.96E+03
P0	BL2	440	6.49E+03
BL1	CL2	451	8.41E+04
BL1	GRN	497	4.99E+03
CL1	GRN	568	3.49E+05
P120	GRN	569	1.14E+05
P60	GRN	569	1.20E+05
P0	GRN	569	1.21E+05
RED	GRN	601	1.43E+05
CL1	CL2	611	1.26E+06
IRP0	GRN	614	3.69E+04
P120	CL2	617	3.90E+05
P60	CL2	617	3.90E+05
P0	CL2	617	3.90E+05
CL1	MT1	619	1.10E+04
P120	MT1	619	3.71E+03
P60	MT1	619	3.71E+03
P0	MT1	619	3.71E+03
IRP0	MT1	619	4.62E+03
CL1	CB1	619	6.06E+04
P120	CB1	620	2.03E+04
P60	CB1	620	2.03E+04
P0	CB1	620	2.03E+04
IRP0	CB1	623	2.19E+04
RED	CL2	650	4.20E+05
HAL	CL2	656	2.64E+04
RED	IR1	702	1.31E+05

(Continued on next page.)

TABLE XIV  
(Continued.)

F1	F2	$\lambda_{\text{cen,NAC}}$	$\lambda_0^{\text{NAC}}$
CL1	MT2	727	1.24E+04
IRP0	MT2	727	6.07E+03
P120	MT2	727	5.37E+03
P60	MT2	727	5.46E+03
P0	MT2	727	6.00E+03
P120	IR1	740	1.71E+05
P60	IR1	740	1.71E+05
P0	IR1	740	1.71E+05
IRP0	CL2	746	4.30E+05
CL1	CB2	750	2.75E+04
IRP0	CB2	750	1.34E+04
P120	CB2	750	1.27E+04
P60	CB2	750	1.27E+04
P0	CB2	750	1.27E+04
CL1	IR1	752	3.92E+05
IRP0	IR1	753	2.03E+05
IR2	IR1	827	4.53E+04
IR2	CL2	862	1.32E+05
CL1	MT3	889	1.06E+04
IRP0	MT3	889	5.30E+03
IR2	IR3	902	4.06E+04
CL1	IR3	930	6.70E+04
IRP0	IR3	930	3.63E+04
CL1	CB3	938	4.70E+03
IRP0	CB3	938	2.53E+03
IR4	IR3	996	6.12E+03
IR4	CL2	1002	7.20E+03

of the target for these filters and combinations. This relation, computed for targets at the heliocentric distance of Saturn (i.e., 9.14 AU) on July 1, 2006, in the middle of the nominal Cassini orbital tour, is

$$S(\text{e}^-/\text{pixel}) = I/F * w_0 * t_{\text{exp}}.$$

To convert to DN, the relation is:

$$\text{DN} = S(\text{e}^-/\text{pixel})/\text{GS}(\text{e}^-/\text{DN}),$$

where GS is the gain state value in  $\text{e}^-/\text{DN}$  given in Table X. The  $\omega_0$  values were calculated starting with the ISS component ground calibrations for the transmission

TABLE XV

The factor,  $\omega_0^{\text{WAC}}$ , relating the brightness of the target,  $I/F$ , to the signal,  $S$  (electrons/pixel), and exposure time in the WAC camera.

F1	F2	$\lambda_{\text{cen, WAC}}$	$\omega_0^{\text{WAC}}$
CL1	VIO	420	8.61E+04
CL1	BL1	460	1.08E+06
CL1	GRN	567	4.76E+06
CL1	CL2	635	1.32E+07
CL1	RED	648	5.86E+06
CL1	HAL	656	3.48E+05
CL1	IRP90	710	3.65E+06
CL1	IRP0	710	3.65E+06
MT2	CL2	728	1.40E+05
MT2	IRP90	728	6.48E+04
MT2	IRP0	728	6.48E+04
CL1	IR1	742	4.00E+06
CB2	IR1	752	2.74E+05
CB2	CL2	752	2.94E+05
CB2	IRP90	752	1.39E+05
CB2	IRP0	752	1.39E+05
IR2	IR1	826	2.56E+05
IR2	CL2	853	5.68E+05
IR2	IRP90	853	2.80E+05
IR2	IRP0	853	2.80E+05
MT3	CL2	890	2.90E+04
MT3	IRP90	890	1.43E+04
MT3	IRP0	890	1.43E+04
IR3	CL2	918	1.58E+05
IR3	IRP90	918	7.81E+04
IR3	IRP0	918	7.81E+04
CB3	CL2	939	8.39E+03
CB3	IRP90	939	4.16E+03
CB3	IRP0	939	4.16E+03
IR4	CL2	1001	9.31E+03
IR4	IRP90	1001	4.62E+03
IR4	IRP0	1001	4.62E+03
IR5	CL2	1028	1.15E+03
IR5	IRP90	1028	5.72E+02
IR5	IRP0	1028	5.72E+02

of the optics, filters, quantum efficiency, shutter performance and gain. Of these, uncertainty in the quantum efficiency (approximately 20%) dominates the uncertainty budget. (In comparison, the uncertainty of stellar fluxes is on the order of 10%, which is the uncertainty we expect to achieve when calibration is complete.) In flight, we relied primarily on photometric standard stars with ancillary information from calibrated observations of Jupiter, Saturn and Saturn's rings.

For the NAC  $\omega_0$  factors, we used standard star images taken during cruise. Specifically, HD339479 images from cruise load C26 were used, as well as Vega and 77 Tau images from loads C37 and C40. Spectra for HD339479 and 77 Tau were taken from the Bruzual-Persson-Gunn-Stryker Spectrophotometric Atlas, Space Telescope Science Institute Data Analysis System (Gunn and Stryker, 1983); the spectrum for Vega was taken from Colina *et al.* (1996).

All images were processed using the CISSCAL calibration software, and aperture photometry was performed using IDL. Filter-specific correction factors were then calculated by taking the ratio of the observed integrated stellar fluxes to the expected values. The resulting correction factors varied smoothly with the central wavelength of the filter combination, and so a quantum efficiency correction function was derived to apply to the system transmission integral. With this correction in place, the images were calibrated yet again, and aperture photometry was performed as before. Residual sensitivity offsets were then taken into account by calculating filter-specific correction factors. The resulting NAC  $\omega_0$  values, which are recorded in Table XIV, have errors on the order of 10–20%, due largely to photometric uncertainty and systematic effects such as the contribution of noise from the horizontal banding (Figure 31) as well as the lack of an adequate dark current model. In general, values for the single broad-band filters are 5–10% less uncertain than those for narrow-band and combination filters.

Due in part to a lack of sufficient standard star images, and also in order to take advantage of as many illuminated pixels as possible, we did not repeat the above analysis for the WAC, but instead used November 2003 approach images of Saturn. Photometry was performed for all available filter combinations, and the resulting disk-and-ring-integrated fluxes were plotted as a function of wavelength for both the NAC and WAC. From this, a quantum efficiency correction was derived analogous to that described earlier for the NAC. No filter-specific correction factors have been calculated yet, as was done for the NAC, and therefore no residual sensitivity offsets have yet been computed. Because of this, and because the WAC sensitivity correction is tied to the accuracy of the NAC analysis, the resultant WAC  $\omega_0$  factors exhibit varying uncertainties on the order of 15–25%, depending on the filter combination.

Tables XIV and XV give the  $\omega_0$  factors for the most common NAC and WAC filters and filter combinations.

### Acknowledgments

A great many people over the last 13.5 years have contributed to the success of the Cassini Imaging Science experiment. It would be an impossible task to name every one. Special thanks go to the engineers at JPL with whom the Imaging Team had the pleasure of working in designing and developing the cameras in the pre-launch years: notable among them are Tom Livermore, William Harris, Cindy Kahn, Len Snyder, and Lloyd Adams. We also thank the scientists, engineers and others across the imaging team and at JPL who have either made significant contributions in the pre-launch years to the calibration of the instrument or are currently responsible for various aspects of the operations and in-flight calibration of the ISS: John Barbara, Michael Belanger, Emma Birath, Rachel Carson, Sebastien Charnoz, Chris Clark, Tilmann Denk, Preston Dyches, Mike Evans, Joe Ferrier, Heidi Finn, Kevin Grazier, Paul Helfenstein, Pauline Helfenstein, Bob Jacobson, Dyer Lytle, Nicole Martin, Dave O'Brien, Leslie Pieri, Jon Proton, Josh Riley, Diane Sherman, Joseph Spitale, Elizabeth Turtle, Ashwin Vasavada, Daren Wilson, Charlie Avis, Amy Culver, John Diehl, James Gerhard, Tina Pavlicek, Candy Hansen, Brad Wallis, and others. We also thank Phillip Dumont at JPL whose code was used to calculate contrasts on Titan.

### References

- Allison, M., Del Genio, A. D., and Zhou, W.: 1995, *Geophys. Res. Lett.* **22**, 2957.  
 Allison, M., Godfrey, D. A., and Beebe, R. F.: 1990, *Science* **247**, 1061.  
 Allison, M.: 2000, *Planet Space Sci.* **48**, 753.  
 Banfield, D., Gierasch, P. J., Bell, M., Ustinov, E., Ingersoll, A. P., Vasavada, A. R., *et al.* : 1998, *Icarus* **135**, 230.  
 Baum, W. A., *et al.*: 1981, *Icarus* **47**, 84–96.  
 Bell, J. F., Cruikshank, D. P., and Gaffey, M. J.: 1985, *Icarus* **61**, 192.  
 Bierhaus, E. B., Chapman, C. R., Merline, W. J., Brooks, S. M., and Asphaug, E.: 2001, *Icarus* **153**, 264–276.  
 Bird, M. K., Dutta-Roy, R., Heyl, M., Allison, M., Asmar, S. W., Folkner, W. M., Preston, R. A., Atkinson, D. H. *et al.*: 2002, *Space Sci. Rev.* **104**, 613.  
 Borderies, N., Goldreich, P., and Tremaine, S.: 1982, *Nature* **299**, 209–211.  
 Borderies, N., Goldreich, P., and Tremaine, S.: 1983, *Icarus* **55**, 124–132.  
 Bosh, A. and Rivkin, A.: 1996, *Science* **272**, 518–521.  
 Brahic, A.: 1977, *Astron. Astrophys.* **54**, 895–907.  
 Brown, M. E., Bouchez, A. H., and Griffith, C. A.: 2002, *Nature* **420**, 795–797.  
 Buratti, B. J., Mosher, J. A., Nicholson, P. D., McGhee, C. A., and French, R. G.: 1998, *Icarus* **136**, 223–231.  
 Buratti, B., Mosher, J. A., and Johnson, T. V.: 1990, *Icarus* **87**, 339–357.  
 Buratti, B. J., and Veverka, J.: 1984, *Icarus* **58**, 254–264.  
 Buratti, B. J.: 1984, *Icarus* **59**, 392–405.  
 Buratti, B. J.: 1985, *Icarus* **61**, 208–217.  
 Buratti, B. J.: 1988, *Icarus* **75**, 113–126.  
 Burns, J. A., *et al.*: 1984, in: *Planetary Rings*, University of Arizona Press, Tucson, p. 200.



- Burns, J. A., Hamilton, D. P., and Showalter, M. R.: 2001, in: Grun, E., Gustafson, B. A. S., Dermott, S. F., and Fechtig, H. (eds.), *Interplanetary Dust*, Springer, Berlin, pp. 641–725.
- Burns, J. A., Kolvoord, R. A., and Hamilton, D. P.: 1989, *An Assessment of Potential Hazards to the Cassini Spacecraft from Debris Along Satellite Orbits. Cassini Mission: Saturn Orbiter Proposal Information Package*, Vol. XIII, JPL D-6464, pp. 6-1–6-23.
- Burns, J. A., Showalter, M. R., Hamilton, D. P., Nicholson, P. D., dePater, I., and Thomas, P. C.: 1999, *Science* **284**, 1146.
- Campbell, D. B., Black, G. J., Carter, L. M., and Ostro, S. J.: 2003, *Science* **302**, 431–434.
- Campbell, J. K. and Anderson, J. D.: 1989, *Astron. J.* **97**, 1485–1495.
- Carr, M. H., *et al.*: 1998, *Nature* **391**, 363–365.
- Chandrasekhar, S.: 1960, *Radiative Transfer*, Dover, New York.
- Chapman, C. R. and McKinnon, W. B.: 1986, in: *Satellites*, University of Arizona Press, Tucson, AZ, p. 492.
- Chapman, C. R., Merline, W. J., Bierhaus, B., and Brooks, S.: 1998, LPSC XXIC, abstract #1927.
- Colas, F., Frappa, E., Gomez, J., Laques, P., Lecacheux, J., and Tagger, M.: 1995, *International Astronomical Union Circular 6129*, Saturn.
- Colina, L., Bohlín, R. C., and Castelli, F.: 1996, in *Observatory Support Group Instrument Science Report (ISR CAL/SCS-008)*.
- Colombo, G., Goldreich, P., and Harris, A. W.: 1976, *Nature* **264**, 344–345.
- Cook, A. F. and Franklin, F. A.: 1970, *Icarus* **13**, 282–291.
- Cooke, M. L.: 1991, 'Saturn's Rings: Radial Variation in the Keeler Gap and C Ring Photometry', *Ph.D. Thesis*, Cornell University.
- Croft, S. K., Lunine, J. I., and Kargel, J.: 1988, *Icarus* **73**, 279–293.
- Cruikshank, D. P., Roush, T. L., Owen, T. C., Geballe, T. R., Dalle, C. M., Ore, B. N., *et al.*: 1999, *Am. Astron. Soc. Bull.* **31**, 302.
- Cruikshank, D. P.: 1981, *Icarus* **41**, 246–258.
- Cruikshank, D. P., Veverka, J., and Lebofsky, L. A.: 1984, in: *Saturn*, University of Arizona Press, Tucson, AZ, pp. 640–667.
- Cruikshank, D. P., Bell, J. F., Gaffey, M. J., Brown, R. H., Howell, R., Beerman, C., *et al.*: 1983, *Icarus* **53**, 90–104.
- Cuzzi, J. N., Lissauer, J. J., and Shu, F. H.: 1981, *Nature* **292**, 703–707.
- Cuzzi, J. N., Lissauer, J. J., Esposito, L. W., Holberg, J. B., Marouf, E. A., Tyler, G. L., *et al.* (eds.), *Planetary Rings*, University of Arizona Press, Tucson, pp. 73–199.
- Cuzzi, J. N., Durisen, R. H., Burns, J. A., and Hamill, P.: 1979, *Icarus* **38**, 54–68.
- Cuzzi, J. N. and Scargle, J. D.: 1985, *Astrophys. J.* **292**, 276–290.
- Cuzzi, J. N. and Burns, J. A.: 1988, *Icarus* **74**, 284.
- Daisaka, H. and Ida, S.: 1999, *Earth Planet Space* **51**, 1195–1213.
- Daisaka, H., Tanaka, H., and Ida, S.: 2001, *Icarus* **154**, 296–312.
- Davies, M. E. and Katayama, F. Y.: 1983a, *J. Geophys. Res.* **88**, 8729–8735.
- Davies, M. E. and Katayama, F. Y.: 1983b, *Icarus* **56**, 603–610.
- Davies, M. E., Colvin, T. R., Oberst, J., Zeitler, W., Schuster, P., Neukum, G., *et al.*: 1998, *Icarus* **135**, 372–376.
- Degawij, J., Andersson, L. E., and Zellner, B.: 1980, *Icarus* **44**, 520–540.
- Del Genio, A. D. and McGrattan, K. B.: 1990, *Icarus* **84**, 29.
- Del Genio, A. D. and Zhou, W.: 1996, *Icarus* **120**, 332–343.
- Del Genio, A. D., Zhou, W., and Eichler, T. P.: 1993, *Icarus* **101**, 1–17.
- Denk, T., Matz, K. D., Roatsch, T., Wolf, U., Wagner, R. J., Neukum, G., *et al.*: 2000, *Lunar Planet. Sci. Conf. XXXI*, abstract no. 1596 (CD-ROM).
- Dermott, S. F. and Thomas, P. C.: 1994, *Icarus* **109**, 241–257.
- Dermott, S. F. and Thomas, P. C.: 1988, *Icarus* **73**, 25–65.

- Dones, L., Cuzzi, J. N., and Showalter, M. R.: 1993, *Icarus* **105**, 184–215.
- Dones, L. and Porco, C. C.: 1989, *Bull. Amer. Astron. Soc.* **21**, 929.
- Dowling, T. E. and Ingersoll, A. P.: 1989, *J. Atmos. Sci.* **46**, 3256.
- Doyle, L. R. and Grün, E.: 1990, *Icarus* **85**, 168–190.
- Durham, W. B. and Stern, L. A.: 2001, *Ann. Rev. Earth Planet. Sci.* **29**, 295.
- Durisen, R. H., Bode, P. W., Cuzzi, J. N., Cederbloom, S. E., and Murphy, B. E.: 1992, *Icarus* **100**, 364–393.
- Dyudina, U. A., Ingersoll, A. P., Vasavada, A. R., and Ewald, S. P.: 2001, *Icarus* **160**, 336–349.
- Dyudina, U., Del Genio, A. D., Ingersoll, A. P., Porco, C. C., West, R. A., Vasavada, A. R. *et al.*: 2004, *Icarus*, in press.
- Ellsworth, K. and Schubert, G.: 1983, *Icarus* **54**, 490–510.
- Engel, S., Lunine, J. I., and Hartmann, W. K.: 1995, *Planet. Space Sci.* **43**, 1059–1066.
- Esposito, L. W., Harris, C. C., and Simmons, K. E.: 1987, *Astrophys. J. Suppl.* **63**, 749–770.
- Esposito, L. W., Cuzzi, J. N., Holberg, J. B., Marouf, E. A., Tyler, G. L., and Porco, C. C.: 1984, in: Gehrels, T., and Matthews, M. S. (eds.), *Saturn*, University of Arizona Press, Tucson, pp. 463–545.
- Esposito, L. W., O’Callaghan, M., and West, R. A.: 1983, *Icarus* **56**, 439–452.
- Estrada, P. R. and Cuzzi, J. N.: 1996, *Icarus* **122**, 251–272.
- Fanale, F. P., *et al.*: 1998, *Icarus* **139**, 179–188.
- Federico, C. and Lanciano, P.: 1983, *Ann. Geophys.* **1**, 469–476.
- Figueredo, P. H., Chuang, F. C., Rathbun, J., Kirk, R. L., and Greeley, R.: 2002, *J. Geophys. Res.* **107**, NO.E5, 10.1029 (2001JE001591).
- Flasar, F. M., Samuelson, R. E., and Conrath, B. J.: 1981, *Nature* **292**, 693–698.
- Flasar, F. M., Samuelson, R. E., and Conrath, B. J.: 1981, *Nature* **292**, 693.
- Franklin, F. A. and Colombo, G.: 1978, *Icarus* **33**, 279–287.
- Franz, O. G., Millis, R. L.: 1975, *Icarus* **24**, 433–442.
- French, R. G. and Nicholson, P. D.: 2000, *Icarus* **145**, 502–523.
- French, R. G., Cuzzi, J. N., Danos, R., Dones, L., and Lissauer, J.: 1998, in: *The Jovian System After Galileo, The Saturnian System Before Cassini-Huygens*, International Symposium, Nantes, France, 11–15 May, 1998.
- French, R. G., Dones, L., and Salo, H.: 2000, *DDA Meeting #31 of the American Astronomical Society*, abstract #08.02.
- French, R. G.: 2003, *Icarus* **162**, 143–170.
- Gault, D. E. and Sonett, C. P.: 1982, *Geol. Soc. Amer.*, Special Paper **190**, 69.
- Gierasch, P. J., Ingersoll, A. P., Banfield, D., Ewald, S. P., Helfenstein, P., Simon-Miller, A., *et al.*: 2000, *Nature* **403**, 628.
- Giese B., Oberst, J., Roatsch, T., Neukum, G., Head, J. W., and Pappalardo, R. T.: 1998, *Icarus* **135**, 303–316.
- Giese, B., Oberst, J., and Kirk, R.: 1996, *ISPRS*, Vol. 31, Part B3, Vienna, pp. 245–250.
- Gladman, B., Kavelaars, J. J., Holman, M., Nicholson, P. D., Burns, J. A., Hergenrother, C. W., *et al.*: 2001, *Nature* **412**, 163.
- Goertz, C. K. and Morfill, G.: 1983, *Icarus* **53**, 219–229.
- Goguen, J., Trippico, M., and Morrison, D.: 1983, *Bull. Am. Astron. Soc.* **15**, 855.
- Goldreich, P. and Tremaine, S. D.: 1978, *Icarus* **34**, 240–253.
- Goldreich, P., Rappaport, N., and Sicardy, B.: 1995, *Icarus* **118**, 414–417.
- Golombek, M. P. and Allison, M. L.: 1981, *Geophys. Res. Lett.* **8**, 1139.
- Gomez, D., Pietro, O., Rodriguez, M. A.: 1996, *Lunar Planet. Sci. Conf.* **27**, 433.
- Grasset, O., Sotin, C., Deschamps, F.: 2000, *Planet. Space Sci.* **48**, 617–636.
- Gresh, D. L., Rosen, P. A., Tyler, G. L., and Lissauer, J. J.: 1986, *Icarus* **68**, 481–502.

- Griffith, C. A., Owen, T., Miller, G., and Geballe, T.: 1998, in: *Paper Presented at 'The Jovian System after Galileo, The Saturnian System before Cassini (Huygens'*, Nantes, France.
- Griffith, C. A., Owen, T., Geballe, T. R., Rayner, J., and Rannou, P.: 2003, *Science* **300**, 628–630.
- Grün, E., Goertz, C. K., Morfill, G. E., and Havnes, O.: 1992, *Icarus* **99**, 191–201.
- Gunn, J. E. and Stryker, L. L.: 1983, *Ap. J. Suppl. Ser.* **52**, 121.
- Haff, P. K., Eviatar, A., and Siscoe, G. L.: 1983, *Icarus* **56**, 426–438.
- Hamilton, D. P. and Burns, J. A.: 1994, *Science* **264**, 550–553.
- Hänninen, J. and Salo, H.: 1994, *Icarus* **108**, 325–346.
- Hänninen, J. and Salo, H.: 1995, *Icarus* **117**, 435–438.
- Hansen, J. E. and Travis, L. D.: 1974, *Space Sci. Rev.* **16**, 527–610.
- Hapke, B.: 1981, *J. Geophys. Res.* **86**, 3039–3054.
- Hapke, B.: 1984, *Icarus* **59**, 41–59.
- Hapke, B.: 1986, *Icarus* **67**, 264–280.
- Harper, D. and Taylor, D. B.: 1993, *Astron. Astrophys.* **268**, 326–349.
- Hartmann, W. K.: 1984, *Icarus* **60**, 56.
- Hillier, J. K. and Squyres, S. W.: 1989, *Bull. Am. Astron. Soc.* **21**, 983.
- Horn, L. J. and Cuzzi, J. N.: 1996, *Icarus* **119**, 285–310.
- Hourdin, F., Talagrand, O., Sadourny, R., Courtin, R., Gautier, D., and McKay, C. P.: 1995, *Icarus* **117**, 358–374.
- Hubbard, *et al.*: 1993, 'The occultation of 28 Sgr by Titan', *Astron. & Astrophys.* **269**, 541–563.
- Hueso, R. and Sanchez-Lavega, A.: 2001, *Icarus* **151**, 257.
- Ingersoll, A. P., Beebe, R. F., Conrath, B. J., and Hunt, G. E.: 1984, in: Gehrels, T., and Matthews, M. S. (eds.), *Saturn*, University of Arizona Press, Tucson, p. 195.
- Ingersoll, A. P., Gierasch, P. J., Banfield, D., Vasavada, A. R., and the Galileo Imaging Team: 2000, *Nature* **403**, 630.
- Ingersoll, A. P., Vasavada, A. R., Little, B., Anger, C. D., Bolton, S. J., Alexander, C., *et al.*: 1998, *Icarus* **135**, 251.
- Ingersoll, A. P.: 1990, *Science* **248**, 308.
- Jankowski, D. G. and Squyres, S. W.: 1988, *Science* **241**, 1322–1325.
- Jarvis, K. S., Vilas, F., Larson, S. M., and Gaffey, M. J.: 2000, *Icarus* **146**, 125–132.
- Jeffreys, H.: 1947, *Monitor. Not. R. Astron. Soc.* **107**, 263–267.
- Johnson, T. V., Veeder, G. J., and Matson, D. L.: 1975, *Icarus* **24**, 428–432.
- Kahn, C. and King, W.: 1996, *Cassini/Huygens: A Mission to the Saturnian System*, SPIE, Vol. 2803, pp. 187–196.
- Kargel, J. S. and Pozio, S.: 1996, *Icarus* **119**, 385–404.
- Kargel, J. S. and Croft, S. K.: 1989, *Lunar Planet. Sci.* **XX**, 500.
- Kargel, J. S., Croft, S. K., Lunine, J. I., and Lewis, J. S.: 1991, *Icarus* **89**, 93–112.
- Kirk, R. L., Howington-Kraus, E., Redding, B., Galuszka, D., Hare, T. M., Archinal, B. A., *et al.*: 2003, *J. Geophys. Res.* **108**, E12, ROV 29-1.
- Kivelson, M. G., *et al.*: 2004, in: Bagenal, F. (ed.), *Jupiter: The Planet, Satellites, and Magnetosphere*, Cambridge University Press, Cambridge.
- Larson, S. M., Fountain, J. W., Smith, B. A., and Reitsema, H. J.: 1981, *Icarus* **47**, 288–290.
- Lemmon, M. T.: 1994, 'Properties of Titan's Haze', *Ph.D. Dissertation*, University of Arizona.
- Lewis, J. S.: 1972, *Icarus* **16**, 241–252.
- Lewis, M. C. and Stewart, G. R.: 2000, *Astron. J.* **120**, 3295–3310.
- Li, L., Ingersoll, A., Vasavada, A. R., Porco, C. C., Del Genio, A. D., and Ewald, S. P.: 2004, *Icarus*, in press.
- Lindal, G. F., Wood, G. E., Hotz, H. B., and Sweetnam, D. N.: 1983, *Icarus* **53**, 348–363.
- Lissauer, J. J.: 1985, *Icarus* **62**, 433–447.
- Lissauer, J. J., Shu, F. H., and Cuzzi, J. N.: 1981, *Nature* **292**, 707–711.

- Lissauer, J. J., Squyres, S. W., and Hartmann, W. K.: 1988, *J. Geophys. Res.* **93**, 13776.
- Little, B., Anger, C. D., Ingersoll, A. P., Vasavada, A. R., Senske, D. A., Breneman, H. H., *et al.*: 1999, *Icarus* **142**, 306.
- Lopes-Gautier, R., *et al.*: 1998, *Icarus* **140**, 243–264.
- Lorenz, R. D.: 1997, *Planet. Space Sci.* **45**, 1009–1019.
- Lucchitta, B. K.: 1980, *Icarus* **44**, 481.
- Lunine, J. I. and Soderblom, L. A.: 2002, *Space Sci. Rev.* **118**, 191–208.
- Lunine, J. I. and Lorenz, R. D.: 1996, *SPIE*, **2803**, 45–54.
- Lunine, J. I. and Stevenson, D. J.: 1985, *Ices in the Solar System*, D. Reidel Publishers, p. 741.
- Lunine, J. I., Lorenz, R. D., and Hartmann, W. K.: 1998, *Planet. Space Sci.* **46**, 1099–1107.
- Malin, M. C., Danielson, G. E., Ravine, M. A., and Soulanille, T. A.: 1992, *J. Geophys. Res.* **97**, 7699–7718.
- Marley, M. S. and Porco, C. C.: 1993, *Icarus* **106**, 508–524.
- Marouf, E. A., Tyler, G. L., and Rosen, P. A.: 1986, *Icarus* **68**, 120–166.
- McCord, T. B., Johnson, T. V., and Elias, J. H.: 1971, *Astrophys. J.* **165**, 413–424.
- McGhee, C., French, R., Dones, L., Cuzzi, J., Salo, H. J., and Danos, R.: 2004, *Icarus*, in press.
- McKinnon, W. B.: 1985, *Bull. Am. Astron. Soc.* **17**, 922.
- Melosh, H. J., Janes, D. M., Jankowski, D. G., and Squyres, S.: 1989, *Science* **245**, 194–196.
- Moore, J. M.: 1984, *Icarus* **59**, 205–220.
- Moore, J. M. and A'Hearn, J. L.: 1983, *J. Geophys. Res.* **88**, 577.
- Moore, J. M., *et al.*: 1998, *Icarus* **140**, 294.
- Moore, J. M., Horner, V. M., and Greeley, R.: 1985, *J. Geophys. Res.* **90**, 785–795.
- Moore, J. M.: 1984, *Icarus* **59**, 205–220.
- Morfill, G., Grun, E., and Johnson, T. V.: 1983, *J. Geophys. Res.* **88**, 5573–5579.
- Murray, C. D. and Dermott, S. F.: 1999, *Solar System Dynamics*, Cambridge University Press, Cambridge.
- Murray, C. D. and Gordon, M., Giulatti-Winter, S. M.: 1997, *Icarus* **129**, 304.
- Namouni, F. and Porco, C.: 2002, *B.A.A.S.* **34**, 884.
- Namouni, F. and Porco, C.: 2002, *Nature* **417**, 45–47.
- Neukum, G., Wagner, R., Wolf, U., Ivanov, B. A., Head III, J. W., Pappalardo, R. T., *et al.*: 1998, *Lunar Planet. Sci. Conf. XXIX*, abstract no. 1742 (CD-ROM).
- Neukum, G.: 1985, *Adv. Space Res.* **5**, 107–116.
- Neukum, G.: 1997, Barbieri, in: C., Rahe, J. H., and Johnson, T. V. (eds.), *Proceedings of the Conference on The Three Galileos: The Man, The Spacecraft, The Telescope*, Padova, Italy, January 7–10, 1997, Kluwer Academic Publishers, Dordrecht, pp. 201–212.
- Nicholson, P. D. and Porco, C. C.: 1988, *J. Geophys. Res.* **93**, 10,209–10,224.
- Nicholson, P. D., Campbell, D. B., French, R. G., Black, G. J., Margot, J. L., Nolan, M.: 2000, *B.A.A.S.* **321**, 2086.
- Nicholson, P. D. *et al.*: 1996, *Science* **272**, 509–515.
- Nicholson, P. D., Hamilton, D. P., Matthews, K., and Yoder, C. F.: 1992, *Icarus* **100**, 464–484.
- Nicholson, P. D., Showalter, M. R., Dones, L., French, R. G., Larson, S. M., Lissauer, J. J., *et al.*: 1996, *Science* **272**, 509.
- Nimmo, F., Pappalardo, R. T., and Giese, B.: 2003, *Icarus* **166**, 21–32.
- Noland, M., Veverka, V., Morrison, D., Cruikshank, D. P., Lazarewicz, A. R., Morrison, N. D., *et al.*: 1974, *Icarus* **23**, 334–354.
- Oberst J., Whlisch, M., Cook, A. C., Roatsch, T., and Jaumann, R.: 1997, *EOS Trans. Am. Geophys. Union* **445**, 450.
- Oberst, J., Schreiner, J. B., Giese, B., Neukum, G., Head, J. W., Pappalardo, R., *et al.*: 1999, *Icarus* **140**, 283–293.

- Oberst, J., Giese, B., Schuster, P., Schreiner, B., Zeitler, W., Wagner, R., Roatsch, T., and Neukum, G.: 1998, in: *Euroconference on The Jovian System After Galileo–The Saturnian System Before Cassini*, May 11–15, Nantes, France, pp. 72–73.
- Oberst, J., Zeitler, W., and Parker, T.: 1999, *EOS Trans. Am. Geophys. Union* **80** (46), 549–553.
- Oberst, J. and Schuster, P.: 2004, *J. Geophys. Res.* **109**, 4003.
- Ockert, M. E., Cuzzi, J. N., Porco, C. C., and Johnson, T. V.: 1987, *J. Geophys. Res.* **92**, 14,969–14,978.
- Owen, T. C., Cruickshank, D. P., Dalle Ore, C. M., Geballe, T. R., Roush, T. L., DeBergh, C.D., *et al.*: 2001, *Icarus* **149**, 160–172.
- Pang, K., Voge, C. C., Rhoads, J. W., and Ajello, J. M.: 1984, *J. Geophys. Res.* **89**, 9459–9470.
- Parmentier, E. M., Squyres, S. W., Head, J. W., and Allison, M. L.: 1982, *Nature* **295**, 290.
- Passey, Q. R.: 1983, *Icarus* **53**, 105.
- Pechmann, J. B. and Ingersoll, A. P.: 1984, *J. Atmos. Sci.* **41**, 3290–3313.
- Plescia, J. B. and Boyce, J. M.: 1985, *J. Geophys. Res.* **90**, 2029.
- Plescia, J. B.: 1987, *Nature* **327**, 201.
- Plescia, J. B.: 1983, *Icarus* **56**, 255–277.
- Polvani, L. M., Wisdom, J., De Jong, E., and Ingersoll, A. P.: 1990, *Science* **249**, 1393.
- Porco, C. C.: 1990, *Adv. Space Res.* **10**, 221–229.
- Porco, C. C. and Danielson, G. E.: 1982, *Astron. J.* **87**, 826–833.
- Porco, C. C. and Danielson, G. E.: 1984, in: Brahic, A. (ed.), *Proceedings of IAU Colloquium #75, Planetary Rings*, CNES, Toulouse, France, p. 219.
- Porco, C. C. and Nicholson, P. D.: 1987, *Icarus* **72**, 437–467.
- Porco, C. C., Pantazopoulou, M., Throop, H., Richardson, D., Quinn, T., Kehoe, T. J. J., *et al.*: 2005, ‘Light Scattering in Saturn’s Rings: Basic Formulation, Ring Thickness and the A Ring Azimuthal Asymmetry’, manuscript in preparation.
- Porco, C. C., Throop, H. B., and Richardson, D. C.: 2001, in: *DPS Meeting #33 of the American Astronomical Society*, abstract #29.01.
- Porco, C. C., Pantazopoulou, M. J., Richardson, D., Quinn, T., and Kehoe, T. J. J.: 1999, in: *DPS Meeting #31 of the American Astronomical Society*, abstract #44.03.
- Porco, C., Nicholson, P. D., Borderies, N. B., Danielson, G. E., Goldreich, P., Holberg, J. B., *et al.*: 1984a, *Icarus* **60**, 1.
- Porco, C., Danielson, G. E., Goldreich, P., Holberg, J. B., and Lane, A. L.: 1984b, *Icarus* **60**, 17–28 (erratum in *Icarus* **61**, 173).
- Porco, C. C. *et al.*: 2003, *Science* **299**, 1469.
- Porco, C. C. and Goldreich, P.: 1987, *Astron. J.* **93**, 724–729.
- Porco, C. C.: 1991, *Science* **253**, 995.
- Porco, C. C., Cuzzi, J. N., Ockert, M. E., and Terrile, R. J.: 1987, *Icarus* **72**, 69–78.
- Prockter, L. M. and Pappalardo, R. T.: 2003, *Lunar Planet. Sci. Conf.* **34**, abstract 1620.
- Poulet, F., Cuzzi, J. N., French, R. G., and Dones, L.: 2002, *Icarus* **158**, 224.
- Prinn, R. G. and Fegley, B.: 1981, *Astrophys. J.* **249**, 308–317.
- Rappaport, N.: 1998, *Icarus* **132**, 36–42.
- Raulin, F. and Owen, T.: 2002, *Space Sci. Rev.* **104**, 377–394.
- Rebiai, R., Scurlock, R. G., and Rest, A. J.: 1984, *Adv. Cryogen. Eng.* **29**, 1005.
- Reynolds, R. T. and Cassen, P. M.: 1979, *Geophys. Res. Lett.* **6**, 121.
- Richardson, D. C.: 1994, *Monitor. Not. R. Astron. Soc.* **269**, 493–511.
- Richardson, D. C.: 1995, *Icarus* **115**, 320.
- Richardson, D. C., Quinn, T., Stadel, J., and Lake, G.: 2000, *Icarus* **143**, 45–59.
- Richardson, J., Lorenz, R. D., and McEwen, A. S.: 2004, *Icarus* **170**, 113–124.

- Roddier, C., Roddier, F., Graves, J. E., and Northcutt, M. J.: 1998, *Icarus* **136**, 50.
- Roe, H. G., De Pater, I., Macintosh, B. A., and McKay, C. P.: 2002, *Astrophys. J.* **581**, 1399–1406.
- Rosen, P. A., Tyler, G. L., Marouf, E. A., and Lissauer, J. J.: 1991, *Icarus* **93**, 25–44.
- Ross, M. N. and Schubert, G.: 1988, *Icarus* **75**, 479–484.
- Ross, M. N. and Schubert, G.: 1989, *Icarus* **78**, 90–101.
- Rossow, W. B. and Williams, G. P.: 1979, *J. Atmos. Sci.* **36**, 377–389.
- Safronov, V. S. and Ruskol, E. L.: 1977, *Planetary Satellites*, University of Tucson Press, Acizona/Tucson pp. 505–512.
- Safronov, V. S.: 1972, 'Evolution of the protoplanetary cloud and formation of the Earth and planets', NASA TT-F-677.
- Safronov, V. S., Perchernikova, G. V., Ruskol, E. L., and Vitjazev, A. V.: 1986, *Satellites*, University of Arizona Press, Tucson, pp. 89–116.
- Sagan, C. and Dermott, S. F.: 1982, *Nature* **300**, 731.
- Sagan, C. and Thompson, W. R.: 1984, *Icarus* **59**, 133.
- Salo, H.: 1992, *Nature* **359**, 619–621.
- Salo, H.: 1995, *Icarus* **117**, 287–312.
- Salo, H., Schmidt, J., and Spahn, F.: 2001, *Icarus* **153**, 295–315.
- Salo, H., Karjalainen, R., and French, R. G.: 2000, in: *DDA Meeting #31 of the American Astronomical Society*, abstract #08.01.
- Sanchez-Lavega, A., Colas, F., Lecacheux, J., Laques, P., Miyazaki, I., and Parker, D.: 1991, *Nature* **353**, 397.
- Sanchez-Lavega, A., *et al.*: 1996, *Science* **271**, 631.
- Sanchez-Lavega, A., Lecacheux, J., Colas, F., Rojas, J. F., and Gomez, J. M.: 1999, *Planet. Space Sci.* **47**, 1277.
- Sanchez-Lavega, A., Perez-Hoyos, F., Rojas, J. F., Hueso, R., and French, R. G.: 2003, *Nature* **423**, 623.
- Schenk, P. M. and Moore, J. M.: 1995, *J. Geophys. Res.* **100**, 19009–19022.
- Schenk, P. M.: 2002, *Nature* **417**, 419–421.
- Schenk, P. M.: 1989, *J. Geophys. Res.* **94**, 3813–3832.
- Schenk, P. M.: 1991, *J. Geophys. Res.* **96**, 1887–1906.
- Schenk, P. M., Chapman, C., Zahnle, K., and Moore, J.: 2004, in: Bagenal, F., Downing, T. E., and McKinnon, W. B. (eds.), *Jupiter: The Planet, Satellites, and Magnetosphere*, Cambridge University Press, Cambridge (chapter 18).
- Schenk, P. M., Wilson, R. R., and Davies, A. G.: 2004, *Icarus* **169**, 98–110.
- Schmidt, J., Salo, H., Spahn, F., and Petzschmann, O.: 2001, *Icarus* **153**, 316–331.
- Schmit, U. and Tscharnuter, W. M.: 1999, *Icarus* **138**, 173–187.
- Schubert, G., Anderson, J. D., Spohn, T., and McKinnon, W. B.: 2004, in: Bagenal, F. (ed.), *Jupiter: The Planet, Satellites, and Magnetosphere*, Cambridge University Press, Cambridge (chapter 13).
- Schubert, G., Stevenson, D. J., and Ellsworth, K.: 1981, *Icarus* **47**, 46.
- Shoemaker, E. M.: 1960, *International Geological Conference XXI*, Norden, vol. 21, p. 418.
- Showalter, M. R., Cuzzi, J. N., Marouf, E. A., and Esposito, L. W.: 1986, *Icarus* **66**, 297–323.
- Showalter, M. R.: 1991, *Nature* **351**, 709–713.
- Showalter, M. R. and Cuzzi, J. N.: 1993, *Icarus* **103**, 124.
- Showalter, M. R., Cuzzi, J. N., and Larson, S.: 1991, *Icarus* **94**, 451.
- Showalter, M. R.: 1996, *Icarus* **124**, 667.
- Showalter, M. R.: 1998, *Science* **282**, 1099.
- Shu, F. H.: 1984, in: Greenberg, R., and Brahic, A. (eds.), *Planetary Rings*, University of Arizona Press, Tucson, pp. 513–561.
- Shu, F. H., Cuzzi, J. N., and Lissauer, J. J.: 1983, *Icarus* **53**, 185–206.



- Sicardy, B., Brahic, A., Ferrari, C., Gautier, D., Lecacheux, J., Lellouch, E., *et al.*: 1990, *Nature* **343**, 350–353.
- Simonelli, D. P., Kay, J., Adinolfi, D., Veverka, J., Thomas, P. C., and Helfenstein, P.: 2000, *Icarus* **138**, 249–255.
- Smith, B. A., Soderblom, L. A., Johnson, T. V., Ingersoll, A. P., Collins, S. A., Shoemaker, E. M., *et al.*: 1979a, *Science* **204**, 951.
- Smith, B. A., Soderblom, L. A., Beebe, R., Boyce, J., Briggs, G., Carr, M., *et al.*: 1979b, *Science* **206**, 927.
- Smith, B. A., *et al.*: 1981, *Science* **212**, 163–191.
- Smith, B. A., *et al.*: 1982, *Science* **215**, 504–537.
- Smith, B. A., *et al.*: 1986, *Science* **233**, 43.
- Smith, B. A., *et al.*: 1990, *Science* **246**, 1422.
- Smith, P. H., Lemmon, M. T., Lorenz, R. D., Sromovsky, L. A., Caldwell, J. J., and Allison, M. D.: 1996, *Icarus* **119**, 336.
- Soter, S.: 1974, Proceedings, IAU Planetary Satellites Conf., Cornell University.
- Squyres, S. W. and Croft, S. K.: 1986, *Satellites*, University of Arizona Press, Tucson, pp. 293–341.
- Squyres, S. W. and Sagan, C.: 1983, *Nature* **303**, 782–785.
- Squyres, S. W., Buratti, B., Veverka, J., and Sagan, C.: 1984, *Icarus* **59**, 426–435.
- Squyres, S. W., Reynolds, R. T., Summers, A. L., and Shung, F.: 1988, *J. Geophys. Res.* **93**, 8779–8794.
- Squyres, S. W., Reynolds, R. T., Cassen, P. M., and Peale, S. J.: 1983, *Icarus* **53**, 319–331.
- Squyres, S. W.: 1980, *Geophys. Res. Lett.* **7**, 593–596.
- Stevenson, D. J.: 1992, *Proceedings of the Symposium on Titan*, Toulouse, France, September 9–12, 1991, ESA SP-338, ESA Publication Division, ESTEC, Noordwijk, The Netherlands, pp. 29–33.
- Stevenson, D. J.: 1982, *Nature* **298**, 142–144.
- Strom, R. G.: 1981, *Lunar Planet. Sci. XII, Suppl. A.*, **7**.
- Tholen, D. J. and Zellner, B.: 1983, *Icarus* **53**, 341–347.
- Thomas, P., Veverka, J., Morrison, D., Davies, M., and Johnson, T. V.: 1983, *J. Geophys. Res.* **88**, 8736–8742.
- Thomas, P. C. and Dermott, S. F.: 1991, *Icarus* **94**, 391–398.
- Thomas, P. C., Black, G. J., and Nicholson, P. D.: 1995, *Icarus* **117**, 128–148.
- Thomas, P. G.: 1988, *Icarus* **74**, 554–567.
- Thomas, P. J. and Squyres, S. W.: 1988, *J. Geophys. Res.* **93**, 14919–14932.
- Thompson, W. T., Lumme, K., Irvine, W. M., Baum, W. A., and Esposito, L. W.: 1981, *Icarus* **46**, 187–200.
- Throop, H. B. and Esposito, L. W.: 1998, *Icarus* **131**, 152.
- Throop, H. B., Porco, C. C., West, R. A., Burns, J. A., Showalter, M. R., and Nicholson, P. D.: 2004, *Icarus*, in press.
- Tobiska, W. K., Woods, T., Eparvier, F., Viereck, R., Floyd, L., Bouwer, D., *et al.*: 2000, *J. Atm. Solar Terr. Phys.* **62** (14), 1233–1250.
- Tokono, T. and Neubauer, F. M.: 2002, *Icarus* **158**, 499–515.
- Tomasko, M. G. and 13 others: 2002, *Space Sci. Rev.* **104**, 469–551.
- Toon, O. B., McKay, C. P., Courtin, R., and Ackerman, T. P.: 1988, *Icarus* **75**, 255.
- Trauger, J. T., Clarke, J. T., Ballester, G. E., Evans, R. W., Burrows, C. J., Crisp, D., *et al.*: 1998, *J. Geophys. Res.* **103**, 20,237.
- Tremaine S.: 2002, *Astron. J.* **125**, 894.
- Turtle, E. P. and Pierazzo, E.: 2001, *Science* **294**, 1326–1328.
- Turtle, E., *et al.*: 1990, *B.A.A.S.* **22**, 1041.
- Turtle, E. *et al.*: 1991, *B.A.A.S.* **23**, 1179.

- Vasavada, A. R., Bouchez, A. H., Ingersoll, A. P., Little, B., Anger, C. D., and the Galileo SSI Team: 1999, *J. Geophys. Res.* **104**, 27,133.
- Vasavada, A. R., Ingersoll, A. P., Banfield, D., Bell, M., Gierasch, P. J., Belton, M. J. S., *et al.*: 1998, *Icarus* **135**, 265.
- Verbiscer, A. and Veverka, J.: 1989, *Icarus* **82**, 336–353.
- Wagner, J. K., Hapke, B. W., and Wells, E. N.: 1987, *Icarus* **69**, 14–28.
- Wagner, R. and Neukum, G.: 1996, *Ann. Geophys.* **14** (Suppl. III), C794.
- Ward, W. R.: 1981, *Geophys. Res. Lett.* **8**, 641–643.
- West, R. A. and Smith, P. H.: 1991, *Icarus* **90**, 330–333.
- West, R. A., Friedson, A. J., and Appleby, J. F.: 1992, *Icarus* **100**, 245–259.
- Wilson, P. and Sagan, C.: 1995, *J. Geophys. Res.* **100**, 7531–7537.
- Wisdom, J. and Tremaine, S.: 1988, *Astron. J.* **95**, 925–940.
- Wisdom, J.: 2004, *Astron. J.* **128**, 484–491.
- Yoder, C. F.: 1979, *Nature* **279**, 767–770.
- Yoder, C. F., Colombo, G., Synnott, S. P., and Yoder, K. A.: 1984, *Icarus* **53**, 431.
- Young, R. E., Walterscheid, R. L., Schubert, G., Seiff, A., Linkin, V. M., and Lipatov, A. N.: 1987, *J. Atmos. Sci.* **44**, 2628–2639.
- Yung, Y. L., Allen, M., and Pinto, J. P.: 1984, *Astrophys. J. Suppl. Ser.* **55**, 465.
- Zahnle, K., Dones, L., and Levison, H. F.: 1998, *Icarus* **136**, 202–222.
- Zahnle, L., Schenk, P., Levison, H., and Dones, L.: 2003, *Icarus* **163**, 263–2889.
- Zebker, H. A., Marouf, E. A., and Tyler, G. L.: 1985, *Icarus* **64**, 531–548.
- Zeitler W. and Oberst, J.: 1998, *J. Geophys. Res.* **104**, 8935–8942.